DISSERTATION

SYNTHESIS OF FLUOROMODIFIED CARBON-RICH ELECTRON ACCEPTORS AND

EXPLORATION OF THEIR STRUCTURAL, ELECTRONIC, AND DEVICE PROPERTIES

Submitted by

Nicholas J. DeWeerd

Department of Chemistry

Doctoral Committee:

Advisor: Steven H. Strauss

Matthew P. Shores
Chris J. Ackerson
Martin J. McCullagh
Martin P. Gelfand

ABSTRACT

SYNTHESIS OF FLUOROMODIFIED CARBON-RICH ELECTRON ACCEPTORS AND

EXPLORATION OF THEIR STRUCTURAL, ELECTRONIC, AND DEVICE PROPERTIES

The electronic and structural characterization of fluoro-modified carbon-rich compounds is critical to the successful implementation of these materials by physicists, biochemists, materials scientists, medicinal chemists, and most significantly for this work, organic electronics chemists. By adding powerful electron-withdrawing groups, the electron acceptor and solid-state structural properties of carbon rich substrates such as polyaromatic hydrocarbons (PAHs) and fullerenes can be improved, making these derivatives attractive semiconductor materials for organic electronics applications. This work will discuss research which has focused on expanding the library of electron acceptor compounds, elucidating the electronic and structural properties of those compounds, and exploring their physicochemical properties, focusing on properties that are important for the performance of organic electronic devices. This was accomplished by exploring reaction conditions which had not been previously reported at pressures and temperatures exceeding the operational limits of conventional reactors, developing purification methods that allow for chromatographic separation of constitutional isomers, and structural characterization of those purified materials by mass spectrometry, NMR, and most importantly X-ray crystallography.

As a complement to this research, the stability of organic electronic active layers was studied to better understand how organic semiconductor active layer's degradation affects device performance over time and to better inform which active layer material properties should be pursued. Based on those findings and literature precedent, one family of compounds, C_{60} and C_{70} fauxhawk fullerenes, found to have favorable characteristics were then utilized in OFET devices as n-type semiconductors resulting in record-setting charge carrier mobilities.

ACKNOWLEDGEMENTS

During my pursuit of this exceedingly elusive and monumentally time-consuming dissertation there are a number of agents in my life I would like to thank for their efforts and support to heave me over this finish line.

First, I would like to thank my family for their continued understanding for my more than decade long career in higher education. "If you liked college just do it again!" they said. "College 2.0!" they said. In this case the "they" is me and the people listening are my exasperated family who simply smile and nod along. You did not complain as I spent holidays working on my computer for hours on end or missing family gatherings entirely to work or run-off early to go take measurements in Chicago. You did not interrupt me as I attempted to excitedly tell you, in as long-winded a version as possible, whatever piece of scientific minutia was the focus of my attention or as I endlessly lamented my continued internment. For these reasons and many more I could never thank you enough in words, but I intend to try by my actions in whatever capacity I can for the rest of my life.

Second, I would like to revisit the first, but give a special shout out to my brother. Jacob, as we have grown older and moved further apart geographically, me in a mountainous paradise and you in America's sweaty armpit, I feel as though we have grown closer together than ever before. I will always remember you as the smurf voiced kid afraid of me sleeping with my door closed because if a murderer entered the house you wanted him to come for me first, (path of least resistance obviously). But now, on top of that image of you is a newer shinier version. A kid/man human hybrid, confident in what he wants in life and unapologetic as he fearlessly and relentlessly pursues it. I hope you have enjoyed the bragging rights you have gained supporting your hopeless older brother because from here on out I will be the one you call when you need help and not the other way around…at least…until you become a multimillionaire by hook or by crook in which case I'm quitting my job and coming to collect for damages to my hand after the Dutch fry incident.

Third, I would like to give special recognition to Zach and Jenn (two n's just this once). You both are like family to me. Sometimes during our collective 12 years of living together you both frustrated me to no end but if anything, that just shows what a close family we really became. When moving to Colorado I wanted to experience new things and say yes when before I would have said no. You both pushed me and still push me to say yes when I want to say no. While it is possible I might have graduated sooner if I had said no a little more often I would not have had nearly as much fun or grown so much as a person. It is well established that when I moved to Colorado I was all but insufferable. If I am any less so now, I have you both in part to thank for it. Thank you for your continued and unending support as I finally catch up to you both in this academic marathon.

Fourth, I would like to thank my advisors, Steve and Olga. I have learned so much from both of you and suspect I will never stop learning from you even as I transcend my student status to be a "scientist". After all, there are something like 50 more crystal structures to be published! Thank you for putting up with my antics. I hope on balance you were able to smile and laugh more than frown in disapproval at my unending shenanigans.

Fifth, I would like to thank my fellow lab mates: Brian, Colin, Kerry, and Matthew. The degree of collaboration and cooperation that we have maintained over the half decade of working together is a model for what any lab should strive for. Between the five of us (I am excluding the "seniors" for simplicity, but they also deserve a lot of credit) we have co-authored seven published papers and will publish a minimum of six more by my count which I see as a testament to our productive, collaborative work environment. Working with you has been one of the greatest pleasures of my life and I hope to be half so lucky to have future co-workers I can rely on as much as you. Kerry in particular has earned a considerable amount of credit for her continued efforts to convert my erratic ramblings into coherent scientific writing and advice on organization and forward progress war-time strategy…always be triaging. I owe each of you a debt of gratitude I am unlikely to be able to repay but if you ever need anything in the future, I would be honored to offer whatever aid I can.

TABLE OF CONTENTS

LIST OF TABLES

LIST OF FIGURES

LIST OF ACRYONYMS AND ABBREVIATIONS

$\odot$ centroid of a molecule or molecular fragment (for SC-XRD intermolecular distances)

anhyd   anhydrous

ANTH   anthracene; $C_{14}H_{10}$ (see drawing on page I-5)

Bn_F perfluorobenzyl; $CF_2C_6F_5$

$C_{70}FHF$ C_{70} fauxhawk fullerene; $C_{70}(cyclo\text{-}CF_2(2\text{-}C_6F_4))$

conc   concentration

CORO   coronene; $C_{24}H_{12}$ (see drawing on page I-5)

CT   charge transfer

CV   cyclic voltammetry

DCE   1,2-dichloroethane; $1,2\text{-}C_2H_4Cl_2$

DCM   dichloromethane; CH_2Cl_2

DFT   density functional theory

EA   gas-phase electron affinity

equiv   equivalent or equivalents

FHF C_{60} fauxhawk fullerene; $C_{60}(cyclo\text{-}CF_2(2\text{-}C_6F_4))$

GTGS   gradient-temperature gas-solid (reactor)

H_2CORO dihydrocoronene; $C_{24}H_{14}$

HEP   heptanes (mixture of isomers; HPLC eluent)

HEX   hexanes (mixture of isomers; HPLC eluent)

HOMO   highest occupied molecular orbital

HPLC   high-pressure liquid chromatography

IE   gas-phase ionization energy

LSP   least squares plane (in X-ray structures)

LUMO   lowest unoccupied molecular orbital

MeCN   acetonitrile

MTR   metal tube reactor

NI-ESI-MS	negative ion electrosprary ionization mass spectrometry (or spectrum)
NMR	nuclear magnetic resonance
oDCB	$ortho$-dichlorobenzene; 1,2-dichlorobenzene; $1,2-C_6H_4Cl_2$
OFET	organic field-effect transitor
OLED	organic light-emitting diode
OOPs	perpendicular out-of-plane displacements of atoms from a least squares plane
OPV	organic photovoltaic
OSC	organic semiconductor
PAH	polycyclic aromatic hydrocarbon
PERY	perylene; $C_{20}H_{12}$ (see drawing on page I-5)
PFF	C_{60} partially fluorinated fauxhawk fullerene; $C_{60}(cyclo\text{-}CH_2(2\text{-}C_6F_4))$
PNTZ	phenothiazine; $C_{12}H_9NS$ (see drawing on page I-5)
PYRN	pyrene; $C_{16}H_{10}$ (see drawing on page I-5)
R_F	perfluoroalkyl
RT	room temperature
SC-XRD	single-crystal X-ray diffraction
TMF	trifluoromethylfullerene; $C_{60}(CF_3)_n$ or $C_{70}(CF_3)_n$
tol	toluene (HPLC eluent)
s.u.	standard uncertainty (for distances in angles in X-ray structures)
UV-vis	ultraviolet-visible (spectroscopy)

INTRODUCTION: AUTHOR'S CONTRIBUTIONS AND MOTIVATION

The overall focus of the author's dissertation research was a class of organic molecules with electron-withdrawing CF_3, CF_2SF_5, $CF_2CF_2SF_5$, $cyclo$-$CH_2(2$-$C_6F_4)$, $cyclo$-$CF_2(2$-$C_6F_4)$, or $cyclo$-C_2F_4 groups or F atoms. The research described in this dissertation includes the synthesis and/or purification and/or physicochemical characterization of polycyclic aromatic hydrocarbons (PAHs), hetero-PAHs, and fullerenes with one or more of these substituents. Drawings of the PAHs, hetero-PAHs, and fullerene substrates that were studied are shown in the figure on page 5. The abbreviations and acronyms used throughout this dissertation are listed on pages 6 and 7.

Chapter 1 describes the design, construction, and use of a high-pressure/high-temperature metal reactor to add CF_3 groups to, and/or substitute H atoms with CF_3 groups on, PAHs, hetero-PAHs, and fullerenes. The substrates studied were anthracene (ANTH), coronene (CORO), perylenetetracarboxylic dianhydride (PTCDA), C_{60}, and C_{70}. The reactions produced mixtures of compounds that were identified spectroscopically. Some of the products had been previously prepared using glass reactors and were previously reported. Some of the products are new compounds that had not been previously reported. This work has been published in a paper with the author of this dissertation as the second of two graduate student co-authors.[1]

Chapter 2 describes a comparison of three different reactors used to prepare $CORO(CF_3)_n$ and $H_2CORO(CF_3)_{7,8}$ derivatives, all of which are new compounds. In addition to $CORO(CF_3)_n$ compounds, four dihydrocoronene derivatives ($H_2CORO(CF_3)_{7,8}$) were prepared, purified by high-pressure liquid chromatography (HPLC), and characterized by cyclic voltammetry (CV), low-temperature gas-phase photoelectron spectroscopy (PES) to determine their electron affinities (EAs; these measurements were made by collaborator Dr. Xue-Bin Wang and graduate student Kerry C. Rippy, but were interpreted by the author by comparison with the published EAs of perylene (PERY) derivatives with 4–7 CF_3 groups, and by single-crystal X-ray diffraction (SC-

XRD). This chapter also includes DFT calculations performed by collaborator Dr. Alexey A. Popov, and interpreted by the author, to determine the most stable isomers of $CORO(CF_3)_n$ derivatives. A manuscript describing the research in Chapter 2, with the author of this dissertation as first author, is in preparation.

Chapter 3 describes syntheses of new C_{60} derivatives with CF_2SF_5 and $CF_2CF_2SF_5$ substituents. The syntheses were performed at Clemson University in consultation with the author, and the reaction mixtures were characterized by the author using HPLC, negative-ion electrospray ionization mass spectrometry (NI-ESI-MS) and ^{19}F NMR spectroscopy. One new compound in particular, $1,7-C_{60}(CF_2CF_2SF_5)_2$, was purified and characterized by NI-ESI-MS and ^{19}F NMR and ultraviolet-visible (UV-vis) spectroscopy. These are the first fullerene derivatives with CF_2SF_5 or $CF_2CF_2SF_5$ substituents. This work has been published in a paper with the author of this dissertation as the second of two graduate student co-authors.[2] Chapter 3 also includes a study to improve the yield of the previously prepared[3] $1,9-C_{60}(cyclo-CF_2(2-C_6F_4))$, known as the faux-hawk fullerene (FHF), and to prepare and characterize three isomers of $C_{70}(cyclo-CF_2(2-C_6F_4))$ (C_{70}FHF). One isomer was characterized by CV, and one by SC-XRD. Part of this work, the improved synthesis of FHF, has been published in a paper with the author of this dissertation as the second of two graduate student co-authors.[4] Finally, Chapter 3 also includes the synthesis and characterization of a partially-fluorinated FHF, $1,9-C_{60}(cyclo-CH_2(2-C_6F_4))$, and a manuscript describing this part of the work is in preparation.

Chapter 4 describes several studies to test the stability of organic photovoltaic (OPV) and organic field-effect transistor (OFET) thin films containing various fullerenes, including FHF and 70-FHF. The author worked in collaboration with scientists at Kent State University and Pacific Northwest National Laboratory for some of the experiments. The author performed other experiments himself when he visited NEXT Energy Technologies during the summer of 2017. Part of this work has been published in a paper with the author of this dissertation as the second of two graduate student co-authors.[4] Other manuscripts are in preparation.

Chapter 5 describes the author's SC-XRD study of charge-transfer (CT) co-crystals. The structure of a 1/2 donor/acceptor CT complex consisting of pyrene (PYRN) as the donor and 2,3,6,7,9,10-ANTH(CF$_3$)$_6$ (ANTH-6-1) as the acceptor revealed a previously unappreciated and unpublished feature of ANTH and pentacene (PENT) structures with perfluoroalkyl (R$_F$) groups on the central C(sp^2) atoms (positions 9 and 10 in ANTH and positions 6 and 13 in PENT): bending of the aromatic core away from planarity is correlated with the conformations of the central CF$_3$ or R$_F$ groups. This led to a DFT study by collaborator Popov, which when interpreted by the author revealed the counterintuitive predictions that bending of the aromatic core of 9,10-ANTH(CF$_3$)$_2$ actually lowers its energy relative to the planar molecule and increases its *EA*. This work has been published in a paper with the author of this dissertation as first author.[5] Additional PAH/PAH(CF$_3$)$_n$ CT co-crystal structures were refined by the author and published in a paper with the author as the fourth of four graduate student co-authors, and two new PYRN/PAH(CF$_3$)$_n$ CT co-crystal structures determined entirely by the author, and not yet been published, are included in this dissertation (PAH = PYRN and phenanthrene (PHEN)). Chapter 5 also includes the first CT co-crystal structures with the strong electron acceptor C$_{60}$F$_{18}$, viz. CORO/(C$_{60}$F$_{18}$)$_2$, PERY/C$_{60}$F$_{18}$, and (PYRN)$_2$/C$_{60}$F$_{18}$. A manuscript describing this work with the author of this dissertation as first author is in preparation.

Chapter 6 describes new phenothiazine (PNTZ) compounds with multiple CF$_3$ substituents. Using product mixtures from high-temperature reactions of PNTZ and CF$_3$I carried out by former graduate student Igor V. Kuvychko, the author isolated and characterized eleven new PNTZ(CF$_3$)$_n$ compounds with n = 3, 4, and 5 by HPLC, ^{1}H and ^{19}F NMR spectroscopy, *EA* measurements (by collaborator Dr. Xue-Bin Wang), and SC-XRD structures of two PNTZ(CF$_3$)$_4$ isomers. A manuscript describing this work with the author of this dissertation as first author is in preparation.

Throughout this dissertation, single-crystal X-ray diffraction is arguably the most important experimental technique used by the author. Chapters 2, 3, and 5 include many new SC-XRD structures, and the results of SC-XRD structure determinations are discussed in Chapter 4. The

motivation for the author to use X-ray diffraction so extensively was that it has been an invaluable tool, if not the most valuable tool, for studying solid-state phenomena since the first X-ray structures were reported in 1913, more than 100 years ago.[6,7] Research involving X-ray diffraction led to 24 Nobel prizes in the first 100 years.[8,9] The first X-ray structures of an organic molecule was a PAH, anthracene.[10,11] The many structures of organic compounds that followed led to unambiguous evidence for some of the most important concepts in chemistry, including the covalent bond, hydrogen bonding, and resonance.[12] It has been said that Linus Pauling's influential book *The Nature of the Chemical Bond*, published in 1939,[12] "introduced chemists to... X-ray crystallography as an important tool for determining structure. Before the book's publication, few chemists had taken notice of the arcane art of crystallography; after its publication no chemist could ignore its value."[13] It has led to innumerable discoveries not only in chemistry but in the fields of geoscience,[14] pharmaceuticals,[15,16] and biology.[17,18] However, it must be said that not every compound the author wished to study could be studied by crystallography: growing diffraction quality single crystals is never a certainty.[19,20] That is why the author also relied on the second most important tool for studying chemical compounds, NMR spectroscopy.[21]
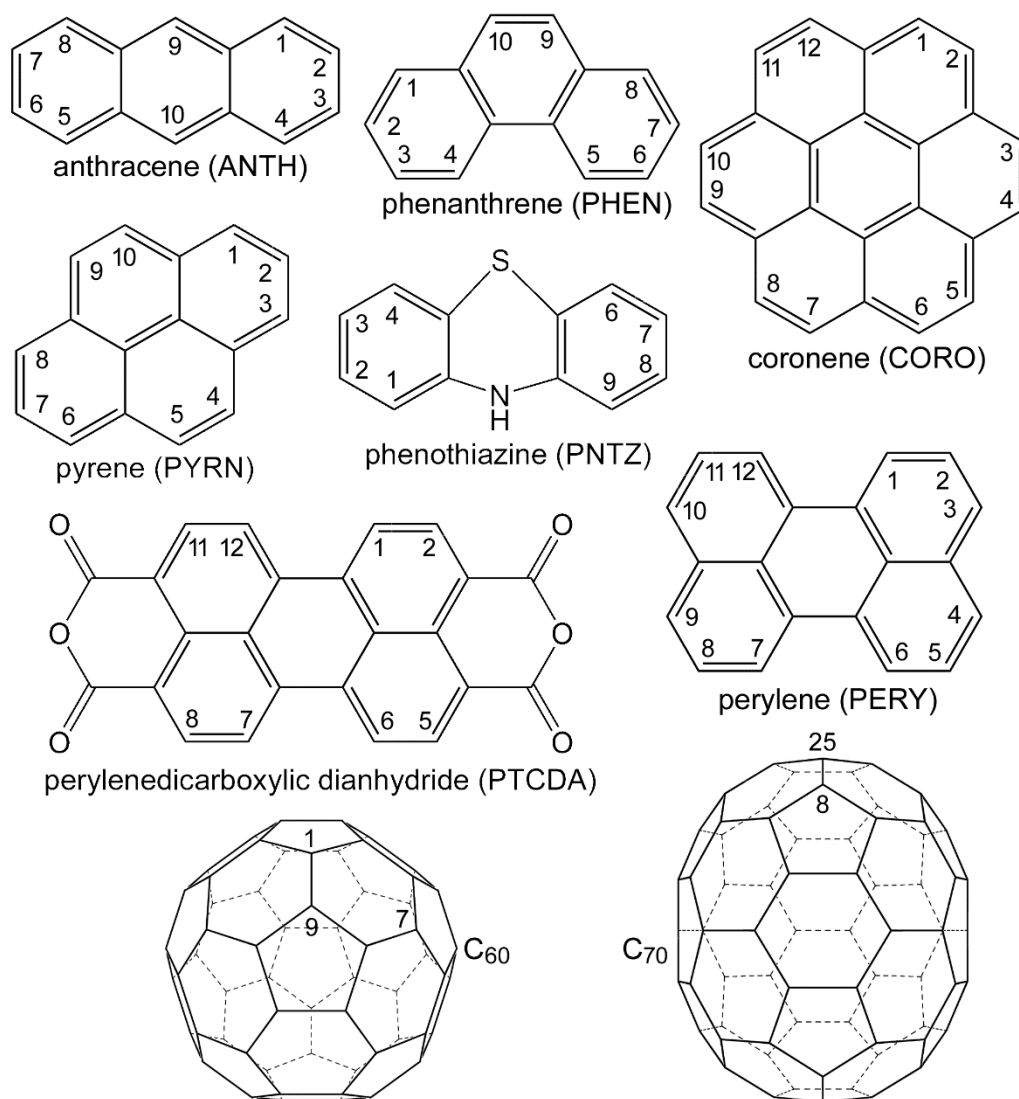
Figure I-1. The PAHs, hetero-PAHs, and fullerenes used in the research reported in this dissertation (PAH = polycyclic aromatic hydrocarbon)

INTRODUCTION REFERENCES

(1)   Bukovsky, E. V.; DeWeerd, N. J.; Strauss, S. H.; Boltalina, O. V. Versatile metal reactor for high-temperature and high-pressure trifluoromethylation of carbon-rich substrates. *J. Fluorine Chem.* **2018**, *210*, 56-64.

(2)   Qing, S.-Y.; DeWeerd, N. J.; Matsnev, A. V.; Strauss, S. H.; Thrasher, J. S.; Boltalina, O. V. Synthesis and Characterization of Pentafluorosulfanyl-Functionalized Fullerenes. *J. Fluorine Chem.* **2018**, *211*, 52-59.

(3)   San, L. K.; Bukovsky, E. V.; Larson, B. W.; Whitaker, J. B.; Deng, S. H. M.; Kopidakis, N.; Rumbles, G.; Popov, A. A.; Chen, Y.-S.; Wang, X.-B.; Boltalina, O. V.; Strauss, S. H. A faux hawk fullerene with PCBM-like properties. *Chem. Sci.* **2015**, *6*, 1801-1815.

(4)   Liu, S.; DeWeerd, N. J.; Reeves, B. J.; San, L. K.; Dahal, D.; Radha Krishnan, R. K.; Strauss, S. H.; Boltalina, O. V.; Lüssem, B. Doped N-Type Organic Field-Effect Transistors Based on Faux-Hawk Fullerene. *Adv. Electron. Mater.* **2019**, *5*, article 1900109.

(5)   DeWeerd, N. J.; Bukovsky, E. V.; Castro, K. P.; Kuvychko, I. V.; Popov, A. A.; Strauss, S. H.; Boltalina, O. V. Steric and electronic effects of CF_3 conformations in acene$(CF_3)_n$ derivatives. *J. Fluorine Chem.* **2019**, *221*, 1-7.

(6)   Bragg, W. H.; Bragg, W. L. The structure of the diamond. *Proc. R. Soc. London, Ser. A* **1913**, *89*, 277-291.

(7)   Bragg, W. L.; Bragg, W. H. The structure of some crystals as indicated by their diffraction of X-rays. *Proc. R. Soc. London, Ser. A* **1913**, *89*, 248-277.

(8)   Authier, A., 100th anniversary of the first crystal structure determinations, Oxford University Press's Academic Insights for the Thinking World, 2013.

(9)   Galli, S. X-ray Crystallography: One Century of Nobel Prizes. *J. Chem. Educ.* **2014**, *91*, 2009-2012.

(10) Mathieson, A. M.; Robertson, J. M.; Sinclair, V. C. The Crystal and Molecular Structure of Anthracene. I. X-ray Measurements. *Acta Crystallogr.* **1950**, *3*, 245-250.

(11) Sinclair, V. C.; Robertson, J. M.; Mathieson, A. M. The Crystal and Molecular Structure of Anthracene. II. Structure Investigation by the Triple Fourier Series Method. *Acta Crystallogr.* **1950**, *3*, 251-256.

(12) Pauling, L.; Cornell University Press: Ithaca, NY, 1939. The Nature of the Chemical Bond

(13) http://scarc.library.oregonstate.edu/coll/pauling/bond/narrative/page46.html.

(14) Armbruster, T.; Danisi Rosa, M. *Highlights in Mineralogical Crystallography*; De Gruyter: Berlin, 2015.

(15) Aitipamula, S.; Vangala, V. R. X-Ray Crystallography and its Role in Understanding the Physicochemical Properties of Pharmaceutical Cocrystals. *J. Indian Inst. Sci.* **2017**, *97*, 227-243.

(16) Deschamps, J. R. X-ray crystallography of chemical compounds. *Life Sci.* **2010**, *86*, 585-589.

(17) Giacovazzo, C. Phasing in crystallography: a modern perspective. *Rend. Fis. Acc. Lincei* **2013**, *24*, 71-76.

(18) Nitta, R.; Imasaki, T.; Nitta, E. Recent progress in structural biology: lessons from our research history. *Microscopy* **2018**, *67*, 187-195.

(19) Elsegood, M.; Carpenter-Warren, C. L. *These crystals will make your crystallographer happy*, 2016.

(20) Watkin, D. J. Chemical crystallography–science, technology or a black art. *Crystallogr. Rev.* **2010**, *16*, 197-230.

(21) NMR Spectroscopy, http://orgchemboulder.com/Labs/Experiments/HandbookNMR.pdf.

CHAPTER 1

DEVELOPMENT OF A NEW METAL TUBE REACTOR FOR RADICAL

TRIFLUOROMETHYLATION REACTIONS AND THE SURPRISING REACTIVITY

OF CARBON-RICH SUBSTRATES AT HIGH PRESSURES

1.1.   INTRODUCTION AND JUSTIFICATION

Gas-solid reactions are an important part of industrial processes with hundreds of examples.[1] Many of these reactions are classified as high temperature and/or high pressure and accordingly specialized reactors are required to deal with these extreme conditions. However, the definition of what is considered a "high" temperature and/or pressure is dependent on the field. For example, in polymer chemistry the polymerization of propylene at 150 °C is described as high temperature while the synthesis of ceramics is often performed at temperatures over 2000 °C. Similarly, pressure ranges can vary from 7000 Torr for the refining of petroleum products, to values greater than 1×10^6 Torr for the Haber-Bosch process.[1] Throughout this dissertation, which is dedicated to the trifluoromethylation of different organic substrates, "high" temperatures and pressures will be considered temperatures exceeding 300 °C and pressures exceeding 2000 Torr. The lower temperature limit is based on the average minimum temperature which is required for the trifluoromethylation of most polycyclic aromatic hydrocarbons, PAHs, and the pressure was determined based on the upper safe operating pressure for glass ampules.

Sealed glass ampule syntheses are the most common method for generating highly substituted, trifluoromethylated carbon-rich substrates, and reactions using these reactors have been reported many times previously by the Strauss-Boltalina research group and others.[2-11] These reactions require skilled glass blowers to perform them safely. Additionally, the highest temperature that can be used for these reactions is approximately 460 °C[12], due to the increase in malleability of glass at higher temperatures, and the highest pressure that can be used is dependent on the diameter of the ampule and the tensile strength of glass. The tensile strength of glass is approximately 22–

32 MPa though it is typically lower due to defects in the glass from handling during manufacture.[12,13] To determine the diameter of the ampule that can be used with a specific pressure, the Barlow equation, shown below, is used. The relationship shows that as the diameter increases the burst pressure decreases.[14]

$$P = \frac{(2S \times t)}{d_o}$$

P represents the burst pressure, *S* represents the tensile strength of the material, *t* is the wall thickness, and d_o is the outside diameter. Using this relationship, the maximum pressure that can be used in a glass ampule is only a few thousand Torr. Thicker walled glass can be used as well as narrower internal diameter ampules to obtain higher pressures like in the case of the ampule synthesis for dodecatrifluoromethyl[60]fullerene[11] but these reactions are dangerous and even the authors caution readers in the application of high-pressure glass ampule reactions. A further consideration, the Barlow relationship shows the virtual impossibility of successfully scaling up these ampule syntheses. If a desireable material was produced and warranted further testing in devices, using glass ampules is not practical.

Electron acceptors with high electron affinity values via the addition of perfluorinated groups are desired by the organic electronics industry because of their improved oxidative stability,[15] hydrophobicity, and their tendency to organize in the solid-state in overlapping π–π stacks.[10,16,17] A possible route to achieve such highly functionalized carbon-rich materials would be to use a large number of equivalents of the trifluoromethylating agent. The reactive gas, CF_3I, has already been shown to be effective in glass ampule reactions but in order to target higher degrees of substitution it is reasonable to assume larger equivalents or in other words, higher pressures, will be needed. Additionally, higher temperature regimes may lead to new reactivity for certain carbon-rich substrates such as fullerenes and larger mass PAHs.

To obtain higher pressures and temperatures specialized reactors are needed. Unfortunately, commercially available reactors capable of withstanding these extreme conditions are very

expensive. This is due to the structural and material constraints required. For example, in order to use reactive gasses like chlorine or fluorine, exotic materials need to be used like Monel or Hasteloy to prevent corrosion of the wetted parts. These materials are expensive to produce and dramatically increase the cost for the product. For a research scale effort these kinds of costs can be prohibitive. A recent quote from Buchiglasuster, a leading manufacturer in pilot plant scale reactors, for two different high pressure and temperature reactors, one made of stainless steel and the other Hastelloy, capable of 5.8×10^3 psi (3.0×10^5 Torr) and 500 or 400 °C cost 30,000 and 60,000 dollars respectively. This quote was for one of their smallest scale reactors with a reaction volume of 100 mL. It is therefore desirable and necessary if one wants to perform reactions that exceed the operational temperatures of sealed glass ampules to design and develop a new low-cost reactor.

It is at this point the high-pressure/high-temperautre reaction industry and the organic electronic field share a common need. In this work, the author reports the design and operation of a new metal tube reactor, MTR, for high-temperature, high-pressure trifluoromethylation of thermally stable carbon-rich substrates, such as PAHs and fullerenes, and present several proof-of-concept experimental results obtained with the new reactor.

The experiments that were performed use a set of substrates chosen for a variety of factors making them optimal test materials for the MTR. The chosen substrates were subjected to elevated temperatures and pressures accessible by the MTR. It should be noted that lower temperatures and pressures can also be used in the MTR, but for the purposes of evaluating reactivity under these extreme conditions, this section will only discuss the high-pressure and high-temperature reactions.

Fullerenes are an ideal class of substrates for exploring these new conditions. Generally, fullerenes have higher sublimation temperatures than most common carbon-rich substrates, furthermore, the reactivity of fullerenes with CF_3I has been well reported by the Strauss-Boltalina lab and others, so the results of these reactions can be compared to previous literature results.[2] This

made evaluating the results of these reactions and the effectiveness of the MTR more straightforward. It was hoped that by using high temperatures and pressures the most thermodynamically stable products would be targeted. Most radical fullerene reactions result in a large distribution of products[2] and so any experimental tool that helps to limit the number of products is an important step towards more selective syntheses, which may ultimately open the doors to applications of trifluoromethylated fullerenes, TMF. Only a few examples of selective trifluoromethylation reactions of fullerenes have been reported: decakis(trifluoromethyl)[70]fullerene, $C_{70}(CF_3)_{10}$, which was made with high selectivity in a flow tube reactor,[18,19] selective synthesis of bis(trifluoromethyl)[60]fullerene, $C_{60}(CF_3)_2$, was developed using a gradient-temperature gas-solid reactor,[20] solution-based reactions to produce various $C_{60}(R_F)_2$ (other than CF_3);[21] and dodeca-trifluoromethyl[60]fullerene, $C_{60}(CF_3)_{12}$ was produced in a sealed ampule reaction as a predominant product.[22,23] Any discoveries leading to increased degrees of control over isomer composition will be an important development since it should be possible to scale these reactions easily.

While the trifluoromethylation of fullerenes was a useful system to test the new reactor due to the wealth of data on TMFs obtained previously, the main goal of the MTR was to explore new reactivity of new substrates and make compounds which were not previously synthesized. To that end, a series of high-pressure and temperature trifluoromethylation reactions of select PAH compounds were performed. In particular, anthracene (ANTH), 3,4,9,10-perylenetetracarboxylic dianhydride (PTCDA), and coronene (CORO) were reacted in the MTR with CF_3I.

The trifluoromethylation of ANTH, like C_{60} and C_{70}, has been thoroughly studied by the Strauss-Boltalina lab so it was a logical choice for a test system to study the effect of higher pressures of CF_3I on PAH functionalization.[6] The main products from the ampule reactions done with ANTH were ANTH$(CF_3)_n$ where n = 6. This compound was very useful in making charge transfer complexes with select PAH donors and elucidating the effect CF_3 conformation has on the bend angle of select acenes which will be discussed in more detail in Chapter 5 of this work.[5]

The second PAH substrate chosen for testing in the MTR was PTCDA. It is a widely used organic semiconductor material, making it an attractive organic substrate for further functionalization.[24] Substitution of the PAH with electron withdrawing groups on the perylene core has already been performed and showed an increase in the electron affinity for the functionalized PAH.[25] PTCDA is also known as a thermally robust organic compound, melting point 350 °C with no reported decomposition, and is insoluble in most organic solvents making solution phase chemistry challenging.[26] These characteristics make it an ideal candidate for testing in the MTR. Additionally, the Strauss-Boltalina lab has already reported that using a gradient-temperature-gas-solid (GTGS) reactor,[20] for the reaction between PTCDA and CF_3I gas at 400 °C, effectively produced (poly)trifluoromethyl derivatives of PTCDA.[27]

The last PAH substrate tested in the MTR was CORO. CORO is commonly referred to as superbenzene for its high degree of stability and chemical resilience to all but the most powerful reagents and consequently most synthetic attempts to derivatize the substrate involve utilizing multi-step bottom up approaches.[28-32] Attempts by the Strauss-Boltalina lab to trifluoromethylate this compound in glass ampules were largely unsuccessful resulting in very low conversion of the starting material and will be discussed here in contrast to the MTR reactions. These factors made coronene an interesting and challenging system to target with the MTR.

In total, five carbon-rich substrates were reacted in the MTR. These reactions resulted in three selective syntheses for trifluoromethylated fullerenes. In the case of 70-8-1, there was not previously a facile synthetic route. Two of the three PAH substrates tested, ANTH and CORO, were converted into previously uncharacterized $H_2ANTH(CF_3)_n$ and $H_2CORO(CF_3)_n$ species with n values greater than six suggesting the *EA* for these compounds will be high. Measurements of the $H_2CORO(CF_3)_n$ *EA* are discussed in Chapter 2. Lastly, a new synthetic route to $PERY(CF_3)_{n \geq 6}$ species was discovered through the conversion of PTCDA. These $PERY(CF_3)_n$ species have n values between six and eight which have not been reported previously.

1.2. RESULTS AND DISCUSSION

1.2.1 Design of the reactor

When considering the design of the reactor, it is helpful to identify a set of experimental criteria that are critical to the reactor's performance. The reactor should possess the following characteristics: (i) low cost, (ii) ease of assembling and disassembling with minimal or no further machining required, (iii) ability to withstand temperatures exceeding 300 °C, (iv) ability to withstand pressures exceeding 2000 Torr, (v) resistance to most reactive gasses, and (vi) replaceable wetted components.

Initial investigation into materials which are capable of (iii) and (iv) quickly leads one to the necessity of a metal reactor thereby narrowing the possible materials that can be used. Beyond the considerably higher tensile strength of steel versus glass, at least 295 vs 7 MPa,[33] the softening temperature of most metals is higher than glass as well.[34] To choose what metal composite is best, a comparison of the heat resistant metal's tensile strength and corrosion resistance was required as a means of satisfying condition (v). The standard in the metallurgical industry is the higher the chromium content of the steel the more resistant it is to corrosion. This is due to an oxide passivation layer formed on the outside of the steel during tempering, which limits the possibility of further reaction of the metal underneath. This anti-corrosive quality is extremely important to this work since while in operation, in addition to the air-free internal conditions, the outside of the reactor will be heated to the reaction temperature, >300 °C, in the presence of air. This will lead to corrosion and eventual degradation of the structural integrity of the steel.[35] Further, the CF_3I reagent dissociates into $CF_3\bullet$ and $I\bullet$, of which the latter can annihilate into I_2, which is corrosive to metal.[36] Utilizing the expertise of HiP Inc., high-pressure equipment supplier, 316L stainless steel was chosen, not just for its higher chromium content, 16–18 weight%, but also its higher tensile strength at elevated temperatures as well.[37] From their catalog of "off-the-shelf" components a 316L stainless steel metal reactor capable of sustained operating temperatures of 520 °C at 20,000 psi was constructed.

The resulting reactor's capacity can range from a few mg to 1000 mg of substrate. The reactor is comprised of a gas tight two-way valve, p.n. 20-12LF9, metal tube, p.n. 20-LM9-12, end cap, p.n. 20-21LF9-C, and two NPT threaded glands and collars to hold the components together, p.n. 20-2LM9 and 20-2L9. The valve is certified to temperatures above the established 300 °C idealized lower limit for the trifluoromethylation of carbon-rich substrates. The reactor tube and cap, the wetted parts, are inexpensive and replaceable, so that as the reactor is used and worn due to slow reaction with $I_2(g)$ and other compounds in the reactor, these parts can be easily replaced. The reactor tube and valve are commercial, off-the-shelf products and are relatively inexpensive. These factors result in a reactor which meets all of the six conditions discussed above. A photograph and schematic of the reactor are shown in Figure 1-1. Total cost of the reactor is approx. 600 dollars and total cost of wet components aka tube, end cap, and replaceable valve stem is approximately 110 dollars.

1.2.2   Operation and parameters of the reactor

The established limitations of the assembled reactor with respect to temperature and pressure are 520 °C and 20,000 psi or 1×10^6 Torr. These limits were established by HiP and should not be exceeded, however, at significantly lower pressures than the 20,000 psi value slightly higher temperatures are possible but the supplier, HiP Inc., should be consulted before any experiments are performed. The packing in the valve stem is made of a flexible graphite-metal composite called Grafoil®, and has been rated to withstand 520 °C, hence the limitation. However, this material is still superior to most valve packing materials, which are generally polymer-based for their ability to deform repeatedly and make a seal, but consequently they have upper operating temperature limits between 200 and 300 °C. The exterior of the valve stem incorporates heat dissipating fins to ensure the valve packing does not get too hot and prematurely degrades causing a leak.

The reactor should be leak-tested before each use to ensure, prior to gas loading, that the valve is seated correctly. In the case of our test experiments, this was done using an electronic barometer, Baratron, and nitrogen gas. The reactor was loaded with a pressure of nitrogen gas and then sealed.

The tubing attaching the Baratron to the reactor was evacuated and then left at static vacuum to observe a pressure increase, and if observed at what rate. The entire reactor as well as the side arm was then evacuated, and the same static measurement was performed. In this way the two leak rates could be compared to discern if there was in fact a real leak. An example of a leak test is shown in Figure 1-2.

An additional variable in the experimental set up was the rate of heating associated with the reactor heating to the reaction temperature. A slow temperature increase could have a significant effect on the reaction time. For simplicity, the reactions which are discussed in Section 1.2.3. of this work are reported without accounting for this variable. The rate of heat transfer is going to be different for each temperature used but an example of the heating rate to the temperature of 425 °C is shown in Figure 1-2. The time required is roughly 40 minutes for the 425 °C temperature to be reached. This measurement was performed by heating a tube furnace to 450 °C and placing the MTR inside the reactor with a K type thermocouple inside the reactor. Because the MTR could not be sealed with the thermocouple inside, hot air is able to escape the reactor and/or mix with the room temperature atmosphere during the measurement which should slow the rate of temperature increase but this experiment should reveal an approximation of the true rate of heat transfer since the temperature exchange between the hot-zone and the outside air should be minimal. It did, however, lower the final equilibrium temperature that can be achieved in this case by 15 °C though the final equilibrium temperature was not reached for 2.5 h.

Even using the more corrosion resistant metal, 316L, $I_2(g)$ can still cause corrosion.[35] To mitigate this, copper powder was employed to ensure I_2 was sequestered as CuI(s). The uptake rate of iodine by copper powder, while not directly measured, was observed using a glass ampule charged with $CF_3I(g)$ and Cu(s) powder. The resulting ampule is shown in Figure 1-3 alongside an image of an analogous ampule where copper powder was not used. At no point during the experiment was purple gas observed in the ampule with Cu powder, suggesting the rate of uptake exceeded the rate of visible $I_2(g)$ formation.

A final concern was the effect high-pressure water can have on steel. After using the MTR valve approximately 400 times (the number of times it was sealed and then reopened) a consistent leak was detected, 0.1 Torr min^{-1}. Multiple experiments were performed to confirm the presence of the leak. Mr. Jimmy Shorkey with the CSU machine shop suggested based on his experience that high-pressure water had eroded the valve stem. The source of the water was unclear as the reactor was evacuated to the zero-point pressure before each reaction, however, careful examination of the IR spectra of the off-gasses from trifluoromethylation reactions suggested the presence of water in the off-gas mixture. Small vibration bands were consistently recorded in the water "grass" region of the spectrum, 3000–3500 wavenumbers, see Figure 1-4. Finally, it was determined that the copper powder, which had been so instrumental in preventing $I_2(g)$ based corrosion, contained a small amount of water on the surface of the particles. Since the amount of water was very small, between 10 and 30 Torr, and would start condensing as the reactor cooled, detection of the water was difficult, however, a consistent IR signal was recorded. The gas IR cell and the reactor were also evacuated exhaustively over multiple days to 10^{-6} Torr to exclude them as the source of the water. Further experiments in the MTR were performed with "dry" copper which was produced by passing reductive $H_2(g)$ over the surface at elevated temperatures using a heat gun. Drying the copper resulted in an observable change in the color of the copper powder from dark orange to light pink.

The activated copper and off-the-shelf copper were used in side-by-side reactions to trifluoromethylate C_{70}. This experiment resulted in a 7% increase in the conversion of C_{70} to TMFs based on the HPLC peak area. More significantly, there was a dramatic change in the IR spectra between the two reactions showing the presence of $C_2F_6(g)$ in the off-gasses from the activated copper reaction. Perfluoroethane was not detected in reactions using off-the-shelf copper, which suggests CF_3 radicals were consumed by the unproductive reaction with water to make CF_3H, detected by IR, and obviously CF_3OH, which was not detected by IR because it is unstable at room temperature.[38,39] Even when "dried" copper was used there was a small signal in the water vapor

region. A direct approximation of the amount of residual water is not possible using these data since the condensation of the water onto the dried IR cell is unavoidable, however, the change in off-gas mixture shows the importance of using anhydrous copper powder.

1.2.3. Trifluoromethylation reactions of fullerenes in the MTR

The first reactions discussed below were performed on the most abundant fullerene, C_{60}. Due to its higher relative abundance in fullerene soot, it is by far the most studied fullerene and so it was the logical first choice for testing the new reactor. C_{60} was reacted with 40.4 equiv of CF_3I or 8.5×10^3 Torr, more than four times the safe operating pressure in glass, at 450 °C, the softening temperature of glass, and yielded a mixture of TMFs and unreacted C_{60}. The product was found to be a mixture of highly soluble TMFs, unreacted C_{60}, and the dominant product dodeca-trifluoromethyl[60]fullerene, $C_{60}(CF_3)_{12}$ with S_6 symmetry, 60-12-1. The most soluble material, which represented the minority of the material, was analyzed by mass spectrometry revealing the presence of TMFs with $n(CF_3) = 12–18$, in accordance with earlier observations.[22,23] To better understand the product composition, a representative fraction was dissolved in C_6D_6 and examined by ^{19}F NMR revealing that only signals attributable to 60-12-1 were detected. The ^{19}F NMR spectrum is shown in Figure 1-5. The signal to noise ratio for the NMR spectrum is poor. It is likely that due to the 60-12-1's low solubility in virtually all solvents except refluxing *o*-DCB that during the course of the NMR experiment, it was precipitating out of the saturated solution.[11] The ^{19}F NMR showed two distinctive multiplets in the $F(CF_3)$ region of the spectrum, which matches well with the previously reported spectrum for 60-12-1.[22,23] The Schlegel diagram showing the addition patterns of the 12 CF_3 groups on the C_{60} cage is also depicted in Figure 1-5. This S_6-$C_{60}(CF_3)_{12}$ isomer has been calculated to have the lowest relative energy of the $C_{60}(CF_3)_{12}$ isomers by DFT making it the most thermodynamically stable compared to other structures.[11] Thus its prevalence among the high-temperature products of the reaction that was carried out in the MTR matches with the proposed hypothesis that preferential formation of thermodynamically stable products occurs.

C$_{70}$, the second most abundant fullerene, has D_5h symmetry and this lower symmetry results in even larger numbers of possible isomers from functionalization. This makes it arguably a more challenging substrate to work with. Since raising the temperature and pressure of the reaction to favor the thermodynamic products worked so well with C$_{60}$ it was also attempted with C$_{70}$. Several reactions were performed to explore the reactivity of C$_{70}$ under these conditions and two noteworthy results were obtained. The HPLC chromatograms and the ^{19}F NMR spectra of those crude product mixtures are shown in Figure 1-6. C$_{70}$ was reacted with 20 equiv of CF$_3$I or 3.5×10^3 Torr and 3.8×10^3 Torr, at 450 °C and 500 °C respectively. For these reactions, higher conversion was achieved by adding fresh CF$_3$I(g) (a total of three times) and evacuating the off-gasses after each reaction period. Analysis of the off-gasses by IR spectroscopy confirmed that all of the CF$_3$I(g) was consumed after only one hour and so the dwell time in each case was only one hour.

After each introduction of additional CF$_3$I(g) conversion of C$_{70}$ occurred with minimal charring of the crude material. More importantly, only one major product was formed in each reaction, deca-trifluoromethyl[70]fullerene, C$_1$-C$_{70}$(CF$_3$)$_{10}$ at 450 °C and octa-trifluoromethyl[70]fullerene, C$_S$-C$_{70}$(CF$_3$)$_8$ at 500 °C. The HPLC and NMR data associated with these reactions are shown in Figure 1-6. Both of these compounds are the lowest relative energy isomers by DFT calculation. Previous work by the Strauss-Boltalina group showed a highly selective synthesis using a flow tube reactor for 70-10-1,[18] however, for 70-8-1 there is not an efficient single-step synthesis.[40] This result shows the possibility of targeted syntheses for the most thermodynamically stable TMF compounds using the MTR and applying different temperatures as a means of synthetic control.

1.2.4. Trifluoromethylation reactions of PAHs in the MTR

For the trifluoromethylation reaction that was performed with ANTH in the MTR, the temperature and number of equivalents of CF$_3$I(g) were chosen to be similar to the previously performed ampule reactions while the volume of the reactor and scale of the reaction were altered resulting in a pressure at the reaction temperature that was an order of magnitude greater than the ampule reactions, as seen in Table 1-1. More specifically, in the case of the reaction between

ANTH and 13.4 equiv of $CF_3I(g)$, the pressure in the reactor reached 11,000 Torr. In comparison, the glass-ampule synthesis of trifluoromethylated ANTH only reached approximately 1000 Torr. It should be noted that the use of Cu powder is a necessity and limitation of the MTR, see Section 1.2.2., but was not used in the ampule reaction.

Figure 1-7 shows the negative-ion electrospray mass spectra (NI-ESI MS) of the crude products from the trifluoromethylation of ANTH in the MTR (bottom panel) and glass ampule (top panel). In the ampule product, the most abundant anion is due to a hexa-substituted derivative, $ANTH(CF_3)_6$, characterized by the Strauss-Boltalina lab previously as the main product of the sealed-ampule reaction.[6] Other minor peaks in the mass spectrum are due to $ANTH(CF_3)_5$ and dihydro-ANTH species, $H_2ANTH(CF_3)_7$, at m/z 655. In the bulk product, the latter comprise only small amounts (<1%, based on the exhaustive product separation in the earlier study[6]). In the MTR crude product mixture, three types of species are observed by mass spectrometry: $ANTH(CF_3)_n$ where $n = 4$ and 5, $H_2ANTH(CF_3)_x$ where $x = 6$ and 7, and dimeric species $H_2ANTH_2(CF_3)_y$ where $y = 10$ and 11, the latter with significantly lower intensities.

It must be stated that the high abundance of the $H_2ANTH(CF_3)_x$ species in the mass spectrum of the MTR product mixture could be explained by the analyte suppression effect.[41] All of the $H_2ANTH(CF_3)_x$ compounds have an x value > 6 and there is no evidence that the n value for $ANTH(CF_3)_n$ exceeds 7; the addition of a single CF_3 group results in an increase to the electron affinity, EA, of the parent PAH by approx. 150–200 meV.[6] This should result in all of the $H_2ANTH(CF_3)_x$ species having a higher EA than the $ANTH(CF_3)_n$ species. However, due to the number of variables that can affect ionization it is not possible to quantify or even approximate the amount of suppression that may be occurring in this case. Additionally, the possibility that the $H_2ANTH(CF_3)_x$ ions formed due to chemical reactions in the ion source of the mass spectrometer can be ruled out as such adduct formation was not observed during the mass spectrometry analysis of pure $ANTH(CF_3)_6$ samples,[6] when using the same conditions as applied for the MTR product analysis.

Alternatively, the relative product distribution of the ANTH(CF$_3$)$_n$ and the H$_2$ANTH(CF$_3$)$_x$ species can be determined by examining the ^{19}F NMR spectra, shown in Figure 1-8. The chemical shifts <-65 ppm must belong to unique CF$_3$ environments since they do not appear in any previously reported spectra for trifluoromethylated PAHs, and by process of elimination must be related to the C(sp^3) atoms formed from the addition of CF$_3$ groups rather than substitution.[6] Further analysis of similar reactions performed on CORO show this assumption to be the most likely assignment of the signals with chemical shifts of -70 ppm. Those reactions will be discussed in more detail in the next section and in Chapter 2. Based on the relative integration of the two different ppm regions, we see the MTR crude product mixture has approximately six times the amount of H$_2$ANTH(CF$_3$)$_x$ species compared to ANTH(CF$_3$)$_n$. This is significantly different than what was observed in the ampule reactions. The ampule reactions by contrast have far fewer unique chemical shifts and therefor a smaller number of unique products making the MTR reaction less selective however, the MTR is a viable route to achieve new H$_2$ANTH(CF$_3$)$_x$ species which have not been studied previously. The ^{19}F NMR of these two crude product mixtures as well as the pure ANTH-6-1 isomer are shown in Figure 1-8.

The second PAH reacted in the MTR, PTCDA, was reacted with CF$_3$I in the MTR at 450 °C and a pressure of 1.2×10^4 Torr, see Table 1-1. Figure 1-9 shows the NI-ESI mass spectra of the crude soluble products of the MTR reaction and, for comparison, two products from sealed ampule reactions carried out at two different temperatures and pressures, one at the same temperature as in the MTR reaction with 600 Torr, and the other at a lower temperature of 390 °C with 400 Torr. The first, and unexpected, observation is that the most intense anions in the mass spectrum of the MTR product could only be assigned to PERY(CF$_3$)$_n$ derivatives and not to PTCDA(CF$_3$)$_n$ compounds, implying that PTCDA itself is not stable under the applied reaction conditions. The anhydride groups on the PTCDA molecule are apparently substituted by CF$_3$ groups yielding PERY(CF$_3$)$_n$, where n = 6, 7, and 8. The second observation was that the degree of trifluoromethylation in the MTR was higher than observed in the glass ampule for the direct high-

temperature trifluoromethylation of the underivatized perylene substrate.[6] The product distribution in the sample from the 450 °C sealed ampule reaction is very similar to that of the MTR crude product spectrum, and the most abundant peak matches the mass to charge ratio for $PERY(CF_3)_8$. By comparing the spectra from both the 390 °C sealed ampule reaction and the 450 °C MTR reaction reveals that a lower reaction temperature increases $PTCDA(CF_3)_n$ production, while suppressing degradation of PTCDA into PERY. Currently, the use of the GTGS reactor, which runs at atmospheric pressure or lower, for trifluoromethylation of PTCDA (or perylene diimide PDIs) appears to be the most efficient approach to the synthesis of $PTCDA(CF_3)_n$. Alternatively, a new synthetic route to new $PERY(CF_3)_{6,7,8}$ species was discovered by the high pressure and temperature degradation of PTCDA in the presence of a large excess of $CF_3I(g)$ utilizing the MTR.

As was previously stated, the last PAH to be tested in the MTR was CORO. The first reaction was performed on 50 mg of CORO at 450 °C and with 1.7×10^4 Torr of $CF_3I(g)$. For comparison, the ampule reactions were performed by Dr. Igor Kuvychko on a smaller amount of material, 16 mg, at lower temperatures, 275 and 360 °C, and with significantly lower pressures of CF_3I, 600 and 1000 Torr. The MTR reaction yielded a sufficient amount of soluble product for a detailed analysis by NI-ESI MS, NMR spectroscopy, and HPLC. While the NMR spectrum of the crude product mixture showed a multitude of chemical shifts the HPLC chromatogram shows only six major fractions. The chromatogram is shown in Figure 1-10. The labeled fractions were isolated and characterized and will be discussed later in Chapter 2 of this work. The NI-ESI mass spectrum showed a set of m/z signals separated by 68 Da, in accordance with the introduction of CF_3 groups in place of hydrogens. Assignment of the molecular compositions of the most abundant peaks resulted in the following general formula for this series: $C_{24}H_{(12-m)+x}(CF_3)_m$, where $m = 7–10$, and $x = 1$, 2, or 4, see Table S2-3 for m/z values. It was concluded that, similar to the ANTH MTR reactions, the CORO MTR reaction proceeds via both substitution and addition of CF_3 radicals resulting in protons bonded to $C(sp^3)$ atoms. These $C(sp^3)$ atom containing species, trifluoromethylated dihydrocoronene compounds, were observed in mass spectra from the ampule

reactions as well despite the lower pressures of CF_3I and the low conversion of the CORO substrate. This result seems to suggest the functionalized CORO derivative, trifluoromethylated coronene, is far more productive to further substitution and subsequent addition than the underivatized CORO substrate. This means that high pressure reaction conditions will kinetically always favor trifluoromethylated dihydrocoronene compounds. Additionally, no species with $C(sp^3)$ atoms aka "extra protons" has fewer than seven CF_3 groups supporting the hypothesis that radical addition is occurring after a specific degree of substitution. This was also observed in the ANTH case.

To test if these dihydrocoronene compounds were a product of the higher pressures of $CF_3I(g)$, another reaction was performed in the MTR using a lower pressure of CF_3I, 7400 Torr, and a larger mass of CORO, 100 mg, overall lowering the amount of CF_3I to 3.4 equiv. This reaction resulted in a distribution of $CORO(CF_3)_n$ derivatives where $n = 1–5$. The resulting HPLC chromatogram for this reaction is shown in Figure 1-11. This reaction led to a number of isolable compounds, which were characterized and will be discussed in greater detail in Chapter 2 of this work. Notably, no species corresponding to dihydrocoronene derivatives were found, as confirmed by NMR spectroscopy.

It is apparent from these PAH reactions that a unique class of trifluoromethylated compounds are now accessible via the MTR. In glass ampule reactions, a large number of substrates have been trifluoromethylated successfully, but these reactions require expert glass blowers and have a limited range of temperatures and pressures. Now, with access to higher pressures, $C(sp^3)$ containing trifluoromethylated PAHs can be synthesized in high yield and with surprising selectivity, at least in the cases of the CORO substrate. The ANTH substrate at high pressures was also converted into a dihydro, $C(sp^3)$ containing PAH, based on mass spectrometry and ^{19}F NMR. In the case of PTCDA, the high pressure trifluoromethylation resulted in a loss of the carbonyl functional groups and a new trifluoromethylated PERY derivative being produced. These newly formed $PERY(CF_3)_n$ compounds have a higher degree of substitution than has been observed for

PERY using glass ampules resulting in the formation of new compounds which are predicted to have higher electron affinities than previously reported. Additionally, by using lower pressures or the same conditions used in glass ampules, trifluoromethylated PAHs without $C(sp^3)$ atoms can be synthesized showing the MTR as a viable alternative reactor to the standard glass ampules.

1.3. CONCLUSION AND FUTURE WORK

The MTR has proven to be an effective high-pressure/high-temperature reactor with an overall lower cost than competing reactors made of more exotic alloys. It has been used to synthesize a variety of compounds including those that had been accessible previously via other published routes and those which have previously not been reported. By combining the improved safety factors and tensile strength of 316L steel, pressures up to a million Torr or 20,000 psi and temperatures as high as 520 °C can be achieved. The MTR is easy to assemble and to use, though care must be taken with respect to residual water and reactive gasses that could shorten the lifetime of the MTR. It is recommended that a leak test be performed before each reaction as well as a calibration of the rate of heat transfer for the target temperatures.

The chemistry, which is now accessible through the MTR, has already been shown to hold exciting possibilities. A targeted and safe synthesis, which is readily accessible via the MTR, has been developed for the S_6 symmetry dodeca-trifluoromethyl[60]fullerene otherwise referred to as 60-12-1 which previously required glass ampules under high enough pressures to condense CF_3I.[11] This synthesis could only be performed with the assistance of an expert glassblower and were even then acknowledged as dangerous reactions. Two $C_{70}(CF_3)_n$ derivatives were synthesized in relatively high yield, deca-trifluoromethyl[70]fullerene 70-10-1 and octa-trifluoromethyl[60]fullerene 70-8-1. This was done by varying the temperature of the reaction from 450 °C to 500 °C and keeping the large excess of equivalents aka a large pressure of $CF_3I(g)$ constant. In the case of 70-8-1 the previous highest yield method required multiple sublimation steps and had a fairly low yield.[40] The results of the high pressure trifluoromethylation of ANTH, PTCDA, and CORO and the implications those results have on the understanding of the unique

23

reactivity of those substrates will be discussed in detail in Chapter 2 but in short, using high pressures of $CF_3I(g)$ has afforded access to a new class of compounds which previously have not been reported. It was also shown that using lower pressures in the MTR results in less dearomatized products and therefore the MTR appears to be a low-cost reusable replacement for glass ampules. Further there are, through HiP, larger diameter reactors that can be purchased though they do come with a necessary decrease in the overall pressure rating due to the Barlow relationship. Large excesses of $CF_3I(g)$ were used with equivalents over 40 times excess and the largest pressure that was reached was in the tens of thousands of Torr which is far below the 500,000 Torr pressure limit on the largest diameter commercial reactor HiP has available.

Future reactions in the MTR would explore the range of PAHs that undergo addition reactions after a number of substitution reactions. The point at which this occurs for each PAH appears to be different based on the compounds tested in this work, ANTH and CORO. PTCDA converted to PERY as a byproduct of the elimination of the carbonyl group but it is logical to assume there is a point where PERY itself would also undergo radical addition and form $C(sp^3)$ atoms. Further studies would explore where these $C(sp^3)$ atoms are produced and if there are any trends dictating their location on the PAH core. Additionally, exploration of other reactive gas reagents would be useful to show the versatility of the MTR. Another variable that could also be explored would be possible changes in product composition as a function of Cu particle size and/or form of Cu that is used. Work reported by Dr. Rippy et. al. showed that the presence of Cu allowed for the formation of regioselective products.[42] It is reasonable to hypothesize that Cu or even the metal composition of the wetted parts of the reactor could have a similar role in MTR reactions for certain substrates. Lastly, a variable beyond the scope of these studies, the slow oxidation of the reactor material could affect the product distribution. Further studies could compare product distribution from identical reactions in both a new and old reactor tube.

1.4. ADDITIONAL RECOGNITION

Table 1-1. Table of high-temperature trifluoromethylation reactions using the metal tube reactor (MTR) or sealed glass ampules

substrate	amount of substrate, mg (mmol)	equiv CF_3I	amount of Cu, g	rxn. temp., rxn time	pressure, Torr	percent conversion[a]
ANTH	55 (0.31)	13.4	2.4	360 °C, 3 h	11300	> 81
ANTH	96 (0.54)	12	—[be]	350 °C, 7 h	760–1000	< 20
PTCDA	50 (0.13)	12	0.65	450 °C, 3 h	12000	< 20
PTCDA	18 (0.05)	12	—[bf]	450 °C, 6 h	600	—
PTCDA	30 (0.08)	12	—[bg]	390 °C, 2 h	400	—
CORO	50 (0.17)	34	4.2	450 °C, 4 h	17000	> 98
CORO	100 (0.33)	3.4	1.9	450 °C, 4 h	3400	80
C_{60}	50 (0.069)	40/48/24[c]	1.8	450 °C, 9 h	8500	67
C_{70}	50 (0.060)	20/20/20[c]	2.3	450 °C, 3 h	3500	44
C_{70}	50 (0.060)	20	2.1	500 °C, 1 h	3800	12
C_{70}	50 (0.060)	20/20/20[c]	2	500 °C, 3 h	3800	48
C_{70}	50 (0.060)	20/20/20[c]	2.2	500 °C, 3 h	3800	66

[a] Percent conversion is defined as the amount of derivatized material relative to the residual starting material. [b] These reactions were carried out using sealed glass ampules (ca. 160[e], 20[f], and 40[g] mL interior volume) without added Cu powder. [c] The product gas was evacuated and a new pressure of CF_3I(g) was added.
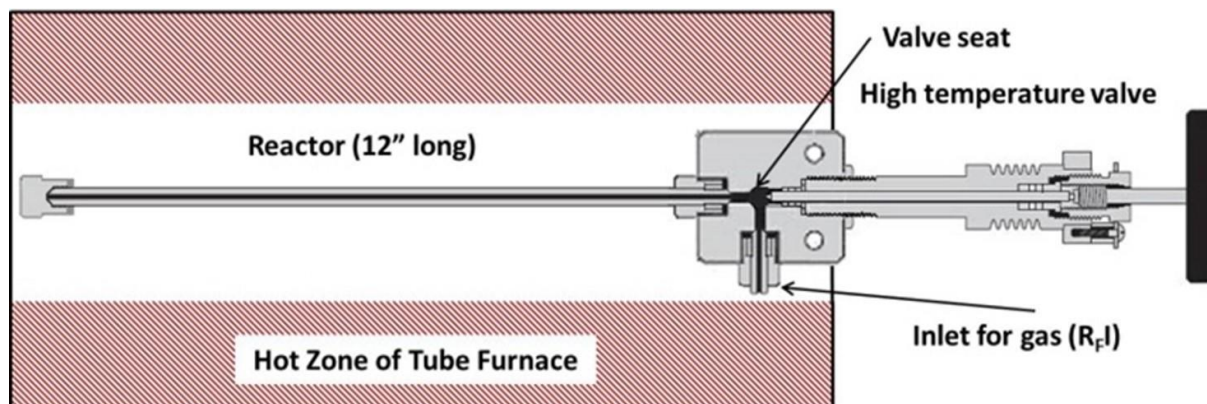
Figure 1-1. (**Top**) Metal tube reactor (MTR) schematic, (**Bottom Left**) Image of the assembled MTR, (**Bottom Right**) MTR set up inside the tube furnace. Firebricks were sculpted and cut to size to stabilize the MTR in the furnace ensuring even heating. A quartz tube was used to hold the firebricks and MTR in position inside the tube furnace.
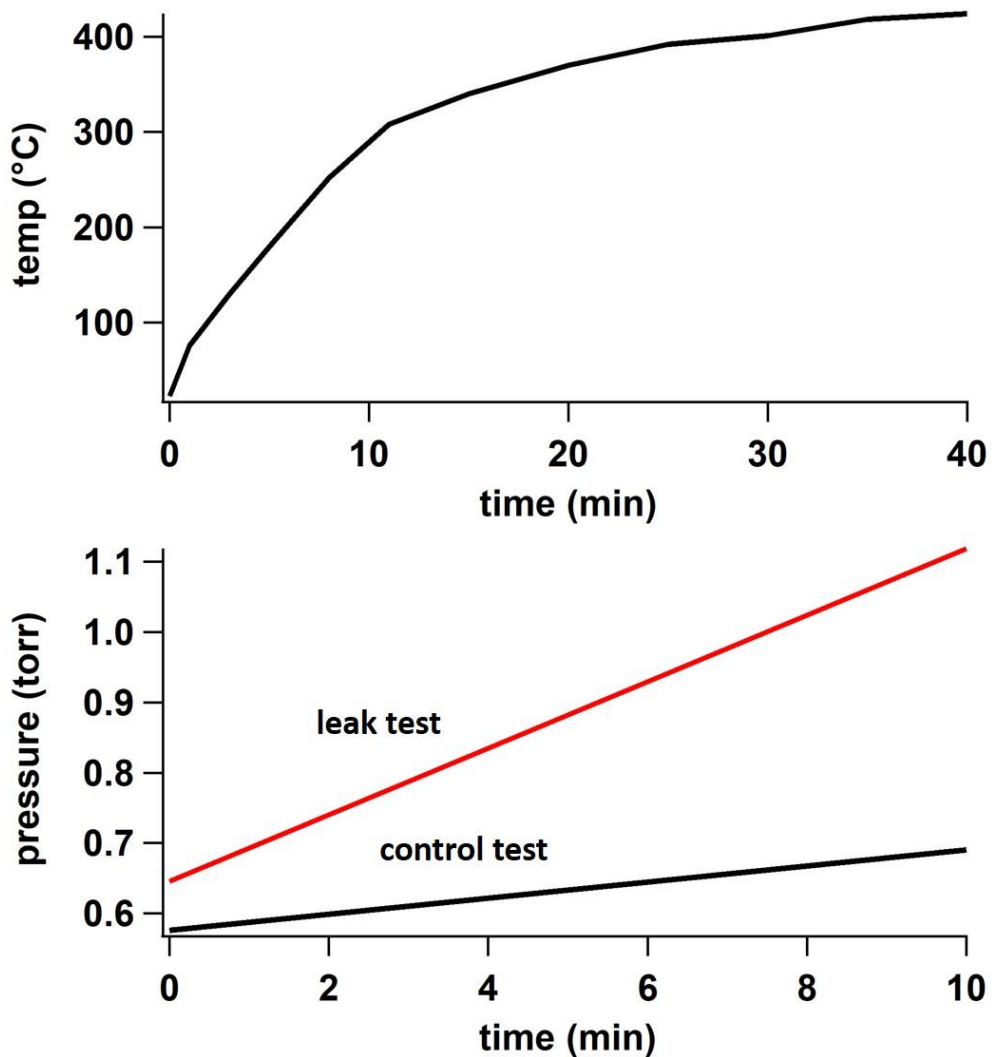
Figure 1-2. (**Top**) A plot of the increase in temperature inside the MTR. For an internal temperature of 425 °C approximately 40 minutes of heating at 450 °C was required. (**Bottom**) Plot of a leak test on the MTR. The control is the leak rate for the manifold and MTR connection, 0.01 Torr min^{-1}, and the leak test is for the sealed MTR into the evacuated manifold, 0.05 Torr min^{-1}. The resulting leak rate of the MTR for this experiment was 0.04 Torr min^{-1}.
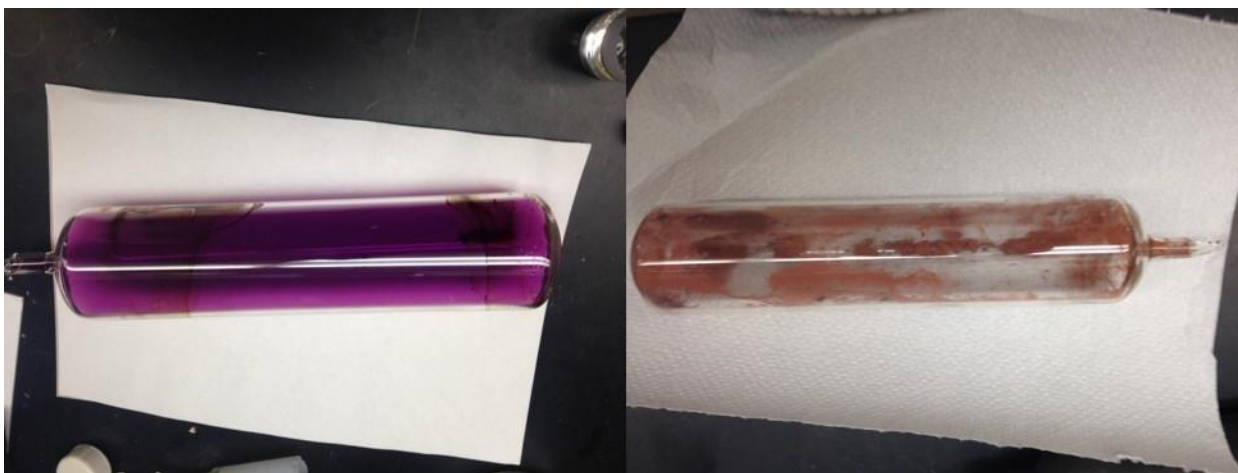
Figure 1-3. Side-by-side ampules charged with CF$_3$I. (**Left**) No Cu$_{(s)}$ was added. (**Right**) Cu$_{(s)}$ was added. The two ampules were heated to allow CF$_3$I bond dissociation to occur and the resulting images show the effect Cu(s) powder has on I$_2$(g) formation. At no point during the test was visible I$_2$(g) formed in the Cu$_{(s)}$ containing ampule.
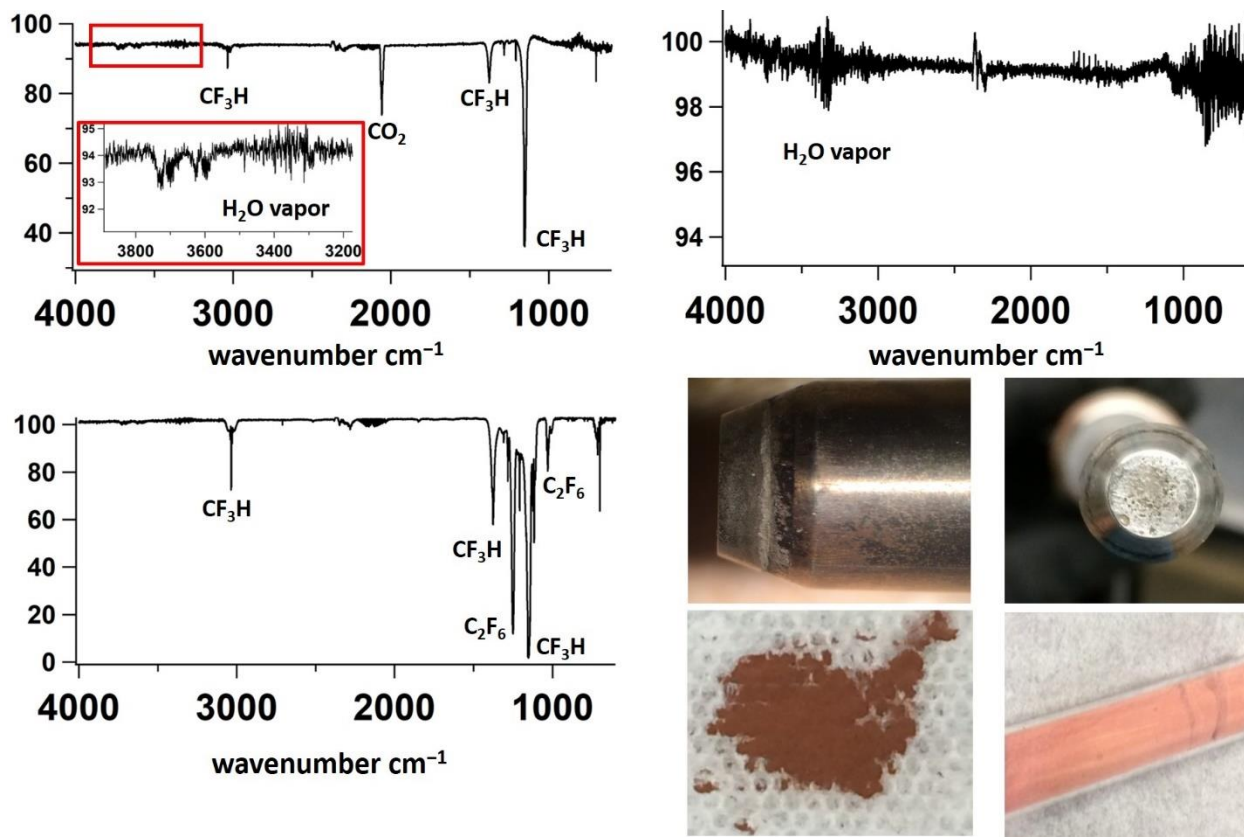
Figure 1-4. (**Top Left**) IR spectrum of the off-gasses from the trifluoromethylation of C_{70}. Stretches characteristic for CF_3H and CO_2 are detected. A small residual signal for water vapor is also detected and shown as an inset. (**Top Right**) IR spectrum of the off-gasses produced by the heating of copper powder. A small signal for water vapor was detected. The gas cell and MTR were rigorously evacuated to exclude them as the source of the water. (**Bottom Left**) IR spectrum of the off-gasses from the trifluoromethylation of C_{70} using the "dried" copper. The increase in C_2F_6 concentration suggests fewer CF_3 radicals are consumed unproductively with water allowing for a more productive trifluoromethylation reaction. (**Bottom Right Top**) Images of the valve stem from the MTR. The erosion of the valve contact point as well as the pitting of the valve stem is indicative of high-pressure water corrosion. (**Bottom Right Bottom**) Copper powder before and after "drying" using elevated temperatures and $H_2(g)$ mediated reduction.
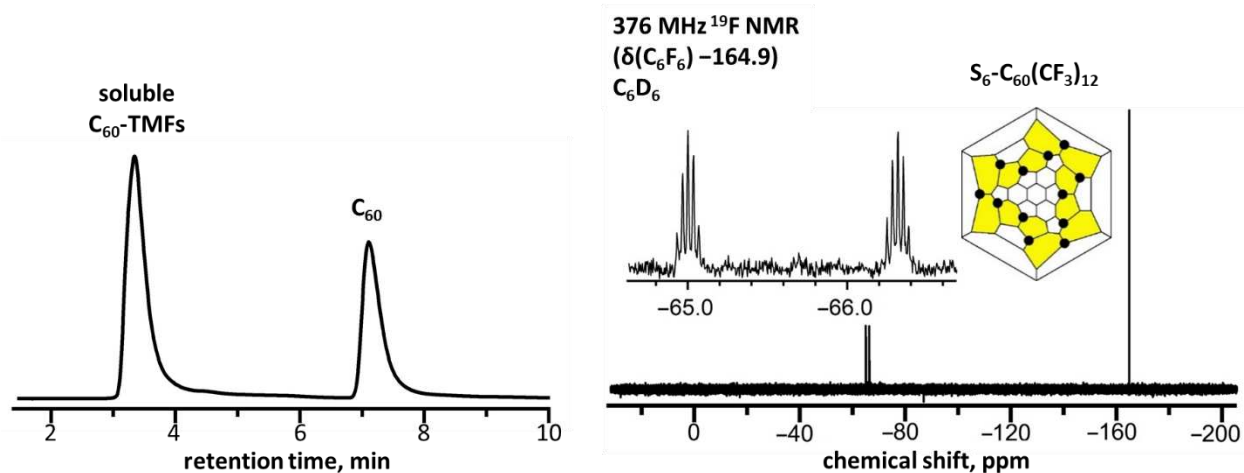
Figure 1-5. (**Left**) The HPLC chromatogram of the crude product mixture from the MTR trifluoromethylation of C_{60}. The earliest eluting fraction contains the soluble TMFs and the later eluting fraction is unreacted C_{60}. The trace was collected for over 30 min but no further signals were detected. 100% toluene, Cosmosil Bucky-M semi-preparative column, 300 nm. (**Right**) The ^{19}F NMR spectrum of the crude product mixture from the MTR trifluoromethylation of C_{60}. The only signal other than the reference (C_6D_6, C_6F_6 δ −164.9) is the distinctive apparent pentets for 60-12-1. The Schlegel diagram of the S_6 point group fullerene is shown as well. The black dots are the locations of the trifluoromethyl groups. The low solubility of 60-12-1 is likely the cause of the poor baseline resolution which is obscuring the other TMF fluorine signals.
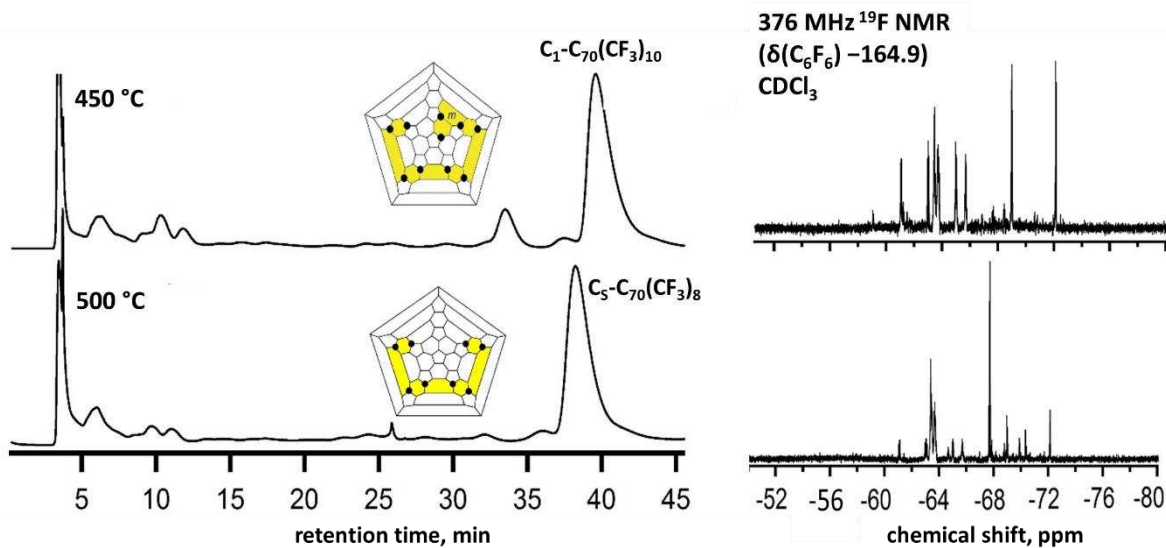
Figure 1-6. (**Left**) The HPLC chromatograms of the crude product mixture from the MTR trifluoromethylation of C_{70} performed at 450 and 500 °C. The two HPLC chromatograms show the remarkable selectivity that can be achieved by only varying the temperature of the reaction. The dominant compounds, C_1-$C_{70}(CF_3)_{10}$ and C_S-$C_{70}(CF_3)_8$ aka 70-10-1 and 70-8-1, are shown in the chromatogram. The Schlegel diagram for each fullerene is shown next to its HPLC peak. (**Right**) The ^{19}F NMR spectra of the crude product mixture from both reactions. The strongest signals are associated with the two main compounds in each reaction.[2] (CDCl$_3$, C$_6$F$_6$ δ −164.9)
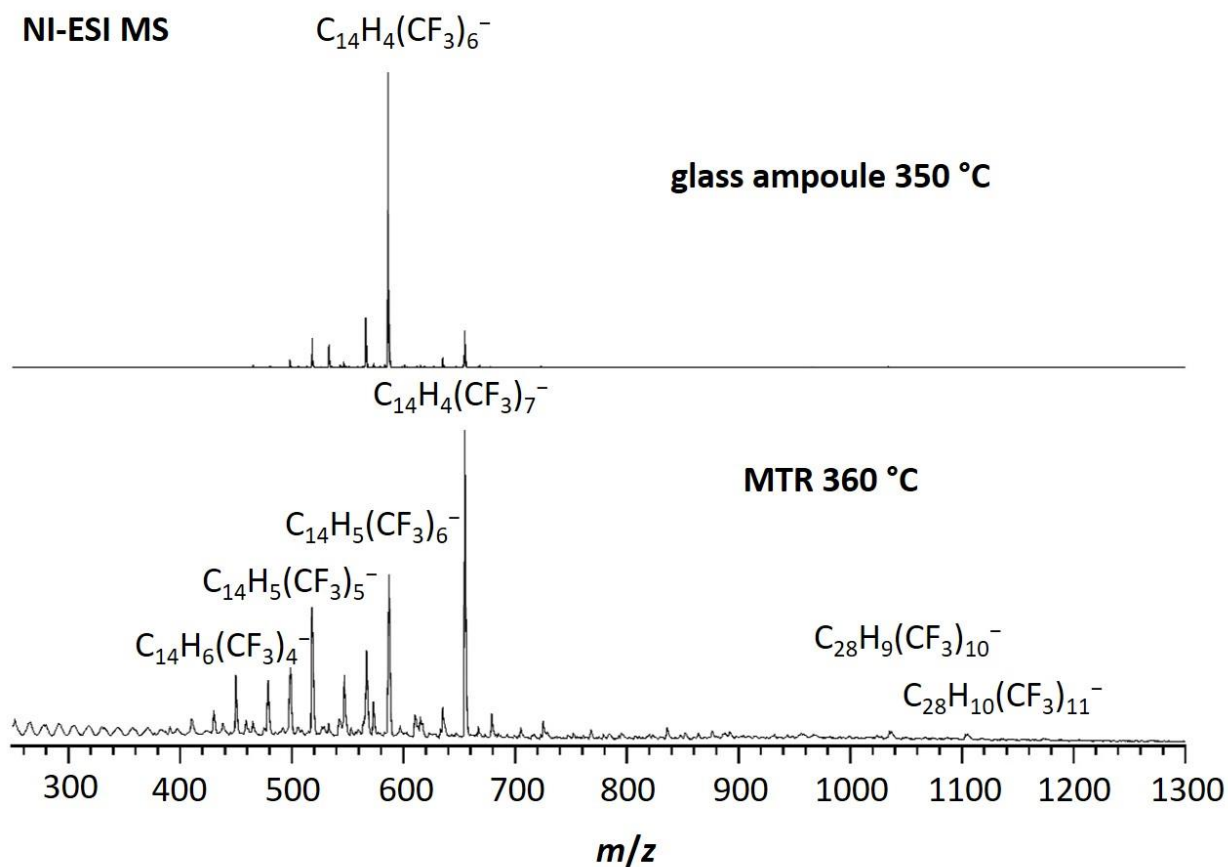
Figure 1-7. (**Top**) NI-ESI MS spectrum of the crude product mixture from the glass ampule trifluoromethylation of ANTH at 350 °C. The dominant isomer is ANTH(CF$_3$)$_6$. (**Bottom**) NI-ESI MS spectrum of the crude product mixture from the MTR trifluoromethylation of ANTH at 360 °C. The largest signal is from H$_2$ANTH(CF$_3$)$_7$ and H$_2$ANTH(CF$_3$)$_6$ where one proton has been lost to gain the negatively charged ion. At significantly lower intensity are the ANTH$_2$(CF$_3$)$_{10}$ and ANTH$_2$(CF$_3$)$_{11}$ signals.
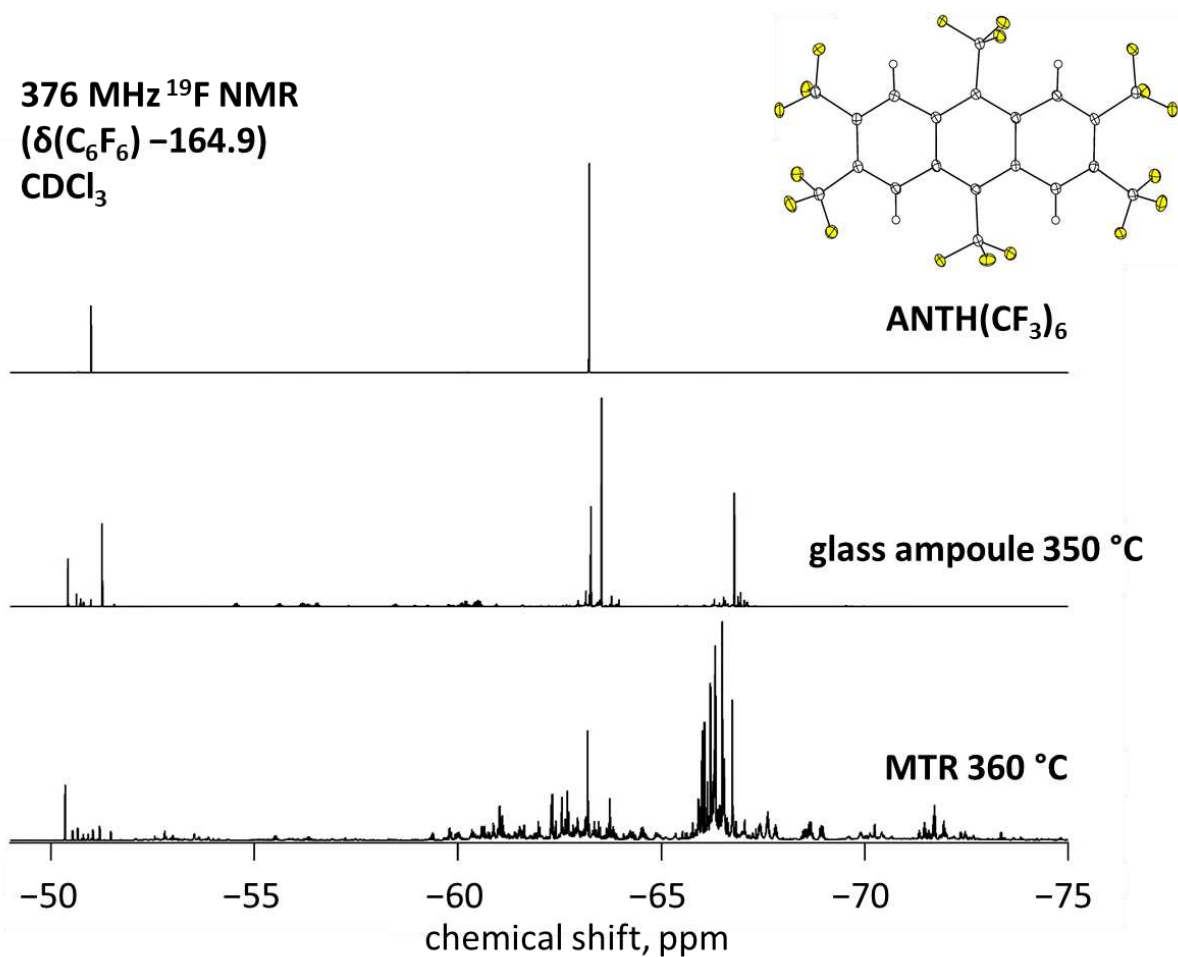
Figure 1-8. ^{19}F NMR spectra of the crude product material from the glass ampule and MTR trifluoromethylation reactions with ANTH, as well as, the spectrum of the pure ANTH(CF$_3$)$_6$ isomer ANTH-6-1. The chemical shifts from −65 to −75 ppm are likely caused by the F(CF$_3$) groups adjacent or attached to C(sp^3) atoms. (CDCl$_3$, C$_6$F$_6$ δ −164.9)
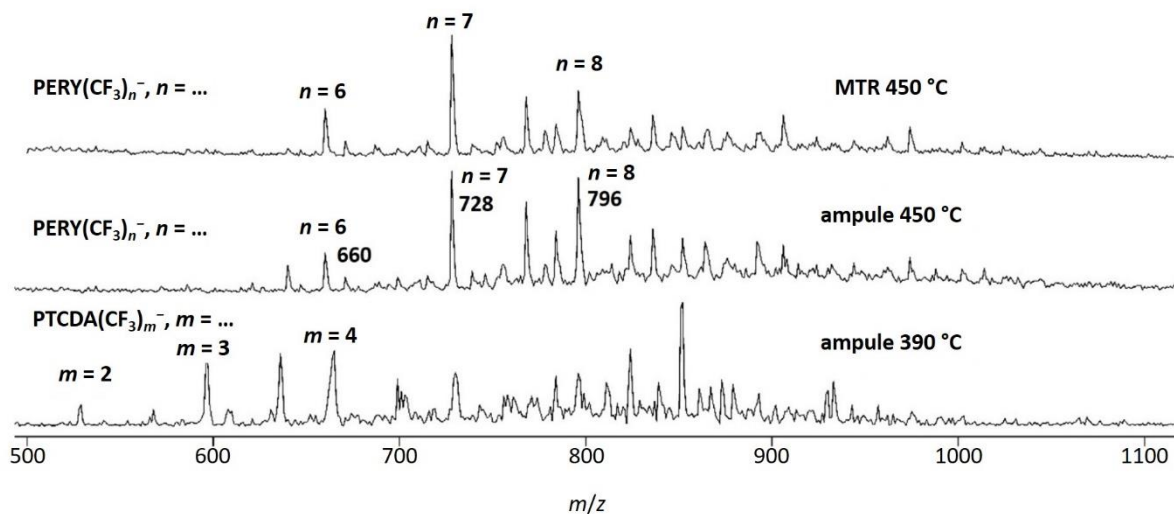
Figure 1-9. Mass spectra of the trifluormethylation of PTCDA in the MTR and in glass ampules. (**Top**) MTR trifluoromethylation of PTCDA at 450 °C resulting in PERY(CF$_3$)$_n^-$ ions. (**Middle**) Glass ampule trifluoromethylation of PTCDA at 450 °C resulting in PERY(CF$_3$)$_n^-$ ions. (**Bottom**) Glass ampule trifluoromethylation of PTCDA at 390 °C resulting in PTCDA(CF$_3$)$_n^-$ ions.

35
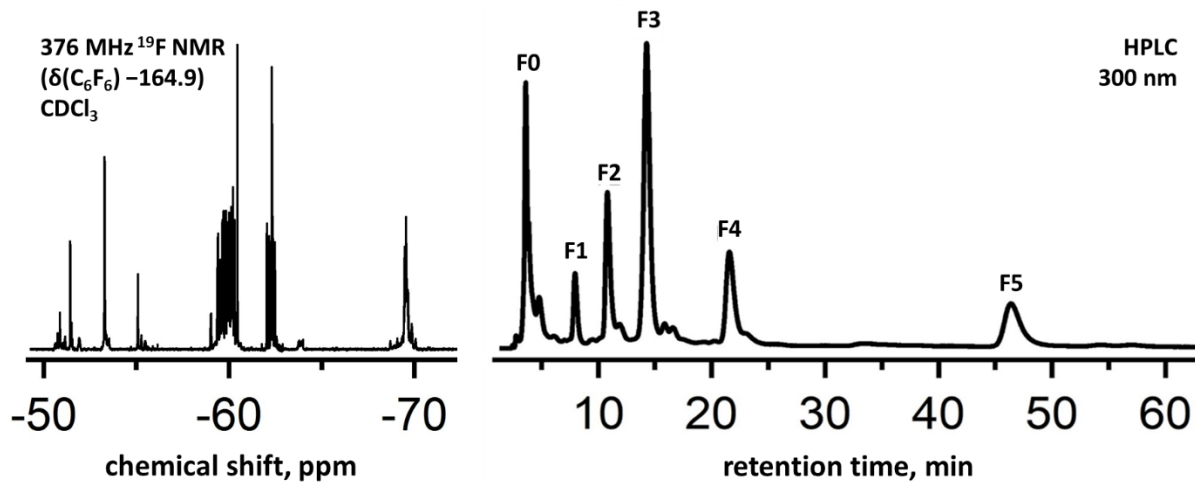
Figure 1-10. (**Left**) ^{19}F NMR spectrum of the crude CORO product mixture from the high-pressure trifluoromethylation in the MTR. (CDCl$_3$, C$_6$F$_6$ δ −164.9) (**Right**) HPLC chromatogram of the crude product from the MTR reaction of CORO (5 mL min^{-1} flow rate, 100% heptane eluent, Cosmosil Buckyprep column (10 × 250 mm)). Numbers designate fractions separated.
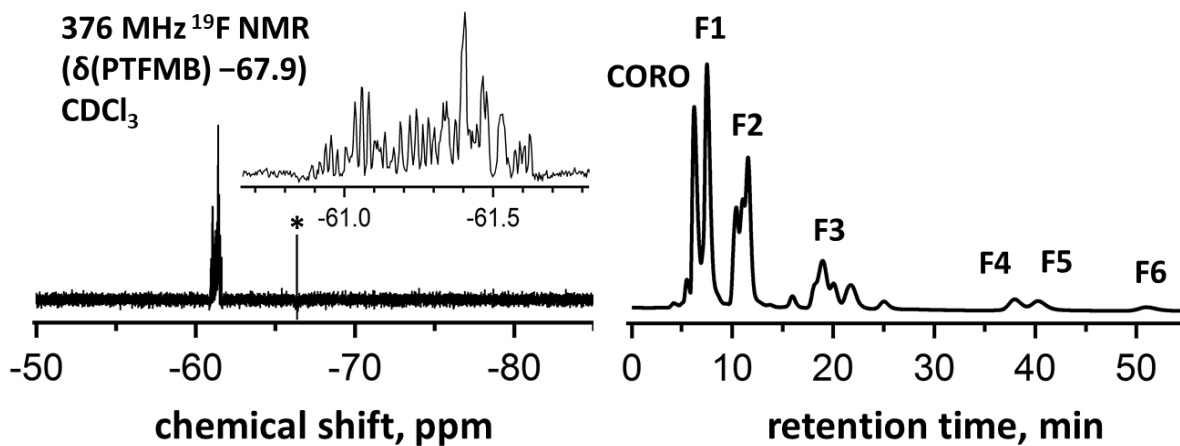
Figure 1-11. (**Left**) The ^{19}F NMR spectrum of the crude product mixture from the low pressure trifluoromethylation of CORO in the MTR. The chemical shift labeled with an asterisk is for the reference. (CDCl$_3$, *para*-trifluoromethylbenzene δ –67.9) (**Right**) HPLC chromatogram of the crude product from the low-pressure MTR reaction of CORO (Cosmosil Buckyprep column (10 × 250 mm), 100% toluene eluent, 5 mL min^{-1} flow rate). Numbers designate the fractions separated.

1.5. REFERENCES

(1)   Kreider, P.; Lipiński, W. High-Temperature Gas–Solid Reactions in Industrial Processes. *Reviews in Mineralogy and Geochemistry* **2018**, *84*, 499-514.

(2)   Boltalina, O. V.; Popov, A. A.; Kuvychko, I. V.; Shustova, N. B.; Strauss, S. H. Perfluoroalkylfullerenes. *Chem. Rev.* **2015**, *115*, 1051-1105.

(3)   Castro, K. P.; Clikeman, T. T.; DeWeerd, N. J.; Bukovsky, E. V.; Rippy, K. C.; Kuvychko, I. V.; Hou, G.-L.; Chen, Y.-S.; Wang, X.-B.; Strauss, S. H.; Boltalina, O. V. Incremental Tuning Up of Fluorous Phenazine Acceptors. *Chem. Eur. J.* **2016**, *22*, 3930-3936.

(4)   Clikeman, T. T.; Bukovsky, E. V.; Kuvychko, I. V.; San, L. K.; Deng, S. H. M.; Wang, X.-B.; Chen, Y.-S.; Strauss, S. H.; Boltalina, O. B. Poly(trifluoromethyl) azulenes: structure and acceptor properties. *Chem. Commun.* **2014**, *50*, 6263-6266.

(5)   DeWeerd, N. J.; Bukovsky, E. V.; Castro, K. P.; Kuvychko, I. V.; Popov, A. A.; Strauss, S. H.; Boltalina, O. V. Steric and electronic effects of CF_3 conformations in acene$(CF_3)_n$ derivatives. *J. Fluorine Chem.* **2019**, *221*, 1-7.

(6)   Kuvychko, I. V.; Castro, K. P.; Deng, S. H. M.; Wang, X.-B.; Strauss, S. H.; Boltalina, O. V. Taming Hot CF_3 Radicals: Incrementally Tuned Families of Polyarene Electron Acceptors for Air-Stable Molecular Optoelectronics. *Angew. Chem. Int. Ed.* **2013**, *52*, 4871-4874.

(7)   Kuvychko, I. V.; Spisak, S. N.; Chen, Y. S.; Popov, A. A.; Petrukhina, M. A.; Strauss, S. H.; Boltalina, O. V. A Buckybowl with a Lot of Potential: C_5-$C_{20}H_5(CF_3)_5$. *Angew. Chem. Int. Ed.* **2012**, *51*, 4939-4942.

(8)   Kuvychko, I. V.; Whitaker, J. B.; Larson, B. W.; Folsom, T. C.; Shustova, N. B.; Avdoshenko, S. M.; Chen, Y.-S.; Wen, H.; Wang, X.-B.; Dunsch, L. Substituent effects in a series of 1,7-$C_{60}(R_F)_2$ compounds (R_F= CF_3, C_2F_5, *n*-C_3F_7, *i*-C_3F_7, *n*-C_4F_9, *s*-C_4F_9, *n*-C_8F_{17}): electron affinities, reduction potentials and *E*(LUMO) values are not always correlated. *Chem. Sci.* **2012**, *3*, 1399–1407.

(9)   San, L. K.; Bukovsky, E. V.; Kuvychko, I. V.; Popov, A. A.; Strauss, S. H.; Boltalina, O. V. Single-Step Gas-Phase Polyperfluoroalkylation of Naphthalene Leads to Thermodynamic Products. *Chem. Eur. J.* **2014**, *20*, 4373-4379.

(10)   Rippy, K. C.; DeWeerd, N. J.; Kuvychko, I. V.; Chen, Y.-S.; Strauss, S. H.; Boltalina, O. V. Fluorination-Induced Evolution of Columnar Packing in Fluorous Triphenylenes and Benzotriphenylenes. *ChemPlusChem* **2018**, *83*, 1067-1077.

(11)   Romanova, N. A.; Papina, T. y. S.; Luk'yanova, V. A.; Buyanovskaya, A. G.; Varuschenko, R. M.; Druzhinina, A. I.; Goryunkov, A. A.; Markov, V. Y.; Panin, R. A.; Sidorov, L. N. S_6 Isomer of $C_{60}(CF_3)_{12}$: Synthesis, properties and thermodynamic functions. *J. Chem. Thermodyn.* **2013**, *66*, 59-64.

(12)   Ashby, M. F. *Materials and the Environment: Eco-Informed Material Choice, 2nd Ed.*; Butterworth-Heinemann: Waltham, MA, 2013.

(13)   Kumar, A.; Kashyap, K.; Hou, M. T.; Yeh, J. A. Strength Improvement of Glass Substrates by Using Surface Nanostructures. *Nanoscale Res. Lett.* **2016**, *11*, 256-256.

(14)   Barlow, P. On the Force Excited by Hydraulic Pressure in a Bramah Press; the Resisting Power of the Cylinder, and Rules for Computing the Thickness of Metal for Presses of Various Powers and Dimensions. *Trans. Inst. Civil Eng.* **1836**, *1*, 133-139.

(15)   Chang, Y. C.; Kuo, M. Y.; Chen, C. P.; Lu, H. F.; Chao, I. On the Air Stability of *n*-Channel Organic Field-Effect Transistors: A Theoretical Study of Adiabatic Electron Affinities of Organic Semiconductors. *J. Phys. Chem. C* **2010**, *114*, 11595-11601.

(16)   Babudri, F.; Farinola, G. M.; Naso, F.; Ragni, R. Fluorinated organic materials for electronic and optoelectronic applications: the role of the fluorine atom. *Chem. Commun.* **2007**, 1003-1022.

(17)   Ragni, R.; Punzi, A.; Babudri, F.; Farinola, G. M. Organic and Organometallic Fluorinated Materials for Electronics and Optoelectronics: A Survey on Recent Research. *Eur. J. Org. Chem.* **2018**, 3500-3519.

(18)   Kareev, I. E.; Kuvychko, I. V.; Popov, A. A.; Lebedkin, S. F.; Miller, S. M.; Anderson, O. P.; Strauss, S. H.; Boltalina, O. V. High-temperature synthesis of the surprisingly stable C_1-

$C_{70}(CF_3)_{10}$ isomer with a *para[7]-meta-para* ribbon of nine $C_6(CF_3)$(2 edge-sharing hexagons. *Angew. Chem. Int. Ed.* **2005**, *44*, 7984-7987.

(19) Shustova, N. B.; Strauss, S. H.; Boltalina, O. V. High-Yield Synthesis of a Single Asymmetric Isomer of $C_{70}(CF_3)_{10}$ by High-Temperature Radical Trifluoromethylation In *Efficient Preparation of Fluorine Compounds*; Roesky, H., Ed.; Wiley: New York, 2012, pp 447-449.

(20) Kuvychko, I. V.; Whitaker, J. B.; Larson, B. W.; Raguindin, R. S.; Suhr, K. J.; Strauss, S. H.; Boltalina, O. V. Pressure effect on heterogeneous trifluoromethylation of fullerenes and its application. *J. Fluorine Chem.* **2011**, *132*, 679-685.

(21) Kuvychko, I. V.; Strauss, S. H.; Boltalina, O. V. Solution-Phase Perfluoroalkylation of C_{60} Leads to Efficient and Selective Synthesis of Bis-Perfluoroalkylated Fullerenes. *J. Fluorine Chem.* **2012**, *143*, 103-108.

(22) Troyanov, S. I.; Dimitrov, A.; Kemnitz, E. Selective synthesis of a trifluoromethylated fullerene and the crystal structure of $C_{60}(CF_3)_{12}$. *Angew. Chem. Int. Ed.* **2006**, *45*, 1971-1974.

(23) Shustova, N. B.; Kareev, I. E.; Kuvychko, I. V.; Whitaker, J. B.; Lebedkin, S. F.; Popov, A. A.; Dunsch, L.; Chen, Y. S.; Seppelt, K.; Strauss, S. H.; Boltalina, O. V. High-temperature and photochemical syntheses of C_{60} and C_{70} fullerene derivatives with linear perfluoroalkyl chains. *J. Fluorine Chem.* **2010**, *131*, 1198–1212.

(24) Zhan, X.; Facchetti, A.; Barlow, S.; Marks, T. J.; Ratner, M. A.; Wasielewski, M. R.; Marder, S. R. Rylene and related diimides for organic electronics. *Adv. Mater.* **2011**, *23*, 268-284.

(25) Ling, M. M.; Erk, P.; Gomez, M.; Koenemann, M.; Locklin, J.; Bao, Z. Air-Stable *n*-Channel Organic Semiconductors Based on Perylene Diimide Derivatives without Strong Electron Withdrawing Groups. *Adv. Mater.* **2007**, *19*, 1123-1127.

(26) Huang, C.; Barlow, S.; Marder, S. R. Perylene-3,4,9,10-tetracarboxylic Acid Diimides: Synthesis, Physical Properties, and Use in Organic Electronics. *J. Org. Chem.* **2011**, *76*, 2386-2407.

(27) Clikeman, T. T.; Bukovsky, E. V.; Wang, X.-B.; Chen, Y.-S.; Rumbles, G.; Strauss, S. H.; Boltalina, O. V. Core Perylene Diimide Designs via Direct Bay- and ortho-

(Poly)trifluoromethylation: Synthesis, Isolation, X-ray Structures, Optical and Electronic Properties. *Eur. J. Org. Chem.* **2015**, 6641-6654.

(28) van de Craats, A. M.; Warman, J. M.; Fechtenkötter, A.; Brand, J. D.; Harbison, M. A.; Müllen, K. Record charge carrier mobility in a room-temperature discotic liquid-crystalline derivative of hexabenzocoronene. *Adv. Mater.* **1999**, *11*, 1469-1472.

(29) Ito, S.; Wehmeier, M.; Brand, J. D.; Kübel, C.; Epsch, R.; Rabe, J. P.; Müllen, K. Synthesis and self-assembly of functionalized hexa-peri-hexabenzocoronenes. *Chem. Eur. J.* **2000**, *6*, 4327-4342.

(30) Zhang, C.; Shi, K.; Cai, K.; Xie, J.; Lei, T.; Yan, Q.; Wang, J.-Y.; Pei, J.; Zhao, D. Cyano- and chloro-substituted coronene diimides as solution-processable electron-transporting semiconductors. *Chem. Commun.* **2015**, *51*, 7144-7147.

(31) Rieger, R.; Kastler, M.; Enkelmann, V.; Müllen, K. Entry to Coronene Chemistry—Making Large Electron Donors and Acceptors. *Chem. Eur. J.* **2008**, *14*, 6322-6325.

(32) Shen, H.-C.; Tang, J.-M.; Chang, H.-K.; Yang, C.-W.; Liu, R.-S. Short and Efficient Synthesis of Coronene Derivatives via Ruthenium-Catalyzed Benzannulation Protocol. *J. Org. Chem.* **2005**, *70*, 10113-10116.

(33) Kasunic, K. J. *Optomechanical Systems Engineering*; Wiley: Hoboken, NJ, 2015.

(34) Association, B. S. S. ASM Specialty Handbook 'Stainless Steels', 2018. Melting temperature ranges for stainless steels

(35) Apostolopoulos, C. A.; Michalopoulos, D. Effect of corrosion on mass loss, and high and low cycle fatigue of reinforcing steel. *J. Mater. Eng. Perform.* **2006**, *15*, 742-749.

(36) Ochar, D. R.; Vermilyea, D. A. Corrosion of Steel by Iodine. *Corrosion* **1968**, *24*, 368-368.

(37) Metals, U. P. *Stainless 316, 316L, 317, 317L.*

(38) Schneider, W. F.; Wallington, T. J.; Huie, R. E. Energetics and Mechanism of Decomposition of CF_3OH. *J. Phys. Chem.* **1996**, *100*, 6097-6103.

(39) Kloeter, G.; Seppelt, K. Trifluoromethanol (CF_3OH) and trifluoromethylamine (CF_3NH_2). *J. Am. Chem. Soc.* **1979**, *101*, 347-349.

(40)   Dorozhkin, E. I.; Ignateva, D. V.; Tamm, N. B.; Goryunkov, A. A.; Khavrel, P. A.; Ioffe, I. N.; Popov, A. A.; Kuvychko, I. V.; Streletskiy, A. V.; Markov, V. Y.; Spandl, J.; Strauss, S. H.; Boltalina, O. V. Synthesis, Characterization, and Theoretical Study of Stable Isomers of $C_{70}(CF_3)_n$ (n = 2, 4, 6, 8, 10). *Chem. Eur. J.* **2006**, *12*, 3876-3889.

(41)   Song, L.; Wellman, A. D.; Yao, H.; Adcock, J. Electron capture atmospheric pressure photoionization mass spectrometry: analysis of fullerenes, perfluorinated compounds, and pentafluorobenzyl derivatives. *Rapid Commun. Mass Spectrom.* **2007**, *21*, 1343-1351.

(42)   Rippy, K. C.; Bukovsky, E. V.; Clikeman, T. T.; Chen, Y.-S.; Hou, G.-L.; Wang, X.-B.; Popov, A. A.; Boltalina, O. V.; Strauss, S. H. Copper Causes Regiospecific Formation of C4F8-Containing Six-Membered Rings and their Defluorination/Aromatization to C4F4-Containing Rings in Triphenylene/1,4-C4F8I2 Reactions. *Chem. Eur. J.* **2016**, *22*, 874-877.

CHAPTER 2

TRIFLUOROMETHYLATION OF CORONENE AND THE NATURE OF RIM BONDS

2.1   INTRODUCTION AND JUSTIFICATION

Coronene, $C_{24}H_{12}$, (CORO), is a D_{6h} polycyclic aromatic hydrocarbon (PAH). As shown in Figure 2-1, it is also referred to as [6]circulene as it is composed of six fused 6-membered aromatic rings surrounding a central hexagon and is considered a useful model for graphene.[1,2] It is a component of the mineral karpatite, and as such, is notable as the only large PAH which occurs naturally in large, pure deposits.[3] It has a large, planar molecular structure and intriguing physical properties, which remain a subject of active debate despite having been studied by astronomers,[4-7] geologists,[3,8,9] theorists,[10,11] environmentalists,[12] physicists,[13] material scientists,[14] and chemists for many decades. In particular, the nature of the rim bonds of coronene (i.e., the six bonds forming the outer periphery of the molecule) remains an active area of interest.[11] These bonds are classically considered to be aromatic, despite CORO not following Huckel's 4n+2 rule. An alternative hypothesis is that the rim bonds have more isolated double bond character, a possibility suggested by the fact that the six rim bonds are shorter than the core bonds, 1.36 Å compared to the accepted 1.4 Å bond distance for idealized C–C aromatic bonds making them more similar in length to idealized C–C double bonds, 1.34 Å.[11,15,16] Calculations based on experimental data by Boldyrev and Fedik support this claim suggesting a bonding model where the outer six rim bonds have more double bond character than the inner core bonds which retain aromatic behavior.[11] This model would support coronene as a molecule with the ability to undergo both electrophilic substitution and addition but after extensive searching there are no examples of CORO undergoing an addition reaction.[17,18] Resolving this question, as well as gaining understanding of CORO's reactivity, has become increasingly important as graphene's potential to revolutionize modern electronics has become clear.[19] Researchers have therefore intensified studies of CORO, both as a model compound, aka a small fragment of graphene,[20,21] and as a precursor for multifunctional electronic materials.[22,23]

In these studies, chemical derivatives of CORO are prepared by either direct functionalization of the CORO substrate or a "bottom-up" approach involving the use of small aromatic building blocks for assembling the desired CORO derivative. The latter approach is generally favored by synthetic chemists, as it allows a rational design of the molecular structures with functional groups in specific locations. In fact, CORO itself was first synthesized in 1932 from a complex anthracene derivative by Scholl, Meyer et al.[24] but the synthesis was laborious and did not result in a measurable yield. The first synthesis of CORO with a reported yield was via a bottom-up approach by Newman et. al. from 7-methyl-1-tetralone in 1940 resulting in a < 1% yield from a six-step method.[25] Since then improvements have been made to the bottom-up synthetic approach largely aided by the ready availability of larger PAH starting materials such as perylene and triphenylene. Numerous CORO derivatives and larger CORO containing PAHs have been prepared using this "bottom-up" approach.[26-32] Such syntheses often involve metal-catalyzed (benzo)annulation of smaller PAHs and results in products including hexabenzocoronene and related compounds,[33,34] CORO imides,[23] methoxylated derivatives and others.[35] The efficiency of these syntheses depends, among other factors, on the availability of the organic precursors. For example, even for the synthesis of the simple monochlorocoronene, three reaction steps were required to prepare a dialkyne functionalized monochlorodihydroanthracene from commercially available anthraquinone, followed by a [Ru]-catalyzed benzocyclization.[36,37]

In contrast, chemical reactions that produce functionalized CORO via direct hydrogen substitution on the coronene core are relatively scarce. Due to its large size and flat shape, CORO has relatively low solubility in organic solvents (e.g., 2.5 mg mL^{-1} in hot toluene) which makes solution-based reactions more difficult with CORO as a substrate than analogous reactions with smaller aromatic molecules.[38] Unless fully substituted products are targeted, the possibility of the formation of partially substituted products (and hence, multiple isomers and compositions) complicates the problem further as it necessitates the development of efficient separation procedures.[39]

Among the few examples of such direct substitutions of CORO, facile nucleophilic substitutions of $C_{24}Cl_{12}$ have been shown to afford fully substituted CORO derivatives.[40] This approach has been used to make several CORO derivatives,[27] including an intriguing sulfur-containing CORO derivative, sulflower.[41] Additionally, the monochloro- substituted coronene mentioned previously was reported as the product of the reaction of CORO and $Cl_{2(g)}$ in a carbon tetrachloride solution in the presence of $AlCl_3$.[42] A thorough literature search has indicated that no fluoro- or perfluoroalkyl substituted CORO derivatives have been made using a direct substitution route prior to this work.

In this work, trifluoromethylation of CORO has been studied for the first time using $CF_3I(g)$ as the trifluoromethylating reagent. While selectivity is difficult to achieve in these reactions (a few exceptions notwithstanding[43]) the typical distribution of the products is partially controlled thermodynamically, i.e., the most abundant products observed experimentally were shown to be of the lowest relative energy according to DFT calculations. Here, we analyze the results of the gas-phase trifluoromethylation of CORO to determine which $CORO(CF_3)_n$ molecules are predicted as the most thermodynamically stable, according to the DFT calculations, and what the maximum degree of CF_3 substitution can be expected considering the bulkiness of the CF_3 groups. We report spectroscopic evidence for the synthesis and characterization of five new trifluoromethylated COROs and in the case of a symmetric $CORO(CF_3)_4$ derivative, a crystal structure showing a high degree of $\pi-\pi$ overlap.

Furthermore, we report the alteration to the CORO aromatic core resulting from addition, rather than substitution of CF_3 groups which results in $C(sp^3)$ atoms. In these cases, the aromatic core shrinks. The resulting fragment can be described as a substituted derivative of a smaller PAH, such as benzo[ghi]perylene in the case of dihydrocoronene derivatives. This unique reactivity, which has been theoretically considered but not previously been observed, yields insight into the fundamental nature of the rim bonds of CORO. In total five unique $H_2CORO(CF_3)_n$ derivatives were characterized spectroscopically and four by X-ray crystallography.

2.2.   RESULTS AND DISCUSSION

2.2.1.   CORO trifluoromethylation reactions

Multiple trifluoromethylation reactions were performed using CF_3I and CORO. In total, three different reactors were used for these reactions: sealed glass ampules, (AMP), the metal tube reactor, (MTR), and the gradient temperature gas-solid reactor, (GTGS) resulting in different products and product distributions.

CORO trifluoromethylation in glass ampules. Three reactions in glass ampules were performed, AMP-1, AMP-2, and AMP-3, the details of which are given in Table 2-1. These reactions were performed by Dr. Igor V. Kuvychko. They utilized an excess of $CF_3I(g)$ to facilitate exhaustive substitution of hydrogens for CF_3 groups to target the highest possible degree of substitution. These reactions resulted in low conversion of the CORO substrate, and only trace amounts of soluble products were recovered. The mass spectrum for the soluble crude material from AMP-1 is shown in Figure 2-2. Interestingly, the trifluoromethylated products that were produced appeared to have extra protons aka *m/z* values two, three, or five mass units higher than expected. While protonation is a viable route for generation of positive ions in the positive mode, it is uncommon when negatively charged species of $PAH(R_F)_n$ compounds are studied. Thus, ruling out that the addition of hydrogens occurred in the ion source of the mass spectrometer, one may tentatively suggest that addition of CF_3 groups requires the formation of $C(sp^3)$ atoms. This results in a modification of the aromatic core of CORO, leaving a smaller core which can be described as a smaller PAH.

Reaction AMP-1 was carried out at 360 °C for 24 h and resulted in the recovery of a very small amount of soluble product and insoluble black char, attributed to degradation. This material was analyzed spectroscopically. The ^1H and ^{19}F NMR spectra were complex with a large number of overlapping signals, indicating low selectivity. However, three distinct regions in the ^{19}F NMR spectrum were noted: δ −55, −60, and −62, indicating three distinct chemical environments of CF_3 groups. Negative-ion electrospray (NI-ESI) mass spectrometry showed several intense peaks in

46

the mass region of 500–800 Da. These peaks are attributed to anionic species described by the general formula $C_{24}H_{n+x}(CF_3)_{12-n}$, ($n = 0$–4; $x = 2, 3, 5$) i.e., some of the CORO rim bonds underwent radical addition.

Reaction AMP-2 was carried out at 275 °C, a lower temperature than AMP-1, to avoid degradation. However, no soluble product was recovered, and little char was observed, indicating that the reaction did not take place at this temperature.

Reaction AMP-3 was carried out at 300 °C, a slightly higher temperature than AMP-2. The reaction time was 10 minutes, to avoid degradation. A small amount of the soluble material collected after the reaction was analyzed by NMR spectroscopy and mass spectrometry. The low conversion of CORO was evidenced by the dominant singlet in the ^{1}H NMR spectrum (δ 8.85). A low intensity ^{19}F NMR spectrum showed weak broad bands with chemical shifts around δ −55 and −60.

The NI-ESI mass spectrometry analysis of the crude product from reaction AMP-3 showed several intense signals with mass separations of 68 Da, consistent with substitution of CF_3 radicals. However, the absolute m/z values do not correspond to the $C_{24}H_{12-n}(CF_3)_n$ formula as expected from the substitution products. Not only do they have 2–5 Da higher mass than expected, but also the mass range extends much further than the m/z of 708 for $C_{24}H_6(CF_3)_6$ species, the largest predicted molecule by DFT calculations which are discussed in Section 2.2.3. Analysis of the isotope distributions allowed for the assignment of the anionic species in the mass spectrum as shown in Figure 2-2. Unexpectedly, the heaviest abundant peak at m/z 1121 corresponds to the species with the formula $C_{24}H_5(CF_3)_{12}^-$, which is most likely formed by a proton detachment from the neutral molecule $C_{24}H_6(CF_3)_{12}$. Under the assumption that the CORO core does not fragment during the reaction, the author proposes a likely explanation for the presence of such $C_{24}H_6(CF_3)_{12}$ species among the products: concurrent with the expected substitution process (one hydrogen exchanged for one CF_3 group), the addition of CF_3 groups has also taken place, producing $C(sp^3)$ atoms. The proposed elementary steps of such a process are shown in Figure 2-3. First, a reaction

between CORO (**1**) and a CF_3 radical leads to a radical adduct (**2**). Then, another CF_3 radical attacks the reactive CORO-CF_3 radical (**2**), with two possible ways for the radicals to annihilate: (i) by removing the hydrogen from the $C(sp^3)$ atom to form a closed-shell CORO(CF_3) species (**3**) by eliminating a CF_3H molecule, and (ii) to attach to the adjacent carbon on the rim and hence make the second $C(sp^3)$ atom resulting in the addition product $H_2CORO(CF_3)_2$ (**4**) with the reduced π system of benzo[ghi]perylene. Apparently, both these processes take place in reaction AMP-3, to generate partially substituted and partially dearomatized species such as the discussed $C_{24}H_6(CF_3)_{12}$. Other high-intensity anions in the mass spectrum were assigned to the species with $n(CF_3)$ = 8, 9, 10, and 11. The molecular precursors for these species were determined as follows: $C_{24}H_6(CF_3)_8$, $C_{24}H_7(CF_3)_9$ $C_{24}H_8(CF_3)_{10}$ and $C_{24}H_7(CF_3)_{11}$. This suggests that in all these species the CORO aromatic core shrinks possibly to analogs of benzo[ghi]perylene, benzopyrene or triphenylene, respectively.

The transformation of a $C(sp^2)$–$C(sp^2)$ bond into a $C(sp^3)$–$C(sp^3)$ bond had not been observed in any of the other non-linear PAH systems studied by the Strauss-Boltalina Lab previously. Noteworthy, characterization of the more common de-aromatization of a central ring on linear PAHs, such as acridine and tetracene had been reported by the author's lab-mates in their Ph.D. theses.[44,45]

CORO trifluoromethylation in the metal tube reactor. In order to explore the reactivity of these H_2CORO compounds further reactions were performed using the previously discussed metal tube reactor, MTR, which was described in detail in Chapter 1 Sections 1.2.1. and 1.2.2.[46] This reactor has several advantages over the glass ampule system. A 20-fold higher pressure can be employed without compromising safety, and scaleup is simple and straightforward, in contrast to sealed glass ampoules. Additionally, temperatures above the glass softening temperature can be utilized in the MTR. These factors allow for a targeted synthesis of these H_2CORO derivatives and if many isomers were produced it was hoped sufficient material could be produced to properly analyze and characterize the products.

Reaction MTR-HP was performed on a larger scale than the glass ampule reactions, AMP-1 through 3, (50 mg vs 5–15.8 mg CORO starting material), at a higher temperature (450 °C vs 275–360 °C) and with a larger excess of $CF_3I(g)$ (17200 Torr vs 600–1000 Torr) than the glass ampule reactions. MTR-HP also utilized Cu metal as a promoter. It yielded a sufficient amount of soluble product that was subjected to a detailed analysis by NI-ESI MS and NMR spectroscopy. The product mixture was separated by HPLC (High Performance Liquid Chromatography) using a Cosmosil Buckyprep semipreparative column with 100% heptane as the eluent. While the NMR analysis indicated the presence of many compounds, the HPLC chromatogram revealed only six major fractions with excellent baseline resolution of a minute or more, as shown in Figure 2-4. The NI-ESI mass spectrum showed a set of peaks separated by 68 Da, in accordance with the introduction of CF_3 groups in place of hydrogens. Assignment of the molecular compositions of the most abundant peaks resulted in the following general formula for this series: $C_{24}H_{12-m+x}(CF_3)_m$, where m = 7–10, and x = 1 and 2. Apparently, similar to reactions AMP-1 and AMP-3, reaction MTR-HP proceeds via both the substitution and addition of CF_3 radicals (see Figure 2-3 for the proposed reaction pathway).

The MTR-HP reaction has higher efficiency than the reactions in glass ampules: (i) significantly higher product yield; (ii) quantitative conversion; (iii) fewer products; and (iv) less degradation. The crude product was separated by HPLC, which resulted in isolation and identification of the major reaction products (designated as fractions F0–F5 in Figure 2-4). Except for fraction F0, five fractions were found to be composed of mostly one compound each (full characterization is given in the supplemental section for this chapter, Appendix A), and fractions F2, F4, and F5 did not require re-purification after one stage of HPLC processing as they contained 95%+ pure single compounds. The NI-ESI MS analysis showed that fractions F2 and F3 contain compounds with formula $C_{24}H_6(CF_3)_8$, whereas fractions F1, F4, and F5 contain compounds with formula $C_{24}H_7(CF_3)_7$, fraction F0 had a range of products $C_{24}H_{7-8}(CF_3)_{9-10,}$ in agreement with the interpretation of the mass spectra.

For the four new compounds isolated from fractions F2–F5, single crystals suitable for X-ray crystallography were grown from organic solutions, and crystallographic data (discussed in Section 2.2.2.) corroborated the proposed molecular compositions based on the MS data.

As expected for PAHs with different π structures, $H_2CORO(CF_3)_n$ derivatives possess a different UV-vis band structure from $CORO(CF_3)_n$ compounds, see Figure S2-32. The most characteristic differences are the new absorption bands in the $H_2CORO(CF_3)_n$ spectra between 325–425 nm. These bands are in good agreement with the UV-vis spectrum of benzo[ghi]perylene and arise from the change of the CORO core to the perylene core.[47]

In addition to the change in electronic band structure, the solubility of the H_2CORO derivatives also increased. It was found that the H_2CORO derivatives were readily soluble in nonpolar alkane solvents. In fact, weak (*ie.* relatively non-polar and non-aromatic) eluent conditions were required to separate the $H_2CORO(CF_3)_n$ isomers. The $H_2CORO(CF_3)_n$ derivatives were readily soluble in heptane and no issues related to insolubility were observed. This is in stark contrast to CORO, which has virtually no solubility in alkane solvents. For comparison unfunctionalized benzo[ghi]perylene is 2.5 times more soluble in heptane than CORO.[48] The difference in solubility of the $H_2CORO(CF_3)_n$ derivatives is believed to be due to the significantly weaker interactions between PAH cores, when compared to CORO. By adding a large number of CF_3 groups (≥ 7), the H_2CORO derivatives π–π interactions are weakened as evidenced by the minimum π–π overlap distances, ≥ 4 Å recorded from X-ray structures of the four isolated isomers. These long π–π distances appear to be due to steric effects associated with the trifluoromethyl groups on both the $C(sp^2)$ and $C(sp^3)$ atoms.

A final piece of evidence to confirm the presence of the $C(sp^3)$ bonded protons was to identify the associated chemical shifts in the ^1H NMR spectra. The NMR spectra for all of the H_2CORO derivatives are shown in Appendix A, figures S2-8 through S2-14. In most cases, low baseline resolution is observed, attributed to the small quantity, (≤ 3 mg) of pure compound isolated.

Using the X-ray structures collected and comparing the NMR spectra of all the isolated isomers several unique chemical shift regions can be identified and reliably assigned in both the ^{1}H and ^{19}F NMR spectra. To show a typical example, the ^{1}H and ^{19}F NMR spectra of H_2CORO-8-1, are shown in Figure 2-5 and the chemical shifts which can be assigned will be discussed. These assignments are consistent with the other H_2CORO(CF$_3$)$_n$ compounds.

The ^{1}H NMR spectrum in Figure 2-5 can be divided into two regions, the aromatic region, with δ values between 9–10, and the relevant aliphatic region, δ values between 5–6. The more shielded range shows the resonances for the allylic C(sp^3) bonded protons which in the case of H_2CORO-8-1 appear at 5.3 and 5.1 ppm. These resonances are significantly deshielded compared to typical allylic protons, 1.5–3.0 ppm,[48] due to the strong electron withdrawing effect of the trifluoromethyl group. In this case, any J_{HH} through bond coupling to the adjacent C(sp^3) bonded proton is not observable, however due to the small amount of isolated material, it may simply be unresolved. In all cases, there is observable J_{HF} spin-spin coupling between the C(sp^3) bonded protons and fluorines on the C(sp^3) bonded trifluoromethyl group with an average coupling constant of 8 Hz (±1 Hz). This spin-spin coupling constant is also observed in the corresponding ^{19}F resonances in the ^{19}F NMR spectrum. This ^{1}H^{19}F coupling is supported by simulation experiments shown in Figure 2-6. All of the coupling constants recorded for both the ^{1}H and ^{19}F resonances for both H_2CORO-8-1 and the other three isolated H_2CORO derivatives are shown in tables S2-4 and S2-5. The second region of chemical shifts have been assigned to the C(sp^2) protons. Excluding the proton bonded to C7, labeled H$_e$ in Figure 2-5, none of the chemical shifts could be definitively assigned to specific protons, however the remaining singlets were still identified ambiguously as belonging to one of the three remaining C(sp^2) bonded protons. The C7 proton was assigned by comparing the structures of all the other H_2CORO(CF$_3$)$_n$ compounds and recognizing the C7 or C8 proton was common to all isomers and of all the ^{1}H NMR spectra only the chemical shift at 9.3 ppm was common to every spectrum. The C(sp^2) bonded proton resonances are deshielded compared to the typical range and in fact are more similar to carboxylic acid protons.[48] However,

the monosubsituted 1-chlorocoronene compound's ^{1}H NMR spectrum shows similar deshielded chemical shifts and therefor supports the assignment of this region to the $C(sp^2)$ bonded protons.[36]

The ^{19}F NMR chemical shifts were also assigned for H_2CORO-8-1, shown in Figure 2-5. Generally, there are four unique chemical shift regions in the fluorine spectra of the H_2CORO(CF_3)$_n$ compounds. The region between δ values −60 and −65 contains resonances from CF_3 groups that are not adjacent to the $C(sp^3)$ region of the molecule and not *ortho-* to any other CF_3 groups. This chemical shift region is the one most commonly observed for the CF_3 groups attached to PAHs and contains all of the singlet resonances.[49]

The region between δ values −70 and −72 has been assigned to resonances arising from the CF_3 groups bonded to a $C(sp^3)$ atom. The CF_3 groups bonded to $C(sp^3)$ atoms exhibit complex J_{FF} coupling and J_{FH} coupling to their neighbors resulting in apparent pentets or multiplets. The complex coupling interactions were deconvoluted by measuring the shortest F···F distances in the H_2CORO-8-1 X-ray structure. That analysis is shown in Figure 2-6. Additionally, the coupling constants were estimated using the Mnova NMR suite. The coupling constants found that most closely match the experimental data are shown in Figure 2-6. The J_{FF} spin-spin coupling is between $C(sp^3)$ bonded CF_3 groups and $C(sp^2)$ bonded CF_3 groups. The simulations as well as the F···F distance analysis show that there is no coupling to the adjacent $C(sp^3)$ bonded CF_3 fluorines. Lastly, in the case of H_2CORO-8-1, the assignment of the $C(sp^3)$ bonded CF_3 fluorine resonances could be made unambiguously due to the additional interaction between the C1 and C3 bonded CF_3 groups. The solid-state structure shows that the C3 and C4 bonded CF_3 groups are twisted out of the plane of the molecule sufficiently to result in an F···F interaction, distance 2.879 Å. This results in the C1 bonded CF_3 group coupling to two different CF_3 groups whereas the C2 bonded CF_3 group only interacts with one other CF_3. This interaction must also occur in solution giving rise to the more complex multiplet for the resonance labeled a in Figure 2-5 and Figure 2-6.

The δ values between −52 and −54 correspond to *ortho-* CF_3 groups. The *ortho-* spin-spin coupled CF_3 groups have J_{FF} values of 16 Hz and appear as either pairs of quartets or in the case

of H_2CORO-8-1 as a quartet, labeled g, and an unresolved broad envelope multiplet, labeled h, due to the added through space coupling to the CF_3 group labeled a. These chemical shifts are the most deshielded of the various chemical shift regions associated with the $H_2CORO(CF_3)_n$ molecules due to the directing effects of the two strongly electron withdrawing groups being adjacent to each other. The simulation experiments most closely resembled the h multiplet when the J_{FF} coupling between h and g was 19 Hz and is listed as such in Figure 2-6.

The region with a δ value between −60 and −61 has been assigned to CF_3 groups adjacent to the $C(sp^3)$ portion of the H_2CORO molecule. In Figure 2-5, the resonance related to the CF_3 group in this chemical environment is labeled c. The CF_3 group labeled h would also be included in this category for H_2CORO-8-1 however it is an exception to this assignment because the directing effects from the *ortho-* CF_3 group g result in h being more deshielded than the typical region, δ −53.

Lastly, as was shown for the C7 and C8 positions in ^1H NMR, the C7 and C8 positions are significant in ^{19}F NMR as well. This position opposite the $C(sp^3)$ region of the molecule is substituted by a CF_3 group in all four of the isolated $H_2CORO(CF_3)_n$ molecules and is consistently observed at −61 ppm as a singlet resulting in a more deshielded chemical shift than any of the other CF_3 groups which are not spin-spin coupled.

This high-pressure reaction in the MTR yielded interesting products which underwent both radical addition and substitution. The reaction yielded significant quantities of new trifluoromethylated dihydrocoronene derivatives which allowed for their structural and electrochemical properties to be characterized. The MTR-HP reaction only produced H_2CORO derivatives. The $CORO(CF_3)_n$ compounds were the original intent of this study and are an important reference point for explaining the formation of the H_2CORO products. A new synthetic method was developed in order to target these products.

CORO trifluoromethylation in the gradient temperature of the gas-solid reactor. With the goal of optimizing CORO trifluoromethylation reactions towards substitution and not addition, a different reactor was used, the Gradient-Temperature Gas-Solid (GTGS) reactor, which had been developed by previous members of the Stauss-Boltalina Lab.[50] It was hypothesized that by allowing the $CORO(CF_3)_n$ compounds to sublime away from the hot-zone, minimal $C(sp^3)$ formation would occur leaving the desired compounds intact. There are multiple advantages to using the GTGS reactor for these reactions. The size of the hot-zone can be varied if needed, to control the residence time of reacting species. The reaction vessel, a transparent quartz thimble, allows visual observation of the changes occurring during the synthesis (e.g., condensation of the volatile products, formation of I_2).

A series of reactions, GTGS-1 through GTGS-6 were carried out under varying experimental conditions as listed in Table 2-1. The $CF_3I(g)$ pressure was varied from 200–700 Torr, reaction time from 1.5–6 hours, varying amounts of starting material, CORO, and amounts of Cu powder were also used. It was found that sublimation of the solid from the reaction zone began almost immediately after the quartz reactor, charged with the reagents, was brought into contact with the hotplate which was preheated. The product was collected by washing the reactor with dichloromethane, dried and then re-dissolved and analyzed by NMR spectroscopy, NI-ESI MS, and separated by HPLC. It was found that a lower $CF_3I(g)$ pressure (reaction GTGS-1) was detrimental to the conversion of CORO, and even at higher pressures of 700 Torr, the conversion into $CORO(CF_3)_n$ was low, most likely due to the escape of CORO to the cold-zone of the reactor by sublimation, prior to CORO's interaction with the CF_3 radicals. By repeating the reaction (one and two times, reactions GTGS-2 and GTGS-3, respectively) with the product collected after the first step of the reaction, the conversion of CORO and the average number of CF_3 substitutions was increased, as evidenced by spectroscopic analyses and HPLC, see Figure S2-23. Addition of Cu powder in these reactions was beneficial, as can be evidenced by comparison of reaction

GTGS-5 (without Cu) with GTGS-2 through GTGS-4, where excess Cu powder was used (see Table 2-1). To determine the molecular compositions of the products, NI-ESI MS was used.

The anionic signals were much weaker than in the mass spectra of AMP-3 or MTR-HP products, and to improve signal intensity the reducing agent TDAE (tetrakis (dimethylamino) ethylene) was added to the solution to ionize neutral species. This revealed m/z values that correspond to the masses of $CORO(CF_3)_{4-5}$. The ^1H and ^{19}F NMR spectra showed a multitude of fluorine and proton resonances where no adjacent CF_3 groups were detected meaning that all of the fluorine signals are singlets. This result suggested that adjacent CF_3 groups were not favored. This conclusion is also in agreement with the DFT calculations which were performed and are discussed in Section 2.2.3. These reactions resulted in six isolable $CORO(CF_3)_n$ compounds, but the isolated yield of these compounds was low, see Table S2-8 for yields. To target higher substitution products selectively glass ampule reactions were preformed using the isolated fractions of $CORO(CF_3)_n$ products.

$CORO(CF_3)_n$ trifluoromethylation in glass ampules. Ampule reactions using underivatized CORO were largely unsuccessful, see Table 2-1, AMP-1 through AMP-3. However, it is possible that a more activated CORO i.e. a previously trifluoromethylated CORO molecule may be a better candidate for further trifluoromethylation in AMP reactions. The results from AMP-1 seemed to suggest this. The crude material from GTGS-6, composed of 20+% residual CORO as well as a mixture of other products, was loaded into an ampule charged with 600 Torr of $CF_3I(g)$. This resulted in a unique distribution of products with the largest concentration being CORO-4 isomers based on HPLC peak area and was repeated with a sample of the crude material from G/A-1 resulting in predominantly CORO-5 isomers, see Table 2-1 and Figure 2-7 where the HPLC chromatograms of the consecutive reactions are shown. This level of control over the product distribution was not observed in the GTGS reactions and it is noteworthy that the best reaction conditions relied on a combination of both methods. Interestingly, the ^{19}F NMR spectrum does not indicate the presence of a CORO-6-1 isomer which would have been a highly symmetric molecule,

55

D_{6h} symmetry. This molecule should have been easily detected, with its six symmetric CF_3 groups resulting in 18 identical fluorines. The NMR spectra are shown in Figure S2-29.

The absence of the CORO-6-1 isomer was puzzling. Therefore, experiments to synthesize CORO-6-1 in any quantity were performed by using an isolated fraction of a mixture of CORO-3 and CORO-4 isomers as the starting material in a GTGS reaction. The crude product from these reactions was analyzed by NI-ESI mass spectroscopy, see Figure S2-25. A parent mass for the CORO-6-1 isomer was not observed after the reaction, however an ion for CORO-6$^-$ +1 m/z, believed to be [CORO-6+H], was observed as well as a signal for a dihydrocoronene derivative with seven CF_3 groups and one missing proton apparently lost during ionization. This evidence supports the argument that formation of the non-aromatic portion of the molecule is more favorable than the formation of the CORO-6-1 isomer.

Karpatite trifluoromethylation in the gradient temperature gas-solid reactor. As was previously stated in Section 2.1., CORO is one of the only PAHs that occurs naturally in a pure form, in the mineral karpatite. By using karpatite as the source of the CORO starting material it was hoped that the predominantly quartz matrix[3] around the CORO material would increase the time that the CORO material spent in the hot-zone, dwell time, either through coordination to the crystalline CORO or by increasing the path length for the CORO material to travel. By increasing the dwell time of the CORO material in the hot-zone the product distribution should be predominantly $CORO(CF_3)_n$ products with a high degree of substitution.

To test if the reactivity of CORO inside the karpatite matrix is different than the commercial CORO sample the ROCK-1 reaction was performed. The HPLC chromatogram of that reaction is shown in Figure S2-26. This reaction shows a large bias for CORO-5 isomers: 47% by HPLC peak area of the total crude material (see Table 2-1). It was also observed that the apparent rate of CORO leaving the hot-zone was low compared to commercial CORO samples. The rate could be observed qualitatively in the GTGS reactions either by the accumulation of material outside the hot-zone or at higher temperatures as a yellow gas rising out of the hot-zone. This apparent slower rate means

56

the material remained in the hot-zone longer and explains the relative increase in CORO-4 and CORO-5 isomers.

To confirm slower sublimation, TGA experiments were performed to compare the rate of sublimation between the commercial and mineral samples. The thermograms are shown in Figures S2-27 and S2-28. In both cases sublimation is evident at 200 °C; however, in the karpatite sample the rate of mass loss is less. The amount of CORO in the mineral sample is not known so more quantitative analysis is not possible. The author also tested the rate of sublimation of CORO crystals which were meticulously collected from the mineral sample. The thermogram for these crystals matched the thermogram profile of the commercial CORO sample showing the difference in the rate of mass loss was due to the CORO material being in contact with the karpatite matrix and does not have to do with the difference in the phase of the CORO starting material since the karpatite material is crystalline and the commercial sample is more amorphous.

2.2.2. X-ray structures of CORO(CF$_3$)$_n$ and H$_2$CORO(CF$_3$)$_n$ compounds

After multiple reactions with multiple reactors a total of 11 CORO and H$_2$CORO trifluoromethyl derivatives were isolated and characterized, see Figure 2-8 and Figure 2-9. It should be noted this number does not take into account the stereochemistry of the H$_2$CORO(CF$_3$)$_n$ compounds. Of those 11 compounds five were characterized by X-ray crystallography. Using the structural confirmation for those compounds, the NMR chemical shifts and mass spectrometry interpretations were confirmed. The NMR spectra for the isolated H$_2$CORO(CF$_3$)$_n$ isomers were assigned where possible and where a determination could not be made reliably, the possible options were shown, see figures S2-8 through S2-14. Of the CORO(CF$_3$)$_n$ compounds, X-ray quality crystals were grown for CORO-4-1 and the dataset that was collected was solved allowing for an analysis of its solid-state properties. All five of the crystal structures were analyzed and analysis of their unique packing motifs are discussed below. The IUPAC numbering schemes of coronene (CORO) and 1,2-dihydrocoronene (H$_2$CORO) are shown in Figure S2-1. All five structures exhibited disorder of one type or another. Modeling of the disorder is discussed in detail

in the supporting information. Bond distances and angles in the disordered portions of the molecules will not be discussed.

Structure of CORO-4-1. A thermal ellipsoid drawing of this molecule is shown in Figure 2-8. The molecule has D_{4h} symmetry. The C and H atoms are rigorously co-planar. The molecules are arranged in stacks parallel to the crystallographic c axis so that every other molecule is rotated 25° with respect to its nearest neighbors in the stack, with the centroids of their central hexagons aligned with the crystallographic c axis, as shown in Figure 2-10, Figure 2-11, and Figure S2-3. The result is that the π systems of nearest neighbor molecules in a stack are 3.61 Å apart. Due to the disorder in this structure no analysis of bond distances can be done but based on the average C–F distance the average s.u. (standard uncertainty) values are 0.003 Å and therefore approximate s.u. values for longer intermolecular distances are 0.006 Å. The degree of overlap of nearest neighbor π systems is significant, ca. 72%. There are stacks of offset parallel molecules in the structure of unsubstituted coronene.[51] The offset results in a much smaller degree of overlap of the π systems of nearest neighbor molecules, as shown in Figure S2-4 (the offset stacks are arranged in a herringbone fashion resulting in 28% overlap of the π system). While it is not possible to

Figure 2-11 shows that the molecules form hexagonal planar arrays parallel to the crystallographic ab plane. The distances between the central hexagon centroids of neighboring molecules in the plane are 13.18 Å (× 4) and 12.48 Å (× 2). Figure S2-5 shows a single plane of major component molecules with the F atoms highlighted as large spheres. Figure S2-6 shows the hexagonal array of stacks with large F atoms to highlight the empty spaces between major component molecules. These spaces may be the reason for the facile rotational disorder of the minor component molecules. The closest intermolecular F···F and F···H distances for molecules in a stack are 3.16 and 2.72 Å, respectively. Two times the van der Waals radius of an F atom is 3.00 Å[52] meaning these distances suggest that the solid-state packing of molecules in CORO-4-1 is not strongly influenced by the interactions between F and H atoms and is primarily influenced by π–π overlap.

Structures of H₂CORO-7-1, H₂CORO-7-2, H₂CORO-8-1, and H₂CORO-8-2. Thermal ellipsoid drawings of these molecules are shown in Figure 2-8. Thermal ellipsoids for the H₂CORO-7-1, H₂CORO-7-2, and H₂CORO-8-1 structures are shown with 50% probability. The H₂CORO-8-2 structure thermal ellipsoids have been constrained to 30% probability due to large amounts of disorder. The standard uncertainties, in angstroms, for these structures are 0.002, 0.006, 0.002, and 0.056.

H₂CORO-7-1. The benzoperylene core is nearly flat deviating from the mean plane 0.017 Å with the carbons adjacent to the $C(sp^3)$ atoms having the largest deviations, (−0.078 C13 and 0.047 C18). H₂CORO-7-1 arranges in a series of interpenetrating molecules making infinite stacks, shown in Figure 2-13 (Left). The distance between molecules is 4.01 Å and the distance between molecules within a column is 8.09 Å. There is minimal overlap of the aromatic cores due to the steric effects of the sp^3 functional groups, 8%, resulting in only four $C(sp^2)$ atoms being directly overlapped. One of the overlapping molecules is overlaid in blue, Figure 2-13 (Right), to better define the two separate molecules. This will be repeated for all of the following structures. The colored region is the area of overlap.

The molecules orient within a plane in a pseudo hexagonal array. Within the array the enantiomers vary as shown in Figure 2-14 (Left) resulting in four *RR* and two *SS* enantiomers bordering a central *RR* isomer. Within a given column the enantiomer alternates between *RR* and *SS*. For example, the next plane above the one shown in Figure 2-14 (Left), would be four *SS* and two *RR* enantiomers bordering an *SS* molecule. Within the pseudo hexagonal array, the distances of the neighboring molecules from the central molecule, measured from the centroid of the central hexagon of each molecule, are 12.12 Å, 13.47 Å (× 2), 14.37 Å (× 2), and 18.26 Å. Within the hexagonal array there are a number of close F···F distances, distances less than 3.0 Å, associated with $C(sp^2)$ bonded CF₃ group F atoms. However, the closest F···F distances are between the F atoms of CF₃ groups attached to core $C(sp^3)$ and $C(sp^2)$ atoms with distances as short as 2.6 Å. For comparison, F atoms on a CF₃ group attached to core $C(sp^3)$ atoms have longer distances with

lengths over 3 Å, but there is one which is shorter at 2.76 Å. Average C–F s.u. value is 0.002 Å and approximate intermolecular distances are 0.004 Å Shown in Figure 2-14 (Right), it is obvious that two dihydrocoronene molecules, alternating enantiomers *RR* and *SS,* are shared between two hexagonal arrays to complete the array. Lastly, within a "plane" of the hexagonal array of molecules there are in fact two separate planes where three molecules, including the central molecule, occupy one plane and the four remaining molecules occupy a separate plane, with the distance between these two being 0.71 Å.

H$_2$CORO-7-2. The benzoperylene core is nearly flat deviating from the mean plane 0.055 Å with the carbons adjacent to the core C(sp^3) atoms having the largest deviations, (−0.267 Å C18 and 0.112 Å C13). As is the case for H$_2$CORO-7-2, the solid-state packing consists of interpenetrating columns with internal column distances of 7.91 Å and the closest distance between nearest molecules of interpenetrating columns being 3.95 Å. The degree of overlap is 15% with eight core C atoms directly overlapped. Similar to H$_2$CORO-7-1, the overlap of the molecules is most heavily influenced by minimizing the steric effects of the CF$_3$ groups. Surprisingly, there are CF$_3$ groups in close proximity to each other unlike in H$_2$CORO-7-1, with F···F distances as short as 2.78 Å. The interpenetrating columns are parallel to each other in both H$_2$CORO-7 structures. Within a given plane all the molecules are coplanar and are the same enantiomer with the next plane above or below being the opposite enantiomer. The planes pack as hexagonal close packed arrays shown in Figure 2-15 (Lower), with distances measured from the centroid of the central hexagon of each molecule, 13.46 Å (× 2), 14.42 Å (× 2), and 14.44 Å (× 2). Average C–F distance s.u. value is 0.006 Å and approximate intermolecular distance s.u. value is 0.012 Å. There are few short intermolecular F···F distances between CF$_3$ groups on core C(sp^2) atoms with the shortest being 2.84 Å. Closer are the distances between F atoms on CF$_3$ groups attached to core C(sp^2) atoms and F atoms on CF$_3$ groups attached to core C(sp^3) atoms, with distances as short as 2.44 Å. Short intramolecular distances, again, are between F atoms on CF$_3$ groups attached to core

$C(sp^3)$ atoms and F atoms on CF_3 groups attached to core $C(sp^2)$ atoms, which are 2.39 and 2.59 Å.

H₂CORO-8-1. The benzoperylene core is slightly flexed resulting in alternating pairs of concave and convex molecules stacking in slip stacked columns of molecules along the *a* axis. This results in deviations from the mean plane, 0.078 Å. The flexing of the core gives rise to the largest deviations from planarity coming from (−0.130 C14 and 0.168 C8), which are at extreme ends of the flexed portion of the molecule. As before, the benzoperylene cores are minimally overlapped, 16%, with interpenetrating columns of molecules. However, unlike the previous H₂CORO-7s the molecules are slip stacked with each molecule translated from the center position. The distance between molecules within the same column depends on whether the pair is flexed towards or away from each other. The concave pair, the molecules are curved towards each other along the *a* axis of the unit cell, is 3.792 Å. The convex pair, the molecules are curved towards each other along the *a* axis of the unit cell, is 4.224 Å. The distance between repeating units is 8.015 Å. Each molecule is coplanar with respect to each other. This is depicted in Figure 2-16 (Top Left).

The molecules pack in hexagonal close packed arrays with the added variable of the core flexing not making a noticeable impact on the structural packing. The distances between central aromatic cores, as measured from the centroid of the central hexagon, are 13.167 Å (× 2), 13.814 Å (× 2), 16.093 Å (× 2). The image depicting the concave convex pairs of molecules between planes Figure 2-16 (Bottom Right), has all non-carbon atoms excluded to minimize confusion and clutter. There are several close intermolecular distances between F atoms on CF_3 groups bonded to core $C(sp^2)$ atoms with the shortest distance being 2.533 Å. Average C–F distance s.u. value is 0.002 Å and approximate intermolecular distance s.u. value is 0.004 Å. The ortho CF_3 groups give rise to more close contacts than in the H₂CORO-7 derivatives due to their twisting out of the plane of the molecule. The intermolecular distance of F atoms bonded to ortho CF_3 groups are 2.446 Å. Both of the CF_3 groups are rotated and bent out of the plane to allow for as much space between F

atoms as possible. Lastly, the short intramolecular F atom distances of F atoms on CF_3 groups bonded to core $C(sp^2)$ and F atoms on CF_3 groups bonded to $C(sp^3)$ atoms are 2.676, 2.732, and 2.877 Å.

H₂CORO-8-2. The benzoperylene core is nearly flat, deviating from the mean plane 0.042 Å. The carbons deviating the most from the mean plane, (−0.166 Å C6 and 0.128 Å C8) are not the carbons closest to the $C(sp^3)$ atoms but are on the opposite end of the molecule. C6 appears to be twisted out of the plane to accommodate the ortho CF_3 groups on C6 and C5. C8 is disordered due to the presence of the H₂CORO-8-3 contaminant. The benzoperylene cores are minimally overlapped, 12%, with four $C(sp^2)$ atoms directly overlapped, and with interpenetrating columns of molecules similar to all other dihydrocoronene structures reported in this work, shown in Figure 2-17. The distance between molecules within the same column is 8.135 Å and the distance between close molecules of interpenetrating columns is 3.866 Å. The molecules pack in a pseudo hexagonal close packed array. The distances between central aromatic cores are 12.803 Å ($\times$ 2), 14.697 Å ($\times$ 2), and 14.774 Å ($\times$ 2). Each plane is comprised of the same enantiomer and all the molecules are coplanar with respect to their core carbon rings. Lastly, the structure has a 2_1 screw axis resulting in two orientations of the molecule within a given array. There is an uneven number of similarly oriented molecules, four and three, and this appears to be the cause of the lower symmetry pseudo hexagonal array. In adjacent planes of molecules, above and below, this molecular orientation is inverted. It should be noted that within a given plane all of the molecules are the same enantiomer. No analysis of the F···F distances was done due to the ambiguity in the bond lengths caused by the co-crystallized superimposed impurity. This impurity identified as H₂CORO-8-3 and is shown in Figure 2-8.

2.2.3. DFT calculations for CORO(CF₃)ₙ compounds and CORO reactivity

We previously demonstrated that for trifluoromethylation reactions of the bowl-shaped PAH corannulene, (CORA, $C_{20}H_{10}$), DFT calculations on the relative energies of the CORA(CF₃)ₙ isomers yielded accurate predictions of the most abundant products.[53] For example, the most stable

isomer, CORA(CF$_3$)$_5$-1 (or CORA-5-1, as used in the literature)[53] was formed in much larger quantities than the next two most stable isomers, CORA-5-2 and CORA-5-3 (energy separations 42.4 and 51.4 kJ mol^{-1} respectively).[54] Qualitatively accurate predictions were also made for isomers of CORA(CF$_3$)$_4$, CORA(CF$_3$)$_6$, and CORA(CF$_3$)$_7$. The absence of the compounds with n(CF$_3$) >7 in the reaction product was consistent with the DFT data on the energetic cost of introducing a bulky CF$_3$ group in the positions adjacent to the other CF$_3$ group, i.e., *ortho*-positions (1,2-CORA(CF$_3$)$_2$ (55.4 kJ mol^{-1}) or *peri*- position (1,12-CORA(CF$_3$)$_2$ (43.9 kJ mol^{-1}).

Table 2-2 lists the results of DFT calculations of relative energies of CORO(CF$_3$)$_n$ isomers. For the CORO(CF$_3$)$_2$, seven low-energy isomers can form (within 4 kJ mol^{-1} of the most stable isomer) in which CF$_3$ groups are separated from each other by at least one carbon. Substitutions in the 1,2 (*ortho*-) or 1,12 (*peri*-) positions result in drastic energy increases of 64 kJ mol^{-1}. This energetic cost is much higher than in the case of 1,2- and 1,10-CORA(CF$_3$)$_2$ isomers, indicating that inter-CF$_3$ repulsion in the planar CORO-2 appears to be stronger than in the bowl-shaped CORA-2. This result was in good agreement with the product distribution for the CORO(CF$_3$)$_n$ compounds. With this in mind, DFT analysis of polysubstituted CORO(CF$_3$)$_n$ was focused on the isomers in which CF$_3$ groups do not occupy unfavorable *ortho*- and *peri*- positions. Because the reaction conditions were high temperatures it is unlikely that the nearly thermodynamic conditions of the synthesis would yield such high-energy products in observable amounts.

Even after eliminating high-energy isomers, in the cases of CORO(CF$_3$)$_3$ and CORO(CF$_3$)$_4$, the numbers of low-energy isomers are high: ten and eleven, respectively. However, for CORO(CF$_3$)$_5$, only three low-energy isomers are possible, and only one isomer of CORO(CF$_3$)$_6$ satisfies the imposed condition, no *ortho*- or *peri*- substitutions. The theoretical calculations suggest that syntheses carried out with an excess of CF$_3$ radicals would yield preferential formation of the following products: one isomer of CORO(CF$_3$)$_4$ (CORO-4-1), two isomers of CORO(CF$_3$)$_5$ (CORO-5-1 and CORO-5-2) and one isomer of CORO(CF$_3$)$_6$. Since trifluoromethylation would be exhaustive (i.e., using a large excess of CF$_3$ radicals) in this example, one of the possible

isomers of CORO(CF$_3$)$_5$ (CORO-5-3), which was isolated, would be converted further to CORO(CF$_3$)$_6$, decreasing the number of final products to four (the structures are shown in Figure 2-18 and the compound names and the abbreviations used in this work are shown in Figure S2-1). The other isomers of CORO(CF$_3$)$_5$ and the isomer of CORO(CF$_3$)$_4$ will not be substituted, as they cannot form low energy isomers.

In reality, complete trifluoromethylation is never achieved and a multitude of CORO(CF$_3$)$_{n<5}$ isomers are indeed produced. Excluding CORO-1-1 and CORO-4-2 which were able to be isolated in a pure form, all other CORO(CF$_3$)$_{n<5}$ coeluted as a complex mixture but by mass spectrometry, their relative distributions could be confirmed. The HPLC chromatogram for GTGS-3 as a representative reaction is shown in Figure 2-19.

2.2.4. Reaction pathways and rim bond reactivity

The high energetic barrier to *peri-* and *ortho-* substitutions limits the number of possible CORO(CF$_3$)$_n$ isomers by limiting the number of possible reaction pathways. However, due to the shrinking number of remaining C(sp^2) bonded protons, the H$_2$CORO(CF$_3$)$_n$ derivatives also have a limited number of pathways for which substitution and/or addition can proceed. The routes to those products starting from their CORO-5 precursors are shown in Figure 2-20. By starting with the three CORO-5 isomers, reaction routes to all five of the isolated H$_2$CORO(CF$_3$)$_n$ products are produced by undergoing first radical addition to one of the *ortho-* protons. The energy for *ortho-* and *peri-* substitution is 64 kJ mol^{-1} based on Dr. Popov's DFT calculations. Therefore, it can be deduced that the energy of the radical addition reaction must be lower than 64 kJ mol^{-1} or else it would likely not occur. Following the radical addition, the aromatic core of the PAH has changed from CORO to H$_2$CORO meaning one of the rim bonds, C1–C2 for H$_2$CORO, has been converted from a double bond to a single bond. This change must result in different thermodynamics for the system because instead of further radical addition reactions, which for CORO were obviously lower in energy than either *peri-* or *ortho-* substitutions, an eighth CF$_3$ group is added via a radical substitution reaction. This substitution must occur in a location which was previously energetically

unfavorable for CORO derivatives, however by examining the isolated $H_2CORO(CF_3)_8$ structures we find that there is one pair of locations for this substitution where the reaction can occur with less steric hinderance than any of the other remaining $C(sp^2)$ bonded protons. Both of the isolated $H_2CORO-7$ isomers have two *peri-* $C(sp^2)$ bonded proton positions, C10 and C11 for $H_2CORO-7$-1 and C8 and C9 for $H_2CORO-7-2$, which are substituted by an eighth CF_3 group to produce the three $H_2CORO(CF_3)_8$ isomers.

Additionally, there is a third $H_2CORO-7$ isomer isolated from the F1 fraction in Figure 2-4. The mass spectrum for this fraction was recorded and the most abundant ion had an *m/z* value of 777 which corresponds to the mass of a $H_2CORO-7^-$ ion with one proton missing, [HCORO-7], see Table S2-3. The most likely source for this species is from the continued reaction of CORO-5-3 to a CORO-6 radical intermediate, rather than CORO-6-1, and then a stable $H_2CORO-7$ isomer. This isomer would have a proton *peri-* to the $C(sp^3)$ region on the C12 atom, see Figure 2-20. The NI-ESI mass spectrum of the crude material from GTGS-4 also shows a 777 *m/z* ion, shown in Figure S2-25. Unfortunately, the NMR spectra for this isomer (not shown) has a poor signal to noise ratio due to the small amount of material isolated and more material and experimentation would be required to say anything definitive about the F1 fraction.

Trifluoromethylated products with more than eight CF_3 groups were never isolated as pure isomers but the F0 fraction, shown in Figure 2-4, was examined by NI-ESI mass spectrometry and showed an *m/z* value of 984 as the most abundant ion corresponding to tetrahydrocoronene derivatives with four $C(sp^3)$ bonded protons, see Table S2-3. The chemical formula would be $C_{24}H_6(CF_3)_{10}$ with four of the six protons bonded to $C(sp^3)$ atoms, two at C1 and C2 and two more on a rim bond which has undergone radical addition and has two CF_3 groups. While no pure tetrahydrocoronene compounds were isolated, a hypothesis can be made which may predict the most likely location for the radical addition based on the bond lengths of the rim bonds in the crystal structures of $H_2CORO(CF_3)_8$ isomers.

It is generally accepted that shorter bonds are known to have a higher bond order and therefore, relative to a longer bond formed from the same pair of atoms, a higher electron density or more accurately a higher electron localization probability making them likely targets for radical attack.[55-59] Additionally, as was previously stated in Section 2.1., but is worth restating here, double bonds preferentially undergo radical addition; aromatic bonds tend to undergo radical substitution.[16-18] Using these rationales, the bond lengths of the rim bonds should be a method by which the most likely sites for radical addition could be predicted. The shortest bonds for H_2CORO-8-1 are the C5–C6 and C9–C10 rim bonds, average distance is 1.356(2) Å. Although the crystal structure containing H_2CORO-8-2 and H_2CORO-8-3 suffers from disorder at the C5–C6 rim bond and therefore cannot be included in this analysis, the C9–C10 rim bond is not disordered and was measured as 1.350 Å (s.u. ±0.0056). The average rim bond distance for H_2CORO-8-1 excluding C5–C6 and C9–C10 is 1.381 Å and if the *ortho-* substituted C3–C4 rim bond is excluded, 1.375 Å. Based on these results the most likely site for radical addition beyond eight CF_3 groups would appear to be the C5–C6 and C9–C10 rim bonds, resulting in the tetrahydrocoronene molecules detected by mass spectrometry.

As a follow up to the initial bond length investigation, the rim bonds C5–C6 and C9–C10 for H_2CORO-7-1 and H_2CORO-7-2 were also analyzed to see if this trend persisted meaning the bonds were shorter than the other bonds in those structures as well and in fact they are, 1.356 Å and 1.358 Å (s.u. 0.0017) for H_2CORO-7-1 and 1.353 Å and 1.344 Å (s.u. 0.0057) for H_2CORO-7-2. The average rim bond distance excluding C5–C6 and C9–C10 for H_2CORO-7-1 and H_2CORO-7-2 is 1.374 Å and 1.372 Å, respectively. A final comparison was made of the rim bonds of benzo[ghi]perylene and perylene, PERY, to rule out the possibility that this arrangement would be common to the H_2CORO PAH without trifluoromethyl functionalization. No crystal structure could be found of dihydrocoronene. The details of this analysis are shown in Table 2-3 but in brief the C5–C6 and C9–C10 rim bonds were longer in the unsubstituted PAHs than in the $H_2CORO(CF_3)_{7,8}$ structures. The reason for these shorter bonds may be a property of the unique

bonding model of the functionalized H_2CORO molecules arising as a product of the specific addition and substitution pattern of the CF_3 groups on the PAH. Other electronic and steric factors may be more important for determining the locations for radical addition but regardless the C5–C6 and C9–C10 rim bonds for the $H_2CORO(CF_3)_{7,8}$ derivatives appear to exhibit the isolated double bond character predicted for CORO by Boldyrev et al.[11]

2.2.5. Electrochemical and electronic properties of $CORO(CF_3)_n$ and $H_2CORO(CF_3)_n$

Due to their large aromatic π systems, CORO and H_2CORO or benzo[ghi]perylene derivatives are of interest in organic electronic research.[29,32,60-62] However, there are only a few examples of CORO molecules with electron withdrawing groups and even fewer examples with fluorinated groups.[32,60,63,64] To compare the effect of the trifluoromethyl groups on the reduction potential and electron affinity of the CORO and H_2CORO substrates, CV and gas phase electron affinity measurements were performed.

Dihydrocoronene compounds exhibit irreversible electrochemical behavior by CV, but the $H_2CORO(CF_3)_n{}^-$ ions generated by chemical reduction with TDAE were stable allowing for the successful collection of the gas phase electron affinity measurement. Three different measurements were recorded using the chemically reduced ions from pure H_2CORO-7-1 and H_2CORO-8-1 and the isomerically impure F0 fraction. The results of the electron affinity measurements are shown in Figure 2-21.

The electron affinity value, *EA*, of the parent PAH, benzo[ghi]perylene, was reported by NIST as 0.42 eV. From the *EA* of H_2CORO-7-1 and H_2CORO-8-1 as well as the parent PAH, a trendline was produced showing the effect of each additional CF_3 resulting in an increase of 0.28 eV. This increase is virtually identical to the effect of trifluoromethylation of perylenes reported by Strauss et al. in 2013 which was expected given the similarities in their respective π systems.[49] More interesting than the similarity in the PERY and H_2CORO *EA*/CF_3 value, is the close linear fit of the perylene slope to the higher *EA* value for the H_4CORO-10 mixture, lowest being 2.42 ± 0.05 eV and 3.71 ± 0.01 eV for the highest, $m/z = 984$, the R^2 value for the least squares fit of the PERY

slope with the H_4CORO-10 3.71 eV value is 0.98. This correlation further supports the mass spectrometry data and would suggest that at least one of the possible tetrahydrocoronene products has a PERY core though unfortunately the relative abundance of these PERY like species cannot be determined. The data also shows that it does not significantly affect the EA/CF_3 group value when the CF_3 group is attached to the $C(sp^3)$ carbon of a dihydro PAH rather than the typical $C(sp^2)$. This observation had been made previously by comparing the EA/CF_3 value of fullerenes and PAHs, but not in an example with such similar molecules.[65]

For the aromatic $CORO(CF_3)_n$ compounds cyclic voltammetry was effective, and they showed quasi-reversible behavior. Unfortunately, these compounds were too difficult to reduce for gas phase electron affinity measurements to be performed.

CV experiments of CORO and $CORO(CF_3)_{4,5}$ compounds were recorded and their $E_{1/2}$ vs. ferrocene values were reported, see Figure 2-22. The addition of a CF_3 group increases the reduction potential by approximately 200 mV making it easier to reduce. With the number of compounds isolated and reported here the addition pattern does not appear to affect the reduction potential, which agrees well with results reported previously by the Strauss-Boltalina research group for other PAHs.[49,66] While the redox event appears quasi-reversible there was some loss of signal on the return oxidation event. This was contributed to CORO compounds interacting and plating onto the platinum and/or silver electrodes. It was found that cleaning of the electrodes was required frequently during these experiments. Also examined was the effect of aromatic solvents on the $E_{1/2}$ value which was assumed to have a significant effect due to the large aromatic π-system. By comparing o-DCB and DME a difference of approximately 150 mV was observed with the lower $E_{1/2}$ value being recorded for the aromatic solvent, see Figure S2-21 for the voltammograms.

2.2.6. Fluorescence quantum yield of H_2CORO-8-1

As a consequence of the changes to the π structure from CORO to H_2CORO, a new set of absorption bands appears for the H_2CORO compounds, see Figure S2-32. The reasoning behind this change in the absorption profile is discussed in greater detail by Nijegorodov et. al but is

largely due to forbidden transitions arising from the higher D_{6h} symmetry as the new aromatic ring is added to the molecule as it transitions from benzo[ghi]perylene to coronene.[67] Since the π structure of H$_2$CORO is analogous to benzo[ghi]perylene, which has been of interest in organic electronic materials for its strong fluorescent properties, the quantum yield for the compound H$_2$CORO-8-1 was recorded. The results are shown in Figure S2-33.

The quantum yield was calculated following the method described by Strickler in 1967 and Castro in 2013.[68,69] With a quantum yield of 40%, the H$_2$CORO-8-1 and presumably all of the H$_2$CORO(CF$_3$)$_n$ compounds have lower quantum yields compared to benzo[ghi]perylene, 70% ($\pm$7%).[67] This could be due to increased flexing of the molecule about the aromatic core compared to the underivatized benzo[ghi]perylene. As the CF$_3$ groups are added the increasing steric strain results in the molecules deviating from planarity as was already discussed earlier in Section 2.2.2. of this work. Further studies are required to make more substantive comparisons.

2.3. MATERIALS AND METHODS

2.3.1. Reagents and general procedures

All reactions were performed with careful efforts to remove oxygen and water from the reactions using classic air-free techniques. This included but was not limited to rigorously drying/reducing the copper powder used with a flow of hydrogen gas and heat, removing the water from the glassware in contact with the reaction by evacuating the glassware while heating it with a flame, and testing for leaks in either the high-pressure reactor or the GTGS reactor prior to use. Upon completion of the reactions, the crude materials were exposed to ambient atmosphere and moisture. This was also the case during HPLC separations.

The following reagents and solvents were obtained from the indicated sources and were used as received or were purified where indicated: CORO (95+%, TCI); trifluoromethyl iodide (99%, SynQuest); copper powder which was purified under a reducing atmosphere of hydrogen and heat (Fischer); dichloromethane (ACS grade 99.6%, Fischer); tetrakis(dimethylamino)ethylene (95+%, Sigma Aldrich); heptane (HPLC grade 99%, Fischer); toluene (ACS grade 99.5%, Fischer);

anhydrous *o*-DCB (99%, Acros Organics); deuterated chloroform (99.8%, Cambridge Isotope Labs); deuterated benzene (99.8%, Cambridge Isotope Labs); perfluorobenzene (99%, Oakwood Products); 1,4-bistrifluoromethylbenzene (99%, Central Glass Co.).

2.3.2. Synthesis of new compounds

For high pressure reactions in the metal tube reactor (MTR), the coronene starting material (50 mg, 0.17 mmol) was mixed as received with copper powder (4.2 or 1.9 g depending on $CF_3I(g)$ pressure) which was purified under a reducing atmosphere of hydrogen and heat. The two components were intimately mixed in a mortar and pestle and then added to a high-pressure reactor described in Chapter 1 of this work. These materials were evacuated until a stable pressure of at least 10^{-5} Torr was reached. At this time trifluoromethyl iodide was introduced at the desired pressure and then condensed to a liquid inside the metal tube reactor using liquid nitrogen. The reactor valve was closed, and the reaction vessel was warmed to room temperature. The reactor was then heated in a tube furnace to the desired temperature and held at that temperature for the duration of the reaction. After the reaction time had elapsed the vessel was removed from the furnace and cooled to room temperature before exposing the sample to the atmosphere. The soluble compounds were removed via repeated washing in dichloromethane and toluene to separate them from any carbonaceous char and bulk copper powder. The resulting solution was filtered and then dried under roto-evaporation.

For reactions using higher equivalents of CF_3I (34 equiv at 17000 Torr at the reaction temperature) the isolated crude material was dissolved in heptane and separated into fractions on a Cosmosil Buckyprep semi-preparative column with heptane as the eluent with a 5 mL min^{-1} flow rate and were detected at 300 nm using an array detector. The compounds resulting in crystal structures eluted at 9.0–10.2 min and at 40.5–42.5 min.

For reactions using lower equivalents of CF_3I in the MTR (7 equiv at 3400 Torr at the reaction temperature) the isolated crude material dissolved in toluene and separated into fractions on a Cosmosil Buckyprep semi-preparative column with toluene as the eluent with a 5 mL min^{-1} flow

rate and were detected at 300 nm using an array detector. Pure compounds were isolated at 6.0–7.0, 14.0–15.0, 20.5–21.2, 32.0–33.5, 35.0–35.5, and 45–50 min. Fractions collected at 6, 32, and 35 min required secondary separation in the same solvent to further purify them. Weakening the eluent mixture with non-aromatic solvents did not result in better separation and both lengthened the separation time and resulted in more overlapping elutes.

Low pressure reactions were performed in the Gradient-Temperature Gas-Solid reactor (GTGS). Details of the reactor can be found in the 2011 paper by Dr. Igor V. Kuvychko et al.[50] CORO solid and copper powder were added to the base of the quartz reactor. After the reactor was sealed it was evacuated and residual water was removed from the glass under evacuation and flame avoiding the reagents at the bottom of the reactor. The desired pressure of $CF_3I(g)$ was loaded into the reactor. The hot-zone was heated to the desired temperature 480 °C[50] and then the reactor was brought into contact with the hot-zone. The reaction was allowed to progress for 30 minutes at which time all the CORO substrate had sublimed away from the reaction base. The reactor was removed from the hot-zone and allowed to cool to room temperature at which time the soluble compounds were extracted in DCM and toluene exhaustively until no blue fluorescence from CORO and CORO products were visible under excitation from a 402 nm laser. This required many washes and repeated sonication events. For reactions involving multiple additions of $CF_3I(g)$, the soluble material was then added back to the reactor with the original copper powder and under evacuation the solvent was completely removed which was verified by a return to the zero-point pressure recorded by an electronic monometer. The same procedure listed above was repeated as many times as was desired.

For GTGS-6 the same experimental conditions were used as previously described and are shown in Table 2-1. The crude material was extracted from the GTGS reactor using DCM or toluene as necessary and then a portion of that solution was added to the prepared ampule. The ampule was evacuated until all residual solvent and atmosphere was removed. The ampule was then charged with $CF_3I(g)$ resulting in a pressure of 600 Torr shown in Table 2-1 following G/A-

1. The G/A-1 reaction was heated to 330 °C and then allowed to cool to room temperature before the ampule was opened and the soluble material was extracted using DCM. A portion of the resulting crude material was then loaded into a new ampule and then the G/A-2 reaction was prepared in the same fashion as was described for G/A-1. The resulting crude materials were analyzed NMR spectroscopy and separated by HPLC.

The karpatite reaction, ROCK-1, was performed using the GTGS reactor using the same methods described for the other GTGS reactions. The karpatite mineral was prepped for the reaction by crushing the mineral sample and then thoroughly grinding it in a mortar and pestle. The resulting powder was used as the karpatite starting material. The karpatite sample does not burn at the temperatures used.

2.3.3. Spectroscopic characterization

^{1}H and ^{19}F NMR spectra were recorded using a Varian INOVA 400 spectrometer operating at 400 and 376 MHz, respectively. Spectra were recorded using a 1 s relaxation time and a 30° pulse angle. The solvent used was deuterated chloroform for $H_2CORO(CF_3)_n$ compounds or deuterated benzene for fully aromatic $CORO(CF_3)_n$ with perfluorinated benzene ($\delta(^{19}F) -164.9$) as an internal standard.

2.3.4. UV-vis Spectroscopy

UV-vis spectra for the comparison of typical $CORO(CF_3)_n$ and $H_2CORO(CF_3)_n$ derivatives were collected using a UV-Vis-NIR Shimadzu UV 3101PC instrument with UVProbe 2.33 software.

2.3.5. Quantum yield determination for H₂CORO-8-1

Quantum yield was recorded as 0.35. The spectra were recorded in cyclohexane with the concentration of the H₂CORO-8-1 being 3.6×10^{-6} M. The standard, quinine hemisulfate monohydrate, was dissolved in 0.105 M $HClO_4$ aqueous solution. The absorption of the standard and the H₂CORO-8-1 sample were matched and the absorption above that point, 385 nm, was kept

below 0.1. The slit width was 2 cm and the step size was 1 nm. The temperature was 25 °C. Spectra were recorded on a Cary 500 UV-vis-NIR spectrophotometer. Fluorescence measurements were recorded using a Horiba Fluorolog-3 with a 450 W Xe lamp and a PMT detector. Samples were degassed by the freeze-pump-thaw method three times and were measured air-free using 1 cm^2 air-free quartz cuvette. Spectra as well as the equation used to calculate the quantum yield are shown in Figure S2-33.

2.3.6. Single-crystal X-ray diffraction

Crystals of CORO-4-1 and the four $H_2CORO(CF_3)_n$ compounds ($n = 7, 8$) were grown by slow evaporation of heptane, chloroform, or benzene-d$_6$ solutions. Diffraction data sets were collected at the Advanced Photon Source at Argonne National Laboratory on beamline 15ID-B and 15ID-D at X-ray wavelengths of 0.40651 or 0.41328 Å (diamond 111 monochromator) with a Bruker D8 goniometer and multi-scan absorption corrections. Unit cell parameters were determined by the least squares fit of the angular coordinates of all reflections. Integrations of all frames were performed using APEX III software, and the structures were solved using SHELXTL/OLEX 2 software. Table S2-1 lists relevant data collection and refinement results for the five structures. Additional details about structure solution and disorder modeling are given in Appendix A.

2.3.7. Gas-Phase photoelectron spectroscopy

Samples of H_2CORO-7-1, H_2CORO-8-1, and a mixture of $H_4CORO(CF_3)_{10}$ isomers were sent to collaborator Dr. Xue-Bin Wang at Pacific Northwest National Laboratory (PNNL) for *EA* measurements. Dr. Wang pioneered the measurement of *EA*s of strong electron acceptors by low-temperature (10–12 K) gas-phase photoelectron spectra of electrospray-ionized samples using an apparatus that couples an electrospray ionization source and a temperature-controlled ion trap to a magnetic-bottle time-of-flight photoelectron spectrometer.[70] In a typical experiment, the electron affinity (*EA*) of a compound is directly measured from the 0–0 transition in the photoelectron spectrum of its one-electron reduced anion. Fresh spray solutions are prepared by adding an aliquot of an acetonitrile solution of the electron-donor compound tetrakis(dimethylamino)ethylene

$(NMe_2)_2C=C(NMe_2)$, TDAE) to a 10^{-3} M solution of the compound in a suitable solvent. The anions produced by the ESI source are guided by two RF-only quadrupoles and directed by a 90° ion bender into a 3D ion trap, where they are accumulated and thermalized via collisions with a background gas (ca. 0.1 mTorr 20/80 H_2/He) for a period of 20–80 ms before being pulsed out into the extraction zone of the time-of-flight mass spectrometer. The mass selected ions are decelerated before being intercepted by the beam from a Nd:YAG probe laser (266 nm; 4.661 eV) in the photo-detachment zone of the magnetic bottle photoelectron analyzer.[70]

2.3.8. Cyclic Voltammetry

Cyclic voltammograms were recorded in an inert atmosphere using a PAR 263 potentiostat/galvanostat and approximately 2 mM *o*-DCB or DME solutions of the analyte with 0.1 M N(*n*-butyl)$_4$BF$_4$ or N(*n*-butyl)$_4$ClO$_4$ as the electrolyte. The electrochemical cell used was equipped with 0.125 mm diameter platinum working and counter electrodes and a 0.5 mm diameter silver reference electrode. The scan rate was 500 mV s^{-1}.

2.4. CONCLUSIONS AND FUTURE WORK

In total, 10 new compounds have been synthesized, isolated, and characterized by a suite of analytical techniques including NMR spectroscopy, mass spectrometry, UV-vis spectroscopy, and single crystal X-ray diffraction. Additionally, their electrochemical properties were characterized by cyclic voltammetry or low temperature PES measurements where appropriate.

From these compounds a set of rules governing the radical substitution of coronene was observed, namely that no *ortho-* or *peri-* positions could be substituted and only after five CF$_3$ groups have been substituted onto the molecule could those higher energy positions be functionalized. When those higher energy positions are functionalized, it is only after radical addition occurs on the C1 and C2 positions of the resulting PAH. This result coupled with crystallographic analysis of the H$_2$CORO compounds as well as several literature compounds leads to new insight into the chemistry of CORO and more specifically about the nature of its rim bonds.

Based on that analysis it has been concluded that the CORO rim bonds are not strictly aromatic as the 'superbenzene' moniker would suggest but in fact are at least capable of being shortened to lengths resembling double bonds possibly as a product of the addition of the electron withdrawing CF_3 substituents. The sights where this shortening of the rim bonds occurred was consistent in all four of the H_2CORO crystal structures, the C5–C6 and C9–C10 bonds. These observations and experimental results suggest that other PAHs could be capable of radical addition under similar conditions, specifically PERY.

Future work on this project could explore the reactivity of PERY to high pressure radical trifluoromethylation to observe if similar addition products can be formed in those cases as well or if this phenomenon is limited to CORO and H_2CORO compounds. This question is based on the bond length analysis shown in Table 2-3 where PERY has bond lengths similar to the underivatized CORO crystal structure.

2.5. ADDITIONAL RECOGNITION

The high pressure trifluoromethylation of CORO was performed with the assistance of Dr. Eric V. Bukovsky and the AMP reactions were performed by Dr. Igor V. Kuvychko. Electron affinity measurements were performed in collaboration with the Pacific Northwest National Lab run by Dr. Xuebin Wang where Dr. Kerry C. Rippy was in attendance and assisted in the collection of the data discussed herein. X-ray diffraction data was collected at the synchrotron source at Argonne National Lab under the supervision of Dr. Yu-Sheng Chen.

Table 2-1. Trifluoromethylation reactions, experimental parameters and major products.

Reaction	CORO (mg)	P(CF$_3$I) (Torr)	Cu (g)	Temp (°C)	Time (h)*	CORO % conv.	ΣCORO-0,1 (%)	ΣCORO-2,3 (%)	ΣCORO-3,4 (%)	ΣCORO-5 (%)
AMP-1	5.3	1000	-	360	24	-	$(C_{22}H_{m+x}(CF_3))_{12-m}$			
AMP-2	5.4	1000	-	275	23	-	no soluble	product	formed	
AMP-3	18	1000	0.5	300	0.17	-	$(C_{24}H_{m+x}CF_3))_{12-m}$			
G/A-1	15.8※	600	-	330	1	-	19	26	42	13
G/A-2	3∴	600	-	330	1	-	8	18	29	45
MTR-HP	50	17200	4.5	450	4	98	2	0	0	0
MTR-LP	100	7400	2	450	4	20**	48	35	12	4
GTGS-1	150	200 x 2	2	480	2	72	54	27	10	3
GTGS-2	50	700 x 2	1.5	480	3	82	67	12	12	5
GTGS-3	50	700 x 3	2	480	1.5	96	22	20	24	24
GTGS-4	31	700 x 3	2.1	480	1.5	-	N/A	N/A	80	20
GTGS-5	60	700 x 3	0	480	6	97	29	32	28	9
GTGS-6	60	700	2.5	480	1	88	33	23	32	12
ROCK-1	2000†	700 x 3	4	480	3	98‡	5	9	21	47

※ Starting material was crude CORO(CF$_3$) products from single GTGS reaction at 700 Torr, GTGS-6. ∴ Starting material from the crude mixture of G/A-1 products. * GTGS reaction times are based on the amount of time required for all visible starting material to sublime from the reaction zone. ** There is no coronene starting material detectable by proton NMR, however it is clearly evident by HPLC and was isolated to confirm this. †This mass is for the sample used for the reaction but a large percentage of the mass is quartz rock which was not separated. ‡ Based on the isolated material extracted from the karpatite substrate. GTGS-4 is a reaction using a mixture of CORO-3 and CORO-4 isomers as the starting material.

Table 2-2. DFT-predicted relative energies of CORO(CF$_3$)$_n$ isomers (n = 2, 3, 4, 5)[a]

n = 2	ΔE		n = 3	ΔE		n = 4	ΔE		n = 5	ΔE
1,7	0.00		1,5,9	0.00		1,4,7,10[b]	0.00		1,3,5,7,10	0.00
1,8	0.33		1,4,8	0.32		1,4,7,9	1.16		1,3, 5,8,10	0.39
1,5	0.46		1,4,7	0.37		1,3,6,9	1.30		1,3,5,7,9[b]	0.42
1,6	0.52		1,5,10	0.43		1,3,6,10	1.63			
1,10	0.85		1,3,7	1.22		1,3,7,9	1.65			
1,4	0.90		1,3,9	1.23		1,3,5,9	2.07			
1,3	2.18		1,3,8	1.61		1,3,8,10	2.74			
1,12	64.15		1,3,10	1.95		1,3,5,10	2.81			
1,2	64.48		1,3,6	2.16		1,3,5,8	2.86			
			1,3,5	3.32		1,3,6,8	2.92			
						1,3,5,7	3.67			

[a] The IUPAC locants on the CORO core are listed under each value of n for each CORO(CF$_3$)$_n$ composition. All relative energies (ΔE) are in kJ mol^{-1}. [b] Isomers that cannot be converted into a higher n(CF$_3$) derivative without avoiding CF$_3$ substituents on *ortho-* or *peri-* positions.

Table 2-3. List of rim C–C bond distances of select PAHs[a]

CORO[b] s.u. 0.003	benzo(PERY)[c] s.u. 0.006	PERY[d] s.u. 0.003	H₂CORO-7-1 s.u. 0.002	H₂CORO-7-2[e] s.u. 0.006	H₂CORO-8-1 s.u. 0.002
1.362	1.410	1.366	1.381	1.377	1.377
1.358	1.383	1.364	1.356[f]	1.353[f]	1.356[f]
1.364	1.406	1.357	1.369	1.367	1.372
1.362	1.404	1.358	1.358[g]	1.344[g]	1.355[g]
1.358	1.380		1.374		1.394
1.364					

[a] All bond distances and their standard uncertainties (s.u.) are given in Å. All distances from this work unless otherwise indicated. [b] Ref. [51]. [c] Ref. [71]. [d] Ref. [72]. [e] The C11–C12 rim bond is excluded due to disorder (see Appendix A). [f] C5–C6 rim bonds. [g] C9–C10 rim bonds.
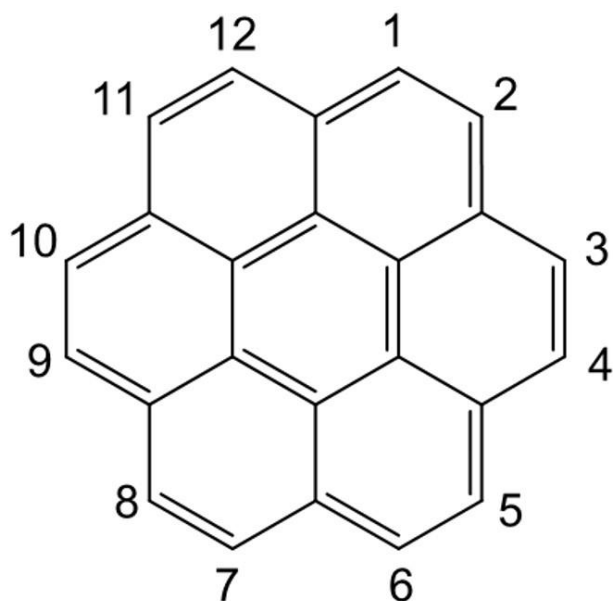
Figure 2-1. (**Left**) The molecular structure and numbering scheme of coronene. (**Right**) A photograph of a 4 × 5 × 3.5 cm sample of the mineral karpatite in the author's private collection (the sample is from the 4th of July Mine in San Benito County, CA). Pale yellow needle-like crystals are a pure phase of coronene, as shown by a ^{1}H NMR spectrum in this work.
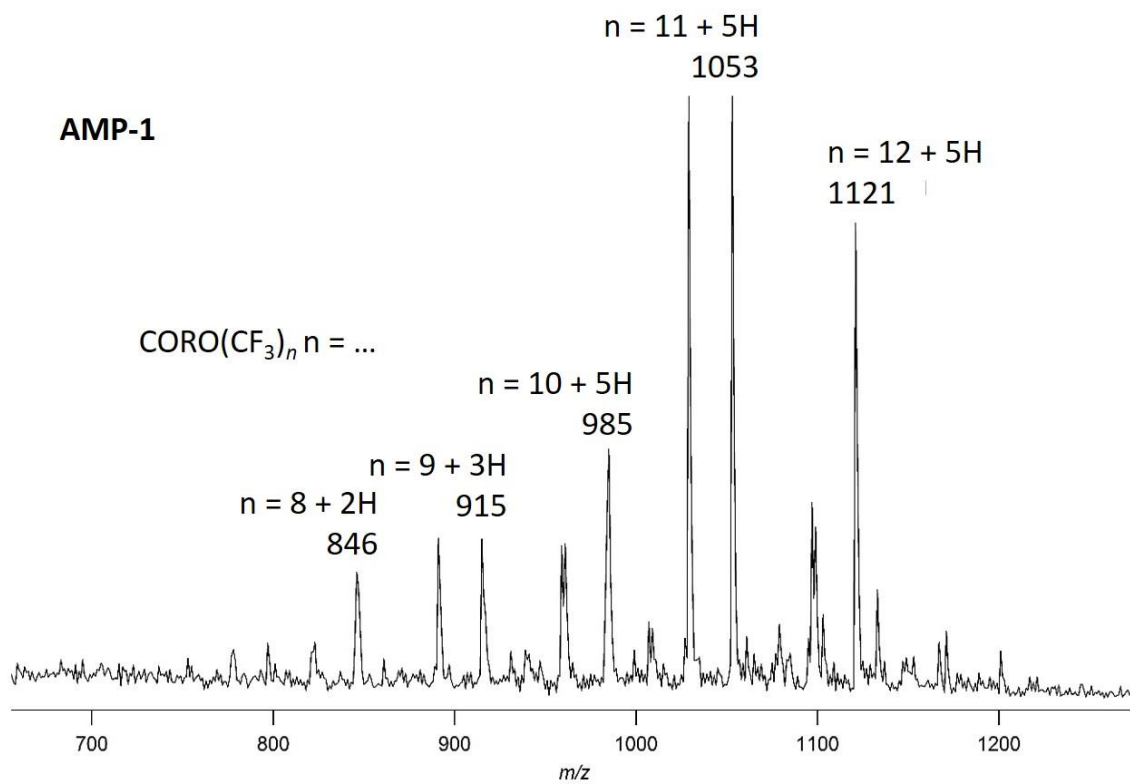
Figure 2-2. Negative-ion electrospray mass spectrum of the crude product of reaction AMP-1.
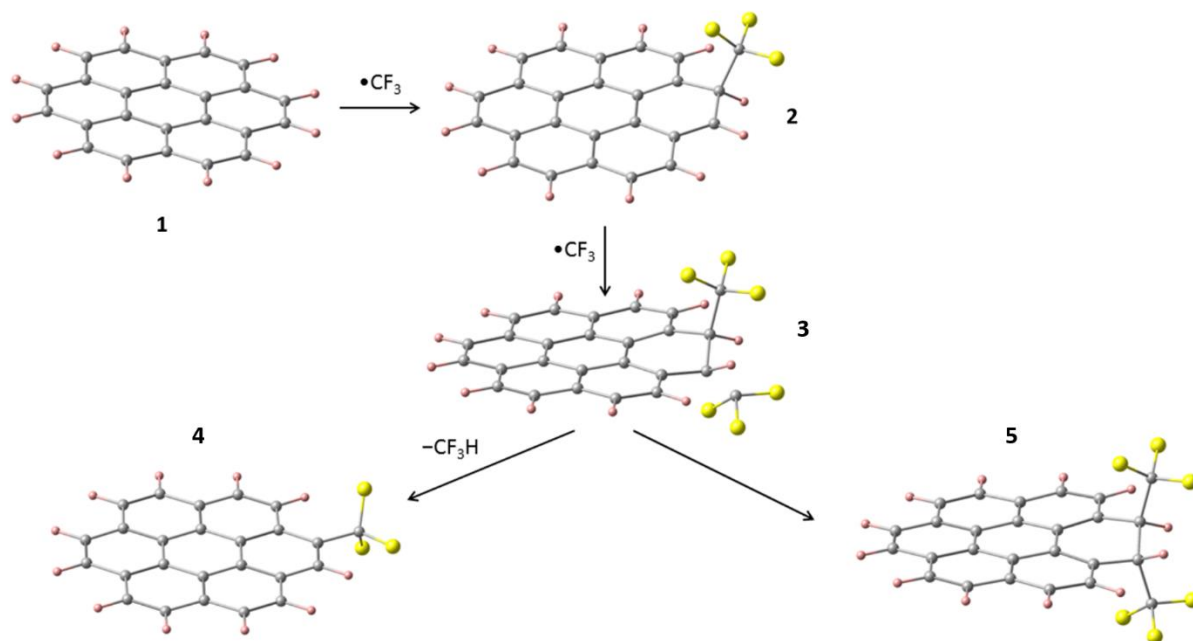
Figure 2-3. Proposed pathway for the CF$_3$ reactivity on CORO. **2** shows the product of the radical CF$_3$ and CORO resulting in radical addition and an HCORO(CF$_3$) radical anion. **3** shows a second CF$_3$ radical either attacking the adjacent C(sp^2) atom or abstracting a proton from the C(sp^3) atom. Step **3** results in either the substitution or addition product shown as **4** and **5** in high-temperature gas-phase trifluoromethylation of CORO substrate.
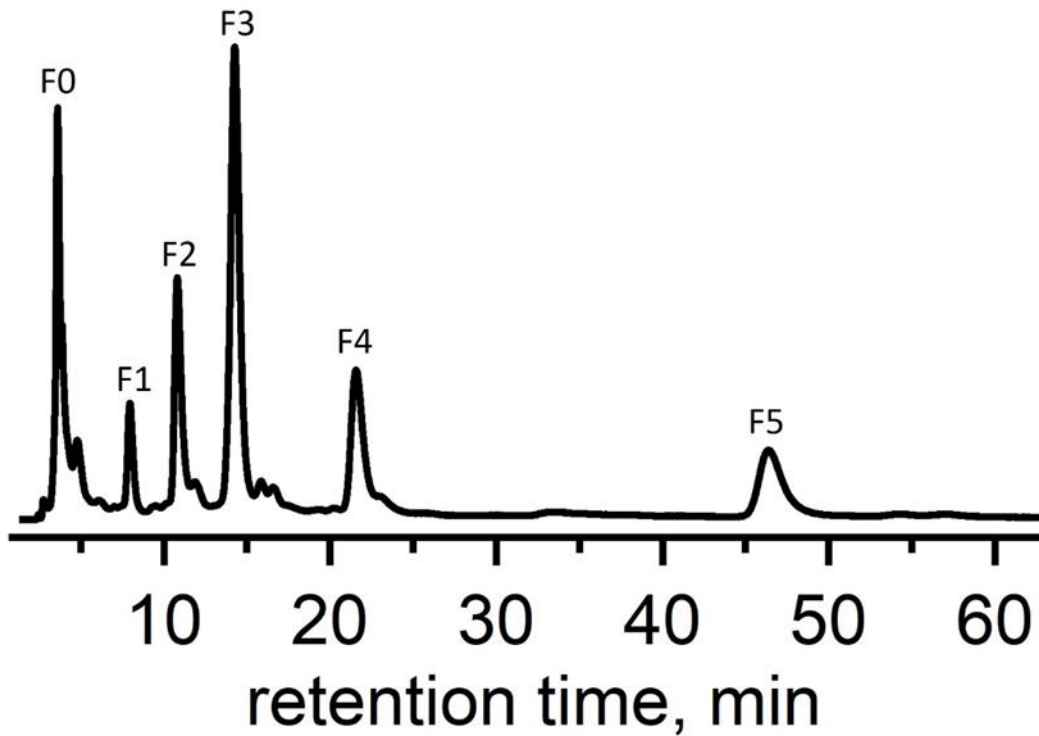
Figure 2-4. HPLC chromatogram of the crude product from reaction M1 (5 mL min^{-1} flow rate, 100% heptane eluent, Cosmosil Buckyprep column (10 × 250 mm)). Numbers designate fractions separated during the HPLC processing, for which spectroscopic analysis was carried out as described in the text.
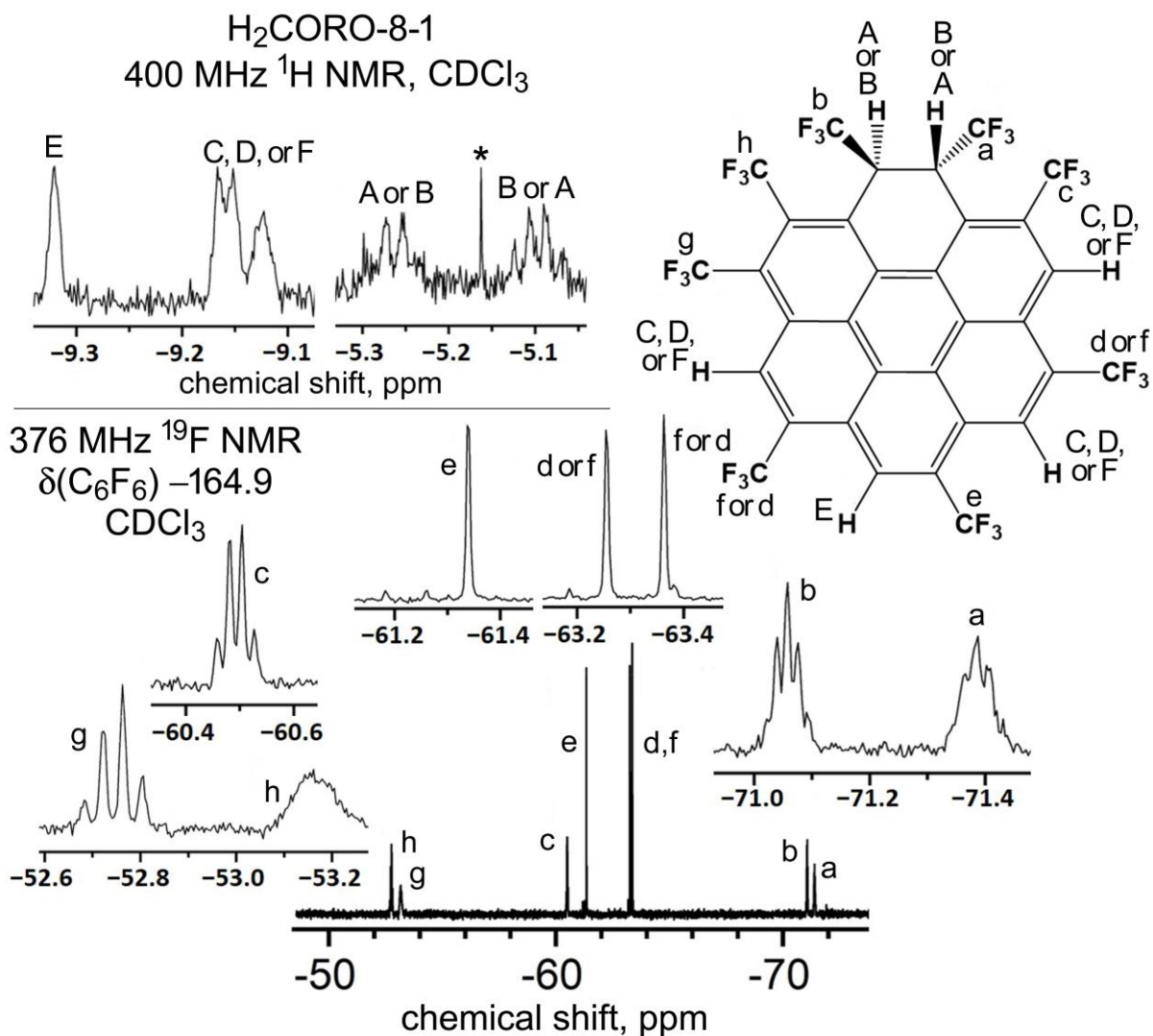
Figure 2-5. ^1H NMR and ^{19}F NMR spectra of H_2CORO-8-1 taken in $CDCl_3$ and referenced to chloroform and C_6F_6, respectively. (**Top**) The sp^3 protons are clearly visible as quartets between δ 5.3 and 5.1. The sharp singlet at δ 5.2, denoted with an asterisk, is due to an unidentified impurity. (**Bottom**) The ^{19}F NMR spectrum shows that there are three unique regions for fluorine environments. The signals between δ −60 and −65 for CF_3 groups not adjacent to the $C(sp^3)$ region of the dihydrocoronene, δ −70 to −72 for CF_3 groups bonded directly to a $C(sp^3)$ atom, and δ −52 to −54 for adjacent CF_3 groups.
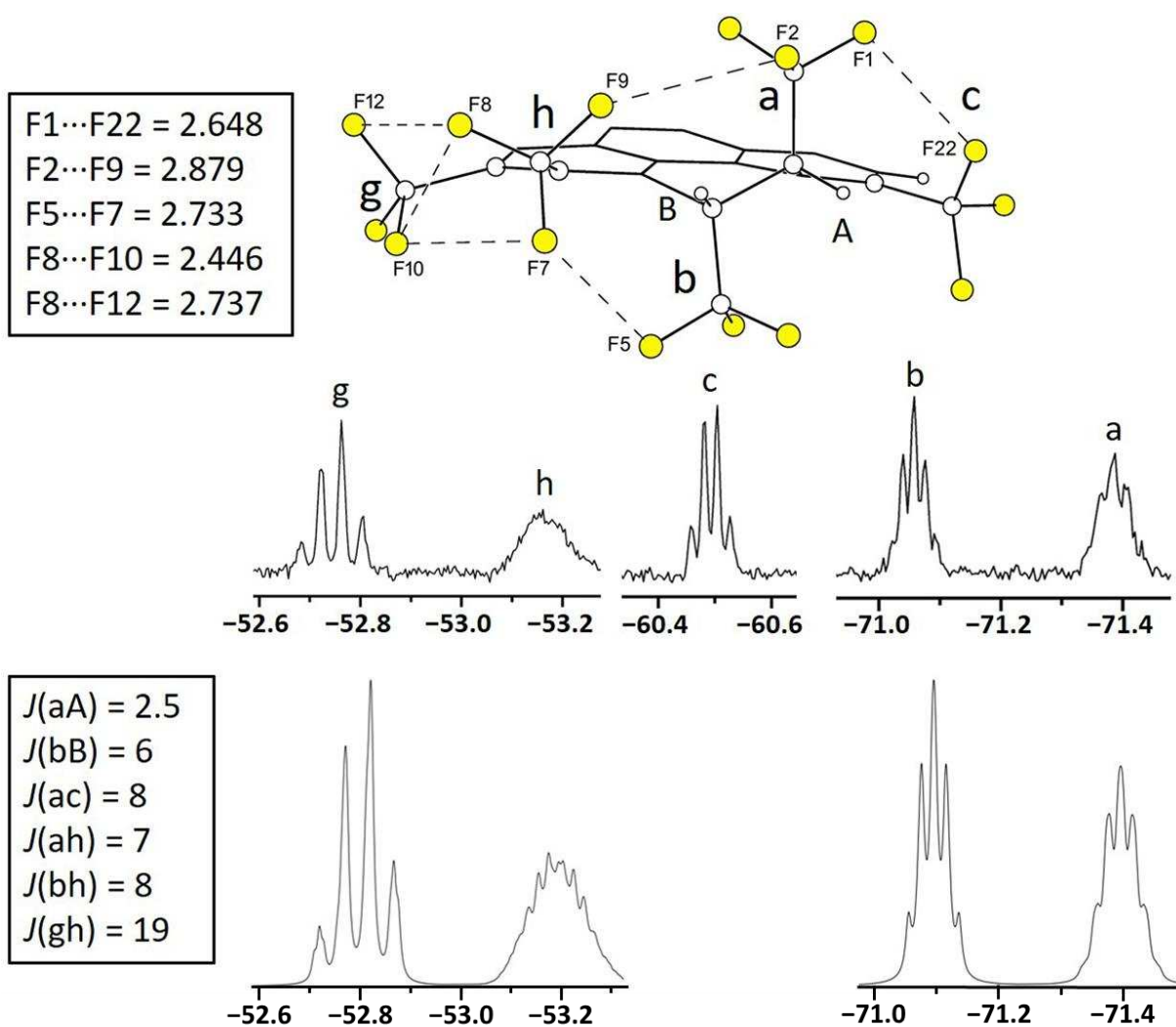
Figure 2-6. J_{FF} coupling analysis of H$_2$CORO-8-1 via (**Top**) solid-state F⋯F distance comparison and (**Bottom**) NMR simulations. F⋯F distances shorter than 3.0 Å are shown (**Top Left**). The simulated coupling constants of the complex multiplets shown in the ^{19}F NMR are shown (**Bottom Left**). CF$_3$ groups with coupled F atoms are labeled as are their corresponding ^{19}F NMR resonances. H atoms which are coupled to C(sp^3) bonded CF$_3$ groups are labeled with capital letters.
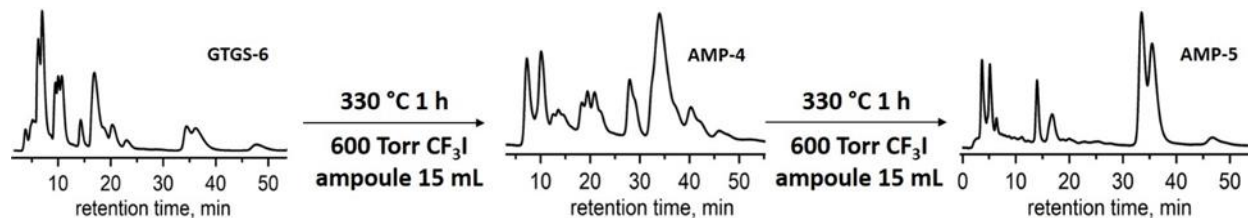
Figure 2-7. HPLC chromatograms showing the progression from the crude trifluoromethylated product from GTGS-6 to the final AMP reaction. The series of reactions appears to show that most CORO products undergo one or two substitutions under the AMP conditions allowing for more control over the reaction progression than is observed from the multiple GTGS reactions.
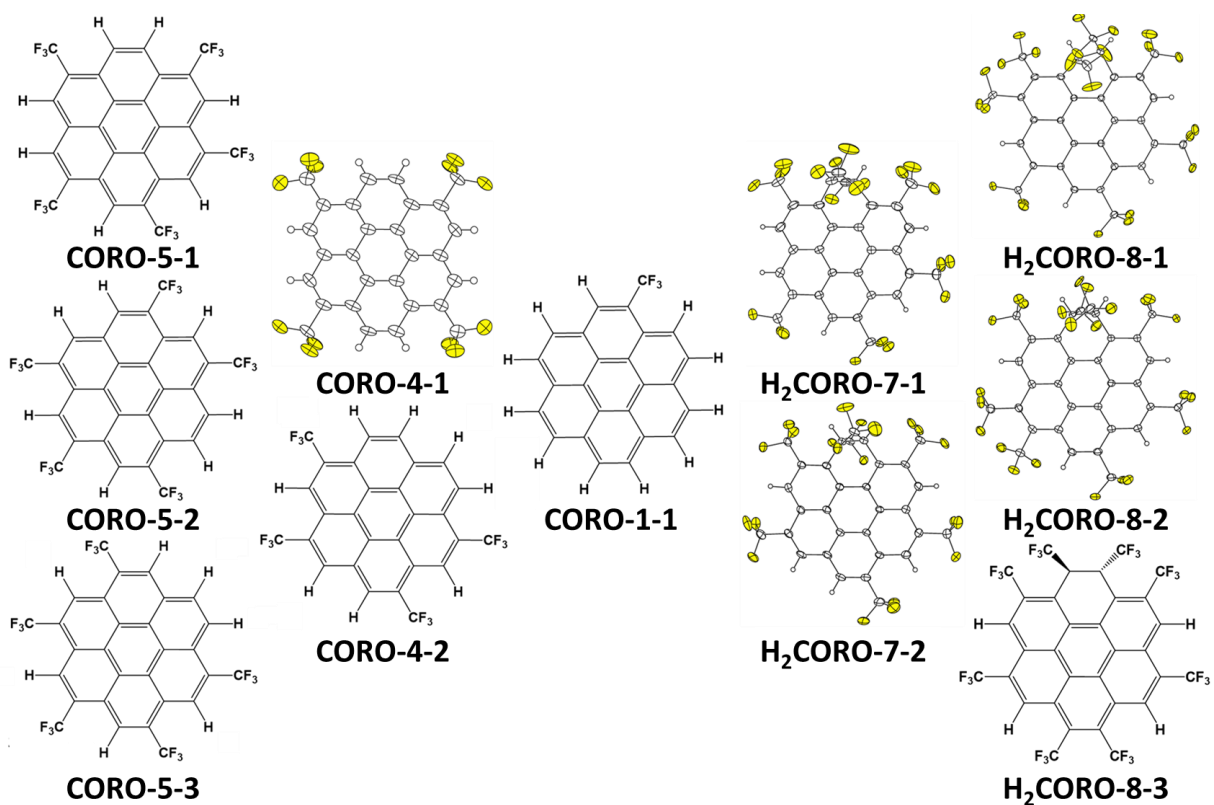
Figure 2-8. The eleven molecular structures of isolated compounds, five of which were confirmed by single-crystal X-ray structures. Additional molecular structures are included with the NMR figures in the supplemental figures.
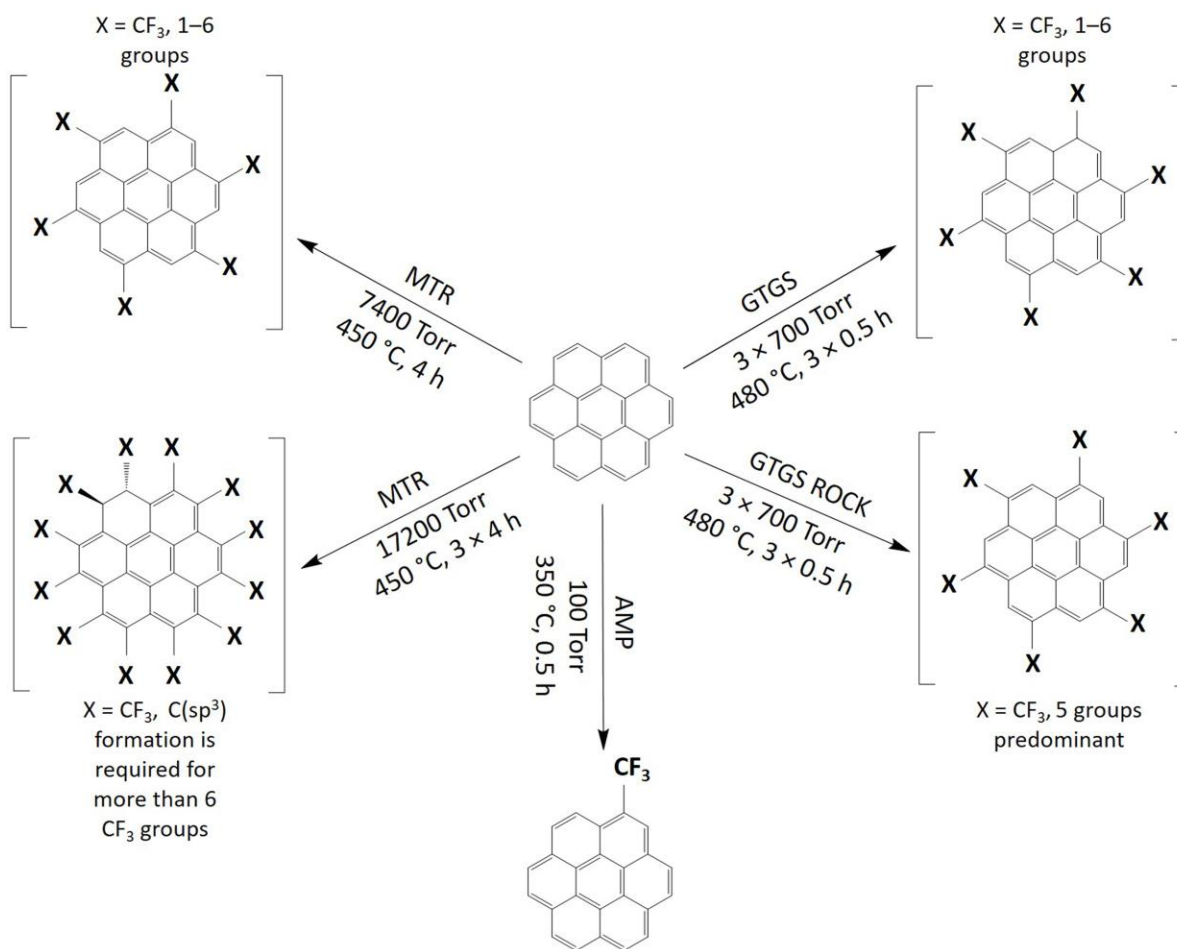
Figure 2-9. Reaction schematic for all the different types of trifluoromethylation reactions performed. The most common type of products from those reactions are shown.
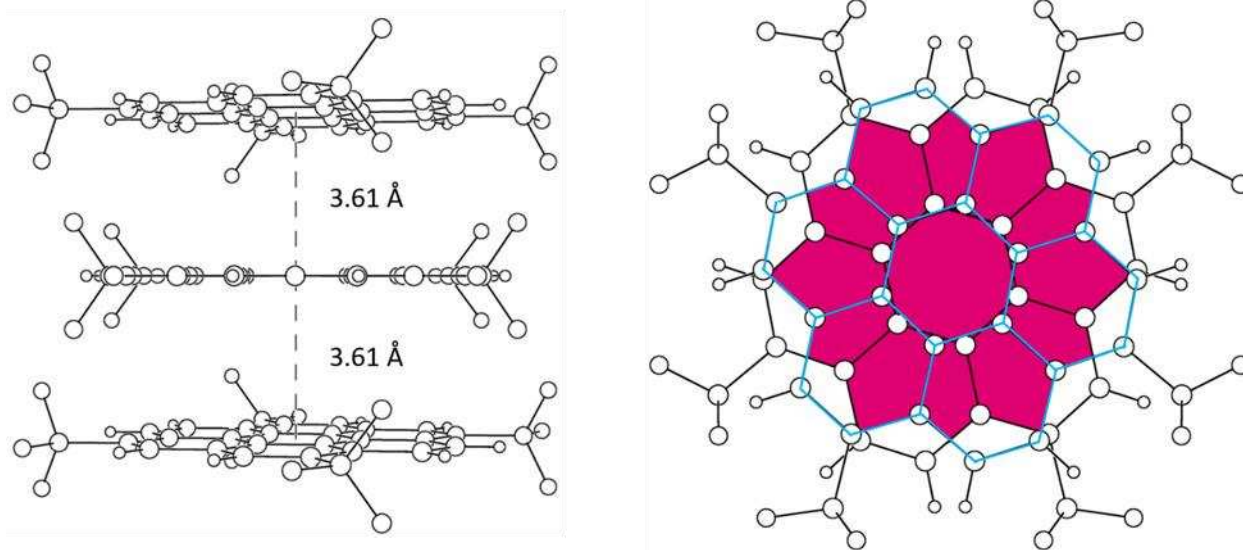
Figure 2-10. (**Left**) Parallel stacking of CORO-4-1 molecules along the crystallographic c axis, resulting in the separation of their rigorously parallel π systems by 3.61 Å. (**Right**) Flat projection drawing showing the degree of π-π overlap between adjacent molecules, which are rotated by 25° relative to one another. The upper molecule is highlighted with blue $C(sp^2)$–$C(sp^2)$ bonds. The amount of π–π overlap is 72%.
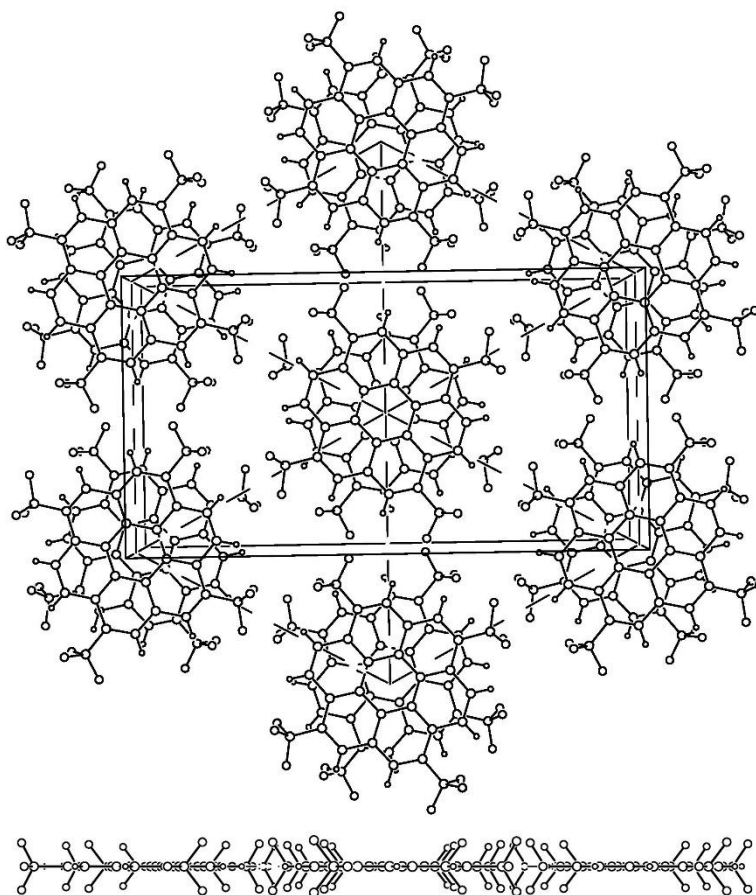
Figure 2-11. (**Top**) Hexagonal array of stacks of molecules in the structure of CORO-4-1. (**Bottom**) One layer of the hexagonal arrays of CORO-4-1 molecules. The layers are parallel to the crystallographic ab plane. The distances between molecular centroids in a given layer, shown with dashed lines, are 13.18 Å ($\times$ 4) and 12.48 Å ($\times$ 2).
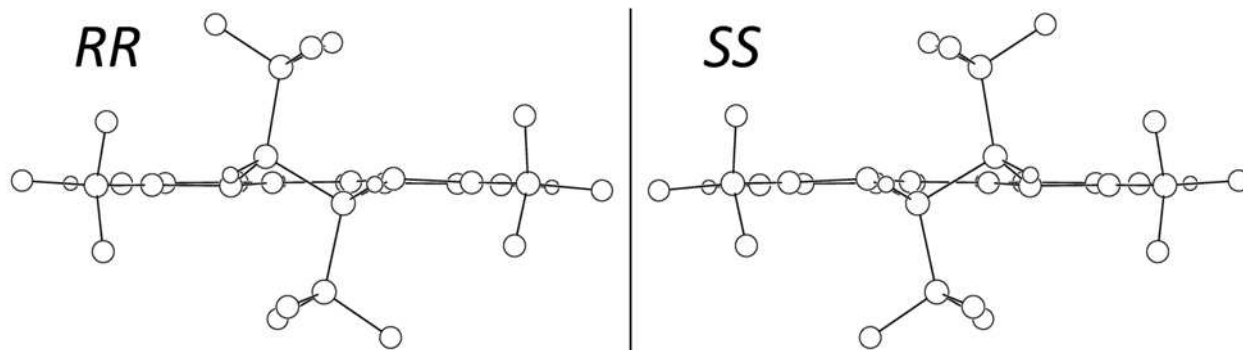
Figure 2-12. Generic $H_2CORO(CF_3)_n$ enantiomers RR and SS, these enantiomers are present in every H_2CORO structure. The difference in orientation of the $C(sp^3)$–$C(sp^3)$ bond gives rise to the two enantiomers resulting in non-superimposable molecules where the functional groups, CF_3 and H, are in alternating orientations. While the percent occupancy of the modeled enantiomers results in all but one of the dihydrocoronene molecules having nonracemic percentages, 61:39 SS:RR respectively for H_2CORO-7-1 for example, the majority enantiomer switches between planes resulting in the total crystal mixture being racemic. More information about the ratio of enantiomers in each model can be found in the supplemental information for this chapter, Appendix A, on pages S2-7 and S2-8.
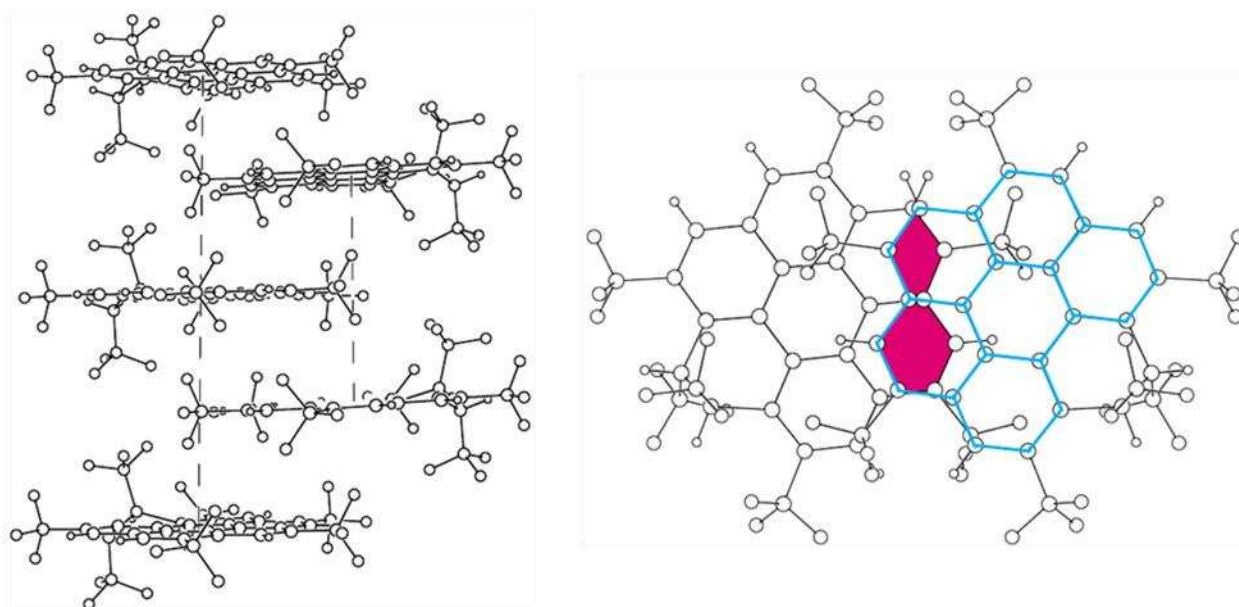
Figure 2-13. (**Lef**t) A column of H_2CORO-7-1 molecules, showing the lateral offset of every other molecule. The perpendicular distance between the central-hexagon centroids of alternating molecules, shown as dashed lines, is 8.085 Å. The closest molecules are in alternating columns with two unique distances for the neighboring molecule above and below being, 3.845 and 4.006 Å between them. The distance is not exactly half of the distance between molecules in the same column because the molecules in the interpenetrating columns are not coplanar resulting in one close distance and one slightly longer distance. (**Right**) Overlap of the two closest molecules of H_2CORO-7-1, the percent overlap is 8% with only four $C(sp^2)$ atoms overlapped. One of the molecules is overlaid in light blue to make the separate molecules more apparent.
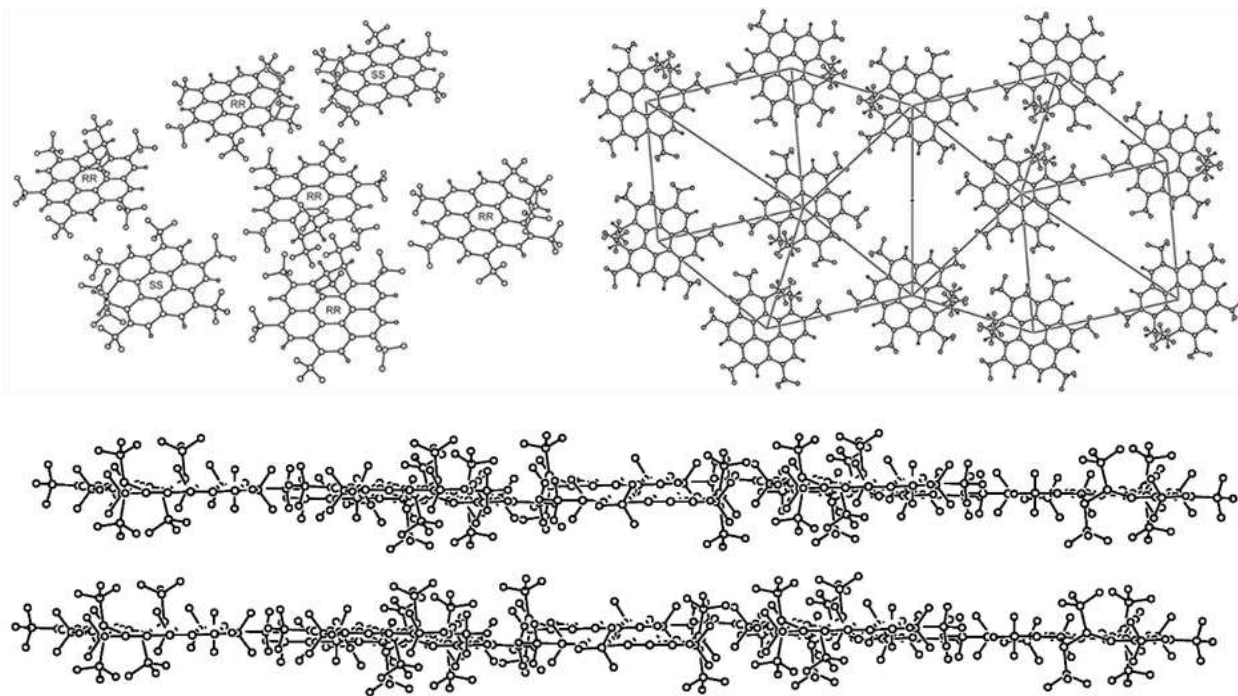
Figure 2-14. (**Top Left**) Six nearest neighbors making up the pseudo hexagonal array. Of the six molecules, four are the *RR* enantiomer and two are the *SS* enantiomer and the center molecule of the array is RR. This packing results in four unique distances measured from the centroid of each molecule, 12.12 Å, 13.47 Å (× 2), 14.37 Å (× 2), and 18.26 Å. (**Top Right**) Drawing showing the unique positions within a full array. Two molecules are shared between neighboring arrays. (**Bottom**) Within each array there are two unique planes, 0.71 Å apart.
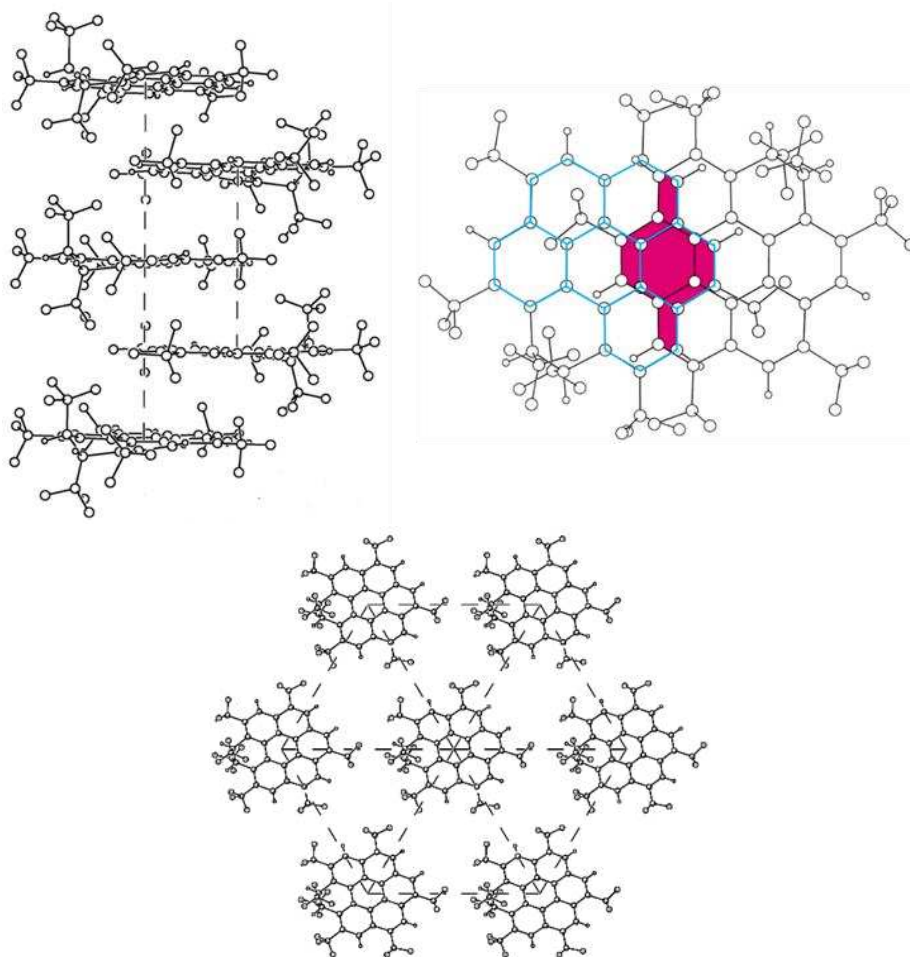
Figure 2-15. (**Top Left**) Interpenetrating columns of H_2CORO-7-2, the distance between molecules in a given column are 7.906 and 3.946 and 3.960 Å between molecules of interpenetrating columns. Again, there are two unique distances between interpenetrating molecules because the two columns of molecules are not coplanar. (**Top Right**) The π-π overlap of H_2CORO-7-2, the percent overlap is 15%. One of the molecules is overlaid in light blue to make the separate molecules more apparent. (**Bottom**) The six nearest neighbors within a single plane making up the hexagonal close packed array. The distances from the central molecule are 13.462 Å ($\times$ 2), 14.422 Å ($\times$ 2), and 14.435 Å ($\times$ 2). Within a single plane all of the molecules are the same enantiomer with each plane being made up of alternating enantiomers.
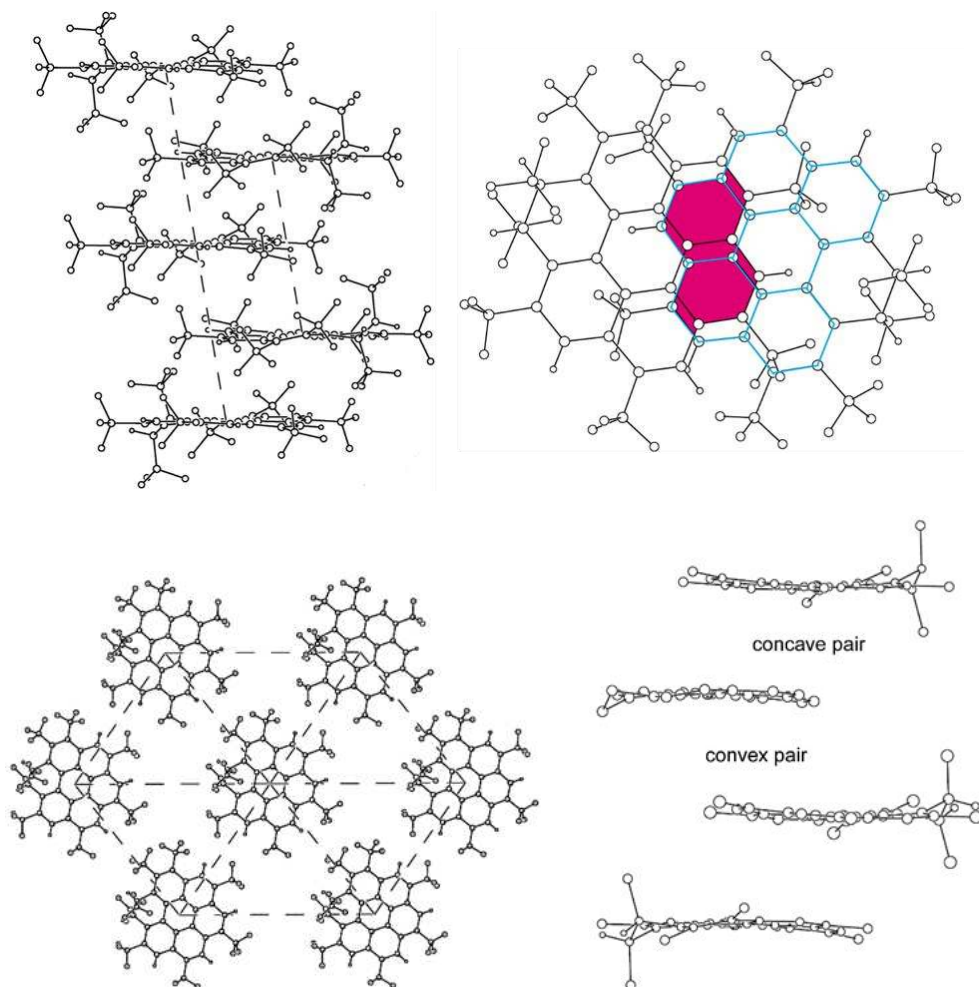
Figure 2-16. (**Top Left**) The interpenetrating columns of H₂CORO-8-1, with the concave pair distance being 3.792 Å while the convex pair is 4.224 Å. The distance between molecules of the same column is 8.015 Å. Notice this distance is always the same since the repeating unit is of course always the same, aka the pair is either both convex or both concave. (**Top Right**) The π–π overlap of H₂CORO-8-1, the percent overlap is 16%, with six C(sp²) atoms being directly overlapped. One of the molecules is overlaid in light blue to make the separate molecules more apparent. (**Bottom Left**) The six nearest neighbors within a single plane making up the hexagonal close packed array. The distances from the central molecule are 13.167 Å (× 2), 13.814 Å (× 2), and 16.093 Å (× 2). Within a single plane all of the molecules are the same enantiomer. (**Bottom Right**) The interpenetrating columns of molecules are comprised of concave and convex pairs.
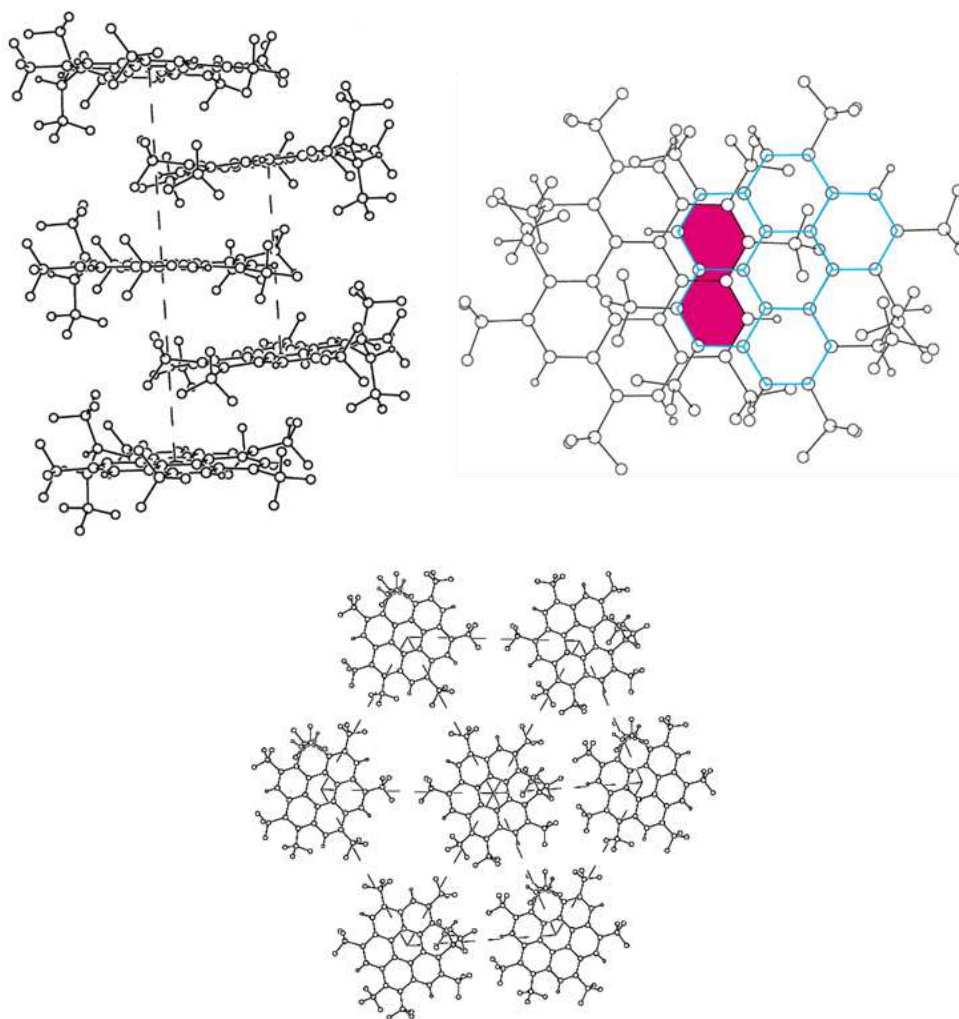
Figure 2-17. (**Top Left**) panel shows the interpenetrating columns of H_2CORO-8-2. The distance between molecules within the same column is 8.135 Å and the distances between close molecules of interpenetrating columns are 3.866 and 4.269 Å. (**Right**) The π–π overlap of H_2CORO-8-2, the percent overlap is 12%, with four $C(sp^2)$ atoms directly overlapped. One of the molecules is overlaid in light blue to make the separate molecules more apparent. (**Bottom**) The six nearest neighbors within a single plane making up the hexagonal close packed array. The distances from the central molecule are 12.803 Å ($\times 2$), 14.697 Å ($\times 2$), and 14.774 Å ($\times 2$). Within a single plane all of the molecules are the same enantiomer.
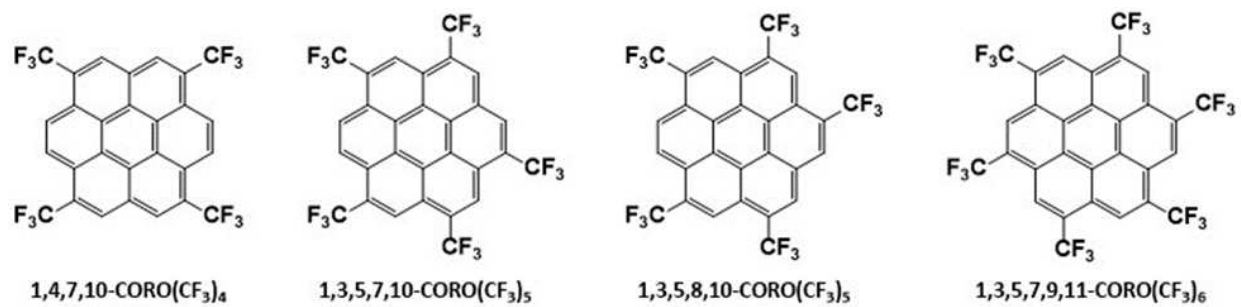
Figure 2-18. Drawings of the molecular structures of the theoretically predicted most stable highly substituted CORO(CF$_3$)$_n$, which do not have CF$_3$ groups on the adjacent carbons.

n = 0,1

n = 2,3

n = 3,4

n = 5

CORO(CF$_3$)$_n$ n = number of CF$_3$ groups
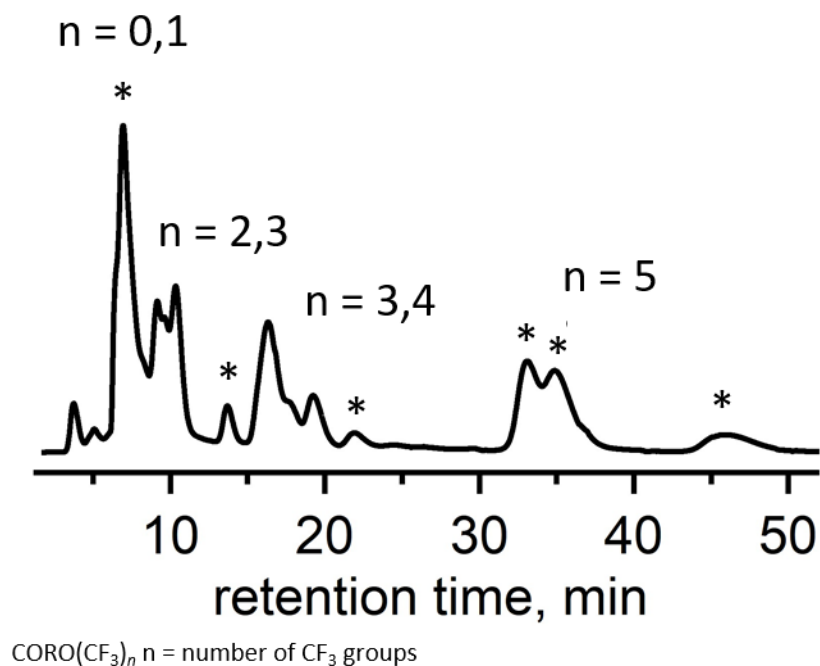
Figure 2-19. HPLC chromatogram from the Buckyprep semipreperative scale separation of GTGS-3. Eluent 100% toluene, flow rate 5 mL/min, and absorption at 300 nm. Peaks identified by an asterisk represent fractions where pure compounds were isolated with either primary or when necessary, secondary separation in the same eluent. The compounds are listed in the order that they elute: CORO-1-1, CORO-4-1, CORO-4-2, CORO-5-1, CORO-5-2, and CORO-5-3. See Table S2-6 for retention times.
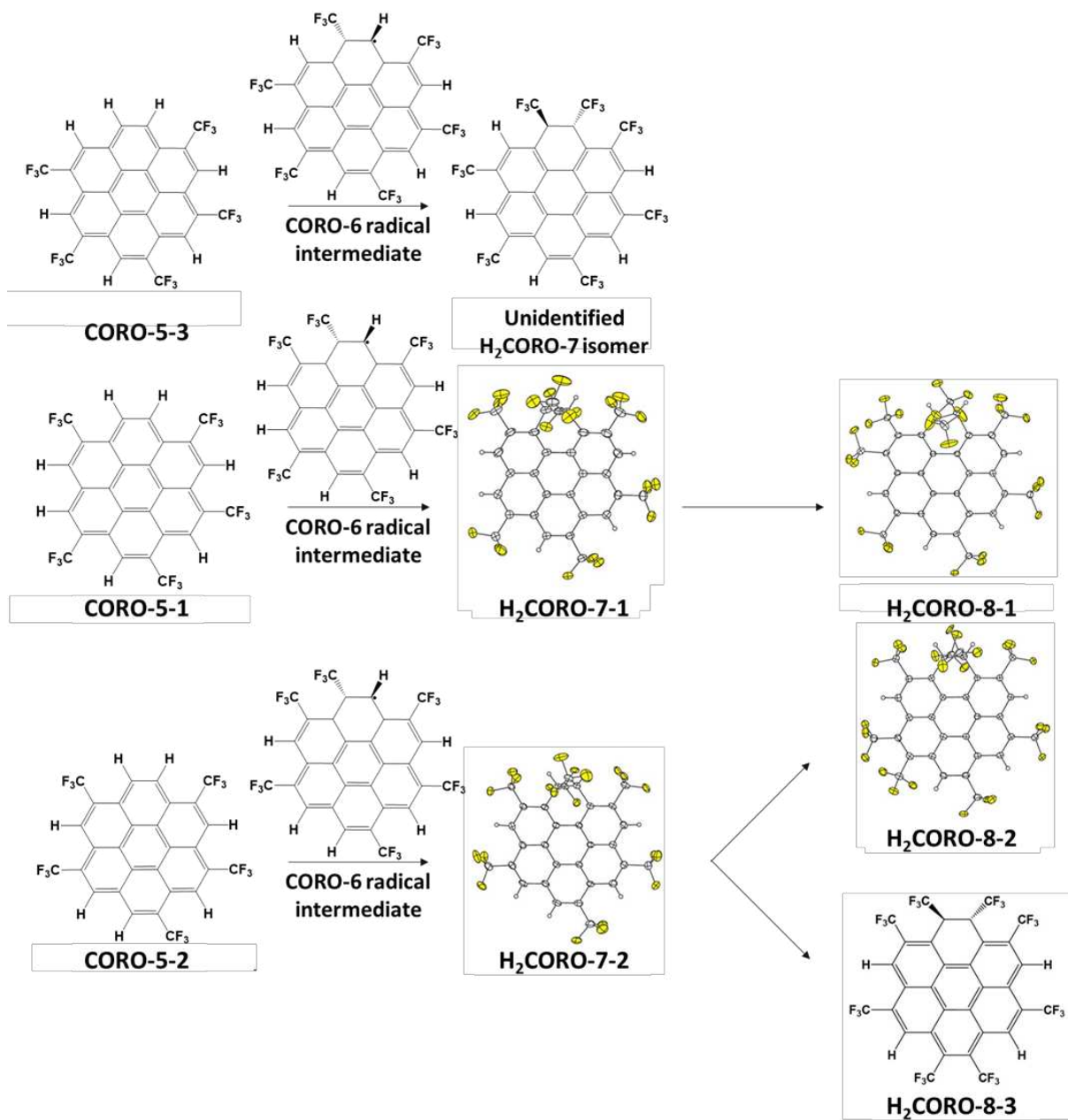
Figure 2-20. Reaction pathways from the CORO-5 isomers to the resulting $H_2CORO(CF_3)_{7,8}$ isomers.

98
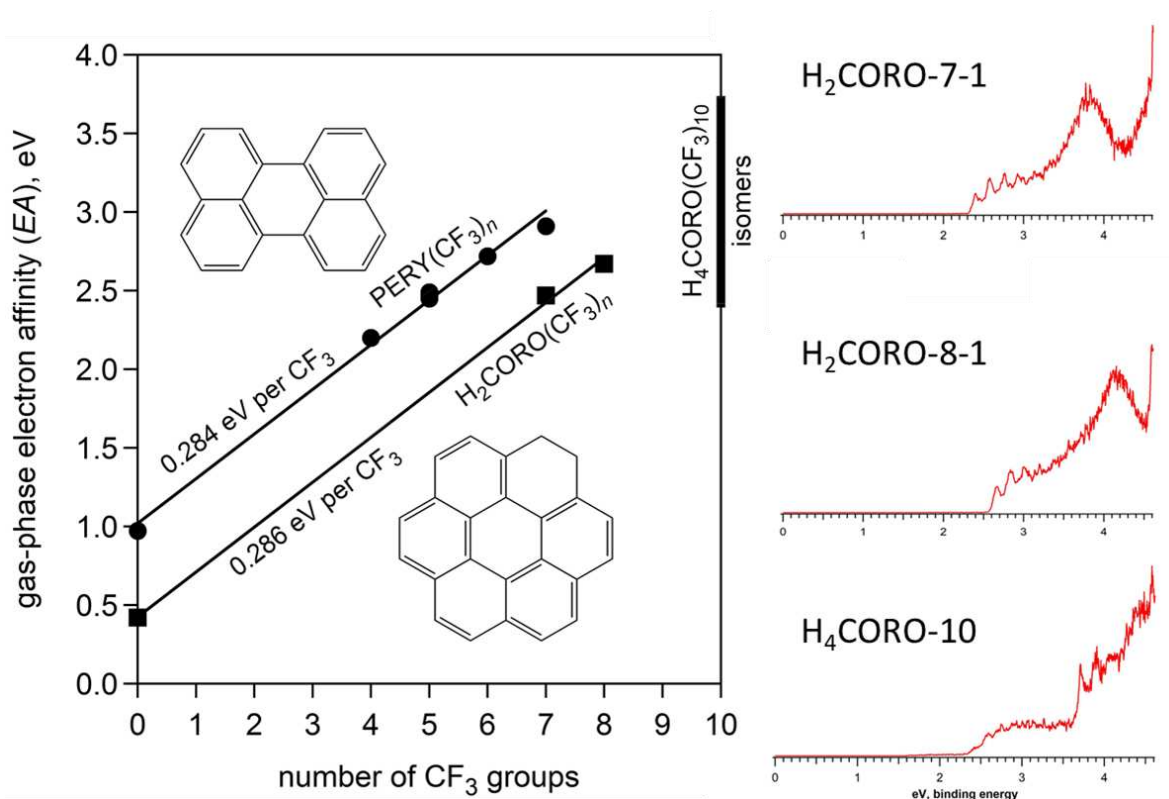
Figure 2-21. Electron affinity of $H_2CORO(CF_3)_n$ derivatives. The (**Top Right**) and (**Middle Right**) drawings show the binding energy plot for the gas-phase electron affinity of H_2CORO-7-1 and H_2CORO-8-1, respectively. H_2CORO-7-1: $EA = 2.40 \pm 0.01$ eV, $m/z = 778$. H_2CORO-8-1: $EA = 2.67 \pm 0.015$ eV, $m/z = 846$. The bottom right drawing shows H_4CORO-10 isomers. No pure isomer was isolated, but the mixture of compounds with $m/z = 984$ exhibited a range of EAs, (the lowest from 2.42 ± 0.05 eV to 3.71 ± 0.01 eV. The effect of adding a single CF_3 group increases the EA by 0.28 eV. Plotted in green are the EA values for trifluoromethylated perylene derivatives which had been previously reported.[49] The effect of a single CF_3 on perylene is very similar to benzo[ghi]perylene, 10 meV spread between the two substrates.
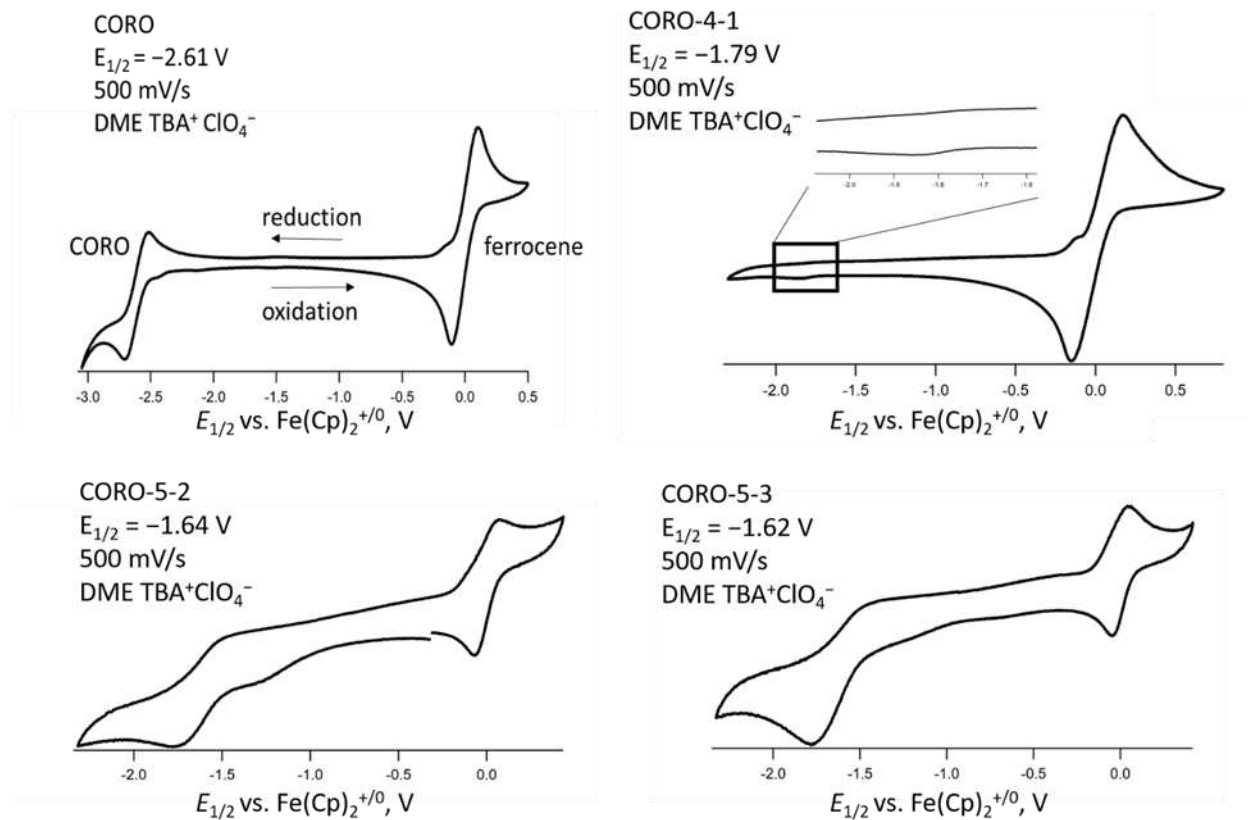
Figure 2-22. Comparison of the cyclic voltammograms of CORO, CORO-4-1, CORO-5-2, and CORO-5-3. All spectra were recorded in dimethoxyethane with tetrabutylamine perchlorate at 500 mV s^{-1}. 200 mV increase per CF$_3$ group.

2.6. REFERENCES

(1)   Zhao, Y.; Truhlar, D. G. A Prototype for Graphene Material Simulation: Structures and Interaction Potentials of Coronene Dimers. *The Journal of Physical Chemistry C* **2008**, *112*, 4061-4067.

(2)   João Paulo Almeida de, M.; Alessandro Henrique de, L.; Georgia Maria Amaral, J.; Welber Gianini, Q.; Cristiano, L.; Indhira Oliveira, M.; Fernando, S. Structural and vibrational study of graphene oxide via coronene based models: theoretical and experimental results. *Materials Research Express* **2016**, *3*, 055020.

(3)   Echigo, T.; Kimata, M.; Maruoka, T. Crystal-chemical and carbon-isotopic characteristics of karpatite (C24H12) from the Picacho Peak Area, San Benito County, California: Evidences for the hydrothermal formation. *Am. Mineral.* **2007**, *92*, 1262-1269.

(4)   Leger, A.; Puget, J. L. Identification of the "unidentified" IR emission features of interstellar dust? *Astron. Astrophys.* **1984**, *137*, L5-L8.

(5)   Rapacioli, M.; Calvo, F.; Joblin, C.; Parneix, P.; Toublanc, D.; Spiegelman, F. Formation and destruction of polycyclic aromatic hydrocarbon clusters in the interstellar medium. *Astron. Astrophys.* **2006**, *460*, 519-531.

(6)   Pathak, A.; Sarre, P. J. Protonated PAHs as carriers of diffuse interstellar bands. *Mon. Not. R. Astron. Soc.: Lett.* **2008**, *391*, L10-L14.

(7)   Rauls, E.; Hornekær, L. Catalyzed routes to molecular hydrogen formation and hydrogen addition reactions on neutral polycyclic aromatic hydrocarbons under interstellar conditions. *Astrophys. J.* **2008**, *679*, 531-536.

(8)   Murdoch, J. Pendletonite, a new hydrocarbon mineral from California. *Am. Mineral.* **1967**, *52*, 611-616.

(9)   Blumer, M. Curtisite, idrialite and pendletonite, polycyclic aromatic hydrocarbon minerals: their composition and origin. *Chem. Geol.* **1975**, *16*, 245-256.

(10)   Popov, I. A.; Boldyrev, A. I. Chemical bonding in coronene, isocoronene, and circumcoronene. *Eur. J. Org. Chem.* **2012**, *2012*, 3485-3491.

(11)   Fedik, N.; Boldyrev, A. I. Insight into The Nature of Rim Bonds in Coronene. *J. Phys. Chem. A* **2018**, *122*, 8585-8590.

(12)   Čupr, P.; Flegrová, Z.; Franců, J.; Landlová, L.; Klánová, J. Mineralogical, chemical and toxicological characterization of urban air particles. *Environ. Int.* **2013**, *54*, 26-34.

(13)   Potticary, J.; Jensen, T. T.; Hall, S. R. Nanostructural origin of blue fluorescence in the mineral karpatite. *Scientific Reports* **2017**, *7*, 9867.

(14)   Dong, W.-K.; Akogun, S. F.; Zhang, Y.; Sun, Y.-X.; Dong, X.-Y. A reversible "turn-on" fluorescent sensor for selective detection of Zn^{2+}. *Sens. Actuators, B* **2017**, *238*, 723-734.

(15)   Robertson, J. M. Bond-length variations in aromatic systems. *Acta Crystallogr.* **1948**, *1*, 101-109.

(16)   Roberts, J. D.; Caserio, M. C. *Basic Principles of Organic Chemistry 2nd Edition*; Addison-Wesley: New York, 1977.

(17)   Anbar, M.; Meyerstein, D.; Neta, P. The reactivity of aromatic compounds toward hydroxyl radicals. *J. Phys. Chem.* **1966**, *70*, 2660-2662.

(18)   Bruckner, R. Electrophilic Additions to the C=C Double Bond In *Organic Mechanisms: Reactions, Stereochemistry and Synthesis*; Harmata, M., Ed.; Springer Berlin Heidelberg: Berlin, 2010, pp 103-156.

(19)   Neto, A. H. C.; Guinea, F.; Peres, N. M. R.; Novoselov, K. S.; Geim, A. K. The electronic properties of graphene. *Rev. Mod. Phys.* **2009**, *81*, 109-162.

(20)   Zhao, Y.; Truhlar, D. G. A Prototype for Graphene Material Simulation: Structures and Interaction Potentials of Coronene Dimers. *J. Phys. Chem. C* **2008**, *112*, 4061-4067.

(21)   Yeamin, M. B.; Faginas-Lago, N.; Albertí, M.; Cuesta, I. G.; Sanchez-Marin, J.; de Merás, A. M. J. S. Multi-scale theoretical investigation of molecular hydrogen adsorption over graphene: coronene as a case study. *RSC Adv.* **2014**, *4*, 54447-54453.

(22)   Yoshida, Y.; Isomura, K.; Kishida, H.; Kumagai, Y.; Mizuno, M.; Sakata, M.; Koretsune, T.; Nakano, Y.; Yamochi, H.; Maesato, M. Conducting π Columns of Highly Symmetric Coronene, The Smallest Fragment of Graphene. *Chem. Eur. J.* **2016**, *22*, 6023-6030.

(23)   Zhang, C.; Shi, K.; Cai, K.; Xie, J.; Lei, T.; Yan, Q.; Wang, J.-Y.; Pei, J.; Zhao, D. Cyano- and chloro-substituted coronene diimides as solution-processable electron-transporting semiconductors. *Chem. Commun.* **2015**, *51*, 7144-7147.

(24)   Scholl, R.; Meyer, K. Synthese des anti-diperi-Dibenz-coronens und dessen Abbau zum Coronen (Hexabenzo-benzol). *Berichte der deutschen chemischen Gesellschaft (A and B Series)* **1932**, *65*, 902-915.

(25)   Newman, M. S. A New Synthesis of Coronene. *J. Am. Chem. Soc.* **1940**, *62*, 1683-1687.

(26)   Kumar, S.; Tao, Y.-T. Contorted Naphtho- and Fluorenocoronenes: Syntheses and Properties of Polycyclic Aromatics beyond Benzo- and Thiophenocoronenes. *Org. Lett.* **2018**, *20*, 2320-2323.

(27)   Wu, D.; Zhang, H.; Liang, J.; Ge, H.; Chi, C.; Wu, J.; Liu, S. H.; Yin, J. Functionalized Coronenes: Synthesis, Solid Structure, and Properties. *J. Org. Chem.* **2012**, *77*, 11319-11324.

(28)   Wurthner, F. Perylene bisimide dyes as versatile building blocks for functional supramolecular architectures. *Chem. Commun.* **2004**, 1564-1579.

(29)   Lütke Eversloh, C.; Li, C.; Müllen, K. Core-Extended Perylene Tetracarboxdiimides: The Homologous Series of Coronene Tetracarboxdiimides. *Org. Lett.* **2011**, *13*, 4148-4150.

(30)   Chen, L.; Li, C.; Mullen, K. Beyond perylene diimides: synthesis, assembly and function of higher rylene chromophores. *J. Mater. Chem. C* **2014**, *2*, 1938-1956.

(31)   Schulze, M.; Philipp, M.; Waigel, W.; Schmidt, D.; Würthner, F. Library of Azabenz-Annulated Core-Extended Perylene Derivatives with Diverse Substitution Patterns and Tunable Electronic and Optical Properties. *J. Org. Chem.* **2016**, *81*, 8394-8405.

(32)   Mao, W.; Zhang, J.; Li, X.; Li, C.; Tian, H. Regioisomerically pure multiaryl coronene derivatives: highly efficient synthesis via bay-extended perylene tetrabutylester. *Chem. Commun.* **2017**, *53*, 5052-5055.

(33)   van de Craats, A. M.; Warman, J. M.; Fechtenkötter, A.; Brand, J. D.; Harbison, M. A.; Müllen, K. Record charge carrier mobility in a room-temperature discotic liquid-crystalline derivative of hexabenzocoronene. *Adv. Mater.* **1999**, *11*, 1469-1472.

(34)	Ito, S.; Wehmeier, M.; Brand, J. D.; Kübel, C.; Epsch, R.; Rabe, J. P.; Müllen, K. Synthesis and self-assembly of functionalized hexa-peri-hexabenzocoronenes. *Chem. Eur. J.* **2000**, *6*, 4327-4342.

(35)	Rieger, R.; Kastler, M.; Enkelmann, V.; Müllen, K. Entry to coronene chemistry—making large electron donors and acceptors. *Chemistry–A European Journal* **2008**, *14*, 6322-6325.

(36)	Shen, H.-C.; Tang, J.-M.; Chang, H.-K.; Yang, C.-W.; Liu, R.-S. Short and Efficient Synthesis of Coronene Derivatives via Ruthenium-Catalyzed Benzannulation Protocol. *J. Org. Chem.* **2005**, *70*, 10113-10116.

(37)	Donovan, P. M.; Scott, L. T. Elaboration of Diaryl Ketons into Naphthalenes Fused on Two or Four Sides: A Naphthoannulation Procedure. *J. Am. Chem. Soc.* **2004**, *126*, 3108–3112.

(38)	Acree Jr., W. H. *Polycyclic Aromatic Hydrocarbons: Binary Non-Aqueous Systems Part I: Solutes A–E*; Oxford University Press: Oxford, 1995.

(39)	Family, H. Aspects of coronene chemistry, Ph.D. dissertation, University of Surrey, 1974.

(40)	Baird, T.; Gall, J. H.; MacNicol, D. D.; Mallinson, P. R.; Michie, C. R. Perchlorocoronene: a novel host precursor. *J. Chem. Soc., Chem. Commun.* **1988**, 1471-1473.

(41)	Dong, R.; Pfeffermann, M.; Skidin, D.; Wang, F.; Fu, Y.; Narita, A.; Tommasini, M.; Moresco, F.; Cuniberti, G.; Berger, R. Persulfurated Coronene: A New Generation of "Sulflower". *J. Am. Chem. Soc.* **2017**, *139*, 2168-2171.

(42)	Nilsson, U. L.; Colmsjö, A. L. Retention characteristics of chlorinated polycyclic aromatic hydrocarbons in normal phase HPLC. I. Chloro-added PAHs. *Chromatographia* **1991**, *32*, 334-340.

(43)	Rippy, K. C.; DeWeerd, N. J.; Kuvychko, I. V.; Chen, Y.-S.; Strauss, S. H.; Boltalina, O. V. Fluorination-Induced Evolution of Columnar Packing in Fluorous Triphenylenes and Benzotriphenylenes. *ChemPlusChem* **2018**, *83*, 1067-1077.

(44)	San, L. K. Strong Fullerene and Polycyclic Aromatic Hydrocarbon Electron Acceptors with Perfluorinated Substituents, Ph.D. dissertation, Colorado State University, 2015.

(45)   Rippy, K. C. Synthesis and Evaluation of Fluorous Polycyclic Aromatic Hydrocarbon Derivatives for Organic Electronics, Ph.D. dissertation, Colorado State University, 2019.

(46)   Bukovsky, E. V.; DeWeerd, N. J.; Strauss, S. H.; Boltalina, O. V. Versatile metal reactor for high-temperature and high-pressure trifluoromethylation of carbon-rich substrates. *J. Fluorine Chem.* **2018**, *210*, 56-64.

(47)   Clar, E. Synthesen von Benzologen des Perylens und Bisanthens. *Chem. Ber.* **1949**, *82*, 46-60.

(48)   The Chemical Shift Index In *Handbook of Proton-Nmr Spectra and Data*; Asahi Research Center Co, L., Ed.; Academic Press: Tokyo, 1987, pp 475-790.

(49)   Kuvychko, I. V.; Castro, K. P.; Deng, S. H. M.; Wang, X.-B.; Strauss, S. H.; Boltalina, O. V. Taming Hot CF_3 Radicals: Incrementally Tuned Families of Polyarene Electron Acceptors for Air-Stable Molecular Optoelectronics. *Angew. Chem. Int. Ed.* **2013**, *52*, 4871-4874.

(50)   Kuvychko, I. V.; Whitaker, J. B.; Larson, B. W.; Raguindin, R. S.; Suhr, K. J.; Strauss, S. H.; Boltalina, O. V. Pressure effect on heterogeneous trifluoromethylation of fullerenes and its application. *J. Fluorine Chem.* **2011**, *132*, 679-685.

(51)   Kataeva, O.; Khrizanforov, M.; Budnikova, Y.; Islamov, D.; Burganov, T.; Vandyukov, A.; Lyssenko, K.; Mahns, B.; Nohr, M.; Hampel, S.; Knupfer, M. Crystal Growth, Dynamic and Charge Transfer Properties of New Coronene Charge Transfer Complexes. *Cryst. Growth Des.* **2016**, *16*, 331-338.

(52)   Bondi, A. van der Waals Volumes and Radii. *J. Phys. Chem.* **1964**, *68*, 441-451.

(53)   Kuvychko, I. V.; Clikeman, T. T.; Dubceac, C.; Chen, Y.-S.; Petrukhina, M. A.; Strauss, S. H.; Popov, A. A.; Boltalina, O. V. Understanding Polyarene Trifluoromethylation with Hot CF_3 Radicals using Corannulene. *Eur. J. Org. Chem.* **2018**, 4233-4245.

(54)   Popov, A. A. Trifluoromethylated Corannulene Derivatives: Thermodynamic Stability and Electron-Accepting Properties In *New Fluorinated Carbons: Fundamentals and Applications*; Boltalina, O. V., Nakajima, T., Eds.; Elsevier: Amsterdam, 2017, pp 91-111.

(55)   Alkorta, I.; Rozas, I.; Elguero, J. Bond Length–Electron Density Relationships: From Covalent Bonds to Hydrogen Bond Interactions. *Struct. Chem.* **1998**, *9*, 243-247.

(56)   Waters, W. A. Radical Addition Reactions. *Nature* **1948**, *162*, 183-183.

(57)   Waters, W. A. The mechanism and kinetics of reactions involving free radicals. *Trans. Faraday Soc.* **1941**, *37*, 770-780.

(58)   Matito, E.; Silvi, B.; Duran, D.; Solà, M. Electron localization function at the correlated level. *J. Chem. Phys.* **2006**, *125*, article 024301.

(59)   Tedder, J. M.; Walton, J. C. The Kinetics and Orientation of Free-Radical Addition to Olefins. *Acc. Chem. Res.* **1976**, *9*, 183-191.

(60)   Hirayama, S.; Sakai, H.; Araki, Y.; Tanaka, M.; Imakawa, M.; Wada, T.; Takenobu, T.; Hasobe, T. Systematic Control of the Excited-State Dynamics and Carrier-Transport Properties of Functionalized Benzo[ghi]perylene and Coronene Derivatives. *Chem. Eur. J.* **2014**, *20*, 9081-9093.

(61)   Hasobe, T.; Ida, K.; Sakai, H.; Ohkubo, K.; Fukuzumi, S. Coronenetetraimide-Centered Cruciform Pentamers Containing Multiporphyrin Units: Synthesis and Sequential Photoinduced Energy- and Electron-Transfer Dynamics. *Chem. Eur. J.* **2015**, *21*, 11196-11205.

(62)   Ida, K.; Sakai, H.; Ohkubo, K.; Araki, Y.; Wada, T.; Sakanoue, T.; Takenobu, T.; Fukuzumi, S.; Hasobe, T. Electron-Transfer Reduction Properties and Excited-State Dynamics of Benzo[ghi]peryleneimide and Coroneneimide Derivatives. *J. Phys. Chem. C* **2014**, *118*, 7710-7720.

(63)   Kowalzik, P.; Atodiresei, N.; Gingras, M.; Caciuc, V.; Schnaebele, N.; Raimundo, J.-M.; Blügel, S.; Waser, R.; Karthäuser, S. Arylthio-substituted coronenes as tailored building blocks for molecular electronics. *Phys. Chem. Chem. Phys.* **2012**, *14*, 1635-1641.

(64)   Pal, A. K.; Li, C.; Hanan, G. S.; Zysman-Colman, E. Blue-Emissive Cobalt(III) Complexes and Their Use in the Photocatalytic Trifluoromethylation of Polycyclic Aromatic Hydrocarbons. *Angew. Chem Int. Ed.* **2018**, *57*, 8027-8031.

(65)   *New Fluorinated Carbons: Fundamentals and Applications*; V., B. O.; Nakajima, T., Eds.; Elsevier: Amsterdam, 2017.^

(66)   Castro, K. P.; Clikeman, T. T.; DeWeerd, N. J.; Bukovsky, E. V.; Rippy, K. C.; Kuvychko, I. V.; Hou, G.-L.; Chen, Y.-S.; Wang, X.-B.; Strauss, S. H.; Boltalina, O. V. Incremental Tuning Up of Fluorous Phenazine Acceptors. *Chem. Eur. J.* **2016**, *22*, 3930-3936.

(67)   Nijegorodov, N.; Mabbs, R.; Downey, W. S. Evolution of absorption, fluorescence, laser and chemical properties in the series of compounds perylene, benzo(ghi)perylene and coronene. *Spectrochim. Acta Part A: Mol. Biomol. Spectrosc.* **2001**, *57*, 2673-2685.

(68)   Strickler, S. J.; Berg, R. A. Relationship between Absorption Intensity and Fluorescence Lifetime of Molecules. *J. Chem. Phys.* **1962**, *37*, 814-822.

(69)   Castro, K. P.; Jin, Y.; Rack, J. J.; Strauss, S. H.; Boltalina, O. V.; Popov, A. A. Perfluoroalkyl [70]-Fullerenes as Robust Highly-Luminescent Fluorocarbons, or Position of One CF_3 Group Matters. *J. Phys. Chem. Lett.* **2013**, *4*, 2500-2507.

(70)   Wang, X. B.; Wang, L. S. Development of a Low-Temperature Photoelectron Spectroscopy Instrument Using an Electrospray Ion Source and a Cryogenically Controlled Ion Trap. *Rev. Sci. Instrum.* **2008**, *79*, 073108.

(71)   White, J. G. The crystal structure of 1:12-benzperylene: a quantitative X-ray investigation. *J. Chem. Soc.* **1948**, 1398-1408.

(72)   Botoshansky, M.; Herbstein, F. H.; Kapon, M. Towards a Complete Description of a Polymorphic Crystal: The Example of Perylene. *Helv. Chim. Acta* **2003**, *86*, 1113-1128.

CHAPTER 3

NEW SYNTHESES TO INTRODUCE FLUORINATED GROUPS TO FULLERENES AND OVERCOMING THE BARRIERS TO SELECTIVITY

3.1. INTRODUCTION AND JUSTIFICATION

Fluorine-rich fullerenes have received a lot of attention as electron withdrawing compounds due to their unique electrochemical properties, improved solubility, improved morphological control, and resistance to oxidation.[1-4] These factors make them possible candidates for semiconductor materials in organic electronics. Therefore, cost effective efficient synthetic routes to new fluorine-rich fullerenes are desired, which includes selectivity for the target compound, high yields, low-cost reagents, one-step synthetic processes and facile purification methods.

However, in fullerene reactions, targeting specific derivatives is always a challenge because of two factors that influence reaction outcome. The first is the thermodynamic barrier to functionalize the pristine fullerene is thermodynamically more unfavorable than subsequent functionalization. Therefore, in a reaction to target a derivatized C_{60} compound like $C_{60}(R)_2$ where R is any functional group, the product will often contain a mixture of the desired fullerene $C_{60}(R)_2$, unreacted C_{60}, and $C_{60}(R)_{n+2}$ where n is an even number. (One nuance to this rule is with respect to cycloadditions which are a large focus in this chapter. In those cases, while R does not increase by even numbers as a rule, there are still two new bonds formed for every subsequent functional group added.) For example, the ΔH_f for the most stable isomer with the composition $C_{60}(CF_3)_2$ is 1111 kJ mol^{-1} and every subsequent stable addition product after that has a negative ΔH_f, resulting in the facile formation of the addition products, $C_{60}(CF_3)_{n+2}$ where n = an even number.[5] In other words the reaction conditions required to convert C_{60} to $C_{60}(CF_3)_2$ are sufficient to easily produce multiple higher addition fullerenes and preventing these subsequent reactions is challenging. This makes control over the product distribution difficult because the number of additions is hard to control. The second factor is the large number of possible isomers of the product with the desired

composition. Even for the lowest composition of $C_{60}(R)_2$, there are 23 theoretically possible isomers. For the same functional group, R, $C_{60}(R)_{10}$ and $C_{70}(R)_{10}$ are theoretically capable of having 7×10^8 and 2×10^{10} isomers, respectively.[6]

Despite these two challenges, it is possible to perform selective fullerene derivative syntheses through optimization and careful control of reaction conditions. For the first factor, limiting the number of equivalents of the reagent can help minimize the number of products which can be formed. This has the drawback of often increasing the reaction time and lowering the percent conversion of the fullerene starting material, but it can make purification easier and the excess unreacted C_{60} can potentially be recovered allowing for further reactions and economical use of reagents. This method has been utilized by the author for several solution phase R_F reactions which will be discussed in the later sections of this chapter.[7,8] The second factor is not as easily overcome by a simple change to reaction methodology but through careful consideration of the specific reaction and the desired products, strategies can be made to improve selectivity and in some cases the yield. For example, the number of possible isomers decreases dramatically if logical assumptions about the range of relative stabilities of the products are considered; calculations reported in 2013 showed that there were not more than 3×10^4 likely isomers for any number of CF_3 functional groups on either C_{60} or C_{70} assuming the relative energies larger than 80 kJ mol^{-1} were excluded.[6] Additionally, the possibility of isomerization from higher relative energy derivatives to lower energy derivatives resulting in accumulation of specific isomers either through thermal treatment during or after the reaction, photolysis, or electrochemically via electrolysis, can further lower the number of products which are likely to be observed.[9-14] For the case of $C_{60}(CF_3)_{10}$, which has the largest number of experimentally identified isomers within a given composition, a total of 27 isomers have been reported.[15] Alternatively, instead of targeting the thermodynamic products, which is the result of all the methods described previously, by controlling the reaction time it is possible to select for kinetic isomers. This principle was utilized by the Strauss-Boltalina research group several times with the Gradient-Temperature Gas-Solid reactor where careful

control of the reaction temperature allowed for the sublimation of the fullerene derivatives produced in the reaction before further additions could take place.[16,17]

In this chapter, the syntheses of new fluorosulfanyl fullerenes and unique [3+2] perfluorocyclo- and partially fluorinated cyclo- groups referred to as fauxhawk functional groups are presented here.[8,18,19] Conditions for the reactions to produce these new products have been thoroughly investigated, and the resulting pure products, when appropriate, have been analyzed for potential uses in organic electronics.

3.2. SYNTHESIS OF PERFLUOROSULFANYL FULLERENES

3.2.1. General Comments

The pentafluorosulfanyl group's effective volume is more than twice that of the comparatively well-studied CF_3 group,[20,21] and is also more electronegative (3.65 vs. 3.36, respectively[22]). Additionally, the pentafluorosulfanyl group is more hydrophobic than the CF_3 group, yet equally hydrolytically stable[20,23] (an important factor since some reaction mixtures are worked up using a water wash[24]). The attachment of flurosulfanyl groups to the cage, or as part of a perfluoroalkyl group attached to the cage, may also increase solubility as was observed for other R_F functionalized fullerenes, such as $1,7\text{-}C_{60}(Bn_F)_2$.[21]

With these attractive properties in mind and in collaboration with Dr. Thrasher's research group at Clemson University in South Carolina, the goals of this research were (i) to see if intact $SF_5CF_2CF_2$ and SF_5CF_2 groups could be added to C_{60} under any conditions and (ii) to find a set of conditions to optimize the preparation of a bis adduct, $C_{60}(CF_2CF_2SF_5)_2$. The longer chain reagent $SF_5CF_2CF_2I$ was chosen for the initial reactions to lessen the possibility that steric hindrance imposed by a bulky SF_5 group might prevent the desired addition product from forming. As was previously mentioned, the SF_5 group is considerably larger than a CF_3 group. In fact, previous efforts to add the SF_5 group to a fullerene were successful using the longer perfluorobutyl chain reagent, $SF_5C_4F_8I$.[25] The second goal was important because the product $C_{60}(CF_2CF_2SF_5)_2$ would likely be a single isomer, $1,7\text{-}C_{60}(CF_2CF_2SF_5)_2$, and therefore it would be easier to purify and

characterize. In principle, the addition of two R_F groups to any of the 60 equivalent $C(sp^2)$ atoms of C_{60} can lead to 23 possible isomers. In practice, however, two R_F groups always add to the *para-* positions of a C_{60} hexagon (i.e., to C1 and C7; see the numbered Schlegel diagram in Figure S3-5) due to steric effects.[21]

This phenomenon is well described in Section 5.1.1 of the perfluoroalkylfullerene review by Strauss et al.,[21] but in brief the thermodynamic cost of adding a bulky addend in the 1,9- or *ortho-* positions is higher than the less sterically strained 1,7- or *para-* positions for C_{60}. For example, the difference in relative DFT calculated energies for adding two CF_3 groups to C_{60} in either the 1,9- or 1,7- positions is 35 kJ mol^{-1} higher in energy for the *ortho-* position. The same experiment with a Br atom, a smaller addend, results in a difference of 14 kJ mol^{-1} in favor of the *para-* position. With the $SF_5CF_2CF_2$- group being considerably bulkier than a trifluoromethyl group it is all but a certainty that the two-addition derivative will add to the *para-* positions as the theoretical *ortho-* addition product would be too thermodynamically unfavorable to form.

The initial conditions chosen for the reactions of C_{60} and $SF_5CF_2CF_2I$ were based on the conditions for the solution-phase synthesis of 1,7-$C_{60}(CF_2CF_2CF_3)_2$ and other 1,7-$C_{60}(R_F)_2$ derivatives using C_{60} and R_FI,[24] which were: 6.9 mM solution of C_{60} in *o*-DCB; 6 or more equiv R_FI; excess Cu powder; 180 °C; and 24–72 h reaction time. It was observed in that work that C_{60} is less soluble in hot *o*-DCB than in room-temperature *o*-DCB,[24] so, except for the initial reaction, lower concentrations of C_{60} in *o*-DCB were used for reactions with $SF_5CF_2CF_2I$ in this work. All synthetic work with $SF_5(CF_2)_nI$ reagents was performed at Clemson University by Dr. Siyan and crude products were shipped to CSU for analysis by the author.

For initial experiments a mixture of C_{60}, C_{70}, and higher fullerenes known as "fullerene extract" was used as the starting material for most of the reactions because it is much less expensive than 99.9% pure C_{60}. In addition, the Strauss-Boltalina research group has shown that the reaction conditions developed using fullerene extract are generally transferable to pure C_{60}.[21,24] Furthermore, C_{70} and higher fullerenes are less reactive than C_{60} with respect to reactions with R_FI

reagents, and therefore separating C_{60} *derivatives* from unreacted C_{70} and higher fullerenes by HPLC is relatively straightforward.[24] The experimental conditions for the 10 reactions studied in this work are summarized in Table 3-1, and HPLC traces, mass spectra, or NMR spectra of reaction mixtures are shown in figures Figure 3-1 through Figure 3-6.

3.2.2. Reaction of 10 mM C_{60} with 6 equiv OF $SF_5CF_2CF_2I$ at 180 °C

This is Reaction 1 (hereinafter Rxn. 1) listed in Table 3-1. During the 72 h reaction, the color of the solution changed from magenta, the color of C_{60}, to dark brown. Excess Cu powder and CuI were removed by filtration, and the solution was dried by rotary evaporation to a dark brown powder, which was soluble in hexane, toluene, and dichloromethane, DCM. Figure 3-1 shows the negative-ion electrospray-ionization, NI-ESI, mass spectrum of the dark brown product mixture dissolved in toluene and acetonitrile, ACN, was used as an eluent. Two sets of peaks are evident in the mass spectrum. There is a progression of five peaks starting at *m/z* 820 and separated by 100 Da that correspond to the molecular ions $C_{60}(C_2F_4)_n^-$ with n = 1–5 (i.e., the mass of $C_{60}(C_2F_4)$ is 820 and the mass of the C_2F_4 moiety is 100 Da). There is another set of four peaks starting at *m/z* 1374 and are also separated by 100 Da that corresponds to the molecular ions $C_{60}(SF_5CF_2CF_2)_2(C_2F_4)_n^-$ with n = 2–5. The ^{19}F NMR spectrum of this mixture of products (not shown) was very complicated, with many overlapping resonances and multiplets. The C_2F_4 substituents are undoubtedly four-membered-ring cycloadducts involving a C_{60} hexagon–hexagon double bond (i.e., a 6,6 junction). The compound 1,9-C_{60}(*cyclo*-C_2F_4) was reported previously (it was prepared by heating C_{60} with 1,2-$C_2F_4I_2$),[25] and its ^{19}F NMR spectrum matches the spectrum of the single compound that corresponds to the n = 1 ion in Figure 3-1 (i.e., after it was separated from a reaction mixture by HPLC). Compounds of C_{60} with multiple *cyclo*-C_2F_4 substituents have not yet been reported, but they are known for C_{70}, one of which was characterized by X-ray crystallography.[26] Note that we did not observe $C_{60}(SF_5)_n$ species among the products of Rxn. 1. This is consistent with the fact that fullerene derivatives with bulky addends or substituents directly bonded to the cage, such as *i*-C_3F_7 and Br, are prone to thermolysis of those substituents at lower

temperatures than derivatives with smaller substituents.[27,28] Furthermore, fullerene derivatives with exohedral C–I bonds are not known.[28]

Several conclusions based on the mass spectrum in Figure 3-1 can be made: (i) the steric bulk of the SF_5 moiety does not prevent the $SF_5CF_2CF_2$ groups from adding to C_{60} (ii) at least two intact $SF_5CF_2CF_2$ groups can add to C_{60} under our reaction conditions, producing stable and isolable products, and (iii) up to five cyclo-C_2F_4 groups can add to C_{60} under these conditions, which must involve C–S bond cleavage at some point. The maximum number of fullerene cage $C(sp^2)$ atoms that were converted to cage $C(sp^3)$ atoms in this reaction are 12, in $C_{60}(CF_2CF_2SF_5)_2(cyclo\text{-}C_2F_4)_5$, one for each of the two (cage)C–$CF_2CF_2SF_5$ bonds plus five pairs for the five cyclo-C_2F_4 adducts, each one involving two adjacent cage $C(sp^3)$ atoms. Since cyclo-C_2F_4 groups add to fullerene 6,6 junctions, the addition pattern(s) for $C_{60}(CF_2CF_2SF_5)_2(cyclo\text{-}C_2F_4)_5$ might involve one cage $C(sp^3)$ on each of the 12 fullerene pentagons. Most $C_{60}(R_F)_n$ derivatives with $n \leq 12$ have addition patterns with one R_F group per pentagon, although a few do not.[21] With "forcing" conditions, compounds such as $C_{60}(n\text{-}C_3F_7)_{14}$ and $C_{60}(n\text{-}C_4F_9)_{14}$ have been observed in complex reaction mixtures.[29]

The following series of reactions are the tentatively proposed pathway shown in equations 1–6 to account for the observed products of Rxn. 1. They are based on what is currently known about reactions of C_{60} with R_FI reagents, with and without excess Cu powder promoter, both in an o-DCB solution at 180 °C[24] and in a hot tube at 320–500 °C[29] (see also ref. 21 for more examples). The pathway is also based on the available literature for the addition of $SF_5CF_2CF_2I$ and $SF_5CF_2CF_2Br$ derived radicals across C=C double bonds[30] (It should be noted that the chemical reactivity of C_{60} is that of an electron-deficient olefin, not an aromatic compound[28]).

$$2SF_5CF_2CF_2I + 3Cu \rightarrow 2SF_4 + 2C_2F_4 + 2CuI + CuF_2 \qquad (1)$$

$$C_{60} + nC_2F_4 \rightarrow C_{60}(C_2F_4)_n \qquad (2)$$

$$SF_5CF_2CF_2I + Cu \rightarrow SF_5CF_2CF_2{}^\bullet + CuI \qquad (3)$$

$$SF_5CF_2CF_2^\bullet + C_{60} \rightarrow [C_{60}CF_2CF_2SF_5]^\bullet \tag{4}$$

$$[C_{60}CF_2CF_2SF_5]^\bullet + SF_5CF_2CF_2I + Cu \rightarrow C_{60}(CF_2CF_2SF_5)_2 + CuI \tag{5}$$

$$C_{60}(CF_2CF_2SF_5)_2 + mC_2F_4 \rightarrow C_{60}(CF_2CF_2SF_5)_2(cyclo\text{-}C_2F_4)_m \tag{6}$$
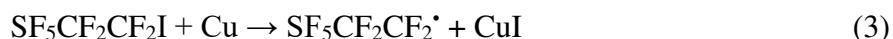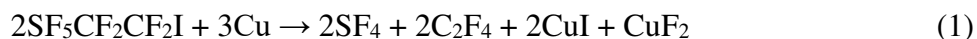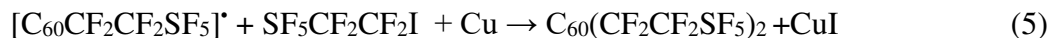
It was noted that SF_4 was detected in the ^{19}F NMR spectrum of the volatile products from the reaction, and therefore it is possible that CuF_2 was also formed as shown in eq. 1. CuF has never been convincingly isolated by anybody despite at least one report to the contrary.[31] If it is produced it decomposes rapidly and so the CuF_2 species would be the only logical option for eq. 1. Other sulfur-containing products may have been present, but this was beyond the scope of this investigation.

3.2.3. Reaction of 5 mM C_{60} with 6 equiv $SF_5CF_2CF_2I$ at 155 °C

These conditions correspond to Rxn. 2 in Table 3-1. The observation of a C_{60} derivative with two intact $CF_2CF_2SF_5$ groups in the Rxn. 1 product mixture was promising. However, all of the products also contained one or more $cyclo\text{-}C_2F_4$ substituents, and if these formed after $SF_5CF_2CF_2$ radicals added to C_{60}, as proposed, then a temperature lower than 180 °C might reduce the rate of the reaction shown in eq. 1 and provide products with more $CF_2CF_2SF_5$ groups and fewer $cyclo\text{-}C_2F_4$ groups. This hypothesis was based on two factors. First, eq. 1 shows four possible products from the decomposition of the $SF_5CF_2CF_2I$ reagent. This results in a reaction where the decomposition of the $SF_5CF_2CF_2I$ reagent is entropically favored leading to an unproductive reaction. Second, the cleavage of the C–SF_5 bond appears to occur readily at the 180 °C temperature used in Rxn. 1 based on the formation of the $cyclo\text{-}C_2F_4$ products. By lowering the temperature, it was hoped that eq. 1, 2, and 6 could be minimized and the reaction would be more selective for $C_{60}(CF_2CF_2SF_5)_n$. Therefore, Rxn. 2 was performed with the same stoichiometry and reaction time as Rxn. 1 but with a lower initial concentration of C_{60} and at 155 °C instead of 180 °C. Figure 3-2 shows the NI-ESI mass spectrum of the product mixture after the same workup was

used as in Rxn. 1 (all of the reactions listed in Table 3-1 were worked up the same way before initial spectroscopic or HPLC analysis).

Although the spectrum is more complicated than the one just described for the Rxn. 1 product mixture, it was immediately obvious that derivatives with up to 11 $CF_2CF_2SF_5$ groups were present. Based on peak intensities of the molecular ions, particularly abundant products included $C_{60}(CF_2CF_2SF_5)_{8,9,10}$ and $C_{60}(CF_2CF_2SF_5)_{4,5,6}(C_2F_4)$. The ^{19}F NMR spectrum and HPLC chromatogram (not shown) confirmed that a complex mixture of derivatives was present, demonstrating that most of the ions present in the mass spectrum did not form by fragmentation of fewer species in the mass spectrometer ion source. Therefore, lowering the reaction temperature to 155 °C resulted in significant suppression of the undesired C–SF_5 bond cleavage, although it did not eliminate it. This led to a series of reactions at even lower temperatures, which will be discussed next.

3.2.4. Optimization of C_{60} + $SF_5CF_2CF_2I$ reaction parameters

As discussed above, beyond demonstrating that $SF_5CF_2CF_2I$ can be used to prepare $C_{60}(CF_2CF_2SF_5)_n$ derivatives, our primary synthetic target was $C_{60}(CF_2CF_2SF_5)_2$ because it would likely be a single isomer. Table 3-1 lists the experimental conditions for Rxns. 3–10, with concentrations of C_{60} that ranged from 3.2 to 5.0 mM, with 4 or 6 equiv $SF_5CF_2CF_2I$, with reaction temperatures of 145 or 140 °C, and with reaction times of 48 and 72 h. The lower temperatures achieved the goal of further limiting the amount of C–SF_5 bond cleavage during the addition of $SF_5CF_2CF_2$ groups to C_{60}.

Rxns. 6 and 8 were the only reactions run for 48 h. Their experimental conditions were identical to confirm that the reactions of C_{60} and $SF_5CF_2CF_2I$ were reproducible with respect to the mixture of products produced, and they will not be discussed further. HPLC chromatograms of crude product mixtures from Rxns. 3–5, 7, and 9, all of which were run at 145 °C, are shown in Figure 3-3 and Figure 3-4. Only Rxn. 10 was run at 140 °C. The HPLC trace of the crude product mixture from Rxn. 10 is also shown in Figure 3-3. In addition, an HPLC chromatogram using a different

eluent and the ^{19}F NMR spectrum of the Rxn. 10 crude product mixture are shown in Figure 3-5 and Figure 3-6, respectively.

Figure 3-3A compares the HPLC chromatograms for Rxns. 3 and 7, both of which had an initial C_{60} concentration of 5.0 mM. They differed in $C_{60}:SF_5CF_2CF_2I$ stoichiometry, 1:4 for Rxn. 3 and 1:6 for Rxn. 7. The greater number of equivs of $SF_5CF_2CF_2I$ resulted in a much higher conversion of C_{60} to products (Rxn. 3), but the ratio of the target derivative $C_{60}(CF_2CF_2SF_5)_2$ (t_R 7 min) to $C_{60}(CF_2CF_2SF_5)_n$ with $n > 2$ ($t_R < 6$ min) was higher in Rxn. 7.

Figure 3-3B compares the HPLC chromatograms for Rxns. 4 and 9, which had the same reaction parameters as Rxns. 3 and 7 except that the initial concentration was 3.2 mM instead of 5.0 mM. Figure 3-3B also allows the comparison of Rxn. 4 with Rxn. 3. With 3.2 mM C_{60} and 6 equiv of $SF_5CF_2CF_2I$ (Rxn. 4), there was less conversion but a higher $C_{60}(CF_2CF_2SF_5)_2:C_{60}(CF_2CF_2SF_5)_{n>4}$ ratio than with 5.0 mM C_{60} and 6 equiv $SF_5CF_2CF_2I$ (Rxn. 3). With 3.2 mM C_{60} and 4 equiv $SF_5CF_2CF_2I$ (Rxn. 9), there was an even higher $C_{60}(CF_2CF_2SF_5)_2:C_{60}(CF_2CF_2SF_5)_{n>4}$ ratio than in Rxn. 4, but there was also a much greater proportion of C–SF_5 bond-cleavage product $C_{60}(c\text{-}C_2F_4)$ (t_R 6.2 min).

HPLC chromatograms for Rxns. 3, 4, and 5 are also compared in Figure 3-4. At 145 °C and with 6 equiv $SF_5CF_2CF_2I$, the lowest initial C_{60} concentration (Rxn. 4) produced more $C_{60}(CF_2CF_2SF_5)_2$ relative to the other products, but of course also had the lowest conversion of C_{60} to products.

Figure 3-3C compares Rxns. 9 and 10, both of which used 4 equiv $SF_5CF_2CF_2I$. The best results were achieved with Rxn. 10, which had the lowest temperature used (140 °C), the lower of the two $C_{60}:SF_5CF_2CF_2I$ stoichiometries used (1:4), but an intermediate initial concentration of C_{60} (4.0 mM). Figure 3-5 shows the HPLC chromatogram of the crude product mixture from Rxn. 10 using a weaker eluent than was used for the chromatograms in Figure 3-3 and Figure 3-4 (i.e., 25/75 v/v toluene/heptane instead of 100% toluene). This chromatogram clearly shows that the predominant

116

Rxn. 10 product was $C_{60}(CF_2CF_2SF_5)_2$. The ^{19}F NMR spectrum of the crude product mixture, shown in Figure 3-6, confirms that the mixture contained $C_{60}(CF_2CF_2SF_5)_2$ as the predominant product with $C_{60}(cyclo\text{-}C_2F_4)$ as the second most abundant product (singlet at $\delta = -114$[25]). The relatively sharp resonances for these two products (*vide infra*) superimposed on much broader features due to the multitude of overlapping resonances of the other products stands in contrast to the NMR spectra of the other crude product mixtures, which are featureless because they contain much less $C_{60}(CF_2CF_2SF_5)_2$, see Figure S3-3. This comparison shows Rxn. 10 as the most selective and a worthy candidate for separation.

3.2.5. Purification and characterization of $C_{60}(CF_2CF_2SF_5)_2$

The $C_{60}(CF_2CF_2SF_5)_2$ product was isolated from the fraction with a t_R *ca.* 18 min as shown in Figure 3-5. The eluent was a binary solvent mixture of toluene and heptane in a 25/75 ratio. In order to avoid decomposition of the desired product either through elimination of the SF_5 group and subsequent *cyclo-* products being formed or elimination of a reactive F^- species from the conversion of SF_5 to SF_4, the fraction was not roto-evaporated at elevated temperatures, as is typical, but was evacuated to dryness without additional heat beyond room temperature. The isolated fraction was analyzed by NI-ESI mass spectrometry and ^{19}F NMR spectroscopy. The initial mass spectrometry analysis that used acetonitrile as the eluent, which was also used for the analysis of the crude product mixtures (see Figure 3-1 and Figure 3-2) showed that besides the signal at *m/z* 1174, due to the molecular anion formed from $C_{60}(CF_2CF_2SF_5)_2$, other peaks were also present, as shown in Figure 3-7, indicating that the fraction might contain more than one compound, even though these signals could not be readily assigned to any of the possible reaction products. However, when the fraction was repurified by HPLC, the mass spectrum did not change. We then examined other ESI eluents, DCM, toluene, and hexanes, to investigate whether the putative "impurity" signals might be due to adduct formation with ionized solvent (and/or any solvent impurities) in the mass spectrometer ion source. The nonpolar solvents, toluene and hexanes, are typically not effective for ESI-MS analysis producing low-intensity mass spectra,

however, in this case, ionization was effective and molecular anions $C_{60}(CF_2CF_2SF_5)_2^-$ were readily formed, indicating that the analyte may possess a relatively high electron affinity (*EA*) (see two lower mass spectra in Figure 3-7). Nevertheless, extensive adduct formation was observed even with these eluents. The solvent DCM was the most prone to adduct formation, and multiple anionic adducts, some identified as a series of $(ClCH_2)_n^-$, adducts that spanned the mass range of 400 Da. It is a highly unusual behavior of the fluoroalkylated fullerenes in the ESI mass spectrometer: CF_3 and longer-chain R_F derivatives of C_{60} typically produce "clean" mass spectra containing only $C_{60}(R_F)_n^-$ and/or $C_{60}(R_F)_{n-1}^-$ anions, with no evidence for the formation of adducts with any of the solvents used in this work. This observation is an indication that the chemical properties of $C_{60}(CF_2CF_2SF_5)_n$ derivatives may be different than those of other PFAFs. Because of these complications, we could not use ESI-MS to determine the purity of the new compound $C_{60}(CF_2CF_2SF_5)_2$. However, it was possible to demonstrate its purity using ^{19}F NMR spectroscopy.

The ^{19}F NMR spectrum of $C_{60}(CF_2CF_2SF_5)_2$ demonstrates that the isomer prepared in this work is indeed 1,7-$C_{60}(CF_2CF_2SF_5)_2$. The spectrum, shown in Figure 3-8, which also includes a drawing of a portion of the proposed structure of the molecule, consists of four regions, two of which are assigned to the SF_5 moiety and two of which are assigned to the two pairs of CF_2 moieties. The SF_5 moiety gives rise to the ab_4 portion of the spectrum, at 62.5 and 42.3 ppm, with $^2J(F_AF_B) =$ 149 Hz, which is similar to the ab_4 sub-spectra of a number of $SF_5CF_2CF_2R$ compounds.[30,32] The two α-CF_2 moieties attached to the C_{60} cage give rise to the $aa'bb'$ multiplet centered at δ −111.2 (where *a* and *a'* represent F_1 and F_1' in one CF_2 moiety and *b* and *b'* represent F_1 and F_1' on the symmetry related α-CF_2 moiety), with $\delta(F_1) = -110.8$, $\delta(F_1') = -111.6$, and $^2J(F_1F_1') = 268 \pm 5$ Hz, cf. the F_1F_1' $aa'bb'$ sub-spectra of 1,7-$C_{60}(CF_2CF_2CF_3)_2$ and 1,7-$C_{60}(CF_2CF_3)_2$,[17] shown in Figure S3-4). Finally, the two β-CF_2 moieties give rise to the *ab* quartet centered at −91.7 ppm, with $\delta(F_2)$ $= -91.5$, $\delta(F_2') = -91.9$, and $^2J(F_2F_2') = 233 \pm 5$ Hz.

The UV-vis spectrum of a toluene solution of $C_{60}(CF_2CF_2SF_5)_2$, shown in Figure 3-9, provides additional confirmation of the proposed addition pattern. There are two bands at 327 and 447 nm,

with weaker bands at 603 and 697 nm. These features are consistent with the *para-* addition pattern

in bis(adducts) of C_{60}, 1,7-$C_{60}(X)_2$ derivatives, including 1,7-$C_{60}(R_F)_2$, several X-ray structures for

which have been reported.[21,24] In contrast, C_{60} bis-adducts with an *ortho-* addition pattern, viz. 1,9-

$C_{60}(X)_2$, have characteristic bands at 328 and 428 nm.

Efforts were made to investigate the electronic properties of 1,7-$C_{60}(CF_2CF_2SF_5)_2$ using cyclic

voltammetry and low-temperature gas-phase photoelectron spectroscopy (LT-PES), both of which

were valuable for the characterization of PFAFs and was used successfully for the analysis of

$H_2CORO(CF_3)_n$ derivatives in Chapter 2 of this work.[17,21] The latter technique can be used to

determine the gas-phase *EA* of molecules as their radical anions can be produced in solution before

injection into the spectrometer.[33,34] The cyclic voltammogram showed irreversible electrochemical

behavior (see Figure S3-8), so an $E_{1/2}(0/-)$ value was not determined. Furthermore, reduction of

$C_{60}(CF_2CF_2SF_5)_2$ by TDAE to produce the required concentration of $C_{60}(CF_2CF_2SF_5)_2^-$ for LT-

PES produced only C_{60}^-. Therefore, not only is the thermal stability of $SF_5CF_2CF_2I$ and

$C_{60}(CF_2CF_2SF_5)_n$ derivatives lower than R_FI compounds and $C_{60}(R_F)_n$ derivatives, the

chemical/electrochemical properties of the SF_5-containing fullerenes are different than those of

other PFAFs.

3.2.6. Reactions of C_{60} and SF_5CF_2I

Only one reaction of C_{60}/C_{70} fullerene substrate with SF_5CF_2I was performed in this work. The

goal was not to prepare a simple derivative such as $C_{60}(CF_2SF_5)_2$ but to see if intact SF_5CF_2 groups

could be added to C_{60}. Therefore, a high stoichiometric ratio (1:30) was used. The initial

concentration of C_{60} in *o*-DCB was 4.2 mM, the reaction temperature was 150–155 °C, and the

reaction time was 76 h. The reaction produced a dark brown solid that was soluble in the same

organic solvents used for the reactions of C_{60} with $SF_5CF_2CF_2I$.

The NI-ESI mass spectrum of the crude products of the reaction is shown in Figure 3-10. None

of the abundant species observed have the formula $C_{60}(CF_2SF_5)_n^-$. Instead, two series of ions,

$C_{60}(CF_3)_n(CF_2SF_5)_m^-$ and $C_{60}(CF_3)_x^-$, were identified in this mass spectrum, which were supported

by MS-MS analysis of the fragmentation patterns for selected ions and isotope distributions. The most abundant ions appear to be $C_{60}(CF_3)(CF_2SF_5)_n^-$, $n = 4–9$, and $C_{60}(CF_3)_2(CF_2SF_5)_m^-$, $m = 3–8$ (Figure 3-10, top panel). The $C_{60}(CF_3)_x^-$ species, $x = 3–5$ were less abundant (Figure 3-10, bottom panel), and from these data alone, it is difficult to ascertain their origin, but it is feasible that they might form via fragmentation of the parent ions $C_{60}(CF_3)_n(CF_2SF_5)_m^-$ in the mass spectrometer ion source.

This unexpected result may indicate that SF_5CF_2I is not thermally stable at 150 °C, and by analogy with the higher analogue $SF_5CF_2CF_2I$, the processes shown in eqs. 7–12 might occur.

$$SF_5CF_2I \ + \ Cu \rightarrow \ [SF_5CF_2]^{\bullet} \ + \ CuI \tag{7}$$

$$C_{60} \ + \ [SF_5CF_2]^{\bullet} \ \rightarrow \ [C_{60}CF_2SF_5)]^{\bullet} \tag{8}$$

$$[SF_5CF_2]^{\bullet} \ \rightarrow \ SF_4 \ + \ CF_3^{\bullet} \tag{9}$$

$$C_{60} + CF_3^{\bullet} \ \rightarrow \ [C_{60}CF_3]^{\bullet} \tag{10}$$

$$[C_{60}CF_3]^{\bullet} \ + \ SF_5CF_2I \ + \ Cu \ \rightarrow \ C_{60}(CF_3)(CF_2SF_5) \ + \ CuI \tag{11}$$

$$[C_{60}CF_2SF_5]^{\bullet} \ + \ SF_5CF_2I \ + \ Cu \ \rightarrow \ C_{60}(CF_3)(CF_2SF_5) \ + \ SF_4 \ + \ CuI \tag{12}$$
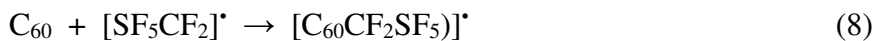
Equations 11 and 12 are based on prior experimental and theoretical work on high-temperature radical additions with fullerenes.[21] The Strauss-Boltalina research group and others previously reported in a few cases the elimination of SF_5^- under basic conditions, and most recently in a few reactions with $SF_5CF_2C(O)Cl$ such eliminations have resulted in the formation of derivatives with terminal CF_3 groups.[35]

The interpretation of the mass spectral data agrees with the ^{19}F NMR spectrum recorded for the crude sample (Figure S3-6). Besides the expected resonances due to fluorine atoms on the SF_5

and CF_2 moieties, a series of multiplets were observed in the "fingerprint" region of the fluorine atoms of CF_3 groups attached to C_{60}, i.e., at $\delta = -65$ to -70.[15] At the same time, signals due to the fluorine atoms directly attached to C_{60} (typical region of $\delta = -150$ to -160)[36] are absent in the ^{19}F NMR spectrum. HPLC analysis of the crude material was carried out in two eluents (as shown in Figure S3-7), and it showed that a very complex, practically inseparable mixture of compounds was present in the sample. The conversion of C_{60} was nearly quantitative but with such a high stoichiometric ratio of C_{60} to SF_5CF_2I it is not surprising. These initial data indicate that multiple additions of CF_2SF_5 groups to C_{60} can be readily accomplished, with the maximum number of additions reaching $n = 9$, as in $C_{60}(CF_3)(CF_2SF_5)_9$ (see Figure 3-10, top panel). This degree of functionalization is only slightly lower than what has been observed previously for perfluoroalkyl derivatives of C_{60} (e.g., for $C_{60}(C_2F_5)_n$, or $C_{60}(n\text{-}C_4F_9)_n$ with $n_{max} = 12$–14).[29] This result shows the increase in steric bulk associated with the SF_5 group when attached to a CF_2 or CF_2CF_2 linker does not have as deleterious an effect on total functionalization as may have been expected. Notably, in the case of $SF_5CF_2CF_2I$ reactions with C_{60}, the maximal degree of addition was even slightly higher, for example with $n_{max} = 11$ by mass spectrometry.

In order to achieve preparation of the isomerically pure $C_{60}(CF_2SF_5)_n$ compounds, further optimization towards more gentle reaction conditions, specifically temperature, will be required to suppress thermally activated fragmentation of the CF_2SF_5 moiety as observed in this study (see eqs. 7–12), and control over stoichiometry of the reaction may assist with improving selectivity. The results of the optimization of the reaction between C_{60} and $SF_5CF_2CF_2I$ indicate that this is a viable and achievable goal for future study.

3.2.7. Conclusion and future work for the pentafluorosulfanyl fullerene

The reactivity of the fullerene C_{60} towards the pentafluorosulfanyl-containing iodides $SF_5CF_2CF_2I$ and SF_5CF_2I was studied herein using solution reaction conditions in the presence of Cu powder. The product distribution in the reactions with $SF_5CF_2CF_2I$ was found to be highly sensitive to the reaction temperature: below 135 °C, the reaction was very slow, while temperatures

above 150 °C gave substantial fragmentation of the $SF_5CF_2CF_2$ group leading to the formation of cycloadducts $C_{60}(C_2F_4)_n$ along with the mixed functionality derivatives. Optimized reaction conditions were found for the synthesis of the bis-derivative $C_{60}(CF_2CF_2SF_5)_2$, and its subsequent isolation and characterization were carried out.

The initial studies of these new materials demonstrated that they possess different properties than previously studied perfluoroalkylfullerenes (PFAFs). The weakness of the S–C bond in the $SF_5CF_2CF_2$ group, compared to the C–C bond in the perfluoroalkyl group is responsible for lower thermal stability and higher chemical/electrochemical reactivity. On the one hand, lower thermal stability of these new fullerene derivatives is a shortcoming for potential applications which require vapor deposition. On the other hand, they have improved solubility compared to most other PFAFs and may become more useful for solution processing and for applications that do not require sublimation or heating above 140 °C. Additionally, the chemical lability of the SF_5 moiety points to the possibility of further derivatizations by replacing them for other functionalities and for designs of self-assembled monolayers (SAMs) on various surfaces taking advantage of the facile detachment of the SF_5 moiety.[37]

For the potential electronic applications of these materials, one would need the knowledge of their frontier orbital energies. The mass spectrometry data obtained in this work provides an indirect indication that the *EA*s of the $C_{60}(CF_2CF_2SF_5)_{2n}$ compounds can be as high as those of perfluoroalkylfullerenes, because they readily ionize in the electrospray ion source, even in nonpolar solvents. While the $C_{60}(CF_2CF_2SF_5)_{2n}$ derivatives were not stable to electrochemical reduction it is possible solid-state measurements, such as inverse photoemission spectroscopy, may be more fruitful for elucidating the electronic properties of these compounds.

3.3. IMPROVED SYNTHESIS AND SEPARATION OF $C_{60}FHF$

3.3.1. General comments

This section will discuss a new method for the synthesis of 1,9-C_{60}(*cyclo*-CF_2(2-C_6F_4)), $C_{60}FHF$, allowing for facile separation resulting in scalable production. The fauxhawk functional

group has a high degree of thermal stability compared to the industry standard for fullerene acceptors, PCBM,[38,39] and can be used in vapor deposited devices.[39,40] This is an important distinction between PCBM and C_{60}FHF, because the PCBM functional group, cyclopropyl phenyl butyric acid methyl ester, isomerizes at elevated temperatures to a [3+2] cycloadduct, iso-PCBM, and other decomposition products.[39] Additionally, for the purposes of organic field effect transistors, OFETs, C_{60}FHF packs 16% more densely than PCBM based on the structural analysis of their solid-state structure by single-crystal x-ray diffraction.[7] Higher density packing in the solid-state has been correlated with higher conductivities in OFETs due to improved charge carrier mobilities.[41] Additionally, the reduction potential of C_{60} and C_{60}FHF have been shown to be within error of each other by solution-phase cyclic voltammetry measurements which means that dopants shown to work well for C_{60} should also be applicable to C_{60}FHF.[19,42] These factors make C_{60}FHF an excellent candidate for organic electronic devices. In fact, vapor-deposited field effect transistors were produced using C_{60}FHF by the collaborators at Kent State University resulting in high conductivities for a fullerene derivative.[7] The details associated with the performance of C_{60}FHF as an intrinsic semiconducting layer material in OFET devices will be discussed in more detail in Chapter 4 of this work.

3.3.2. Synthesis of C_{60}FHF

The first synthesis of C_{60}FHF was reported in 2015 by Dr. Long San et al.[19] It utilized a two-step reaction, which required (i) synthesis and isolation of a hydrofullerene precursor, 1,9-$C_{60}(CF_2C_6F_5)H$, by a laborious high-performance liquid chromatography (HPLC) separation and then (ii) a reaction of the hydrofullerene with proton sponge to form the final product, C_{60}FHF, which required further purification by HPLC to remove residual unreacted hydrofullerene, 1,7-$C_{60}(CF_2C_6F_5)_2$, and/or C_{60}. (The mechanism by which bisperfluorobenzyl fullerene was produced in the second step of the reaction from purified $C_{60}(CF_2C_6F_5)H$ is not well understood and the product was not produced in any meaningful quantity, <5% of the product mixture.) This two-step synthetic strategy will be referred to in the remainder of this text as Method 1. Specific variations

between reactions are reported in Section 3.6. It was also reported that C_{60}FHF could be synthesized in a single-step reaction, but only with a low yield of 7%. These factors made it difficult to synthesize large amounts of purified C_{60}FHF for device studies, therefore, a series of optimization experiments were continued by Dr. Long San, that were aimed at improving the yield of C_{60}FHF, scaling up the reaction, and decreasing the overall time required for preparation and purification.

The most significant change to the reported procedure[19] involved decreasing the number of reaction steps from two to one. Dr. San achieved this by introducing an organic base, pyridine, in the starting reaction mixture, which allowed the process of deprotonation of the hydrofullerene to occur *in situ*.[38] The data and experiments discussed from Dr. San's work were recorded in his laboratory notebooks and digital records stored by the Strauss-Boltalina research group and are summarized here by the author and in the 2019 paper reporting the one-step synthesis of C_{60}FHF of which the author is the second of six graduate student co-authors.[7] The one-step synthetic strategy utilizing pyridine as an internal organic base will be referred to for the remainder of the text as Method 2 and as before, specific reaction details will be reported in Section 3.6. Figure 3-11 shows the effect adding pyridine to the reaction mixture had on the product distribution, i.e. no residual hydrofullerene is present when pyridine is used. Not only did this innovation make the second step unnecessary, but it also allowed for the relative amounts of the reagents, i.e., tributyl tin hydride (SnH) and perfluorobenzyl iodide (Bn_FI) to be lowered. For example, going from the published 10 equiv SnH and 20 equiv Bn_FI[19] to 4 and 8 equiv, respectively, a single-step synthesis yielded 14% C_{60}FHF. Other reaction parameters were varied by Dr. San, such as reaction time, C_{60} concentration, and the mode of addition of the base (dropwise or all at once), each resulting in incremental improvements. Good reproducibility was demonstrated by performing the reaction on a 250 mg scale of C_{60}.

At this point the author of this dissertation continued this work in order to further optimize the reaction with a focus on making the reaction practical for larger scales of production so that more

device studies could be performed. Dr. San's experiments indicated to the author that the outcome of the reaction was strongly dependent on the presence of trace amounts of moisture (in solvents, reagents, and even glassware). Evidence for this conclusion could be qualitatively observed by the indirect relationship between the concentration of pyridine and the optimal concentration of the SnH. It is well documented that SnH is water sensitive due to the relative acidity of water compared to the hydride atom and in fact aqueous solutions are regularly used as a means of removing unwanted residual SnH or other reactive organotin reagents.[43] When Dr. San added pyridine, a drying agent, the observed optimal concentration of both reagents went down, Bn_FI by 60% and SnH by 40% from the original published conditions.[19] It was rationalized that this decrease in the optimal concentration of the reagents was due to fewer equiv of the reagents being lost to the unproductive reaction with water.

As a test of this hypothesis, the author performed a ^{1}H NMR experiment using the SnH reagent used by Dr. San dissolved in the undried o-DCB and a minimal amount of dried $CDCl_3$ as a locking agent. This experiment showed only 10% of the hydride was present. The chemical shift for the hydride is slightly shifted from the literature value of 5.1 ppm to 4.8 ppm likely due to solvent effects from the o-DCB.[44] That spectrum is shown in Figure S3-9.

It was deduced that the excess of reagents, in the 2015 reaction[19] and to a lesser extent the initial pyridine reactions, reacted with water which made reliably predicting the optimal concentration of the reagents difficult since the presence of residual moisture varied by season and age of the undried solvent. In other words, following the reagents unproductive reaction with water the remaining number of equivalents was unknown and so a large excess was used to ensure the remaining concentration was sufficient for the reaction to proceed. As a consequence of the required excess of reagents, Dr. San optimized the reaction time to 2 h, which prevented the majority of the product mixture from being multiple addition products: $C_{60}(Bn_F)_{x>2}$, $C_{60}(H)_{x>2}$, and $C_{60}(Bn_F)_{x\geq1}(H)_{y\geq1}$ where the resulting totals are always even numbers and for the mixed functional group species both x and y could not be equal to one.

To remove variability in the optimal conditions due to water and further reduce the amount of excess reagent as well as undesired multiple addition side products, an advanced protocol for the rigorous exclusion of moisture was developed including flame drying the glassware and drying all of the solvents and reagents used using a combination of 3 Å mol sieves and Schlenk line techniques. This resulted in a further reduction in the optimal amounts of reagents, going from 4 equiv SnH and 8 equiv Bn_FI to 1.1 equiv for both reagents. It also, as predicted, improved selectivity towards $C_{60}FHF$, which, in turn, significantly facilitated purification. An isolated yield of 22% of 99% pure $C_{60}FHF$ was achieved in a one-step synthesis and one-stage HPLC purification. The reaction is scalable, and more reagent and eluent-economical than previously reported. These additional improvements on the work done originally by Dr. San and then continued by the author resulted in an efficient synthesis that allowed for the production of $C_{60}FHF$ to perform a wide range device studies.[7] Those studies will be discussed in Chapter 4 of this work. Details of the modified synthesis are discussed in Section 3.6.2. of this chapter.

3.3.3. Conclusions and future work for the synthesis of $C_{60}FHF$

By removing residual water and decreasing the number of equivalents used in the reaction the selectivity and overall yield of the $C_{60}FHF$ synthesis has been improved from 7% yield in a single step to 22%. Further optimization of the concentration of C_{60} in the reaction as well as the optimal temperature and duration for the reaction should be explored to further increase the yield. Fellow graduate student, Brian J. Reeves, has had success further optimizing this synthesis and published his improvements in 2019.[40]

3.4. SYNTHESIS OF C_{70} FAUXHAWK

3.4.1. General comments

With the appealing physical and electrochemical properties of $C_{60}FHF$: thermal stability, high packing density, and a reduction potential closely matched by the parent fullerene; it was desirable to apply the synthesis developed for $C_{60}FHF$ to C_{70}. The C_{70} fullerene as well as its monoadducts, most notably $PC_{70}BM$, have been in great demand as high-performing electron acceptor materials

for a wide range of applications, including OFETs,[45] OPVs,[46] and record-holding perovskite photovoltaics.[47,48] The fullerene C_{70} in at least one respect is a more challenging substrate than C_{60} because of its lower symmetry, D_{5h}. This lower symmetry can result in more monoadduct isomers than an analogous reaction with C_{60}. For example, $PC_{70}BM$, is synthesized as a mixture of isomers which are very difficult to separate requiring recycling HPLC systems to isolate the dominant isomer with a high degree of purity.[49-53]

3.4.2. DFT calculations of the relative stability of $C_{70}FHF$ isomers

Before the synthesis of $C_{70}FHF$ was performed, DFT calculations were performed by Dr. Popov to predict which isomers would be the most stable. With the large number of possible isomers, relative energy calculations are a useful tool for predicting major products. The results of the DFT calculations of the relative energies of the most stable $C_{70}FHF$ isomers as well as their frontier orbital energies are given in Table 3-2 (a complete list is given in Table S3-3 and S3-4).

The two lowest-energy isomers are 25,8- and 8,25- , (isomers a1 and a2 in Table 3-2), the third most stable isomer is separated by only 15.2 kJ mol^{-1}, whereas the fourth isomer is 38 kJ mol^{-1} less stable than the 25,8-isomer. The calculations showed that those three isomers should be the dominant products in the product mixture, assuming thermodynamic conditions. In total, the first 12 lowest relative energy isomers were analyzed. These isomers as well as the corresponding Schlegel diagrams for the three lowest energy derivatives are shown in Figure 3-12. The calculated frontier orbital energies of C_{60}, C_{70}, PCBM, and $C_{60}FHF$ are also shown for comparison.

3.4.3. A single step synthesis for $C_{70}FHF$ derivatives

Dr. San made efforts to synthesize $C_{70}FHF$ derivatives utilizing the reaction conditions reported for the synthesis of $C_{60}FHF$ in 2015, aka Method 1.[19] A summary of those efforts is reported in his dissertation.[54] Two HPLC chromatograms showing his product distribution when chlorobenzene or o-DCB was the solvent is included for comparison between Method 1 and Method 2 in Figure 3-13. The author of this dissertation's success improving the synthesis of $C_{60}FHF$ inspired his efforts to apply the new reaction to C_{70}. The improved synthetic approach

involved the addition of an organic base, pyridine, *in situ* during the reaction of C_{70} with Bn_FI and SnH, which resulted in the formation of the fauxhawk derivatives in one stage.[7,40] Reaction **2a**, performed by the author using Method 2, was first carried out in chlorobenzene and yielded a product that contained three isomers of $C_{70}FHF$ and a large amount of unreacted C_{70}, as shown in the HPLC chromatogram in Figure 3-13. When *o*-DCB was used as the solvent in reaction **2b**, the conversion improved, and larger amounts of $C_{70}FHF$ isomers were made. Notably, no amount of $C_{70}Bn_FH$ compounds were detected in the product indicating that pyridine is an effective base for the quantitative deprotonation of the $C_{70}(Bn_F)H$ isomers, consistent with the $C_{60}FHF$ chemistry. HPLC separation of the product resulted in the isolation of the pure $C_{70}FHF$-3 isomer in the fraction eluting at t_R = 9 min and a 2:1 mixture of $C_{70}FHF$-1 and $C_{70}FHF$-2 in the fraction eluting at t_R = 10 min, whereas a broad unresolved fraction eluting at t_R = 2.8–8 min was identified as a complex mixture of bis- and tris- fauxhawk derivatives, and it was not studied further. Numerous attempts were made to separate the $C_{70}FHF$-1 and $C_{70}FHF$-2 isomers, which included varying eluents, flow rate, and stationary phase but with no success.

The NMR and UV-vis spectra for the two fractions were recorded. The NMR spectra are shown in Figure 3-14 and the UV-vis spectra are shown in Figure S3-12 and S3-13. A distinctive feature which further reinforces the assignment of $C_{70}FHF$-3, is the AB quartet shown in the inset of Figure 3-14. The small difference in chemical environment for the two fluorines on the CF_2 functional group where one fluorine is over a pentagon and the other is over a hexagon gives rise to the unique multiplet. This phenomenon has been observed previously and is useful in characterizing the different isomers of C_{70} derivatives.[7] Table S3-1 shows the full list of chemical shifts for the three $C_{70}FHF$ fullerenes. The chemical shifts for $C_{70}(Bn_F)H$-1 is also in Table S3-1 The band maxima for the UV-vis spectra for the mixture of $C_{70}FHF$-1 and $C_{70}FHF$-2 as well as the pure isomer, $C_{70}FHF$-3, are listed in Table S3-2.

Overall, reaction **2b** afforded the isolation of 26% $C_{70}FHF$-1 and $C_{70}FHF$-2 isomers and 7% of $C_{70}FHF$-3. The unreacted C_{70} can be easily collected for recycling. The reaction can be readily

scaled up further if larger (multigram) amounts of the materials are needed in the future. More than 100 mg of the C_{70}FHF-1 and C_{70}FHF-2 mixture and the pure C_{70}FHF-3 isomer were produced and used in OFET devices. The results from those experiments will be discussed in Chapter 4.

3.4.4. Electrochemistry of C_{70}FHF derivatives

In order to use C_{70}FHF compounds in organic electronic devices, like OFETs, the reduction potentials need to be well matched with the architecture of the device. In Chapter 4, the benefits of matching the source and drain LUMO energies with the *n*-type intrinsic layer is discussed for C_{60}FHF based devices which highlights the importance of well characterized materials. experiments were conducted to measure these characteristics for the C_{70}FHF materials. For C_{70}FHF-3, a pure sample was used for these experiments, but since only a small amount of the pure C_{70}FHF-1 isomer was ever synthesized the mixture of C_{70}FHF-1 and C_{70}FHF-2 was used. This was necessary to determine the behavior of the mixture since the mixture, which could be produced in large quantities, was going to be used in the devices. The cyclic voltammogram of both samples are shown in Figure 3-15. The $E_{1/2}$ (1st reduction) versus ferrocene for the mixture and for C_{70}FHF-3 is −1.11 and −1.09 V, respectively. The voltammograms were both collected in *o*-DCB with 1.0 M concentration of the supporting electrolyte, tetrabutyl ammonium tetrafluoroborate (TBA BF$_4$), at a cycle rate of 250 mV s^{-1}. The difference of 20 mV is within the ±10 mV error of our measurement and so these values are, within the precision of the measurement, the same. This similarity in reduction potential means that both materials should function similarly in the same device architectures excluding any solid-state packing differences between the two materials. An additional advantage is that these compounds, like C_{60}FHF vs. C_{60}, are within error of the $E_{1/2}$ (1st reduction) versus ferrocene of C_{70} in the same solvent, −1.11 V. This result makes it possible to test devices which have been optimized for C_{70} with C_{70}FHF derivatives.

3.4.5. Solid-state packing and crystal structure of C_{70}FHF-1

From Dr. San's synthesis efforts, pure C_{70}FHF-1 was isolated and a single crystal X-ray dataset was collected. At the time of Dr. San's dissertation only a preliminary structure was able to be

obtained and therefore no packing or structural properties were discussed. Following the author's synthesis of $C_{70}FHF$ isomers by a one-step method the author resolved to solve the dataset. The now publishable structure is discussed here. The structure contains two $C_{70}FHF$-1 molecules in the formula unit and one CS_2 molecule. The structure of one of the two nearly-identical 25,8-$C_{70}(CF_2(2'-C_6F_4))$ molecules is shown in Figure 3-16 (thermal ellipsoid plots of both molecules are shown in Figure S3-23). The molecules are packed in hexagonal arrays in layers in crystallographic bc planes, as shown in Figure 3-17. The C_{70} centroids in these layers are co-planar with an average deviation from their least-squares plane of ± 0.06 Å (the C_{70} centroids, hereinafter denoted with the symbol $\odot$, are defined by the 10 triple-hexagon junction $C(sp^2)$ atoms around the fullerene equator). The six $\odot \cdots \odot$ distances within the fullerene layers range from 10.03 to 11.02 Å and average 10.63 Å. The fullerene layers are stacked along the crystallographic a axis separated by either a layer of fluorous fauxhawk substituents or a layer of CS_2 molecules, as shown in Figure 3-18. Each fullerene centroid is within 11.32 Å from ten other centroids. The average of the 10 $\odot \cdots \odot$ distances is 10.71 Å for one molecule and 10.78 Å for the other molecule. Additional drawings are shown in Figures S3-24 and S3-25.

There are several relevant structures of C_{70} fullerene derivatives with a single cycloadduct attached to the C8–C25 or the C7–C22 bond that have been used to fabricate heterojunction photovoltaic materials. In the solvent-free structure of the methanofullerene 8,25-$C_{70}(C(4'$-$C_6H_4(O$-nBu$)_2)$, there are only six $\odot \cdots \odot$ distances shorter than 13.3 Å, as shown in Figure 3-19.[48] They range from 10.34 to 10.83 Å and average 10.67 Å. In the solvent-free structure of the methanofullerene 8,25-$C_{70}(C(Ph)(C_3H_6COOMe)$, there are seven $\odot \cdots \odot$ distances shorter than 13.8 Å, as shown in Figure 3-19.[49] They range from 10.20 to 10.99 Å and average 10.60 Å. Interestingly, in the structure of the hexane solvate of the same derivative, shown in Figure 3-19, there are also seven $\odot \cdots \odot$ distances with essentially the same range and average.[51] In the CS_2 solvate of 7,22-$C_{70}(C_6H_4(CH_2)_2)$, there are nine $\odot \cdots \odot$ distances shorter than 13.8 Å, as shown in Figure 3-19.[55] They range from 10.21 to 11.15 Å and average 10.58 Å. The CS_2 solvate of its

isomer, $1,6$-$C_{70}(C_6H_4(CH_2)_2)$, has a very similar packing pattern, with nine $\odot\cdots\odot$ distances shorter than 14.0 Å, as shown in Figure 3-19.[55] The $\odot\cdots\odot$ distances range from 10.21 to 11.12 Å and average 10.58 Å.

This comparative analysis shows that the planar fauxhawk substituent in $25,8$-$C_{70}(CF_2(2'$-$C_6F_4))$ allows the fullerene cages to pack more densely (i.e., to pack with more 10–11 Å $\odot\cdots\odot$ distances) than in the solvent-free methanofullerene structures or in the CS_2 solvate of $7,22$-$C_{70}(C_6H_4(CH_2)_2)$. Of the C_{70} derivatives shown in Figure 3-19, only $PC_{70}BM$ and $C_{70}FHF$ were used in OFETs, and the electron mobility reported for the former range from 10^{-3} to 0.1 cm^{-1} V^{-1} s^{-1},[55] which is consistent with its low-density molecular packing in the crystals. The results of the $C_{70}FHF$ OFET devices will be discussed in Chapter 4.

The two isomers of *o*-xylene monoadducts of C_{70} exhibit very tight packing motifs and similar parameters, despite the difference in the addend location, however, no data on their OFET performance have been reported. On the other hand, the C_{60} *o*-xylene monoadduct (abbreviated as OXCMA) (only one isomer exists due to higher molecular symmetry of the fullerene cage) has been studied intensely both as a *n*-type semiconductor in OFETs, and as an electron acceptor in OPVs. The high mobility of 2.28 cm^2 V^{-1} s^{-1} was reported for the *n*-doped OFETs, and 0.5 cm^2 V^{-1} s^{-1} for the undoped OFETs.[56] Analysis of the packing in the single crystals[57] shows that each OXMCA molecule has ten nearest neighbors with the $\odot\cdots\odot$ distances ranging from 9.87–10.09 Å and average 9.95 Å.

Whether the structure packing of $25,8$-$C_{70}(CF_2(2'$-$C_6F_4))$ and $7,22$-$C_{70}(CF_2(2'$-$C_6F_4))$ are sufficiently different to have led to the observed difference in the thin-film conductivities we have measured for these $C_{70}FHF$ isomers will have to await the crystallization and X-ray structure of $7,22$-$C_{70}(CF_2(2'$-$C_6F_4))$. At this time, crystallization attempts have not yet resulted in good-quality crystals.

3.4.6. Conclusions and future work for C_{70}FHF research

In conclusion three new C_{70}FHF molecules have been synthesized by a new one-step method. This synthesis can be readily scaled making it possible to produce devices with the C_{70}FHF molecules. The isolated yield of this reaction is 26% for the C_{70}FHF-1 and 2 mixture and 7% for C_{70}FHF-3. The cyclic voltammogram of the C_{70}FHF molecules was measured and the reduction potentials for the three molecules are within error of the reduction potential for C_{70}. This is in agreement with the behavior of C_{60}FHF and C_{60}. The crystal structure data of C_{70}FHF-1 were collected and compared to other similar fullerenes. This analysis shows that the packing density of C_{70}FHF-1 is high relative to other C_{70} fullerenes and is encouraging for the potential of these materials as OFET active layers.

Further research into C_{70}FHF fullerenes will focus on developing separation techniques for the two currently inseparable isomers and optimizing the yield of the reaction. It is possible that a recycling solvent HPLC system could separate the two isomers as was done with PC$_{70}$BM.[58] If the isomers could be separated, then structural and electronic studies attempting to find differences between the two fullerenes would be useful for understanding their performance in OFET devices.

3.5. SYNTHESIS AND CHARACTERIZATION OF A PARTIALLY FLUORINATED C_{60} FAUXHAWK FULLERENE

3.5.1. General comments

As has already been established, many of the highest efficiency organic electronic devices are produced with PCBM as the electron acceptor.[38,39,59] This means the majority of organic donor molecules for OPV devices and device architectures have been designed to match the electronic properties of PCBM. PCBM has a higher LUMO, (more positive), than C_{60} making it harder to reduce, and so C_{60}FHF is not optimal for the donors which were optimized to be used with PCBM. PCBM's reduction potential is 90 mV more positive than the reduction potential of C_{60} and C_{60}FHF.[19] One approach to make a sublimable PCBM alternative, is to synthesize a fauxhawk fullerene derivative with the thermally stable [3+2] moiety with fewer electron withdrawing

fluorines. Such a molecule could be used in solution processed OPV devices with PCBM compatible donors or sublimed for deposition processed devices making it a highly versatile acceptor. Additionally, many of the new high efficiency donor and acceptor materials utilize fluorinated groups to improve their conductivity and material properties.[60,61] Fluorinated donors and acceptors when used together in a bulk heterojunction have already been shown to improve photoconductance so a fluorinated PCBM like acceptor that could be sublimed and solution processed would be ideal.[62] This new derivative was made using pentafluorobenzyl bromide which is 77% per mole cheaper than the perfluorobenzyl iodide reagent used to make $C_{60}FHF$, an attractive factor for potential industrial applications.[63,64] This new fullerene is called the partially fluorinated C_{60} fauxhawk fullerene, $1,9\text{-}C_{60}(cyclo\text{-}CH_2(2\text{-}C_6F_4))$ or $C_{60}PFF$.

3.5.2. Optimization of the $C_{60}(PFB)H$ synthesis

The first attempt to synthesize a new partially fluorinated fauxhawk fullerene, $C_{60}PFF$, used pentafluorobenzyl bromide (PFB-Br) and SnH using the original two-step synthesis of $C_{60}FHF$ reported in the 2015 paper, Method 1.[19] This reaction resulted in only 7.6% yield of $1,9\text{-}C_{60}(CH_2C_6F_5)H$, $C_{60}(PFB)H$. When compared with the literature reported yield for $1,9\text{-}C_{60}(CF_2C_6F_5)H$, 35%, this significant drop in conversion was attributed to the apparent lower reactivity of PFB-Br compared to Bn_FI. The C–Br bond is stronger than the C–I bond by as much as 70 kJ mol^{-1}.[65] In order to synthesize $C_{60}PFF$ from $C_{60}(PFB)H$ in a large enough yield to perform characterizations on both compounds and study their electrochemical behavior as well as the differences in the chemistry of the $C_{60}FHF$ and the $C_{60}PFF$ systems, the $C_{60}(PFB)H$ synthesis was improved.

The first attempt at the synthesis of $C_{60}(PFB)H$, Rxn. 3A, resulted in a large amount of multiple addition products and minimal conversion of C_{60}. For example, $C_{60}((CH_2C_6F_5)H)_2$ and $C_{60}((CH_2C_6F_5)H)_3$ were identified by mass spectrometry in the crude product mixture. To reduce the number of multiple additions and selectively target the single addition product multiple adjustments to the synthetic conditions were made. The C_{60} concentration in solution was

decreased by 4 mM, from the published concentration of 5.6 mM. In conjunction with the decrease in concentration, the temperature was decreased from 165 °C to 140–145 °C. The solvent was also changed from *o*-DCB to chlorobenzene. As a consequence of lowering the temperature of the reaction and the fullerene concentration in solution, the time required for the reaction to reach completion increased from 2 to 24 h. The change in product distribution between Rxn. 3A and the optimized reaction, Rxn. 3B, is shown in Figure 3-20. More generally the changes made to the conditions were done to decrease the formation of the fullerene derivatives with multiple addends. Optimization of the reaction conditions resulted in an increase from 7.6% to 40% yield of the $C_{60}(PFB)H$ based on HPLC peak area.

3.5.3. Separation and characterization of $C_{60}(PFB)H$

HPLC separation of $C_{60}(PFB)H$ was done using a Cosmosil Buckyprep column with an eluent mixture of 80/20 toluene/heptane. $C_{60}(PFB)H$ was identified as a peak eluting from 6–7.25 min. The isolated $C_{60}(PFB)H$ was characterized by mass spectrometry, NMR, and UV-vis spectroscopy as shown by figures Figure 3-21, Figure 3-22, and S3-26. The ^1H NMR shows two singlets, a peak at 6.6 and 4.9 ppm for the cage proton and the CH_2 benzyl protons, respectively. These chemical shifts are in good agreement with literature reported shifts for similar compounds.[66] The ^{19}F NMR spectrum shows three aromatic fluorine resonances integrating to 2:1:2. The UV-vis spectrum of $C_{60}(PFB)H$ shows the characteristic absorption band at 420 nm that has been shown to occur for *ortho*-addition fullerene compounds.[17,25] The mass spectrum of this fraction was recorded using an NI-APCI instrument. The spectrum shows a peak for 902 *m/z* as expected for the $C_{60}(PFB)H$. It also shows a peak for 882 *m/z*, the expected mass to charge ratio for 1,9-$C_{60}(cyclo-CH_2(2-C_6F_4))$, ($C_{60}PFF$). To explain how this signal could be present in the spectrum, efforts to further purify the isolated $C_{60}(PFB)H$ material were undertaken to identify if $C_{60}PFF$ could be produced as a minor product and co-eluting, however it was discovered that $C_{60}PFF$ co-elutes with C_{60} under the separation conditions used (Cosmosil Buckyprep semipreparative column, 100% toluene eluent, 5 mL min^{-1}). Additionally, the NMR spectra of $C_{60}(PFB)H$ did not show any evidence for additional

134

derivatized fullerenes. The more likely explanation is that following ionization in the mass spectrometer, $C_{60}(PFB)H$ is able to lose a hydrogen fluoride molecule and undergo annulation in the timescale of the experiment.

3.5.4. Synthesis of $C_{60}PFF$

Following the published synthesis for $C_{60}FHF$,[19] using the purified $C_{60}(PFB)H$ material, an air-free one-electron reduction reaction using cobaltocene was performed, Rxn. 4A. Attempts were also made to use proton sponge, as was shown to be effective for the synthesis of $C_{60}FHF$,[19] however, no reaction was observed apparently due to the more negative reduction potential of $C_{60}(PFB)H$ versus the perfluorinated hydrofullerene. Upon addition of 1 equiv of cobaltocene to the $C_{60}(PFB)H$ solution, the color of the mixture changed from brown to dark green indicating the reduction of the fullerene derivative. Following a period of several days, the solution returned to a dark brown color and was exposed to air to continue the reaction workup. The time required for the reaction to go to completion was determined by monitoring the reaction mixture by ^{19}F NMR. The solution was run through a silica gel column to remove residual cobaltocene and cobaltocenium salts from the product mixture. The filtered solution was dried and examined by HPLC and NMR. The HPLC chromatogram was collected using a Cosmosil Buckyprep column with 100% toluene as the eluent. The chromatogram showed three distinct peaks as shown by Figure 3-23. The first was identified as residual $C_{60}(PFB)H$, by NMR. The second peak was identified by NMR and mass spectrometry as $C_{60}PFF$. The ^{19}F NMR spectrum of $C_{60}PFF$ is shown in Figure 3-21 (bottom). The 10-minute fraction was identified as the para addition bis benzyl compound, $1,7\text{-}C_{60}(C_6F_5)_2$, $C_{60}(PFB)_2$, by NMR, UV-vis spectroscopy, and mass spectrometry. This compound was reported previously by Nakamura et al.[67]

The presence of $C_{60}(PFB)_2$ was confusing at first, primarily because the reaction starting material was isolated $C_{60}(PFB)H$. It was not obvious how the $C_{60}(PFB)H$ could react to form $C_{60}(PFB)_2$ and not produce an equal amount of C_{60}. The "missing C_{60}" was believed to be co-eluting with $C_{60}PFF$ and so efforts were made to isolate the missing fullerene material. Using

slightly modified separation coditions, Cosmosil Bucky-M column with the same eluent and flow rate, $C_{60}PFF$ and C_{60} were able to be separated. This result showed that under reducing conditions, although the intended annulation event does occur, approximately 10% by HPLC peak area of the initial $C_{60}(PFB)H$ starting material is converted to C_{60} and $C_{60}(PFB)_2$. This is a result that was not observed by San et al in the synthesis of $C_{60}FHF$ showing a clear difference in the chemical stability of $C_{60}(PFB)H$.[19]

3.5.5. Separation and characterization of $C_{60}PFF$

First-stage separation of $C_{60}PFF$ was achieved using the Cosmosil Buckyprep column with 100% toluene as the eluent. This separation resulted in the isolation of $C_{60}PFF$ along with C_{60}. Secondary separation was performed using the Cosmosil Bucky-M column and the same eluent, 100% toluene. This produced pure $C_{60}PFF$, which was characterized by NMR, mass spectrometry, and UV-vis spectroscopy.

The ^{19}F NMR spectrum obtained is indicative of the fauxhawk functional group showing four fluorine chemical shifts which integrate to one with respect to each other, see Figure 3-21. The ^{1}H NMR shows a singlet with a chemical shift at 5.1 ppm. Using 1,4-bistrifluoromethylbenznene, PTFMB, as a reference for the proton and fluorine spectra the peak in the [1] NMR was integrated with respect to the fluorines resulting in an integration of two for the peak in the ^{1}H NMR versus the fluorine signals, allowing this peak at 5.1 ppm to be definitively assigned to the α protons. The mass spectrum of $C_{60}PFF$ shows a signal for 882 *m/z* which matches the molecular weight of $C_{60}PFF$. Lastly, the UV-vis spectrum for the compound shows a similar feature at 425 nm as observed for the $C_{60}(PFB)H$ indicating an *ortho*-addition pattern, see Figure S3-27.

The stability of $C_{60}PFF$ to sublimation was also evaluated. $C_{60}FHF$ can be sublimed at 7 mTorr at a temperature of 300 °C based on experiments performed by the author. In order for $C_{60}PFF$ to be used in deposition-based organic electronic devices it must be stable to sublimation. At 7 mTorr $C_{60}PFF$ was readily sublimed at 350 °C with minimal decomposition as shown by the comparison of the HPLC chromatograms of the material before and after sublimation shown in Figure S3-28.

It is interesting that the sublimation temperature of $C_{60}PFF$ is 50 °C higher than $C_{60}FHF$. This increase in sublimation temperature suggests stronger intermolecular forces within the solid material. Unfortunately, a crystal structure has not been obtained for this compound despite exhaustive attempts to prepare single crystals so no analysis of the solid-state packing of $C_{60}PFF$ can be performed. The solubility of $C_{60}PFF$ is low compared to other derivatized fullerenes. The solubility in toluene, for example, was measured to be 0.4 mg mL^{-1}. The final isolated yield of $C_{60}PFF$ after the two reactions was only 8% with the isolated yield from the conversion of $C_{60}(PFB)H$ to $C_{60}PFF$ only being 29%.

3.5.6. Electrochemistry of $C_{60}(PFB)H$ and $C_{60}PFF$

The cyclic voltammogram of $C_{60}(PFB)H$ and $C_{60}PFF$ have been recorded and compared to C_{60} and $C_{60}FHF$, see Figure 3-24. With the first reduction of C_{60} set as the zero-point $C_{60}FHF$ has an $E_{1/2}$ of zero as well. This results in $C_{60}FHF$ having an $E_{1/2}$ 0.09 V more positive than PCBM according to measurements made by the Strauss Group previously under the same conditions.[19] $C_{60}PFF$ has an $E_{1/2}$ of −0.07 V with respect to the first reduction of C_{60}. Since the $E_{1/2}$ value can be used to estimate the LUMO energy[68] of the fullerene acceptor it is apparent that the goal of making a fullerene acceptor with the a similar LUMO to PCBM has been achieved given the error of this measurement is ±10 mV.

The cyclic voltammogram of $C_{60}(PFB)H$ was recorded as well and shows and interesting feature in the voltammogram. The return oxidation wave shows a non-reversible reduction event. This increase is believed to be due to a chemical change undergone by the $C_{60}(PFB)H$. This behavior has also been observed for the hydrofullerene precursor for $C_{60}FHF$. This reduction event is hypothesized to be associated with the intermediate formed after the loss of HF or F$^-$ generating a charged species. Evidence for this can be found by comparing the relative heights of the reduction and return oxidation of $C_{60}(PFB)H$. The return oxidation event is smaller than the initial reduction suggesting some of the material has been lost, presumably to the loss of HF or F$^-$. This explanation

is in agreement with the observed m/z value for $C_{60}PFF$ when the mass spectrum of $C_{60}(PFB)H$ is recorded.

3.5.7. One-pot synthesis of $C_{60}PFF$

Due to the instability of $C_{60}(PFB)H$ and the multiple stages of separation required to isolate $C_{60}PFF$, the synthesis reported in sections 3.5.2. and 3.5.4. of this work was not viable for large-scale production. In order to make enough material for testing organic electronic devices, a more scalable synthesis was needed and so the synthesis developed for $C_{60}FHF$, referred to here as Method 2, was adapted for $C_{60}PFF$, Rxn. 4B. The objective was to observe if the scalability and ease of separation afforded by Method 2 would significantly increase the isolated yield of $C_{60}PFF$.

The method 2 reaction to synthesize $C_{60}PFF$, Rxn. 4B, closely mirrored the conditions used for the $C_{60}FHF$ one-pot synthesis with the only change being the PFB-Br concentration was doubled to account for the observed lower reactivity of the bromide reagent. A second reaction, Rxn. 4C, was performed using the expected 1:1:1 ratio of fullerene substrate to SnH and PFB-Br but the reaction resulted in a minimal change to the isolated yield, 12% for Rxn. 4B and 8% for Rxn. 4C. For both reactions, dried solvents were used as well as the addition of the anhydrous 10% by volume pyridine.

The one-pot synthesis of $C_{60}PFF$, as was the case for $C_{60}FHF$, did not result in any residual $C_{60}(PFB)H$ which could be detected by ^{19}F NMR spectroscopy, see Figure 3-25. The isolated yield of the best $C_{60}PFF$ reaction of the two was only 12% which was only slightly better than the optimized Method 1 synthesis. However, the yield based on HPLC peak area was 35%. This large discrepancy was observed consistently for $C_{60}PFF$ reactions and is likely due to the low solubility of $C_{60}PFF$ resulting in loss of the material throughout the purification process. For example, after the end of the separation shown in Figure 3-25 which utilized chlorobenzene as the eluent to improve solubility, the HPLC column was washed with excess chlorobenzene resulting in multiple

milligrams of material eluting from the column. In both cases this material was predominantly C_{60}PFF with C_{60} also present.

Attempts were made to purify C_{60}PFF by alternative means to minimize the loss of material. Recrystallization was attempted using a variety of solvents including but not limited to CS_2 and hot toluene but in all cases the resulting filtrate contained a significant portion of C_{60}PFF, and the precipitate was contaminated with C_{60} as well as other minor product fullerenes. Attempts at purification by flash chromatography were also not successful with either toluene, chlorobenzene, o-DCB, or CS_2 as an eluent. C_{60}PFF was not mobile on silica gel in any of the mentioned solvent mixtures and could not be removed from the silica gel after it was deposited even with extended sonication of the gel. Purification by sublimation resulted in the co-sublimation of C_{60} and C_{60}PFF as well.

3.5.8. Conclusion and future work for C_{60}PFF

The successful synthesis of two new fullerenes, C_{60}(PFB)H and C_{60}PFF, was developed and both compounds were characterized by UV-vis spectroscopy, NMR spectroscopy, mass spectrometry, and cyclic voltammetry. An efficient synthesis for the production of C_{60}(PFB)H was achieved with an isolated yield of 27%. This compound was also used as a precursor to make C_{60}PFF in a synthesis resulting in a 29% yield based on the C_{60}(PFB)H starting material. An unexpected byproduct in the form of C_{60}(PFB)$_2$ was formed as well during this reaction. The mechanism for this side reaction is not known but shows the potential for further functionalization of the CH_2 benzyl protons. C_{60}PFF, was also synthesized in a one-pot synthesis using pyridine as an internal base. While the reaction resulted in a 35% yield based on HPLC peak area the isolated yield was only 12%. This dramatic drop in yield was attributed to the loss of material due to C_{60}PFF's low solubility, 0.4 mg mL^{-1}. A multitude of methods other than HPLC were attempted to purify C_{60}PFF but none were successful including sublimation.

In order to use C_{60}PFF in organic electronic devices the solubility issues must be addressed to allow for higher yields, or an alternative purification method must be developed. Alternatively, to

address the original intent of this project, a $C_{60}PFF$ derivative could be synthesized with organic solubilizing groups, such as hexyl groups, which could increase the solubility of the fullerene and potentially make purification easier while not significantly changing the frontier orbital energy. This would hopefully result in a solution processable, sublimation stable, fullerene acceptor with a reduction potential similar to PCBM.

3.6. MATERIALS AND METHODS

3.6.1. Reagents and general procedures

The following reagents and solvents were obtained from the indicated sources and were used as received or were purified where indicated: Chlorobenzene (99.5%, Aldrich Chemicals). 1,2-dichlorobenzene (99% dried over CaH_2, Acros Organics). C_{60} (99.5%, MTR Limited). C_{70} (98.0+%, MTR Limited). 2,3,4,5,6-pentafluorobenzyl bromide (98%, Oakwood Chemicals). tri-n-butyl tin hydride (95%, Strem Chemical). Cobaltocene purified by sublimation and stored under nitrogen in a glovebox (Strem Chemical). Benzonitrile dried over 3 Å molecular sieves (99+%, Sigma Aldrich). Pyridine (99%, dried over CaH_2 Acros Organics). Deuterated benzene (99.5%, Cambridge Isotope Laboratories, Incorporated). Deuterated chloroform (99.8%, Cambridge Isotope Laboratories, Incorporated). Perfluorobenzene (99%, Oakwood Products). 1,4–bistrifluoromethyl benzen (99%, Central Glass Co.). Toluene (99.9%, Fischer Scientific). Carbon disulfide (98%, Alfa Aesar). 1,8-bis(dimethylamino)-naphthalene (Proton Sponge) purified by sublimation and stored in a purified-dinitrogen filled glovebox (Sigma-Aldrich). Silica gel high purity with an average pore size of 60 Å, 70–230 mesh, (Sigma Aldrich).

3.6.2. Synthesis of new compounds

$C_{60}(CF_2CF_2SF_5)_2$. The compound C_{60} (18.7 mg, 0.026 mmol) was mixed with *o*-DCB 6 mL in a 10 mL Schlenk flask equipped with a PTFE-protected high-vacuum valve and a magnetic stir bar. The flask was placed in an ultrasonic water bath for 1 h, and then the mixture was stirred overnight to form a homogeneous solution. To the liquid obtained, 4 equiv of $SF_5CF_2CF_2I$ (16.6 μL, 0.104 mmol) was added using a micro syringe, then 1.85 g of copper powder was carefully transferred

into the flask. The Schlenk flask was connected to a vacuum line to remove air, and then the reaction vessel was placed in an oil bath that had been heated to 145 °C. The color of the solution changed from violet to deep brown during the period of heating. After 72 h, the reaction flask was cooled with cold water and then stored in a refrigerator overnight. The reaction mixture was then filtered, and the resulting solid residue was washed with o-DCB. A deeply brown-colored crude product mixture was collected after removing the solvent via high vacuum at 55 °C. The crude product was separated by HPLC on a Cosmosil Buckyprep semipreparative column with a mixture of toluene/heptane in a 25/75 ratio as the eluent.

Scalable C$_{60}$FHF. C$_{60}$, 200 mg (0.2 mmol) was added to a clean and flame dried Schlenk flask, under a flush of nitrogen. The flask was then sealed under a positive pressure of nitrogen and opened again in a UHP nitrogen, glovebox. Anhydrous o-DCB, (35 mL, resulting fullerene concentration 6.0 mM), was added along with a stir bar and 1.1 equiv of tributyl tin hydride (82 µL). At this time anhydrous pyridine, 10% by volume, (3.5 mL) was added to the crude solution. The reaction flask was then sealed and sonicated for approximately 15 minutes or until all C$_{60}$ was dissolved. Afterwards, under a flush of nitrogen 1.1 equiv of perfluorobenzyl iodide (48 µL) was added via a glass syringe. The flask was then resealed under a positive pressure and all remaining gasses were removed from both the solution and the head space of the flask via the freeze-pump-thaw method. After 3 freeze-pump-thaw cycles, and the degassed solution had warmed to approximately room temperature, the reaction flask was placed in a 145 °C oil bath with stirring for 16 h. After the reaction period the solution had changed from a dark purple to brown. The resulting solution was then transferred to a round bottom flask in air and roto-evaporated to near dryness. The dark brown sludge was washed with heptane, sonicated, and then roto-evaporated to azeotrope any remaining o-DCB. This procedure was repeated 3 times. The resulting brown powder was dissolved in toluene and was then separated by HPLC on a Cosmosil Buckyprep column with 100% toluene as the eluent with a flow rate of 5 mL min^{-1}.

Method 1 for C$_{70}$(Bn$_F$)H-1 and C$_{70}$FHF-1. These reactions were performed by Dr. Long San but are included here for comparison to the Method 2 reactions to make C$_{70}$FHF derivatives. The compound C$_{70}$ (100 mg, 0.119 mmol) was dissolved in 45 mL of chlorobenzene in a Kontes tube with 400 µL of perfluorobenzyl iodide and 320 µL of tributyl tin hydride, 20 and 10 equiv respectively. The reaction mixture was sonicated until all of the C$_{70}$ was dissolved. The reaction mixture was degassed using the freeze-pump-thaw method three times and then under evacuation was sealed and heated to 145 °C for 1.25 h. The crude reaction mixture was allowed to cool to room temperature and then all volatiles were removed via evacuation. The crude reaction mixture was separated on a Cosmosil Buckyprep semipreparative column with toluene at 5 mL min^{-1}. C$_{70}$(Bn$_F$)-1 was isolated and was dissolved in anhydrous oxygen free benzonitrile. To this solution, excess proton sponge was added, and the reaction mixture was allowed to react at room temperature for two days. After two days the reaction was evacuated until all volatiles were removed. The crude material was separated by HPLC in the same conditions reported for step one.

Method 2 for C$_{70}$FHF. The compound C$_{70}$ (40 mg, 0.048 mmol) was added under a flow of nitrogen to a 25 mL Schlenk flask which was flame dried under vacuum prior to addition. A flea stir bar was also added to the flask. Under a pressure of nitrogen a rubber septum was used to seal the flask and was then wired shut. The sealed flask was then pumped into a glovebox where anhydrous and degassed *o*-DCB was added to the flask, 4.8 mL for a 0.01 M solution, after removing the septum. Also added to the flask was 1.1 equiv, 14.1 µL, of tributyltin hydride with a 25 µL syringe. The septum was replaced and removed from the glovebox. The solution was sonicated briefly, usually less than 1 minute, to dissolve all of the residual solid C$_{70}$. Under a purge of nitrogen, introduced through the side arm of the flask the septum was removed and 1.1 equiv, 8.2 µL, of perfluorobenzyl iodide was added via a syringe to the solution. To the open flask a reflux condenser was attached which had been adapted with a tubing adapter to allow for a flow of nitrogen as well. This was done with an inline bubbler and rubber bands to prevent an over pressure and to allow for a blow out in the event an overpressure occurred without allowing in

142

oxygen. The nitrogen flow was then regulated to a few bubbles every 30 seconds and the solution was heated to 145 °C and stirred for 3 hours. After 3 hours, anhydrous pyridine, 10% by volume or 0.48 mL, which was dried over calcium hydride, was added to the stirring heated solution. This solution was allowed to continue stirring and heating for another hour. The solution was then exposed to air and the o-DCB was removed under evacuation. After nearly all of the visible liquid was evaporated, heptane was added to the crude solid and sonicated. The solution was then roto-evaporated to dryness. This was done three times. The resulting crude solid was washed with approximately 15–20 mL of heptane by adding the heptane to the flask containing the solid and sonicating the crude mixture. The mixture was then filtered. The filtrate was put away for later purification as it was found to contain some $C_{70}FHF$ compounds and could be purified by long term evacuation under dynamic vacuum to remove residual high boiling liquids, and the remaining solid which was now a fine dark brown powder was dissolved in CS_2 and removed from the filter paper. The CS_2 was removed under a stream of air and then evacuated for approximately an hour to ensure complete removal of the solvent.

Method 1 for $C_{60}(PFB)H$ and $C_{60}PFF$. The compound C_{60} (200 mg, 0.278 mmol) was dissolved in 170 mL of o-DCB (1.6 mM). To the solution, 10 equiv of 2,3,4,5,6-pentafluorobenzyl bromide was added followed by 5 equiv of (n-butyl)$_3$ tin hydride. The reaction mixture was degassed by three consecutive freeze-pump-thaw cycles. The degassed mixture was left under vacuum and heated to between 140–145 °C for 24 h. The resulting brown solution was dried under vacuum. The solid product mixture was dissolved in toluene and separated on the Cosmosil Buckyprep semi-preparative column with a 100% toluene mobile phase with a 5 mL min^{-1} flow rate. $C_{60}(PFB)H$ was isolated from the crude reaction mixture to give an isolated yield of 27%. In an air-free nitrogen gas environment $C_{60}(PFB)H$, 5 mg (0.007 mmol), was dissolved in approximately 1.5 mL of rigorously dried/air-free benzonitrile. To this brown solution 1 equiv of cobaltocene was added via a 0.1 M cobaltocene solution in rigorously dried benzonitrile. After the addition of cobaltocene the solution became dark green indicating the fullerene had been reduced. The

reaction was allowed to progress for 90 h. The total reaction time was determined by ^{19}F NMR monitoring. After the reaction appeared to have reached completion, the solution had returned to a dark brown color. The reaction mixture was then passed through a silica gel column to remove any residual cobaltocene and dried. C_{60}PFF was isolated using a two-stage separation technique. The crude reaction material was separated using the Buckyprep semi-preparative column with a 100% toluene mobile phase and a 5 mL min^{-1} flow rate to separate it from any unreacted C_{60}(PFB)H. This resulted in a mixture of C_{60} and C_{60}(PFF) in a single fraction. The second stage of separation used the Bucky-M semi-preparative column with a 100% toluene mobile phase and a flow rate of 5 mL min^{-1} resulting in the separation of C_{60}PFF from C_{60}. The isolated yield was 29% based on C_{60}(PFB)H.

Method 2 for C$_{60}$PFF. The compound C_{60} (200 mg, 0.278 mmol) was added under a flow of nitrogen to a 150 mL Kontes flask which was flame dried under vacuum prior to addition. A stir bar was also added to the flask. Under a pressure of nitrogen, the flask was sealed. The sealed flask was then pumped into a glovebox where anhydrous o-DCB, 110 mL, was added for a 2.5 mM solution based on C_{60}. Also added to the flask was 1.1 equiv, 82 µL, of tributyltin hydride and anhydrous pyridine, 10% by volume. The Kontes flask was sealed and removed from the glovebox. The solution was sonicated briefly, usually less than 1 minute, to dissolve all of the residual solid C_{60}. Under a purge of nitrogen, introduced through the side arm of the flask, the Kontes valve was removed and 2.1 equiv, 88 µL, of pentafluorobenzyl bromide was added via a 250 µL syringe to the solution. The flask was then sealed, and all gasses were removed via the freeze-pump-thaw method which was repeated three times. The flask was allowed to warm to room temperature and then placed into a hot oil bath at 160 °C. The reaction was allowed to proceed for 16 h. The solution was then exposed to air and the o-DCB and pyridine was removed under evacuation. After nearly all of the visible liquid was evaporated, heptane was added to the crude oily solid and sonicated. The solid was suspended and then filtered. The heptane insoluble solid was washed with CS_2 and removed from the filter. The solution was then evacuated to dryness. The crude solid was dissolved

144

in a gross excess of toluene, more than 100 mL, to ensure complete dissolution of the crude solid. The elute was separated on a Cosmosil buckyprep semi-preparative stationary phase in 100% toluene at 5 mL min^{-1} and the desired product, C_{60}PFF, was collected with C_{60} which co-elutes. The fullerene mixture was then evacuated to dryness and was re-dissolved in approximately 50 mL of chlorobenzene and separated by HPLC chromatography on the Cosmosil Bucky-M stationary phase at 4 mL min^{-1}. Isolated yield for this reaction was 12%.

3.6.3. Spectroscopic characterization

^{1}H and ^{19}F NMR spectra were recorded using a Varian INOVA 400 spectrometer operating at 400 and 376 MHz, respectively. Spectra were recorded using a 1 s relaxation time and a 30° pulse angle. The solvent used was deuterated chloroform or a mixture of deuterated chloroform and carbon disulfide in a 1/9 ratio when higher concentrations were required.

3.6.4. UV-vis spectroscopy

UV-vis spectra were collected using a UV-Vis-NIR Shimadzu UV 3101PC instrument with UVProbe 2.33 software.

3.6.5. High pressure liquid chromatography

HPLC was conducted using a Shimadzu liquid chromatography instrument (CBM-20A control module, SPD-20A UV-vis detector set to 300 nm, LC-6AD pump, manual injector valve.) The HPLC columns utilized were 10 mm I.D. X 250 nm COSMOSIL Buckyprep column and 10 mm I.D. 250 nm COSMOSIL Bucky-M prep column (Nacalai Tesque, Inc.). The eluent was ACS grade toluene or HPLC grade heptane in a mixture of a specified ratio at a flow rate of 5 mL min^{-1} unless otherwise stated.

3.6.6. Mass spectrometry

A 2000 Finnigan LCQ-DUO spectrometer was utilized to record negative ion atmospheric pressure chemical ionization (NI-APCI) and negative ion electrospray ionization (NI-ESI) mass spectra with acetonitrile or toluene as a carrier solvent.

3.6.7. Cyclic voltammetry

Cyclic voltammograms were recorded in an inert atmosphere using a PAR 263 potentiostat/galvanostat and approximately 2 mM *o*-DCB solutions analyte with 0.1 M N(*n*-butyl)$_4$BF$_4$ as the electrolyte. The electrochemical cell used was equipped with 0.125 mm diameter platinum working and counter electrodes and a 0.5 mm diameter silver reference electrode. The scan rate was 250 mV s^{-1}.

3.6.8. Single-crystal X-ray diffraction

Crystals of C$_{70}$FHF-1 suitable for diffraction were by slow evaporation of carbon disulfide solution. Diffraction data were collected at the Advanced Photon Source at Argonne National Laboratory on beamline 15ID-B, using a diamond 111 monochromator, an X-ray wavelength of 0.46051 Å, and a Bruker D8 goniometer, and multi-scan absorption corrections. Unit cell parameters were determined by the least squares fit of the angular coordinates of all reflections. Integrations of all frames were performed using APEX III software, and the structures were solved using SHELXTL/OLEX 2 software.

3.7. CONCLUSIONS

In summary, several new solution phase fullerene reactions to add R$_F$ and fluorinated and partially fluorinated *cyclo-* groups are reported. Efforts were made by the author to make the reactions as selective as possible. For the addition of perfluoroalkyl pentafluorosulfanyl groups, lowering the temperature from 180 °C, which was shown to be successful for the synthesis of C$_{60}$(R$_F$)$_2$, to 140 °C resulted in a more selective reaction with the majority product being, C$_{60}$(CF$_2$CF$_2$SF$_5$)$_2$. The number of equivalents of SF$_5$CF$_2$CF$_2$I reagent was also decreased from six to four which decreased the number of multiple addition products. The major product, C$_{60}$(CF$_2$CF$_2$SF$_5$)$_2$, was characterized by ^{19}F NMR and NI-ESI mass spectrometry. The product was found to form multiple different solvent adducts with even weakly coordinating solvents such as DCM and *n*-hexane.[69] This behavior suggests the strong electron withdrawing affect the CF$_2$CF$_2$SF$_5$ group has. Unfortunately, the gas-phase electron affinity and cyclic voltammogram

for this compound was not successfully recorded apparently due to its rapid decomposition upon reduction. The perfluorocyclobutane C_{60} monoadduct and other similar perfluoro *cyclo-* derivatives were identified in the crude reactions by mass spectrometry. These decomposition products appear to be the result of an annulation reaction following the loss of the pentafluorosulfanyl group.

An improved synthetic method for making fauxhawk functionalized fullerenes in a one-pot reaction, referred to in this work generally as Method 2, was developed for $C_{60}FHF$. This synthetic approach differed from the literature reported method, Method 1, by performing the reaction anhydrously allowing the number of equivalents of SnH and Bn_FI to be decreased from 10 and 20 to 1 and 1 equiv respectively. Additionally, this method utilizes the organic base, pyridine, to deprotonate the hydrofullerene, $C_{60}(CF_2C_6F_5)H$, during the reaction which then undergoes an annulation rearrangement to form $C_{60}FHF$. This technique was pioneered by Dr. San and allows the reaction to be performed in one-step without additional purification to isolate the hydrofullerene. This method allowed for the scalable production of $C_{60}FHF$ with an isolated yield of 22% and minimal multiple addition products making separation relatively facile. Further improvements to this synthesis have been made by fellow researcher Brian J. Reeves resulting in 37% isolated yield.[40]

Method 2 was applied to C_{70} as well with minor alterations to the reaction conditions. This resulted in at least three different $C_{70}FHF$ isomers. The combined isolated yield of the three isomers is 33%. The yield of $C_{70}FHF-1$ is 17%, $C_{70}FHF-2$ is 9%, and $C_{70}FHF-3$ is 7%. The two major isomers, $C_{70}FHF-1$ and 2, were inseparable and so were characterized as a mixture. The reduction potential of the mixture and $C_{70}FHF-3$ were recorded by cyclic voltammetry and were found to be within error of each other -1.11 and -1.09 V, respectively. These values are also within error of the reduction potential of C_{70} which is consistent with the electrochemical behavior of $C_{60}FHF$ with respect to C_{60}. Thanks to research efforts by Dr. San, a single crystal dataset of $C_{70}FHF-1$ was obtained and was able to be modeled by the author. This allowed the solid-state

packing of the $C_{70}FHF$-1 isomer to be characterized. It was found to pack in a similar ordered fashion as $C_{60}FHF$ with the same number of fullerene nearest neighbors, 10.[19] This ordered structure as well as the high packing density, 1.850 g cm^{-3}, lead the author to pursue using the $C_{70}FHF$-1 and 2 mixture in OFET devices. The results from those experiments are discussed in Chapter 4 of this work.

Lastly, in an attempt to make a fullerene based organic electron acceptor with a similar reduction potential to PCBM and also able to be utilized in deposition processed organic devices the synthesis of $C_{60}PFF$ was developed. $C_{60}PFF$ was produced using syntheses adapted from Methods 1 and 2 but neither resulted in high yields with the highest yielding reactions being 8% and 12% for the adapted syntheses respectively. These low yields make pursuing $C_{60}PFF$ as an organic electronic material impractical as of this report. $C_{60}PFF$ is also unique with respect to the other FHF derivatives that have been produced, because of its low solubility. In toluene it has a solubility of only 0.4 mg mL^{-1}.

In total, six unique syntheses were developed, and six new fluorine rich fullerenes were synthesized and characterized. Special care was made to optimize the syntheses to be as selective as possible by controlling for variables like temperature, reagent concentration, reaction duration, and residual moisture content. Two scalable synthesis to make $C_{60}FHF$ and $C_{70}FHF$ derivatives were reported allowing for hundreds of milligrams of material to be produced which was used to make OFETs which are discussed in Chapter 4 of this work.

3.8. ADDITIONAL RECOGNITION

Synthesis of the $C_{60}(CF_2CF_2SF_5)_n$ and $C_{60}(CF_2SF_5)_n$ compounds was carried out by Dr. Siyan Qing under the supervision of Dr. Joseph Thrasher at Clemson University in collaboration with the author.[8] Development of Method 1 for the synthesis of $C_{70}FHF$ derivatives was done by Dr. Long San and he performed the initial efforts to use pyridine as an internal base for the conversion of $C_{60}(Bn_F)H$ into $C_{60}FHF$.[7] Dr. Long San also grew the single crystal of $C_{70}FHF$-1. Efforts to collect the gas-phase electron affinity values for select compounds were made by Dr. Xuebin Wang

at Pacific Northwest National Labs. DFT calculations were performed by Dr. Alexey Popov. X-ray diffraction data was collected at the synchrotron source at Argonne National Lab under the supervision of Dr. Yu-Sheng Chen.

Table 3-1. Experimental conditions for reactions of C_{60} or fullerene substrate with $SF_5CF_2CF_2I^a$

rxn. no.	mass of substrate, mg	C_{60} conc., mM^b	# equiv. $SF_5CF_2CF_2I$	temp., °C	rxn. time, h	MS, NMR, or HPLC trace
1	C_{60}/C_{70}, 18.7	10.0	6	180	72	Fig. 3-1
2	C_{60}/C_{70}, 18.7	5.0	6	155	72	Fig. 3-2
3	C_{60}/C_{70}, 18.7	5.0	6	145	72	Figs. 3-3A, 3-4
4	C_{60}/C_{70}, 18.7	3.2	6	145	72	Figs. 3-3B, 3-4
5	C_{60}/C_{70}, 18.7	4.0	6	145	72	Fig. 3-4
6	C_{60}/C_{70}, 18.7	5.0	6	145	48	
7	C_{60}/C_{70}, 18.7	5.0	4	145	72	Fig. 3-3A
8	C_{60}/C_{70}, 18.7	5.0	6	145	48	
9	C_{60}/C_{70}, 18.7	3.2	4	145	72	Figs. 3-3A, 3-3B
10	C_{60}, 18.7	4.0	4	140	72	Figs. 3-5, 3-6

[a] The solvent was 1,2-$C_6H_4Cl_2$ (*o*-DCB); C_{60}/C_{70} = fullerene substrate = 75% C_{60}/24% C_{70} with ca. 1% higher fullerenes. [b] The listed concentration is for C_{60} (it does not include C_{70} when fullerene substrate was used).

Table 3-2. DFT-calculated relative energies and frontier orbital energies of $C_{70}FHF$ isomers, $C_{60}FHF$, $PC_{60}BM$, and parent fullerenes C_{60} and C_{70}.[a]

	dE, kJ mol^{-1}	HOMO, eV	LUMO, eV	ΔLUMO (vs C_{70}), eV	$E_{1/2}^{0/-}$, V	LUMO, eV (from $E_{1/2}$)[b]
	0.0	−5.735	−4.106	0.004	−1.05[c]	−4.05
$C_{70}FHF\_a2$	0.7	−5.730	−4.117	−0.008	−1.05[c]	−4.05
$C_{70}FHF\_b$	15.2	−5.665	−4.158	−0.048	−1.07[c]	−4.03
$C_{70}FHF\_d$	38.0	−5.548	−4.387	−0.277	-	
$C_{70}FHF\_e$	65.3	−5.613	−4.714	−0.604	-	
C_{70}		−5.824	−4.110	0.000	−1.01[d]	−4.05
C_{60}		−5.823	−4.173	−0.063	−1.03[d]	−4.07
$C_{60}FHF$		−5.723	−4.228	−0.119	−1.03[d]	−4.07
$PC_{60}BM$		−5.493	−4.009	0.100	−1.12[d]	−3.98
$OXC_{60}MA$					−1.12[e]	−3.98

[a] Calculated by collaborator Dr. Alexey A. Popov using the basis set PBE-D3BJ/def2-TZVP. [b] Calculated using −5.1 eV for the $Fe(Cp)_2^{+/0}$ redox couple (ref. [70]). [c] This work. [d] From ref. [71]. [e] From ref. 56 (LUMO recalculated here for consistency).

Table 3-3. Reaction conditions for the synthesis of $C_{60}(PFB)H$ and $C_{60}PFF^a$

reaction	time, h	temp., °C	solvent	conc., mM	PFB-Br (equiv)	SnH (equiv)	yield, %
Rxn. 3A[b]	2	16	o-DCB	5.6	10	5	7.6[d]
Rxn. 3B[b]	24	145	CB	1.6	10	5	27
Rxn. 4A[c]	90	RT	anhydrous BN	4.7	N/A	N/A	29[e]
Rxn. 4B[c]	16	160	o-DCB	2.5	2.1	1.1	12
Rxn. 4C	16	160	anhydrous o-DCB[e]	2.5	1.1	1.1	8

[a] Abbreviations: temp. = temperature; conc. = concentration; RT = room temperature; PFB-Br = perfluorobenzyl bromide; o-DCB = o-dichlorobenzene; CB = chlorobenzene; BN = benzonitrile. [b] The synthetic target was $C_{60}(PFB)H$. [c] The synthetic target was $C_{60}(PFF)$. [c] abbreviation for chlorobenzene. [d] The yield is based on HPLC peak area. [e] The yield is based on the amount of $C_{60}(PFB)H$ starting material.
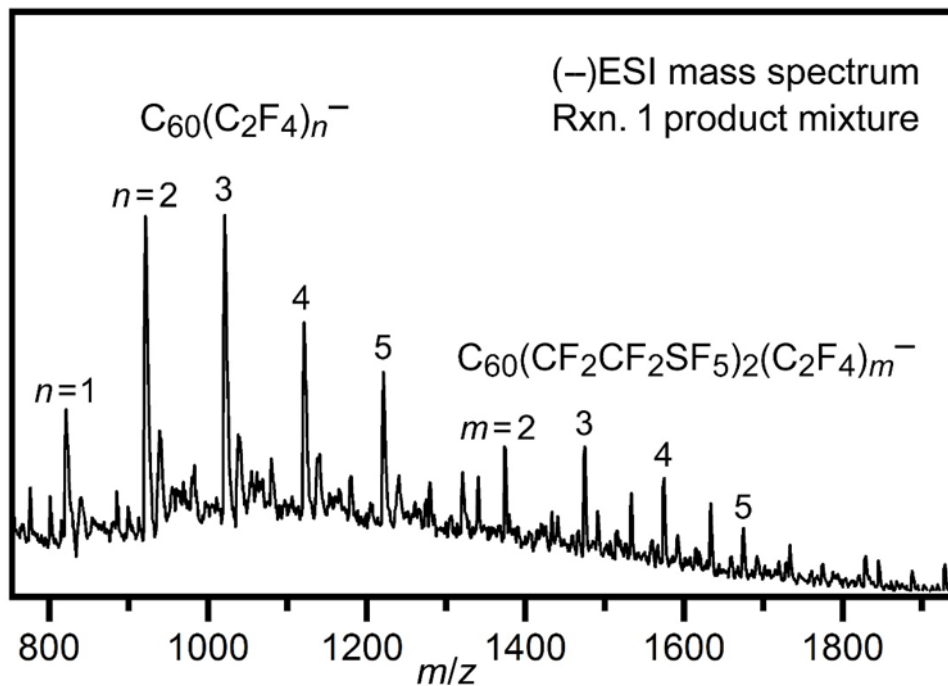
Figure 3-1. NI-ESI mass spectrum of the crude product mixture from the reaction of C_{60} and $SF_5CF_2CF_2I$ in $1,2\text{-}C_6H_4Cl_2$ at 180 °C (Rxn. 1 in Table 3-1).
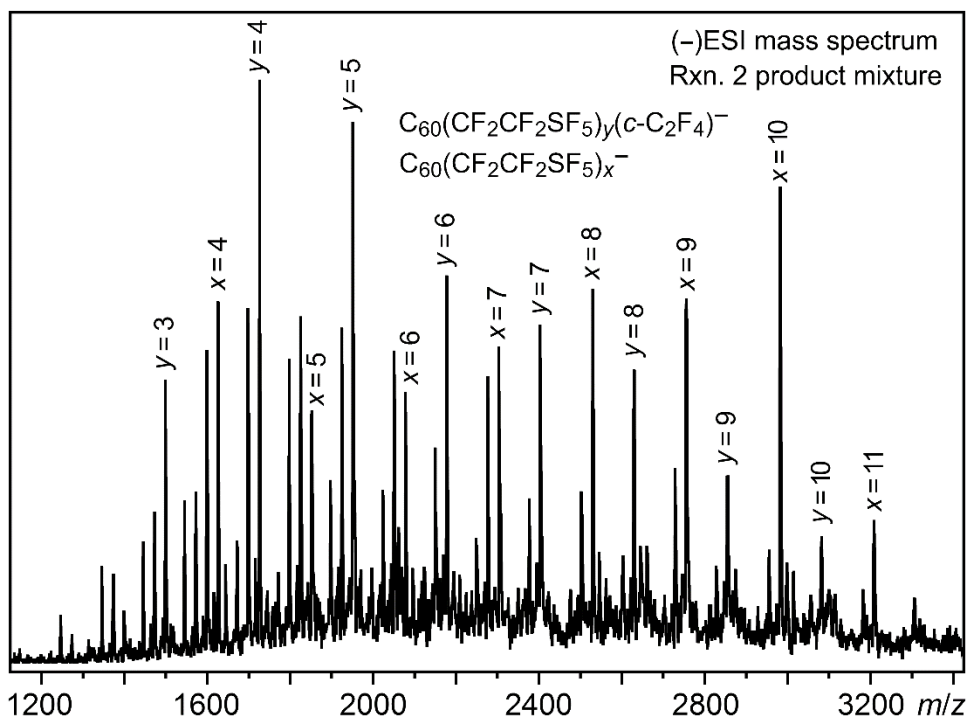
Figure 3-2. NI-ESI mass spectrum of the crude product mixture from the reaction of C_{60} and $SF_5CF_2CF_2I$ in 1,2-$C_6H_4Cl_2$ at 155 °C (Rxn. 2 in Table 3-1). The *cyclo-* modifier is abbreviated as *c* for simplicity.
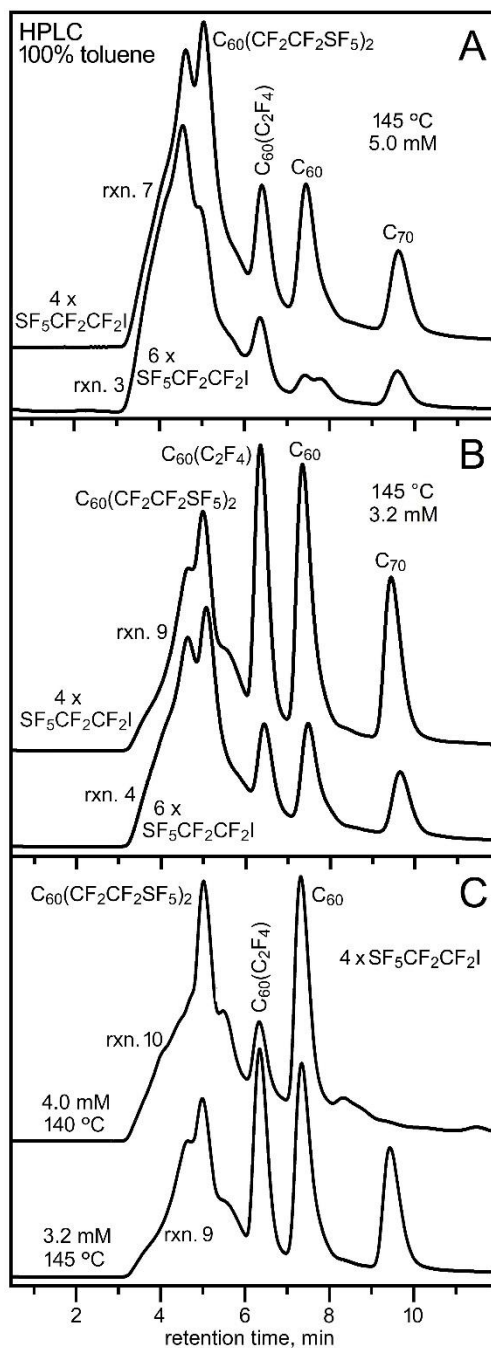
Figure 3-3. HPLC chromatogram of the crude product mixtures from reactions of C_{60} and $SF_5CF_2CF_2I$ in 1,2-$C_6H_4Cl_2$ listed in Table 3-1. Part A: Rxns. 3 and 7. Part B: Rxns. 4 and 9. Part C: Rxns. 9 and 10. The initial millimolar concentration of C_{60} in each reaction is shown.
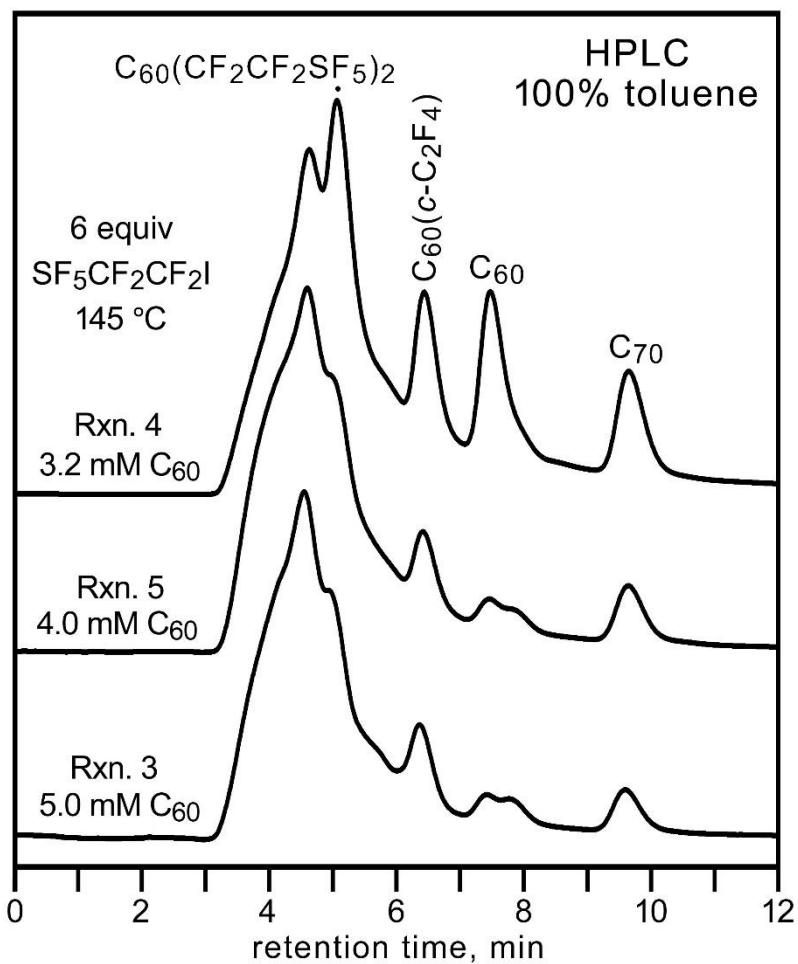
Figure 3-4. HPLC chromatograms of the crude product mixtures from Rxns. 3, 4, and 5 of C_{60}/C_{70} fullerene extract with $SF_5CF_2CF_2I$ in $1,2\text{-}C_6H_4Cl_2$ (see Table 3-1). The *cyclo-* modifier is abbreviated as *c* for simplicity.
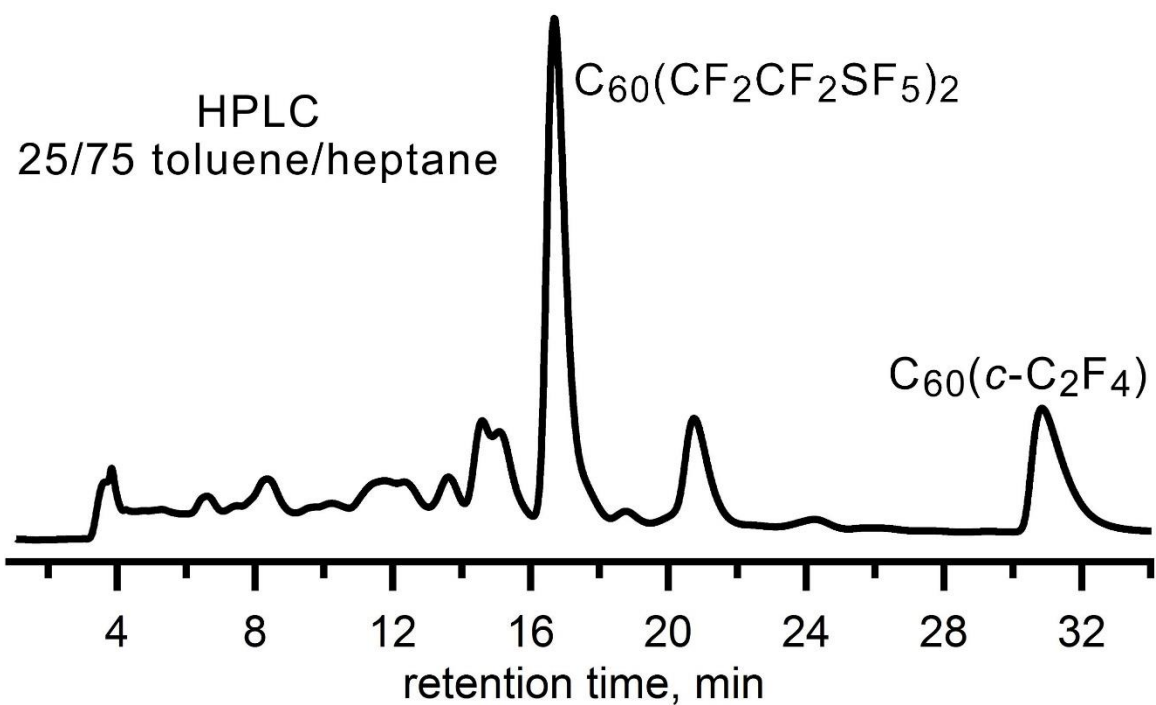
Figure 3-5. HPLC chromatogram (Cosmosil BuckyPrep, 25/75 v/v toluene/heptane eluent, 5 mL min^{-1}) of the crude product of the reaction of C_{60} and $SF_5CF_2CF_2I$ in 1,2-$C_6H_4Cl_2$ at 140 °C (Rxn. 10 in Table 3-1). The chromatogram does not show the elution of unreacted C_{60}, which was washed from the column with toluene after 40 min. The *cyclo-* modifier is abbreviated as *c* for simplicity.
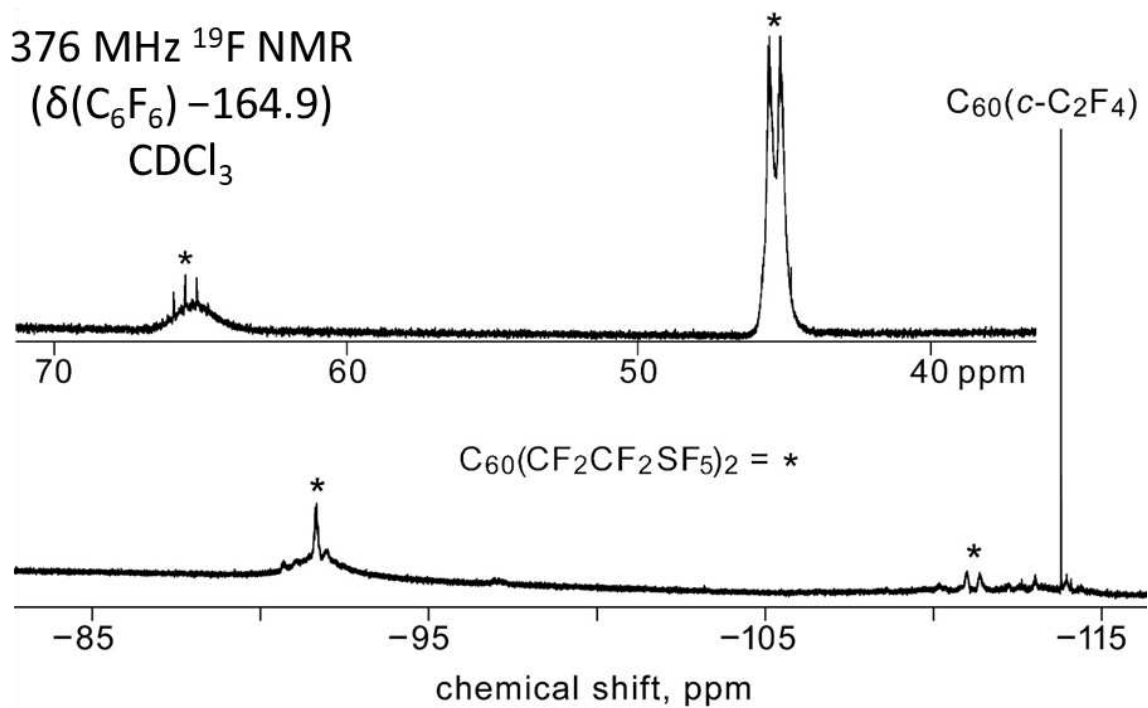
Figure 3-6. The 376 MHz ^{19}F NMR spectrum of a CDCl$_3$ solution of the crude product mixture from the reaction of C$_{60}$ and SF$_5$CF$_2$CF$_2$I in 1,2-C$_6$H$_4$Cl$_2$ at 140 °C. (Rxn. 10 in Table 3-1). The resonances and multiplets marked with asterisks are assigned to 1,7-C$_{60}$(CF$_2$CF$_2$SF$_5$)$_2$. The *cyclo*-modifier is abbreviated as *c* for simplicity.
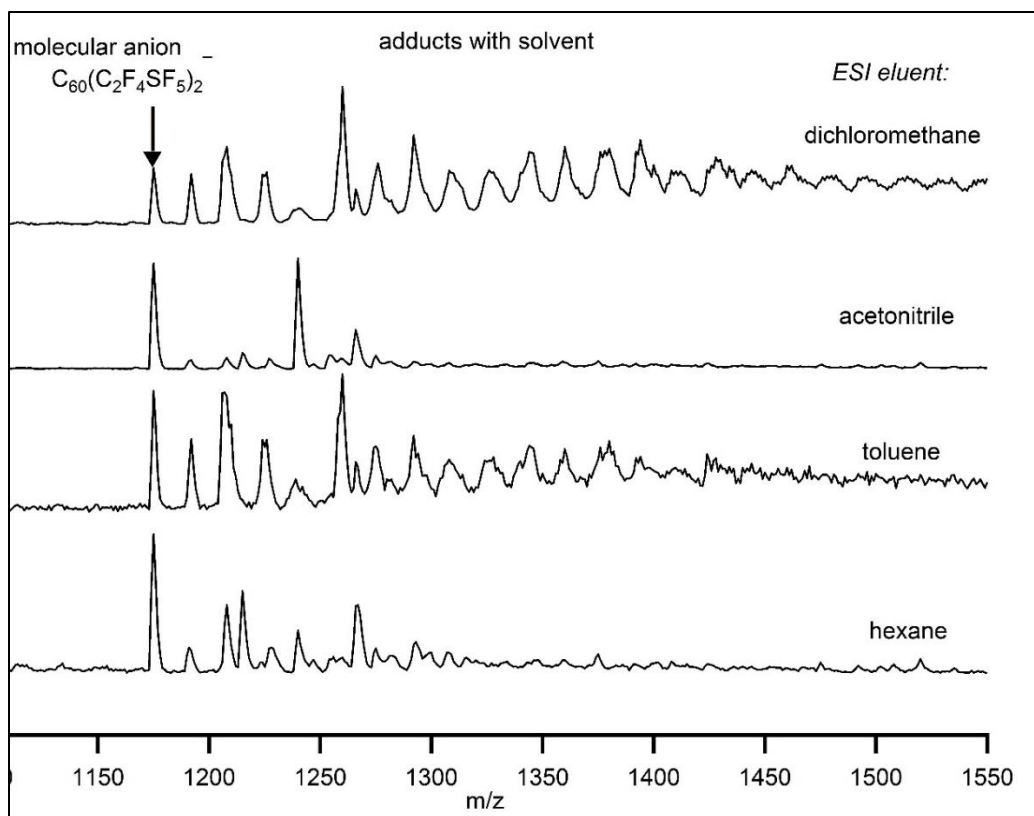
Figure 3-7. NI-ESI mass spectra of the 17 min retention-time HPLC fraction in Figure 3-5 in different eluents (1,7-$C_{60}(CF_2CF_2SF_5)_2$). The main peak in the mass spectrum recorded in hexane at *m/z* 1174 corresponds to the molecular anion $C_{60}(CF_2CF_2SF_5)_2^-$.
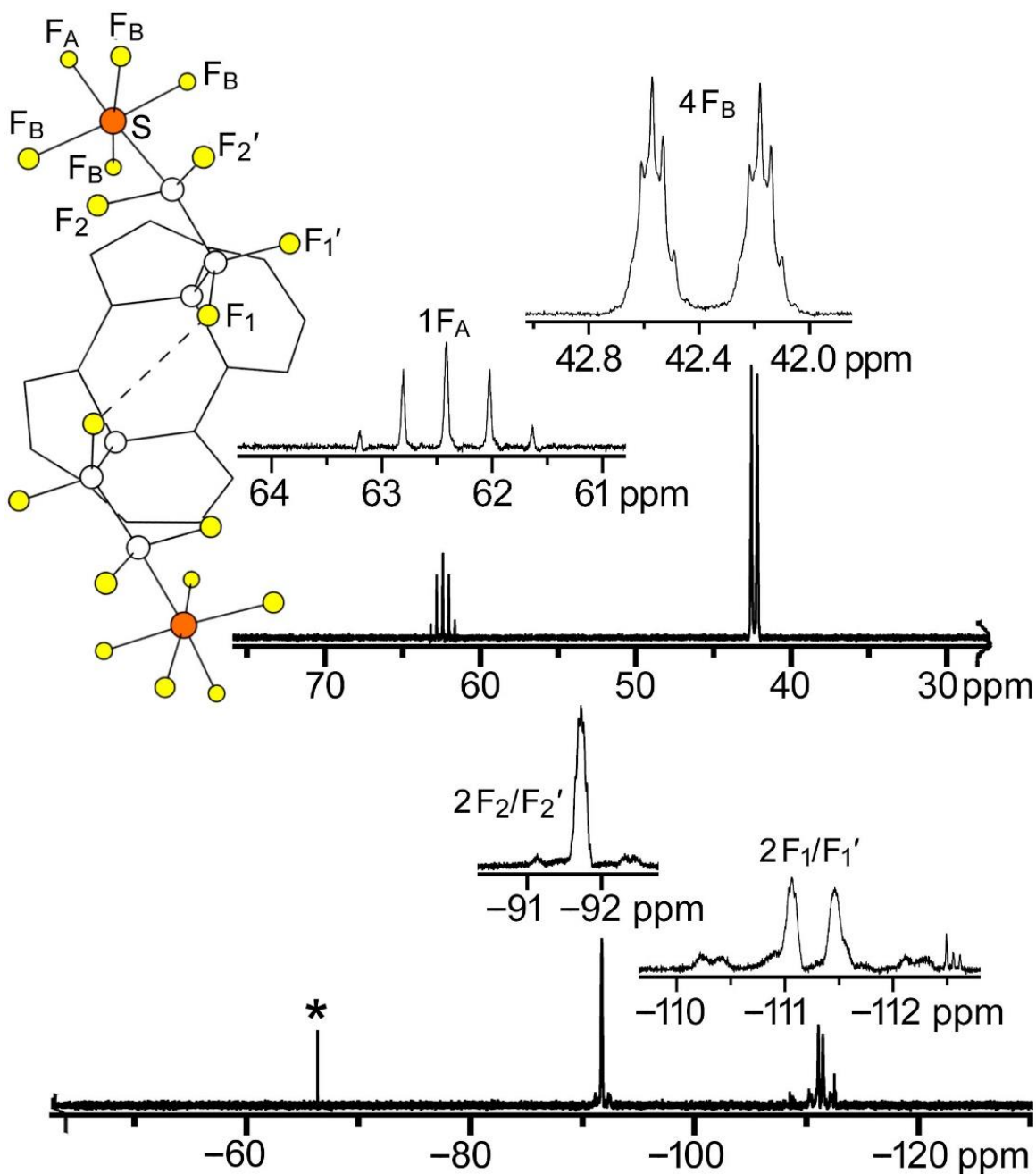
Figure 3-8. The ^{19}F NMR spectrum of 1,7-$C_{60}(CF_2CF_2SF_5)_2$ (CDCl$_3$; *para*-$C_6H_4(CF_3)_2$, PTFMB, int. std. δ −67.9). A drawing of a portion of the proposed structure is shown. An F atom on each of the α-CF_2 moieties are ca. 2.7 Å apart over the shared C_{60} hexagon, as in many $C_{60}(R_F)_n$ derivatives with *para*-$C_{60}(R_F)_2$ hexagons on the fullerene surface (see Ref. 21 and references therein).
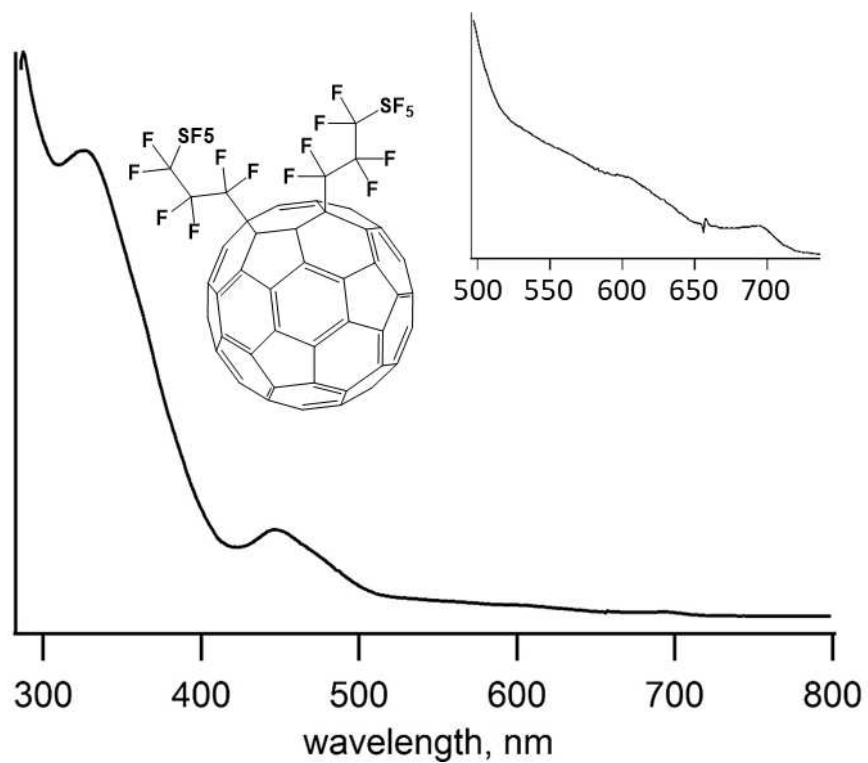
Figure 3-9. UV-vis spectrum of 1,7-$C_{60}(CF_2CF_2SF_5)_2$ solution in toluene. Insets: expanded 500–800 nm range of the spectrum and a drawing of proposed molecular structure. Intensity jump at 670 nm (see insert) is an instrument artifact.
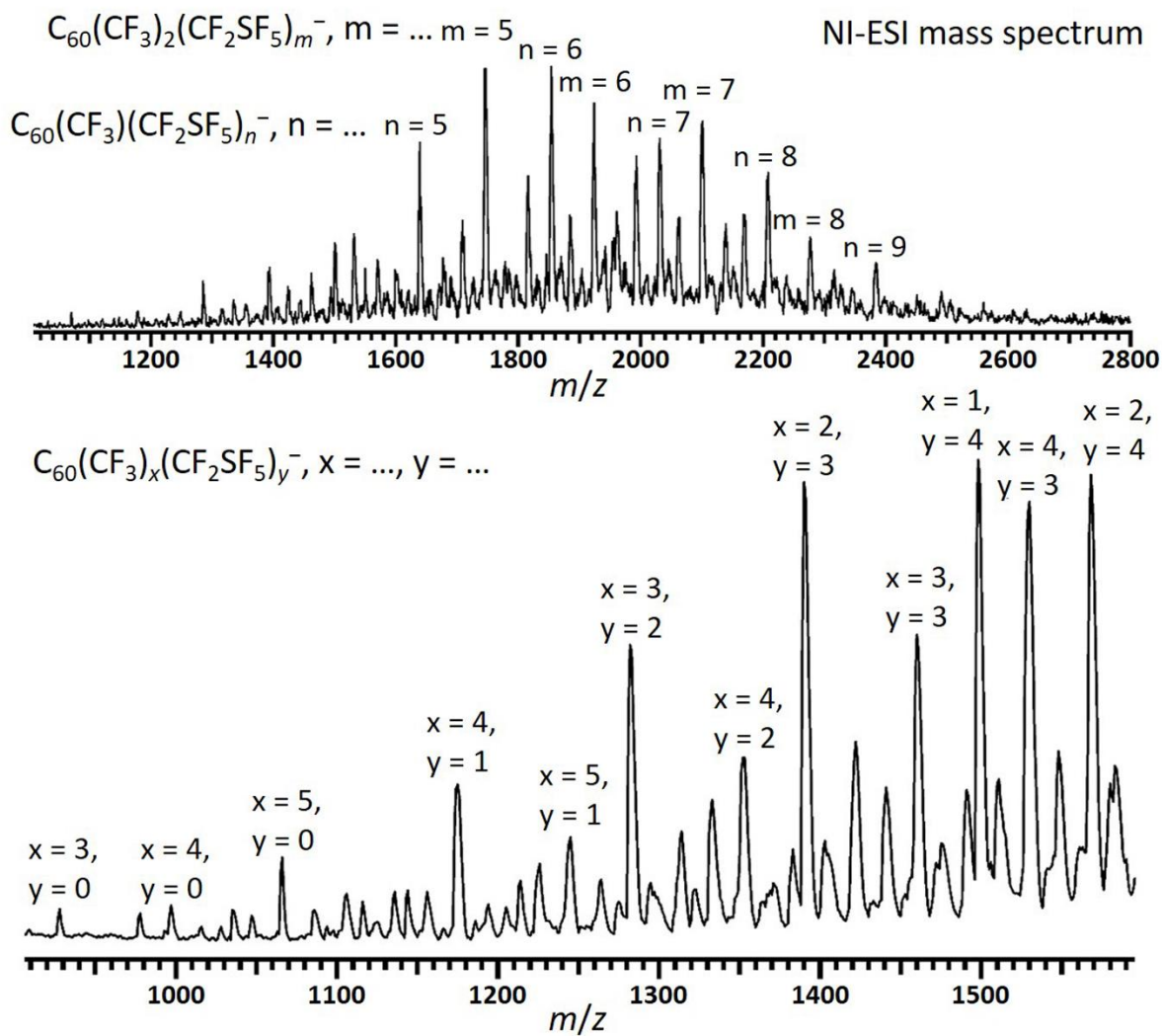
Figure 3-10. NI-ESI mass spectrum of the crude product of the reaction of C_{60} and SF_5CF_2I in *o*-DCB at 150 °C. (**Top**) Full mass range. (**Bottom**) Expansion of the *m/z* 900–1600 region.

376 MHz ^{19}F NMR
(δ(C$_6$F$_6$) −164.9)
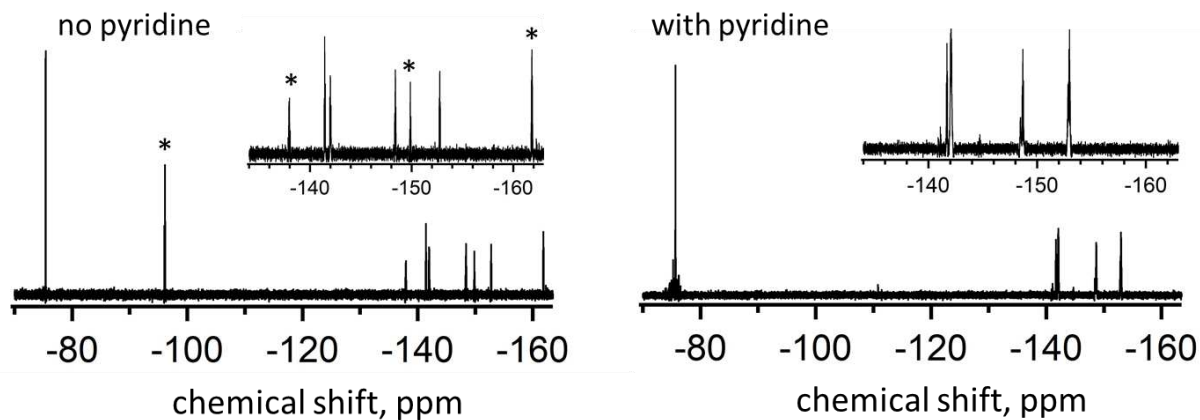
Figure 3-11. ^{19}F NMR spectra of the crude products from two reactions to synthesize C$_{60}$FHF performed under identical conditions, except for the use of pyridine. Spectra were recorded in a 9:1 mixture of CS$_2$ and CDCl$_3$ int. std. C$_6$F$_6$. (**Left**) shows the product mixture from a reaction without pyridine. The signals with asterisks are due to the hydrofullerene. (**Right**) shows that use of pyridine results in the quantitative conversion of the hydrofullerene into C$_{60}$FHF in one step.
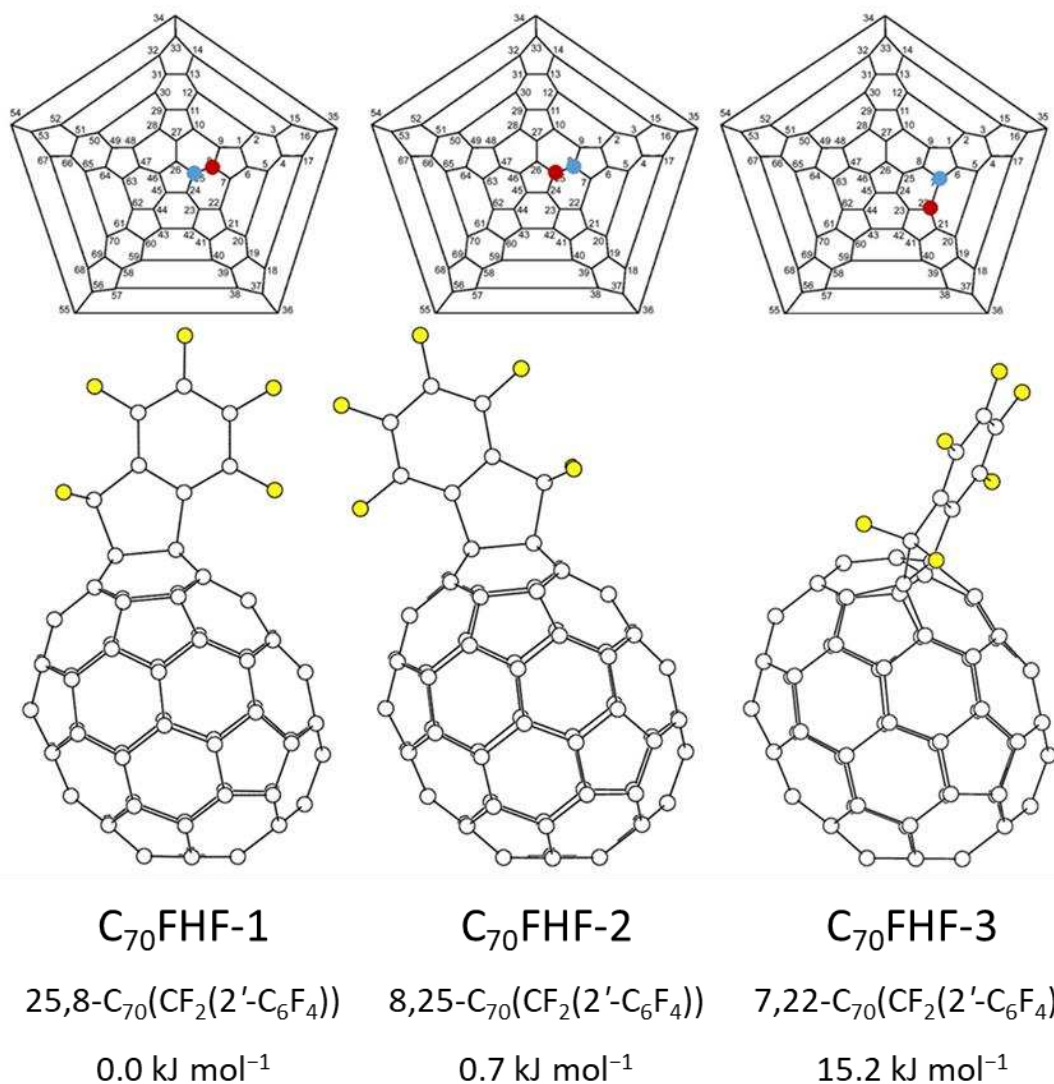
Figure 3-12. (**Top**) Schlegel diagrams of the three isomers of C_{70} faux hawk derivatives prepared and characterized in this work. Red dot shows the addition site for $CF_2(Bn_F)$ moiety, blue dot represents the site for annulation. (**Bottom**) DFT-optimized molecular structures of the isomers, abbreviated names, IUPAC numbering and relative energies. Note that alternative (non-IUPAC) notations for these isomers are used in the literature: 25,8-, 8, 25-, and 6,22 are α1, α2 and β, respectively.[52]
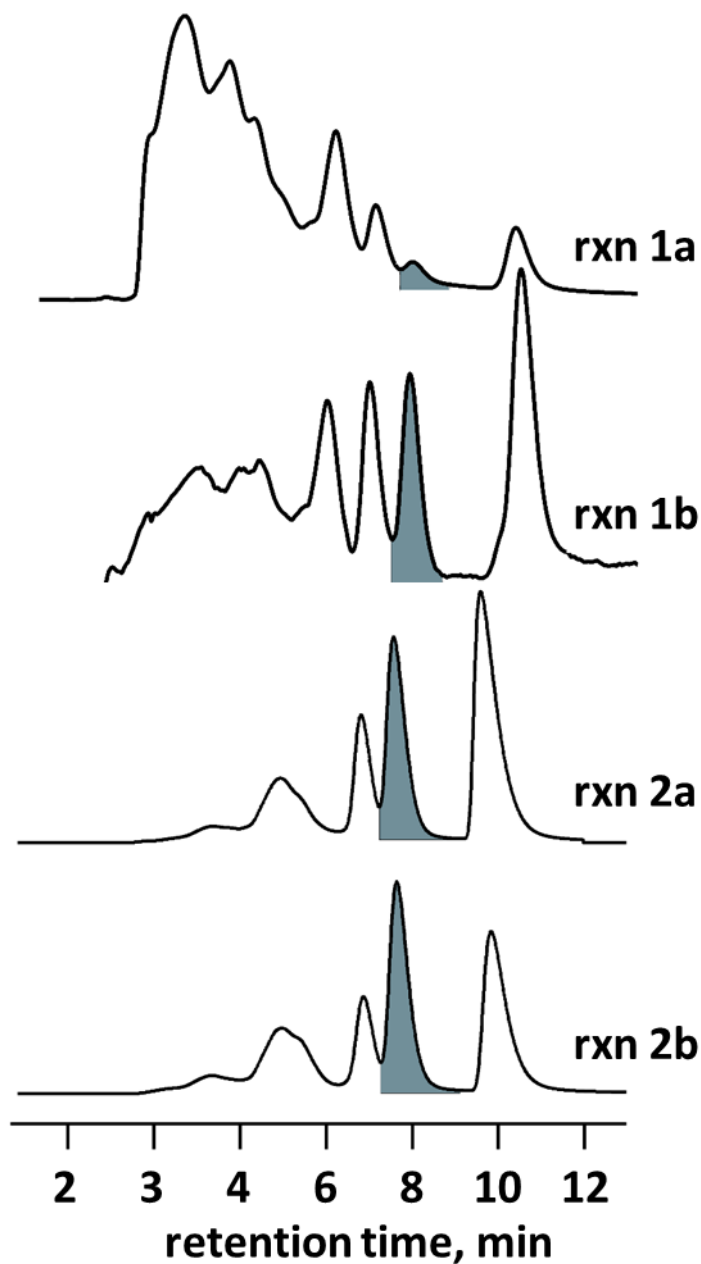
Figure 3-13. HPLC chromatograms (100% toluene, UV detection 300 nm) of crude reaction products prepared by Dr. San using Method 1 in chlorobenzene, (rxn **1a**), and in *o*-DCB (rxn **1b**); and reactions prepared by the author using Method 2 in chlorobenzene (rxn **2a**) and in *o*-DCB (rxn **2b**). Highlighted in grey is the fraction containing a mixture of two major $C_{70}FHF$ isomers. The highest yield (largest peak area relative to total crude) is achieved in reaction **2b**.
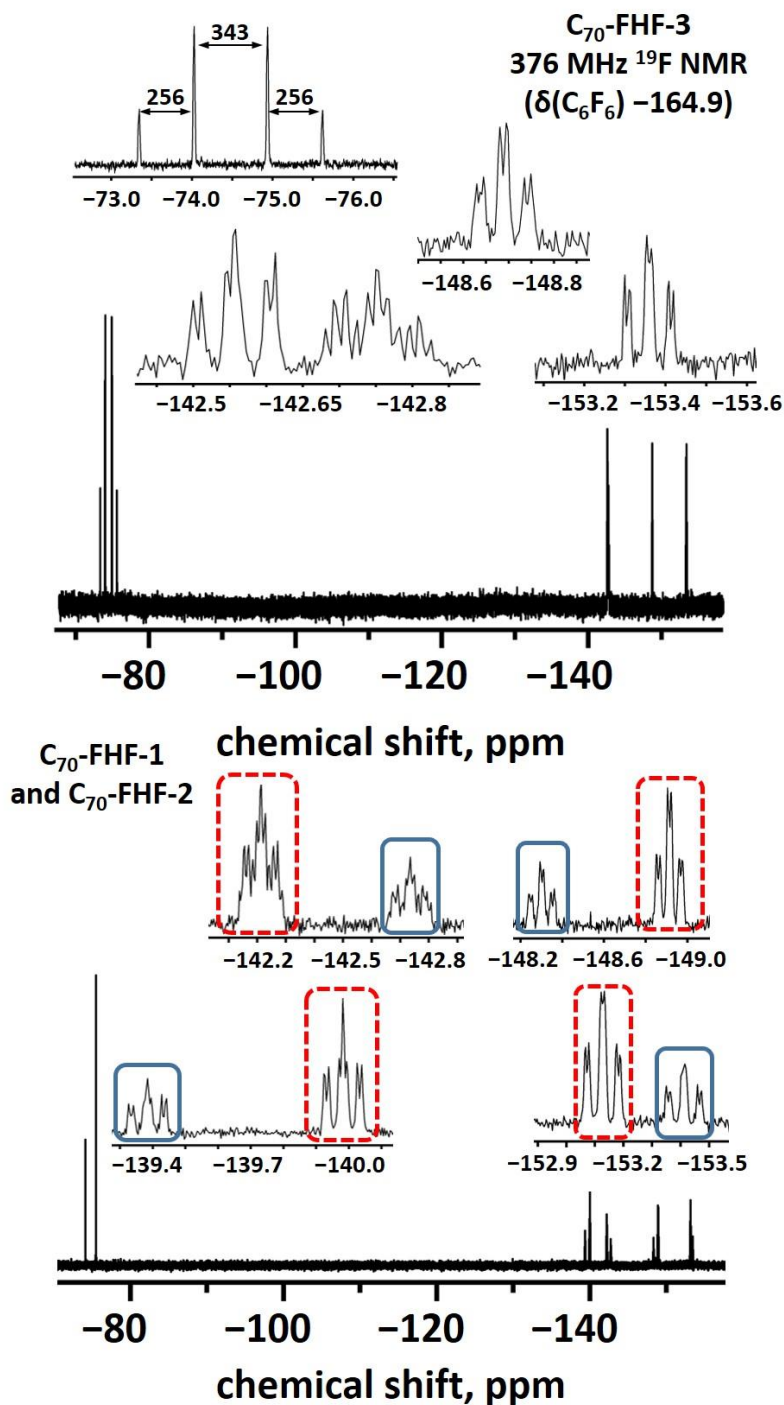
Figure 3-14. (**Left**) ^{19}F NMR of $C_{70}FHF$-3. The inset shows the AB quartet distinctive for the 7,22 addition pattern. Coupling constants are shown in Hz. (**Right**) ^{19}F NMR of $C_{70}FHF$-1, red, and $C_{70}FHF$-2, blue, mixture used for OFETs, dominant compound $C_{70}FHF$-1. Recorded in a 9/1 mixture of $CS_2/CDCl_3$. (C_6F_6 int. std. (δ −164.9)).
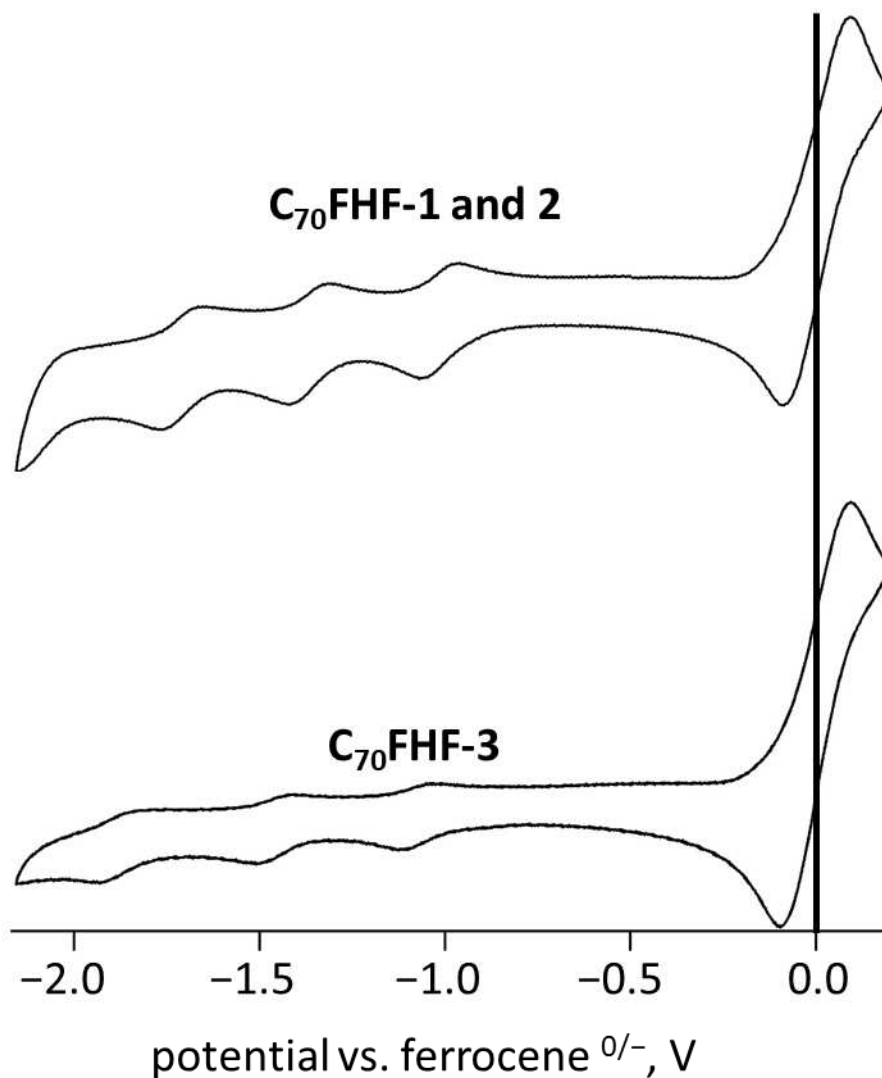
Figure 3-15. (**Top**) Cyclic voltammogram of C_{70}-FHF-1 and 2 mixture versus ferrocene recorded in 0.1 M TBABF$_4$ o-DCB solution with a cycle rate of 250 mV s^{-1}. $E_{1/2}$ (1st red.) vs Ferrocene -1.11 V. (**Bottom**) Cyclic voltammogram of C_{70}-FHF-3 versus ferrocene recorded in 0.1 M TBABF$_4$ o-DCB solution with a cycle rate of 250 mV s^{-1}. $E_{1/2}$ (1st red.) vs Ferrocene -1.09 V.
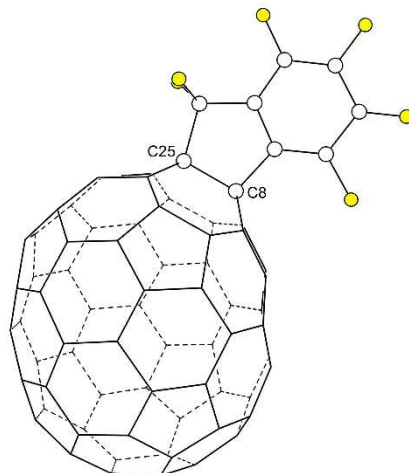
Figure 3-16. The structure of 25,8-$C_{70}(CF_2(2'-C_6F_4))$. The molecule is oriented so that the original C_{70} C_5 axis is aligned with the long axis of the page. The faux hawk substituent C atoms, C25, and C8 are nearly co-planar with an average out-of-plane deviation of ±0.03 Å. Note the 10 triple-hexagon junctions around the C_{70} equator.
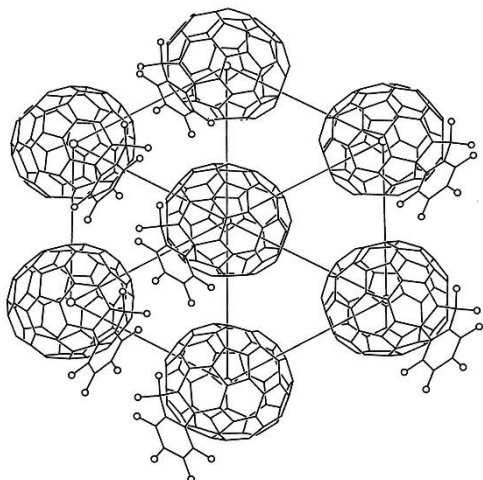
Figure 3-17. The hexagonal array of fullerene molecules in the structure of 25,8-$C_{70}(CF_2(2'-C_6F_4))$. The circles in the center of the C_{70} moieties represent the centroids ($\odot$) of the 10 triple-hexagon junction $C(sp^2)$ atoms. The centroids are nearly co-planar, with an average deviation from their least-squares plane of ±0.06 Å. The $\odot\cdots\odot$ distances within the fullerene layers range from 10.03 to 11.02 Å and average 10.63 Å. The crystallographic *bc* plane is in the plane of the page.

169
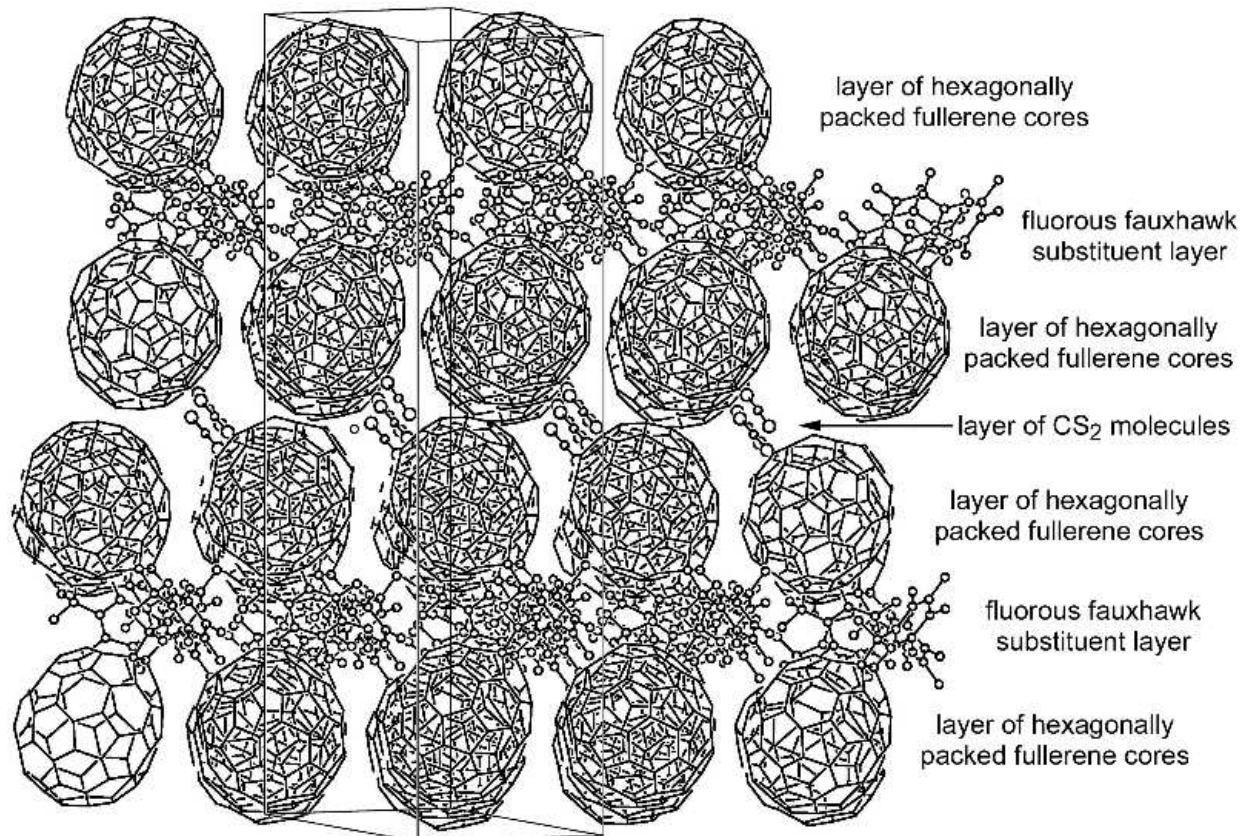
Figure 3-18. The hexagonal layers of fullerenes in the structure of 25,8-$C_{70}(CF_2(2'-C_6F_4))$ are stacked along the crystallographic *a* axis and are separated by either their fluorous fauxhawk substituents or a layer of CS_2 solvate molecules. The orthorhombic unit cell is also shown.

8,25-C_{70}(C(4'-C_6H_4(O-nBu)$_2$
six neighbors
10.34–10.83 Å (av. 10.67 Å)

8,25-C_{70}(C(Ph)(C_3H_6COOMe))
seven neighbors
10.20–10.99 Å (av. 10.60 Å)

8,25-C_{70}(C(Ph)(C_3H_6COOMe))×C_6H_{14}
seven neighbors
10.21–11.15 Å (av. 10.58 Å)

7,22-C_{70}(C_6H_4(CH$_2$)$_2$)
nine neighbors
10.21–11.15 Å (av. 10.58 Å)

C_{70}FHF-1: 25,8-C_{70}(CF$_2$(2'-C_6F_4))
ten neighbors
10.03–11.32 Å (av. 10.67 Å)

1,6-C_{70}(C_6H_4(CH$_2$)$_2$)
nine neighbors
10.22–11.12 Å (av. 10.58 Å)
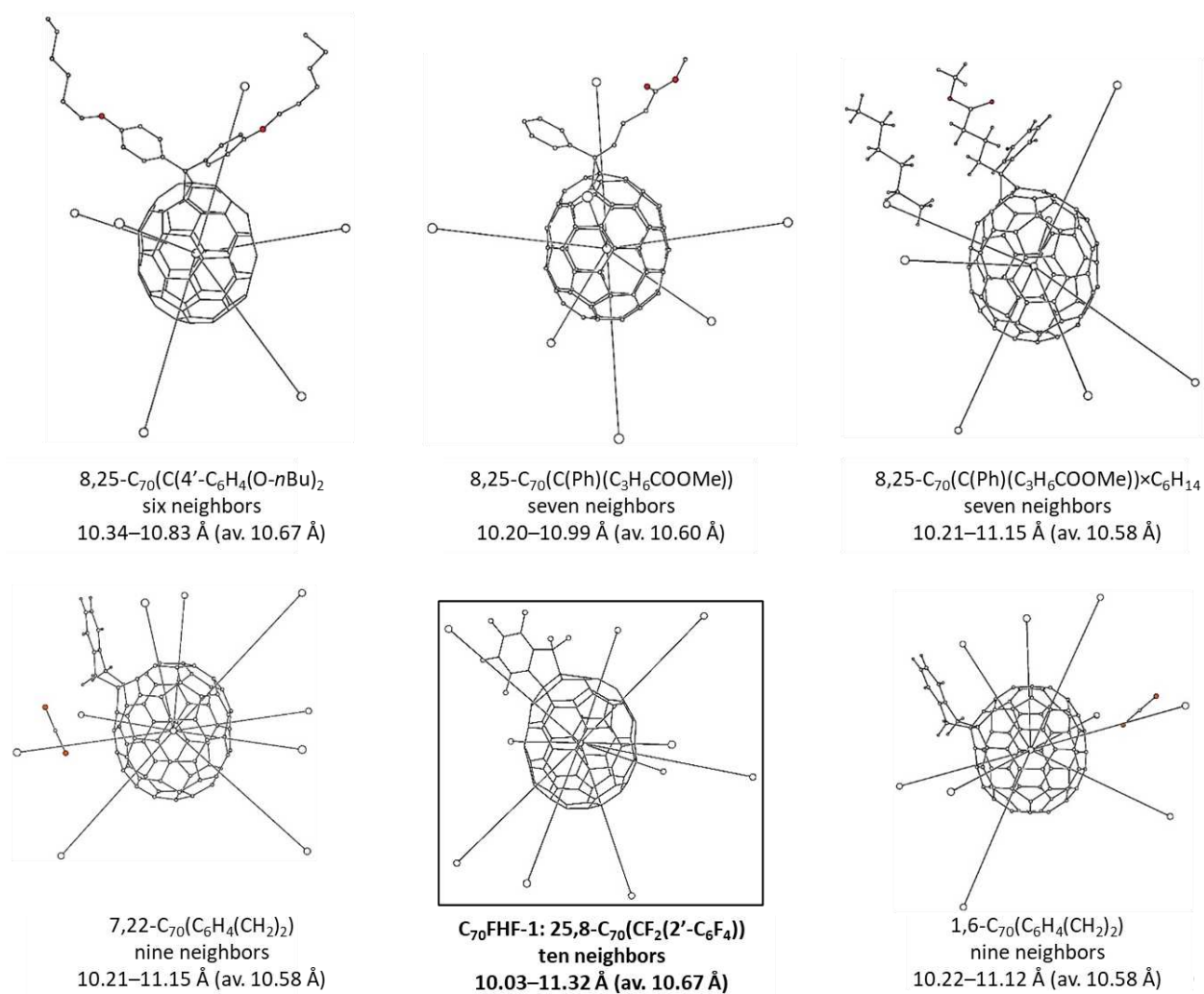
Figure 3-19. The packing of fullerene centroids (large circles) in the structures of C_{70} monoadducts from the literature (see text for more detail) and C_{70}FHF-1 (in the solid frame) from this work. The number of the nearest neighbors, the range of the $\odot\cdots\odot$ centroid-centroid distances and average distances (in parentheses) are calculated from the single-crystal X-ray data.

171
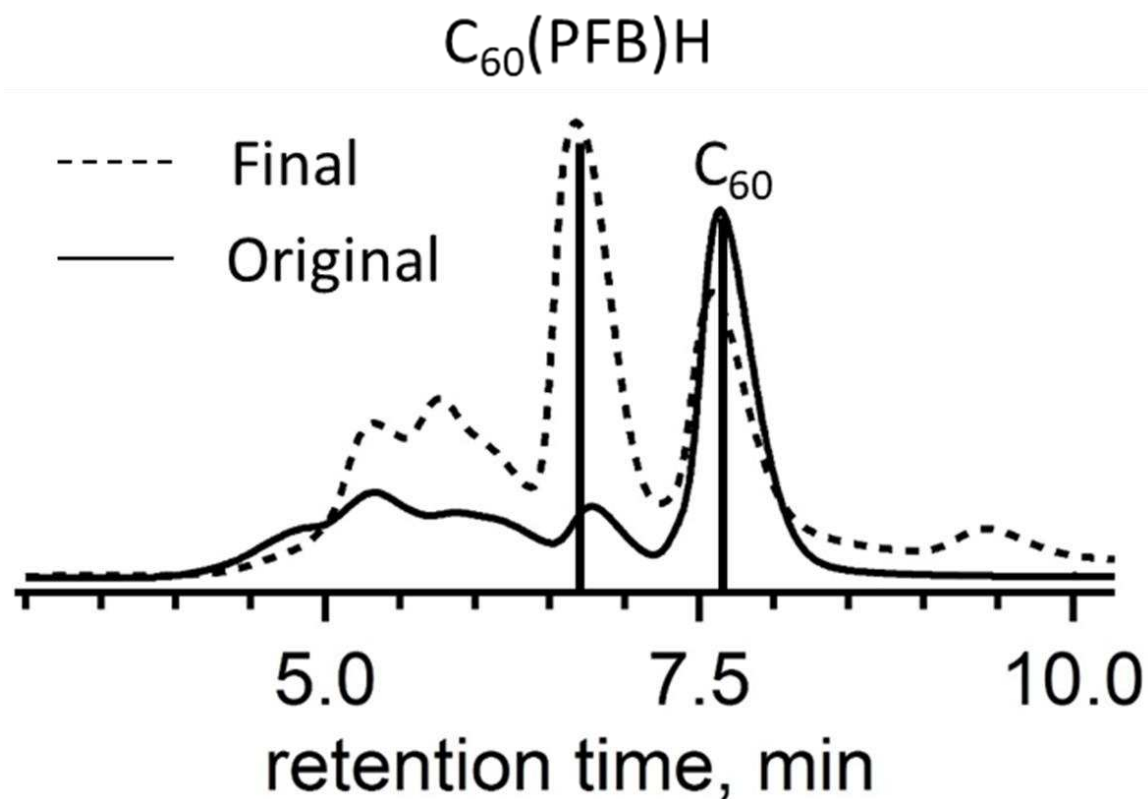
Figure 3-20. Comparison of the initial synthesis of $C_{60}(PFB)H$ versus the optimized reaction. Separated on a Cosmosil Buckyprep semipreparative scale column, eluent 100% toluene, 5 mL min^{-1}, 300 nm. The initial conditions were the same used for the published synthesis of 1,9-$C_{60}(CF_2C_6F_5)H$. The reaction was modified by diluting the concentration of C_{60} from 5.6 mM to 1.6 mM, decreasing the temperature from 165 °C to 145°C, and increasing the reaction time to 24 h from 2 h.
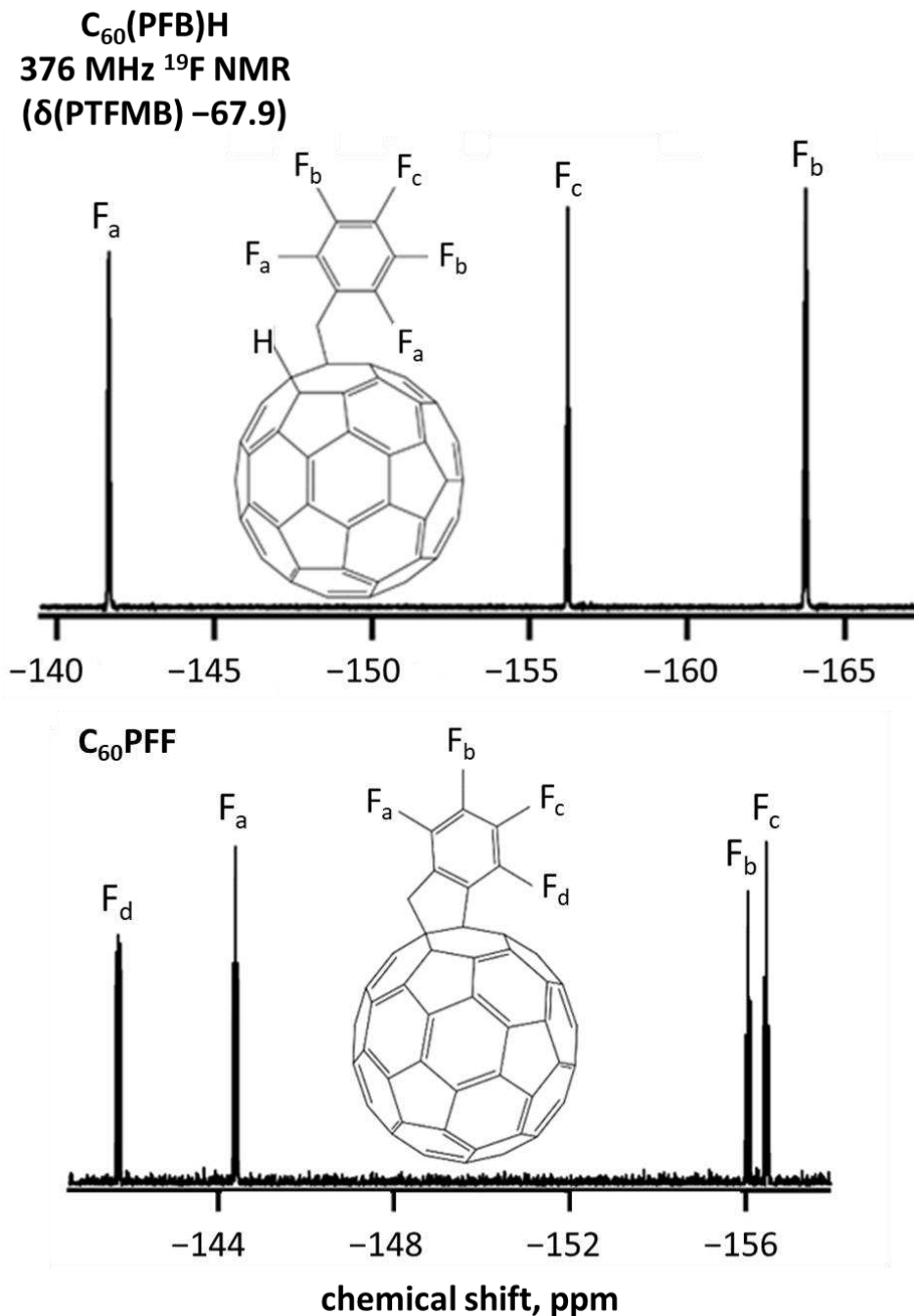
Figure 3-21. The ^{19}F NMR spectrum of $C_{60}(PFB)H$ (**Top**) and $C_{60}PFF$ (**Bottom**), all the peaks have been assigned based on integration, shielding, and multiplicity. (PTFMB int. std. ($\delta -67.9$)). (**Top**) The integration values are 2 to 1 to 2 with $F_c = 1$, F_a $\delta -141.7$, F_c $\delta -156.2$, and F_b $\delta -163.2$. The solvent used was deuterated chloroform ($CDCl_3$). (**Bottom**) Each signal integrates to 1, F_a δ -144.7, F_b $\delta -156.5$, F_c $\delta -156.9$, and F_d $\delta -141.2$. The solvent used was $CDCl_3$.
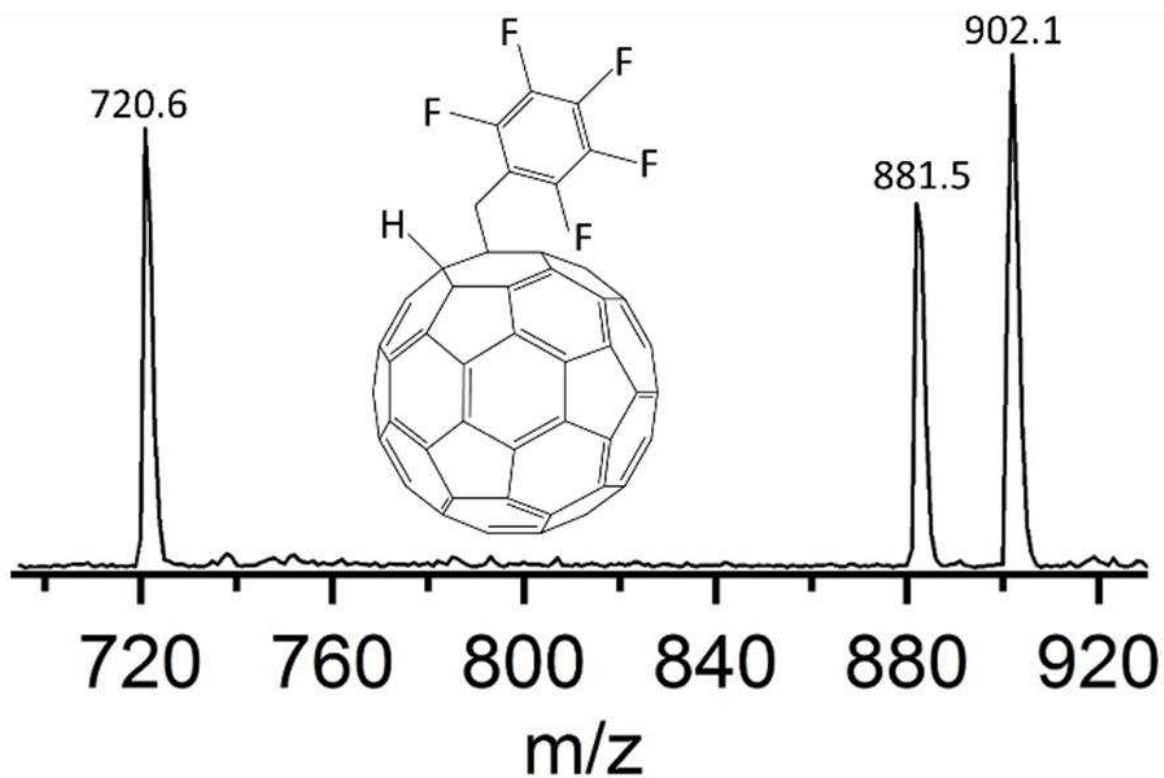
Figure 3-22. NI-ESI Mass spectrum of $C_{60}(PFB)H$ showing masses equivalent to C_{60} and $C_{60}PFF$. Eluent was acetonitrile. The mass of $C_{60}(PFB)H$, 902.1 *m/z*, is accompanied by the mass associated with the annulated product, $C_{60}PFF$, 881.5 *m/z*.
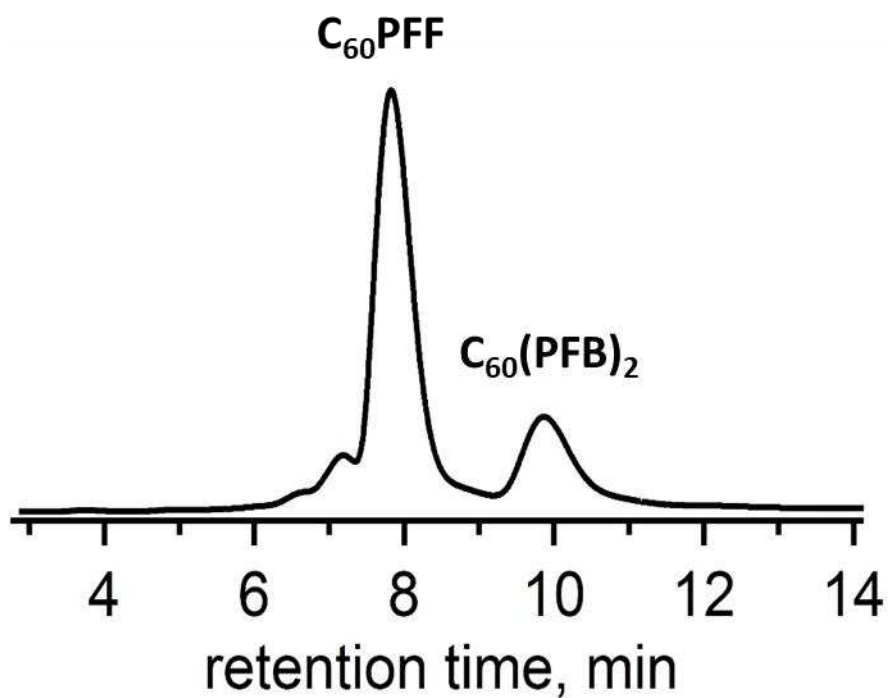
Figure 3-23. HPLC chromatogram of the crude material from rxn 4A. Separation conditions: eluent 100% toluene, stationary phase Cosmosil Buckyprep semipreparative column, flow rate 5 mL min^{-1}, and 300 nm detection wavelength. The *para-* addition bis pentafluorobenzyl fullerene compound, $C_{60}(PFB)_2$, is labeled for clarity.
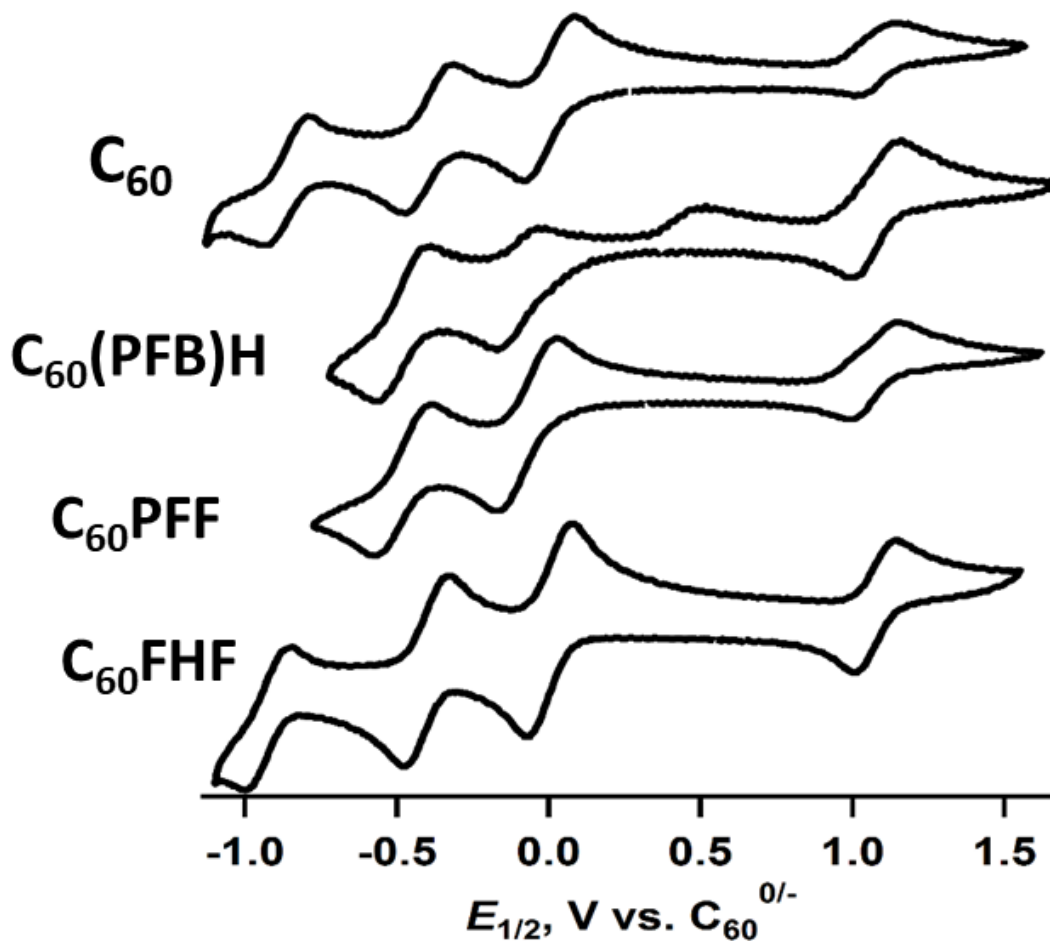
Figure 3-24. The cyclic voltammograms for C60, $C_{60}(PFB)H$, $C_{60}PFF$, and $C_{60}FHF$. The zero point has been set as the first reduction potential of C_{60}. Ferrocene was used as an internal standard. The voltammograms were recorded using 0.1 M $N(n\text{-butyl})_4BF_4$ in o-DCB as an electrolyte. The $E_{1/2}$ (1st red.) vs C_{60} for $C_{60}PFF$ is -0.07 V. The extra reduction event at 0.5 V for $C_{60}(PFB)H$ is believed to be associated with the charged intermediate formed after the loss of HF.
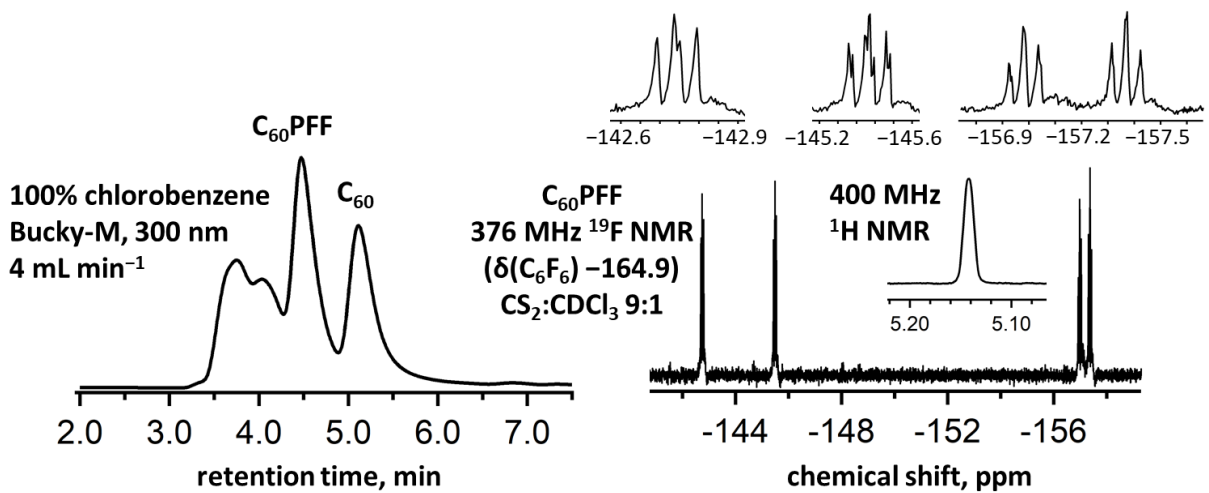
Figure 3-25. (**Left**) HPLC chromatogram for the one pot synthesis of $C_{60}PFF$. (**Right**) ^{19}F NMR of $C_{60}PFF$ in $CS_2/CDCl_3$ 9/1. No unreacted $C_{60}(PFB)H$ is present, both fullerenes co-elute in 100% toluene on the Cosmosil Bucky-M stationary phase and the residual $C_{60}(PFB)H$ would be evident by NMR.

3.9. REFERENCES

(1)   Anthopoulos, T. D.; Tanase, C.; Setayesh, S.; Meijer, E. J.; Hummelen, J. C.; Blom, P. W. M.; de Leeuw, D. M. Ambipolar organic field-effect transistors based on a solution-processed methanofullerene. *Adv. Mater.* **2004**, *16*, 2174–2179.

(2)   Ryno, S. M.; Ravva, M. K.; Chen, X.; Li, H.; Brédas, J.-L. Molecular Understanding of Fullerene – Electron Donor Interactions in Organic Solar Cells. *Adv. Eng. Mater.* **2017**, *7*, article 1601370.

(3)   Cui, C.; Li, Y.; Li, Y. Fullerene Derivatives for the Applications as Acceptor and Cathode Buffer Layer Materials for Organic and Perovskite Solar Cells. *Adv. Eng. Mater.* **2017**, *7*, article 1601251.

(4)   Hosseini, V. K.; Ahmadi, M. T.; Afrang, S.; Ismail, R. Current Analysis and Modeling of Fullerene Single-Electron Transistor at Room Temperature. *J. Electron. Mater.* **2017**, *46*, 4294–4298.

(5)   Romanova, N. A.; Papina, T. y. S.; Luk'yanova, V. A.; Buyanovskaya, A. G.; Varuschenko, R. M.; Druzhinina, A. I.; Goryunkov, A. A.; Markov, V. Y.; Panin, R. A.; Sidorov, L. N. S_6 Isomer of $C_{60}(CF_3)_{12}$: Synthesis, properties and thermodynamic functions. *J. Chem. Thermodyn.* **2013**, *66*, 59-64.

(6)   Ignateva, D. V.; Goryunkov, A. A.; Ioffe, I. N.; Sidorov, L. N. Trifluoromethylation of Fullerenes: Kinetic and Thermodynamic Control. *J. Phys. Chem. A* **2013**, *117*, 13009-13017.

(7)   Liu, S.; DeWeerd, N. J.; Reeves, B. J.; San, L. K.; Dahal, D.; Radha Krishnan, R. K.; Strauss, S. H.; Boltalina, O. V.; Lüssem, B. Doped N-Type Organic Field-Effect Transistors Based on Faux-Hawk Fullerene. *Adv. Electron. Mater.* **2019**, *5*, article 1900109.

(8)   Qing, S.-Y.; DeWeerd, N. J.; Matsnev, A. V.; Strauss, S. H.; Thrasher, J. S.; Boltalina, O. V. Synthesis and Characterization of Pentafluorosulfanyl-Functionalized Fullerenes. *J. Fluorine Chem.* **2018**, *211*, 52-59.

(9)   Gakh, A. A.; Tuinman, A. A. 'Fluorine dance' on the fullerene surface. *Tetrahedron Lett.* **2001**, *42*, 7137-7139.

(10)   Kako, M.; Sugiura, T.; Miyabe, K.; Yasui, M.; Yamada, M.; Maeda, Y.; Guo, J. D.; Nagase, S.; Akasaka, T. Preparation, Structural Determination, and Characterization of Electronic Properties of [5,6]- and [6,6]-Carbosilylated $Sc_3N@I_h$-C_{80}. *Chem. Asian J.* **2017**, *12*, 1391-1399.

(11)   Ueda, M.; Imai, N.; Yoshida, S.; Yasuda, H.; Fukuyama, T.; Ryu, I. Scalable Flow Synthesis of [6,6]-Phenyl-C_{61}-butyric Acid Methyl Ester (PCBM) using a Flow Photoreactor with a Sodium Lamp. *Eur. J. Org. Chem.* **2017**, 6483-6485.

(12)   Kessinger, R.; Fender, N. S.; Echegoyen, L. E.; Thilgen, C.; Echegoyen, L.; Diederich, F. Selective Electrolytic Removal of Bis(alkoxycarbonyl)methano Addends from C60 Bis-adducts and Electrochemical Stability of C_{70} Derivatives. *Chem Eur. J.* **2000**, *6*, 2184-2192.

(13)   Kessinger, R.; Gómez-López, M.; Boudon, C.; Gisselbrecht, J.-P.; Gross, M.; Echegoyen, L.; Diederich, F. Walk on the Sphere: Electrochemically Induced Isomerization of C_{60} Bis-adducts by Migration of Di(alkoxycarbonyl)methano Bridges. *J. Am. Chem. Soc.* **1998**, *120*, 8545-8546.

(14)   Cai, T.; Slebodnick, C.; Xu, L.; Harich, K.; Glass, T. E.; Chancellor, C.; Fettinger, J. C.; Olmstead, M. M.; Balch, A. L.; Gibson, H. W.; Dorn, H. C. A Pirouette on a Metallofullerene Sphere: Interconversion of Isomers of *N*-Tritylpyrrolidino I_h $Sc_3N@C_{80}$. *J. Am. Chem. Soc.* **2006**, *128*, 6486-6492.

(15)   Bukovsky, E. V.; Larson, B. W.; Clikeman, T. T.; Chen, Y. S.; Popov, A. A.; Boltalina, O. V.; Strauss, S. H. Structures and structure-related electronic properties of new $C_{60}(CF_3)_{10}$ isomers. *J. Fluorine Chem.* **2016**, *185*, 103–117.

(16)   Kuvychko, I. V.; Whitaker, J. B.; Larson, B. W.; Raguindin, R. S.; Suhr, K. J.; Strauss, S. H.; Boltalina, O. V. Pressure effect on heterogeneous trifluoromethylation of fullerenes and its application. *J. Fluorine Chem.* **2011**, *132*, 679-685.

(17)   Kuvychko, I. V.; Whitaker, J. B.; Larson, B. W.; Folsom, T. C.; Shustova, N. B.; Avdoshenko, S. M.; Chen, Y.-S.; Wen, H.; Wang, X.-B.; Dunsch, L. Substituent effects in a series of 1,7-$C_{60}(R_F)_2$ compounds (R_F= CF_3, C_2F_5, *n*-C_3F_7, *i*-C_3F_7, *n*-C_4F_9, *s*-C_4F_9, *n*-C_8F_{17}): electron

affinities, reduction potentials and *E*(LUMO) values are not always correlated. *Chem. Sci.* **2012**, *3*, 1399–1407.

(18)　Bukovsky, E. V.; DeWeerd, N. J.; Strauss, S. H.; Boltalina, O. V. Versatile metal reactor for high-temperature and high-pressure trifluoromethylation of carbon-rich substrates. *J. Fluorine Chem.* **2018**, *210*, 56-64.

(19)　San, L. K.; Bukovsky, E. V.; Larson, B. W.; Whitaker, J. B.; Deng, S. H. M.; Kopidakis, N.; Rumbles, G.; Popov, A. A.; Chen, Y.-S.; Wang, X.-B.; Boltalina, O. V.; Strauss, S. H. A faux hawk fullerene with PCBM-like properties. *Chem. Sci.* **2015**, *6*, 1801-1815.

(20)　Sowaileh, M. F.; Hazlitt, R. A.; Colby, D. A. Application of the Pentafluorosulfanyl Group as a Bioisosteric Replacement. *ChemMedChem* **2017**, *12*, 1481–1490.

(21)　Boltalina, O. V.; Popov, A. A.; Kuvychko, I. V.; Shustova, N. B.; Strauss, S. H. Perfluoroalkylfullerenes. *Chem. Rev.* **2015**, *115*, 1051-1105.

(22)　Saethre, L. J.; Berrah, N.; Bozek, J. D.; Børve, K. J.; Carroll, T. X.; Kukk, E.; Gard, G. L.; Winter, R.; Thomas, T. D. Chemical Insights from High-Resolution X-ray Photoelectron Spectroscopy and ab Initio Theory: Propyne, Trifluoropropyne, and Ethynylsulfur Pentafluoride. *J. Am. Chem. Soc.* **2001**, *123*, 10729–10737.

(23)　Savoie, P. R.; Welch, J. T. Preparation and Utility of Organic Pentafluorosulfanyl-Containing Compounds. *Chem. Rev.* **2014**, *115*, 1130–1190, and references therein.

(24)　Kuvychko, I. V.; Strauss, S. H.; Boltalina, O. V. Solution-Phase Perfluoroalkylation of C_{60} Leads to Efficient and Selective Synthesis of Bis-Perfluoroalkylated Fullerenes. *J. Fluorine Chem.* **2012**, *143*, 103-108.

(25)　Larson, B. W. Synthesis and characterization of fluorine-containing C60 derivatives and their charge transfer photophysics in organic photovoltaics, Ph.D. Dissertation, Colorado State University, 2013.

(26)　Gruzinskaya, N. I.; Silin, A. I.; Pimenova, A. S.; Khavrel, P. A.; Markov, V. Y.; Sidorov, L. N.; Kemnitz, E.; Troyanov, S. I. Synthesis and structure of cycloperfluoroalkylated derivatives of C_{70}, $C_{70}(C_2F_4)$ and $C_{70}(C_4F_8)_n$, *n* = 1–6. *New J. Chem.* **2010**, *34*, 243–249.

(27)   Shustova, N. B.; Kuvychko, I. V.; Peryshkov, D. V.; Whitaker, J. B.; Larson, B. W.; Chen, Y. S.; Dunsch, L.; Seppelt, K.; Popov, A. A.; Strauss, S. H.; Boltalina, O. V. Chemical tailoring of fullerene acceptors: synthesis, structures and electrochemical properties of perfluoroisopropylfullerenes. *Chem. Commun.* **2011**, *47*, 875–877.

(28)   Hirsch, A.; Brettreich, M. *Fullerenes: Chemistry and Reactions*; John Wiley & Sons: Weinheim, 2006.

(29)   Shustova, N. B.; Kareev, I. E.; Kuvychko, I. V.; Whitaker, J. B.; Lebedkin, S. F.; Popov, A. A.; Dunsch, L.; Chen, Y. S.; Seppelt, K.; Strauss, S. H.; Boltalina, O. V. High-temperature and photochemical syntheses of C_{60} and C_{70} fullerene derivatives with linear perfluoroalkyl chains. *J. Fluorine Chem.* **2010**, *131*, 1198–1212.

(30)   Dudzinski, P.; Matsnev, A. V.; Thrasher, J. S.; Haufe, G. Ambiphilic Properties of $SF_5CF_2CF_2Br$ Derived Perfluorinated Radical in Addition Reactions Across Carbon–Carbon Double Bonds. *Org. Lett.* **2015**, *17*, 1078–1081, and references therein.

(31)   Ebert, F.; Woitinek, H. Kristallstrukturen von Fluoriden. II. HgF, HgF_2, CuF und CuF_2. *Z. Anorg. Allg. Chem.* **1933**, *210*, 269-272.

(32)   Winter, R. W.; Dodean, R.; Smith, J. A.; Anilkumar, R.; Burton, D. J.; Gard, G. L. Site directed synthesis of mono and disubstituted SF_5-polyfluoroalkyl benzenes. *J. Fluorine Chem.* **2005**, *126*, 1202–1214.

(33)   Wang, X. B.; Chi, C. X.; Zhou, M. F.; Kuvychko, I. V.; Seppelt, K.; Popov, A. A.; Strauss, S. H.; Boltalina, O. V.; Wang, L. S. Photoelectron Spectroscopy of $C_{60}F_n^-$ and $C_{60}F_m^{2-}$ (n = 17, 33, 35, 43, 45, 47; m = 34, 46) in the Gas Phase and the Generation and Characterization of C_1-$C_{60}F_{47}^-$ and D_2-$C_{60}F_{44}$ in Solution. *J. Phys. Chem. A* **2010**, *114*, 1756–1765.

(34)   Larson, B. W.; Whitaker, J. B.; Wang, X. B.; Popov, A. A.; Rumbles, G.; Kopidakis, N.; Strauss, S. H.; Boltalina, O. V. Electron Affinity of Phenyl-C_{61}-Butyric Acid Methyl Ester (PCBM). *J. Phys. Chem. C* **2013**, *117*, 14958–14964.

(35)   Dudziński, P.; Matsnev, A. V.; Thrasher, J. S.; Haufe, G. Synthesis of SF_5CF_2-Containing Enones and Instability of This Group in Specific Chemical Environments and Reaction Conditions. *J. Org. Chem.* **2016**, *81*, 4454-4463.

(36)   Kniaz, K.; Fischer, J. E.; Selig, H.; Vaughan, G. B. M.; Romanow, W. J.; Cox, D. M.; Chowdhury, S. K.; McCauley, J. P.; Strongin, R. M.; Smith, A. B. Fluorinated fullerenes: synthesis, structure, and properties. *J. Am. Chem. Soc.* **1993**, *115*, 6060-6064.

(37)   Clikeman, T. T.; Schmaltz, T.; Halik, M.; Hirsch, A.; Strauss, S. H.; Boltalina, O. V. Formation of Perfluoroalkyl Fullerene Alkylphosphonic Acid Self-Assembled Monolayers on Aluminum Oxide. *ECS J. Solid State Sci. Technol.* **2017**, *6*, M3163–M3167.

(38)   Tuktarov, A. R.; Khuzin, A. A.; Dzhemilev, U. M. Light-controlled molecular switches based on carbon clusters. Synthesis, properties and application prospects. *Russ. Chem. Rev.* **2017**, *86*, 474-509.

(39)   Larson, B. W.; Whitaker, J. B.; Popov, A. A.; Kopidakis, N.; Rumbles, G.; Boltalina, O. V.; Strauss, S. H. Thermal [6,6] → [6,6] Isomerization and Decomposition of PCBM (Phenyl-C_{61}-butyric Acid Methyl Ester). *Chem. Mater.* **2014**, *26*, 2361-2367.

(40)   Reeves, B. J.; Brook, C. P.; Gerdes, O.; Deng, S. H.; Yuan, Q.; Wang, X.-B.; Strauss, S. H.; Boltalina, O. V.; Walzer, K. Fluorous Fullerene Acceptors in Vacuum-Deposited Photovoltaic Cells. *Solar RRL* **2019**, *3*, article 1900070.

(41)   Mas-Torrent, M.; Rovira, C. Role of Molecular Order and Solid-State Structure in Organic Field-Effect Transistors. *Chem. Rev.* **2011**, *111*, 4833-4856.

(42)   Lüssem, B.; Keum, C.-M.; Kasemann, D.; Naab, B.; Bao, Z.; Leo, K. Doped Organic Transistors. *Chem. Rev.* **2016**, *116*, 13714-13751.

(43)   Le Grognec, E.; Chrétien, J.-M.; Zammattio, F.; Quintard, J.-P. Methodologies Limiting or Avoiding Contamination by Organotin Residues in Organic Synthesis. *Chem. Rev.* **2015**, *115*, 10207-10260.

(44)   Heumann, L. V.; Keck, G. E. A New Construction of 2-Alkoxypyrans by an Acylation−Reductive Cyclization Sequence. *Org. Lett.* **2007**, *9*, 1951-1954.

(45)   Haddock, J. N.; Zhang, X.; Domercq, B.; Kippelen, B. Fullerene based *n*-type organic thin-film transistors. *Org. Electron.* **2005**, *6*, 182-187.

(46)   Meng, L.; Zhang, Y.; Wan, X.; Li, C.; Zhang, X.; Wang, Y.; Ke, X.; Xiao, Z.; Ding, L.; Xia, R. Organic and solution-processed tandem solar cells with 17.3% efficiency. *Science* **2018**, *361*, 1094-1098.

(47)   Said, A. A.; Xie, J.; Zhang, Q. Recent Progress in Organic Electron Transport Materials in Inverted Perovskite Solar Cells. *Small* **2019**, *15*, article 1900854.

(48)   Vidal, S.; Izquierdo, M.; Filippone, S.; Fernandez, I.; Akin, S.; Seo, J. Y.; Zakeeruddin, S. M.; Gratzel, M.; Martin, N. Site-selective Synthesis of β-[70]PCBM-like Fullerenes: Efficient Application in Perovskite Solar Cells. *Chem. Eur. J.* **2019**, *25*, 3224-3228.

(49)   Umeyama, T.; Miyata, T.; Jakowetz, A. C.; Shibata, S.; Kurotobi, K.; Higashino, T.; Koganezawa, T.; Tsujimoto, M.; Gélinas, S.; Matsuda, W. Regioisomer effects of [70]fullerene mono-adduct acceptors in bulk heterojunction polymer solar cells. *Chem. Sci.* **2017**, *8*, 181-188.

(50)   Umeyama, T.; Imahori, H. Isomer Effects of Fullerene Derivatives on Organic Photovoltaics and Perovskite Solar Cells. *Acc. Chem. Res.* **2019**, *52*, 2046-2055.

(51)   Umeyama, T.; Shibata, S.; Igarashi, K.; Takahara, S.; Higashino, T.; Seki, S.; Imahori, H. Enantiomerically Separated α-[70]PCBM for Organic Photovoltaics. *Chem. Lett.* **2017**, *46*, 1001-1003.

(52)   Umeyama, T.; Shibata, S.; Miyata, T.; Igarashi, K.; Koganezawa, T.; Imahori, H. Regioisomer effects of [70]PCBM on film structures and photovoltaic properties of composite films with a crystalline conjugated polymer P3HT. *RSC Adv.* **2017**, *7*, 45697-45704.

(53)   Zhan, X. X.; Lin, M. S.; Lu, X. Z.; Tang, X. Y.; Xu, Y. Y.; Wang, T.; Deng, L. L.; Xie, S. Y.; Huang, R. B.; Zheng, L. S. Formulation of $PC_{71}BM$ isomers in P3HT-based polymer solar cells. *Sol. Energ. Mat. Sol. C* **2018**, *176*, 340-345.

(54)   San, L. K. Strong Fullerene and Polycyclic Aromatic Hydrocarbon Electron Acceptors with Perfluorinated Substituents, Ph.D. dissertation, Colorado State University, 2015.

(55)   Yang, W.-W.; Li, Z.-J.; Li, S.-H.; Wu, S.-L.; Shi, Z.; Gao, X. Reductive Activation of C_{70} Equatorial Carbons and Structurally Characterized C70 δ-Adduct with Closed [5,6]-Ring Fusion. *J. Org. Chem.* **2017**, *82*, 9253-9257.

(56)   Yu, H.; Cho, H.-H.; Cho, C.-H.; Kim, K.-H.; Kim, D. Y.; Kim, B. J.; Oh, J. H. Polarity and Air-Stability Transitions in Field-Effect Transistors Based on Fullerenes with Different Solubilizing Groups. *ACS Appl. Mater. Interfaces* **2013**, *5*, 4865-4871.

(57)   Mamada, M.; Katagiri, H.; Sakanoue, T.; Tokito, S. Crystal Structure and Theoretical Investigation of Charge-transport Properties of Fullerene Derivatives. *Chem. Lett.* **2016**, *45*, 1421-1424.

(58)   Zhan, X. X.; Zhang, X.; Dai, S. M.; Li, S. H.; Lu, X. Z.; Deng, L. L.; Xie, S. Y.; Huang, R. B.; Zheng, L. S. Tailorable $PC_{71}BM$ Isomers: Using the Most Prevalent Electron Acceptor to Obtain High-Performance Polymer Solar Cells. *Chem Eur. J.* **2016**, *22*, 18709-18713.

(59)   Nelson, J. Polymer:fullerene bulk heterojunction solar cells. *Mater. Today* **2011**, *14*, 462-470.

(60)   Fan, Q.; Méndez-Romero, U. A.; Guo, X.; Wang, E.; Zhang, M.; Li, Y. Fluorinated Photovoltaic Materials for High-Performance Organic Solar Cells. *Chem. Asian J.* **2019**, *14*, 3085-3095.

(61)   Babudri, F.; Farinola, G. M.; Naso, F.; Ragni, R. Fluorinated organic materials for electronic and optoelectronic applications: the role of the fluorine atom. *Chem. Commun.* **2007**, 1003-1022.

(62)   Garner, L. E.; Larson, B. W.; Oosterhout, S. D.; Owczarczyk, Z. R. R.; Olson, D. C.; Kopidakis, N.; Boltalina, O. V.; Strauss, S. H.; Braunecker, W. A. In *2017 IEEE 44th Photovoltaic Specialist Conference* 2017, p 1–4. Improving photoconductance of fluorinated donors with fluorinated acceptors

(63)   2,3,4,5,6-Pentafluorobenzyl   bromide,   Sigma-Aldrich, https://www.sigmaaldrich.com/catalog/product/aldrich/101052?lang=en&region=US.

(64)   Heptafluorobenzyl   iodide,   SynQuest-Labs,
http://synquestlabs.com/product.html?id=18974.

(65)   Cottrell, T. L. *The Strengths of Chemical Bonds*; Butterworths: London, 1958.

(66)   Yang, W.-W.; Li, Z.-J.; Gao, X. Reaction of C_{60}^{2-} with Organic Halides Revisited in DMF: Proton Transfer from Water to RC_{60}^{-} and Unexpected Formation of 1,2-Dihydro[60]fullerenes. *J. Org. Chem.* **2010**, *75*, 4086-4094.

(67)   Li, C.-Z.; Matsuo, Y.; Niinomi, T.; Sato, Y.; Nakamura, E. Face-to-face C_6F_5-[60]fullerene interaction for ordering fullerene molecules and application to thin-film organic photovoltaics. *Chem. Commun.* **2010**, *46*, 8582-8584.

(68)   Maccoll, A. Reduction Potentials of Conjugated Systems. *Nature* **1949**, *163*, 178-179.

(69)   Díaz-Torres, R.; Alvarez, S. Coordinating ability of anions and solvents towards transition metals and lanthanides. *Dalton Trans.* **2011**, *40*, 10742-10750.

(70)   Cardona, C. M.; Li, W.; Kaifer, A. E.; Stockdale, D.; Bazan, G. C. Electrochemical Considerations for Determining Absolute Frontier Orbital Energy Levels of Conjugated Polymers for Solar Cell Applications. *Adv. Mater.* **2011**, *23*, 2367-2371.

(71)   Ruff, A.; Qian, X.; Porfyrakis, K.; Ludwigs, S. Effect of the Type and Number of Organic Addends on Fullerene Acceptors for *n*-Type Electronic Devices: Redox Properties and Energy Levels. *ChemistrySelect* **2018**, *3*, 5778-5785.

CHAPTER 4

STABILITY IN FULLERENE-BASED ORGANIC PHOTOVOLTAICS AND
IMPROVING MOBILITY EXPECTATIONS FOR FULLERENE DERIVATIVES

4.1. INTRODUCTION AND JUSTIFICATION

Since their discovery in 1985, fullerenes have been investigated for their organic electronic material prooperties.[1] They have been utilized in a wide range of research areas in the field including but not limited to: superconductivity,[2,3] field-effect transistors,[4,5] photovoltaics,[6] and photodetectors.[7,8] Specifically, fullerenes function as impressive electron acceptor materials for these applications. For example, fullerene derivatives have been used as electron acceptors in OPVs with percent conversion efficiencies, PCE, over 17%[9] and the pristine fullerene, C_{60}, in n-type OFET devices with reported charge transport mobilities over 10 cm^2 V^{-1} s^{-1}.[10] The high performance of C_{60} in these electron acceptor applications is attributable to a number of factors, including their high degree of π–π conjugation leading to efficient charge delocalization,[11,12] low HOMO-LUMO gap,[12] low reorganization energy for electron transfer,[13,14] and redox stability up to six reduction events.[15,16]

Among the industries which have utilized fullerenes in the field of organic electronics, two will be discussed in this work: organic photovoltaics (OPVs)[14] and organic field-effect transistors (OFETs).[10] Both technologies benefit from a number of fullerene properties including electrochemical and morphological tunability,[17,18] low electrical impedance,[19] and the potential to be highly flexible.[20,21] These properties allow for niche applications including wearable electronics,[22] bio-compatible organic electronic medical devices,[23] and the components to produce flexible computers[24] to name a few.[25]

First, the advantages of OPVs for application in outer space are investigated. Interest in this application stems from their potential stability with respect to particle bombardment and relatively low weight compared to other photovoltaic technologies. Next, a study of the device lifetime for

OPV active layers made of phenyl-C_{60}-butyric acid methyl ester, PCBM, is presented. PCBM is an industry leading OPV material, but the degradation mechanisms for PCBM in devices are poorly understood. Finally, the performance of fluoromodified fullerenes, $C_{60}FHF$ and $C_{70}FHF$, as active layers in OFET devices is investigated. Interest in fluoromodification stems from the fact that it has been shown as a reliable way to improve device performance,[26,27] improving active layer morphology for charge transport,[28] improving percent conversion efficiency in OPVs, and improving both electron and hole mobilities in *n*-type and *p*-type OFETs respectively. [27,29-31]

4.2. STABILITY OF ORGANIC PHOTOVOLTAIC ACTIVE LAYERS FOR SPACE APPLICATIONS

4.2.1. General Comments

One potential benefit of OPV materials that has yet to be rigorously explored is a property that is common to all organic electronic materials: they are made of low Z contrast atoms aka predominantly first row elements like carbon. These materials should be more resistant to the high energy particle bombardment that occurs in between Earth's thermosphere and lower bounds of the exosphere, one of the most desirable regions for satellite orbits.[32] This region of space is called low earth orbit, LEO. LEO has a sufficiently high flux of high energy particles that satellites and their solar cells regularly degrade.[33,34] One method suggested to combat this was the use of heavy Z number atom materials as shielding.[33] This has been presented as an expensive but necessary measure to prolong the functional lifetime of satellites in LEO.[33] Alternatively, it was hypothesized by the author that rather than attempting to deflect high energy particles; devices could be made with low Z number materials. These materials would be less likely to interact with these high energy particles, thereby decreasing the rate at which they degrade.

In support of this theory is the fact that low atomic number atoms have long been understood by both X-ray crystallographers and electron microscopists as the most challenging materials to study[35,36] because these measurements rely on interactions with the electron cloud and, to a lesser extent, the atomic nucleus.[37,38] When the atomic number of an atom is low that means it is

effectively a "smaller" target and results in fewer interactions with the incident source.[35,36] While this property makes organic molecules more challenging to study with these techniques, it also implies that organic materials will be more robust to bombardment in outer space, as fewer high energy particle interactions will occur. To evaluate this hypothesis work was performed to study the radiation tolerance of OPV films as well as their tolerance to the vacuum and thermal environment in space.

4.2.2. OPV active layer evacuation and thermal stability testing

In total, four different experiments were performed to measure OPV device's suitability to space applications. The Yield × Mobility value of the active layers was recorded before and after the films were subjected to prolonged vacuum exposure and thermal cycling. The Yield × Mobility value shows the number of charge carriers present in the active layer film under illumination. It was recorded using a Time Resolved Microwave Conductivity (TRMC) instrument at the National Renewable Energy Lab. Yield × Mobility values have been used as a measure of the potential performance of OPV active layers and so are a useful figure of merit for evaluating the performance of the active layers.[39] All testing, film production, and data analysis was done in collaboration with Dr. Long K. San, a research group member at the time.

OPV active layers were produced by Dr. Long K. San using the drop cast method and the films were deposited on 1 cm quartz slides. The bulk heterojunction solutions used to prepare active layers were 30/70 by weight mixtures of the acceptor fullerene and P3HT. The three fullerenes which were used were $C_{60}FHF$, PCBM, and, for the evacuation and thermal cycling experiments, C_{60}. The synthesis and potential use of $C_{60}FHF$ as an organic semiconductor was discussed in Chapter 3. PCBM is by far the most frequently studied OPV acceptor and is the current industry standard for fullerene-based OPV acceptor materials.[40-42]

In total, three active-layer blends were prepared in triplicate, Table 4-1. Samples with the letter A are samples that were not subjected to the evacuation test. Samples with the letter B or C were subjected to the evacuation tests. The initial and final masses of the quartz substrate with the

deposited (drop cast) active layer blend were measured and recorded pre- and post-evacuation. The uncertainty in the mass balance is ±0.0001 g. The recorded mass loss was negligible for the films with the largest being 0.3 mg from an initial mass of 670 mg however; Table 4-1 shows that there appears to be a significant impact on the Yield × Mobility value. These differences are attributed to the lack of homogeneity in the active layer films. Due to the use of the drop cast method, the film thickness was not the same for all samples, and this irregularity gave rise to a range of Yield × Mobility values that cannot be correlated to any influences from the evacuation testing. More interesting was the effect that thermal cycling had on the Yield × Mobility values.

In order to simulate the effect of the temperature range experienced in LEO and in accordance with the functional requirements of the Air Force, the active layer films were thermally cycled from −78 °C to 100 °C. The films were held at the desired temperature for 45 minutes and then moved to the next temperature for an additional 45 minutes. This cycling was repeated for 24 h and then again for an additional 48 h resulting in the B and C measurements shown in Table 4-1. This cycling was done in a nitrogen atmosphere using a specially designed air-tight chamber. Details of how the chamber was constructed and tested are given in Section 4.6.2. The Yield × Mobility value shows improvement between the repeated measurements of the same films pre- and post-thermal cycling suggesting improved film morphology following additional thermal annealing. The improvement in performance following thermal annealing has been observed previously for active layers using P3HT and PCBM.[43] Following annealing, P3HT has been shown to reorganize into a better morphology via its glass-phase transition resulting in better device performance and so this reorganization appears to occur for the $C_{60}FHF$ and C_{60} films as well. This healing ability could be an important variable in the longevity of OPV devices in LEO where the temperature fluctuations should result in the active layers recovering some of their lost performance due to radiation exposure over time.

4.2.3. OPV active layer radiation testing

Two different radiation tests, UV irradiation and proton bombardment, were performed on the active-layer materials. UV-vis spectroscopy was used to measure the effect of radiation on the films. By using UV-vis instead of TRMC, we were able to minimize the delay between irradiation and the recording of the measurements removing any possible variables related to environmental effects. UV-vis and TRMC have been used by the OPV field to study potential performance changes of active layers as the degree of photo-absorption is tied to potential device efficiency and the Yield × Mobility figure of merit derived from TRMC measurements.[44] All the films tested were blends of P3HT and C_{60}FHF or PCBM.

For the proton bombardment studies, it was necessary to determine a target exposure dose to simulate the radiation environment in LEO. This approximation is not trivial since the flux in LEO is region dependent and radiation sources are variable and unpredictable including the sun, cosmic rays, and the trapped radiation belts generated by the Earth's magnetic field.[34,45] The target dose chosen was 14 krads since this represented an upper average value for radiation tolerant devices which are commonly between 5 and 20 krads[46] and was suggested by our collaborators at Vector Sum as an average annual dose.

The samples were exposed to UV radiation at CSU by placing them ca. 5 in. from a 450 W high-pressure mercury-arc lamp, set up shown in Figure S4-2, and proton bombardment by a 3 MeV proton beam using a 9SDH-2 NEC Pelletron in Dr. Vaithiyalingam Shutthanandan's lab at PNNL.

UV Irradiation

The two films tested were thermally cycled at 100 °C for 45 minutes and at −78 °C for 45 minutes for a total of 24 h. The thin films were placed ca. 5" from the lamp and were irradiated for a total of 87 h. UV-vis spectra taken after various exposure times and are shown in Figure 4-1.

The C_{60}FHF sample had visibly deteriorated after irradiation (i.e., there was a noticeable color change from a uniform dark brown-purple film to a lighter yellow color) and a concomitant decrease in absorption band intensities was observed. However, the PCBM sample maintained a similar UV-vis spectrum throughout most of the experiment. This could be attributed to the oxidation of PCBM which helped to stabilize the P3HT polymer,[44] whereas the oxidation of C_{60}FHF did not occur or did not have a stabilizing effect on the P3HT. This stabilizing effect that PCBM has on P3HT could be an important factor in prolonging the lifetime of OPV devices in space however, it should be noted that these experiments were performed in air whereas the actual application would be in the vacuum of space. It is possible that without an oxygen source the stabilizing oxidation of PCBM would not occur. Experiments to elucidate the susceptibility of PCBM to degradation under one sun illumination in an inert atmosphere as a neat film were also performed and will be discussed in Section 4.3.2.

Proton bombardment

Four samples (FHF-A, FHF-B, PCBM-A, and PCBM-B) were used for this proton bombardment experiment. The A moniker corresponds to no thermal treatment and the B moniker corresponds to thermal treatment via the cycling method used in Section 4.2.2. The UV-vis spectra were recorded prior to proton bombardment. Each thin film was analyzed twice, the second measurement with the film rotated by 180°, and their spectra were averaged. The samples were subsequently shipped to Dr. Shutthanandan's lab at Pacific Northwest National Labs for proton bombardment experiments. A beam of 3 MeV H^+ ions was used to irradiate each sample with a 14 krad dose. The UV-vis spectra of the samples were recorded after they were irradiated. The spectra before and after annealing are shown in Figure 4-2.

The films showed UV-vis spectroscopic evidence for degradation in all cases except for PCBM-A. The UV-vis peak intensities increased significantly for sample PCBM-A. A possible explanation was that there was an irregularity with the UV-vis spectrum before bombardment either due to sample position or the film being inhomogeneous prior to bombardment and then

annealing from the heat of the bombardment experiment resulted in a more uniform film but a repeat experiment is needed. Regardless, each film was subjected to a second round of annealing at 100 °C for 24 h under an inert atmosphere. This resulted in an improvement in the active layer absorption characteristics for all four samples. This may be the result of radiation recovery; however, further characterization of the fullerene/polymer blends must be performed.

4.2.4. Conclusions and future work for OPV radiation tolerances

In summation, OPV active layer films were subjected to evacuation, thermal cycling, UV irradiation, and proton bombardment to gauge their suitability for space applications, study their radiation tolerance, and evaluate if low Z number materials have any advantage over higher Z number materials currently in use in the space industry. While without further rigorous testing a definitive statement on suitability cannot be made it was convincingly shown that OPV active layer materials are resilient to prolonged vacuum exposure and thermal cycling between −78 °C and 100 °C. These are important properties advantageous for space applications. An improvement in the active layer's Yield × Mobility value was observed after the thermal cycling for both C_{60} and $C_{60}FHF$ films. UV-vis measurements of thermally cycled PCBM active layers show the absorption profile improved after annealing and this is a well-documented behavior of OPV active layers including PCBM/P3HT blends.[43]

As for the radiation tests, degradation of the films was observed in both the UV and proton bombardment experiments. However, through thermal annealing the devices were able to recover some of their absorption profile suggesting that as the satellite's position with respect to the sun changes some of the lost performance due to degradation could be regained.

While the results from these experiments are promising, many additional experiments would need to be done before OPVs could be deemed suitable for space applications. One expansion of this work for example would be to include fully functioning OPV devices to confirm that the changes in the Yield × Mobility value and absorption profile correspond to changes in the percent conversion efficiency of the devices. Full devices have more components that may be affected by

the LEO environment and need to be evaluated before OPV devices can be used in space applications. Studies using X-rays to irradiate OPV devices have been done and showed charge build up at the electrode interfaces lowered the open circuit voltage, V_{oc}, and thereby the power conversion efficiency, PCE.[47,48] An additional variable that could not be tested in our irradiation experiments was the effect a lower current of ions (decreasing the concentration of ions per second) would have on the device's degradation. This is especially important for the proton bombardment studies where an entire annual radiation dose was delivered in a tenth of a second. This high flux bombardment may result in additional degradation than it would be observed in the actual application for the duration of 12 months. Additionally, a lower flux may result in no appreciable degradation at all if the healing of the devices after thermal annealing continued to occur competing with the rate of degradation.

Preliminary electron bombardment studies at CSU were also performed with 30 kV electrons which resulted in minimal degradation to the C_{60}FHF/P3HT active layer. However, prior to the complete irradiation of the film, sample charging resulting in an arc event forced the experiment to be ended prematurely. More studies with higher energy electron sources would be needed to better evaluate the active layers tolerance to high energy electrons which are prevalent in the LEO environment.[34] Additionally, while rare, >10 MeV protons and as high as hundreds of MeV impacts are possible[33,45] and should be evaluated for their effect on OPV active layers.

4.3. DEGRADATION STUDIES OF PCBM

4.3.1. General Comments

While OPVs have made great strides with respect to their efficiencies from the first experiments with fullerene/polymer bulk heterojunctions[6] in the early 90s to recent reports of multijunction devices reaching record efficiencies of >17% PCE values[9] there still remain significant challenges to wide-scale adoption of OPV devices in commercial markets. One such challenge is improving device lifetimes. Currently, undesirable processes such as photo-initiated degradation reactions, transport layer stability, and electrode degradation result in shorter device

lifetimes than the industry viable 10-year lifetime benchmark.[49] Additionally, inconsistencies with stock material purity and chemical variability of the high performance active-layer materials make research into understanding mitigating the specific degradation mechanisms for any given device challenging. Therefore, research into this area has lagged behind efforts to develop new donor-acceptor materials and new high efficiency devices. Now that efficiencies have comfortably surpassed the industry viable 10% efficiency mark with some ternary devices reaching >17% efficiency,[50] a renewed focus on device lifetimes is warranted.

In collaboration with NEXT Energy Technologies, a research effort was made to identify and characterize the kinds of compounds which are produced during the degradation of PCBM under illumination. To limit the number of experimental variables, neat films of PCBM were studied rather than complete devices. The PCBM films stability to illumination in an inert environment and in air was studied. As discussed in Section 4.2., PCBM is considered one of the best performing acceptors in the fullerene based OPV acceptor market, making it the most logical target compound for this study. Previous work by McGehee et al., followed similar experimental procedures.[51] Their work concluded that the dominant degradation compound formed under illumination was dimerized PCBM molecules, based on APCI mass spectrometry. The work by the author, as will be discussed in this section, agrees well with those experimental results and uses their work to identify some of the degradation species as dimerized PCBM molecules. Furthering McGehee et al.'s work, aged PCBM films were analyzed by the author with the intent of identifying new degradation species. Those efforts resulted in the discovery of oxidized PCBM molecules and in this section the identification and characterization of those compounds as well as their effect on OPV devices will be discussed.

4.3.2. Aging of PCBM films

Before the PCBM films were made, the purity of the PCBM starting material was confirmed by ^{1}H NMR, HPLC, and mass spectrometry. This is an important step in any device-oriented study because small impurities and even trace amounts of solvents have been shown to affect device

performance.[52,53] The results of those analyses show that the PCBM sample is 97+% pure with a 3% toluene impurity, which could potentially be removed by evacuation. The ^{1}H NMR spectra and chromatogram for these analyses are shown in figures S4-3 through S4-5 and a description of those results is included in Section 4.6.4.

Following the purity analysis, PCBM films were produced by the author via solution processing using the production facilities at NEXT Energy Technologies' lab in Santa Barbara, California. The films were produced from a 40 mg mL^{-1} PCBM chlorobenzene solution. Details about the conditions and how the films were treated are included in Section 4.6.5. Following their production, the films were handled in either an inert atmosphere or in air and were aged under 1 sun illumination under the same conditions. In both groups one of the films was not illuminated and was stored in the dark as a control, and the other films were exposed to one sun illumination for either 24 or 100 h. The aged material was extracted from the films and analyzed by HPLC and ^{1}H NMR. The results of those experiments are shown in Figure 4-3.

Analysis of the HPLC chromatograms shows that the films that were never exposed to air have the largest amount of degradation based on the HPLC peak area. It should be noted that these observations do not take into account any differences in the extinction coefficients of the different species. The compounds eluting after 8 min are hypothesized to be dimerized PCBM molecules based on similar results shown by McGehee et al.[51] This result matches well with the literature that shows dimerization of fullerenes occurring less frequently in air than in inert atmospheres.[54] The air-exposed samples show the amount of dimerized fullerenes generated reaches a max peak area of 26% and then stops. This has been explained by O_2's ability to quench the T_1 excited state for C_{60} which is required to form fullerene dimers.[54] The air-aged films were produced in an oxygen-free glovebox and were only exposed to air when the illumination study began, therefore the initial dimerization that occurs in the first day may be correlated with the amount of time required for oxygen to diffuse through the film. It has been shown before that C_{60} films stored in an argon atmosphere retain a percentage of argon even after being removed from the argon

atmosphere and, in the presence of oxygen that argon is displaced over time.[55] To test this a film kept in the dark in air and allowed to equilibrate with the ambient atmosphere prior to illumination may show even less dimerization.

Dimerization of PCBM has been linked to a drop in the short circuit current, J_{sc}, for OPV devices and so based only on the HPLC data it could be concluded that to minimize performance loss PCBM-based solar cells should be exposed to air. However, upon careful examination of both the HPLC and ^{1}H NMR data, discrepancies in the relative ratio of degradation products to PCBM become apparent. The air-exposed films only have a maximum composition of 26% by peak area of dimerized PCBM, however the ^{1}H NMR spectra show as high as 58% of the starting PCBM material has degraded. The ^{1}H NMR percent degradation values are based on the methoxy region of the spectrum. The PCBM methoxy group is useful for analysis and quantification of the various PCBM-like compounds present in the sample via ^{1}H NMR because they are three times the intensity of a signal representing one proton and are not coupled to any other protons allowing for a sharp singlet. The differences between the HPLC chromatograms and ^{1}H NMR spectra of films aged in argon is less significant, 9%, and so this suggests there are some species which are unaccounted for and occur in a larger quantity on the air-exposed films. It was hypothesized these compounds would likely be oxidized PCBM species, O_x-PCBM. There have been several studies on the oxidation of neat fullerenes, which show it can occur at both elevated temperatures and under illumination, both of which are unavoidable aspects of OPV device operation.[55,56] Studies to elucidate the rate of PCBM oxidation as well as the electronic and chemical structure of the resulting O_x-PCBM derivatives have also been performed.[57-59]

To look for the missing PCBM degradation products, likely O_x-PCBM species, the samples aged in air and argon were reanalyzed by HPLC using the similar separation conditions as shown in Figure 4-3 but with a weaker eluent mixture to improve the separation by increasing the retention times. A mixture of 60/40 toluene/heptane was found to be the most effective. This resulted in the

two chromatograms shown in Figure 4-4. From those chromatograms it is clear that some previously unobserved species were co-eluting with PCBM.

4.3.3. Synthesis and characterization of O$_x$-PCBM

In order to determine if the new species detected in the aged films were actually O$_x$-PCBM species, a reference sample of O$_x$-PCBM was needed. Using *m*-chloroperoxybenzoic acid (*m*CPBA) as an oxidant and following a synthesis as described by Balch et. al,[60] a reaction was performed to oxidize PCBM. From this reaction, crude material was recovered that was then characterized by ^{1}H NMR, HPLC, and mass spectrometry, which confirmed the presence of O$_x$-PCBM.

The mass spectra of the PCBM starting material and the O$_x$-PCBM crude material are shown in Figure S4-6. The O$_x$-PCBM crude material showed an *m/z* value of 926 which is indicative of an O$_x$-PCBM species with one oxygen atom. As a control experiment, the PCBM starting material was also measured using the same conditions as the O$_x$-PCBM and showed only the mass for PCBM, 910 *m/z*. For these measurements field desorption mass spectrometry was used because it is a solvent-free ionization method. The previous characterization of PCBM by mass spectrometry using NI-ESI, using an eluent, showed a signal at *m/z* 926 for the oxidized PCBM species, see Figure S4-5. This species could have formed during the ionization experiment as a reaction with the eluent and/or dissolved oxygen so field desorption was a better ionization method for these experiments.

It is not trivial to quantify the concentration of O$_x$-PCBM in the crude sample from only mass spectrometry, so after the presence of O$_x$-PCBM was confirmed, ^{1}H NMR spectroscopy was used to measure the ratio of methoxy chemical shifts, which do not correspond to PCBM, relative to the remaining PCBM methoxy chemical shift. The spectrum, shown in Figure 4-5, displays the methoxy region, δ 3.6–3.8, which integrates to 36 mol% of the total integration area including the PCBM starting material. It should be noted that this method of quantification cannot distinguish between other derivatives of PCBM that may form, aka compounds with a methoxy group in a

197

similar environment to PCBM. For example, this method would not allow for the exclusion of any dimerized PCBM molecules present in the O_x-PCBM sample. To confirm the concentration of PCBM oxides, the O_x-PCBM sample was also analyzed by HPLC in 60/40 toluene/heptane on the Buckyprep column used for the analysis of the aged films, shown in Figure 4-6.

The HPLC chromatograms in Figure 4-6 show that with 100% toluene as the eluent PCBM and O_x-PCBM co-elute and only in the weaker eluent mixture, 60/40 toluene/heptane, do the new peaks for the O_x-PCBM species elute following PCBM. Note the t_R for the O_x-PCBM species is the same as the t_R for the unidentified species in the air-aged films shown in Figure 4-4. This evidence supports the conclusion that the compounds identified as possible O_x-PCBM species in Figure 4-4 are correctly assigned.

Further confirmation of the presence of O_x-PCBM in both the air- and argon-aged films was achieved by comparing the ^{1}H NMR spectra of O_x-PCBM and the films. There is a good agreement between the spectra, and in all three spectra there is one significant intense signal with a chemical shift at 3.6 ppm indicating that there is at least one oxide compound if not more in both aged films. This result was unexpected in the argon-aged sample where oxygen was not supposed to be present. This high degree of agreement between the spectra of the O_x-PCBM sample and the aged films is surprising. It could be assumed there should be chemical shifts which are unique to at least the argon-aged sample due to the relatively high concentration of fullerene dimers compared to PCBM.

The O_x-PCBM concentration based on HPLC peak area relative to PCBM is only 25% compared to the 36% shown in the ^{1}H NMR experiment, however, there is no baseline resolution between the two peaks and so the O_x-PCBM concentration may be under-represented. For further studies the concentration of O_x-PCBM was assumed to be 30%.

With confirmation that O_x-PCBM is present in the aged PCBM films, OPV devices could be made using the resources at NEXT Energy Technologies to study the effect that O_x-PCBM has on the OPV device figures of merit.

4.3.4. O_x-PCBM-doped OPV devices

In order to evaluate the effect O_x-PCBM species have on device performance, OPV devices were made by the author at NEXT Energy Technologies' lab in Santa Barbara, California with varying percentages of O_x-PCBM. Devices were made using a small-molecule donor which has been shown to work well with fullerene acceptors[61] referred to here as SMD. The SMD molecule, 7,7'-(4,4-bis(2-ethylhexyl)-4H-silolo[3,2-b:4,5-b']dithiophene-2,6-diyl)bis(6-fluoro-4-(5'-hexyl-[2,2'-bithiophen]-5-yl)benzo[c][1,2,5]thiadiazole), is shown in Figure S4-7. A small-molecule donor was chosen for the study because the recently reported highest efficiency OPV devices have been made with small-molecule donors and acceptors making a study of the degradation characteristics of a non-polymer-based device warranted.[9,62-65] A schematic of the device architecture as well as an image of a mock-up of the active-layer films are shown in Figure S4-8. Actual photos from inside NEXT Energy Technologies' lab were not permitted to protect intellectual property rights.

A total of 11 devices were made, two controls with no O_x-PCBM and three devices for each O_x-PCBM concentration of the selected three. Each device has four pairs of electrodes resulting in 12 data points for each concentration of O_x-PCBM and eight data points for the two control devices. The variability in the devices gave rise to the box and whisker plots shown in Figure 4-8. The devices were tested under an approximation of one sun irradiation for 100 h, in an argon atmosphere. Three different concentrations of O_x-PCBM were tested 0.3%, 3%, and 30% as well as a control device with 0%. The resulting device characteristics, shown in Figure 4-8, show that with increasing oxide concentration there is a linear drop in efficiency.

The morphology of the spin-cast active layer films could have changed due to the addition of the O_x-PCBM. Morphology control is critical to good device performance.[66-68] This may prevent

the devices reaching an optimal morphology resulting in a lower PCE. An additional effect may be that the O_x-PCBM species are acting as trap states with lower LUMO energies than PCBM preventing the efficient delocalization of charges.[44,69,70]

In these experiments, it has been shown that the presence of O_x-PCBM has a deleterious effect on device efficiencies. This implies that the susceptibility of the acceptor to oxidation is an important factor to consider when designing OPV devices. Furthermore, it is important to understand the effect that O_x-PCBM has on the device lifetime. To probe this effect, the devices were exposed to one sun illumination and continuously monitored for changes in efficiency. The results of that experiment are shown in Figure 4-9. The device lifetimes for the O_x-PCBM doped devices show that, although the effect of the O_x-PCBM over time does not appear deleterious to the device characteristics, it does increase the initial drop off in efficiency recorded in the first 100 h, aka the burn-in phenomenon shown by many OPV devices.[49,65] The burn-in for all the devices was more severe as the concentration of O_x-PCBM was increased.

The cause of OPV device burn-in is a highly active area of study, so these data showing a direct relationship between the burn-in of a set of devices and the concentration of O_x-PCBM are an important finding.[49,65,71-73] Even more significant is that following the burn-in period, the devices stabilize suggesting the effect is burn-in specific. Since burn-in is observed in virtually all OPV devices it is unlikely that O_x-PCBM is the sole cause, however, there is no doubt that in these devices it is directly contributing to the severity of the burn-in efficiency loss.

4.3.5. Conclusions and future work for PCBM based OPV degradation studies

Aging studies of PCBM were conducted revealing a host of interesting data. In agreement with the literature, PCBM films aged under one sun in an inert atmosphere undergo degradation, which has been associated with dimerization of PCBM.[51] This degradation was minimal in the air exposed films apparently due to oxygen's ability to quench the T_1 transition state required for photoinitiated dimerization.[54] What had not been shown before was the exact degree to which PCBM films could be degraded by photo-illumination in air since the oxidized fullerenes had not

been observed via HPLC or NMR before. The photo-oxidation of PCBM and fullerenes in general is still an active area of study.[55,59,74] After it was confirmed that O_x-PCBM could be formed in PCBM films, efforts were made to synthesize O_x-PCBM using *m*CPBA, which had been shown to be effective for the oxidation of C_{60}.[60] Following characterization of the O_x-PCBM material by mass spectrometry, HPLC, and ^{1}H NMR; devices using SMD and PCBM were made with varying concentrations of O_x-PCBM. Devices with high O_x-PCBM concentrations showed a significant drop in efficiency. This is the first time this experiment has been performed, to the best of the author's knowledge. The oxidation of PCBM is assumed to occur more gradually in the presence of either a donor or if the device is encapsulated. Therefore, the lifetime performance of the devices with O_x-PCBM was also of interest. The lifetime data showed a dramatic burn-in event for the higher concentration O_x-PCBM devices, 3% and 30%. Following the severe initial drop in PCE, the efficiency loss rate for the devices slowed down suggesting the oxidation of PCBM during manufacturing could account for some of the burn-in that is observed in OPV devices. In addition to the degradation studies performed on PCBM films, $PC_{70}BM$ was also studied. The data associated with that work are shown in figures S4-9 and S4-10. While no devices were fabricated, the studies did confirm the resistance of $PC_{70}BM$ to dimerization which has been reported previously.[51] The air-aged $PC_{70}BM$ films showed significantly more degradation than the argon aged films, likely in the form of $PC_{70}BM$-oxide species similar to PCBM.

The next steps for this research would be to confirm that the drop in initial device efficiency is tied to the presence of O_x-PCBM and is not due to the morphology of the devices that contain higher concentrations of the O_x-PCBM mixture since the solution used to spin cast the active layers contained the O_x-PCBM as an additive. This could be evaluated using SAXs and comparing the diffractogram profiles of the doped devices to the control devices. Additionally, $PC_{70}BM$ oxide species could be synthesized following a similar synthesis as reported here for PCBM and doped devices could be made to examine if the burn-in specific degradation is common to both fullerene acceptors.

4.4. ORGANIC FIELD-EFFECT TRANSISTORS USING C$_{60}$FHF

4.4.1. General Comments

While the majority of the fullerene-based organic electronics research field has focused its efforts to utilize fullerenes in OPV research, a growing area of research has found success using fullerenes in *n*-type OFETs. The first fullerene-based OFET was reported in 1995 by Haddon et. al. using C$_{60}$ and then one year later with C$_{70}$.[4,11] Fullerene-based OFETs have reached as high as 10 cm^2 V^{-1} s^{-1} in 2012 using C$_{60}$ single crystals.[75] However, the progress made with C$_{60}$ has not been achieved with fullerene derivatives.[10] Out of the overall 88 C$_{60}$ derivatives summarized in a recent review by Zhang et al.,[10] only the *o*-xylene C$_{60}$ monoadduct OXCMA reported by Yu et al. showed a maximum mobility above 0.3 cm^2 V^{-1} s^{-1} (maximum mobility of 0.5 cm^2 V^{-1} s^{-1} average mobility of 0.16 cm^2 V^{-1} s^{-1}).[76] Reasons for this poor performance vary from poor organization in the solid-state to high resistance source and drain contacts. Despite this, interest in using fullerene derivatives remains, as they have the potential to be solution processed and, with their wide range of LUMO energies, could be used in devices with varying gate potentials and device architectures.[10]

In order to move this industry forward, new fullerene derivatives with a high packing density, ordered solid-state packing, reversible reduction behavior to multiple redox events, high electron affinity, and thermal stability are needed.[77-80] The fullerene derivative, C$_{60}$FHF, has those characteristics. Therefore, work was done in a collaboration between the Strauss-Boltalina Research group and Dr. Lussem's lab at Kent State University in Ohio to make OFET devices to evaluate C$_{60}$FHF's behavior as an *n*-type OFET material.[81]

For those experiments to be feasible, a significant amount of C$_{60}$FHF was needed (between 150 and 200 mg). For this amount, the original 2015 synthesis[82] was not practical due to difficulties with scalability, so a new scalable synthesis of C$_{60}$FHF was developed. This method was discussed in Chapter 3 of this work. The improved synthesis resulted in preparation of 100+ mg samples in a single-step reaction and allowed for the systematic study of the performance of C$_{60}$FHF in

vacuum-processed organic field-effect transistors, in particular, the influence of contact and channel doping on the performance of the transistors. By deriving an analytical solution for the drain current of an *n*-doped OFET operated in saturation, it is shown that the subthreshold swing of doped transistors can be optimized by using a transfer doping approach, i.e. by including a bulk dopant layer at the interface between organic semiconductor and gate dielectric instead of a mixed doped layer. The optimized devices achieved a charge carrier mobility of 0.35 $cm^2\,V^{-1}s^{-1}$, which is among the highest performances for fullerene derivates.

4.4.2. OFET device design with $C_{60}FHF$

All design, fabrication, and measurements of $C_{60}FHF$ OFET devices was performed by Dr. Shiyi Liu at Kent State University in Dr. Bjorn Lussem's lab. The general design of the OFETs studied here is shown in Figure 4-10. The parameters varied within each series are listed in Table 4-3.

The transistors consist of an aluminum gate electrode with a dielectric Al_2O_3 layer on its surface, (50 nm in series #1 and #2, 5 nm in series #3), which helps regulate the threshold voltage due to its higher capacitance and decreases the number of trap states from metal hydroxyl groups.[83] To increase the stability of the transistors, the oxide layer is covered either by a thin layer of tetratetracontane, TTC, (series #1 and #2)[84] or by a self-assembled monolayer of phosphonic acid (series #3) which has been shown to passivate the trap states in the dielectric layer and also create a crystalline template for the intrinsic layer, $C_{60}FHF$, which can improve transconductance.[85] At the interface between the intrinsic layer consisting of $C_{60}FHF$, a thin layer (thickness of 0, 1, 2, and 4 Å) of the *n*-dopant *o*-MeO-DMBi-I[86] is deposited by vacuum deposition to control the threshold voltage of the transistors.[87]

Finally, in order to study the contact resistance of these devices, two different contact geometries are used, shown in Figure 4-10. In the first contact geometry (series #2 and #3), a 25 nm heavily *n*-doped (8 wt.%) layer of C_{60} (C_{60}/*o*-MeO-DMBI-I) and a thin layer (2 nm) of the *n*-

dopant (*o*-MeO-DMBI-I) is deposited as the injection layer, which is known to generate a quasi-ohmic contact to reduce the injection losses.[88] This arrangement is of special interest in the case of $C_{60}FHF$ because of the minimal difference in LUMO energy between C_{60} and $C_{60}FHF$.[82] By doping the C_{60} layer the transconductance and therefore the injection rate should increase. Finally, in the second series of devices, gold contacts are used as a reference material for a common metal source/drain contact (series #1). In order to ensure the horizontal conductivity on electrodes, all contacts are covered by an aluminum film (60 nm) on top of the source and drain contacts.

4.4.3. Performance of $C_{60}FHF$ OFETs

The series of devices listed in Table 4-3 and Figure 4-10 were all examined for their stability to repeated cycling before measurements of their device characteristics were recorded. All of the devices produced were shown to be sufficiently stable for measurements. An example of the devices is shown in Figure 4-11.

The drain and gate currents are stable over the range of gate-source potentials cycled, 1–10 V. Additionally, the drift in the threshold voltage is minimal for both the *n*-doped C_{60} and Au contacts. This is the first hurdle for a new OFET and in the case of the $C_{60}FHF$ devices there is no detectable hysteresis which would indicate degradation of the devices. Following confirmation of the device's stability the full set of device characteristics could be measured.

One parameter which was evaluated and shows one of the beneficial characteristics of $C_{60}FHF$ was the source/drain resistance when *n*-doped C_{60} was used versus Au. As previously stated in Section 4.4.2., the LUMO difference between C_{60} and $C_{60}FHF$ is minimal and so there should be a minimal energy barrier for charge carriers at the interface. Additionally, it has been shown that *n*-doped C_{60} can form an ohmic contact between a metallic source electrode and the organic semiconductor in the intrinsic layer resulting in a minimized contact resistance.[89] With an ohmic contact the resistance should follow Ohm's Law meaning the current and voltage should respond linearly as opposed to a rectifying contact which would have non-linear behavior.[90] This is an important characteristic of the device and $C_{60}FHF$'s behavior as an OFET semiconductor because

one of the main factors affecting OFET performance (besides the intrinsic mobility of the organic semiconductors) is the large contact resistance at the common inorganic source and drain interfaces.[90]

In Figure 4-12, the output characteristics of OFETs using an n-doped C_{60} injection layer and OFETs using Au contacts are compared. At identical operation conditions, i.e. identical gate-source voltage, V_{GS}, and drain/source voltage, V_{DS}, the transistors using Au contacts show a lower drain current, I_D. This reduction in I_D correlates with an increased contact resistance, R_C, plotted in Figure 4-12. Whereas OFETs using Au contacts show a contact resistance of several MΩmm, the R_C is reduced by the inclusion of the doped layer to 0.4 MΩmm. Furthermore, the dependency of the R_C on the V_{GS} is greatly reduced for the OFETs with doped layers, which will make the calculation of the charge-carrier mobility of the corresponding OFETs more reliable. This is an important consideration given the over estimation of charge-carrier mobility in the past by not accounting for the high R_C between organic and metal interfaces.[91]

Lastly, the electron mobility of the device is an important characteristic for any OFET. This value is most commonly used as the figure of merit to determine the value of new intrinsic layer materials.[10] It was expected that $C_{60}FHF$ should have a high charge-carrier mobility because of its dense packing allowing for more facile charge diffusion through the material. A comparison of the crystal packing density and number of nearest neighbors of $C_{60}FHF$[82] and two solvent-free crystal structures of C_{60}[92] and PCBM[93] is shown in Figure 4-13. The density of the crystalline $C_{60}FHF$ is 16% higher than that of $PC_{60}BM$ with only 1.1% larger molar mass.

After, optimizing the dopant layer thickness for the gate-intrinsic layer contact an impressive average charge-carrier mobility of 0.34 $cm^2\,V^{-1}\,s^{-1}$ was achieved. This value is one of the highest reported for a fullerene derivative.[10] Figure 4-14 shows the effect of varying the dopant thickness on charge mobility for the TTC dielectric layers. Experiments were also performed using self-assembled monolayers as the gate-intrinsic layer contact material but resulted in a lower electron mobility average.

For devices made with *n*-doped C_{60} contacts the highest mobility recorded was for a device with a dopant thickness of 0.2 nm and beyond that there is a slight drop in mobility. For the Au contacts the optimal dopant thickness was achieved with thicker dopant layers and the charge mobility was considerably lower at lower dopant thicknesses. This difference between the two contacts is consistent with the observations made with respect to the near ohmic contacts between the *n*-doped C_{60} source and drain contacts and the intrinsic layer showing improved transconductance for the less optimal Au contact at higher dopant thicknesses.

4.4.4. Conclusion for C_{60}FHF OFET Devices

OFET devices using C_{60}FHF as an intrinsic semiconductor material were produced. The C_{60}FHF devices were found to be stable with no detectable hysteresis after 100 cycles at varying gate voltages. Additionally, there was no significant drift in the threshold voltage. With the stability of the devices confirmed, experiments were undertaken to optimize the charge mobility of the OFET devices in the reported configuration with C_{60}FHF. The OFET devices with *n*-doped C_{60} contacts had minimal contact resistance as was expected since the LUMO levels of C_{60} and C_{60}FHF are approximately within error of each other. This ohmic resistance was compared to the Au contacts as a control for common inorganic contacts and the contact resistance for the *n*-doped C_{60} contacts was only 0.4 MΩmm while the Au contacts were as high as 6 MΩmm at higher gate source voltages. The dopant thickness as well as the dielectric layer thickness and material were optimized as well. The optimal configuration with the highest charge mobility was found for device series #2 with a 2 nm gate-intrinsic layer dopant contact, TTC as a dielectric layer, and *n*-doped C_{60} as the drain and source contacts resulting in an impressive charge mobility of 0.34 cm^2 V^{-1}s^{-1}. This mobility is among some of the highest reported for C_{60} based OFET derivatives.

4.5. C_{70}FHF BASED OFET DEVICES

4.5.1. General comments

While C_{60} and certain derivatives have shown the most promise as an *n*-type semiconductor C_{70} as well as other higher fullerenes have lagged behind.[10] The justification that has been used

for these results are (i) the smaller HOMO-LUMO gap for higher fullerenes and (ii) the lower symmetry for higher fullerenes including C_{70} results in poor electron transport properties.[10] This trend seems to extend to fullerene derivatives as well with the mobilities for C_{60} derivatives being higher than the analogous C_{70} derivatives. Table S4-1 shows a number of C_{60} and C_{70} OFET devices's charge mobilities including both pristine and derivatized fullerenes and in all cases the C_{70} materials performed worse than the C_{60} analogs. This trend was studied formally among other structural variables in the 2012 paper by Li et al.[94]

However, the results shown and discussed in this section reveal that this trend is not absolute. OFET devices made using $C_{70}FHF$ as an intrinsic material actually had higher mobilities than the $C_{60}FHF$ devices reported in Section 4.4 of this work. The $C_{70}FHF$ devices were made using the same parameters as the $C_{60}FHF$ devices and were optimized for the dopant and dielectric film thicknesses showing these results as a fair comparison of the two material properties. Additionally, a third material was tested, $C_{70}FHF$-3, which had demonstrably worse charge carrier mobilities. The electronic properties of these two materials are largely the same and so these results show an example where the structural differences in the solid-state packing is, apparently, singularly responsible for the differences in device performance.

4.5.2. OFET device design with $C_{70}FHF$

The same device architecture used for $C_{60}FHF$ OFET devices was used for $C_{70}FHF$. A bottom gate/top contact OFET geometry as shown in Figure 4-10 was also used for $C_{70}FHF$ devices. As before, the material used for the source and drain contacts was varied. Two $C_{70}FHF$ series, #5 and #7 utilize the n-doped C_{60} contacts and #4 and #6 use Au. The n-dopant used in all cases was o-MeO-DMBI-I which was shown to effectively dope C_{60} in the $C_{60}FHF$ devices.[81]

All device variations were performed for the 2:1 mixture of $C_{70}FHF$-1 and $C_{70}FHF$-2 first described in Chapter 3 of this work and for the pure compound $C_{70}FHF$-3, leading to OFET series #4 to #7 listed in Table 4-4.

4.5.3. Performance of C_{70}FHF OFETs

Figure 4-15 shows the device behavior for series #4 – #7. Devices using an *n*-doped C_{60} contact are shown in the left drawings and the devices utilizing Au contacts are shown on the right. Devices made using the isomer mixture, C_{70}FHF-1 and C_{70}FHF-2, are shown in the top drawings and the devices made using the pure C_{70}FHF-3 isomer are shown on the bottom of Figure 4-15. All the devices produced exhibit good hysteresis, a high on/off ratio, and a low threshold voltage. The contact resistance, as was seen for C_{60}FHF devices, is lowest for the *n*-doped C_{60} contacts. Contact resistance drops from 2.10 MΩmm at V_{GS} = 7 V to 0.85 MΩ mm at V_{GS} = 10 V for the *n*-doped contacts and 48.67 MΩmm at V_{GS} = 7 V to 33.28 MΩmm at V_{GS} = 10 V for the Au contacts. The large difference in resistivity at the source/drain contacts is consistent with the results already discussed for the C_{60}FHF devices.

In Figure 4-15, the influence of the thickness of the dopant layer at the gate dielectric/intrinsic layer interface is shown as well. As the dopant layer thickness increases the threshold voltage, V_{th}, shifts to a slightly lower value. This follows the expected trend for the shift to ohmic contact resistance as the dopant layer was increased which was seen for C_{60}FHF as well.

The average electron mobility is summarized in Figure 4-16 for the 2:1 mixture of C_{70}FHF-1 and C_{70}FHF-2 in the left drawing and the right drawing for C_{70}FHF-3. Overall, the mobility of the isomer mixture, C_{70}FHF-1 and C_{70}FHF-2, is 0.6 cm^2 V^{-1}s^{-1}, more than twice as high as the mobility of the C_{70}FHF-3 isomer, 0.27 cm^2 V^{-1}s^{-1}. Within the margin of error, the influence of the contact material on the (effective) mobility can be neglected for all variations.

The charge mobility drops as the dopant layer thickness is increased. This result suggests that the addition of the doped layer on top of the gate dielectric may have an effect on the morphology of the C_{70}FHF layer. This result is in contrast to Figure 4-14 which showed increasing dopant layer thickness improved charge mobility for the C_{60}FHF devices with Au contacts and had a minimal impact on the *n*-doped C_{60} devices, series #1 and #2. However, even for the thickest dopant layer,

the mobility is above 0.3 cm^2 V^{-1} s^{-1} (for the 2:1 mixture of C$_{70}$FHF-1 and C$_{70}$FHF-2) and 0.18 cm^2 V^{-1} s^{-1} (for isomer C$_{70}$FHF-3).

4.5.4. Conclusion for C$_{70}$FHF OFET Devices

In this section the author reports the impressive performance of C$_{70}$FHF isomers as intrinsic materials in OFETs. The charge mobility of the C$_{70}$FHF compounds in the case of the isomer mixture out-performed the C$_{60}$ analog. This is unusual because pure compounds tend to have more crystalline morphologies and therefore better charge transport. Furthermore, at optimal conditions the mobility of the 2:1 C$_{70}$FHF-1 and C$_{70}$FHF-2 isomer mixture was almost double that of the similarly optimized C$_{60}$FHF, 0.6 versus 0.34 cm^2 V^{-1} s^{-1} respectively. An additional isomer of C$_{70}$FHF, C$_{70}$FHF-3, which was able to be isolated in a pure form, was tested and showed slightly worse performance than the isomer mixture with a maximum charge mobility of 0.27 cm^2 V^{-1} s^{-1}. The reason for this difference in performance is assumed to be related to differences in the structural packing of the two materials since their electrochemical properties are within error of each other as was discussed in Chapter 3.

The structure of C$_{70}$FHF-1, which was discussed in detail in Chapter 3, is similar to the structure of C$_{60}$FHF and has a nearly identical packing density, 1.850 vs. 1.885 g cm^{-3}, respectively, and packs with ten nearest fullerene neighbors. However, since the devices reported here were made with a 2:1 mixture of C$_{70}$FHF-1 and C$_{70}$FHF-2. Since crystals of the latter compound suitable for X-ray diffraction could not be isolated, no further discussion of the structural properties of this material can be made. This is also true for the devices made with C$_{70}$FHF-3.

Future research will focus on characterizing the structural properties of the two unique intrinsic layer materials after they have been sublimed onto the device surface. While it may not be possible to grow crystals of the two materials, especially from mixtures of the compounds, the deposited films could be studied using an electron microscopy technique such as SEM or a diffraction technique such as SAXs assuming the source flux, such as a synchrotron, is large enough to

compensate for the low Z number atoms. The results of such experiments could be more informative about the nature of the intrinsic layer material and may explain the drop in charge-carrier mobility as the dopant thickness was increased. Additionally, devices made with the pure C_{70}FHF-1 isomer, which has been structurally characterized, would show whether using the mixture of compounds was advantageous or disadvantageous with respect to device performance.

4.6. MATERIALS AND METHODS

4.6.1. Reagents and general procedures

The following reagents and solvents were obtained from the indicated sources and were used as received: aluminum (99.999%, Sigma Aldrich); gold (99.999%, Sigma Aldrich); o-MeO-DMBI-I (99.9%, Lumtech); C_{60} for OFET contacts (99.99%, Creaphys GmbH); 1,2-dichlorobenzene (99%, Acros Organics); P3HT (97+%, Sigma Aldrich); C_{60} for OPV films (99.5%, MTR Ltd.); PCBM (97%, Nano-C); PC$_{70}$BM (97%, Nano-C); anhydrous chlorobenzene (99%, Sigma-Aldrich); toluene (99.9%, Fischer Scientific); carbon disulfide (98%, Alfa Aesar); chloroform (99%, Fischer); chloroform-d (CDCl$_3$, 99.8%, Cambridge Isotope); HPLC grade heptane (99%, Fischer); and 7,7′-[4,4-Bis(2-ethylhexyl)-4H-silolo[3,2-b:4,5-b′]dithiophene-2,6-diyl]bis[6-fluoro-4-(5′-hexyl-[2,2′-bithiophen]-5-yl)benzo[c][1,2,5]thiadiazole ("SMD", 97%, NEXT Energy Technologies). The compound m-chloroperbenzoic acid (m-CPBA) was obtained from Sigma-Aldrich with 85% purity and was recrystallized from chloroform.

4.6.2. OPV active layer film production

OPV active layers were made from a 30:70 weight % fullerene/polymer solution from o-DCB. The films were drop casted and allowed to dry in air with a single directional air flow using a fume hood. The only polymer used was poly-3-hexylthiophene (P3HT). The fullerenes used were C_{60}, 1,9-C_{60}(fauxhawk) (C_{60}FHF), and phenyl-C_{60}-butyric acid methyl ester (PCBM).

4.6.3. Thermal annealing chamber development

The chambers were made by sealing 1.25 in. NPT red brass pipes with two 1.25 in. NPT red brass caps each using gas-utility polytetrafluoroethylene (PTFE) tape. A glass tube was inserted

in each hollow brass apparatus, and several glass 3 dram vials were placed in the glass tubes. Each active-layer polymer/fullerene composite films to be tested was deposited, in triplicate, on quartz time-resolved microwave conductivity (TRMC) sample slides, which were placed in the 3 dram vials and labeled according to film composition. The design is shown in Figure S4-1.

In order to confirm that each of the apparatuses were air-tight, they were tested for their ability to hold water at the temperatures used in the thermal cycling experiments, −78 to 100 °C. This experiment effectively explored the design's steam tightness with one end of the pipe sealed and not meant to be opened again while the other was able to be opened and closed repeatedly without significant damage to the system.

Water (10 mL) was added to each apparatus. It was reproducibly sealed by measuring the length of exposed thread. Each hollow-pipe brass/glass apparatus was placed in an oven at 100 °C for 24 h. After the heating period was completed, the apparatus was opened and the amount of water it contained was measured. In this way, it was determined that each assembled apparatus was effectively air-tight at 100 °C.

Following this test, the chamber seals were tested following thermal cycling. The chambers were assembled, and 10 mL of water was added. The chambers were cycled approximately every 12 h from 100 °C to −78 °C for 48 h. To maintain −78 °C a foam cooler was placed inside of a larger, plastic cooler. The interior cooler and the space between the outer and interior cooler was filled with dry ice, shown in Figure S4-1. The temperature inside of the foam cooler was found to be stable at −76 °C using a K-type thermocouple. At the end of the test, an average of 9.7 mL of water was collected with the losses due to some water which remained inside the chamber showing the seal was maintained even after prolonged cycling.

4.6.4. Proton bombardment

The hydrogen ions were accelerated to 3.0 MeV by a National Electrostatics Corporation (NEC) Pelletron tandem accelerator. The beam was rastored across the films to give uniform

coverage. A 3 MeV proton (H$^+$) beam was obtained by irradiating the sample at a total dose per film of 4.17×10^{17} ions/cm^2 at a current of 0.3 nA for 107 ms. The dose size was calculated by converting the recommended dose size of 14 krad to ions cm^{-2}.

4.6.5. PCBM purity determination

Before the PCBM samples were used to make the films for the illumination experiments their purity was assessed by NMR, HPLC, and mass spectroscopy. To ensure that no contaminants were introduced in the PCBM sample during the NMR analysis, the ^{1}H NMR spectra of the neat NMR solvents were collected in the same NMR tubes that were subsequently used for the analysis of the PCBM sample. This allowed for the elimination of any solvent based impurities arising from contamination of the NMR tubes. These experiments showed that even at high PCBM concentrations, 0.01 M, no observable non-solvent proton-containing impurities were present. There is a small but detectable amount of a toluene impurity (δ 7.0–7.2 and 2.4) likely left over from the original purification. The full spectrum of PCBM is shown in Figure S4-3 and the chemical shifts are in agreement with the reported values.[41]

To further probe the sample for other potential non-volatile impurities as well as identify the retention time for PCBM in our HPLC system, the HPLC chromatogram of PCBM was collected in 100% toluene with a flow rate of 5 mL min^{-1}. The chromatogram is shown in Figure S4-4.

The trace shows there are no detectable impurities. The inset shown in Figure S4-4, shows the chromatogram at 100X magnification. There is an unidentified residual solvent peak at the dead volume (or first sample elution point). Most importantly, we can tentatively conclude there are no significant concentrations of multi-adduct PCBM derivatives present in this sample. Those adducts would have appeared in the HPLC trace as separate peaks, most likely with retention times shorter than that of PCBM. Furthermore, we can deduce that there are no detectable amounts of C$_{60}$ in the sample, which would have not been detected by ^{1}H NMR. C$_{60}$ would have eluted as a second peak at 8 minutes in this separation regime.

One cannot completely rule out that some impurities can co-elute with PCBM, so further elaboration of analysis is possible. For example, by modifying the mobile phase to increase the retention of fullerenes, one can detect co-eluting compounds. This technique was used in later studies.

Lastly, negative ion electrospray ionization mass spectrometry, NI-ESI MS, was used to further rule out the presence of any fullerene contaminants with a different composition than PCBM that may have co-eluted with PCBM. The mass spectrum of the PCBM sample is shown in the supplemental information section for this chapter, Figure S4-5. Use of more polar solvents, e.g., acetonitrile, resulted in the extensive adduct formation in the ion source complicating analysis of the sample composition so only toluene was used as the carrier solvent.

There is a low-intensity signal at m/z 926. With a mass separation of 16 Da from PCBM, this ion is most likely due to an oxidized PCBM derivative. This ion may have been formed in the ion source of the mass spectrometer as a result of the ionization process in the presence of residual water or oxygen. There is also a peak identified as the parent ion C_{60} at m/z 720. This peak appears to be the result of fragmentation of the PCBM parent ion since the HPLC trace did not show a detectable quantity of C_{60}. From these analyses it can be concluded that PCBM has a high compositional purity and was sufficiently pure to use in the degradation studies.

4.6.6. Variability in PCBM vendor purity

Using the methodology described above multiple PCBM vendor samples were analyzed for purity. In one case, the sample was found to be contaminated by the 5,6 isomer of PCBM rather than the more stable 6,6-PCBM isomer that is commonly referred to as PCBM. For this section and for the related figures and figure captions PCBM will be referred to as 6,6-PCBM for clarity. The 5,6-PCBM contaminant was found to have a deleterious effect on device performance and so the characterization of that impurity is reported here for the benefit of the literature.

For privacy reasons the vendor name will not be disclosed and will be referred to as Vendor X for the purposes of this work. The ^{1}H NMR spectrum of the Vendor X PCBM sample was recorded in a mixture of 9:1 CS_2:$CDCl_3$ and compared to the verified sample of PCBM from Nano-C discussed in Section 4.6.5. The spectra are shown in Figure 4-17 and a more detailed spectrum of the Vendor X PCBM sample is shown in Figure 4-18. From this spectrum the chemical shifts of the 5,6-PCBM impurity were identified and matched well to the chemical shifts reported by Hummelen.[95] In order to characterize the impurity further, the 5,6-PCBM was separated from the major isomer, 6,6-PCBM by HPLC using an eluent mixture of 60/40 toluene/heptane. The HPLC chromatograms associated with the separation are shown in Figure 4-19. Upon isolation the F1 fraction, 6,6-PCBM, was yellow in solution and the F2 fraction, 5,6-PCBM, was a dark purple color. Using the isolated fractions, the UV-vis spectra were recorded and the band maxima were matched to the literature reported values[95] adding an additional confirmation that the contaminant was the 5,6-PCBM isomer.

The synthesis reported by Hummelen[95] utilizes the 5,6-PCBM isomer as the starting material for the final step in the multi-step process to produce 6,6-PCBM which is commonly used in organic electronic devices. It is important for future researchers to be aware of this possible contaminant so they can take appropriate steps to either remove the 5,6 isomer or convert it into the 6,6 isomer.

4.6.7. PCBM film production

PCBM films were made via spin casting from a 40 mg/mL solution of PCBM in chlorobenzene. The films were spin casted at 760 rpm for 40 s which was found to give the most uniform coverage while simultaneously resulting in the thickest film. The films were cast in a nitrogen filled glovebox and thermally annealed at 90 °C for 10 min. The films were evacuated over 24 h in a glovebox antechamber to remove residual chlorobenzene from the films. Three films were brought into an argon glovebox. Two of those three films were placed under 1 sun illumination and were continuously exposed for 24 h and 100 h respectively. The third film was

kept in the dark in the glovebox for the duration of the experiment. Three other films were exposed to air and 2 were aged under the same conditions as previously described in air and the final film was stored in the dark for the duration of the experiment. The resulting films were either scraped in a glovebox or in air depending on the initial aging conditions for each film, Air-aged films were scraped in air and argon aged films were scraped in a glovebox atmosphere. The Ar-aged films were packed under nitrogen in air-tight gasket sealed vessels and the Air-aged films were packaged in air in the same vessels. Both containers were wrapped in aluminum to exclude light and shipped to CSU for analysis.

4.6.8. Chemical oxidation of PCBM

A sample of chemically oxidized PCBM was synthesized using meta-chloroperoxybenzoic acid (*m*CPBA) as an oxidant[60] in a dilute solution (0.01 M) of PCBM in chloroform. The solution was washed with water after resting for 4 h and then washed with a dilute solution of NaOH (0.01 M) to remove residual acid. The solution was washed with water again three times and then with chloroform, which was roto-evaporated to dryness. The resulting crude material, referred to as O_x-PCBM in this document, was analyzed by mass spectrometry (MS), ^{1}H NMR, and HPLC.

4.6.9. SMD:PCBM device fabrication

The devices were made with 0%, 0.3%, 3%, and 30% PCBM-oxide. These devices were constructed in an inverted architecture using SMD as a small molecule donor. This has been shown to produce devices with PCE efficiencies greater than 6% with PCBM as the acceptor. All of the doped devices were made using the same device structure. Device structure: hole blocking layer polyethylenimine and glycerol diglycidylether (PEI:DEG) | BHJ | electron blocking layer vapor deposited $MoO_{(x)}$ | vapor deposited Al. All device layers were spin coated unless otherwise stated.

4.6.10. C_{60}FHF and C_{70}FHF OFET fabrication

The C_{60}FHF and C_{70}FHF OFETs were assembled on glass substrates, which are cleaned by a sequence of ultrasonication in D.I. water, acetone, methanol and isopropanol, and were dried under a stream of nitrogen. To assemble the dielectric gate, which includes the gate oxide and a

passivation layer, an aluminum film of 150 nm is deposited by thermal evaporation and structured by shadow masks to form the gate patterns.

For TTC based OFETs (series #1 and #2), 50 nm of aluminum oxide was used as the dielectric gate material, which was grown by anodization according to the reports by Majewski et al..[96] The thickness of the aluminum oxide was controlled by the terminating voltage of anodization. Afterwards, substrates were annealed for 2 h at a temperature of 70 °C. Finally, a passivation layer (40 nm film of TTC) was deposited onto the aluminum oxide to complete the dielectric gate. Before the evaporation of the organic semiconductors, substrates with a dielectric gate were annealed for another 2 h at a temperature of 70 °C.

For SAMs based OFETs (series #3), aluminum oxide was grown by oxygen plasma according to the reports by Klauks, et al.[97] Afterwards, the samples are immersed in 5 mM solution of N-tetradecylphosphonic acid (TDPA) for 18 h to form a passivation layer of self-assembled monolayers (SAMs) on the oxide surface.[85] The samples are rinsed by isopropanol and again dried by nitrogen gas. Finally, samples are annealed for 20 min at 70 °C in a nitrogen filled glovebox.

The dopant film was deposited in a single evaporation run with different thicknesses at an evaporation rate of 0.1 Å s^{-1}. Afterwards, 40 nm of an intrinsic fauxhawk fullerene film was thermally deposited at a rate of 0.5 Å s^{-1}.

The injection layer was deposited and patterned by a drain/source shadow mask, followed by 60 nm of aluminum film to ensure a high conductivity throughout the drain/ source electrodes. For OFETs with a gold injection layer, 20 nm of gold was thermally deposited as the injection layer. For OFETs with an n-type C_{60} injection layer, the heavily doped C_{60} film (25 nm, 8 wt.% of C_{60}: o-MeO-DMBI-I) was deposited by co-evaporation. During the co-evaporation, the doping concentration was controlled by the ratio of the evaporation rate between C_{60} and the corresponding n-dopant o-MeO-DMBI-I. Here, the rate of C_{60} was kept at 0.5 Å s^{-1}. Furthermore,

a thin film of the pure n-dopant (2 nm, *o*-MeO-DMBI-I) was deposited on top of the *n*-type C_{60} injection layer to further enhance the injection.

The vacuum chamber and deposition tool are manufactured by Angstrom Inc. The base pressure of the vacuum chamber is in the range of 5×10^{-8} Torr. The transistors are characterized by a Keithley SCS-4200 semiconductor parameter analyzer inside the glovebox at room temperature (300 K). The level of oxygen and moisture in the glovebox are controlled and remained below 0.1 ppm.

4.7. CONCLUSIONS

A wide range of applied research has been performed to advance the field of fullerene based organic electronics. Work was done to evaluate using OPV devices in space applications. These materials would be well suited to instruments with low power consumptions and minimal operational windows, cubesats. At this time, it has been shown that OPV active layers were resilient to prolonged vacuum and thermal cycling in the temperature and pressure ranges experienced in space. Additionally, thermal cycling resulted in a measurable improvement in the Yield × Mobility value of the active layer films.

Preliminary radiation exposure studies were performed but more work is needed before any conclusions about the viability of OPV devices in space can be made, however a promising result is that the degradation in the films due to high energy proton and photon bombardment was able to be reversed to some extent by thermal cycling of the OPV active layers.

Aging studies of PCBM films were performed in air and in an inert Ar atmosphere. While it had been shown previously that the PCBM degrades in an inert atmosphere and less so in air apparently due to dimerization of the fullerene[51] it had not been shown that in air while the dimerization is inhibited due to singlet oxygen's ability to quench the T_1 excited state[54] oxidation of the fullerene does occur. The discovery of the previously unidentified O_x-PCBM species in the aged material was achieved by HPLC using weaker eluent conditions than had been previously

reported and was confirmed by careful analysis of the ^{1}H NMR spectra of the samples correlated with the HPLC chromatogram peak areas in the literature separation conditions.

The effect of O_x-PCBM on the device performance was measured by synthesizing O_x-PCBM and intentionally adding it to OPV devices. These studies showed that, as expected, the O_x-PCBM had a deleterious effect on the device performance and specifically the fill factor.

Since the oxidation of PCBM is likely an unavoidable part of any PCBM based OPV overtime the effect O_x-PCBM has on device lifetime was also investigated. Unexpectedly, the most significant result was that the presence of O_x-PCBM had a minimal impact on the prolonged performance of the OPV devices and the loss rate became effectively stable after the first 250 h. However, the devices initial drop in performance, commonly referred to as burn-in, was dramatically affected. In the highest O_x-PCBM concentrations the majority of the devices did not have a measurable PCE value shortly after the first 100 h of illumination. This result may have important implications both in device processing and in attempts to fundamentally understand the causes of device burn-in which remains an active area of study.[49,65,71-73]

Lastly, OFET devices were produced utilizing fauxhawk fullerene materials synthesized by the author. The original devices were made using C_{60}FHF. These devices showed impressive charge carrier mobilities with an average of 0.34 cm^2 V^{-1}s^{-1}. These devices were found to have minimal hysteresis and optimal device architecture was found through controlled varying of the dopant thickness layer and source/drain contact materials. By utilizing o-MeO-DMBI-I N-doped C_{60} contact layers were produced and these had the highest charge mobilities with C_{60}FHF.

Following this success more devices were prepared using two different C_{70}FHF materials, a mixture of 2:1 C_{70}FHF-1 and C_{70}FHF-2, and C_{70}FHF-3. Both of these materials, contrary to the general consensus in the literature, outperformed or matched the performance of the C_{60}FHF devices. Most impressive was the C_{70}FHF isomer mixture which achieved an average charge mobility of 0.6 cm^2 V^{-1}s^{-1}, one of the highest mobilities reported for a fullerene derivative in an

n-type OFET device. This result suggests previous conclusions about the cause of lower mobilities for C_{70} based OFETs may need to be re-evaluated.

4.8. ADDITIONAL RECOGNITION

The fabrication of the drop cast OPV bulk heterojunction films was performed by Dr. Long K. San. Dr. Long K. San was critical to the experimental design of the radiation exposure studies. The proton bombardment experiments were performed in Dr. Vaithiyalingam Shutthanandan's lab at Pacific Northwest National Lab. The electron bombardment studies were performed at Colorado State University with the assistance of Dr. Roy Geiss. Dr. Geiss also supplied the author, going beyond the normal call of his responsibilities as a Central Instrument Facilities Analytical Specialist, with several primary literature sources for radiation degradation of carbon rich sources which were invaluable in understanding the results of the experiments and were also useful in later work associated with PCBM aging experiments. The aging experiments were performed at NEXT Energy Technologies lab in Santa Barbara, California with advice and assistance from the excellent team of engineers and chemists there. The OFET devices were produced at Kent State University by the always impressive Dr. Shiyi Liu in Dr. Bjorn Lussem's research lab.

Table 4-1. Effect of prolonged evacuation and thermal cycling of the active layer films measured by changes in the Yield × Mobility value.

sample	$\varphi\Sigma\mu$ $(cm^2\ V^{-1}{\cdot}s^{-1})^a$	% change	$\varphi\Sigma\mu$ $(cm^2\ V^{-1}{\cdot}s^{-1})^b$	% change
C60-A	0.025		0.009	
C60-B	0.022	11	0.011	23
C60-C			0.049	460
FHF-A	0.016		0.005	
FHF-B	0.009	42	0.007	33
FHF-C			0.020	240
PCBM-A	0.014			
PCBM-B	0.016	16	0.011	

[a] Yield × Mobility value was recorded for samples that were not evacuated (A) and samples which were evacuated (B). [b] Yield × Mobility value was recorded for samples that were not thermally cycled (A) and samples which were thermally cycled (B) and samples which were thermally cycled again (C).

Table 4-2. Summary of PCBM films and degradation conditions.

film	light			atmosphere	
	no exposure	24 h	100 h	air	Ar
A1	X			X	
A2	X				X
B1		X		X	
B2		X			X
C1			X	X	
C2			X		X

Table 4-3. Summary of $C_{60}FHF$ OFET Devices

OFET series	#1	#2	#3
thickness of Al_2O_3 gate oxide	50 nm	50 nm	5 nm
passivation layer	TTC (40 nm)	TTC (40 nm)	SAM
injection layer	Au	n-doped C_{60}	n-doped C_{60}
thickness of dopant layer	0, 1, 2, or 4 Å	0, 1, 2, or 4 Å	0, 1, 2, or 4 Å
channel length	100, 150, 200, 250, 300, or 350 µm		

Table 4-4. Summary of $C_{70}FHF$ OFET Devices

OFET series	#4	#5	#6	#7
Semiconductor	$C_{70}FHF$-1: $C_{70}FHF$-2 (2:1) 20 nm	$C_{70}FHF$-1: $C_{70}FHF$-2 (2:1) 20 nm	$C_{70}FHF$-3 18 nm	$C_{70}FHF$-3 18 nm
thickness of Al_2O_3 gate oxide [nm]	50	50	50	50
passivation layer	TTC (40 nm)	TTC (40 nm)	TTC (40 nm)	TTC (40 nm)
injection layer	Au	*n*-doped C_{60}	Au	*n*-doped C_{60}
thickness of dopant layer [Å]		0,1,2,4		
channel length [μm]		100, 150, 200, 250, 300, 350		
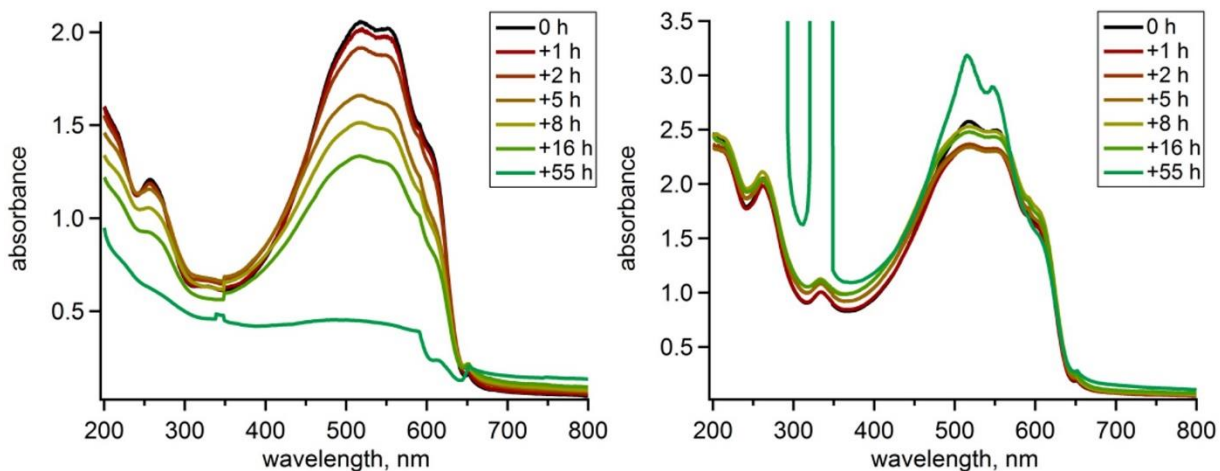
Figure 4-1. UV-vis spectra taken after UV exposure of OPV active layers over time. (**Left**) $C_{60}FHF$:P3HT film (**Right**) PCBM:P3HT film. Both films were thermally cycled in the thermal stability test described in Section 4.2.2.
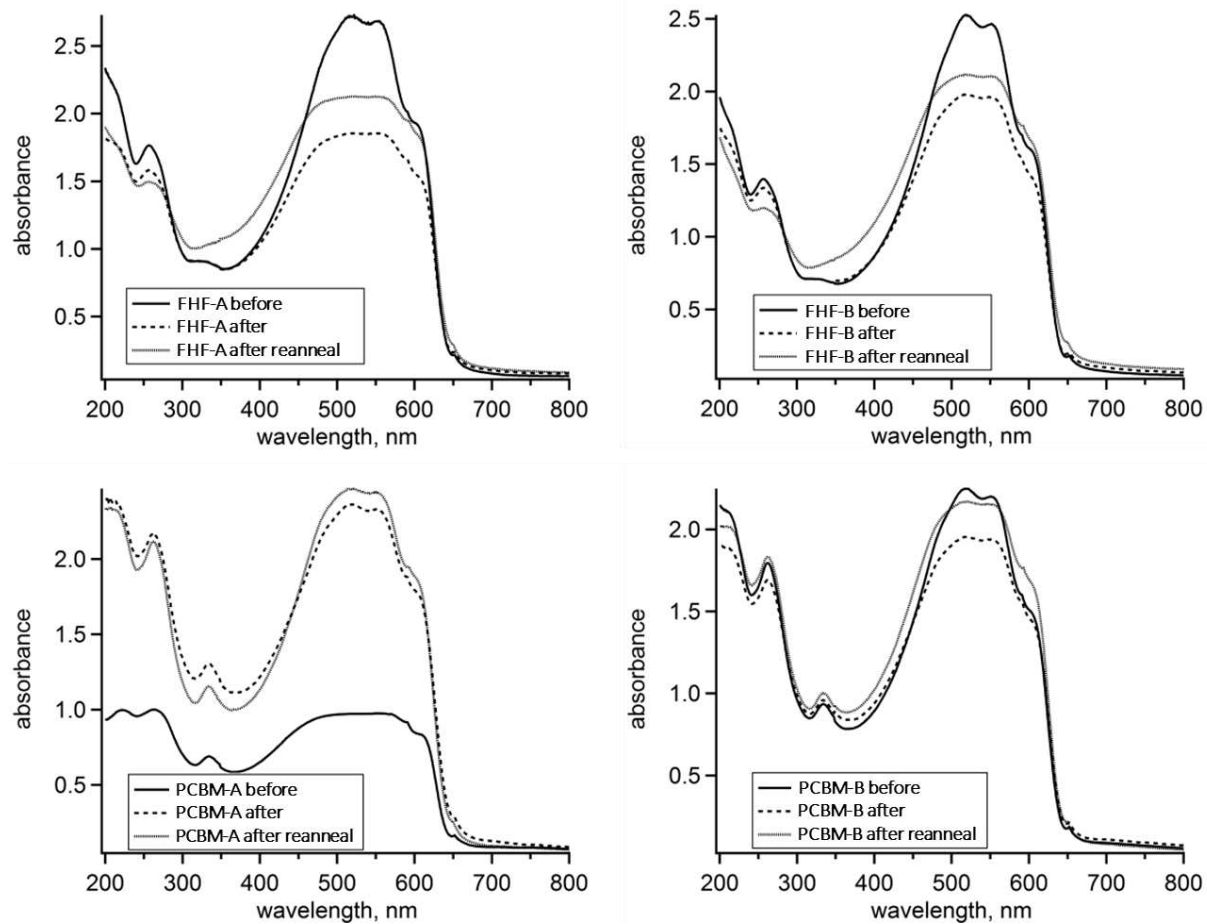
Figure 4-2. (**Top**) C_{60}FHF:P3HT UV-vis spectra pre and post proton bombardment. (**Bottom**) PCBM/P3HT UV-vis spectra pre and post proton bombardment. Samples labeled A were not thermally cycled; samples labeled B were thermally cycled.
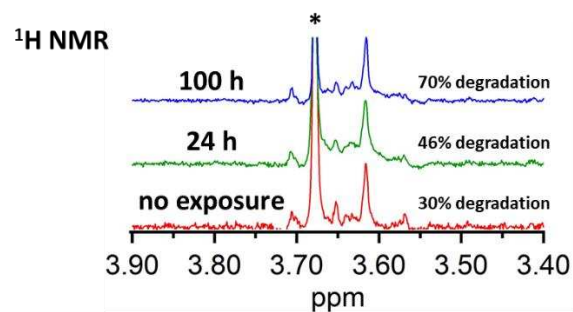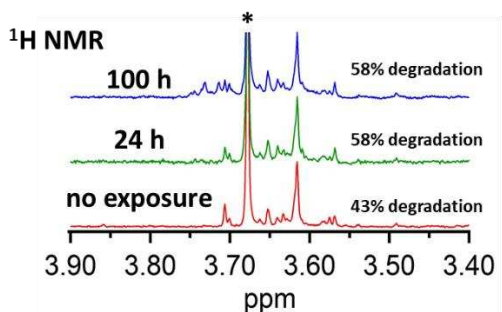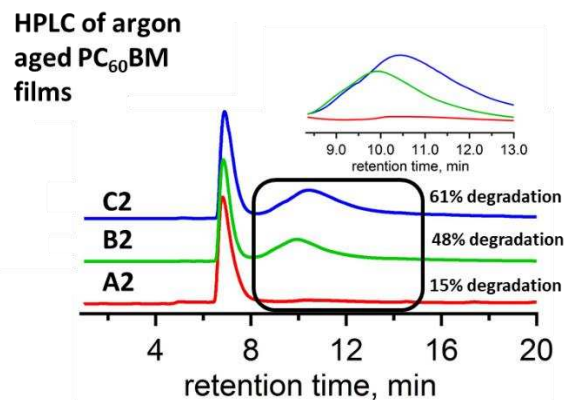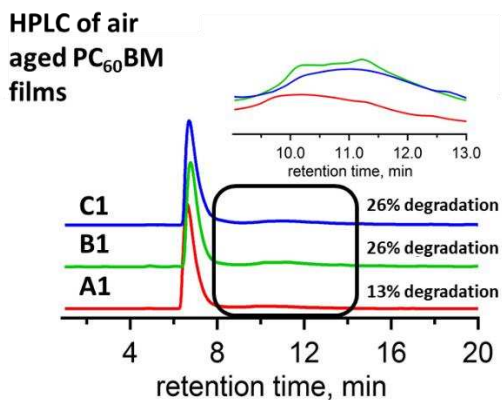
Figure 4-3. (**Left**) Drawings depicting the effects of increasing durations of illumination under ambient air. (**Right**) Drawings depicting the effects of increasing durations of illumination under an inert argon atmosphere. (**Top**) HPLC chromatograms for the films showing the percentage of the peak area not included in the PCBM peak. The inset shows a zoomed in view of the degradation product region of the chromatogram. (**Bottom**) NMR spectra for the films showing the percentage of peak area not accounted for by PCBM's methyl ester chemical shift. The asterisk shows the chemical shift for PCBM. No exposure refers the two films with no illumination.
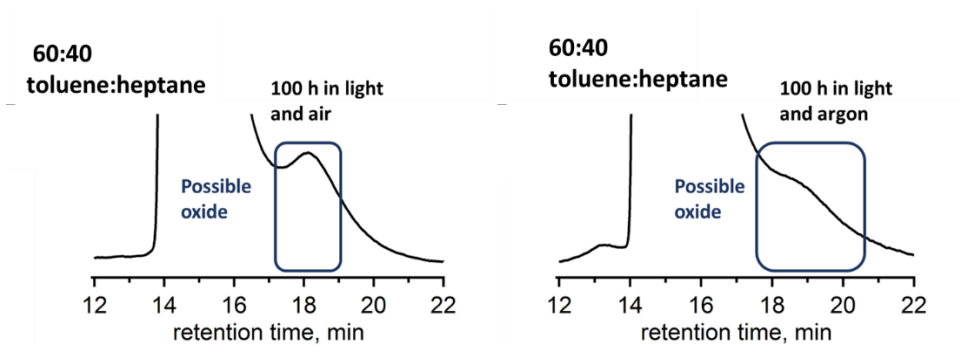
Figure 4-4. HPLC chromatograms of two PCBM films illuminated in air (**Left**) and in argon (**Right**) for 100 h. In both chromatograms a new peak is visible eluting between 18 and 20 min. The large peak eluting between 14 and 18 min is PCBM.
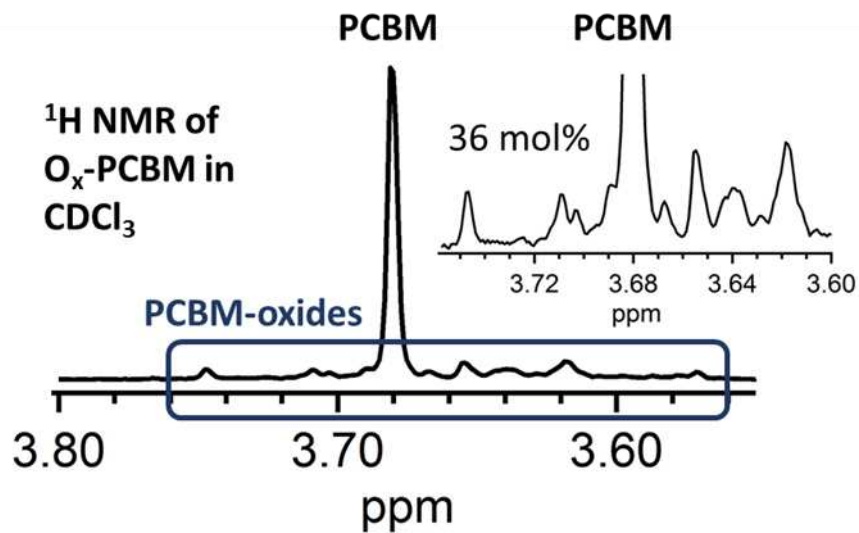
Figure 4-5. The ^{1}H NMR spectrum of the O_x-PCBM sample is shown. Only the methoxy region is shown because it is the most informative part of the spectrum. Based on integration of the methoxy region the sample was found to contain 36 mol% PCBM-oxide.
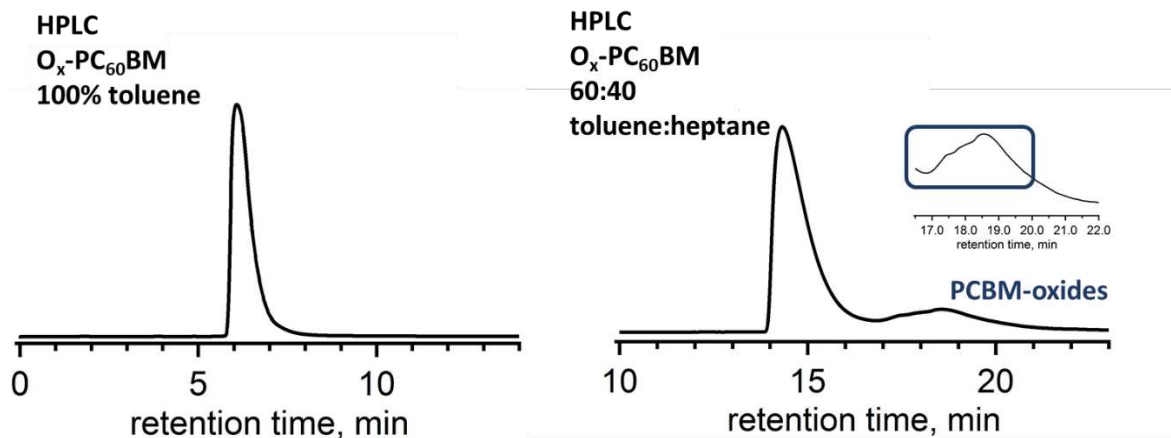
Figure 4-6. (**Left**) Chromatogram was collected using 100% toluene as the eluent and (**Right**) was collected using 60/40 toluene/heptane. The oxidized species co-elute between 17 and 21 minutes under these conditions as shown by the inset on the right panel. The amount of PCBM-oxide fraction based on peak area is 30%. However, this analysis cannot account for compounds that may still remain hidden beneath the PCBM peak and Therefore it is possible that the PCBM-oxide concentration is under-represented.
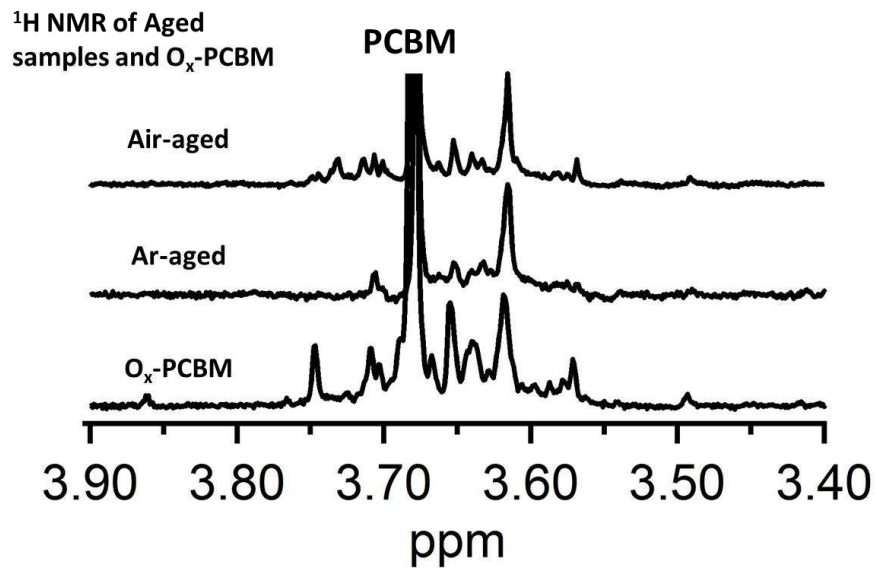
Figure 4-7. Stacked ^{1}H NMR spectra of the O_x-PCBM, air-aged, and argon, Ar, aged showing the fingerprint methoxy region. The signal at 3.6 ppm is common to all three of the spectra.
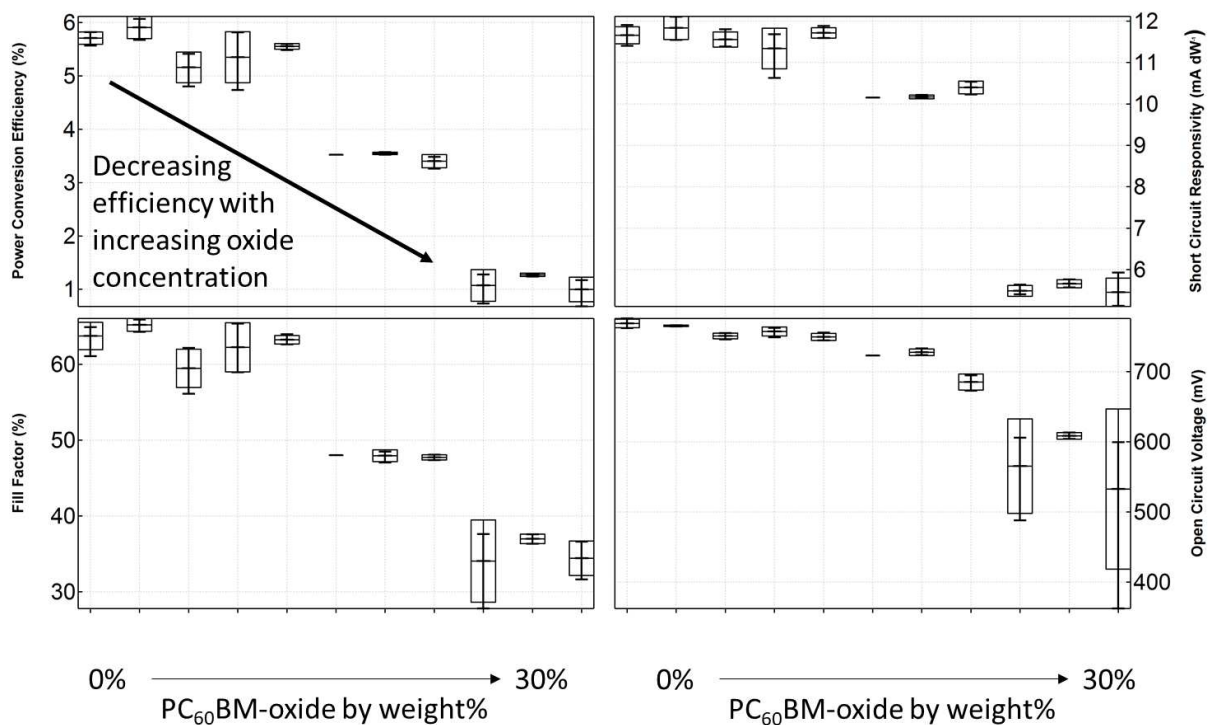
Figure 4-8. The oxide doped devices were measured for their initial efficiency. As the weight% of O_x-PCBM increases from 0% to 0.3% to 3% to 30% the efficiency of the device drops off linearly with the control devices having a percent conversion efficiency of approximately 6% and the highest weight% devices 1% or less. The box and whisker plots are generated by the four different electrodes on each device and represent the deviation between all four of the fingers on each device.
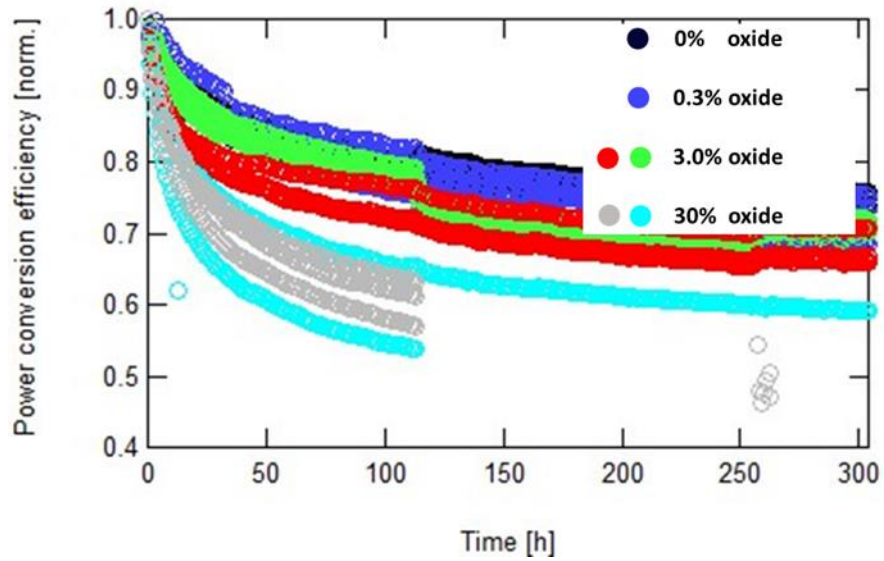
Figure 4-9. First 300 h of device lifetime. The control devices as well as the 0.3% devices have comparable initial losses in the first 100 h (burn-in). The 3% devices perform worse with a more substantial burn-in but eventually asymptotically level off. Lastly, the 30% devices fail more than 75% of the time after the initial burn-in. This is likely due to the severity of the burn-in leaving the actual efficiency to be negligible. All efficiencies shown here are normalized to one.
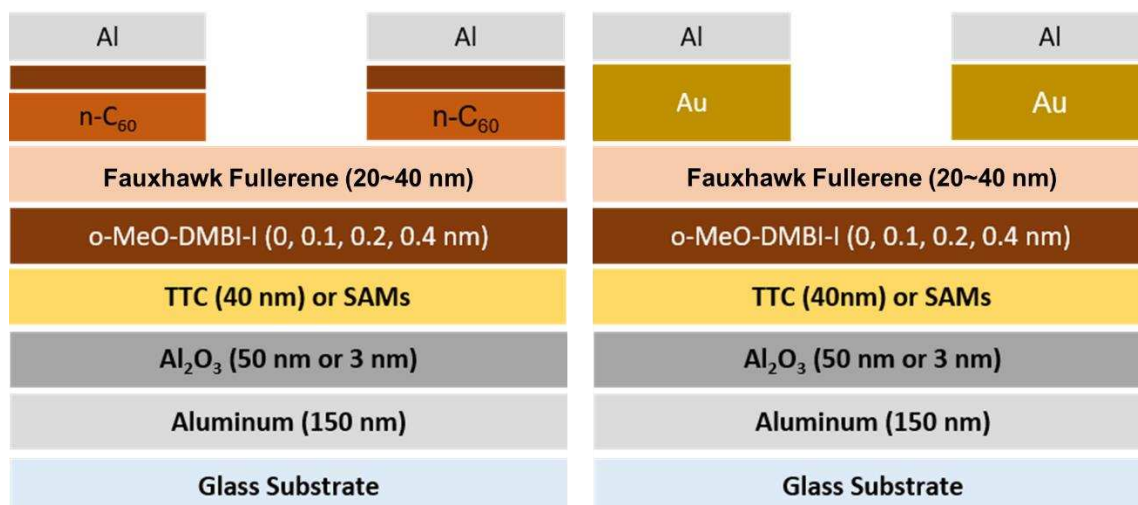
Figure 4-10. The design of OFETs used to study the performance of fauxhawk fullerenes. The p-junction material for the source and drain is aluminum with an n-doped contact layer between the FHF layer (intrinsic n-type layer). Two different contact layers were used, n-doped C_{60} (**Left**) and gold (**Right**). Furthermore, a thin layer of the n-dopant, o-MeO-DMBI-I, full structure shown in Figure S4-12 was introduced between the dielectric gate and the intrinsic FHF layer to control the threshold voltage of these transistors. The gate dielectric Al_2O_3 is either covered by a thin layer of tetratetracontane (a 44 carbon n-alkyl chain), TTC, or by a self-assembled monolayer (SAM) made from the deposition of phosphonic acid.
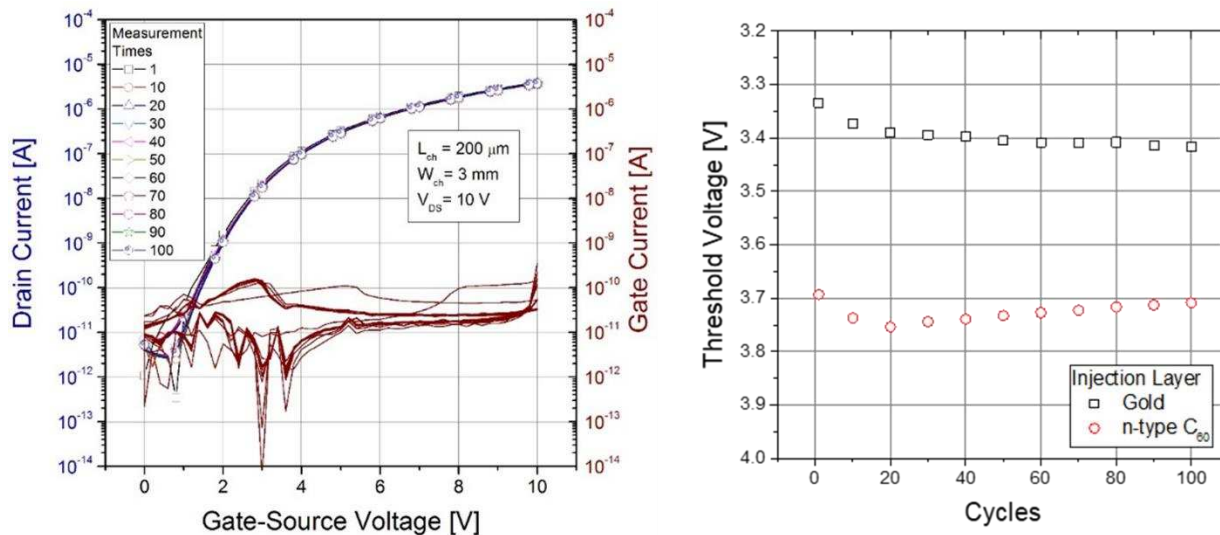
Figure 4-11. (**Left**) Stability of an OFET with the device configuration #1 described in Table 4-3 (no channel doping). No significant change in the transfer characteristic is observed for 100 cycles. (**Right**) Threshold voltage for one transistor from series #1 with Au contacts and for one transistor from series #2 with n-doped C_{60} contacts, both without channel doping. In both geometries, the threshold voltage shown remains stable under repeated cycling.
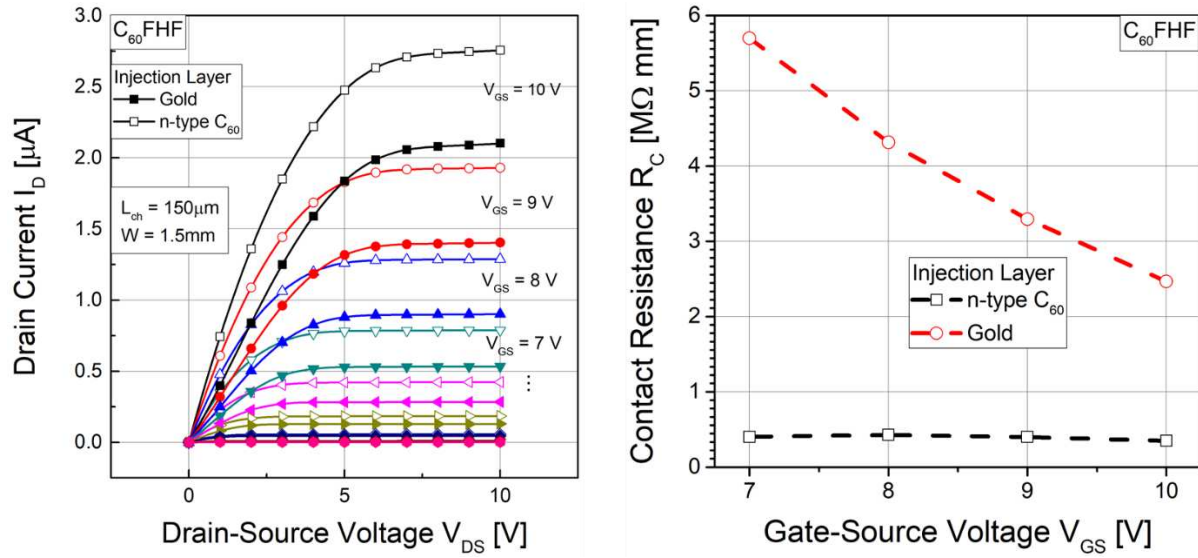
Figure 4-12. Influence of contact resistance on transistor performance. (**Left**) shows the output characteristic of transistors with Au source and drain contacts and *n*-doped C_{60} source and drain contacts showing the *n*-doped C_{60} contact devices have the highest currents, another measure of the higher transconductance, lower resistance, in those contacts. (**Right**) displays the dependence of the contact resistance on the gate source voltage.
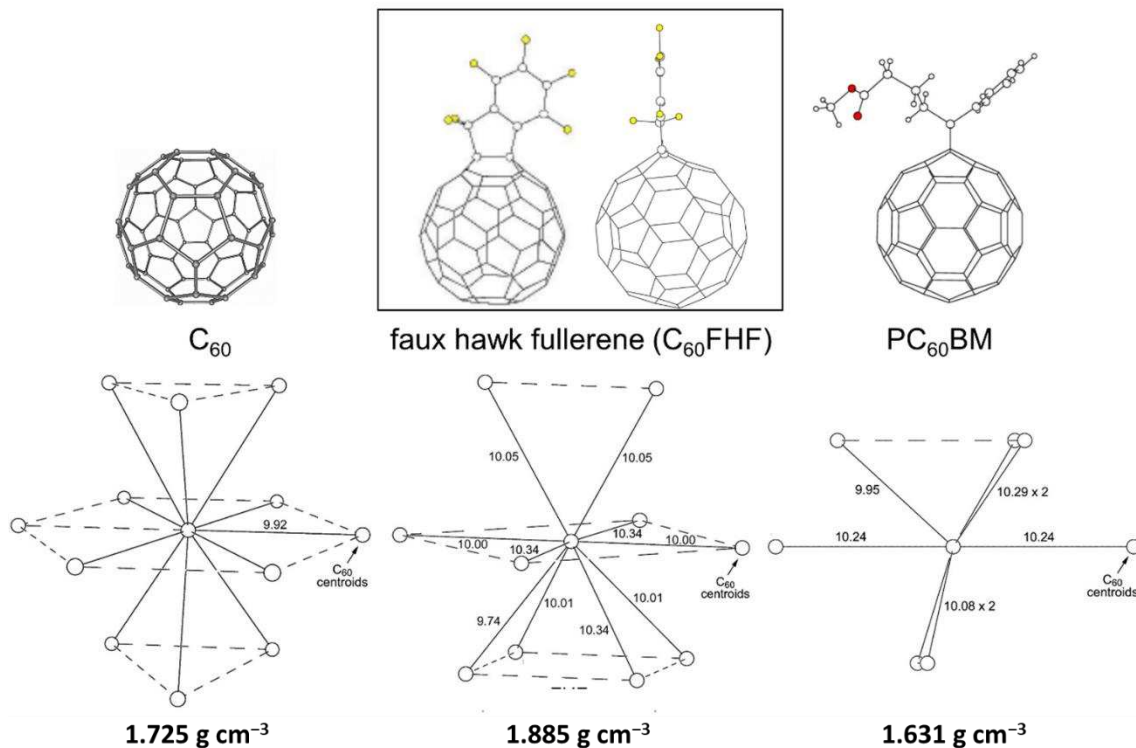
Figure 4-13. (**Top**) Drawings of molecular structures of C_{60} (**Top Left**), C_{60}FHF (two views) (**Top Middle**) and PC$_{60}$BM (**Top Right**). (**Bottom**) The nearest-neighbor centroid packing patterns in the single-crystal X-ray structures of C_{60} (**Bottom Left**) with twelve nearest neighbors,[92] C_{60}FHF (**Bottom Middle**) with ten nearest neighbors,[82] and PC$_{60}$BM (**Bottom Right**) with seven nearest neighbors.[93] The experimental crystal packing densities are shown as well.
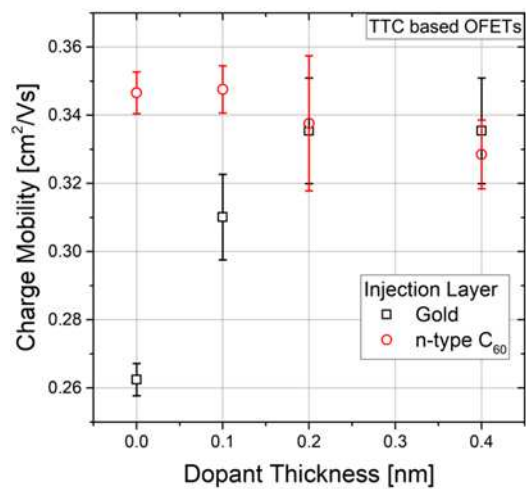
Figure 4-14. Influence of gate channel doping layer thickness on the charge carrier mobility of $C_{60}FHF$:TTC based OFETs (series #1 and #2, each data point contains results from eight devices.)
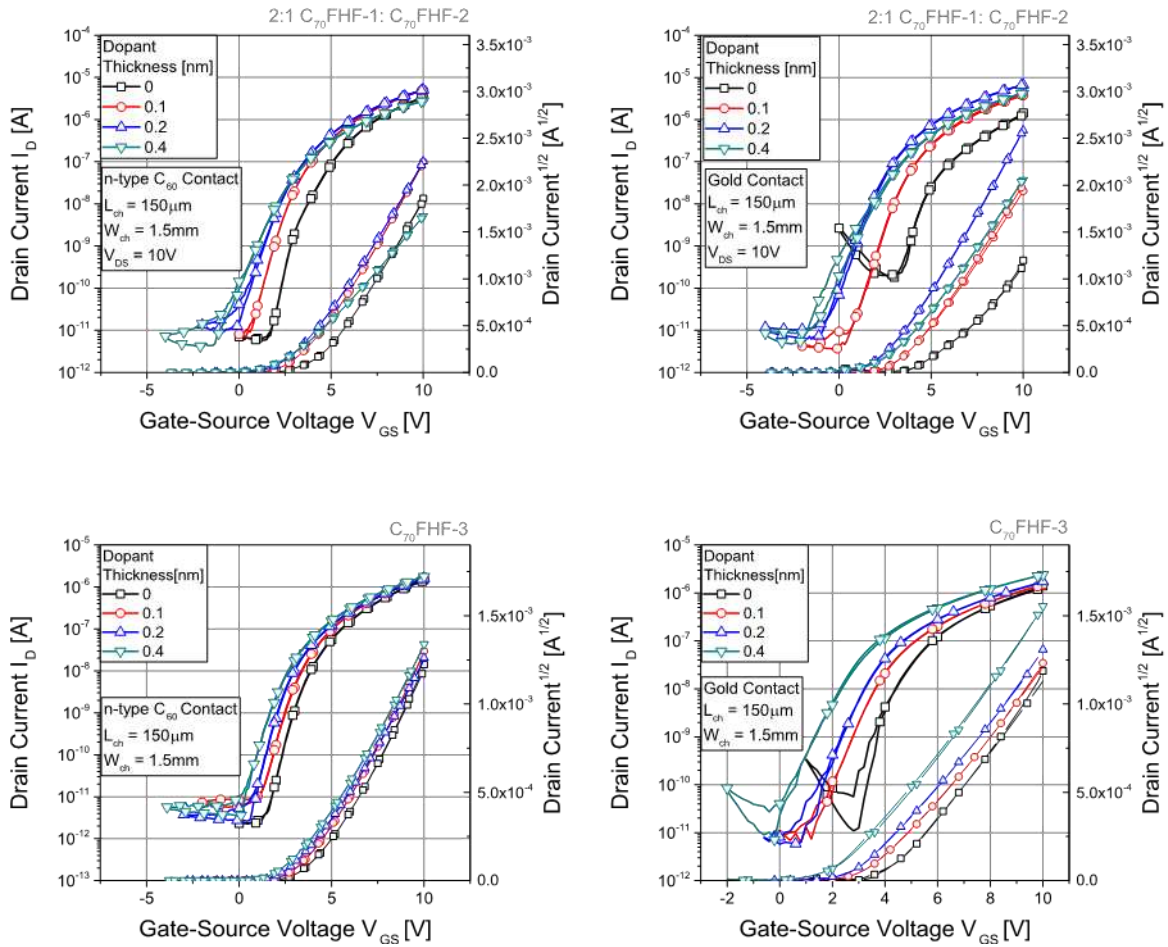
Figure 4-15. Transfer characteristic of OFETs (**Top**) using a 2:1 mixture of $C_{70}FHF$-1 and $C_{70}FHF$-2 (series #4 and #5); and (**Bottom**) isomer $C_{70}FHF$-3 (series #6 and #7). Whereas the transistors shown (**Left**) use *n*-doped C_{60} as the injection layer (series #4 and #6), (**Right**) use Au contacts (series #5 and #7).
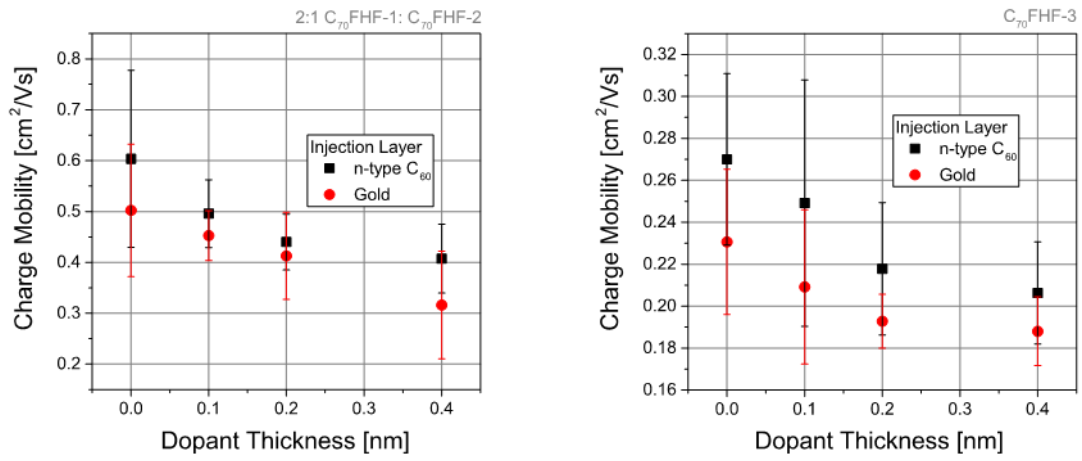
Figure 4-16. Average electron mobility of transistors using $C_{70}FHF-1:C_{70}FHF-2$ (2:1) (**Left**) and $C_{70}FHF-3$ (**Right**).
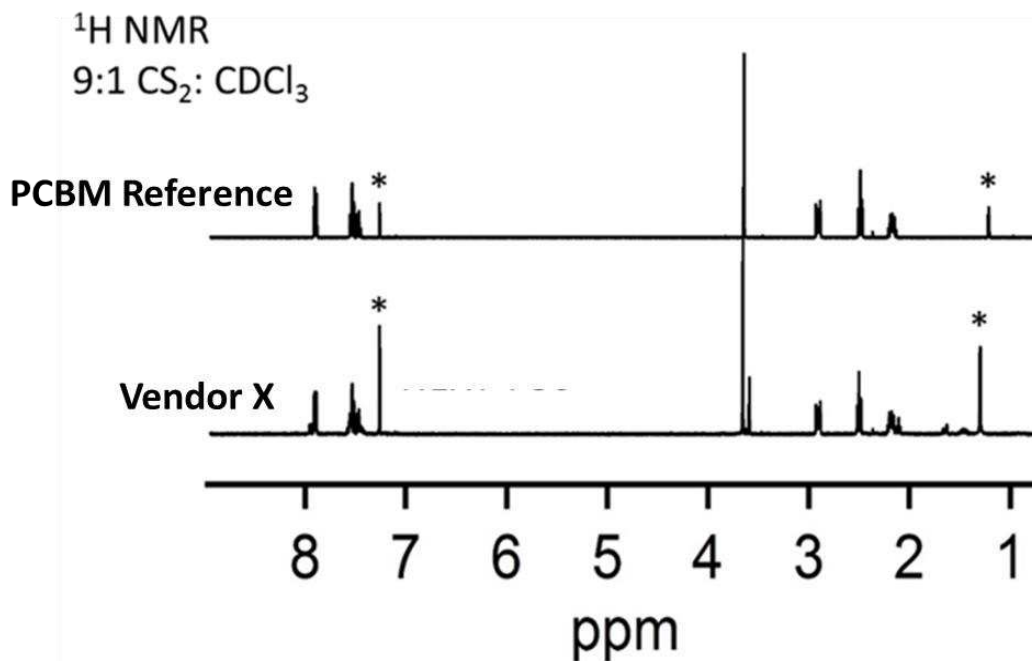
Figure 4-17. Stacked ^{1}H NMR spectra for the PCBM reference sample and Vendor X. The spectrum of the Vendor X sample shows several peaks that are not observed in the spectrum of the reference PCBM sample. These signals were identified as 5,6-PCBM. Asterisk labeled peaks are residual chloroform and water in the NMR solvent.
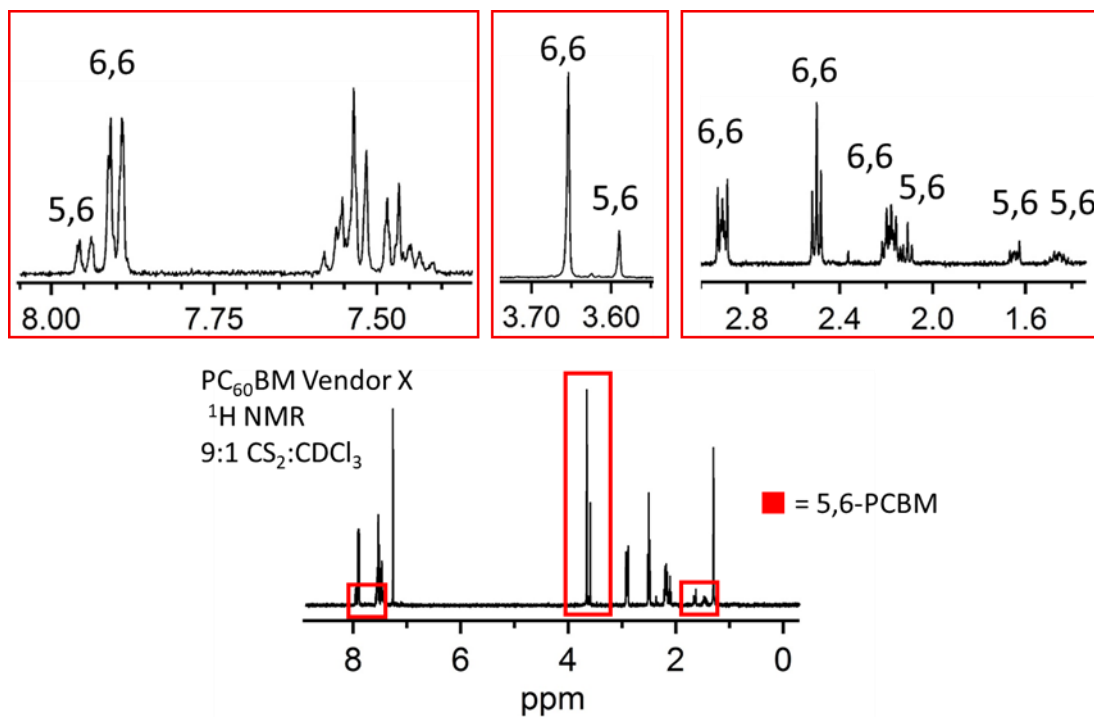
Figure 4-18. The ^{1}H NMR spectrum of the Vendor X PCBM sample. Red boxes highlight regions with additional peaks which are not attributed to PCBM.[95] Inset (**Top Middle**) shows the singlets due to methoxy protons on PCBM (δ 3.7) and on the 5,6-PCBM impurity (δ 3.60), the latter is estimated as 20 mol% relative to PCBM. The ratio of signals assigned to PCBM and 5,6-PCBM are consistent in both the aromatic and aliphatic regions.
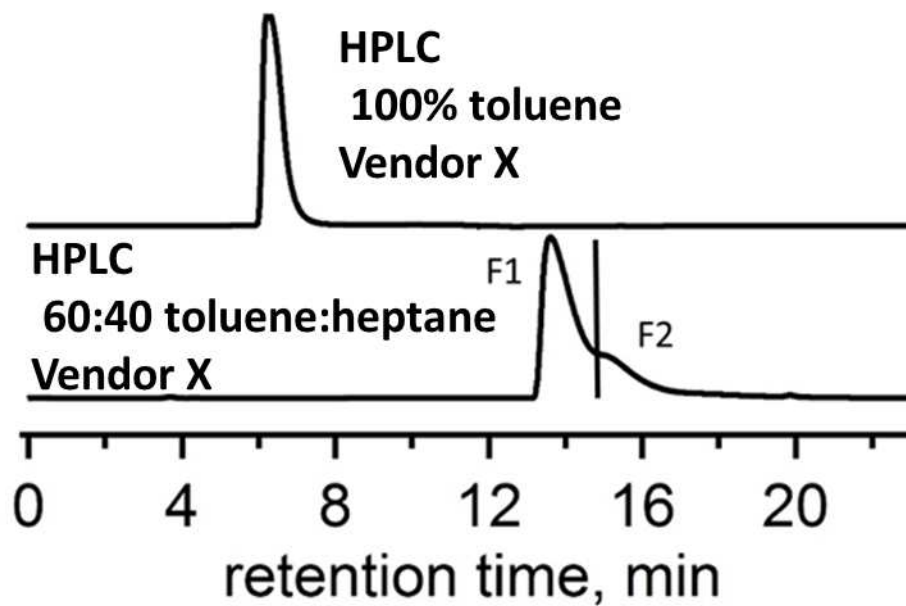
Figure 4-19. HPLC chromatograms for the Vendor X sample in 100% toluene and 60:40 toluene heptane. The line through the lower trace shows where the F1 and F2 fractions were collected.
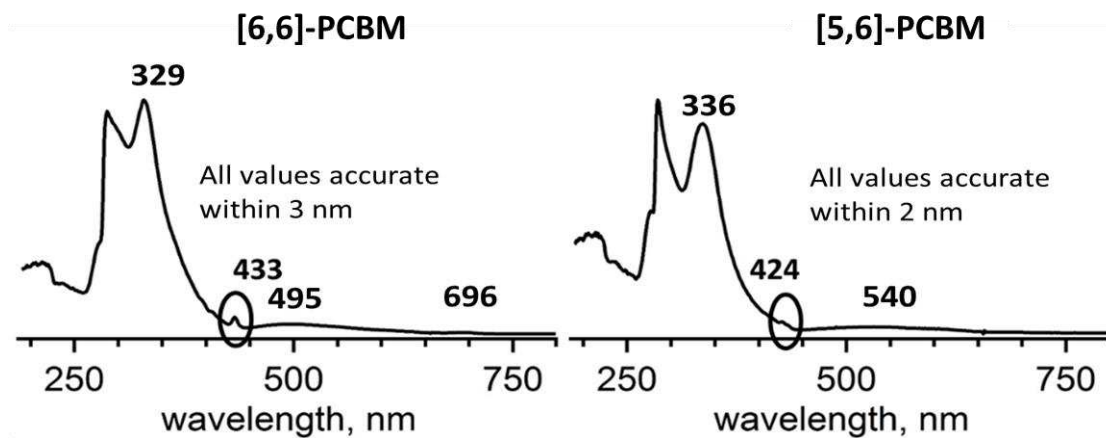
Figure 4-20. The UV-vis spectra of F1 and the F2. The UV-vis spectra were recorded in the eluent mixture for the HPLC separation, 60:40 toluene heptane. The characteristic absorption bands are outlined on both spectra. The band maxima agree well with the literature values for both the [6,6] and [5,6] respectively.[95]

4.9. REFERENCES

(1)   Kroto, H. W.; Heath, J. R.; O'Brien, S. C.; Curl, R. F.; Smalley, R. E. C_{60}: Buckminsterfullerene. *Nature* **1985**, *318*, 162-163.

(2)   Margadonna, S.; Prassides, K. Recent Advances in Fullerene Superconductivity. *J. Solid State Chem.* **2002**, *168*, 639-652.

(3)   Kortan, A. R.; Kopylov, N.; Glarum, S.; Gyorgy, E. M.; Ramirez, A. P.; Fleming, R. M.; Zhou, O.; Thiel, F. A.; Trevor, P. L.; Haddon, R. C. Superconductivity in barium fulleride. *Nature* **1992**, *360*, 566-568.

(4)   Haddon, R. C.; Perel, A. S.; Morris, R. C.; Palstra, T. T. M.; Hebard, A. F.; Fleming, R. M. C_{60} thin film transistors. *Appl. Phys. Lett.* **1995**, *67*, 121-123.

(5)   Spanggaard, H.; Krebs, F. C. A brief history of the development of organic and polymeric photovoltaics. *Sol. Energ. Mat. Sol. C* **2004**, *83*, 125-146.

(6)   Sariciftci, N. S.; Smilowitz, L.; Heeger, A. J.; Wudl, F. Semiconducting polymers (as donors) and buckminsterfullerene (as acceptor): photoinduced electron transfer and heterojunction devices. *Synth. Met.* **1993**, *59*, 333-352.

(7)   Guo, F.; Xiao, Z.; Huang, J. Fullerene Photodetectors with a Linear Dynamic Range of 90 dB Enabled by a Cross-Linkable Buffer Layer. *Adv. Opt. Mater.* **2013**, *1*, 289-294.

(8)   Shi, L.; Liang, Q.; Wang, W.; Zhang, Y.; Li, G.; Ji, T.; Hao, Y.; Cui, Y. Research Progress in Organic Photomultiplication Photodetectors. *Nanomaterials-Basel* **2018**, *8*, article 713.

(9)   Meng, L.; Zhang, Y.; Wan, X.; Li, C.; Zhang, X.; Wang, Y.; Ke, X.; Xiao, Z.; Ding, L.; Xia, R.; Yip, H.-L.; Cao, Y.; Chen, Y. Organic and solution-processed tandem solar cells with 17.3% efficiency. *Science* **2018**, *361*, 1094-1098.

(10) Zhang, Y.; Murtaza, I.; Meng, H. Development of fullerenes and their derivatives as semiconductors in field-effect transistors: exploring the molecular design. *J. Mater. Chem. C* **2018**, *6*, 3514-3537.

(11) Haddon, R. C. C_{70} Thin Film Transistors. *J. Am. Chem. Soc.* **1996**, *118*, 3041-3042.

(12) Bendikov, M.; Wudl, F.; Perepichka, D. F. Tetrathiafulvalenes, Oligoacenenes, and Their Buckminsterfullerene Derivatives: The Brick and Mortar of Organic Electronics. *Chem. Rev.* **2004**, *104*, 4891-4946.

(13) Umeyama, T.; Imahori, H. Isomer Effects of Fullerene Derivatives on Organic Photovoltaics and Perovskite Solar Cells. *Acc. Chem. Res.* **2019**, *52*, 2046-2055.

(14) He, Y.; Li, Y. Fullerene derivative acceptors for high performance polymer solar cells. *Phys. Chem. Chem. Phys.* **2011**, *13*, 1970-1983.

(15) Nakanishi, T.; Ohwaki, H.; Tanaka, H.; Murakami, H.; Sagara, T.; Nakashima, N. Electrochemical and Chemical Reduction of Fullerenes C_{60} and C_{70} Embedded in Cast Films of Artificial Lipids in Aqueous Media. *J. Phys. Chem. B* **2004**, *108*, 7754-7762.

(16) Xie, Q.; Perez-Cordero, E.; Echegoyen, L. Electrochemical detection of C_{60}^{6-} and C_{70}^{6-}: Enhanced stability of fullerides in solution. *J. Am. Chem. Soc.* **1992**, *114*, 3978-3980.

(17) Shi, Y.; Peng, L.; Ding, Y.; Zhao, Y.; Yu, G. Nanostructured conductive polymers for advanced energy storage. *Chem. Soc. Rev.* **2015**, *44*, 6684-6696.

(18) Zhang, J.; Xu, W.; Sheng, P.; Zhao, G.; Zhu, D. Organic Donor–Acceptor Complexes as Novel Organic Semiconductors. *Acc. Chem. Res.* **2017**, *50*, 1654-1662.

(19) Koutsouras, D. A.; Hama, A.; Pas, J.; Gkoupidenis, P.; Hivert, B.; Faivre-Sarrailh, C.; Di Pasquale, E.; Owens, R. M.; Malliaras, G. G. PEDOT:PSS microelectrode arrays for hippocampal cell culture electrophysiological recordings. *MRS Commun.* **2017**, *7*, 259-265.

(20)   Garnier, F.; Horowitz, G.; Peng, X.; Fichou, D. An all-organic "soft" thin film transistor with very high carrier mobility. *Adv. Mater.* **1990**, *2*, 592-594.

(21)   Lei, T.; Peng, R.; Song, W.; Hong, L.; Huang, J.; Fei, N.; Ge, Z. Bendable and foldable flexible organic solar cells based on Ag nanowire films with 10.30% efficiency. *J. Mater. Chem. A* **2019**, *7*, 3737-3744.

(22)   Chow, P. C. Y.; Someya, T. Organic Photodetectors for Next-Generation Wearable Electronics. *Adv. Mater.* **2019**.

(23)   Feron, K.; Lim, R.; Sherwood, C.; Keynes, A.; Brichta, A.; Dastoor, P. C. Organic Bioelectronics: Materials and Biocompatibility. *Int. J. Mol. Sci.* **2018**, *19*, article 2382.

(24)   Xiang, D.; Wang, X.; Jia, C.; Lee, T.; Guo, X. Molecular-Scale Electronics: From Concept to Function. *Chem. Rev.* **2016**, *116*, 4318-4440.

(25)   Shi, W.; Guo, Y.; Liu, Y. When Flexible Organic Field-Effect Transistors Meet Biomimetics: A Prospective View of the Internet of Things. *Adv. Mater.* **2019**.

(26)   Fan, Q.; Méndez-Romero, U. A.; Guo, X.; Wang, E.; Zhang, M.; Li, Y. Fluorinated Photovoltaic Materials for High-Performance Organic Solar Cells. *Chem. Asian J.* **2019**, *14*, 3085-3095.

(27)   Ragni, R.; Punzi, A.; Babudri, F.; Farinola, G. M. Organic and Organometallic Fluorinated Materials for Electronics and Optoelectronics: A Survey on Recent Research. *Eur. J. Org. Chem.* **2018**, 3500-3519.

(28)   Reichenbächer, K.; Süss, H. I.; Hulliger, J. Fluorine in crystal engineering—"the little atom that could". *Chem. Soc. Rev.* **2005**, *34*, 22-30.

(29)   Kim, M.; Park, W.-T.; Park, S. A.; Park, C. W.; Ryu, S. U.; Lee, D. H.; Noh, Y.-Y.; Park, T. Controlling Ambipolar Charge Transport in Isoindigo-Based Conjugated Polymers by Altering

Fluorine Substitution Position for High-Performance Organic Field-Effect Transistors. *Adv. Funct. Mater.* **2019**, *29*, article 1805994.

(30)   Zhao, W.; Li, S.; Yao, H.; Zhang, S.; Zhang, Y.; Yang, B.; Hou, J. Molecular Optimization Enables over 13% Efficiency in Organic Solar Cells. *J. Am. Chem. Soc.* **2017**, *139*, 7148-7151.

(31)   Chatterjee, S.; Ie, Y.; Seo, T.; Moriyama, T.; Wetzelaer, G.-J. A. H.; Blom, P. W. M.; Aso, Y. Fluorinated naphtho[1,2-c:5,6-c']bis[1,2,5]thiadiazole-containing π-conjugated compound: synthesis, properties, and acceptor applications in organic solar cells. *NPG Asia Mater.* **2018**, *10*, 1016-1028.

(32)   Ackerman, S. A.; Platnick, S.; Bhartia, P. K.; Duncan, B.; L'Ecuyer, T.; Heidinger, A.; Skofronick-Jackson, G.; Loeb, N.; Schmit, T.; Smith, N. Satellites See the World's Atmosphere. *Meteor. Monogr.* **2018**, *59*, article 4.

(33)   Badavi, F. F. Exposure estimates for repair satellites at geosynchronous orbit. *Acta Astron.* **2013**, *83*, 18-26.

(34)   Suparta, W.; Zulkeple, S. K. Spatial Analysis of Galactic Cosmic Ray Particles in Low Earth Orbit/Near Equator Orbit Using SPENVIS. *J. Phys.: Conf. Ser.* **2014**, *495*, article 012040.

(35)   Yamashita, S.; Kikkawa, J.; Yanagisawa, K.; Nagai, T.; Ishizuka, K.; Kimoto, K. Atomic number dependence of Z contrast in scanning transmission electron microscopy. *Sci Rep* **2018**, *8*, article 12325.

(36)   Bracewell, B. L.; Veigele, W. J. Elemental X-Ray Cross Sections at Selected Wavelengths In *Advances in X-Ray Analysis: Volume 15*; Heinrich, K. F. J., Barrett, C. S., Newkirk, J. B., Ruud, C. O., Eds.; Springer US: Boston, MA, 1972, pp 352-364.

(37) Brill, R. Determination of Electron Distribution in Crystals by Means of X Rays In *Solid State Physics*; Seitz, F., Turnbull, D., Ehrenreich, H., Eds.; Academic Press: New York, 1968; Vol. 20, pp 1-35.

(38) Bovin, J. O.; Wallenberg, R.; Smith, D. J. Imaging of atomic clouds outside the surfaces of gold crystals by electron microscopy. *Nature* **1985**, *317*, 47-49.

(39) Piris, J.; Kopidakis, N.; Olson, D. C.; Shaheen, S. E.; Ginley, D. S.; Rumbles, G. The Locus of Free Charge-Carrier Generation in Solution-Cast $Zn_{1-x}Mg_xO$/Poly(3-hexylthiophene) Bilayers for Photovoltaic Applications. *Adv. Funct. Mater.* **2007**, *17*, 3849-3857.

(40) Tuktarov, A. R.; Khuzin, A. A.; Dzhemilev, U. M. Light-controlled molecular switches based on carbon clusters. Synthesis, properties and application prospects. *Russ. Chem. Rev.* **2017**, *86*, 474-509.

(41) Larson, B. W.; Whitaker, J. B.; Popov, A. A.; Kopidakis, N.; Rumbles, G.; Boltalina, O. V.; Strauss, S. H. Thermal [6,6] → [6,6] Isomerization and Decomposition of PCBM (Phenyl-C_{61}-butyric Acid Methyl Ester). *Chem. Mater.* **2014**, *26*, 2361-2367.

(42) Nelson, J. Polymer:fullerene bulk heterojunction solar cells. *Mater. Today* **2011**, *14*, 462-470.

(43) Marsh, R. A.; Hodgkiss, J. M.; Albert-Seifried, S.; Friend, R. H. Effect of Annealing on P3HT:PCBM Charge Transfer and Nanoscale Morphology Probed by Ultrafast Spectroscopy. *Nano Lett.* **2010**, *10*, 923-930.

(44) Reese, M. O.; Nardes, A. M.; Rupert, B. L.; Larsen, R. E.; Olson, D. C.; Lloyd, M. T.; Shaheen, S. E.; Ginley, D. S.; Rumbles, G.; Kopidakis, N. Photoinduced Degradation of Polymer and Polymer-Fullerene Active Layers: Experiment and Theory. *Adv. Funct. Mater.* **2010**, *20*, 3476-3483.

(45)   Badhwar, G. D. The Radiation Environment in Low-Earth Orbit. *Rad. Res.* **1997**, *148*, S3-S10.

(46)   Sinclair, D.; Dyer, J. In *27th Annual AIAA/USU Conference on Small Satellites* 2013. Radiation Effects and COTS Parts in SmallSats

(47)   Devine, R. A. B.; Mayberry, C.; Kumar, A.; Yang, Y. Origin of Radiation Induced Damage in Organic P3HT:PCBM Based Photocells. *IEEE Trans. Nuc. Sci.* **2010**, *57*, 3109-3113.

(48)   Li, G.; Yang, Y. Radiation induced damage and recovery in poly(3-hexyl thiophene) based polymer solar cells. *Nanotech.* **2008**, *19*, article 424014.

(49)   Zhang, Y.; Samuel, I. D. W.; Wang, T.; Lidzey, D. G. Current Status of Outdoor Lifetime Testing of Organic Photovoltaics. *Adv. Sci.* **2018**, *5*, article 1800434.

(50)   Nisato, G.; Lupo, D.; Ganz, S. *Organic and Printed Electronics: Fundamentals and Applications*; Jenny Stanford Publishing: Singapore, 2016.

(51)   Heumueller, T.; Mateker, W. R.; Distler, A.; Fritze, U. F.; Cheacharoen, R.; Nguyen, W. H.; Biele, M.; Salvador, M.; von Delius, M.; Egelhaaf, H.-J.; McGehee, M. D.; Brabec, C. J. Morphological and electrical control of fullerene dimerization determines organic photovoltaic stability. *Energ. Environ. Sci.* **2016**, *9*, 247-256.

(52)   Chang, L.; Bonekamp, J.-B.; Meerholz, K.; Moule, A.; Moulé, A. Effect of Trace Solvent on the Morphology of P3HT:PCBM Bulk Heterojunction Solar Cells. *Adv. Funct. Mater.* **2011**, *21*, 1779-1787.

(53)   Mateker, W. R.; Douglas, J. D.; Cabanetos, C.; Sachs-Quintana, I. T.; Bartelt, J. A.; Hoke, E. T.; El Labban, A.; Beaujuge, P. M.; Frechet, J. M. J.; McGehee, M. D. Improving the long-term stability of PBDTTPD polymer solar cells through material purification aimed at removing organic impurities. *Energ. Environ. Sci.* **2013**, *6*, 2529-2537.

(54) Zhou, P.; Dong, Z.-H.; Rao, A. M.; Eklund, P. C. Reaction mechanism for the photopolymerization of solid fullerene C_{60}. *Chem. Phys. Lett.* **1993**, *211*, 337-340.

(55) Wohlers, M.; Bauer, A.; Belz, T. The mechanism of oxidation of fullerenes with molecular oxygen. *Preprints of Papers, Am. Chem. Soc., Div. Fuel Chem.* **1996**, *41*, 108-112.

(56) Dattani, R.; Gibson, K. F.; Few, S.; Borg, A. J.; DiMaggio, P. A.; Nelson, J.; Kazarian, S. G.; Cabral, J. T. Fullerene oxidation and clustering in solution induced by light. *J. Colloid Interface Sci.* **2015**, *446*, 24-30.

(57) Shogo, Y.; Junji, M.; Yasumasa, S.; Miho, S.; Liang, C.; Hiroyuki, S. MALDI-TOF MS Study of the Photooxidation of PCBM and Its Suppression by P3HT. *Chem. Lett.* **2015**, *44*, 339-341.

(58) Anselmo, A. S.; Dzwilewski, A.; Svensson, K.; Moons, E. Photodegradation of the electronic structure of PCBM and C_{60} films in air. *Chem. Phys. Lett.* **2016**, *652*, 220-224.

(59) Brumboiu, I. E.; Ericsson, L.; Hansson, R.; Moons, E.; Eriksson, O.; Brena, B. The influence of oxygen adsorption on the NEXAFS and core-level XPS spectra of the C_{60} derivative PCBM. *J. Chem. Phys.* **2015**, *142*, article 054306.

(60) Balch, A. L.; Costa, D. A.; Noll, B. C.; Olmstead, M. M. Oxidation of Buckminsterfullerene with *m*-Chloroperoxybenzoic Acid. Characterization of a C_s Isomer of the Diepoxide $C_{60}O_2$. *J. Am. Chem. Soc.* **1995**, *117*, 8926-8932.

(61) Ko Kyaw, A. K.; Gehrig, D.; Zhang, J.; Huang, Y.; Bazan, G. C.; Laquai, F.; Nguyen, T.-Q. High open-circuit voltage small-molecule *p*-DTS(FBTTh$_2$)$_2$:ICBA bulk heterojunction solar cells – morphology, excited-state dynamics, and photovoltaic performance. *J. Mater. Chem. A* **2015**, *3*, 1530-1539.

(62) Anthony, J. E. Small-Molecule, Nonfullerene Acceptors for Polymer Bulk Heterojunction Organic Photovoltaics. *Chem. Mater.* **2011**, *23*, 583-590.

(63) Collins, S. D.; Ran, N. A.; Heiber, M. C.; Nguyen, T.-Q. Small is Powerful: Recent Progress in Solution-Processed Small Molecule Solar Cells. *Adv. Energ. Mater.* **2017**, *7*, article 1602242.

(64) Chen, W.; Zhang, Q. Recent progress in non-fullerene small molecule acceptors in organic solar cells (OSCs). *J. Mater. Chem. C* **2017**, *5*, 1275-1302.

(65) Burlingame, Q.; Tong, X.; Hankett, J.; Slootsky, M.; Chen, Z.; Forrest, S. R. Photochemical origins of burn-in degradation in small molecular weight organic photovoltaic cells. *Energ. Environ. Sci.* **2015**, *8*, 1005-1010.

(66) Ray, B.; Nair, P.; Alam, M. Unraveling the Role of Morphology on Organic Solar Cell Performance. *arXiv* **2010**, *1011*, article 0956.

(67) Gaspar, H.; Figueira, F.; Pereira, L.; Mendes, A.; Viana, J. C.; Bernardo, G. Recent Developments in the Optimization of the Bulk Heterojunction Morphology of Polymer: Fullerene Solar Cells. *Materials (Basel)* **2018**, *11*, article 2560.

(68) Agostinelli, T.; Lilliu, S.; Labram, J. G.; Campoy-Quiles, M.; Hampton, M.; Pires, E.; Rawle, J.; Bikondoa, O.; Bradley, D. D. C.; Anthopoulos, T. D.; Nelson, J.; Macdonald, J. E. Real-Time Investigation of Crystallization and Phase-Segregation Dynamics in P3HT:PCBM Solar Cells During Thermal Annealing. *Adv. Funct. Mater.* **2011**, *21*, 1701-1708.

(69) Teuscher, J.; Brauer, J. C.; Stepanov, A.; Solano, A.; Boziki, A.; Chergui, M.; Wolf, J.-P.; Rothlisberger, U.; Banerji, N.; Moser, J.-E. Charge separation and carrier dynamics in donor-acceptor heterojunction photovoltaic systems. *Struct. Dyn.* **2017**, *4*, article 061503.

(70) Speller, E. M. The significance of fullerene electron acceptors in organic solar cell photo-oxidation. *J. Mater. Sci. Technol.* **2017**, *33*, 924-933.

(71)   Lee, J.; Kim, J. W.; Park, S. A.; Son, S. Y.; Choi, K.; Lee, W.; Kim, M.; Kim, J. Y.; Park, T. Study of Burn-In Loss in Green Solvent-Processed Ternary Blended Organic Photovoltaics Derived from UV-Crosslinkable Semiconducting Polymers and Nonfullerene Acceptors. *Adv. Energ. Mater.* **2019**, *9*, article 1901829.

(72)   Sung, Y.; Huang, Y.; Chien, F. A.; Tsao, C. Mechanism and Analysis of Thermal Burn-In Degradation of OPVs Induced by Evaporated HTL. *IEEE J. Photov.* **2019**, *9*, 694-699.

(73)   Yang, X.-Y.; Niu, M.-S.; Qin, C.; Bi, P.-Q.; Chen, Z.-H.; Feng, L.; Liu, J.-Q.; Hao, X.-T. Unraveling the unstable amorphous phase evolution effect on burn-in loss in polymer-fullerene solar cells. *Org. Electron.* **2019**, *71*, 156-163.

(74)   Weu, A.; Kress, J. A.; Paulus, F.; Becker-Koch, D.; Lami, V.; Bakulin, A. A.; Vaynzof, Y. Oxygen-Induced Doping as a Degradation Mechanism in Highly Efficient Organic Solar Cells. *ACS Appl. Energ. Mater.* **2019**, *2*, 1943-1950.

(75)   Li, H.; Tee, B. C. K.; Cha, J. J.; Cui, Y.; Chung, J. W.; Lee, S. Y.; Bao, Z. High-Mobility Field-Effect Transistors from Large-Area Solution-Grown Aligned C60 Single Crystals. *J. Am. Chem. Soc.* **2012**, *134*, 2760-2765.

(76)   Yu, H.; Cho, H.-H.; Cho, C.-H.; Kim, K.-H.; Kim, D. Y.; Kim, B. J.; Oh, J. H. Polarity and Air-Stability Transitions in Field-Effect Transistors Based on Fullerenes with Different Solubilizing Groups. *ACS Appl. Mater. Interfaces* **2013**, *5*, 4865-4871.

(77)   Facchetti, A. Semiconductors for organic transistors. *Mater. Today* **2007**, *10*, 28-37.

(78)   Chang, Y. C.; Kuo, M. Y.; Chen, C. P.; Lu, H. F.; Chao, I. On the Air Stability of *n*-Channel Organic Field-Effect Transistors: A Theoretical Study of Adiabatic Electron Affinities of Organic Semiconductors. *J. Phys. Chem. C* **2010**, *114*, 11595-11601.

(79)   Hasegawa, T.; Takeya, J. Organic field-effect transistors using single crystals. *Sci. Technol. Adv. Mater.* **2009**, *10*, article 024314.

(80)   Guo, X.; Baumgarten, M.; Müllen, K. Designing π-conjugated polymers for organic electronics. *Prog. Polym. Sci.* **2013**, *38*, 1832-1908.

(81)   Liu, S.; DeWeerd, N. J.; Reeves, B. J.; San, L. K.; Dahal, D.; Radha Krishnan, R. K.; Strauss, S. H.; Boltalina, O. V.; Lüssem, B. Doped N-Type Organic Field-Effect Transistors Based on Faux-Hawk Fullerene. *Adv. Electron. Mater.* **2019**, *5*, article 1900109.

(82)   San, L. K.; Bukovsky, E. V.; Larson, B. W.; Whitaker, J. B.; Deng, S. H. M.; Kopidakis, N.; Rumbles, G.; Popov, A. A.; Chen, Y.-S.; Wang, X.-B.; Boltalina, O. V.; Strauss, S. H. A faux hawk fullerene with PCBM-like properties. *Chem. Sci.* **2015**, *6*, 1801-1815.

(83)   Jang, S.; Son, D.; Hwang, S.; Kang, M.; Lee, S.-K.; Jeon, D.-Y.; Bae, S.; Lee, S. H.; Lee, D. S.; Kim, T.-W. Hybrid dielectrics composed of Al_2O_3 and phosphonic acid self-assembled monolayers for performance improvement in low voltage organic field effect transistors. *Nano Converg.* **2018**, *5*, article 20.

(84)   Kraus, M.; Richler, S.; Opitz, A.; Brütting, W.; Haas, S.; Hasegawa, T.; Hinderhofer, A.; Schreiber, F. High-mobility copper-phthalocyanine field-effect transistors with tetratetracontane passivation layer and organic metal contacts. *J. Appl. Phys.* **2010**, *107*, article 094503.

(85)   Klauk, H.; Zschieschang, U.; Pflaum, J.; Halik, M. Ultralow-power organic complementary circuits. *Nature* **2007**, *445*, 745-748.

(86)   Wei, P.; Oh, J. H.; Dong, G.; Bao, Z. Use of a 1*H*-Benzoimidazole Derivative as an *n*-Type Dopant and To Enable Air-Stable Solution-Processed *n*-Channel Organic Thin-Film Transistors. *J. Am. Chem. Soc.* **2010**, *132*, 8852-8853.

(87) Lüssem, B.; Keum, C.-M.; Kasemann, D.; Naab, B.; Bao, Z.; Leo, K. Doped Organic Transistors. *Chem. Rev.* **2016**, *116*, 13714-13751.

(88) Blochwitz, J.; Fritz, T.; Pfeiffer, M.; Leo, K.; Alloway, D. M.; Lee, P. A.; Armstrong, N. R. Interface electronic structure of organic semiconductors with controlled doping levels. *Org. Electron.* **2001**, *2*, 97-104.

(89) Canzler, T. W.; Denker, U.; Fadhel, O.; Huang, Q.; Rothe, C.; Werner, A. Application of redox doping in OTFTs. *Proc. SPIE* **2008**, *7054*, article 70540O.

(90) Liu, C.; Xu, Y.; Noh, Y.-Y. Contact engineering in organic field-effect transistors. *Mater. Today* **2015**, *18*, 79-96.

(91) Bittle, E. G.; Basham, J. I.; Jackson, T. N.; Jurchescu, O. D.; Gundlach, D. J. Mobility overestimation due to gated contacts in organic field-effect transistors. *Nature Commun.* **2016**, *7*, article 10908.

(92) Liu, S.; Lu, Y.-J.; Kappes, M. M.; Ibers, J. A. The Structure of the C60 Molecule: X-Ray Crystal Structure Determination of a Twin at 110 K. *Science* **1991**, *254*, 408-410.

(93) Paternò, G.; Warren, A. J.; Spencer, J.; Evans, G.; Sakai, V. G.; Blumberger, J.; Cacialli, F. Micro-focused X-ray diffraction characterization of high-quality [6,6]-phenyl-C_{61}-butyric acid methyl ester single crystals without solvent impurities. *J. Mater. Chem. C* **2013**, *1*, 5619-5623.

(94) Li, C.-Z.; Chueh, C.-C.; Yip, H.-L.; Zou, J.; Chen, W.-C.; Jen, A. K. Y. Evaluation of structure–property relationships of solution-processible fullerene acceptors and their *n*-channel field-effect transistor performance. *J. Mater. Chem.* **2012**, *22*, 14976-14981.

(95) Hummelen, J. C.; Knight, B. W.; Lepeq, F.; Wudl, F.; Yao, J.; Wilkins, C. L. Preparation and Characterization of Fulleroid and Methanofullerene Derivatives. *J. Org. Chem.* **1995**, *60*, 532-538.

(96)   Majewski, L. A.; Schroeder, R.; Voigt, M.; Grell, M. High performance organic transistors on cheap, commercial substrates. *J. Phys. D: Appl. Phys.* **2004**, *37*, 3367-3372.

(97)   Klauk, H. Will We See Gigahertz Organic Transistors? *Adv. Electron. Mater.* **2018**, *4*, article 201700474.

CHAPTER 5

SINGLE-CRYSTAL X-RAY DIFFRACTION STRUCTURES OF PAH/PAH(CF$_3$)$_n$ AND PAH/C$_{60}$F$_{18}$ CHARGE-TRANSFER CO-CRYSTALS

5.1. INTRODUCTION

The study of donor/acceptor charge-transfer co-crystals (CT/CCs) is an exciting area of research because of their possible applications in organic electronics.[1] CT/CCs have a number of advantages over normal organic semiconductor materials. For example, the crystallization process can exclude impurities which can decrease trap state concentration and non-linear voltage behavior in OFETs.[1,2] In addition, the ability to readily tune both structural and electronic properties make CT/CCs attractive materials with which to design molecular electronics.[3-5]

Although donor/acceptor co-crystals of PAHs and fluorinated PAHs (i.e., PAH(F)$_n$) have been studied for many years (e.g., co-crystals of perfluoronaphthalene with pyrene[6] and fluorene[7]), co-crystals of PAHs and PAH(CF$_3$)$_n$ derivatives have only recently been published. The only one published before 2019 was the structure of PYRN/AZUL-5-1, published in 2014 (AZUL-5-1 = 1,2,3,5,7-azulene(CF$_3$)$_5$).[8] In 2019 the structure of the donor/acceptor co-crystal PYRN/(ANTH-6-1)$_2$ was published in a paper in which the author of this dissertation is the first author (ANTH-6-1 = 2,3,6,7,9,10-anthracene(CF$_3$)$_6$).[9] The structure of this co-crystalline charge-transfer complex will be discussed in this chapter. The structures of seven additional PAH/PAH(CF$_3$)$_n$ donor/acceptor co-crystalline charge-transfer complexes were also published in 2019.[10] In a continuation of the investigation of PAH/PAH(CF$_3$)$_n$ CT/CCs, the author studied the structures of two new CT/CCs, PYRN/PHEN-5-1 and PYRN/PYRN-5-4, and they are also discussed in this chapter (PHEN-5-1 = 1,3,6,7,9-phenanthrene(CF$_3$)$_5$; PYRN-5-4 = 1,3,5,7,9-pyrene(CF$_3$)$_5$). These two structures have not yet been published, but a manuscript is in preparation in which the author of this dissertation will be the first author.

This chapter also includes the author's determination of three CT/CC structures with PAH donors and the fluorofullerene acceptor $C_{60}F_{18}$, viz. $(PYRN)_2/C_{60}F_{18}$, $CORO/(C_{60}F_{18})_2$, and $PERY/C_{60}F_{18}$ (PERY = perylene). Despite the fact that $C_{60}F_{18}$ is known to be a strong electron acceptor with an estimated electron affinity of 3.1–3.2 eV,[11] before this work no CT complexes of $C_{60}F_{18}$ had been studied, either in solution or in the solid state. The three $PAH/C_{60}F_{18}$ structures in this chapter are rare examples of CT/CCs with a 2-dimensional donor and a 3-dimensional, spheroidal acceptor.

5.2. PAH/PAH(CF₃)ₙ CHARGE-TRANSFER CO-CRYSTAL STRUCTURES

5.2.1. General comments

PAH/PAH$(CF_3)_n$ donor/acceptor CT/CCs were the focus of a 2019 paper by Castro et al.[10] The PAH donors included ANTH, CORO, PERY, and PYRN. The PAH$(CF_3)_n$ acceptors included trifluoromethyl derivatives of ANTH, AZUL, PYRN, and triphenylene. Except for the structure of PYRN/(ANTH-6-1)$_2$ discussed below, the PAH/PAH$(CF_3)_n$ CT complexes were found to pack in hexagonal arrays of columnar stacks, with alternating donors and acceptors that exhibit a high degrees of π–π overlap.[10]

It is well known that CF_3 substituents are prone to 2-, 3-, and 4-fold rotational disorder about their $C–CF_3$ bonds in solid state structures.[12] With the assistance of chemistry department crystallographer Brian S. Newell, the author conducted a search of the Cambridge Structural Database (CSD) in December 2018 and determined that there are nearly 40,000 published X-ray structures of organic molecules with at least one CF_3 group, and of these more than 20,000 exhibit rotational or positional CF_3 disorder. This is not surprising in view of the fact that barriers to rotation of CF_3 groups in solids are small, and the relative energies of different orientation minima can be even smaller. For example, the barrier to rotation of the CF_3 group in crystalline 3-PHEN(CF_3), which exhibits a 2-fold rotational disorder,[13] is 11.5(7) kJ mol^{-1}.[14] In the isolated molecule, the DFT-predicted barrier is only 1.7 kJ mol^{-1}.[13] (The way that the CSD interprets disordered groups is by showing the minor part of the disorder as non-bonded atoms. Therefore,

we searched for structures with at least one CF_3 group and at least three non-bonded F atoms. The search also returned several positive hits if the CF_3 group is positionally disordered with another group in the molecule.) It should be noted that lowering the data collection temperature can decrease the rotational disorder but the degree of disorder is largely affected by the structural intermolecular forces interacting with the CF_3 group. For example, in all of the structures reported here the temperature for the collection was 100 K.

5.2.2. The Structure of PYRN/PYRN-5-4

A thermal ellipsoid plot of PYRN/PYRN-5-4 is shown in Figure 5-1. The structure confirms that PYRN-5-4 is the isomer 1,3,5,7,9-PYRN$(CF_3)_5$, which distinguishes it from three other isomers of PYRN$(CF_3)_5$.[15,16] Figure 5-2 shows additional drawings of PYRN/PYRN-5-4. The upper drawing shows the infinite D/A/D/A stacking of PYRN donor (D) and PYRN-5-4 acceptor (A) molecules along the diagonal of the crystallographic *ac* plane. If the center of the PYRN-5-4 molecule central C–C bond is located at the unit cell origin ([0,0,0]), the center of the third PYRN-5-4 molecule along the stack is located at [1,0,1], a distance of 14.60 Å. In the similar structure of PYRN/PYRN-6-2, the distance between every third PYRN-6-2 acceptor center is 14.23 Å (in this case the donors and acceptors are stacked along the crystallographic *a* axis; PYRN-6-2 = 1,2,4,6,8,9-PYRN$(CF_3)_6$).[10]

The aromatic cores of both the PYRN donor and the PYRN-5-4 acceptor are essentially planar. The average out-of-plane displacement (OOP) of the PYRN C(sp^2) atoms from their least-squares plane is 0.012 Å (the range is −0.022 to +0.022 Å). The average OOP of the PYRN-5-4 C(sp^2) atoms from their least-squares plane is 0.032 Å (the range is −0.066 to +0.073 Å). The dihedral angles of the PYRN-5-4 least-squares plane to the PYRN C(sp^2) least-squares planes on either side of the PYRN-5-4 least-squares plane are 0.7° and 1.4°. The D/A/D/A... stacks are packed in the usual hexagonal array (not shown).

The lower drawings in Figure 5-2 show the areas of donor/acceptor π–π overlap on either side of the PYRN-5-4 acceptor. The PYRN donor is oriented the same way and is in the plane of the

page in both drawings. The shaded area of the D/A overlap is different on the two sides of the acceptor. Nevertheless, there are eight acceptor $C(sp^2)$ atoms that overlap the donor π system on *both* sides of the donor. The average OOPs of the acceptor $C(sp^2)$ atoms from the PYRN $C(sp^2)$ least-squares plane are 3.578 Å on one side (3.532–3.604 Å) and 3.510 Å on the other side (3.476–3.566 Å). These average D/A OOPs are similar to those in seven other stacked PAH/PAH(CF$_3$)$_n$ CT/CC structures, which ranged from 3.49 to 3.61 Å.[10] However, they are ca. 0.3 Å larger than the average OOP for a PYRN D/A CT/CC structure with a planar acceptor (i.e., all acceptor atoms in a plane), such as the 3.24 Å average OOP in PYRN/tetrafluorobenzoquinone.[17] This may be due to the steric requirements of the CF$_3$ groups in PYRN-5-4 and the other PAH acceptors with multiple CF$_3$ groups.

5.2.3. The Structure of PYRN/PHEN-5-1

A thermal ellipsoid plot of PYRN/PHEN-5-1 is shown in Figure 5-3. The $C(sp^2)$ atoms of the PYRN molecule are co-planar to an average OOP of 0.023 Å (−0.043 to +0.045 Å), and the $C(sp^2)$ atoms of the PHEN-5-1 molecule are co-planar to an average OOP of 0.013 Å (−0.027 to +0.025 Å). The aromatic cores of the PYRN and PHEN-5-1 molecules are essentially parallel. The dihedral angle between the PYRN and PHEN-5-1 $C(sp^2)$ least-squares planes is only 0.5°.

The PYRN and PHEN-5-1 molecules are arranged in D/A/D/A stacks along the crystallographic b axis, as shown in Figure 5-4. There are seven donor $C(sp^2)$ atoms that overlap the acceptor π system, with an average OOP of 3.521 Å (3.457–3.553 Å), as also shown in Figure 5-4. This is similar to the average OOPs in PYRN/PYRN-5-4. The major axes of PYRN and PHEN-5-1 are rotated 15.4° with respect to one another.

Parallel D/A/D/A... stacks are packed in a hexagonal array, as shown in Figure 5-5. The parallel-stack packing in PYRN/PHEN-5-1 stands in contrast to the structures of PHEN-5-1 itself[15] and PYRN itself,[18] both of which exhibit stacks oriented ca. 90° to one another in herringbone type patterns.

5.2.4. The Structure of PYRN/(ANTH-6-1)$_2$

A thermal ellipsoid plot showing the PYRN donor and ANTH-6-1 acceptor in the X-ray co-crystal structure of PYRN/(ANTH-6-1)$_2$ is shown in Figure 5-6. Unlike the stacked structures described above, this structure consists of discrete, centrosymmetric [ANTH-6-1/PYRN/ANTH-6-1] ([A/D/A]) triplet complexes of nearly parallel molecules (the donor/acceptor least-squares-planes dihedral angle is 1.6°). Drawings of the triplet complex, the PYRN/ANTH-6-1 π–π overlap, and the way that they pack in the lattice are shown in Figure 5-7.

The discrete [ANTH-6-1/PYRN/ANTH-6-1] ([A/D/A]) complexes of nearly-parallel molecules are packed in herringbone sandwich layers in crystallographic [1,0,1] planes such that the PYRN centroids (⊙) are rigorously co-planar. The [A/D/A] complexes in each layer form a pseudo-square net depicted with dashed lines in Figure 5-7: all ⊙···⊙ distances are 12.37 Å and the ⊙···⊙···⊙ angles that define the nearly-square rhombus are 81.4 and 98.6°. The PYRN least-square planes are tilted 84.6° from the 101 plane; the PYRN least-square planes in neighboring [A/D/A] sandwiches in the [1,0,1] planes are tilted 81.4° relative to one another. The layers of [A/D/A] complexes above and below the layer shown in Figure 5-7 are displaced by *b*/2 (the lower right drawing in Figure 5-7 is oriented so that the *b* axis is the long axis of the page).

The distance between the ANTH-6-1 centroid and the PYRN centroid is 3.516 Å. There are seven acceptor C(sp^2) atoms that overlap the donor π system, with an average OOP of 3.621 Å and a range of 3.523–3.732 Å. This is a wider range of π–π overlap OOPs than in the other PAH/PAH(CF$_3$)$_n$ CT/CC structures because the ANTH-6-1 aromatic core is bent (i.e., domed). Let us define the bend angle, θ, as shown in Figure 5-8. It is the supplementary angle formed by bending the two outer benzenoid rings of ANTH or ANTH derivatives at a hypothetical hinge connecting the central C(sp^2) atoms, C9 and C10. Figure 5-8 shows that θ is 13.5° for the ANTH-6-1 molecule in the structure of PYRN/(ANTH-6-1)$_2$.

The bend angle, as defined above, can be generalized for acenes with an odd number of rings. For pentacene (PENT) and its derivatives, θ will be defined as the supplementary angle formed by

bending the two outer naphthalenoid portions of PENT at a hypothetical hinge connecting the central $C(sp^2)$ atoms, which for PENT are C6 and C13. Interestingly, there are two X-ray structures of 6,13-PENT(CF$_3$)$_2$. In the $P2_1/c$ polymorph, θ is 0.0° (i.e., the PENT aromatic core is flat).[19] In the $P2_1/n$ polymorph, the PENT aromatic core is bent and θ is 16.8°, as shown in Figure 5-8.[20]

5.2.5. The Structure of ANTH-6-1 and the Connection Between Acene Aromatic Core Bending and R$_F$ Conformations in 9,10-ANTH(R$_F$)$_2$ and 6,13-PENT(R$_F$)$_2$ Derivatives

After determining the structure of PYRN/(ANTH-6-1)$_2$, with its bent, θ = 13.5° ANTH-6-1 molecule, and after finding two X-ray structures of PENT(CF$_3$)$_2$ in the literature, one flat[19] and one bent,[20] the author decided to investigate the structure of ANTH-6-1 in the absence of a PAH donor molecule to see if bending of the ANTH-6-1 aromatic core was a general phenomenon or was unique to the structure of PYRN/(ANTH-6-1)$_2$. A preliminary structure of ANTH-6-1 was published in 2013, but a more precise structure with as little disorder as possible was required for the comparison to be meaningful. Therefore, the author solved and refined the structure of a synchrotron radiation X-ray diffraction data set collected by another member of the Strauss-Boltalina group. The results and analysis in this section of Chapter 5 were published in 2019, with the author of this dissertation as first author.[9]

Drawings of the structure of ANTH-6-1 are shown in Figure 5-9. It can be seen that the bend angle θ is 7.4°, only about half of the value in PYRN/(ANTH-6-1)$_2$. There are three other CT/CC structures with ANTH-6-1 as the acceptor, ANTH/ANTH-6-1, PERY/ANTH-6-1, and (CORO)$_2$/ANTH-6-1, and in all three structures the ANTH-6-1 core is flat and θ = 0.0°.[10] These results, in addition to the two polymorphs of 6,13-PENT(CF$_3$)$_2$, initially suggested that crystal packing forces were responsible for bending the acene aromatic cores in ANTH-6-1, PYRN/(ANTH-6-1)$_2$, and $P2_1/n$ 6,13-PENT(CF$_3$)$_2$ relative to the flat cores they have in the other structures and the presumably flat cores they would have in the isolated (i.e., gas-phase) molecules.

However, DFT calculations reported in the 2017 Yamada et al. paper predicted that the lowest energy structure for an isolated 6,13-PENT(CF$_3$)$_2$ molecule is bent, with θ = 19.1°, an even larger

angle, by 2.3°, than exhibited by the molecule in the $P2_1/n$ polymorph.[20] Furthermore, the bent conformation was predicted to be 9.0 kJ mol^{-1} more stable than the flat conformation with $\theta =$ 0.0°.[20] At this point, collaborator Dr. Alex Popov was asked to calculate the lowest energy conformation of ANTH-6-1, and he also found that the $\theta = 0.0°$ was not the lowest energy structure. Instead, the structure of ANTH-6-1 with $\theta = 17.5°$ was 5.7 kJ mol^{-1} more stable than when the molecule was forced to adopt the $\theta = 0.0°$ conformation. (A previous DFT optimization of ANTH-6-1 reported did not report the bend angle,[21] but when the coordinates of that structure were analyzed for this work it was found that $\theta = 13.8°$.) It became clear that the stable, *intrinsic* molecular structures of ANTH-6-1 and 6,13-PENT(CF$_3$)$_2$ have significantly bent aromatic cores. Based on these results, the author of this dissertation concluded that crystal packing forces, rather than being responsible for *bending* the acene cores in ANTH-6-1, PYRN/(ANTH-6-1)$_2$, and $P2_1/n$ 6,13-PENT(CF$_3$)$_2$, are actually responsible for *flattening* the acene cores in $P2_1/c$ 6,13-PENT(CF$_3$)$_2$ and the other ANTH-6-1 CT/CC structures.

When all of these X-ray and DFT optimized structures were examined next to each other, as shown in Figure 5-10, a clear pattern emerged. When the CF$_3$ groups on the acene central C(sp^2) atoms are eclipsed with respect to one another, as in DFT and $P2_1/n$ 6,13-PENT(CF$_3$)$_2$,[20] DFT ANTH-6-1 (this work), and the ANTH-6-1 molecule in the X-ray structure of PYRN/(ANTH-6-1)$_2$ (this work), the acene core is bent and $\theta = 13.5–19.1°$. When the CF$_3$ groups are staggered, as in $P2_1/c$ 6,13-PENT(CF$_3$)$_2$[19] and the ANTH-6-1 molecule in the X-ray structure of ANTH/ANTH-6-1 and two other PAH/ANTH-6-1 CT/CC X-ray structures,[10] the acene core is flat and $\theta = 0.0°$. When the CF$_3$ groups are partway between eclipsed and staggered, as in the X-ray structure of ANTH-6-1 (this work), the core is bent, but not as much as when the CF$_3$ groups are staggered (θ is only 7.4°).

Additional DFT calculations by Dr. Popov are summarized in the graphs shown in Figure 5-11. The results show that the energy of unsubstituted ANTH is raised when the aromatic core is bent by any angle, and its relative energy is 18 kJ mol^{-1} when θ is 17.0°. In contrast, the energy of

DFT-optimized 9,10-ANTH(CF$_3$)$_2$ (a hypothetical molecule) is lowest when θ is 17.0° and is 10.5 kJ mol^{-1} when θ is 0.0°.

The generality of the connection between ANTH core bending and the eclipsed or staggered conformations of CF$_3$ or CF$_2$R$_F$ conformations is further supported by five related X-ray structures that were found in a literature search (R$_F$ = n-C$_x$F$_{2x+1}$). These are 2,6,9,10-ANTH(n-C$_8$F$_{17}$)$_4$, with staggered central CF$_2$R$_F$ groups and θ = 0.0°,[22] 2,6-bis((4-methoxyphenyl)ethynyl)-9,10-ANTH(CF$_3$)$_2$, with staggered CF$_3$ groups and θ = 0.0°,[23] 2-phenylethynyl-9,10-ANTH(CF$_3$)$_2$, with eclipsed CF$_3$ groups and θ = 14.6°,[23] and 9,10-ANTH(CF$_3$)(n-C$_8$F$_{17}$) and 9,10-ANTH(CF$_3$)(n-C$_6$F$_{13}$), both with eclipsed central groups and both with θ = 18.0°.[23]

Note that the definition of θ and the connection between the magnitude of θ and the relative conformations of the central CF$_3$ and/or CF$_2$R$_F$ groups in acene derivatives was developed in the course of the work reported in this dissertation. Neither the degree of acene core bending (or lack thereof) nor the conformations of the central groups in the X-ray structures described above were discussed in the papers reporting those structures. All of these were determined in this work using the fractional coordinates for the X-ray structures in the crystallographic information files for the published structures, which were downloaded from the Cambridge Crystallographic Data Centre.

5.2.6. PAH/PAH(CF$_3$)$_n$ Structures: Summary and Conclusions

The structure of ANTH-6-1 and three D/A CT/CC structures PYRN/(ANTH-6-1)$_2$, PYRN/PYRN-5-4, and PYRN/PHEN-5-1 were determined and their packing was described. All four of the structures suffered from some form of trifluoromethyl disorder, either positional or rotational or both. Trifluoromethyl rotational disorder is not surprising as a survey of the frequency with which CF$_3$ disorder occurs in the structures deposited in the CCDC revealed that more than half of the trifluoromethyl containing crystal structures suffer from some form of CF$_3$ disorder.

Two of the PAH/PAH(CF$_3$)$_n$ CT/CCs, PYRN/PHEN-5-1 and PYRN/PYRN-5-4 pack similarly in overlapping stacks of D/A/D/A… with average OOPs between the donor and acceptor molecules ranging between 3.521 and 3.578 Å with between 7 and 8 C(sp^2) donor atoms

overlapping the acceptor molecules. Close π–π distances and a high degree of π–π overlap between donor and acceptor is suspected to result in better charge transport in potential organic electronic applications and so these figures of merit are promising. However, other PYRN/A CT/CCs, such as PYRN/tetrafluorobenzoquinone,[17] pack with smaller OOPs apparently as a result of the steric bulk of the CF_3 groups.

Additionally, the third PAH/PAH(CF$_3$)$_n$ CT/CC, PYRN/(ANTH-6-1)$_2$, structure was determined and the packing was reported. This CT/CC packed as A/D/A triplet complexes oriented in herringbone layers. While the number of overlapping donor C(sp^2) atoms is seven as in PYRN/PHEN-5-1, the OOPs between the A/D/A molecules range from 3.523 to 3.732 Å due to the bending of the ANTH-6-1 acceptor. An analysis of both the ANTH-6-1 structure as well as the acceptor molecules in the PYRN/(ANTH-6-1)$_2$ CT/CC structure revealed both molecules were bent with bend angles, θ, of 7.4° and 13.5°. A literature search for other bent acene derivatives revealed this phenomenon also occurred in a number of other 9,10-ANTH(R$_F$) and 6,13-PENT(R$_F$) structures, with θ as large as 18°.[23] DFT calculations by collaborator Dr. Alexey Popov revealed that this phenomenon was not due to packing forces, as had been originally suspected, but instead the bent structures were the lowest relative energy conformations based on the results from the analysis of the optimization of the 9,10-ANTH(CF$_3$) and 6,13-PENT(CF$_3$) DFT-structures. The effect was found to be dependent on the confirmation of the R$_F$ group, either staggered or eclipsed, the acceptors were flat or bent respectively and the flat and staggered arrangements reported in some crystal structures was due to packing forces.

5.3. PAH/C$_{60}$F$_{18}$ CHARGE-TRANSFER CO-CRYSTAL STRUCTURES

5.3.1. General comments

The fluorinated fullerene $C_{60}F_{18}$ was first prepared in macroscopic quantities in 1996[24] following its observation in 1995 by Olga V. Boltalina in the Thermochemistry Laboratory at Moscow State University in the mass spectrum of the volatile products produced from a mixture of C_{60} and K_2PtF_6 heated in a Knudsen cell attached to the mass spectrometer.[25] It is a very polar

molecule, with the 18 F atoms on a set of contiguous fullerene $C(sp^3)$ atoms confined to one hemisphere of C_{60},[26,27] as shown in Figure 5-12. This figure also includes a Schlegel diagram showing the IUPAC fullerene numbering scheme for this derivative. (A Schlegel diagram is a planar graph of a polyhedron drawn without any of its edges crossing.[28])

One interesting fact about $C_{60}F_{18}$ is its 45 min retention time on a Nacalai Tesque Buckyprep HPLC column (toluene eluent).[29] This stands in contrast to the short retention times (same column, same eluent) of C_{60} (7 min)[29] and fluorofullerenes with 24 or more F atoms distributed symmetrically on both hemispheres, T_h-$C_{60}F_{24}$ (2.9 min)[30] and C_3-$C_{60}F_{36}$ (3.5 min).[31] The Buckyprep column stationary phase contains PYRN moieties (specifically pyrenylpropyl groups).[32] Although X-ray diffraction studies of crystals of $C_{60}F_{18}$ containing aromatic solvents such as toluene, xylenes, and hexamethylbenzene have been published,[33] before this work no co-crystal structure of $C_{60}F_{18}$ with any PAH had been reported.

5.3.2. The Structure of PERY/$C_{60}F_{18}$

Drawings of this X-ray crystal structure are shown in Figures 5-14, 5-15, 5-16, and 5-17. It has a 1/1 D/A stoichiometry. Both molecules are located on special positions, PERY on an inversion center and $C_{60}F_{18}$ on a two-fold axis that is parallel to the crystallographic a axis. Therefore, only half of the atoms of each molecule are unique.

The structure consists of alternating close-packed layers of $C_{60}F_{18}$ and close-packed layers of PERY molecules, as shown in Figures 5-14 and 5-15. Let the centroids of the 60 C atoms of the fullerene be defined by the letter S, and the centroids of the 20 C atoms of the PERY molecules be defined by the letter P, then the least-squares plane of the S and P centroids are individually rigorously co-planar and the two least-squares planes are perfectly parallel to one another. The perpendicular distance between those planes is 5.950 Å. The S···S distances are 9.848 (×2), 10.839 (×2), and 11.499 (×2) Å. The P···P distances are 10.338 (×4) and 11.499 (×2) Å. If one connects the $C_{60}F_{18}$ 60 C atom centroid to the centroid of the $C_{60}F_{18}$ benzenoid ring, that vector is tilted 69°

from four of their nearest neighbor molecules in the plane and parallel to the two nearest neighbor molecules in the plane.

The planes of $C_{60}F_{18}$ molecules and PERY molecules are parallel to the crystallographic ac planes and are stacked in the direction of the crystallographic b axis of the orthorhombic unit cell, as shown in Figure 5-16. The PERY molecules are "sandwiched" between two $C_{60}F_{18}$ molecules in two planes, as shown in Figure 5-17, and make close approaches to a fullerene hexagon in each of those two $C_{60}F_{18}$ molecules. The PERY least-squares plane is in the plane of the page in Figure 5-17, and the two fullerene hexagons that are shown are both tilted 14.1° from that plane and are parallel to one another.

There is a parallel between this structure and the structure of the hexamethylbenzene (HMB) solvate of $C_{60}F_{18}$.[33] In that structure, there are planes of $C_{60}F_{18}$ molecules and planes of HMB molecules in crystallographic ab planes. The planes are stacked in the direction of the crystallographic c axis in the orthorhombic unit cell, and the planes of the molecules are 5.45 Å apart.[33]

5.3.3. The Structure of CORO/($C_{60}F_{18})_2$

Drawings of this X-ray crystal structure are shown in Figures 5-18 and 5-19. It has a 1/2 D/A stoichiometry. There are two unique $C_{60}F_{18}$ molecules with nearly identical structures. The CORO molecule is located on a crystallographic center of inversion resulting in two rotationally disordered half-CORO molecules on either side of the two neighboring $C_{60}F_{18}$ molecules. Layers of CORO molecules are separated by double layers of $C_{60}F_{18}$ molecules. The layers are parallel to the crystallographic bc plane and are stacked parallel to the a axis. The CORO centroid planes and $C_{60}F_{18}$ centroids planes are rigorously parallel. The perpendicular distance between the CORO plane and the $C_{60}F_{18}$ close-packed planes above and below is 6.486 Å.

The CORO $\odot\cdots\odot$ distances are 10.325 × 4 and 11.093 × 2 Å. The average CORO $\odot\cdots\odot$ distance is 10.581 Å, which is nearly the same as the 10.645 Å average $\odot\cdots\odot$ distance between the $C_{60}F_{18}$ molecules in the close-packed planes in that structure. The geometric constraints of the

lattice requires that the area of the close-packed hexagonal array of CORO centroids must be equal to the area of the close-packed hexagonal array of $C_{60}F_{18}$ centroids. The CORO molecules are tilted with respect to the plane of their centroids by 21.8°. The dihedral angle between the planes of adjacent CORO molecules are either 0.00° or 27.2°.

The structure of solvent-free $C_{60}F_{18}$ was first published by Goldt, Boltalina, et al. in 2002.[26] A much higher resolution structure was published in the 2007 charge-density paper by Hübschle, Luger, Boltalina, et al.[27] The space group is *Cc*, which is non-centric. Therefore, crystals of solvent-free $C_{60}F_{18}$ are polar, but this was not discussed in either paper. The double layers of $C_{60}F_{18}$ molecules in the structure of CORO/$(C_{60}F_{18})_2$ can be compared with the layers of $C_{60}F_{18}$ molecules in the structure of solvent-free $C_{60}F_{18}$. The comparison is shown in Figures 5-20. The $C_{60}F_{18}$ molecules in the solvent-free structure are not packed as tightly in the plane, shown in Figure 5-20 *left* (average $\odot\cdots\odot$ = 11.115 Å), as in the close packed planes of fullerenes in the structure of CORO/$(C_{60}F_{18})_2$ (average $\odot\cdots\odot$ = 10.655 Å). However, the $\odot\cdots\odot$ distances between the central molecule in solvent-free $C_{60}F_{18}$ to molecules in planes above and below the plane shown above are 9.601×2 and 11.273×4 Å (average = 10.716 Å). The perpendicular distance between planes of $C_{60}F_{18}$ molecules in the solvent-free structure is 8.276 Å. The perpendicular distance between the planes of $C_{60}F_{18}$ molecules in CORO/$(C_{60}F_{18})_2$ is 9.278 Å. The difference in interplanar spacing is ca. 1.0 Å (9.278 Å − 8.276 Å).

These differences are clearly a result of the different orientations of the molecules with respect to the close-packed planes. This can be seen in the drawings in Figure 5-21. In solvent-free $C_{60}F_{18}$, the benzenoid hexagon is tilted 29.4° from the plane of the C_{60} centroids, allowing the layers to approach more closely than in CORO/$(C_{60}F_{18})_2$, in which the fullerene benzenoid hexagon is nearly perpendicular to the close-packed layer (the tilt angle is 88.4°). In solvent-free $C_{60}F_{18}$, the fullerene dipoles are all oriented in the same general direction, resulting in the formation of polar crystals. This is also true for the double layers of $C_{60}F_{18}$ molecules in CORO/$(C_{60}F_{18})_2$. However, in the co-crystal structure the dipoles in alternate double layers point in opposite directions.

5.3.4. The Structure of $(PYRN)_2/C_{60}F_{18}\cdot CH_2Cl_2$

This structure is significantly different than the CT/CC structures of $PERY/C_{60}F_{18}$ and $CORO/(C_{60}F_{18})_2$ in that neither the PYRN donors nor the $C_{60}F_{18}$ acceptors form layers. Drawings of the structure are shown in Figures 5-22 and 5-23. There are ribbons of fullerenes in a triangular array, with $\odot\cdots\odot$ distances of 10.258 ($\times$ 2) and 13.374 Å. The fullerene centroids in the ribbons are rigorously co-planar. There are ribbons 1.096 Å above and 1.096 Å below each ribbon, forming a stairstep array of ribbons that can be thought of as forming a corrugated plane of fullerenes. Two ribbons with centroid planes 1.096 Å apart (i.e., the perpendicular distance between the ribbon planes is 1.096 Å) are shown in Figure 5-22.

The PYRN molecules do not form planar arrays, and there are no PYRN–PYRN π–π overlaps. Each $C_{60}F_{18}$ molecule is surrounded by a complex array of three other $C_{60}F_{18}$ molecules ($\odot\cdots\odot$ = 10.258 ($\times$ 2) and 13.374 Å) and nine PYRN molecules ($\odot\cdots\odot$ = 6.526, 6.586, 11.017, 11.323, and 11.796 Å to one unique PYRN and 6.540, 7.980, 9.668, and 10.699 Å to the other unique PYRN molecule; the PYRN centroids are defined by the centroid of the central C–C bond). Some drawings are shown in Figure 5-23. The drawing on the upper left corresponds to a $C_{60}F_{18}$ molecule nearly in the center of a unit cell (centroid coordinates [0.5, 0.59836, 0.50978]). The drawing on the upper right is an array of PYRN molecules, showing the lack of any π–π overlap. The drawings at the bottom of Figure 5-23 are rotated versions of the upper left drawing.

Figure 5-24 shows the most interesting aspect of the structure of $(PYRN)_2/C_{60}F_{18}\cdot CH_2Cl_2$. The upper and middle sets of drawings show the three PYRN molecules (H atoms omitted for clarity) and the three fullerene hexagons with which they form π–π overlap interactions. In each of the upper set of drawings, the PYRN $C(sp^2)$ atoms are colored blue and the fullerene hexagon $C(sp^2)$ atoms, labeled with their IUPAC locants, are colored brown. In each of the middle set of drawings, the perpendicular distances, in Å, of the fullerene hexagon $C(sp^2)$ atoms to the PYRN least-squares plane are indicated. The red hexagons in the Schlegel diagram indicate the three fullerene hexagons that have π–π overlap interactions with the three PYRN molecules.

The possibility of strong π–π interactions of *multiple* PYRN molecules with a $C_{60}F_{18}$ molecule may be the reason that the retention time of $C_{60}F_{18}$ on an HPLC column with a PYRN stationary phase is so much longer than the retention times for C_{60}, $C_{60}F_{24}$, and $C_{60}F_{36}$ on the same column with the same eluent, as discussed above in Section 5.3.1.

5.3.5. PAH/$C_{60}F_{18}$ Structures: Summary and Conclusions

Three PAH/$C_{60}F_{18}$ CTCC structures with PAH donors varying in size from the four fused ring system of PYRN to the large seven fused ring system of CORO are reported. Their packing and unique structural features have been discussed. All three of the structures have different D/A stoichiometric ratios showing the variability in the structure orientations and packing as a function of the D/A ratio. Most interesting is the apparent relationship between the donor PAH size and packing. In the PYRN structure, the smallest PAH donor used, the structure has complex packing with the donor PAH molecules oriented in a complex array of $C_{60}F_{18}$ and PYRN molecules allowing three PYRN molecules to coordinate to a single $C_{60}F_{18}$ molecule resulting in three separate π–π interactions. These interactions clearly result in an overall larger interaction than the possible π–π interactions between PYRN molecules of which there are none. This strong affinity between PYRN and $C_{60}F_{18}$ is believed to be responsible for the long t_R for $C_{60}F_{18}$ on the PYRN based stationary phase of the Buckyprep column. In contrast, the larger donor PAHs, PERY and CORO, form ordered stacked layers of D/A/D and D/A/A/D layers. This change in packing orientation is apparently in response to the steric differences between PYRN and the larger PAHs.

5.4. MATERIALS AND METHODS

5.4.1. Reagents and general procedures

The compounds ANTH-6-1, PHEN-5-1, and PYRN-5-4 were prepared by former group member Karlee P. Castro. Pyrene (98%, Alfa Aesar) and ACS grade dichloromethane (DCM) were used as received. Single crystals of PYRN/PHEN-5-1, PYRN/PYRN-5-4, PYRN/(ANTH-6-1)$_2$, and ANTH-6-1 were grown by slow evaporation of DCM solutions.

The following reagents and solvents were obtained from the indicated sources and were used as received or were purified where indicated: PYRN (98%, Alfa Aesar); CORO (95+%, TCI); PERY (98%, Alfa Aesar); $C_{60}F_{18}$ prepared by Dr. Boltalina and used as received; DCM (99%, Fisher Scientific); 1,2-dichloroethane (98+%, Fisher Scientific); ANTH-6-1 (98+%, prepared as previously described[34]).

5.4.2. X-ray crystallography for PAH/PAH(CF$_3$)$_n$

Synchrotron radiation X-ray diffraction data for PYRN/PHEN-5-1, PYRN/PYRN-5-4, and ANTH-6-1 were collected at the Advanced Photon Source at Argonne National Laboratory on ChemMatCARS Sector 15 beamline, using a diamond 111 monochromator, an X-ray wavelength of 0.41328 Å, a Bruker D8 goniometer, and multi-scan absorption corrections. Unit cell parameters were determined by the least squares fit of the angular coordinates of all reflections. Integrations of all frames were performed using APEX III software, and the structures were solved using SHELXTL/OLEX 2 software.

X-ray diffraction data for PYRN/(ANTH-6-1)$_2$ were collected using a Bruker Kappa APEX 2 CCD diffractometer equipped with a sealed X-ray tube (λ=0.71073 Å) and a graphite monochromator in the X-ray laboratory in the Department of Chemistry at Colorado State University. The data reduction was performed with the Bruker APEX 2 suite of software, a semiempirical absorption correction was applied using SCALE, and the structure was solved and refined using SHELXTL/OLEX 2 software.

Crystallographic data collection and final refinement parameters for PYRN/PHEN-5-1 and PYRN/PYRN-5-4 are listed in Table 5-1. Crystallographic data collection and final refinement parameters for PYRN/(ANTH-6-1)$_2$ and ANTH-6-1 are listed in Table 5-2.

The ANTH-6-1 structure has a completeness of only 93.8%. This is a common issue with data sets collected at the Advanced Photon Source with low symmetry space groups (in this case $P\overline{1}$) due to instrument time constraints associated with the synchrotron source. The resolution cut-off

was optimized for the highest completeness possible. The PYRN(ANTH-6-1)$_2$ co-crystal structure has a disordered CF$_3$ group on the C9 position of the unique ANTH-6-1 molecule. The disorder appears to be due to a combination of rotational and positional disorder brought on by the flexing of the ANTH aromatic core. The angle of the C9–CF$_3$ bond was determined to be 15° based on the generation of a mean plane for the central ring and calculating the angle of the CF$_3$ group with respect to this plane using C9 as the third point of a right triangle. This deviation from the plane resulted in small amounts of flexing in the position of the core generating noticeable changes in the position of the F atoms on the disordered CF$_3$ group. However, there was not enough electron density to support a second carbon to build a positional disorder model because this part of the disorder was <10% based on the free variable for the F atoms. Therefore, the positional disorder was ignored and the CF$_3$ group was modeled as a simple 2-fold rotational disorder refined on a free variable, resulting in overly acute F–C–F angles and a combination of slightly elongated or shortened C–F bond distances for the disorder model depending on whether the fluorines were close to the electron density above or in the middle of the CF$_3$ group. To deal with this, the C–F distances and F–C–F angles were constrained using the DFIX and DANG commands. The thermal ellipsoids, as a result of this complex disorder, were prolated beyond acceptable ADP max/min ratios and were further constrained using a combination of ISOR and EADP commands as required to minimize the unaccounted for electron density while still generating a structure which made "good" chemical sense. As a result, no analysis of the bond distances or angles for the disordered CF$_3$ group is warranted.

5.4.3. X-ray crystallography for PAH/C$_{60}$F$_{18}$

Crystals of PAH/C$_{60}$F$_{18}$ CT complexes suitable for diffraction were grown by slow evaporation of dichloromethane solutions. Diffraction data were collected at the Advanced Photon Source at Argonne National Laboratory on beamline 15ID-D, using a diamond 111 monochromator, an X-ray wavelength of 0.41328 Å, a Bruker D8 goniometer, and multi-scan absorption corrections. Unit cell parameters were determined by the least squares fit of the angular coordinates of all

reflections. Integrations of all frames were performed using APEX III software, and the structures were solved using SHELXTL/OLEX 2 software. Crystallographic data collection and final refinement parameters for all three structures are listed in Table 5-3.

The $CORO/(C_{60}F_{18})_2$ CT/CC structure was rotationally disordered about two CORO positions. In order to model the presumed two-part disorder, ISOR and SAME commands were used to build the second half-coronene moiety. There is a large residual electron density in the structure, 1.8 e^- $\mathring{A}^{-3}$, which is believed to be due to a disordered DCM molecule occupying space between the fullerenes. Unfortunately, the SQUEEZE function was not able to remove this residual electron density, apparently due to its close proximity between the two fullerenes. The $(PYRN)_2/C_{60}F_{18}$ crystal has an inversion twin that was modeled using the inversion twin law with a BASF value of 0.32. The CT/CC structure of $PERY/C_{60}F_{18}$ differs from the other two in that it is a 1/1 donor/acceptor structure and exhibits no disorder.

5.4.4. UV-vis spectroscopy of $PAH/C_{60}F_{18}$

The author attempted to find charge-transfer maxima for the CT complexes in UV-vis spectra of DCM solutions of the $PAH/C_{60}F_{18}$ mixtures using an Agilent 8453 UV-visible spectrophotometer. No meaningful results were obtained due to a combination of the background spectral bands of $C_{60}F_{18}$, the apparently small charge-transfer complex equilibrium constants, and the limited solubility of the CT complexes. However, photographs of mixtures of $C_{60}F_{18}$ and CORO, PYRN, or PERY were clearly a different color, if only slightly, then solutions of the individual compounds, as shown in Figure 5-13. In addition, the photographs show reddish solid particles of the CT complexes in the mixtures of $C_{60}F_{18}$ and CORO and of $C_{60}F_{18}$ and PERY, which are presumably microcrystalline particles of the sparingly soluble CT complexes.

5.5. CONCLUSIONS

In summary, six CTCC structures and one $PAH(CF_3)_n$ structure have been reported. Of the $PAH/PAH(CF_3)_n$ structures, $PYRN/(ANTH-6-1)_2$, was reported in a publication of which the

272

author was first author.[9] This structure in complement with the structure of ANTH-6-1, also reported here, literature structures of PENT(R_F) derivatives, and DFT calculations by Dr. Popov revealed a unique behavior of 9,10- functionalized ANTH(R_F) and 6,13- functionalized PENT(R_F) derivatives that show the preferred structure of these compounds is bent when the R_F group is in an eclipsed orientation. The other two PAH/PAH(CF$_3$)$_n$ CTCC structures reported here pack similarly and have notably small OOP distances with both structures averaging to 3.550 Å and a high degree of π–π overlap with 7 and 8 overlapping $C(sp^2)$ atoms. In the case of PYRN/PYRN-5-4, this structure has the added benefit of being the first time this acceptor has been reported or characterized in any way.

Lastly, a series of three PAH/C$_{60}$F$_{18}$ CTCC structures are reported. The three structures reveal a possible trend where the packing of the PAH/C$_{60}$F$_{18}$ CTCC is dependent on the size of the PAH with the smaller PAH, PYRN, forming three π–π interactions with the fullerene leading to complex packing with no π–π overlap between the PYRN molecules and the larger PAHs, PERY and CORO, forming alternating layers of D/A molecules. Understanding the driving forces for D/A packing will hopefully lead to the intelligent design of desirable organic-metal materials like TTF/TCNQ.[35]

5.6. ADDITIONAL RECOGNITION

Crystals of ANTH-6-1 and PAH/ANTH-6-1 CTCCs were grown by Dr. Karlee Castro. Crystals of PYRN/PHEN-5-1 and PYRN/PYRN-5-4 were grown by Dr. Kerry Rippy. Highly pure, 98+%, C$_{60}$F$_{18}$ was provided by Dr. Olga V. Boltalina. Relative energy DFT calculations of PAH(R_F) bend angles and CF$_3$ confirmations were performed by Dr. Alexey Popov.

Table 5-1. Crystal data collection and final refinement parameters for PYRN/PHEN-5-1 and PYRN/PYRN-5-4[a]

compound	PYRN/PHEN-5-1	PYRN/PYRN-5-4
empirical formula	$C_{35}H_{15}F_{15}$	$C_{37}H_{15}F_{15}$
molecular weight, g mol^{-1}	720.47	744.49
habit, color	needle, yellow green	needle, orange yellow
space group, Z	$P2_1/n$, 4	$P2_1/n$, 4
a, Å	19.4835(17)	13.1130(15)
b, Å	7.1938(5)	18.135(2)
c, Å	20.9156(19)	13.3312(15)
α, deg	90	90
β, deg	109.073(2)	112.978(2)
γ, deg	90	90
V, Å^3	2770.6(4)	2918.7(6)
T, K	100	100
ρ_{calc}, g cm^{-3}	1.727	1.694
$R(F)$ $(I>2\sigma(I))^{b}$	0.0352	0.0821
$wR(F^2)$ [all data]^{b}	0.1069	0.2422
GooF	1.035	1.030
C–C bond precision, Å	0.0011	0.0076

[a] PHEN-5-1 = 1,3,6,7,9-phenanthrene(CF$_3$)$_5$; PYRN-5-4 = 1,3,5,7,9-pyrene(CF$_3$)$_5$; PYRN = pyrene. [b] $R(F) = \Sigma||F_o|-|F_c||/ \Sigma|F_o|$; $wR(F^2) = (\Sigma[w(F_o^2 - F_c^2)^2/ \Sigma[w(F_o^2)^2])^{1/2}$.

Table 5-2. Crystal data collection and final refinement parameters for ANTH-6-1 and PYRN/(ANTH-6-1)$_2$[a]

compound	ANTH-6-1	PYRN/(ANTH-6-1)$_2$
empirical	$C_{20}H_4F_{18}$	$C_{56}H_{18}F_{36}$
molecular weight, g mol^{-1}	586.23	687.35
habit, color	plate, colorless	plate, red
X-ray wavelength, Å	0.41328	0.71073
space group, Z	$P\overline{1}$, 2	$P2_1/n$, 2
a, Å	8.6246(6)	10.7122(4)
b, Å	10.2747(6)	18.7549(7)
c, Å	11.1904(7)	12.3835(4)
α, deg	97.2580(10)	90
β, deg	105.0760(10)	91.632(2)
γ, deg	101.2270(10)	90
V, Å^3	922.64(10)	2486.91(15)
T, K	100(2)	120(2)
ρ_{calc}, g cm^{-3}	2.110	1.836
$R(F)$ $(I > 2\sigma(I))$[b]	0.0382	0.0417
$wR(F^2)$ [all data][b]	0.0928	0.1047
GooF	1.079	1.032
C–C bond precision, Å	0.0020	0.0024
CCDC deposition number	1883531	1883534

[a] ANTH-6-1 = 2,3,6,7,9,10-anthracene(CF$_3$)$_6$; PYRN = pyrene.
[b] $R(F) = \Sigma||F_o|-|F_c||/\Sigma|F_o|$; $wR(F^2) = (\Sigma[w(F_o^2 - F_c^2)^2/\Sigma[w(F_o^2)^2])^{1/2}$.

Table 5-3. Crystal data collection and final refinement parameters for $(PYRN)_2/C_{60}F_{18}$, $CORO/(C_{60}F_{18})_2$, and $PERY/C_{60}F_{18}$[a]

compound	$(PYRN)_2/C_{60}F_{18}$	$CORO/(C_{60}F_{18})_2$	$PERY/C_{60}F_{18}$
empirical formula	$C_{105}H_{22}F_{18}$	$C_{144}H_{12}F_{36}$	C80H12F18
molecular wt., g mol^{-1}	1552.01	2425.54	1314.90
habit, color	needle, purple	plate, red	plate, dark green
space group, Z	$P2_12_12_1$, 4	$P2_1/c$, 4	$Pnma$, 4
a, Å	13.3741(8)	44.872(4)	11.4988(8)
b, Å	19.5758(12)	11.1086(9)	23.8011(16)
c, Å	22.2815(12)	17.4423(15)	17.1844(11)
α, deg	90	90	90
β, deg	90	96.759(2)	90
γ, deg	90	90	90
V, Å^3	5833.5(6)	8633.9(13)	4703.1(5)
T, K	100	100	150
ρ_{calc}, g cm^{-3}	1.767	1.866	1.857
$R(F)$ $(I>2\sigma(I))$[a]	0.0338	0.0960	0.0535
$wR(F^2)$ [all data][a]	0.0857	0.2552	0.1713
GooF	1.027	1.058	0.991
C–C bond precision, Å	0.0040	0.0085	0.0025

[a] PYRN = pyrene; CORO = coronene; PERY = perylene.
[b] $R(F) = \Sigma||F_o|-|F_c||/ \Sigma|F_o|$; $wR(F^2) = (\Sigma[w(F_o^2 - F_c^2)^2/ \Sigma[w(F_o^2)^2])^{1/2}$.
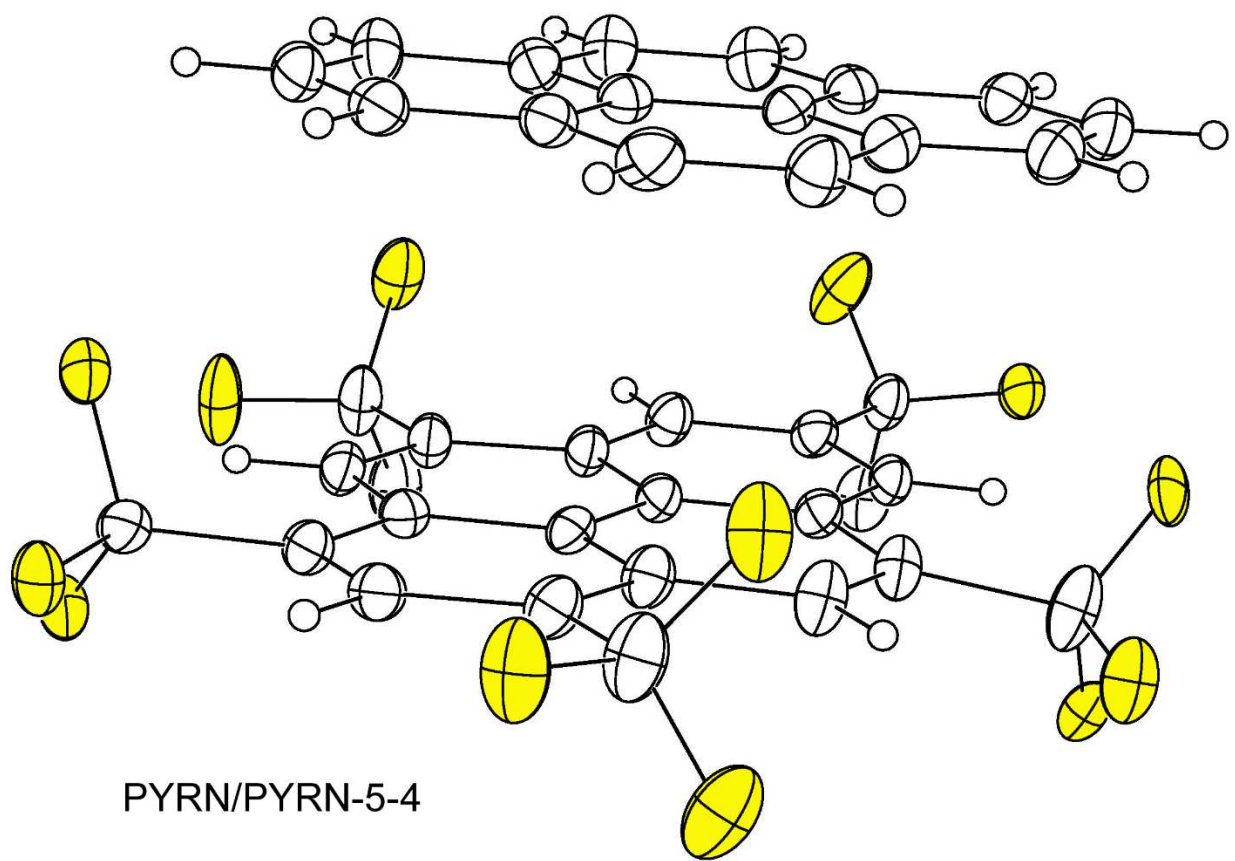
Figure 5-1. A thermal ellipsoid plot of the pyrene (PYRN) donor and the PYRN-5-4 acceptor in the X-ray co-crystal structure of PYRN/PYRN-5-4 (25% probability ellipsoids except for H atoms; F atoms are colored yellow). The separation of the molecules is to scale. Three other isomers of $PYRN(CF_3)_5$ with different CF_3 distribution patterns were published in 2013 (ref. [15]).
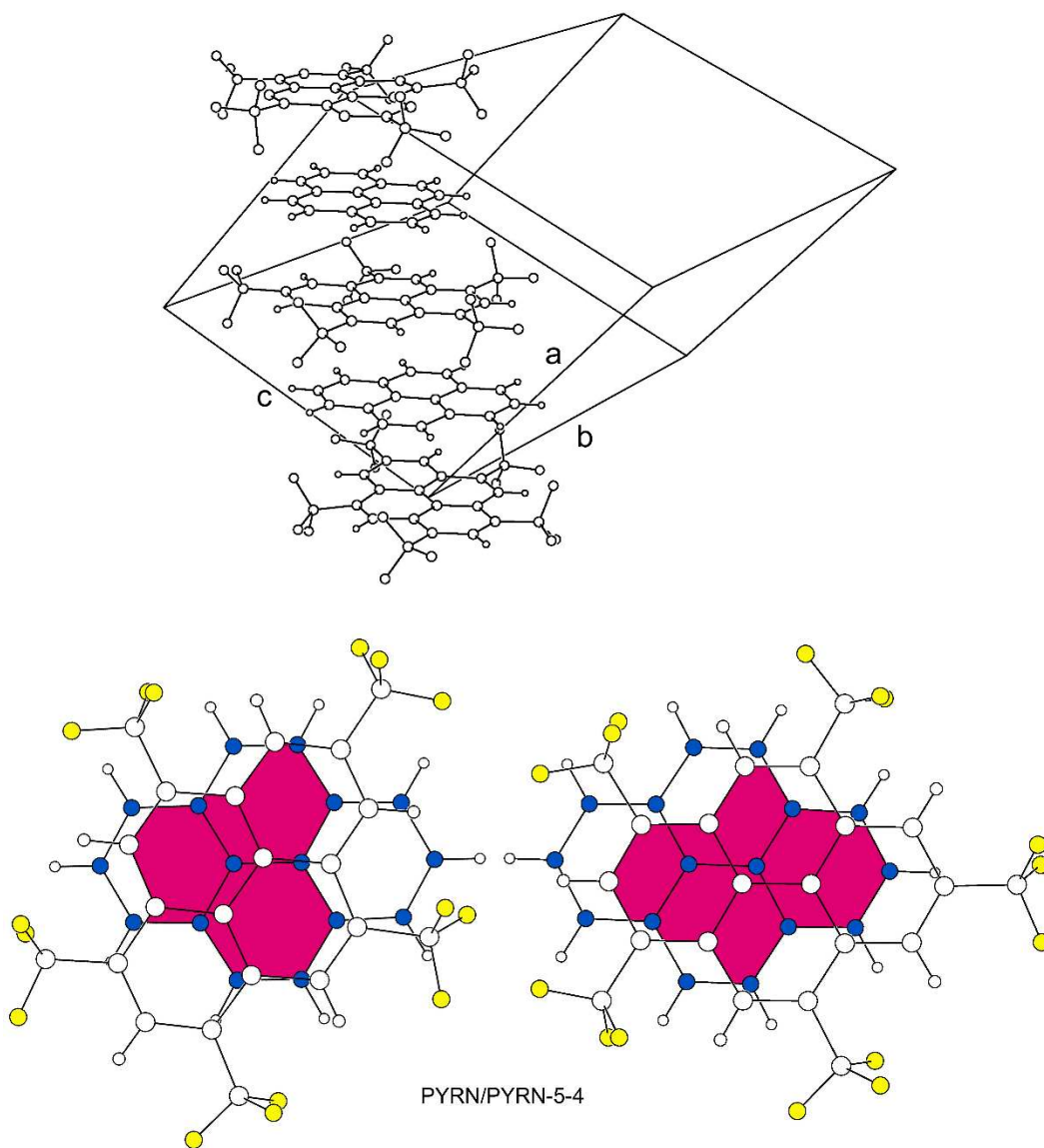
Figure 5-2. Drawings of the structure of PYRN/PYRN-5-4. The upper drawing shows the unit cell and the stacking of molecules along the diagonal of the crystallographic *ac* plane. The lower drawings show the areas of donor/acceptor π–π overlap on either side of the PYRN-5-4 acceptor.

278
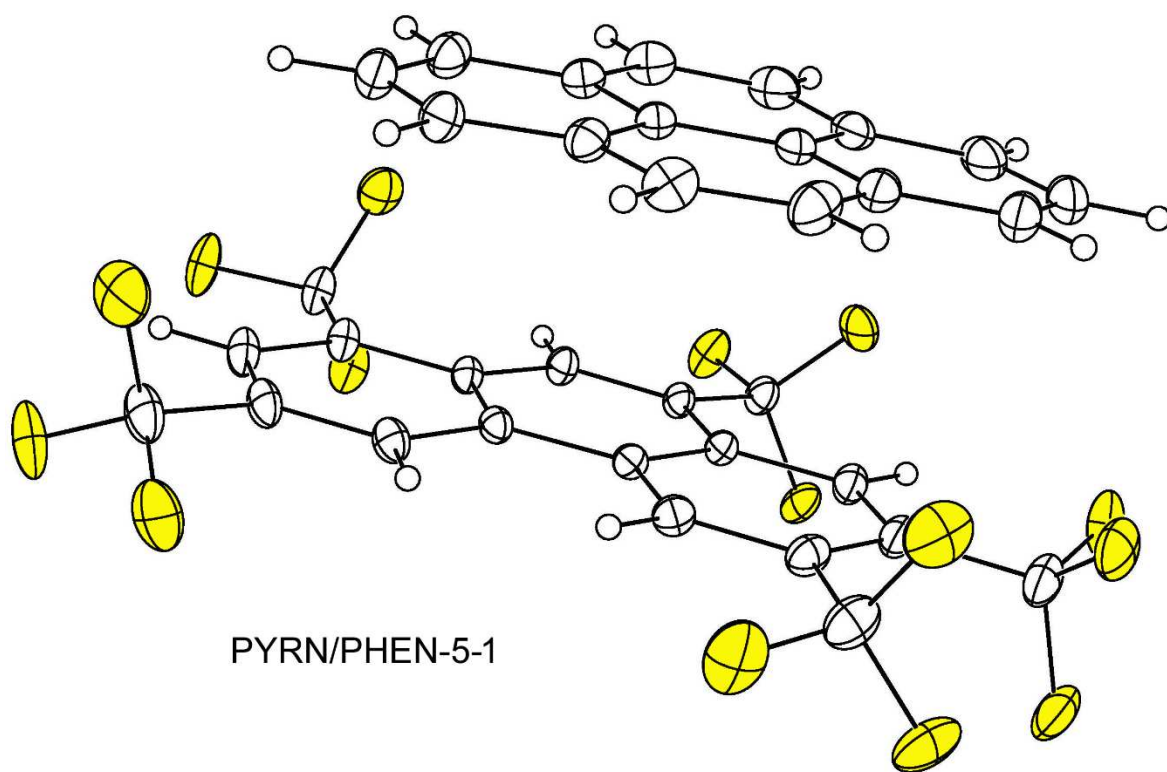
PYRN/PHEN-5-1

Figure 5-3. A thermal ellipsoid plot of the PYRN donor and the PHEN-5-1 acceptor in the X-ray co-crystal structure of PYRN/PHEN-5-1 (50% probability ellipsoids except for H atoms; F atoms are colored yellow). The separation of the molecules is to scale.
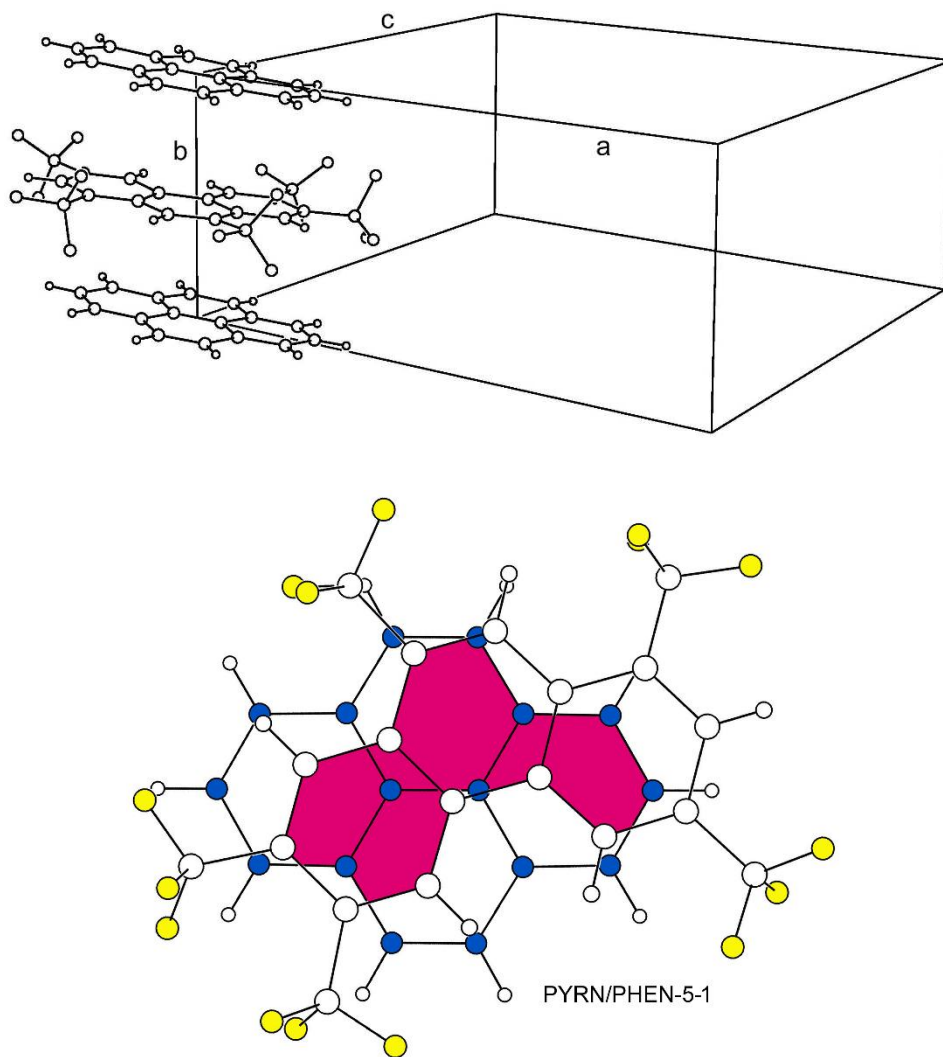
Figure 5-4. Drawings of the co-crystal structure of PYRN/PHEN-5-1. The upper drawing shows the unit cell and the D/A/D/A stacking of PYRN donor (D) and PHEN-5-1 acceptor (A) molecules along the crystallographic *b* axis. The lower drawing show the area of donor/acceptor π–π overlap.
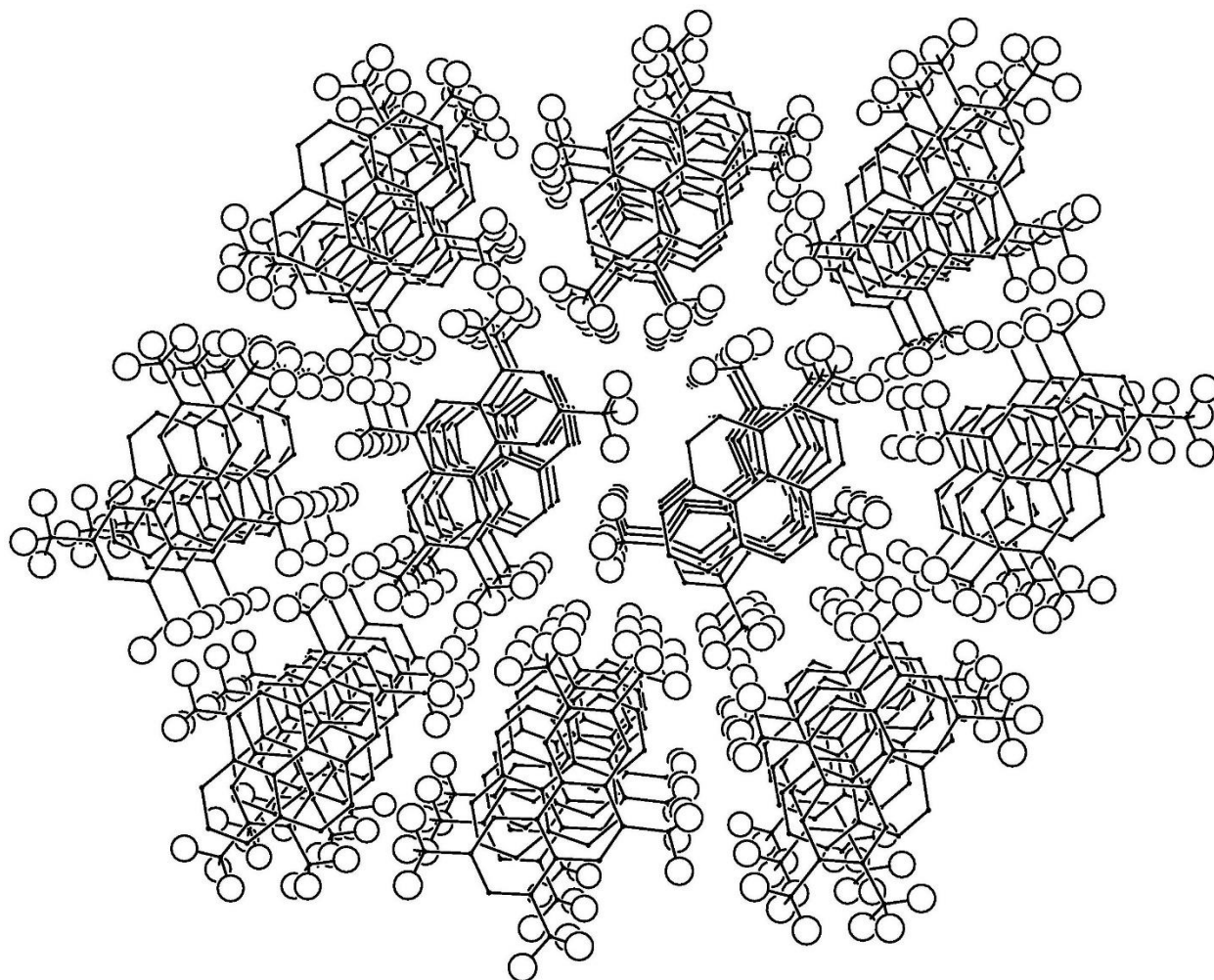
Figure 5-5. Drawing of the hexagonal arrangement of parallel D/A/D/A stacks in the co-crystal structure of PYRN/PHEN-5-1. The H atoms have been removed for clarity, and the F atoms of PHEN-5-1 are shown as large circles.
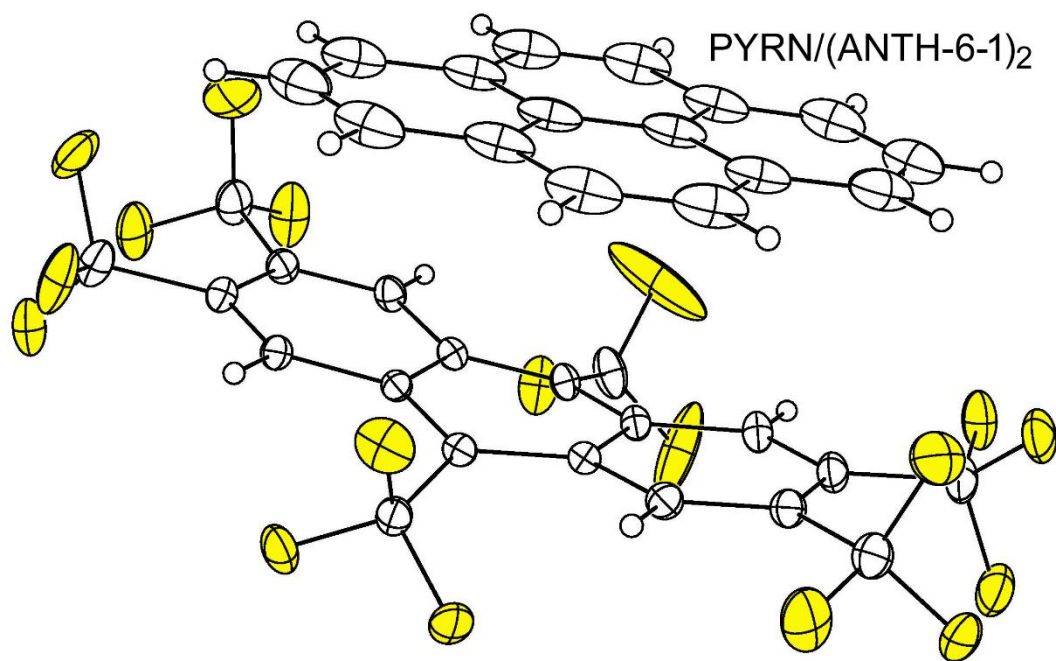
Figure 5-6. A thermal ellipsoid plot of the PYRN donor and ANTH-6-1 acceptor in the X-ray co-crystal structure of PYRN/(ANTH-6-1)$_2$ (50% probability ellipsoids except for H atoms; F atoms are colored yellow). The separation of the molecules is to scale.
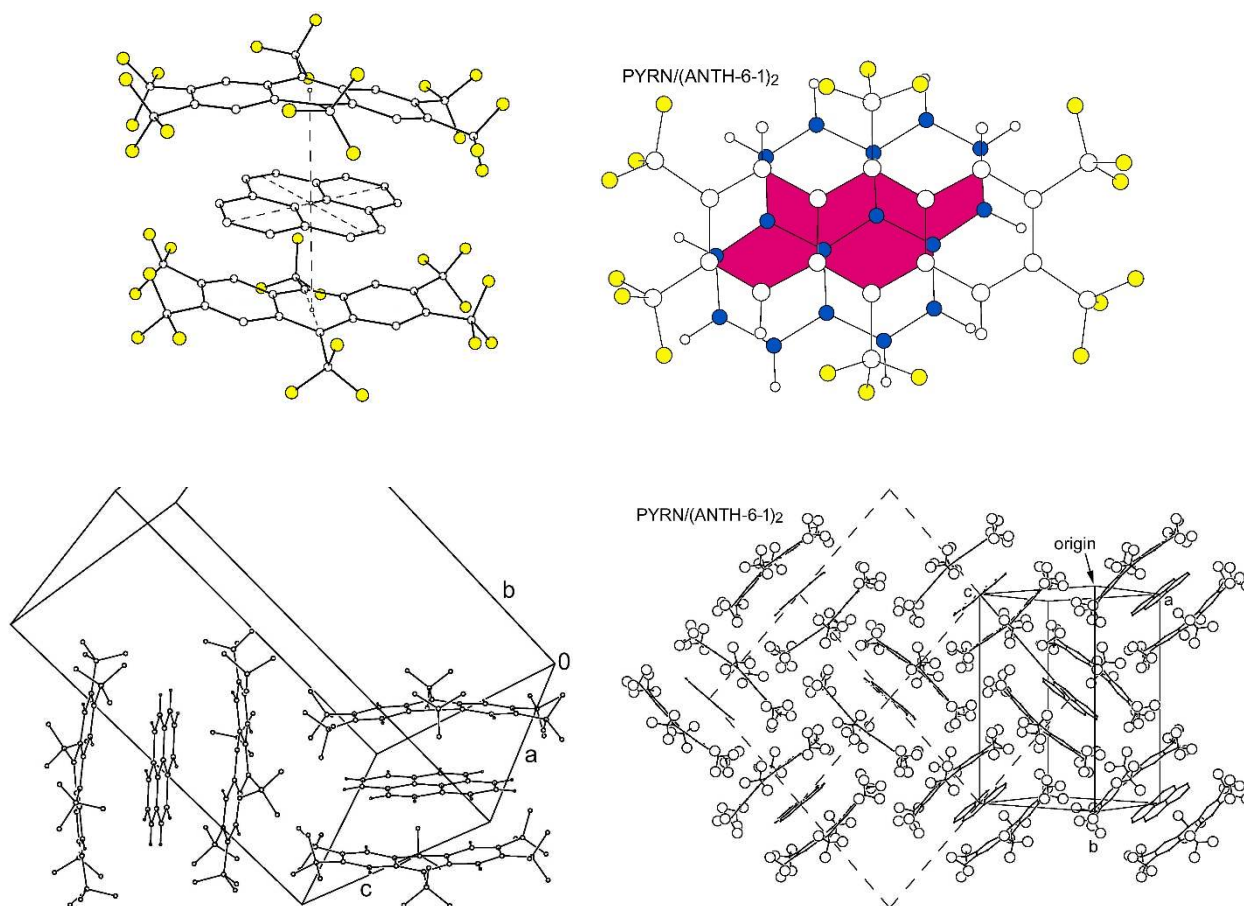
Figure 5-7. Drawings of the co-crystal structure of PYRN/(ANTH-6-1)$_2$. The upper left drawing shows the discrete ANTH-6-1/PYRN/ANTH-6-1 triplet sandwich complex. The distance between the ANTH-6-1 centroid and the PYRN centroid is 3.516 Å. The upper right drawing shows the area of donor/acceptor π–π overlap. The lower drawings show the packing of the triplet complexes in the lattice.
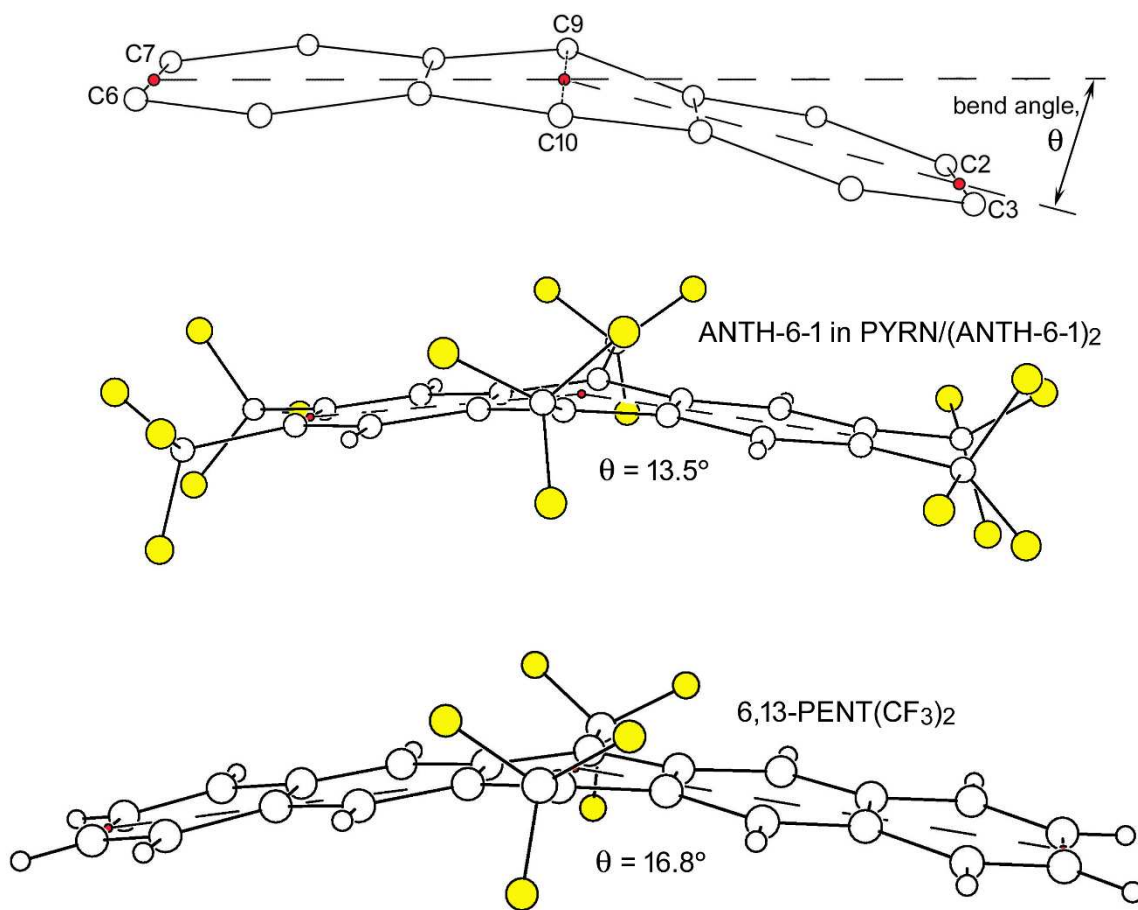
Figure 5-8. (**Top**) The definition of the bend angle in ANTH and ANTH derivative structures, and by analogy in PENT and PENT derivative structures. (**Middle**) Drawings of the ANTH-6-1 molecule in the co-crystal structure PYRN/(ANTH-6-1)$_2$, showing that the bend angle θ is 13.5°. (**Bottom**) Drawing of the 6,13-PENT(CF$_3$)$_2$ molecule from the X-ray structure published in ref. [20], showing that $\theta = 16.8°$.

ANTH-6-1

θ = 7.4°
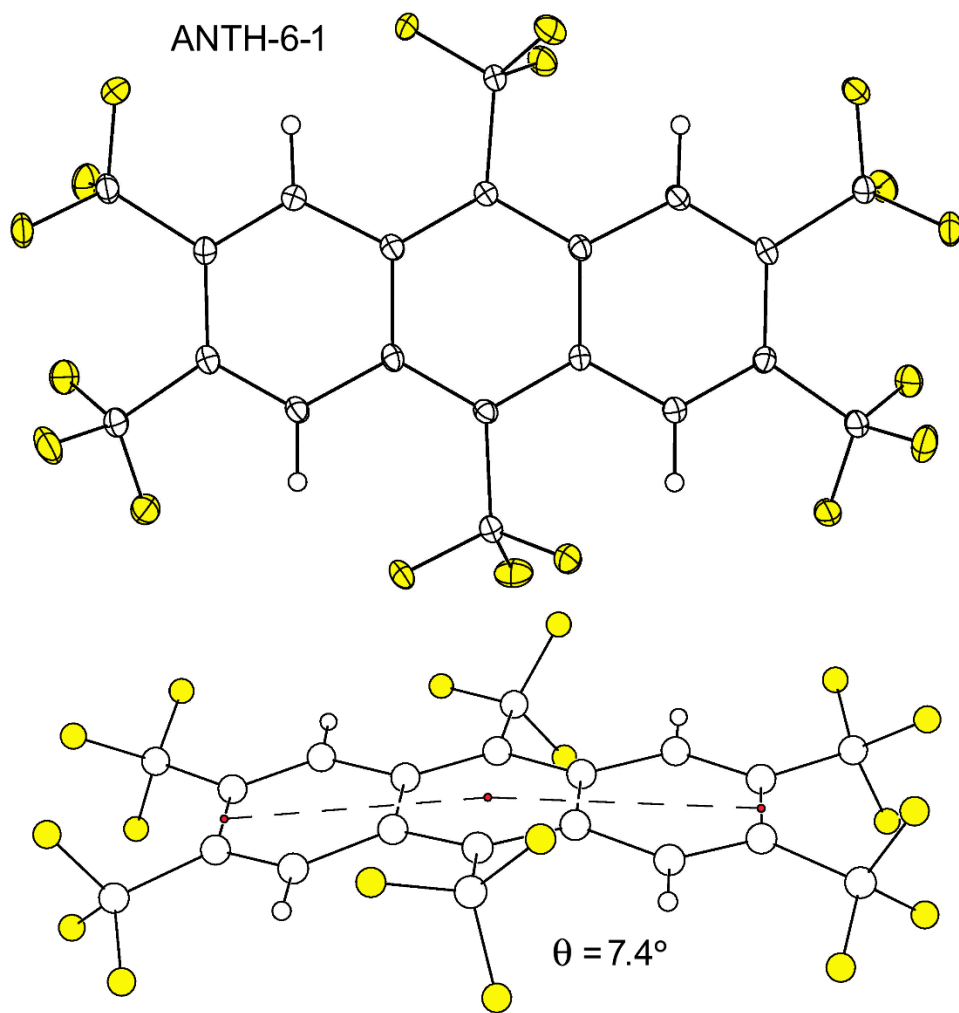
Figure 5-9. (**Top**) Thermal ellipsoid plot of the ANTH-6-1 molecule in its single-crystal X-ray structure (50% probability ellipsoids except for H atoms; F atoms are colored yellow). (**Bottom**): A side view of the ANTH-6-1 molecule, showing that the bend angle θ, defined in Figure 5-8, is 7.4°.
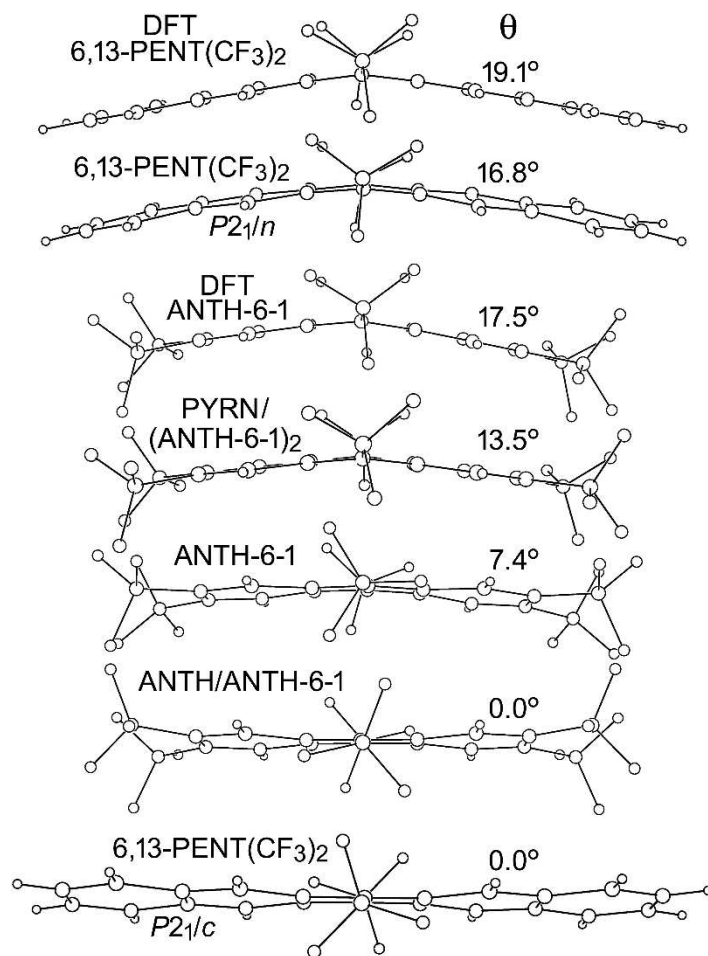
Figure 5-10. Side views of the X-ray and DFT-optimized structures of ANTH-6-1 (this work), the P2$_1$/c and P2$_1$/n X-ray structures of 6,13-PENT(CF$_3$)$_2$ (refs. 19 and 20, respectively), and the lowest-energy DFT-optimized structure of 6,13-PENT(CF$_3$)$_2$ (ref. 20). The acene bending angle θ, defined in Figure 5-8, is shown for each structure.
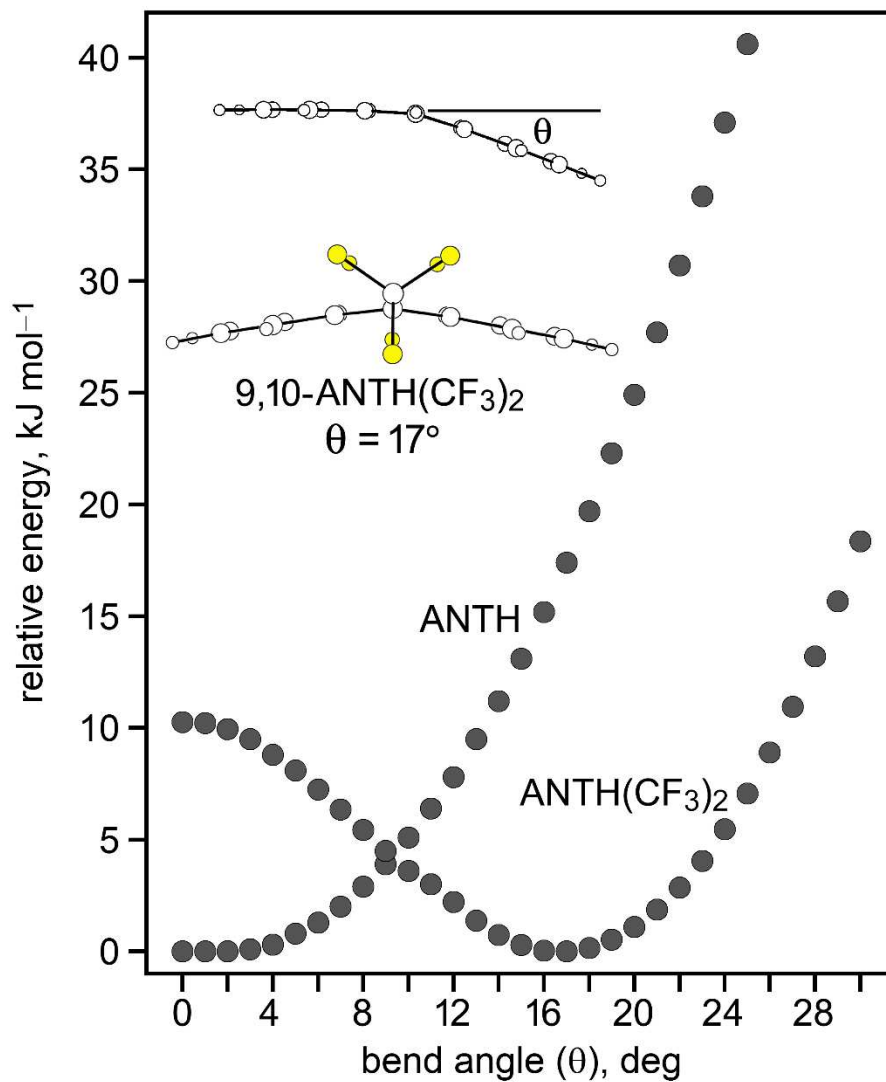
Figure 5-11. DFT calculations by collaborator Dr. Alexey A. Popov. These results show that the energy of unsubstituted ANTH is raised when the aromatic core is bent by any angle, and its relative energy is 18 kJ mol^{-1} when θ is 17.0°. In contrast, the energy of DFT-optimized 9,10-ANTH(CF$_3$)$_2$ (a hypothetical molecule) is lowest when θ is 17.0° and is 10.5 kJ mol^{-1} when θ is 0.0°.
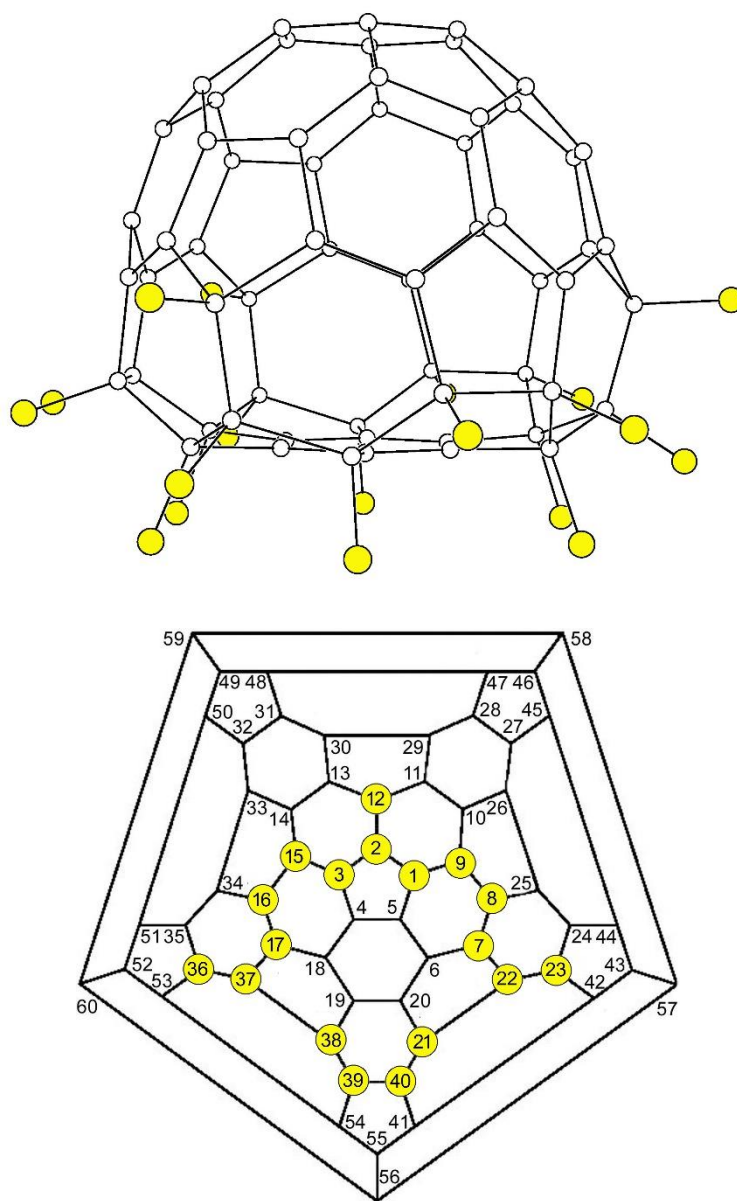
Figure 5-12. The structure of the C_{3v} symmetry molecule $C_{60}F_{18}$ determined by single-crystal X-ray diffraction (refs. 26 and 27). Also shown is a Schlegel diagram showing the distribution of F atoms on 18 contiguous C atoms (indicated with yellow circles) and their IUPAC locants (from ref. 36). The IUPAC name of $C_{60}F_{18}$ is 1,2,3,7,8,9,12,15,16,17,21,22,23,36,37,38,39,40-octadecafluoro-1,2,3,7,8,9,12,15,16,17,21,22,23,36,37,38,39,40-octadecahydro($C_{60}I_h$)[5,6]fullerene.
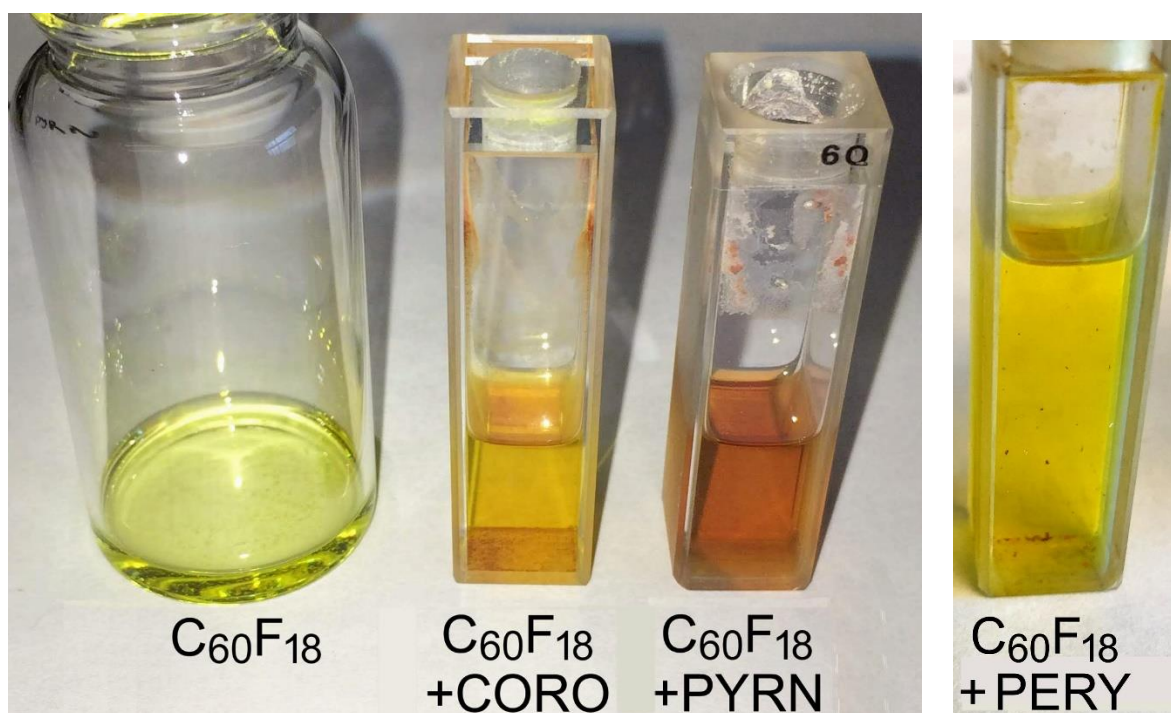
Figure 5-13. Dichloromethane solutions of $C_{60}F_{18}$ and of mixtures of $C_{60}F_{18}$ and either CORO, PYRN, or PERY. Note the reddish precipitates in the CORO/$C_{60}F_{18}$ and PERY/$C_{60}F_{18}$ mixtures, which are presumably microcrystalline particles of the sparingly soluble CT complexes.
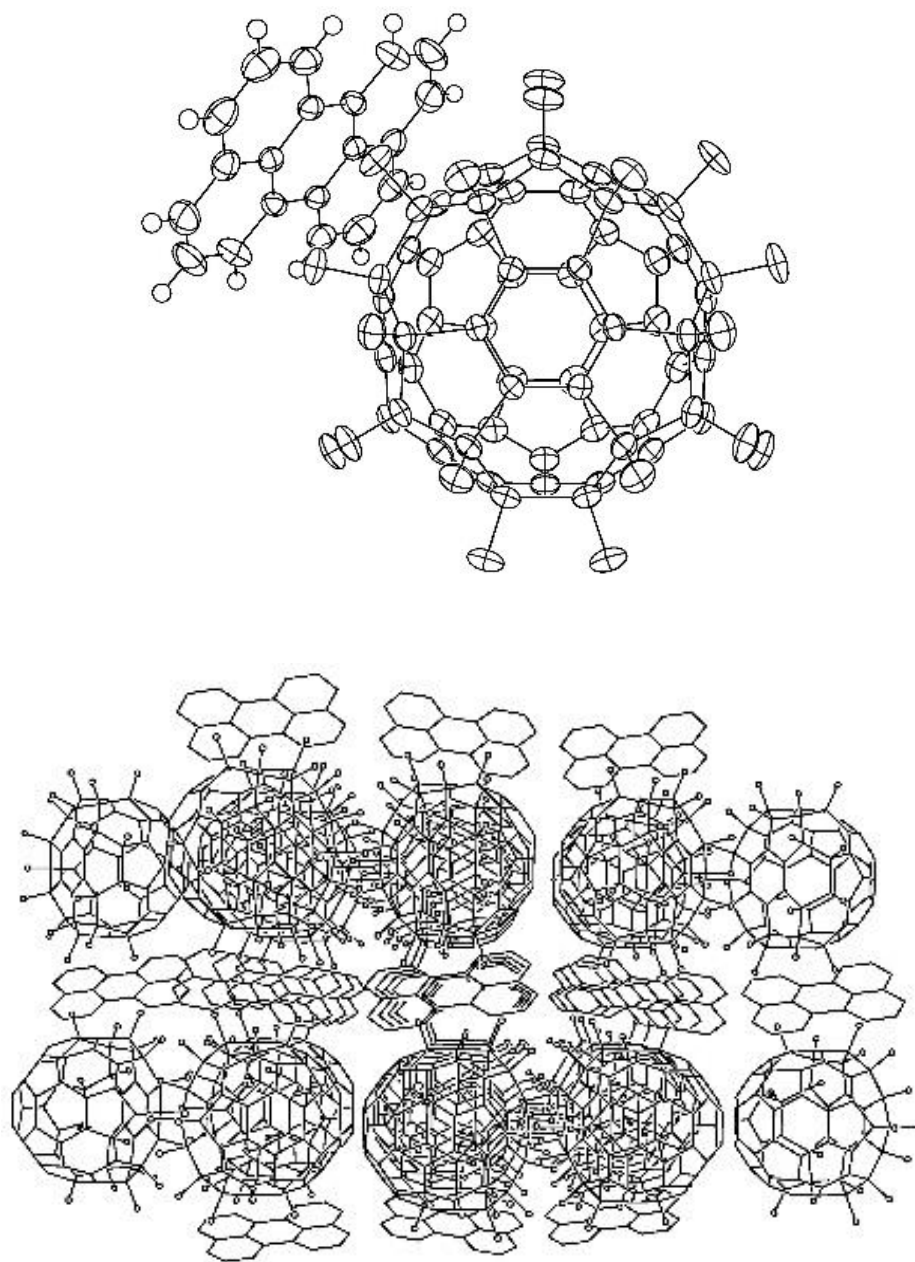
Figure 5-14. The X-ray crystal structure of PERY/$C_{60}F_{18}$. (**Top**) drawing shows is a thermal ellipsoid plot (50% probability ellipsoids except for H atoms). (**Bottom**) drawing show the packing of alternate layers of PERY and $C_{60}F_{18}$ molecules. The layers are in the crystallographic *ac* planes and are stacked along the *b* axis.
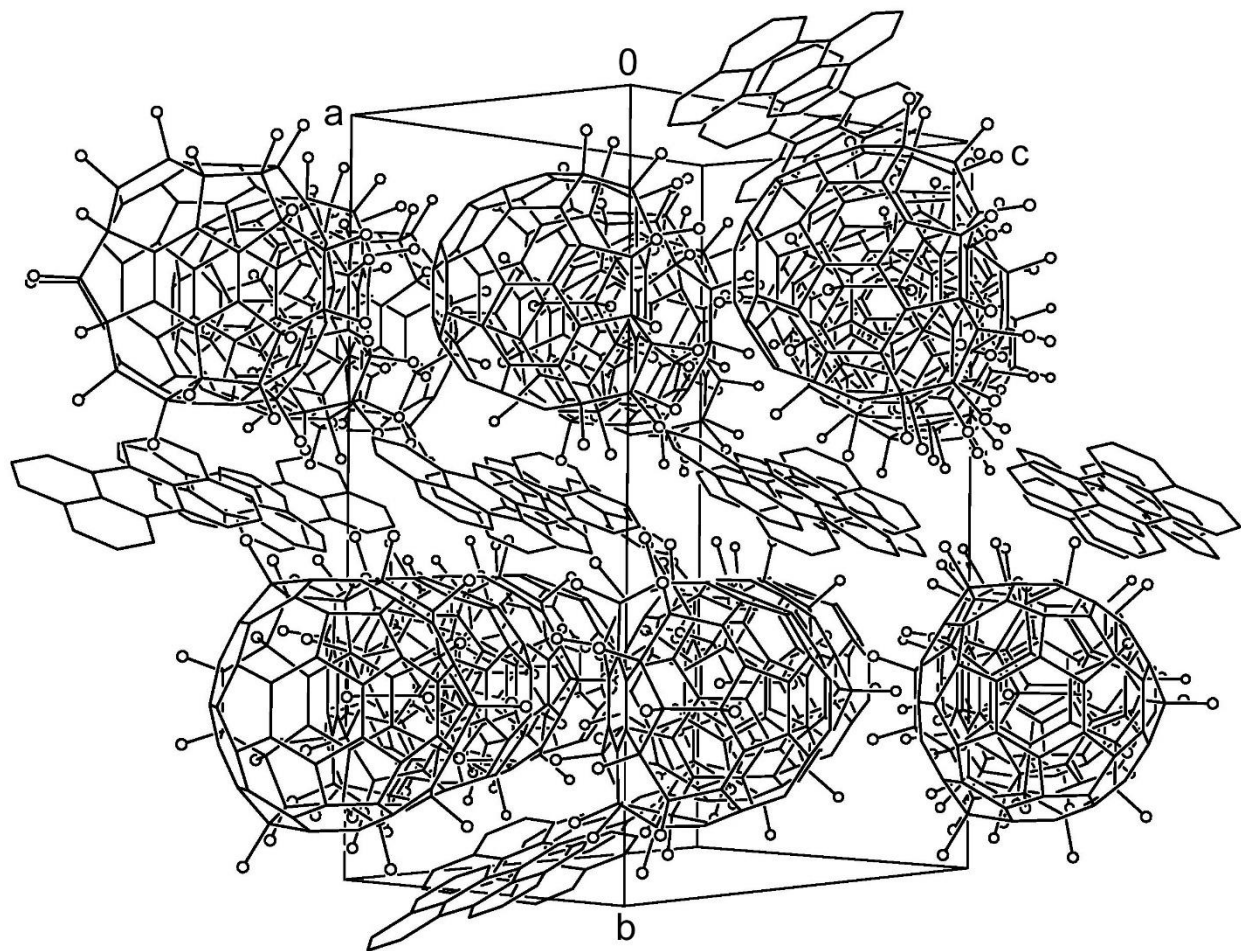
Figure 5-15. The structure of PERY/$C_{60}F_{18}$, showing the layers of molecules in parallel to the crystallographic *ac* planes and the stacking of the layers along the crystallographic *b* axis of the orthorhombic unit cell (H atoms have been removed for clarity, and F atoms are shown as spheres of arbitrary size). The distance between the rigorously parallel least-squares planes of molecular centroids is 5.950 Å.
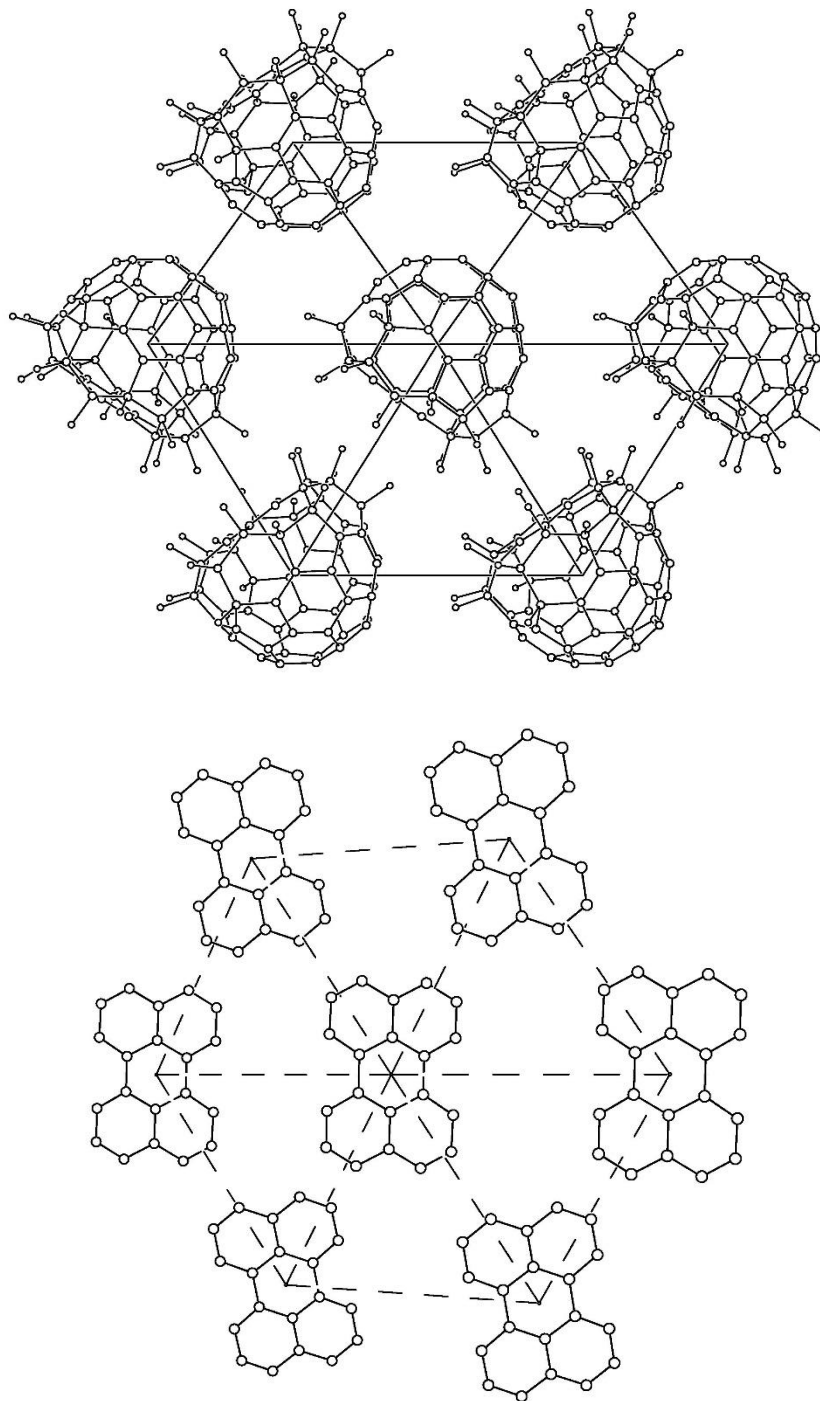
Figure 5-16. The layers of $C_{60}F_{18}$ and PERY molecules in the CT/CC structure of PERY/$C_{60}F_{18}$. The fullerene $\odot\cdots\odot$ distances are 9.848 (×2), 10.839 (×2), and 11.499 (×2) Å. The PERY $\odot\cdots\odot$ distances are 10.338 (× 4) and 11.499 (×2) Å.
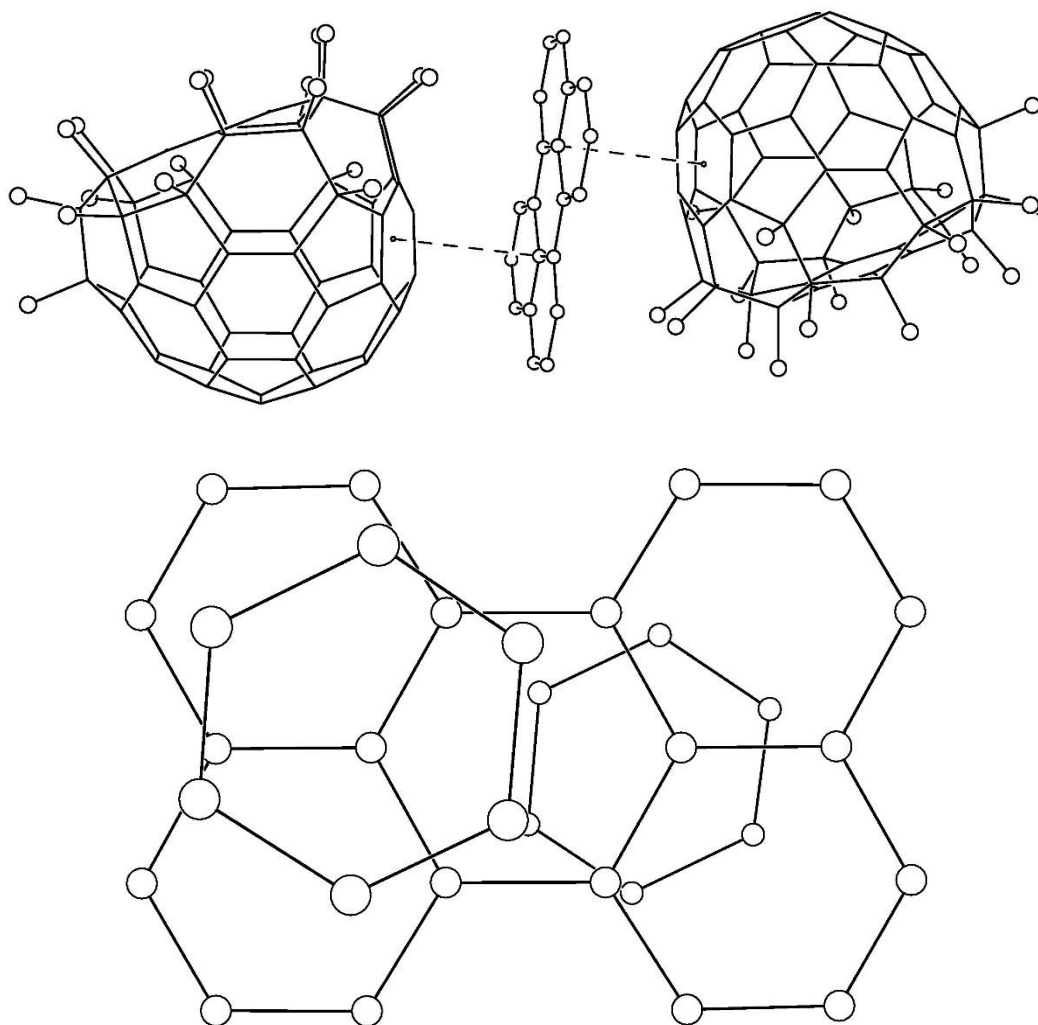
Figure 5-17. Drawings of portions of the structure of PERY/$C_{60}F_{18}$. The PERY least-squares plane is tilted 14.1° from the closest hexagon in two fullerene molecules. The distances shown with dotted lines in the upper drawing between the center of the fullerene hexagons and the closest PERY atom is 3.43 Å (the PERY least-squares plane is in the plane of the page; H atoms have been omitted for clarity).
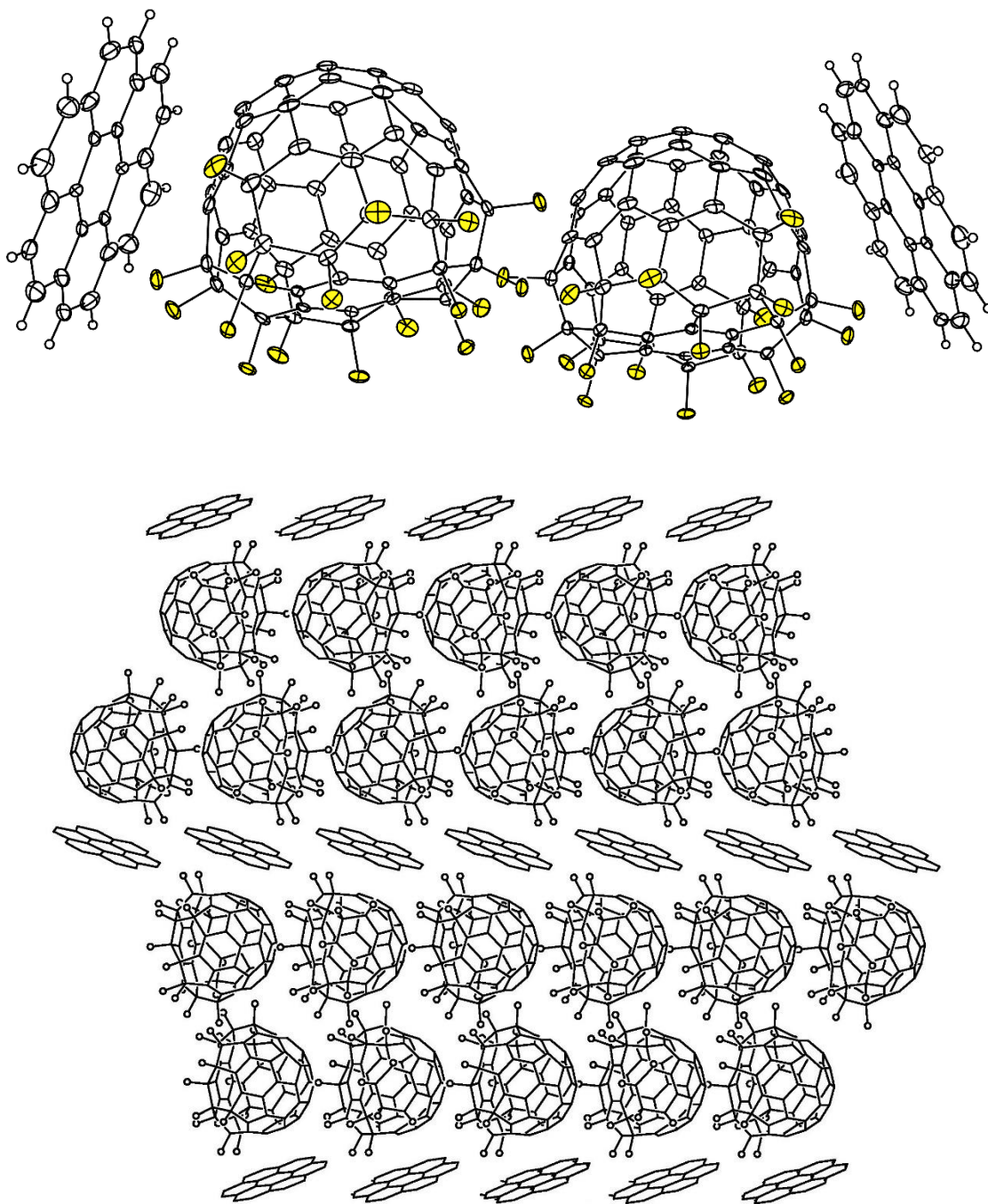
Figure 5-18. The structure of CORO/(C$_{60}$F$_{18}$)$_2$. (**Top**) drawing is a thermal ellipsoid plot (50% probability ellipsoids except for H atoms; F atoms are colored yellow). (**Bottom**) drawing shows the stacking of layers of CORO molecules and double layers of C$_{60}$F$_{18}$ molecules.
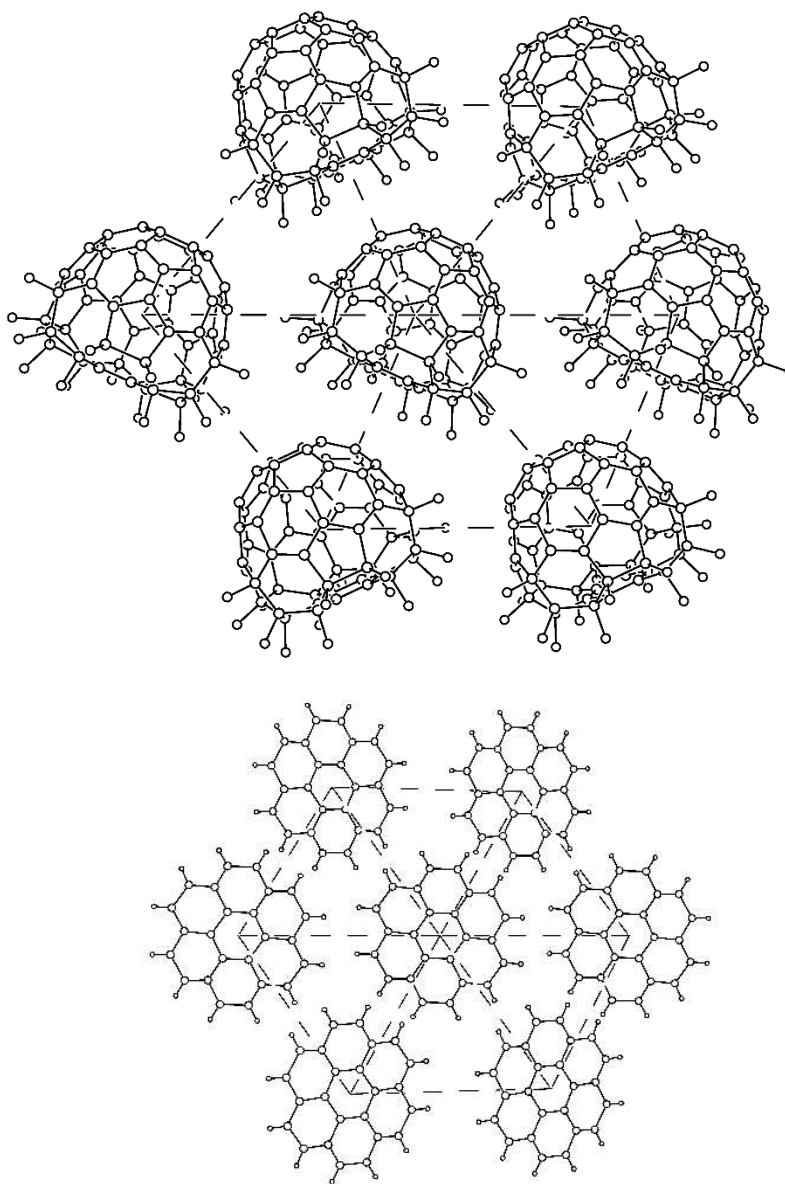
Figure 5-19. The layers of $C_{60}F_{18}$ and CORO molecules in the structure of CORO/$(C_{60}F_{18})_2$. The fullerene $\odot\cdots\odot$ distances are 9.534 (×2), 11.093 (×2), and 11.307 (×2) Å. The CORO $\odot\cdots\odot$ distances are 10.332 (× 4) and 11.093 (×2) Å, which are similar to the PERY $\odot\cdots\odot$ distances in the structure of $C_{60}F_{18}$/PERY (see Figure 5-16).
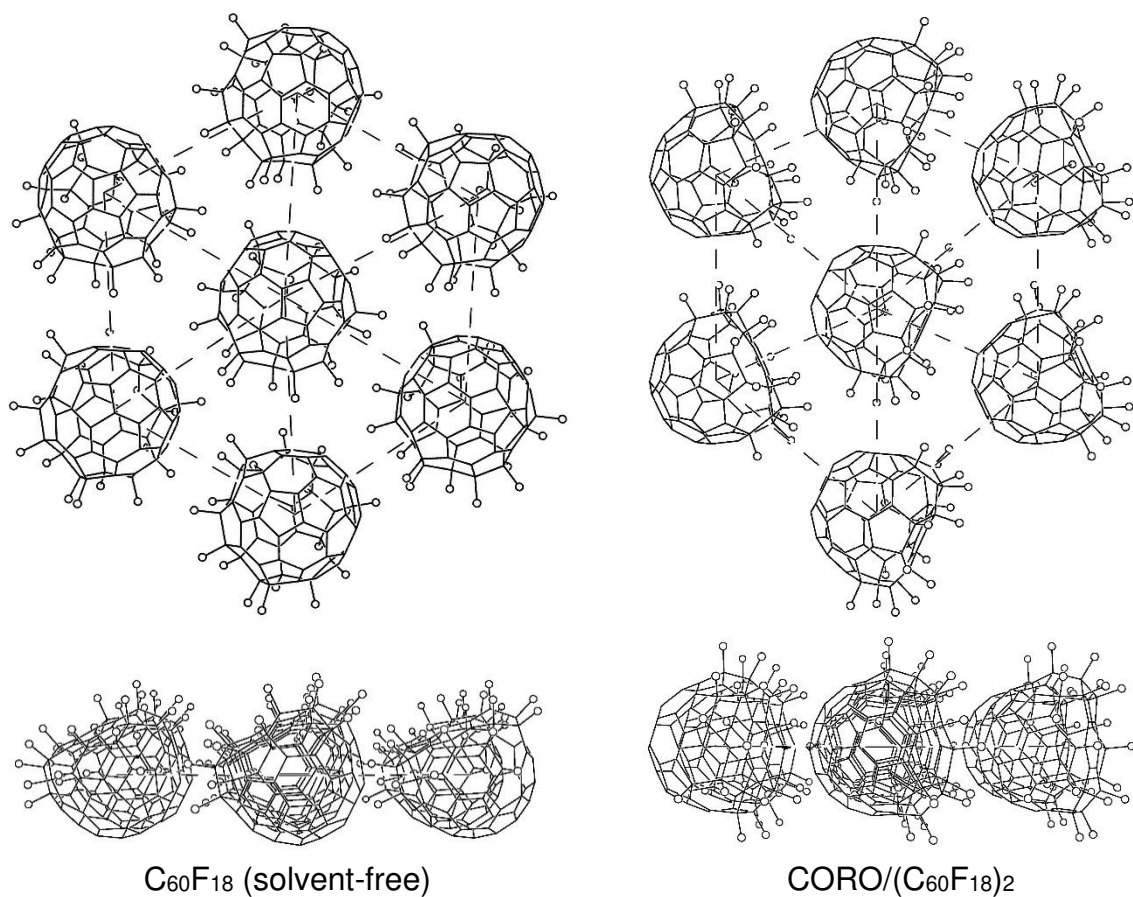
Figure 5-20. Comparison of the $C_{60}F_{18}$ layers in the structures of solvent-free $C_{60}F_{18}$ (refs. 26 and 27) and the CT/CC structure CORO/$(C_{60}F_{18})_2$ (this work; see also Figure 5-21). The $\odot\cdots\odot$ distances within the close-packed layers in the solvent free structure are 10.810 (×2), 11.037 (×2), and 11.502 (×2) Å and average 11.115 Å. The $\odot\cdots\odot$ distances within the close-packed layers in the structure of CORO/$(C_{60}F_{18})_2$ are 9.534 (×2), 11.093 (×2), and 11.307 (×2) Å and average 10.655 Å.

296

C$_{60}$F$_{18}$ (solvent free)
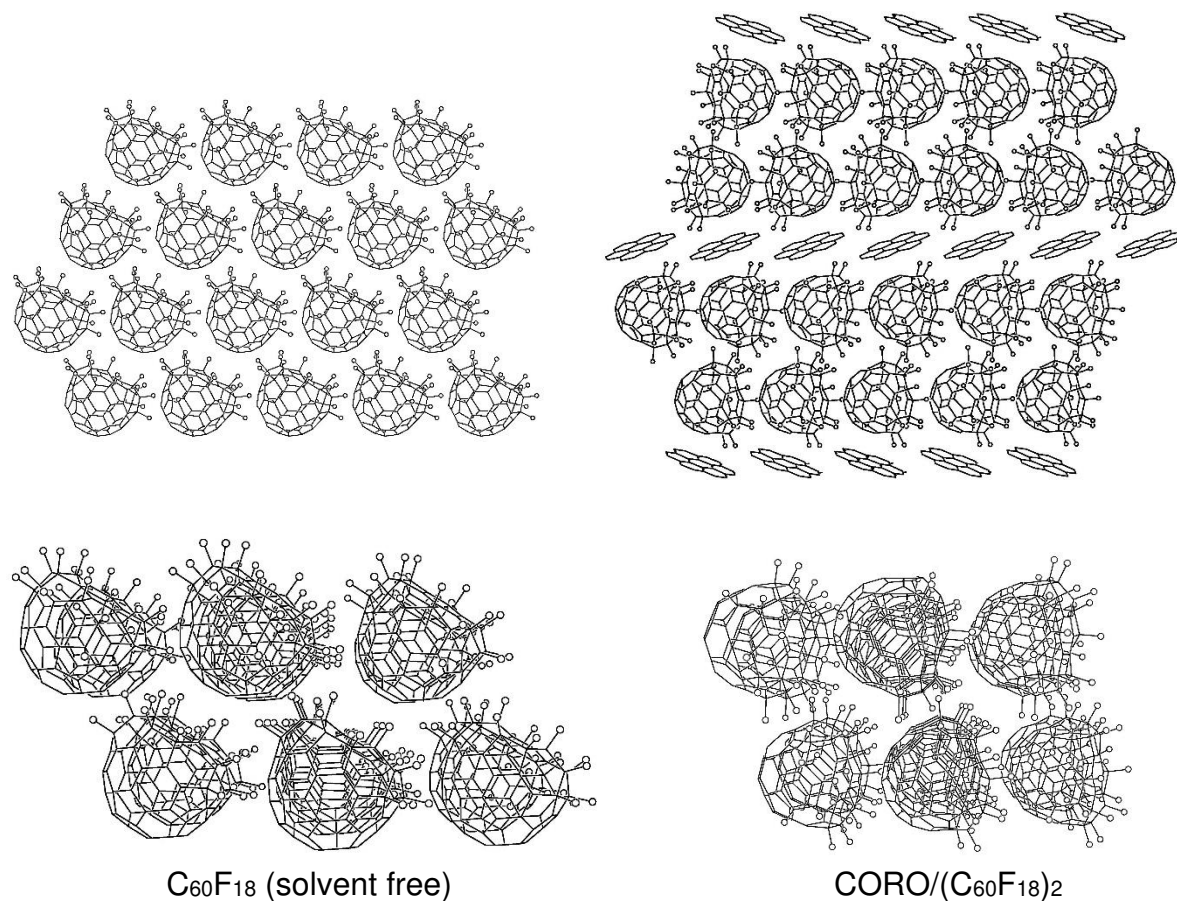
CORO/(C$_{60}$F$_{18}$)$_2$

Figure 5-21. Further comparison of the C$_{60}$F$_{18}$ layers in the structures of solvent-free C$_{60}$F$_{18}$ (refs. 26 and 27) and the CT/CC structure CORO/(C$_{60}$F$_{18}$)$_2$ (this work; see also Figure 5-20). The difference in interplanar spacing is ca. 1.0 Å (9.278 Å − 8.276 Å). In solvent-free C$_{60}$F$_{18}$, the fullerene dipoles are all oriented in the same general direction, resulting in the formation of polar crystals. This is also true for the double layers of C$_{60}$F$_{18}$ molecules in CORO/(C$_{60}$F$_{18}$)$_2$. However, in the co-crystal structure the dipoles in alternate double layers point in opposite directions.
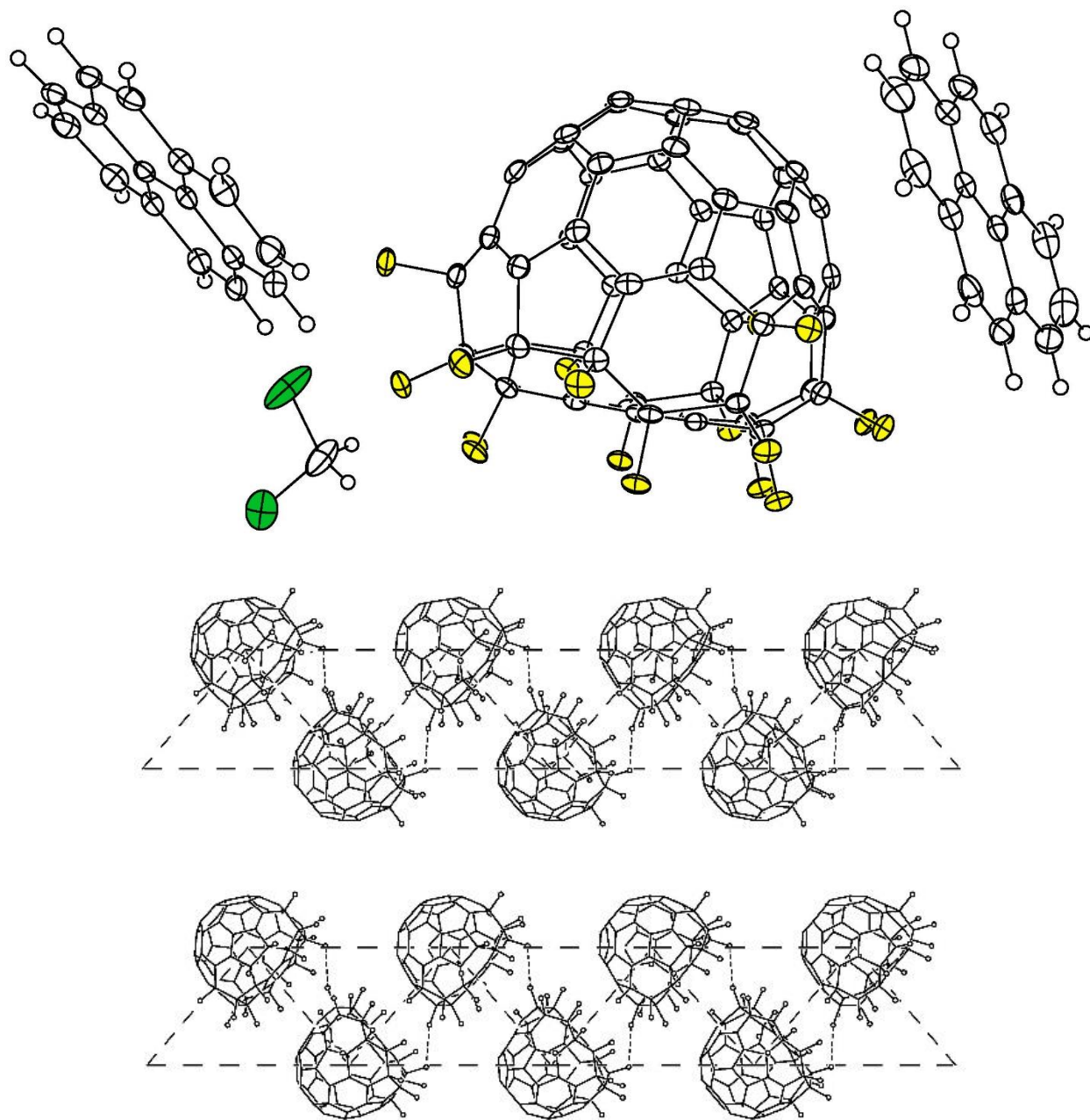
Figure 5-22. The structure of (PYRN)$_2$/C$_{60}$F$_{18}$·CH$_2$Cl$_2$. (**Top**) drawing is a thermal ellipsoid plot (50% probability ellipsoids except for H atoms; F and Cl atoms are colored yellow and green, respectively). (**Bottom**) drawing shows the ribbons of fullerene centroid (⊙) triangles with ⊙···⊙ distances of 10.258 (×2) and 13.374 Å. The perpendicular distance between the ribbon planes is 1.096 Å.
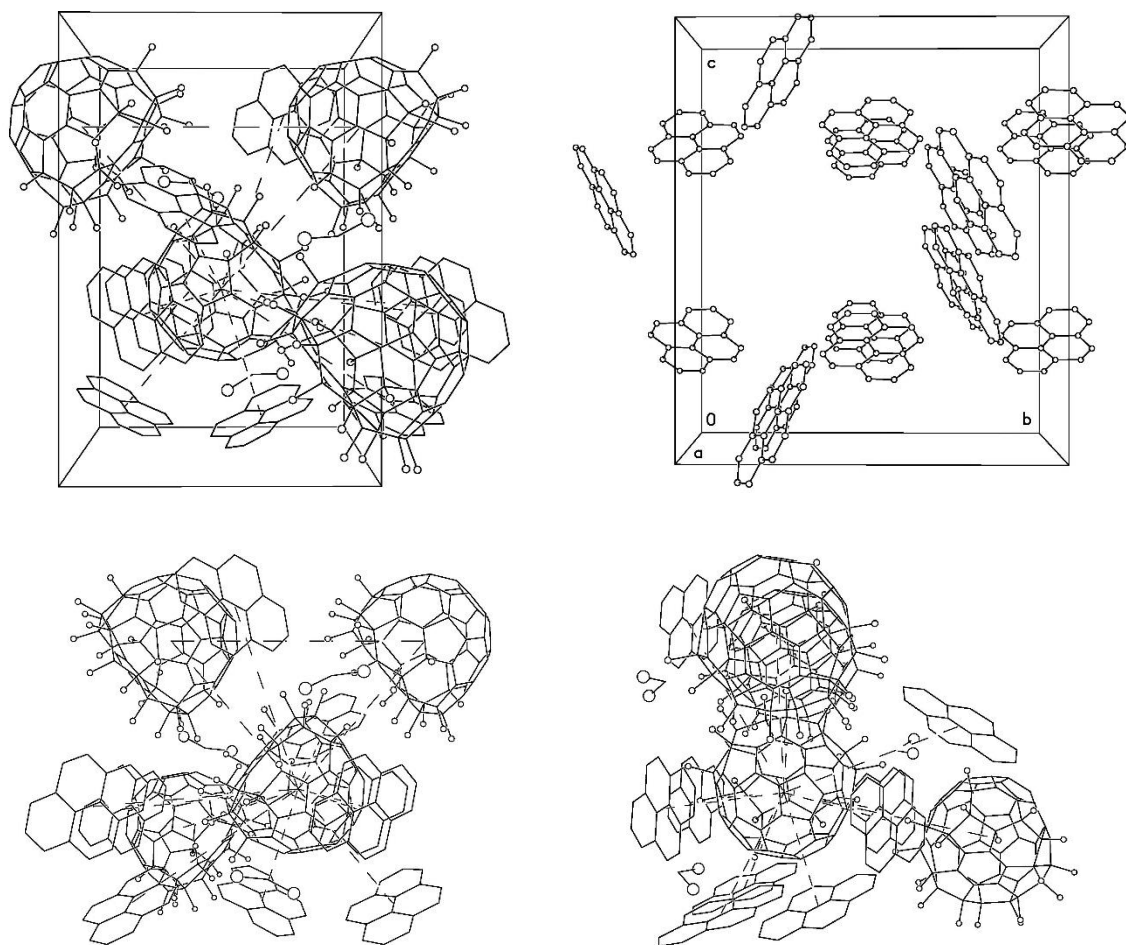
Figure 5-23. Drawings of the structure of $(PYRN)_2/C_{60}F_8 \cdot CH_2Cl_2$ (H atoms and the CH_2Cl_2 molecules omitted for clarity). Each $C_{60}F_{18}$ molecule is surrounded by a complex array of three $C_{60}F_{18}$ molecules ($\odot \cdots \odot = 10.258$ (×2) and 13.374 Å) and nine PYRN molecules ($\odot \cdots \odot = 6.526$, 6.586, 11.017, 11.323, and 11.796 Å to one unique PYRN and 6.540, 7.980, 9.668, and 10.699 Å to the other unique PYRN (the PYRN centroids are defined by the centroid of the central C–C bond). The drawing on the upper left corresponds to a $C_{60}F_{18}$ molecule nearly in the center of a unit cell (centroid coordinates [0.5, 0.59836, 0.50978]). The drawing directly below on the upper right is an array of PYRN molecules, showing the lack of any PYRN–PYRN π–π overlap. The bottom drawings are rotated versions of the upper left drawing.

299
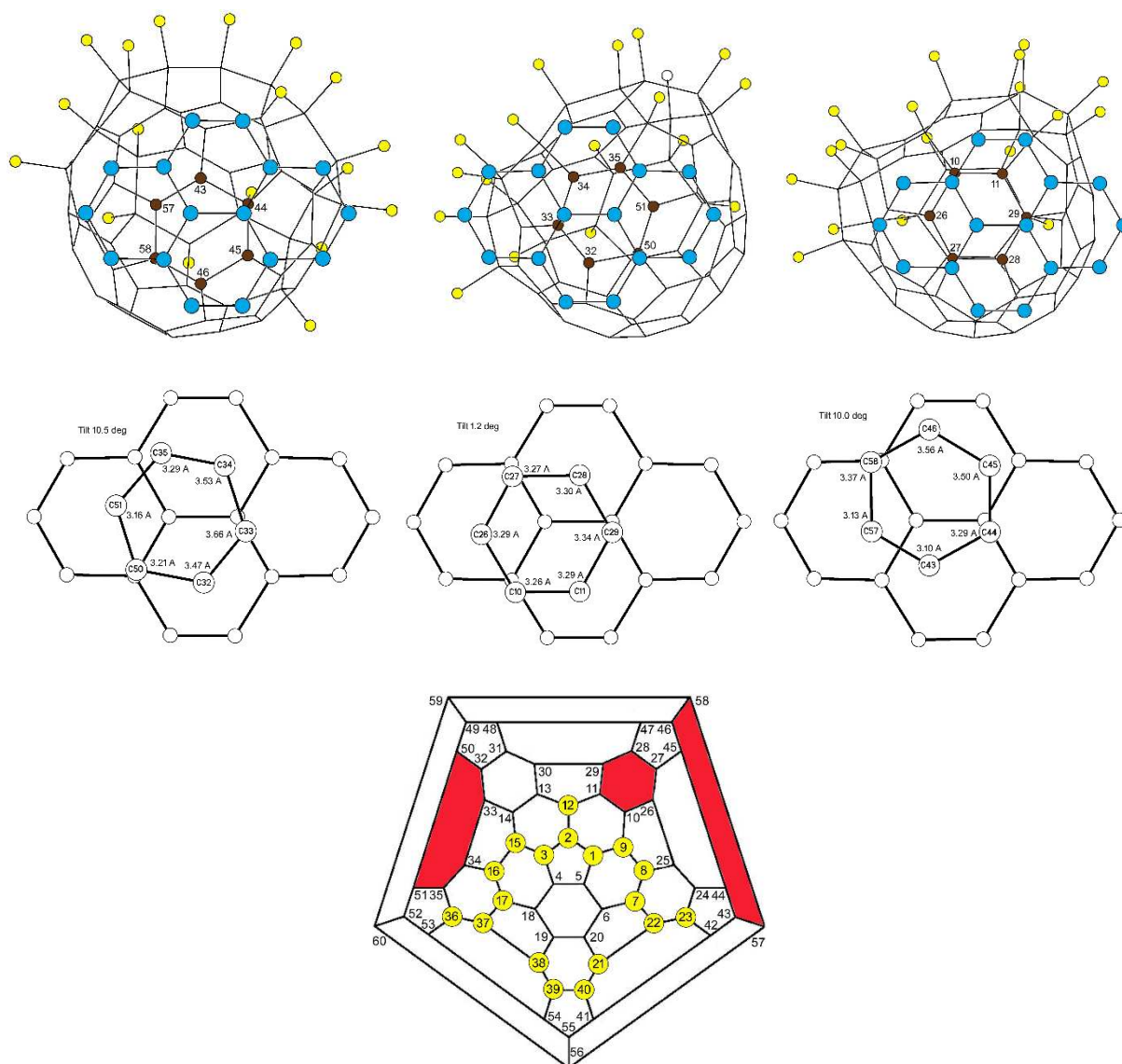
Figure 5-24. The structure of (PYRN)$_2$/C$_{60}$F$_{18}$·CH$_2$Cl$_2$. (**Top and Middle**) drawings show the three PYRN molecules (H atoms omitted for clarity) and the three fullerene hexagons with which they form π–π overlap interactions. In each of the upper set of drawings, the PYRN C(sp^2) atoms are colored blue and the fullerene hexagon C(sp^2) atoms, labeled with their IUPAC locants, are colored brown. In each of the middle set of drawings, the perpendicular distances, in Å, of the fullerene hexagon C(sp^2) atoms to the PYRN least-squares plane are indicated. The red hexagons in the Schlegel diagram indicate the three fullerene hexagons that have π–π overlap interactions with the three PYRN molecules.

300

5.7. REFERENCES

(1)   Zhang, J.; Xu, W.; Sheng, P.; Zhao, G.; Zhu, D. Organic Donor–Acceptor Complexes as Novel Organic Semiconductors. *Acc. Chem. Res.* **2017**, *50*, 1654-1662.

(2)   Stallinga, P.; Gomes, H. L. Modeling electrical characteristics of thin-film field-effect transistors: II: Effects of traps and impurities. *Synth. Met.* **2006**, *156*, 1316-1326.

(3)   Rieger, R.; Enkelmann, V.; Müllen, K. Charge-Transfer Controlled Crystallization of a Model Oligomer for Donor-Acceptor-Polythiophenes. *Materials* **2010**, *3*, 1904-1912.

(4)   Colombo, V.; Presti, L. L.; Gavezzotti, A. Two-component organic crystals without hydrogen bonding: structure and intermolecular interactions in bimolecular stacking. *CrystEngComm* **2017**, *19*, 2413-2423.

(5)   Goud, N. R.; Matzger, A. J. Impact of Hydrogen and Halogen Bonding Interactions on the Packing and Ionicity of Charge-Transfer Cocrystals. *Cryst. Growth Des.* **2017**, *17*, 328-336.

(6)   Collings, J. C.; Roscoe, K. P.; Thomas, R. L.; Batsanov, A. S.; Stimson, L. M.; Howard, J. A. K.; Marder, T. B. Arene-perfluoroarene interactions in crystal engineering. Part 3. Single-crystal structures of 1 : 1 complexes of octafluoronaphthalene with fused-ring polyaromatic hydrocarbons. *New J. Chem.* **2001**, *25*, 1410–1417.

(7)   Collings, J. C.; Batsanov, A. S.; Howard, J. A. K.; Marder, T. B. Arene–perfluoroarene interactions in crystal engineering. Part 14. 1:1 Complexes of octafluoronaphthalene with fluorene and 9,10-dihydrophenanthrene. *Can. J. Chem.* **2006**, *84*, 238–242.

(8)   Clikeman, T. T.; Bukovsky, E. V.; Kuvychko, I. V.; San, L. K.; Deng, S. H. M.; Wang, X.-B.; Chen, Y.-S.; Strauss, S. H.; Boltalina, O. B. Poly(trifluoromethyl) azulenes: structure and acceptor properties. *Chem. Commun.* **2014**, *50*, 6263-6266.

(9)   DeWeerd, N. J.; Bukovsky, E. V.; Castro, K. P.; Kuvychko, I. V.; Popov, A. A.; Strauss, S. H.; Boltalina, O. V. Steric and electronic effects of CF_3 conformations in acene$(CF_3)_n$ derivatives. *J. Fluorine Chem.* **2019**, *221*, 1-7.

(10)   Castro, K. P.; Bukovsky, E. V.; Kuvychko, I. V.; DeWeerd, N. J.; Chen, Y.-S.; Deng, S. H. M.; Wang, X.-B.; Popov, A. A.; Strauss, S. H.; Boltalina, O. V. PAH/PAH(CF$_3$)$_n$ Donor/Acceptor Charge-Transfer Complexes in Solution and in Solid-State Co-Crystals. *Chem. Eur. J.* **2019**, *25*, 13547-13565.

(11)   Ohkubo, K.; Taylor, R.; Boltalina, O. V.; Ogo, S.; Fukuzumi, S. Electron transfer reduction of a highly electron-deficient fullerene, C$_{60}$F$_{18}$. *Chem. Commun.* **2002**, 1952-1953.

(12)   Beckmann, P. A.; Reingold, A. L. ^{1}H and ^{19}F spin-lattice relaxation and CH$_3$ or CF$_3$ reorientation in molecular solids containing both H and F atoms. *J. Chem. Phys.* **2016**, *144*, article 154308, and references therein.

(13)   Wang, X.; Mallory, F. B.; Mallory, C. W.; Bechmann, P. A.; Reingold, A. L.; Franci, M. M. CF$_3$ Rotation in 3-(Trifluoromethyl)phenanthrene. X-ray Diffraction and ab Initio Electronic Structure Calculations. *J. Phys. Chem. A* **2006**, *110*, 3954-3960.

(14)   Beckmann, P. A.; Rosenberg, J.; Nordstrom, K.; Mallory, C. W.; Mallory, F. B. CF$_3$ Rotation in 3-(Trifluoromethyl)phenanthrene: Solid State ^{19}F and ^{1}H NMR Relaxation and Bloch-Wangsness-Redfield Theory. *J. Phys. Chem,. A* **2006**, *110*, 3947-3953.

(15)   Kuvychko, I. V.; Castro, K. P.; Deng, S. H. M.; Wang, X.-B.; Strauss, S. H.; Boltalina, O. V. Taming Hot CF$_3$ Radicals: Incrementally Tuned Families of Polyarene Electron Acceptors for Air-Stable Molecular Optoelectronics. *Angew. Chem. Int. Ed.* **2013**, *52*, 4871-4874.

(16)   Castro, K. P. Dissertation, Colorado State University, 2015.

(17)   Bock, H.; Sievert, M.; Schödel, H.; Kleine, M. Interactions in crystals .88. Donor/acceptor complexes of alkylbenzenes, pyrene or perylene and tetrahalogen-*p*-benzoquinones: Structures and properties. *Z. Naturforsch. B* **1996**, *51*, 1521–1537.

(18) Frampton, C. S.; Knight, K. S.; Shankland, N.; Shankland, K. Single-crystal X-ray diffraction analysis of pyrene II at 93 K. *J. Mol. Struct.* **2000**, *520*, 29-32.

(19) Schwaben, J.; Münster, N.; Breuer, T.; Klues, M.; Harms, K.; Witte, G.; Koert, U. Synthesis and Solid-State Structures of 6,13-Bis(trifluoromethyl)- and 6,13-Dialkoxypentacene. *Eur. J. Org. Chem.* **2013**, 1639-1643.

(20)   Yamada, S.; Kinoshita, K.; Iwama, S.; Yamazaki, T.; Kubota, T.; Yajima, T.; Yamamoto, K.; Tahara, S. Synthesis of perfluoroalkylated pentacenes and evaluation of their fundamental physical properties. *Org. Biomol. Chem.* **2017**, *15*, 2522-2535.

(21)   Sun, H.; Putta, A.; Billion, M. Arene Trifluoromethylation: An Effective Strategy to Obtain Air-Stable *n*-Type Organic Semiconductors with Tunable Optoelectronic and Electron Transfer Properties. *J. Phys. Chem. A* **2012**, *116*, 8015-8022.

(22)   Sun, H.; Tottempudi, U. K.; Mottishaw, J. D.; Basa, P. N.; Putta, A.; Sykes, A. G. Strengthening $\pi-\pi$ Interactions While Suppressing $Csp^2-H\cdots\pi$ (T-Shaped) Interactions via Perfluoroalkylation: A Crystallographic and Computational Study That Supports the Beneficial Formation of 1-D $\pi-\pi$ Stacked Aromatic Materials. *Cryst. Growth Des.* **2012**, *12* 5655-5662.

(23)   Yamada, S.; Kinoshita, K.; Iwama, S.; Yamazaki, T.; Kubota, T.; Yajima, T. Development of novel synthetic routes to bis(perfluoroalkyl)-substituted anthracene derivatives. *RSC Adv.* **2013**, *3*, 6803-6806.

(24)   Boltalina, O. V.; Markov, V. Y.; Taylor, R.; Waugh, M. P. Preparation and characterisation of $C_{60}F_{18}$. *Chem. Commun.* **1996**, *2549-2550*.

(25)   Boltalina, O. V.; Markov, V. Y.; Lukonin, A. Y.; Avakjan, T. V.; Ponomarev, D. B.; Sorokin, I. D.; Sidorov, L. N. Mass Spectrometric Measurements of the Equilibrium Constants of Ion Molecular Reactions of Fullerenes, Fluorine Derivatives and Endohedrals. Electron and Fluorine Affinity Estimates In *Recent Advances in the Chemistry and Physics of Fullerenes and Related Materials*; Kadish, K. M., Ruoff, R. S., Eds.; Electrochemical Society: Pennington, N.J., 1995; Vol. 95-10, pp 1395-1408.

(26)   Goldt, I. V.; Boltalina, O. V.; Sidorov, L. N.; Kemnitz, E.; Troyanov, S. I. Preparation and crystal structure of solvent free $C_{60}F_{18}$. *Solid State Sci.* **2002**, *4*, 1395-1401.

(27)   Hübschle, C. B.; Scheins, S.; Weber, M.; Luger, P.; Wagner, A.; Koritsánszky, T.; Troyanov, S. I.; Boltalina, O. V.; Goldt, I. V. Bond Orders and Atomic Properties of the Highly Deformed Halogenated Fullerenes $C_{60}F_{18}$ and $C_{60}Cl_{30}$ Derived from their Charge Densities. *Chem. Eur. J.* **2007**, *13*, 1910-1920.

(28)   Schlegel, V. *Theorie der homogen zusammengesetzten Raumgebilde* Blockmann & Sohn: Dresden, Germany, 1883.

(29)   Goryunkov, A. A.; Kareev, I. E.; Ioffe, I. N.; Popov, A. A.; Kuvychko, I. V.; Markov, V. Y.; Goldt, I. V.; Pimenova, A. S.; Serov, M. G.; Avdoshenko, S. M.; Khavrel, P. A.; Sidorov, L. N.; Lebedkin, S. F.; Mazej, Z.; Zemva, B.; Strauss, S. H.; Boltalina, O. V. Reaction of C_{60} with $KMnF_4$. Isolation and Characterization of a New Isomer of $C_{60}F_8$ and Re-evaluation of the Structures of $C_{60}F_7(CF_3)$ and the Known Isomer of $C_{60}F_8$. *J. Fluorine Chem.* **2006**, *127*, 1423-1435.

(30)   Denisenko, N. I.; Troyanov, S. I.; Popov, A. A.; Kuvychko, I. V.; Zemva, B.; Kemnitz, E.; Strauss, S. H.; Boltalina, O. V. T_h-$C_{60}F_{24}$. *J. Am. Chem. Soc.* **2004**, *126*, 1618-1619.

(31)   Boltalina, O. V.; Street, J. M.; Taylor, R. $C_{60}F_{36}$ consists of two isomers having T and C_3 symmetry. *J. Chem. Soc., Perkin Trans. 2* **1998**, 649-654.

(32)   https://www.nacalai.co.jp/global/cosmosil/column/11.html, accessed January 2020.

(33)   Troyanov, S. I.; Boltalina, O. V.; Kuvychko, I. V.; Troshin, P. A.; Kemnitz, E.; Hitchcock, P. B.; Taylor, R. Molecular and Crystal Structure of the Adducts of $C_{60}F_{18}$ with Aromatic Hydrocarbons. *Fuller. Nanotub. Carbon Nanostruct.* **2002**, *10*, 243-260.

(34)   Kuvychko, I. V.; Castro, K. P.; Deng, S. H. M.; Wang, X.-B.; Strauss, S. H.; Boltalina, O. B. Taming Hot CF_3 Radicals: Incrementally Tuned Families of Polyarene Electron Acceptors for Air-Stable Molecular Optoelectronics. *Angew. Chem. Int. Ed.* **2013**, *52*, 4871–4874.

(35)   Weger, M. Theory of the Electrical Conductivity of Organic Metals In *The Physics and Chemistry of Low Dimensional Solids. NATO Advance Study Institutes Series (Series C - Mathematical and Physical Sciences)*; Alcácer, L., Ed.; Springer Netherlands: Dordrecht, 1980; Vol. 56, pp 77-100.

(36)   Powell, W. H.; Cozzi, F.; Moss, G. P.; Thilgen, C.; Hwu, R. J. R.; Yerin, A. Nomenclature for the C_{60}-I_h and C_{70}-$D_{5h(6)}$ Fullerenes (IUPAC Recommendations 2002). *Pure Appl. Chem.* **2002**, *74*, 629-695.

CHAPTER 6

TRIFLUOROMETHYLPHENOTHIAZINE DERIVATIVES,
COMPOUNDS WITH CF₃···H–N HYDROGEN BONDING

6.1. INTRODUCTION AND JUSTIFICATION

Phenothiazine (10*H*-phenothiazine, PNTZ) and its derivatives have been rigorously studied as tranquilizers, antimalarials, antipsychotics, biological stains, dyes, and pigments ever since PNTZ was prepared in 1883.[1-5] More recently, PNTZ and various derivatives have been studied for OPV and other organic electronic applications, especially as a donor molecule in donor/acceptor CT complexes.[4,6-10] PNTZ is a non-planar hetero-tricyclic molecule with a bend angle of 28°, as shown in Figure 6-1. It is not completely aromatic, although its X-ray structure showed that the N atom is flattened from a true $N(sp^3)$ trigonal pyramid (the sum of the three angles around the N atom is 352.6°;[11] cf. 332.7° for NMe_3).

Although $PNTZ(F)_n$ (n = 1–4)[12] and 2-,[13] 3-,[12] and 4-$PNTZ(CF_3)$[14] have been reported, no *EA*s of any PNTZ derivative has been reported, and none has been studied as a possible electron acceptor. Several years ago, our laboratory set out to prepare $PNTZ(CF_3)_n$ derivatives with $n \geq 3$. Several high-temperature reactions of PNTZ and CF_3I were carried out by former graduate student Igor V. Kuvychko and initial HPLC separation of the crude product mixture into seven fractions was carried out by former graduate student Long K. San. Each of the seven fractions contained multiple $PNTZ(CF_3)_n$ compounds. The author's contribution to this work is the further HPLC separation of each of the seven fractions, from which eleven pure $PNTZ(CF_3)_n$ compounds were isolated and characterized by ¹H and ¹⁹F NMR spectroscopy and, for two isomers of $PNTZ(CF_3)_4$, SC-XRD. In addition, four compounds were sent to collaborator Dr. Xue-Bin Wang for possible *EA* determinations using low-temperature PES.

6.2. PURIFICATION OF PNTZ(CF₃)ₙ DERIVATIVES

The PNTZ(CF$_3$)$_n$ derivatives were synthesized by Dr. Kuvychko and details of the synthesis are shown in Section 6.4.2. Dr. San performed an initial separation of the crude material in acetonitrile generating seven fractions, see Figure 6-2. One of those fractions, F2, was further separated by Dr. San in a mixture of 25/75 toluene/heptane as the eluent and the second fraction from that separation was identified and characterized by the author as PNTZ-4-1. The fractions were then evaporated to dryness. The author re-dissolved each of the seven dried fractions in MeOH and further separated Fractions F1 and F3–F7 with the same HPLC column using MeOH as the eluent with a flow rate of 5 mL min^{-1}. These constituted the second stage of HPLC purification. Pure PNTZ(CF$_3$)$_n$ compounds were isolated only from fractions F2–F5. The second-stage chromatograms of first-stage fractions F3, F4, and F5 are shown in Figure 6-3. As discussed in the NMR section below, seven PNTZ(CF$_3$)$_n$ compounds with ≥ 95 mol% purity were isolated by second-stage purification of fractions F2–F5, one isomer of PNTZ(CF$_3$)$_3$, four isomers of PNTZ(CF$_3$)$_4$, and one isomer of PNTZ(CF$_3$)$_5$. Additionally, four more PNTZ(CF$_3$)$_4$ isomers were identified in impure fractions but could be reliably structurally assigned by NMR, see Figure 6-12. Note that the amounts of material in first-stage fractions F2, F3, F4, and F5 that were available to the author for second-stage purification were 11, 14, 11, and 13 mg, respectively. First-stage fractions F1, F6, and F7 did not yield any pure PNTZ(CF$_3$)$_n$ compounds and will not be discussed further. Table 6-1 lists the seven purified PNTZ(CF$_3$)$_n$ compounds, the second-stage fraction from which they were isolated, and IUPAC locants and abbreviations (the locants came from analysis of their ^{1}H and ^{19}F NMR spectra discussed in Section 6.3.2.).

6.3. CHARACTERIZATION OF PNTZ(CF₃)ₙ COMPOUNDS

6.3.1. The structure of PNTZ(CF₃)₄

The structure of PNTZ-4-2 (orthorhombic, $P2_12_12_1$) was modeled as a two-component inversion twin with a 60% majority component. The CF$_3$ group attached to C9 exhibited a two-

fold rotational disorder. It was refined with a free variable, and the dominant disordered portion was modeled with 81% occupancy. The structure of PNTZ-4-3 (monoclinic, $P2_1$) has low precision due to poor crystal quality and unresolved twinning (the C–C s.u. is 0.01 Å). The structure contains two unique PNTZ-4-3 molecules with almost identical conformations. Higher symmetry space groups were evaluated but no solutions were generated and none of the standard tests returned concerns about missed symmetry.

Thermal ellipsoid plots of the two compounds, confirming their substitution patterns, 1,3,7,9-PNTZ(CF$_3$)$_4$ for PNTZ-4-2 and 1,2,7,9-PNTZ(CF$_3$)$_4$ for PNTZ-4-3, are shown in Figure 6-4. Drawings of the molecules in another orientation are shown in Figure 6-5. The molecules adopt bent, butterfly-like conformations. The outer six-membered aromatic rings, bearing the CF$_3$ groups, are planar in both structures. The central C$_4$NS hexagons adopt similar boat configurations in the two structures. The molecules are domed, or bent, in a way that is reminiscent of the bending observed with ANTH-6-1 and similar compounds discussed in Chapter 5. The two halves of the PNTZ molecules are bent with respect to the N···S vector, as shown in Figure 6-1. The bend angle is 27.8° in unsubstituted PNTZ,[11] 33.0° in PNTZ-4-2, and 36.0°/35.2° for the two unique molecules in PNTZ-4-3, but is only 22.4° in singly-substituted 2-PNTZ(CF$_3$).[15] The bend angle in DFT optimized PNTZ-4-2 is 32.3°, close to the value in the X-ray structure, but the bend angle in DFT optimized unsubstituted PNTZ is 34.3°, considerably larger than in the X-ray structure.[16] Therefore, the bending of PNTZ and its derivatives about the N···S vector may depend on crystal packing forces in much the same way as the bending of ANTH-6-1, discussed in Chapter 5, varied from 0° to 13.5° from one crystal structure to another.[17]

Both PNTZ-4-2 and PNTZ-4-3 pack in their respective lattices in very similar ways, as shown in Figure 6-6 for both structures, in Figure 6-7 for the structure of PNTZ-4-3, and in Figure 6-8 for the structure of PNTZ-4-2. The densities are the same to within 1.5%, 1.910 g cm^{-3} for PNTZ-4-2 and 1.938 g cm^{-3} for PNTZ-4-3. The molecules form stacks, with very little offset, along the crystallographic b axis in PNTZ-4-2 and along the a axis in PNTZ-4-3. Molecules of PNTZ-4-3

are chiral, and adjacent molecules along the stacks are opposite enantiomers. Molecules of PNTZ-4-2 have idealized C_s symmetry. The N⋯S centroids of molecules along each stack are 3.86 Å apart in PNTZ-4-2 and 3.83 or 3.89 Å apart in PNTZ-4-3, and the vectors connecting an N⋯S centroid with the centroids in the molecules above and below subtend angles of 164° in PNTZ-4-2 and 163° in PNTZ-4-3. The stacks form hexagonal arrays, as shown in Figure 6-8, with intermolecular F⋯F contacts as short as 2.80 Å (twice the van der Waals radius of an F atom is 2.94 Å[18]). More importantly, as far as the ^{19}F NMR spectra of the $PNTZ(CF_3)_n$ derivatives are concerned (see below), intramolecular F⋯F contacts between the pair of *ortho* CF_3 groups in PNTZ-4-3 are 2.59(1) and 2.62(1) Å in one molecule (shown with dashed lines in Figure 6-4) and 2.55(1) and 2.62(1) Å in the second molecule.

Unsubstituted PNTZ[11] and 2-PNTZ(CF_3)[15] both adopt herringbone packing patterns in their respective crystals, in contrast to the stacked packing in PNTZ-4-2 and PNTZ-4-3. This parallels the observations by the Strauss-Boltalina group that $PAH(CF_3)_n$ derivatives with three or more CF_3 groups tend to form structures with stacks of molecules (e.g., 1,4,7,10-CORO(CF_3)$_4$ (Chapter 2), 2,3,6,8,9,10-ANTH(CF_3)$_6$ (Chapter 5), 1,4,7,10-PERY(CF_3)$_4$,[19] 1,3,9-PHZN(CF_3)$_3$,[20] and 1,3,4,6,8-PYRN(CF_3)$_5$[19]) whereas unsubstituted PAHs tend to form herringbone structures (e.g., ANTH,[21] PERY,[22] PHZN,[23] and PYRN[24]).

6.3.2. NMR spectroscopy of $PNTZ(CF_3)_n$

The ^{19}F NMR spectrum of purified PNTZ-5-1 is shown in Figure 6-10. The ^{19}F NMR spectra of the nine other $PNTZ(CF_3)_n$ compounds are shown in Figures Figure **6-11** and Figure **6-12**, and a representative ^{1}H NMR spectrum of PNTZ-4-1 is shown in Figure 6-13. Chemical shifts and coupling constants are listed in Table 6-2. The ^{1}H NMR spectra are consistent with the structural assignments based on the ^{19}F NMR spectra. Three $PNTZ(CF_3)_4$ derivatives, PNTZ-4-2, PNTZ-4-4, and PNTZ-4-9 have C_s symmetry. The other compounds are asymmetric. The spectra shown in Figures Figure **6-10**,Figure **6-11**, and Figure **6-12** clearly show evidence for CF_3 groups that are on $C(sp^2)$ atoms *ortho* to one or two $C(sp^2)$ atoms bearing a CF_3 group. This evidence is the

presence of pairs of quartets, or a quartet and a more complex multiplet, in the ^{19}F spectra of PNTZ-3-1, PNTZ-4-1, PNTZ-4-3, PNTZ-4-5, PNTZ-4-7, PNTZ-4-8, and PNTZ-5-1, with $^5J_{FF}$ coupling constants of 14–16 Hz. The presence of an *ortho* pair of CF_3 groups in PNTZ-4-3 was proven by its X-ray crystal structure. As discussed below, the presence of pairs of quartets or quartets-of-quartets (apparent septets, as in multiplet e in the ^{19}F NMR spectrum of PNTZ-5-1) is the hallmark of intramolecular "through-space" coupling between the F atoms in neighboring CF_3 groups.[25]

The following paragraph is paraphrased from sections about through-space J_{FF} coupling in refs. 25 and 26. Some might argue that the term "through-space coupling" is a misnomer since true through-space coupling involving zero orbital overlap (e.g., dipolar coupling) is not observed in liquid NMR spectra. (This is because dipole-dipole interactions in an isotropically tumbling molecule are averaged to zero.) However, NMR spectroscopists have used the term for more than 50 years to describe Fermi contact coupling by direct overlap of F atom lone-pair orbitals, as opposed to Fermi contact coupling through the σ and π framework of a molecule.[27,28] It is now widely accepted that significant spin-spin J coupling between proximate F nuclei (i.e., ≤ 3.2 Å) that are separated by four or more bonds (i.e., $^{\geq 4}J_{FF}$) is predominantly mediated through space, as just defined.[29-38] A convincing example is the 17 Hz $^{398}J_{FF}$ coupling observed[39] for the F atoms on 6-fluorotryptophan residues (Trp5 and Trp133) in a dihydrofolate reductase-NADPH-MTX protein complex, which Oldfield later showed was mediated entirely by through-space coupling (F$\cdots$F = 2.98 Å).[40]

As noted in the previous section, the structure of PNTZ-4-3 exhibited intramolecular F$\cdots$F distances of 2.55(1)–2.62(1) between the F atoms on the *ortho* CF_3 groups attached to PNTZ $C(sp^2)$ atoms C1 and C2. These CF_3 groups are rapidly rotating about their respective $C(sp^2)$–CF_3 single bonds. Therefore, the observed 16 Hz J_{FF} values are time averages: the average coupling constant between *each* of the F atoms on one CF_3 group with *each* of the F atoms on the other CF_3 group over all possible conformations. Figure 6-14 shows the orientation of the *ortho* pair of CF_3 groups in the crystal structure of PNTZ-4-3. In solution, there would be 18 different conformations for

these two CF_3 groups, and F15 would be ca. 2.6 Å from F16, and would experience through-space coupling with F16, in only four of those 18 conformations. For the 14 other conformations, the distance between F15 and F16 would be >> 3 Å, and the through-space J_{FF} value for those two F atoms would be effectively zero. Therefore, 16 Hz is the average of four non-zero J_{FF} values and 14 zero J_{FF} values, and according to this analysis the "instantaneous" J_{FF} coupling constant for these two CF_3 groups is expected to be approximately 72 Hz (i.e., 4x ÷ 18 = 16 Hz, x = 72 Hz).

The above analysis is supported by ^{19}F NMR spectra and X-ray crystal structures of perfluoro-alkylated derivatives of C_{60}. First, consider the isolated $para$-$C_6(CF_3)_2$ hexagon in the X-ray crystal structure of 1,6,11,16,18,24,27,36,41,57-$C_{60}(CF_3)_{10}$,[41] which is shown in Figure 6-14. The F⋯F distance between F23 on one CF_3 group and F27 on the other CF_3 group is 2.621(5) Å. In solution, the ^{19}F NMR spectrum of this compound exhibits two quartets with J_{FF} = 14 Hz for these rapidly rotating CF_3 groups,[26] and it was suggested that the nonzero component of the time-averaged J_{FF} value would be ca. 126 Hz (i.e., 9 × 14 Hz, because any pair of F atoms experiences the nonzero coupling only one-ninth of the time). Next, consider one of the three isolated $para$-$C_6(i$-$C_3F_7)_2$ hexagons in the X-ray crystal structure of 1,7,16,30,36,47-$C_{60}(i$-$C_3F_7)_6$,[42] also shown in Figure 6-14. The two central F atoms are 2.655(4) Å apart in the X-ray structure. The size and shape of the perfluoroisopropyl groups dictates that this is probably the only possible conformation for these two groups in solution. Consequently, the two F atoms are ca. 2.7 Å apart 100% of the time, and the J_{FF} value for these F atoms was found to be 160 Hz.[43]

The ^{19}F NMR spectra of the $H_2CORO(CF_3)_7$ and $H_2CORO(CF_3)_8$ compounds discussed in Chapter 2 also exhibited quartets (and quartets-of-quartets or more complex multiplets) for neighboring CF_3 groups with J_{FF} values ranging from 7 to 16 Hz (e.g., see Figures 2-5, 2-6 and S2-9. Figure 2-6 shows six F⋯F contacts shorter than 2.9 Å between five contiguous CF_3 groups, three attached to CORO $C(sp^2)$ atoms and two attached to the CORO $C(sp^3)$ atoms.

Returning to the ^{19}F NMR spectra of the $PNTZ(CF_3)_n$ compounds, some of the multiplets in the spectrum of PNTZ-5-1 in Figure 6-10 (and the spectra of PNTZ-4-3 and PNTZ-4-7 in Figures

Figure 6-11 and Figure 6-12, respectively) show evidence of $^{7}J_{FF}$ coupling between the CF_3 groups on C1 and C9 (i.e., between the CF_3 groups "next to" the N atom) and J_{FH} coupling between those CF_3 groups and the N–H proton. First of all, singlet a, and multiplets c and e, in the ^{19}F NMR spectrum of PNTZ-5-1 do not require additional comment. Next, multiplet b is not a singlet, therefore CF_3 group b must be coupled to the N–H proton (note that the signal for isolated CF_3 group a is a singlet). But if that were all, it would be a doublet, not a complex multiplet. In addition, multiplet d shows that CF_3 group d is not just coupled to CF_3 group e, because then it would be a simple quartet, like the quartet for CF_3 group c, not the complex multiplet d that was observed. Therefore, CF_3 group d must also be coupled to the N–H proton. But if that were all, it would be a quartet of doublets, and it is not as simple as that. A simulation of multiplet d using the program MNova is shown in Figure 6-15. The lowest simulated spectrum includes 16 Hz J_{FF} coupling to CF_3 group e and 4 Hz coupling to the N–H proton. Only when an additional 4 Hz J_{FF} coupling to CF_3 group b is included does the simulated multiplet d match experimental multiplet d. The simulation of multiplet b, shown in Figure 6-16, confirms that CF_3 group b exhibits 4 Hz J_{bd} as well as 4 Hz J_{bH} coupling.

The bent structure of the $PNTH(CF_3)_n$ compounds is probably why there is measurable 4 Hz J_{FH} coupling to the N–H proton in PNTZ-5-1 and five $PNTZ(CF_3)_4$ isomers, and why there is measurable, 4 Hz J_{FF} coupling between the CF_3 groups on opposite sides of the N atom in PNTZ-5-1 and PNTZ-4-3. Figure 6-17 shows part of the X-ray crystal structure of PNTZ-4-3, with F2$\cdots$F11 = 3.27 Å, F2$\cdots$H = 2.28 Å, and F11$\cdots$H = 2.00 Å. In contrast, Figure 6-17 includes a comparison with the corresponding part of the X-ray structure of 1,3,6,8,10-$ANTH(CF_3)_5$,[19] which does not have a bent aromatic core and which does not exhibit the same type of J_{FF} and J_{FH} coupling in its ^{19}F NMR spectrum.[19] The corresponding distances in 1,3,6,8,10-$ANTH(CF_3)_5$, F1$\cdots$F4 = 3.64 Å, F1$\cdots$H9 = 2.42 Å, and F4$\cdots$H9 = 2.43 Å, are significantly longer than in PNTZ-4-3.

Long-range C–F$\cdots$H–C[5,6] J_{FH} values of 1–15 Hz were reported as long ago as 1966 and have been referred to, since then, as "through-space" coupling,[44-48] in much the same way as long-range

J_{FF} coupling has been called through-space coupling.[29-38] However, the presumed through-space $^5J_{FH}$ coupling in PNTZ-5-1 and PNTZ-4-3 cannot be mediated by the same mechanism as the $^5J_{FF}$ and $^7J_{FF}$ through-space couplings in those compounds because H atoms do not have lone pairs to overlap with F atom lone pairs. Instead, the $^5J_{FH}$ couplings are probably mediated by overlap of F atom lone pairs with the N–H σ^* antibonding orbital. In this way, this intramolecular "long-range, through-space" coupling is neither long-range nor through-space, but is J_{FH} spin-spin coupling through a weak, insipient (C)F···H–N hydrogen bond. Intramolecular J_{FH} coupling of the same magnitude as in PNTZ-5-1 and PNTZ-4-3, and with the similar (C)F···H(N) distances, have been attributed to (C)F···H–N hydrogen bonding in a number of compounds.[49-53] Drawings of some of the molecules reported in these references, including one with a CF_3 group coupled to an N–H proton,[49] are shown in Figure 6-18.[50,52]

6.3.3. Gas-phase photoelectron spectroscopy of PNTZ(CF$_3$)$_n$

In this work, solutions of PNTZ-3-1, PNTZ-4-1, PNTZ-4-2, and PNTZ-5-1 in CH_3CN containing TDAE were used by Dr. Wang. The resulting photoelectron spectra are shown in Figure 6-19 and the results from these spectra are listed in Table 6-4. It became obvious that the spectra did not show the electron photodetachment energies for gas-phase [PNTZ(CF$_3$)$_n$]$^-$ anions, because the EAs of the neutral PNTZ(CF$_3$)$_n$ derivatives could not possibly exceed 3 eV. That tentative conclusion was based on the known EAs of PAH(CF$_3$)$_n$ derivatives, including 2.80(2) eV for ANTH-6-1[19] (DFT value = 2.86[54]), 2.40(2) eV for 1,3,6,8,10-ANTH(CF$_3$)$_5$,[19] 1.795(20) eV for 1,3,5,7-naphthalene(CF$_3$)$_4$ (DFT value = 1.745),[54] and 2.60(1) eV for 1,4,6,9-phenazine(CF$_3$)$_4$.[20] The conclusion was verified by asking collaborator Dr. Alexey A. Popov to calculate the EAs of PNTZ-3-1, PNTZ-4-1, PNTZ-4-2, and PNTZ-5-1. Those results, which ranged from 0.92 to 1.46 eV, are listed in Table 6-4.

The current interpretation of the PES spectra in Figure 6-19 is that the anions for which electron photodetachment energies were measured were deprotonated anions, [PNTZ(CF$_3$)$_n$ − H]$^-$, and these are the molecular ions shown next to each PES spectrum. Unlike the other PAH(CF$_3$)$_n$

compounds that have had their *EA*s determined by Dr. Wang at PNNL,[19,20,54,55] PNTZ has an acidic proton (pK_a = 22.7 in dimethylsulfoxide[56]), and PNTZ derivatives with multiple electron-withdrawing CF_3 groups would be expected to be orders of magnitude more acidic than unsubstituted PNTZ. Therefore, the indicated values are the gas-phase electron affinities of the putative radicals formed by removing the H atom from the N atom, not the electron affinities of the intact protonated molecules. Dr. Popov also calculated their *EA*s by DFT. The measured values range from 3.33(5) to 3.67(5) eV, and the DFT predicted values range from 2.80 to 3.39 eV.

6.4. MATERIALS AND METHODS

6.4.1. Reagents and general procedures

The following reagents and solvents were obtained from the indicated sources and were used as received or were purified where indicated: PNTZ (98%, Sigma Aldrich); Trifluoromethyl iodide (99% SynQuest); dichloromethane (ACS grade, Fischer); methanol ACS grade (99%, Fischer); acetonitrile (ACS grade, Fischer); sodium thiolsulfate (99+%, Fischer); deuterated chloroform (99.8%, Cambridge Isotope Labs); toluene (99.9%, Fischer Scientific); heptane HPLC grade (98%, Fischer); and perfluorobenzene (Oakwood Products).

6.4.2. Synthesis of PNTZ(CF₃)ₙ

Kuvychko's synthesis of PNTZ(CF_3)$_n$ compounds involved heating PNTZ (200 mg, 1.00 mmol) with CF_3I (ca. 10 mmol) in a sealed glass ampule in a manner similar to reactions reported previously by the Strauss-Boltalina group.[19,20] (The pressure in the ampule before heating was ca. 600 Torr.) The sealed ampule was heated stepwise from 300 °C to 330 °C over a period of 30 minutes with 10 °C step increases. The ampule was held at 330 °C for 7 h, then cooled to RT. The reaction product was extracted with DCM and washed with aqueous $Na_2S_2O_3$ to remove the I_2 by-product. The DCM layer was evaporated to dryness, yielding 133 mg of a mixture of PNTZ(CF_3)$_n$ compounds.

6.4.3. Spectroscopic characterization

Proton and ^{19}F NMR spectra of first-stage and second-stage purification fractions evaporated to dryness and re-dissolved in $CDCl_3$ were recorded using a Varian INOVA 400 spectrometer operating at 400 and 376 MHz, respectively. The ^{19}F NMR spectra of first-stage purification fractions F4 and F5, which contained multiple products, and of second-stage purification fractions F3F1–F3F3, F4F1–F4F7, and F5F1–F5F4 are shown in Figure 6-9.

6.4.4. X-ray crystallographic data collection for PNTZ(CF$_3$)$_4$

Crystals of two PNTZ(CF$_3$)$_4$ isomers suitable for diffraction, PNTZ-4-2 and PNTZ-4-3, were grown by slow evaporation of methanol solutions. Diffraction data were collected by the author at the Advanced Photon Source at Argonne National Laboratory on beamline 15ID-D, using a diamond 111 monochromator, an X-ray wavelength of 0.41328 Å, a Bruker D8 goniometer, and multiscan absorption corrections. Unit cell parameters were determined by the least squares fit of the angular coordinates of all reflections. Integrations of all frames were performed using the Bruker APEX III suite of software, and the structures were solved by the author using SHELXTL/OLEX 2 software. Table 6-2 lists crystallographic data collection and final refinement parameters.

6.4.5. Photoelectron spectroscopy

Samples of PNTZ-3-1, PNTZ-4-1, PNTZ-4-2, and PNTZ-5-1 were sent to collaborator Dr. Xue-Bin Wang at Pacific Northwest National Laboratory (PNNL) for *EA* measurements. A discussion of a typical experiment is included in Section 2.6.3. of this work.

6.5. CONCLUSIONS AND FUTURE WORK

The high-temperature reaction of PNTZ with CF$_3$I produced a mixture of compounds from which eleven PNTZ(CF$_3$)$_n$ were successfully isolated and characterized. The structures of PNTZ-4-2 and PNTZ-4-3 form structures with close-packed arrays of stacks of molecules, unlike the

herringbone structures of unsubstituted PNTZ and 2-PNTZ(CF$_3$). The bend angles are greater than in unsubstituted PNTZ and 2-PNTZ(CF$_3$), and the greater bend may be responsible, in part, for the tendency of PNTZ-4-2 and PNTZ-4-3 to form molecular stacks in their respective crystals.

The NMR spectra of the PNTZ(CF$_3$)$_n$ derivatives revealed J_{FH} coupling of CF$_3$ groups to the N–H proton that is probably mediated by donation of an F atom lone pair to the N–H σ* antibonding orbital, and J_{FF} coupling between ortho pairs of CF$_3$ groups and CF$_3$ groups on opposite sides of the N atom that is mediated by through-space Fermi-contact overlap of F atom lone pairs. The bending of the hetero-tricyclic core of these compounds is believed to be responsible for the observed J_{FH} coupling, by bringing the F atoms and the H atom closer together than if the PNTZ core were flat.

Attempts to measure EAs of four PNTZ(CF$_3$)$_n$ derivatives were thwarted by deprotonation to the anions upon electrospray ionization. Therefore, the EAs measured were those of the neutral N-deprotonated radicals. Nevertheless, DFT calculations by collaborator Dr. Alexey A. Popov predicted that the four EAs would range from 0.92 to 1.46 eV, only about one-third to one-half of the EAs of other tricyclic PAHs and heteroPAHs with 3, 4, or 5 CF$_3$ groups.[19,20] Therefore, PNTZ(CF$_3$)$_n$ derivatives will not be suitable electron acceptors for charge-transfer co-crystals with high conductivities, even though they may very well form segregated-stack co-crystals with PAH donors.

In potential future work, if one wanted to measure the EAs of similar molecules with the PNTZ core, it might be possible to add multiple CF$_3$ groups to N-MePNTZ, a derivative of PNTZ that has an even larger bend angle ($\theta = 40.3°$) than the derivatives of PNTZ discussed in this chapter. Using N-MePNTZ(CF$_3$)$_n$ derivatives, if they can be prepared, for low-temperature gas-phase PES EA measurements would avoid the deprotonation of the N atom that prevented the EA measurements of the PNTZ(CF$_3$)$_n$ compounds studied by the author and discussed in this chapter.

6.6. ADDITIONAL RECOGNITION

The synthesis of trifluoromethylated phenothiazine derivatives was performed by Dr. Igor V. Kuvychko. First-stage separation of the crude reaction material was performed by Dr. Long San. Electron affinity measurements were performed in collaboration with the Pacific Northwest National Lab run by Dr. Xuebin Wang X-ray diffraction data was collected at the synchrotron source at Argonne National Lab under the supervision of Dr. Yu-Sheng Chen.

Table 6-1. IUPAC locants and abbreviations for the seven purified $PNTZ(CF_3)_n$ compounds and the second-stage HPLC purification fraction from which they were isolated[a]

compound	abbreviation	second-stage HPLC fraction	retention time, min[b]
2,3,7 or 8-phenothiazine$(CF_3)_3$	PNTZ-3-1	F5F2	12
1,4,7,8-phenothiazine$(CF_3)_4$	PNTZ-4-1	F2F2	—[c]
1,3,7,9-phenothiazine$(CF_3)_4$	PNTZ-4-2	F3F2	8.5
1,2,7,9-phenothiazine$(CF_3)_4$	PNTZ-4-3	F4F3	11
1,4,6,9-phenothiazine$(CF_3)_4$	PNTZ-4-4	F4F7	12
1,3,6,7-phenothiazine$(CF_3)_4$	PNTZ-4-5	F5F3	16
1,3,6,9-phenothiazine$(CF_3)_4$	PNTZ-4-6	F3F1	8
1,2,6,9-phenothiazine$(CF_3)_4$	PNTZ-4-7	F4F4	24
2,3,6,8-phenothiazine$(CF_3)_4$	PNTZ-4-8	F4F2[d]	10.5
2,4,6,8-phenothiazine$(CF_3)_4$	PNTZ-4-9	F4F2[d]	10.5
1,2,3,7,9-phenothiazine$(CF_3)_5$	PNTZ-5-1	F4F6	15.5

[a] See Figure 6-1 for a key to the IUPAC locants for phenothiazine. [b] Buckyprep semi-preparative HPLC column, MeOH eluent, 5 mL min^{-1}. [c] First-stage HPLC fraction F2 was separated using 25:75 toluene:heptane, not MeOH. [d] Compounds PNTZ-4-8 and PNTZ-4-9 co-eluted in 2nd stage HPLC fraction F4F2.

Table 6-2. Crystallographic data collection and final refinement parameters

compound	PNTZ-4-2[a]	PNTZ-4-3[b]
empirical formula	$C_{16}H_5F_{12}NS$	$C_{16}H_5F_{12}NS$
empirical formula wt., g mol^{-1}	471.27	471.27
molecular formula	1,3,7,9-$(C_{12}H_5NS)(CF_3)_4$	1,2,7,9-$(C_{12}H_5NS)(CF_3)_4$
habit, color	needle, colorless	needle, colorless
data collection site	Advanced Photon Source	Advanced Photon Source
X-ray wavelength, Å	0.41328	0.41328
crystal system	orthorhombic	monoclinic
space group, Z	$P2_12_12_1$, 4	$P2_1$, 4
a, Å	7.6445(13)	7.626(2)
b, Å	8.8006(15)	24.337(7)
c, Å	24.364(4)	8.704(3)
α, deg	90	90
β, deg	90	90.726(5)
γ, deg	90	90
V, Å^3	1639.1(5)	1615.2(8)
T, K	100(2)	100(2)
ρ_{calc} (g cm^{-3})	1.910	1.938
$R(F)$ $(I > 2\sigma(I))$[c]	0.0560	0.0626
$wR(F^2)$ [all data][c]	0.1435	0.1584
GOF	1.034	1.028

[a] PNTZ-4-2 = 1,3,7,9-phenothiazine$(CF_3)_4$. [b] PNTZ-4-3 = 1,2,7,9-phenothiazine$(CF_3)_4$.
[c] $R(F) = \Sigma||F_o| - |F_c|| / \Sigma|F_o|$; $wR(F^2) = (\Sigma[w(F_o^2 - F_c^2)^2] / \Sigma[w(F_o^2)^2])^{1/2}$.

Table 6-3. The ^{1}H and ^{19}F NMR chemical shifts, relative intensities, and coupling constants for PNTZ(CF$_3$)$_n$ derivatives[a]

PNTZ-3-1 ^{1}H: δ 6.7 (bd s, 1H); 7.0 (s, 1H); 7.1 (s, 1H); 7.3 (s, 1H); 7.4 (s, 1H).

^{19}F: δ = −62.4 (q, 3F, J = 14 Hz); −63.1 (q, 3F, J = 14 Hz); −65.9 (s, 3F).

PNTZ-4-1 ^{1}H: δ 6.8 (bd, 1H); 7.0 (s, 1H); 7.4 (d, 1H, J = 8 Hz); 7.5 (d, 1H, J = 8 Hz); 7.5 (s, 1H).

^{19}F: δ −62.2 (q, 3F, J = 14 Hz); −63.0 (q, 3F, J = 14 Hz); −64.4 (s, 3F); −65.3 (s, 3F).

PNTZ-4-2 ^{1}H: δ 7.4 (s, 2H); 7.5 (bd m, 1H); 7.6 (s, 2H).

^{19}F: δ −64.5 (s, 6F, J_{FH} ≈ 4 Hz); −66.0 (s, 6F).

PNTZ-4-3 ^{1}H: δ 7.2 (s, 1H); 7.4 (s, 1H); 7.4 (m, 1H); 7.5 (m, 1H); 7.8 (bd s, 1H).[b]

^{19}F: δ −58.5 (m, 3F, J = 4, 16 Hz, J_{FH} = 4 Hz); −61.5 (q, 3F, J = 16 Hz); −64.3 (sp, 3 F, J = 4 Hz, J_{FH} = 4 Hz); −65.9 (s, 3F).

PNTZ-4-4 ^{1}H: δ 7.8 (d, 2H, J = 8 Hz); 8.1 (d, 2H, J = 8 Hz).[c]

^{19}F: δ −62.8 (s, 6F); −64.9 (s, 6F, J_{FH} ≈ 4 Hz).

PNTZ-4-5 ^{1}H: δ 7.3 (s, 1H); 7.7 (bd s, 1H); 7.8 (s, 1H); 9.0 (d, 1H, J = 9 Hz); 9.2 (d, 1H[d]).

^{19}F: δ −59.6 (q, 3F, J = 16 Hz); −61.0 (q, 3F, J = 16 Hz); −64.8 (s, 3F, J_{FH} ≈ 4 Hz); −65.7 (s, 3F).

PNTZ-4-6 ^{1}H: δ 7.6 (s, 1H); 7.6 (bd s, 2H); 7.4 (d, 1H, J = 9 Hz).

^{19}F: δ −64.4 (bd s, 3F); −64.6 (bd s, 3F); −65.2 (s, 3F); −65.8 (s, 3F).

PNTZ-4-7 ^{1}H: δ 7.5 (d, 1H); 7.5 (d, 1H); 7.4 (d, 2H)

^{19}F: δ −58.2 (m, 3F, J = 4 Hz, 16 Hz, J_{FH} = 4 Hz); −61.4 (q, 3F, J = 4 Hz, 16 Hz); −64.6 (bd m, 3F); −65.2 (s, 3F).

PNTZ-4-8 ^{1}H: δ 7.5 (s, 2H); 7.5 (s, 2H)

^{19}F: δ −62.3 (q, 3F, J = 14 Hz); −63.0 (q, 3F, J = 14 Hz); −65.3 (s, 3F); −66.5 (s, 3F).

PNTZ-4-9 ^{1}H: δ 7.6 (s, 1H); 7.5 (s, 1H); 7.5 (s, 1H); 7.5 (s, 1H).

^{19}F: δ −64.4 (d, 6F, J = 4 Hz); −65.0 (s, 6F).

Table 6-3. (continued) The ^{1}H and ^{19}F NMR chemical shifts, relative intensities, and coupling constants for PNTZ(CF$_3$)$_n$ derivatives[a]

PNTZ-5-1　^{1}H: δ 7.4 (s, 1H); 7.5 (s, 1H); 7.6 (s, 1H); 7.7 (bd m, 1H).[e]

^{19}F: δ = −56.7 (h, 3F, J = 16 Hz); −58.3 (m, 3F, J = 4 Hz, 16 Hz, J_{FH} = 4 Hz); −60.9

(q, 3F, J = 16 Hz); −64.0 (h, 3F, J = 4 Hz, J_{FH} = 4 Hz); −66.1 (s, 3F).

---

[a] See Figures Figure **6-5** and Figure **6-6** for the IUPAC locants for each compound. The operating frequencies of the spectrometer were 400 MHz for ^{1}H NMR spectra and 376 MHz for ^{19}F NMR spectra. The solvent was CDCl$_3$. The chemical shifts are referenced to residual CHCl$_3$ in CDCl$_3$ solvent (δ 7.27) for ^{1}H NMR spectra and to a small amount of added C$_6$F$_6$ (δ −164.9) for ^{19}F NMR spectra. Abbreviations: s, singlet; d, doublet; q, quartet; m, multiplet; bd, broad. All J coupling constants are J_{FF} unless otherwise indicated. [b] The spectrum contains signals at δ 7.4 and 7.6 due to a small amount of PNTZ-4-2. [c] No observable signal for the N–H proton. [d] This doublet is poorly resolved, but it is assumed that J = 9 Hz. [e] This compound is unique in that it there is J_{FF} coupling between the CF$_3$ groups on C1 and C9.

Table 6-4. Experimental and DFT predicted electron affinities (*EA*s)[a]

compd	experimental *EA*, eV[b]	DFT predicted *EA*, eV[c]
PNTZ	—	−0.51
2-PNTZ(CF$_3$)	—	0.079
PNTZ-3-1	—	0.92
PNTZ-4-1	—	1.10
PNTZ-4-2	—	1.11
PNTZ-4-3	—	1.01
PNTZ-5-1	—	1.46
PNTZ-3-1− H$^\bullet$	3.54(1)[d]	2.80
PNTZ-4-1 − H$^\bullet$	3.33(5)[d]	2.91
PNTZ-4-2 − H$^\bullet$	3.43(5)[d]	2.94
PNTZ-5-1 − H$^\bullet$	3.67(5)[d]	3.39

[a] PNTZ = phenothiazine (see Figure 6-1 for structure and IUPAC locants). The experimental values are for the neutral radical formed by removing the H atom attached to the N atom in the parent compound. [b] Determined by low-temperature gas-phase photoelectron spectroscopy by collaborator Dr. Xue-Bin Wang at Pacific Northwest National Laboratory (Richland, WA). The samples were provided by the author. [c] DFT predicted *EA*s at the B3LYP/ma-def2-TZVPP level of theory were calculated by collaborator Dr. Alexey A. Popov at the Leibniz Institute for Solid State and Materials Research (Dresden, Germany). [d] The nature of the species that gave rise to the PES spectra in Figure 6-19 is assumed to be the anion formed by the removal of H$^+$ during the electrospray ionization process.

phenothiazine (PNTZ)
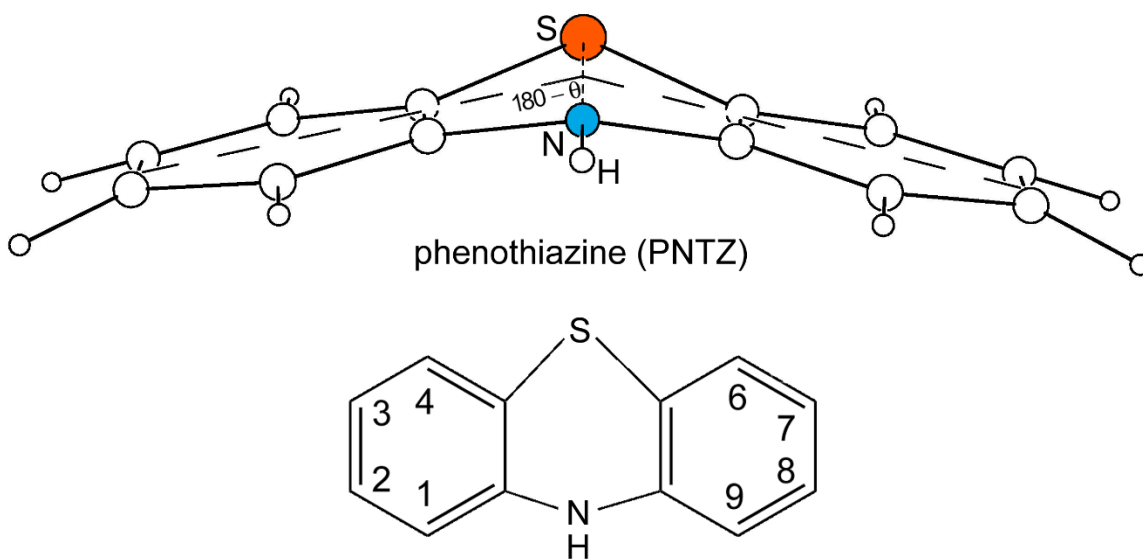
Figure 6-1. The structure of the hetero-tricyclic molecule phenothiazine (10*H*-phenothiazine; PNTZ). The upper drawing was made from the X-ray coordinates published in ref. [11], and shows the definition of the bend angle θ: 180° minus the angle formed by vectors connecting the midpoints of each of the outermost C–C bonds and the midpoint of the N···S vector. The IUPAC locants are shown in the bottom drawing.
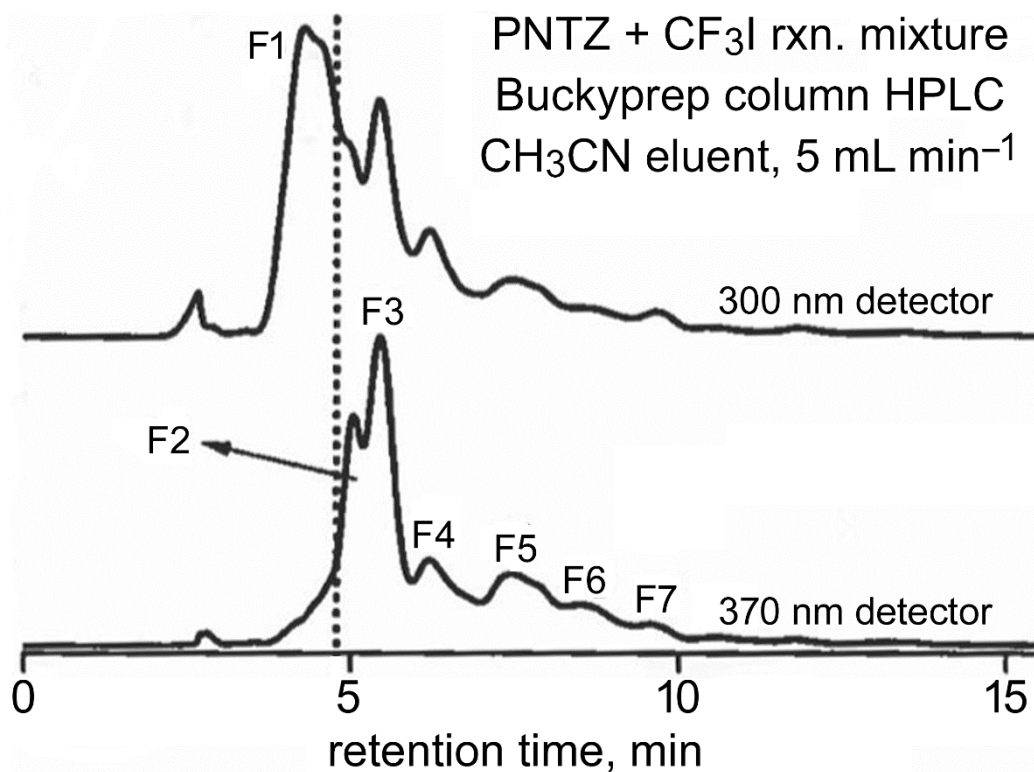
Figure 6-2. HPLC chromatograms of the crude product mixture from the high-temperature reaction of phenothiazine (PNTZ) and CF_3I. These chromatograms were recorded by former graduate student Dr. Long K. San and show the seven fractions that were further purified by the author to obtain eleven PNTZ$(CF_3)_n$ derivatives.
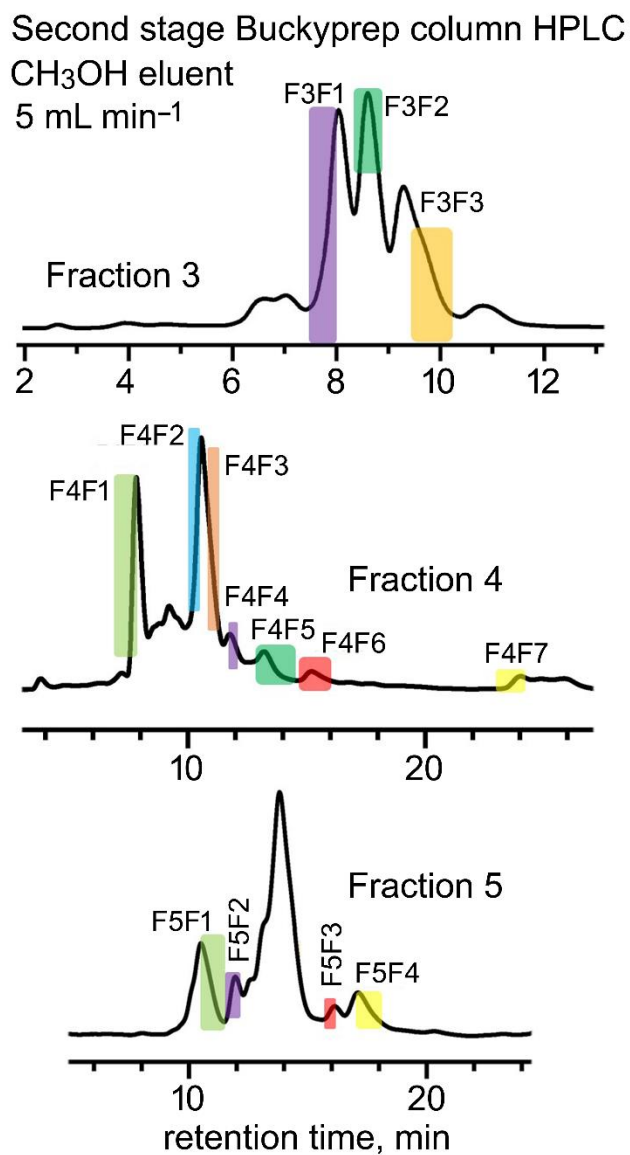
Figure 6-3. Second-stage HPLC separation of Fractions 3, 4, and 5 (see Figure 6-2) using CH₃OH as the eluent. The second stage separation of Fraction 2, performed by Dr. Long San, (not shown) using 25:75 toluene:heptane as the eluent resulted in three peaks, one of which contained pure 1,4,7,8-PNTZ(CF₃)₄ (PNTZ-4-1).
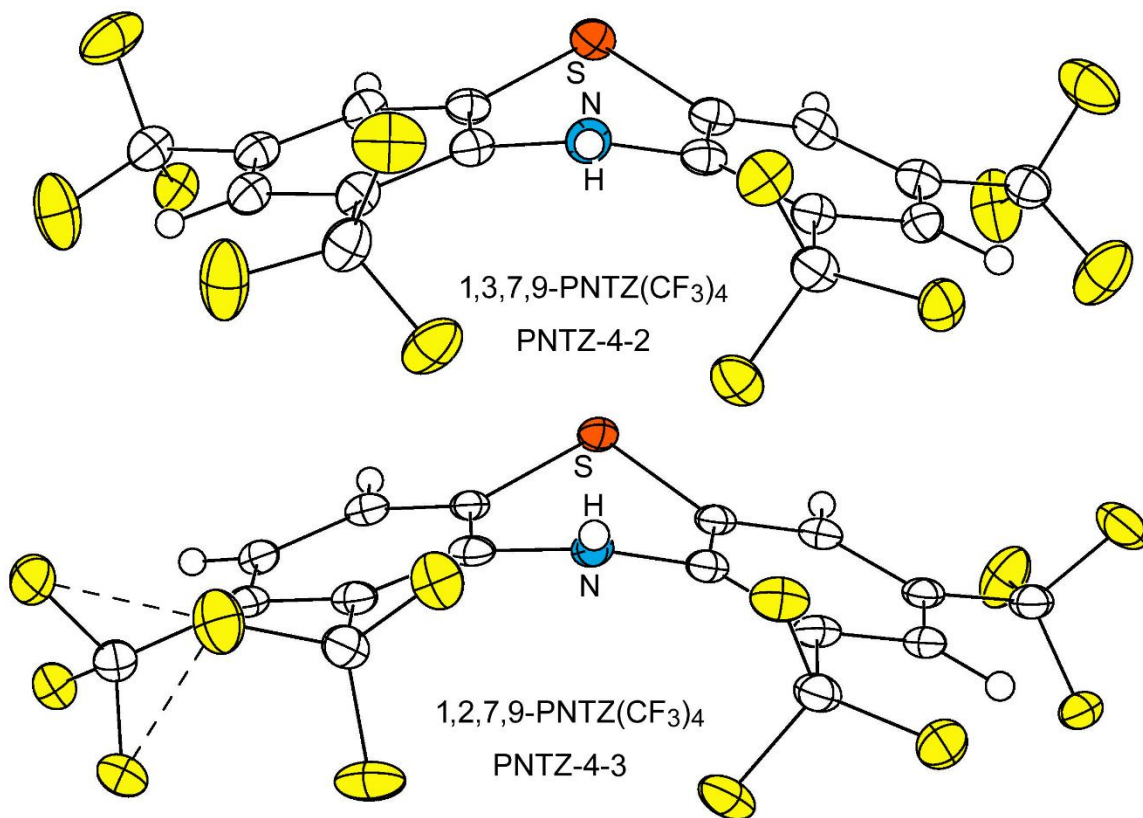
Figure 6-4. Drawings of the X-ray diffraction structures of PNTZ-4-2 and PNTZ-4-3 (30% probability ellipsoids except for H atoms, which are shown as spheres of arbitrary size). The F atoms are colored yellow. The short intramolecular F···F contacts of 2.58(1) and 2.62(1) Å in the structure of PNTZ-4-3 are shown with dashed lines. Only one of the two unique virtually identical molecules of PNTZ-4-3 is shown. The corresponding F···F distances in the second molecule are 2.55(1) and 2.59(1) Å.
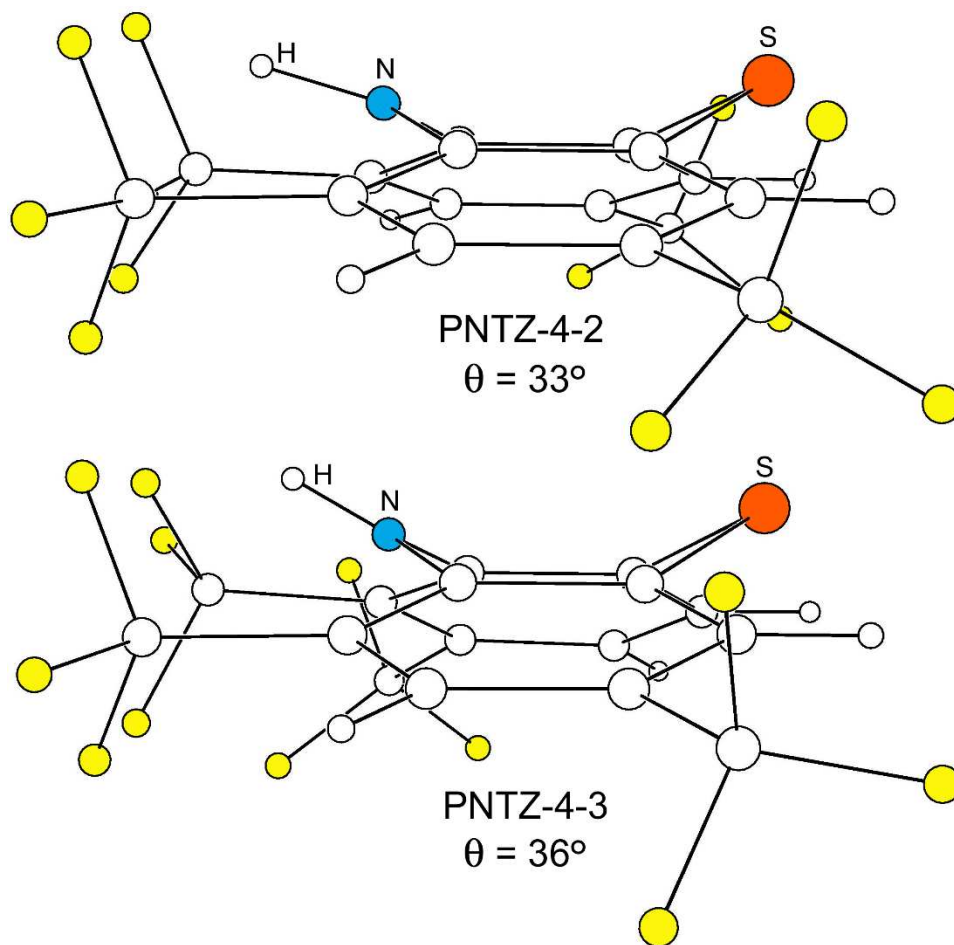
Figure 6-5. The bent, or domed, structures of 1,3,7,9-PNTZ(CF$_3$)$_4$ (PNTZ-4-2) and 1,2,7,9-PNTZ(CF$_3$)$_4$ (PNTZ-4-3). The F atoms are colored yellow. The bend angles, θ, defined in Figure 6-1, are shown. Note that the N atoms are almost completely flattened from a tetrahedral configuration to a trigonal-planar configuration.
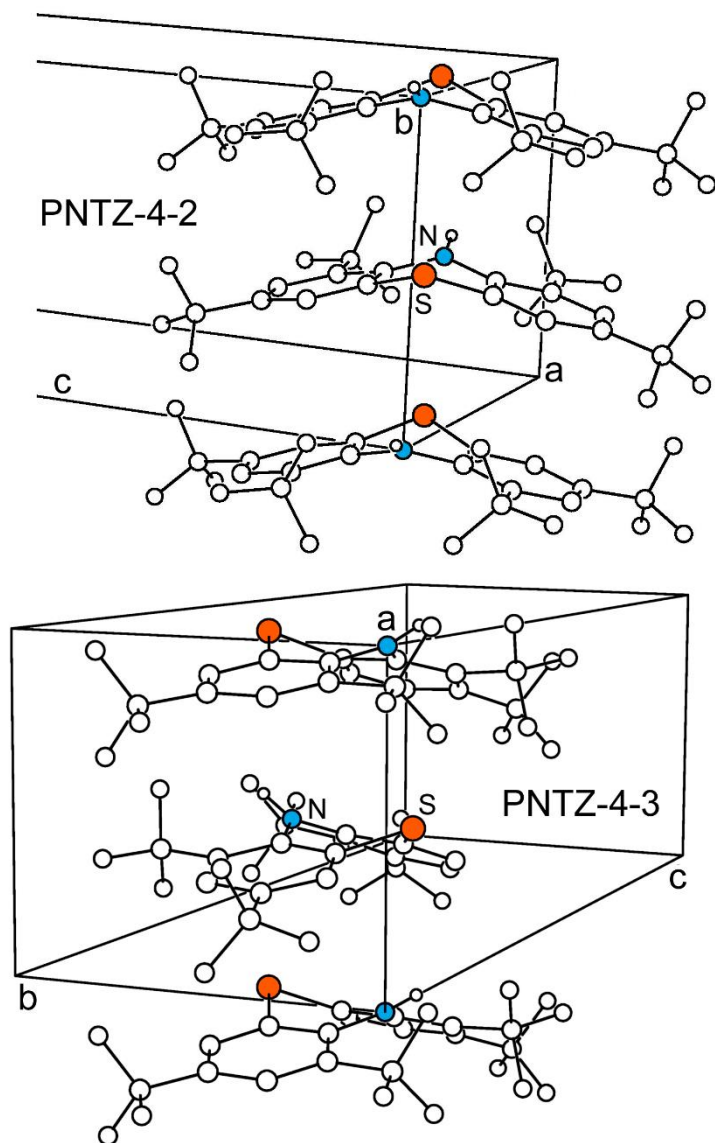
Figure 6-6. The structures of 1,3,7,9-PNTZ(CF$_3$)$_4$ (PNTZ-4-2; upper drawing) and 1,2,7,9-PNTZ(CF$_3$)$_4$ (PNTZ-4-3; lower drawing). The molecules form stacks so that the N atoms (and the S atoms) in every other molecule are aligned along the *b* axis in PNTZ-4-2 and along the *a* axis in PNTZ-4-3.
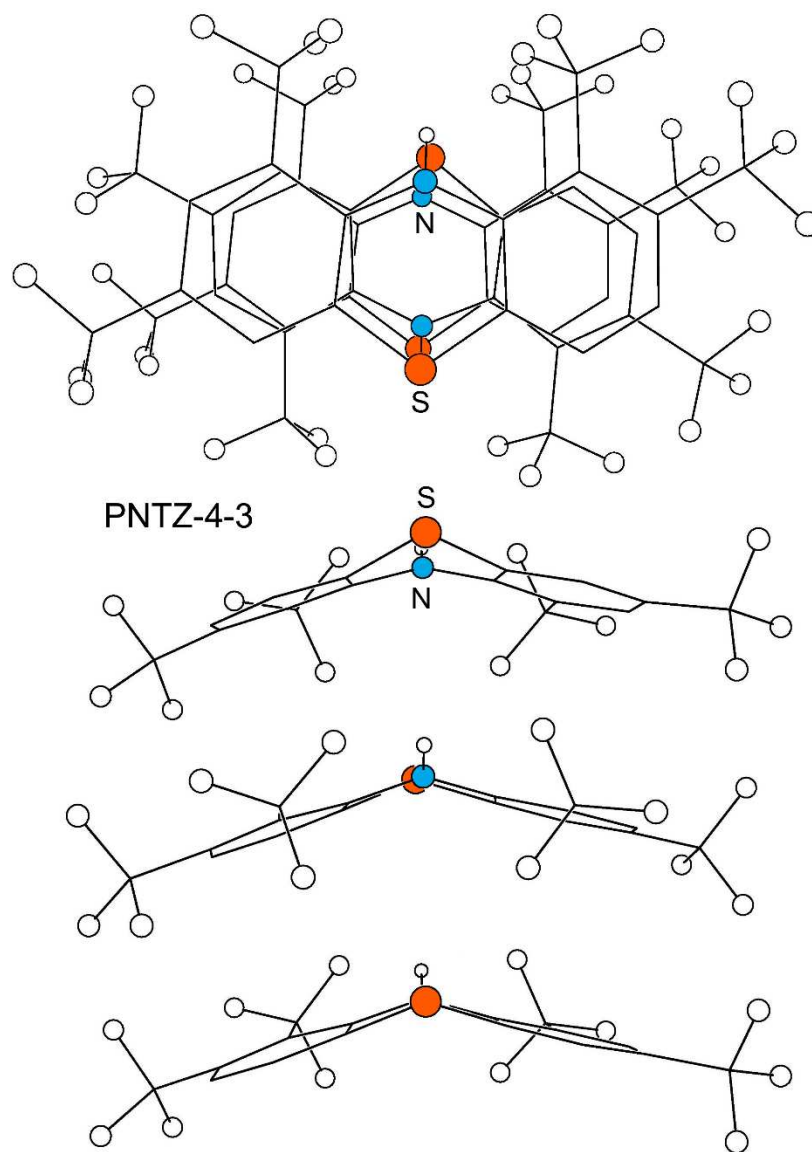
PNTZ-4-3

Figure 6-7. Perpendicular views of part of the structure of 1,2,7,9-PNTZ(CF$_3$)$_4$ (PNTZ-4-3), The nearly-superimposed molecules form chevron-like stacks, with the N⋯S vector turned 180° in every other molecule in the stack. Similar drawings of the molecules in the structure of PNTZ-4-2 (not shown) demonstrate that they are stacked in virtually the same way.
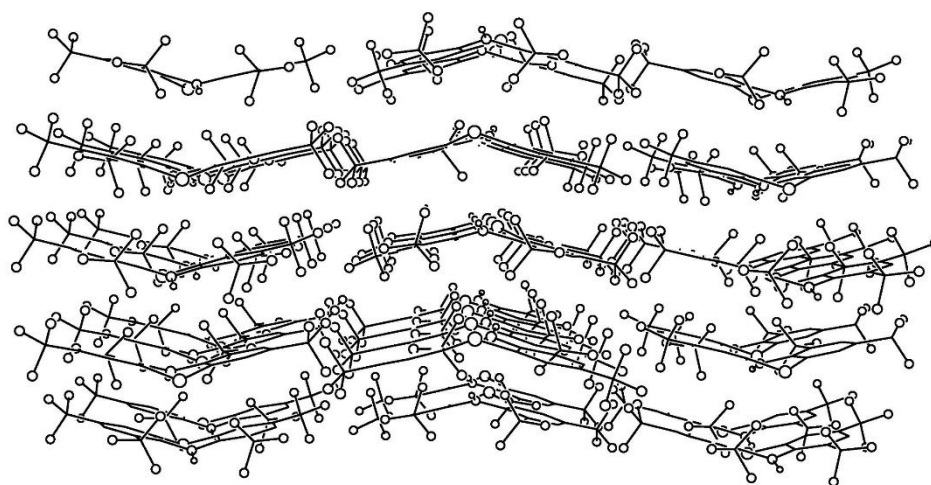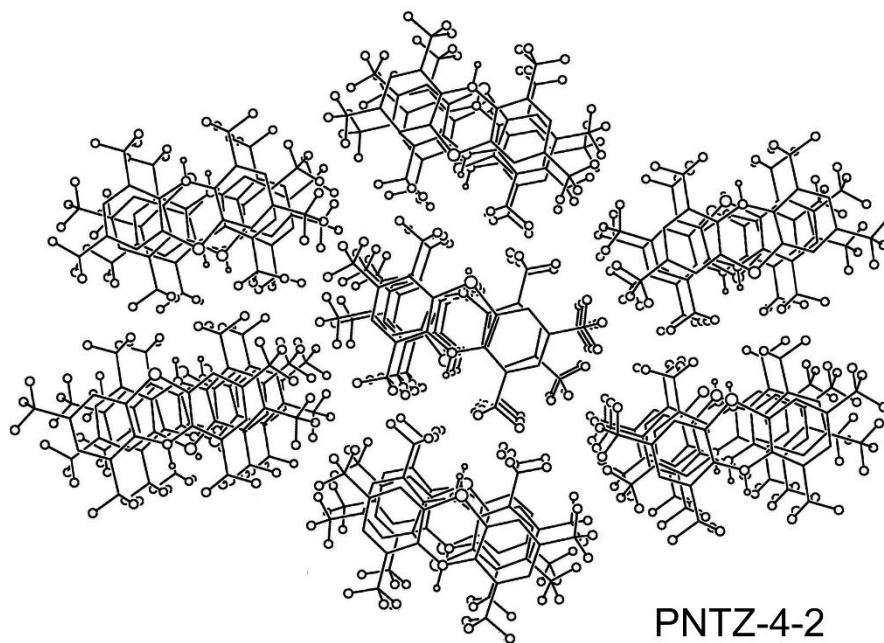
PNTZ-4-2

Figure 6-8. Perpendicular views of part of the structure of 1,3,7,9-PNTZ(CF$_3$)$_4$ (PNTZ-4-2). The upper drawing shows the close-packed array of stacks of molecules. Similar drawings of the molecules in the structure of PNTZ-4-3 (not shown) demonstrate that they are stacked in virtually the same way.
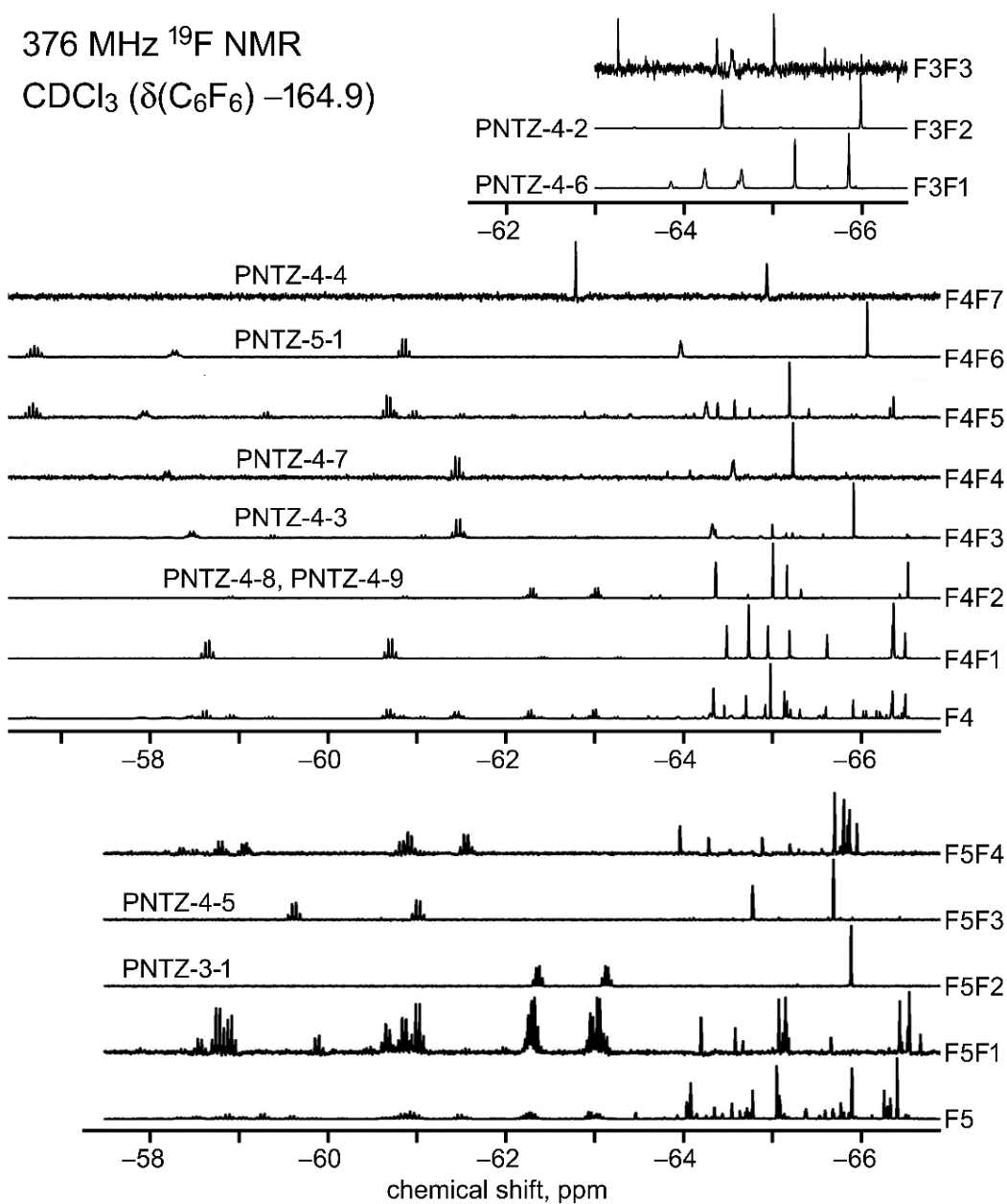
Figure 6-9. The ^{19}F NMR spectra of first- and second-stage PNTZ(CF$_3$)$_n$ HPLC fractions (see Figures Figure *6-2* and Figure **6-3**; the second-stage purification of first-stage fraction F2, from which PNTZ-4-1 was isolated, is not shown). Nine of the 15 second-stage fractions each resulted in the isolation of a single PNTZ(CF$_3$)$_n$ compound. Second-stage fraction F4F2 contained a 1:2 mixture of two compounds, PNTZ-4-8 and PNTZ-4-9. Drawings of the molecules are shown in Figures Figure **6-10**, Figure **6-11**, and Figure **6-12**. The IUPAC locants are shown in the aforementioned three figures and are also listed in Table 6-1.
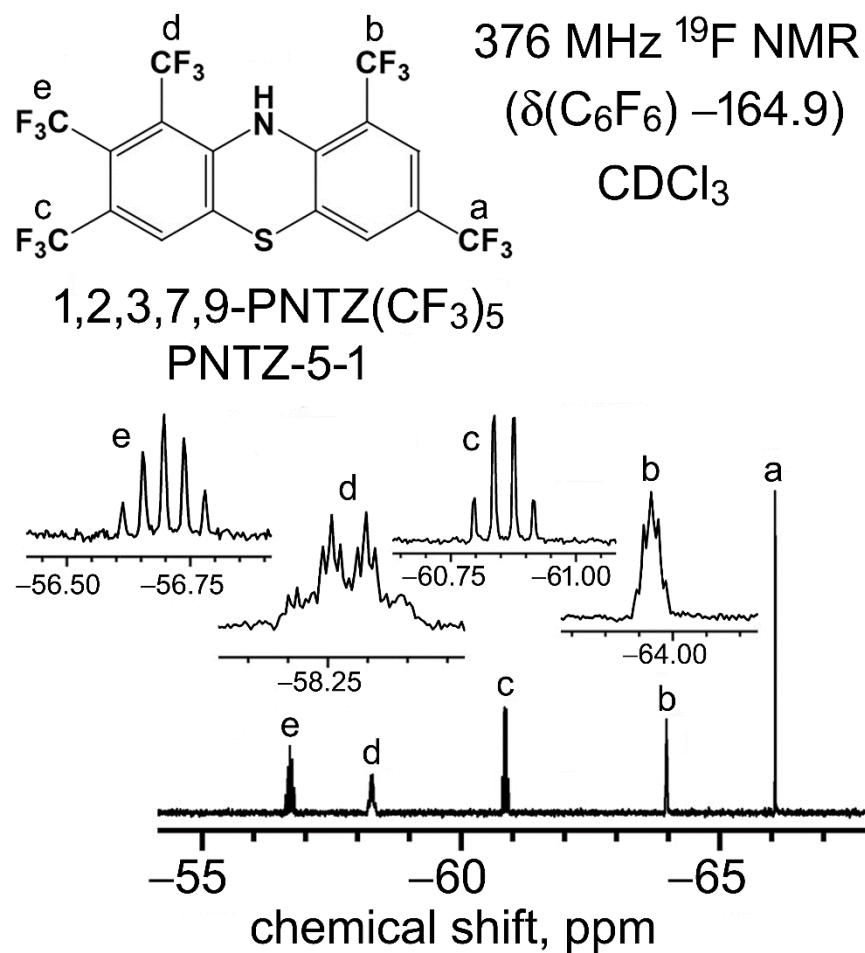
Figure 6-10. The ^{19}F NMR spectrum of PNTZ-5-1 (1,2,3,7,9-PNTZ(CF$_3$)$_5$), which was isolated from Fraction F4F6 of the second-stage HPLC purification (see Figure 6-9).
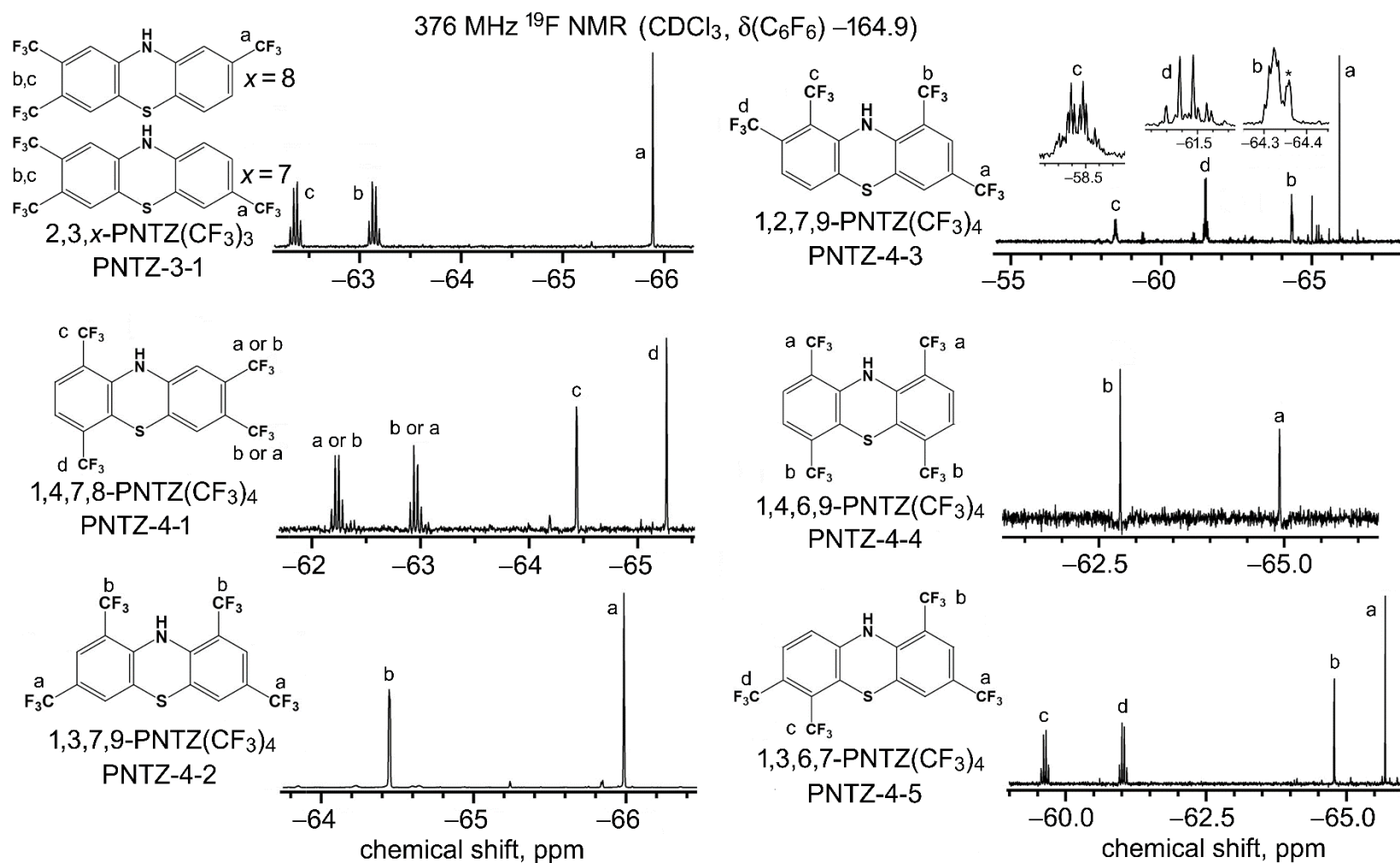
Figure 6-11. The ^{19}F NMR spectra of PNTZ-3-1 and five of the nine isomers of PNTZ(CF$_3$)$_4$. Peak assignments and IUPAC locants are shown.
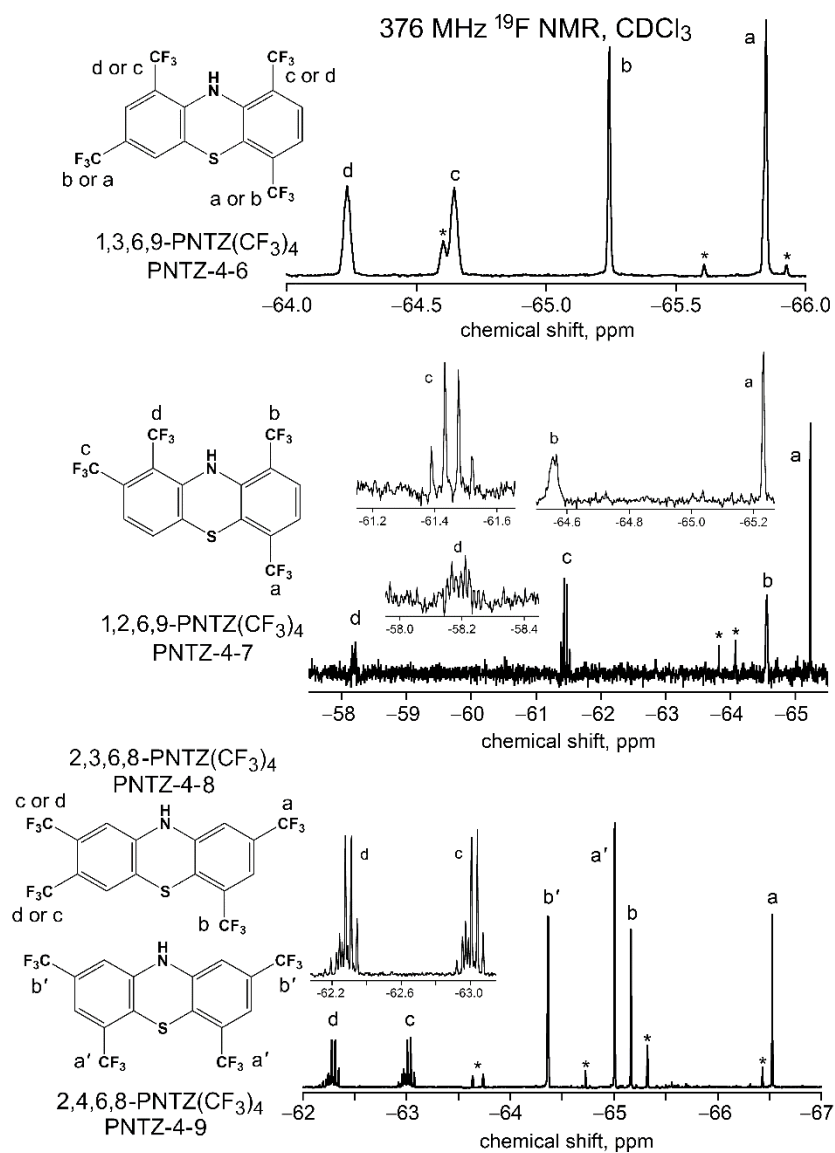
Figure 6-12. The ^{19}F NMR spectra of four of the nine PNTZ(CF$_3$)$_4$ isomers. The sample for the bottom spectrum was second-stage HPLC fraction F4F2, which contained a 1:2 mixture of PNTZ-4-8 and PNTZ-4-9. Peak assignments and IUPAC locants are shown.
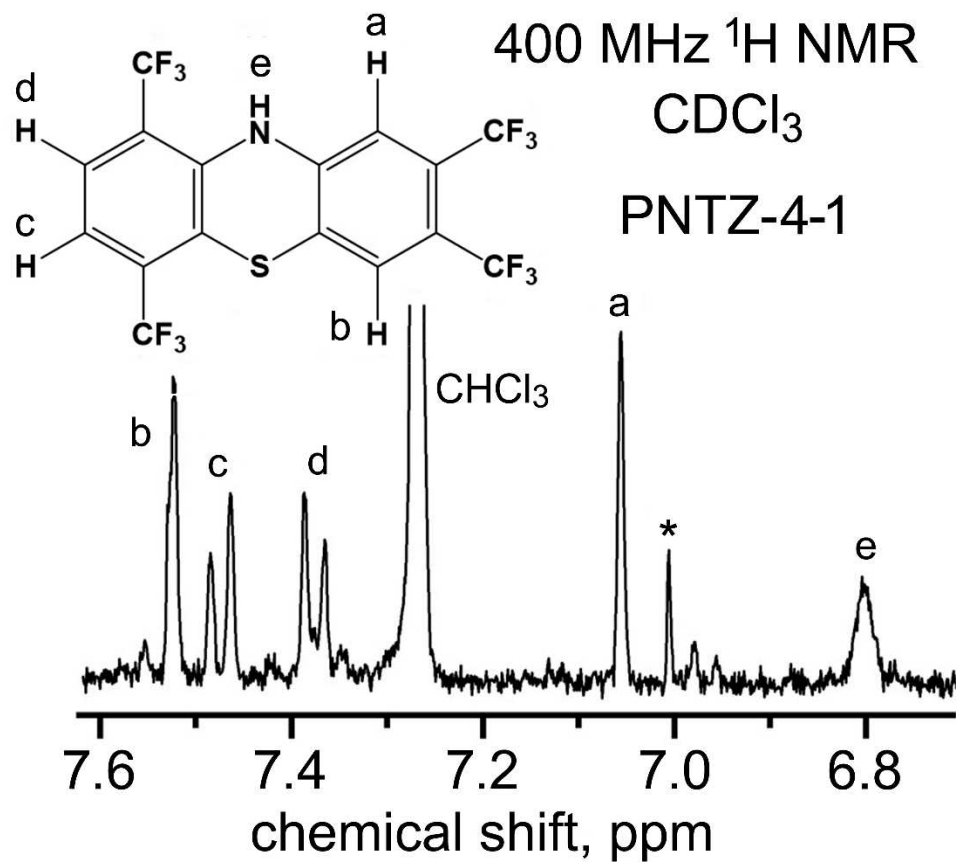
Figure 6-13. The 400 MHz ^{1}H NMR spectrum of 1,4,7,8-PNTZ(CF$_3$)$_4$ (PNTZ-4-1). Peak assignments are shown.

334
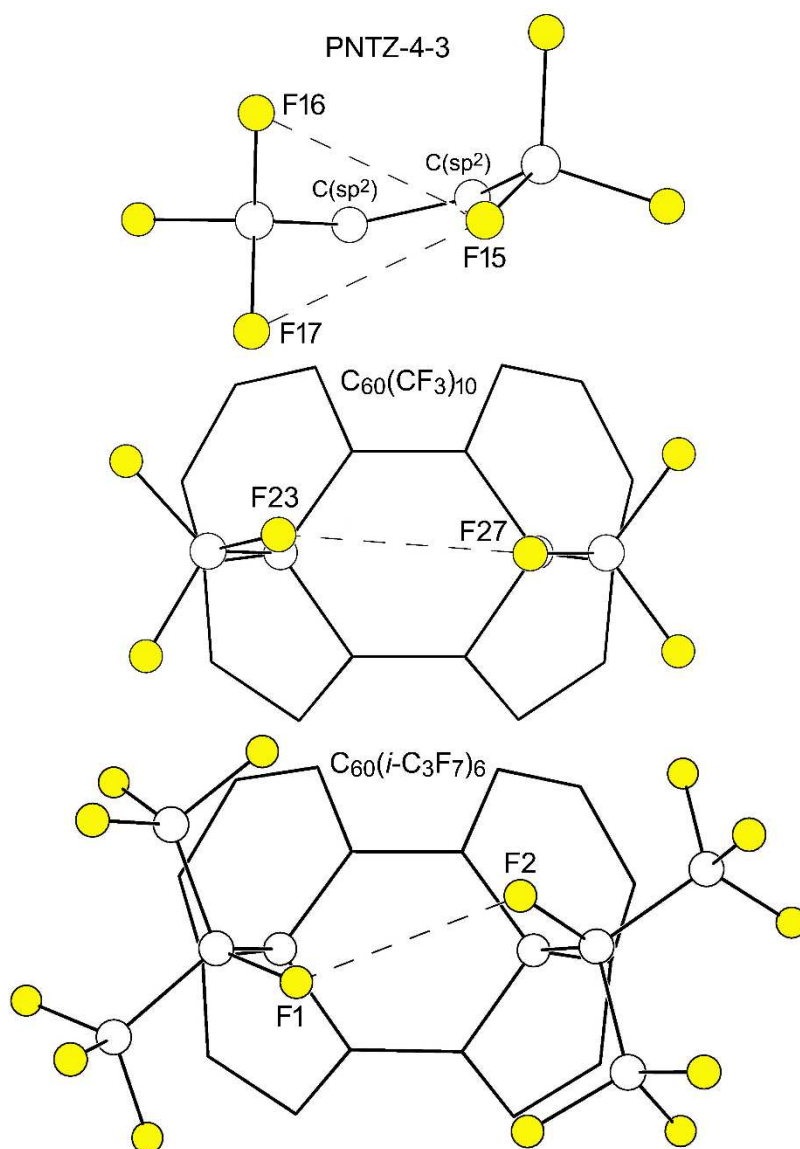
Figure 6-14. Portions of the X-ray crystal structures of PNTZ-4-3 (this work), 1,6,11,16,18,24,27,36,41,57-$C_{60}(CF_3)_{10}$ (ref. [41]), and 1,7,16,30,36,47-$C_{60}(i$-$C_3F_7)_6$ (ref. [42]). The F15⋯F16 and F15⋯F17 distances in PNTZ-4-3 are 2.55(1) and 2.59(1) Å. The F23⋯F27 distance in $C_{60}(CF_3)_{10}$ is 2.621(5) Å. The F1⋯F2 distance in $C_{60}(i$-$C_3F_7)_6$ is 2.655(4) Å.
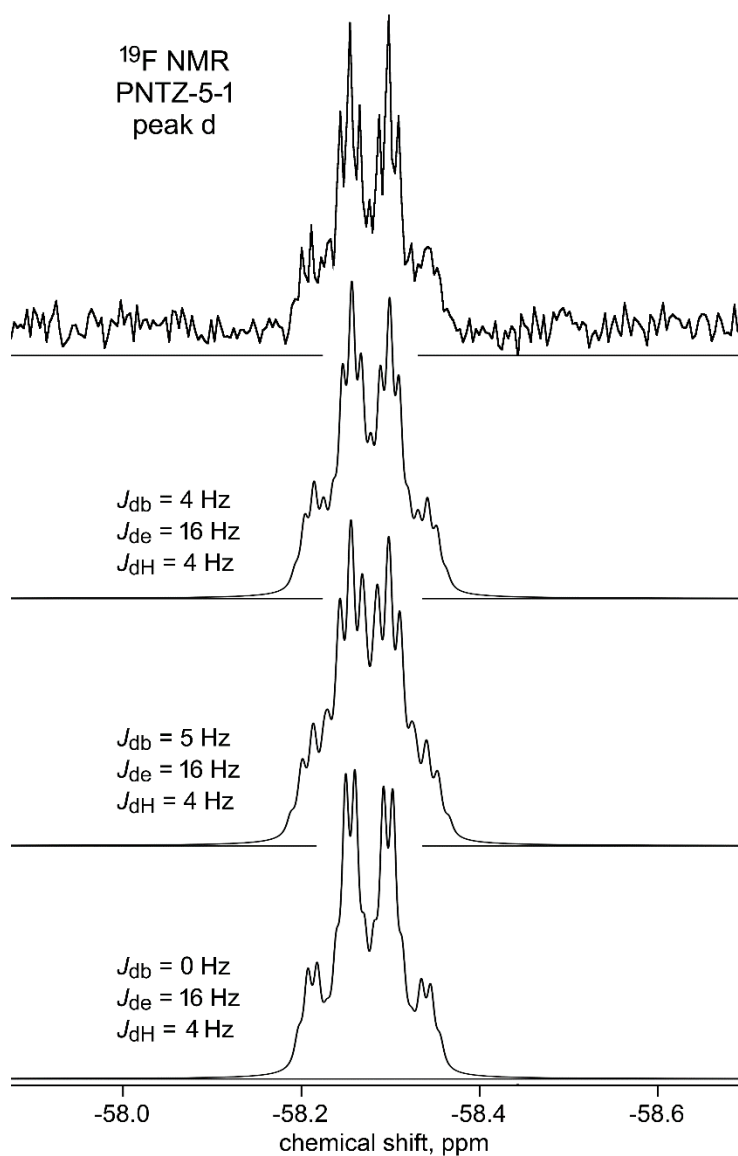
Figure 6-15. Experimental and simulations of multiplet d in the ^{19}F NMR spectrum of PNTZ-5-1 (see Figure 6-10 for a key to the multiplet abbreviations). The lower two simulations show that 4 Hz J_{db} and 4 Hz J_{dH} coupling are both necessary to match the experimental multiplet. See also Figure 6-16.
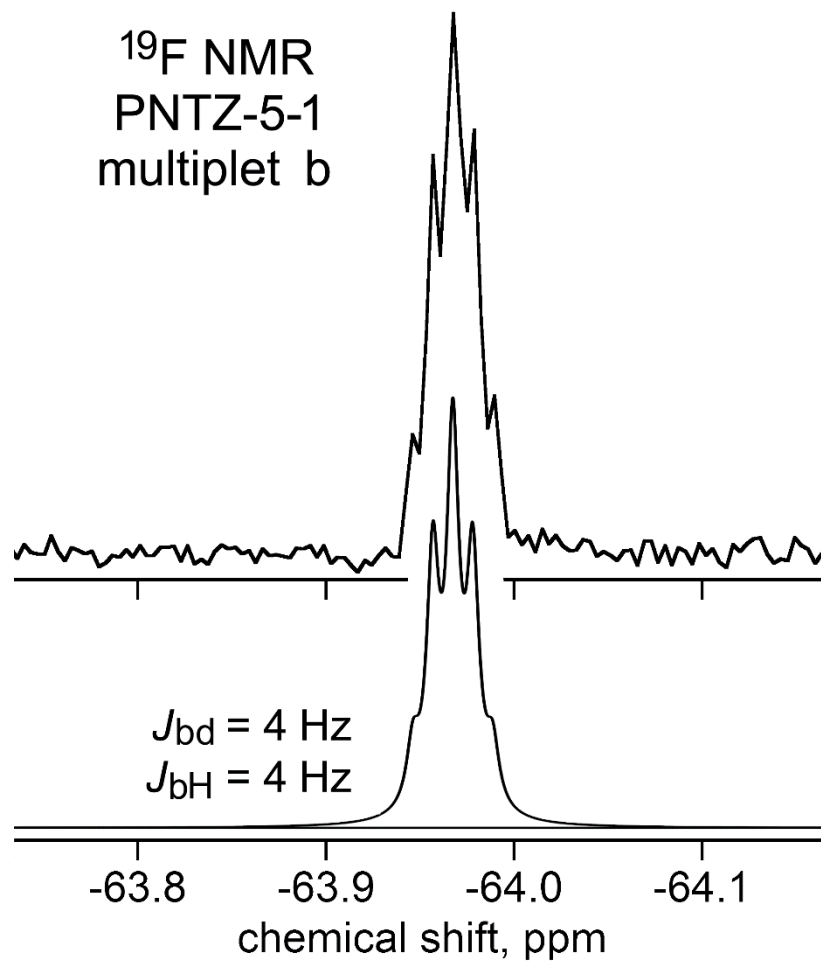
Figure 6-16. Experimental and simulation of multiplet b in the ^{19}F NMR spectrum of PNTZ-5-1 (see Figure 6-10 for a key to the multiplet abbreviations). The simulation shows that 4 Hz J_{db} and 4 Hz J_{bH} coupling match the experimental multiplet. See also Figure 6-15.
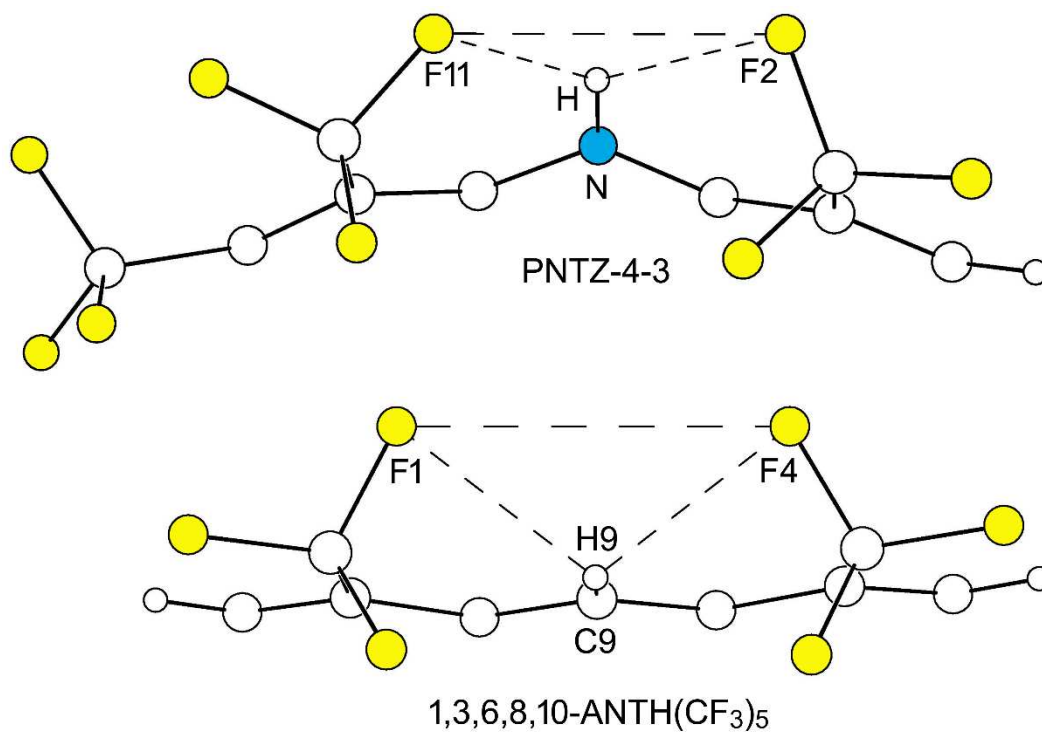
Figure 6-17. Portions of the X-ray crystal structures of PNTZ-4-3 (this work) and 1,3,6,8,10-ANTH(CF$_3$)$_5$ (ref. [19]). The F2$\cdots$F11, F2$\cdots$H, and F11$\cdots$H distance in PNTZ-4-3 are 3.27, 2.28, and 2.20 Å, respectively. The F1$\cdots$F4, F1$\cdots$H9, and F4$\cdots$H9 distances in ANTH(CF$_3$)$_5$ are 3.64, 2.42, and 2.43 Å, respectively.
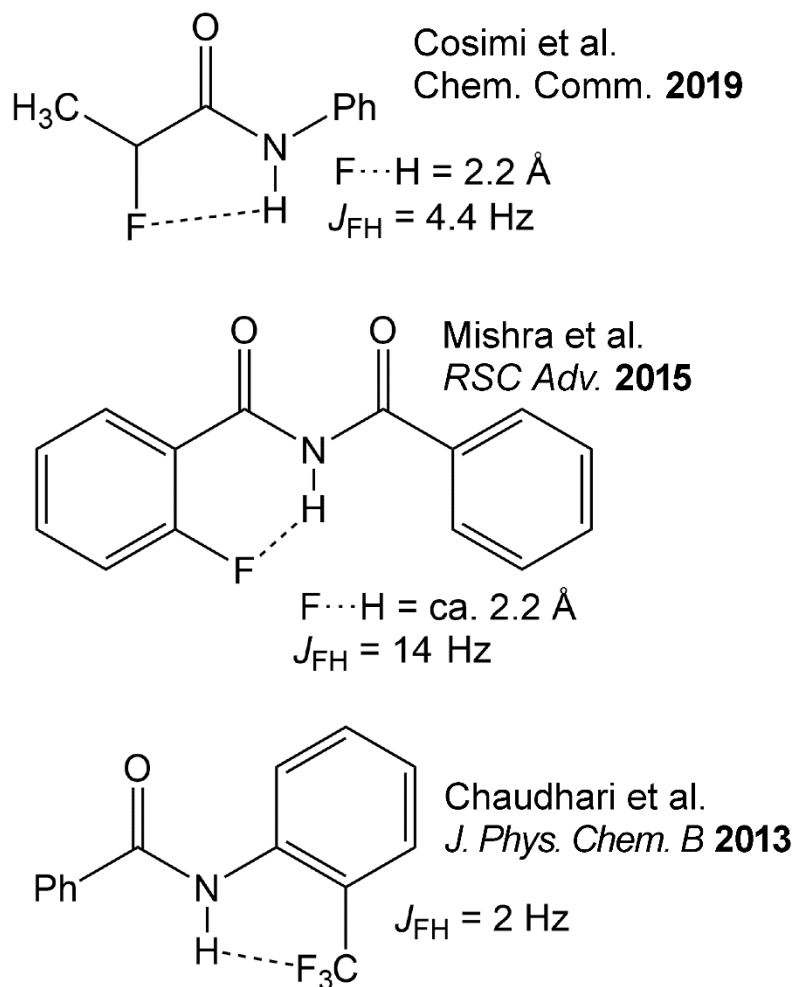
Figure 6-18. Several compounds with weak (C)F···H–N hydrogen bonding that exhibit $^{4,5}J_{FH}$ coupling measured by NMR spectroscopy: Cosimi et al. (ref. [52]); (Mishra et al. (ref. [50]); and Chaudhari et al. (ref. [49]).
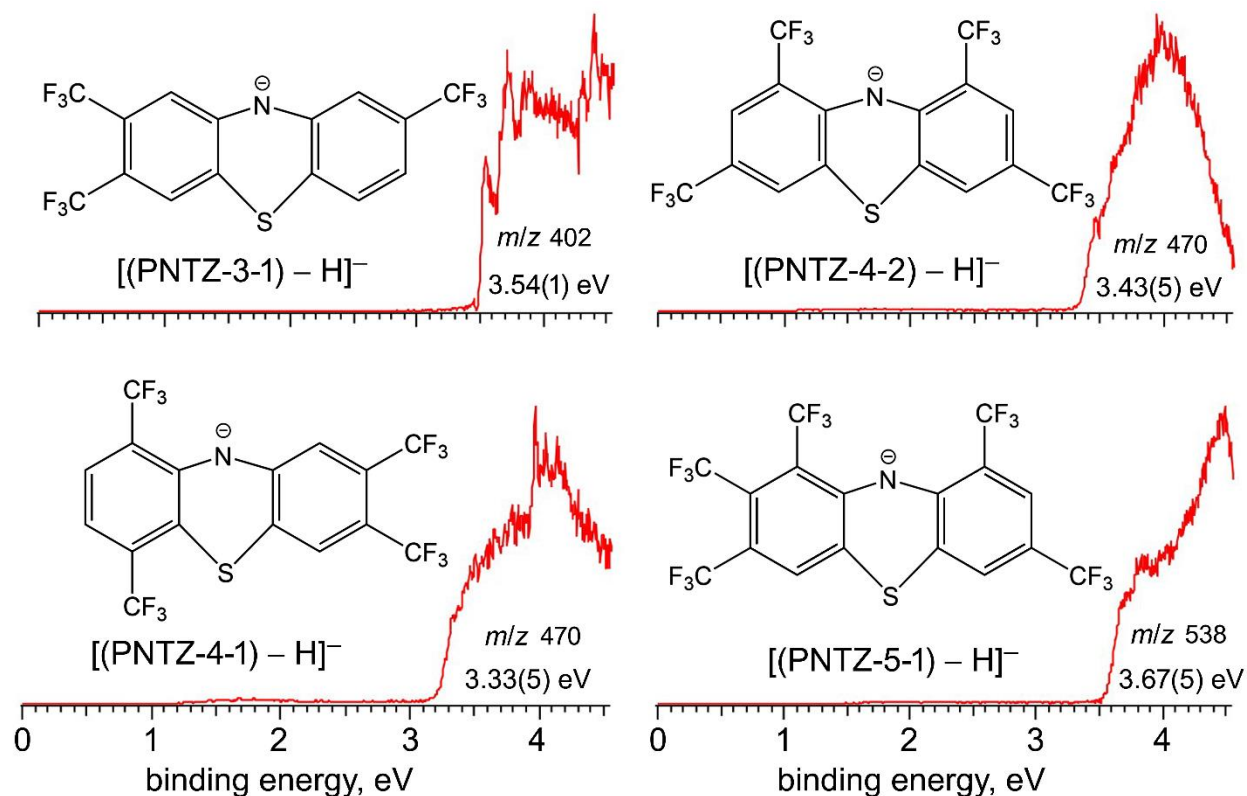
Figure 6-19. Low-temperature gas-phase photoelectron spectra of electrospray-ionized samples of PNTZ-3-1, PNTZ-4-1, PNTZ-4-2, and PNTZ-5-1. The solutions that were electrosprayed into the ionization chamber were CH_3CN solutions containing $(NMe_2)_2C=C(NMe_2)_2$, and the species giving rise to the spectra are most likely the N-deprotonated anions of each compound. Therefore, the indicated values are the gas-phase electron affinities of the putative radicals formed by removing the H atom from the N atom, not the electron affinities of the intact protonated molecules.

6.7. REFERENCES

(1)   Bernthsen, A. Zur Kenntniss des Methylenblau und verwandter Farbstoffe. *Ber. Deut. Chem. Ges.* **1883**, *16*, 2896–2904.

(2)   Massie, S. P. The Chemistry of Phenothiazine. *Chem. Rev.* **1954**, *54*, 797-833.

(3)   Domelsmith, L. N.; Munchausen, L. L.; Houk, K. N. Photoelectron Spectra of Psychotropic Drugs. 2. Phenothiazine and Related Transquilizers. *J. Am. Chem. Soc.* **1977**, *99*, 6506–6514.

(4)   Onoabedje, E. A.; Egu, S. A.; Okoro, U. C. Effect of acceptor strength on optical, electrochemical and photovoltaic properties of phenothiazine-based small molecule for bulk heterojunction organic solar cells. *J. Mol. Struct.* **2019**, *1175*, 956–962.

(5)   Szymańska, M.; Majerz, I. Geometry and electron density of phenothiazines. *J. Mol. Struct.* **2020**, *1200*, article 127095.

(6)   Li, Z.; Dong, Q.; Li, Y.; Xu, B.; Deng, M.; Pei, J.; Zhang, J.; Chen, F.; Wen, S.; Gao, Y.; Tian, W. Design and synthesis of solution processable small molecules towards high photovoltaic performance. *J. Mater. Chem.* **2011**, *21*, 2159-2168.

(7)   Zhang, W.-W.; Mao, W.-L.; Hu, Y.-X.; Tian, Z.-Q.; Wang, Z.-L.; Meng, Q.-J. Phenothiazine−Anthraquinone Donor−Acceptor Molecules: Synthesis, Electronic Properties and DFT-TDDFT Computational Study. *J. Phys. Chem,. A* **2009**, *113*, 9997–10004.

(8)   Sharma, G. D.; Anil Reddy, M.; Ramana, D. V.; Chandrasekharam, M. A novel carbazole–phenothiazine dyad small molecule as a non-fullerene electron acceptor for polymer bulk heterojunction solar cells. *RSC Advances* **2014**, *4*, 33279-33285.

(9)   Revoju, S.; Biswas, S.; Eliasson, B.; Sharma, G. D. Effect of acceptor strength on optical, electrochemical and photovoltaic properties of phenothiazine-based small molecule for bulk heterojunction organic solar cells. *Dyes Pigments* **2018**, *149*, 830-842.

(10)   Al-Busaidi, I. J.; Haque, A.; Al Rasbi, N. K.; Khan, M. S. Phenothiazine-based derivatives for optoelectronic applications: A review. *Synth. Met.* **2019**, *257*, article 116189.

(11) McDowell, J. J. H. The crystal and molecular structure of phenothiazine. *Acta Crystallogr., Sect. B* **1976**, *32*, 5-10.

(12) Roe, A.; Little, W. F. The Preparation of Some Fluoro- and Trifluoromethyl Phenothiazines, and Some Observations Regarding Determination of Their Structures by Infrared Spectroscopy. *J. Org. Chem.* **1955**, *20*, 1577-1590, and references therein.

(13) Smith, N. L. Synthesis of Phenothiazine Derivatives For Use As Antioxidants. *J. Org. Chem.* **1950**, *15*, 1125-1130.

(14) Craig, P. N.; Nodiff, E. A.; Lafferty, J. J.; Ullyot, G. E. New Trifluoromethylphenothiazine Derivatives. *J. Org. Chem.* **1957**, *22*, 709-711.

(15) Phelps, D. W.; Cordes, A. W. The dihedral angle of 2-(trifluoromethyl)phenothiazine. *J. Heterocycl. Chem.* **1976**, *13*, 625-627.

(16) DeWeerd, N. J.; Kuvychko, I. V.; San, L. K.; Strauss, S. H.; Boltalina, O. V. Synthesis and Structures of Phenothiazine(CF$_3$)$_n$ Derivatives. **2020**, manuscript in preparation.

(17) DeWeerd, N. J.; Bukovsky, E. V.; Castro, K. P.; Kuvychko, I. V.; Popov, A. A.; Strauss, S. H.; Boltalina, O. V. Steric and electronic effects of CF$_3$ conformations in acene(CF$_3$)$_n$ derivatives. *J. Fluorine Chem.* **2019**, *221*, 1-7.

(18) Bondi, A. van der Waals Volumes and Radii. *J. Phys. Chem.* **1964**, *68*, 441-451.

(19) Kuvychko, I. V.; Castro, K. P.; Deng, S. H. M.; Wang, X.-B.; Strauss, S. H.; Boltalina, O. V. Taming Hot CF$_3$ Radicals: Incrementally Tuned Families of Polyarene Electron Acceptors for Air-Stable Molecular Optoelectronics. *Angew. Chem. Int. Ed.* **2013**, *52*, 4871-4874.

(20) Castro, K. P.; Clikeman, T. T.; DeWeerd, N. J.; Bukovsky, E. V.; Rippy, K. C.; Kuvychko, I. V.; Hou, G.-L.; Chen, Y.-S.; Wang, X.-B.; Strauss, S. H.; Boltalina, O. V. Incremental Tuning Up of Fluorous Phenazine Acceptors. *Chem. Eur. J.* **2016**, *22*, 3930-3936.

(21) Brock, C. P.; Dunitz, J. D. Temperature dependence of thermal motion in crystalline anthracene. *Acta Crystallogr., Sect. B: Struct. Sci. Cryst. Eng. Mater.* **1990**, *46*, 795-806.

(22) Botoshansky, M.; Herbstein, F. H.; Kapon, M. Towards a Complete Description of a Polymorphic Crystal: The Example of Perylene. *Helv. Chim. Acta* **2003**, *86*, 1113-1128.

(23) Lee, T.; Rong, H.; Lin, H. Y.; Lee, H. L. Continuous Co-Crystallization As a Separation Technology: The Study of 1:2 Co-Crystals of Phenazine−Vanillin. *Cryst. Growth Des.* **2012**, *12*, 5897-5907.

(24) Frampton, C. S.; Knight, K. S.; Shankland, N.; Shankland, K. Single-crystal X-ray diffraction analysis of pyrene II at 93 K. *J. Mol. Struct.* **2000**, *520*, 29-32.

(25) Kareev, I. E.; Santiso Quińones, G.; Kuvychko, I. V.; Khavrel, P. A.; Ioffe, I. N.; Goldt, I. V.; Lebedkin, S. F.; Seppelt, K.; Strauss, S. H.; Boltalina, O. V. Variable-Temperature ^{19}F NMR and Theoretical Study of 1,9- and 1,7-C60F(CF$_3$) and C_s- and C_1-$C_{60}F_{17}$(CF$_3$): Hindered CF$_3$ Rotation and Through-Space J_{FF} Coupling. *J. Am. Chem. Soc.* **2005**, *127*, 11497-11504, and references therein.

(26) Kareev, I. E.; Kuvychko, I. V.; Lebedkin, S. F.; Miller, S. M.; Anderson, O. P.; Seppelt, K.; Strauss, S. H.; Boltalina, O. V. Synthesis, Structure, and ^{19}F NMR Spectra of 1,3,7,10,14,17,23,28,31,40-C_{60}(CF$_3$)$_{10}$. *J. Am. Chem. Soc.* **2005**, *127*, 8362-8375.

(27) Petrakis, L.; Sederholm, C. H. NMR Fluorine-Fluorine Coupling Constants in Saturated Organic Compounds. *J. Chem. Phys.* **1961**, *35*, 1243-1248.

(28) Brey, W. S.; Ramey, K. C. Temperature Dependence of Fluorine Nuclear Spin-Spin Coupling Constants. *J. Chem. Phys.* **1963**, *39*, 844-845.

(29) Cavagna, F.; Schumann, C. Non-Bond F-F Nuclear Spin Couplings II. Hexafluoropropene Trimers. *J. Magn. Reson.* **1976**, *22*, 333-344.

(30) Contreras, R. H.; Peralta, J. E.; Giribet, C. G.; Ruiz de Azua, M. C.; Facelli, J. C. Advances in Theoretical and Physical Aspects of Spin-Spin Coupling Constants In *Annual Reports on NMR Spectroscopy*; Academic Press Ltd.: London, 2000; Vol. 41, pp 55-184.

(31) Mallory, F. B.; Mallory, C. W.; Butler, K. E.; Lewis, M. B.; Xia, A. Q.; Luzik, J., E. D.; Fredenburgh, L. E.; Ramanjulu, M. M.; Van, Q. N.; Franci, M. M.; Freed, D. A.; Wray, C. C.; Hann, C.; Nerz-Stormes, M.; Carroll, P. J.; Chirlian, L. E. Nuclear Spin-Spin Coupling via Nonbonded Interactions. 8. The Distance Dependence of Through-Space Fluorine-Fluorine Coupling. *J. Am. Chem. Soc.* **2000**, *122*, 4108-4116.

(32)   Bryce, D. L.; Wasylishen, R. E. Ab initio Characterization of Through-Space Indirect Nuclear Spin-Spin Coupling Tensors for Fluorine-X (X = F, C, H) Spin Pairs. *J. Mol. Struct.* **2002**, *602*, 463-472.

(33)   San Fabian, J.; Westra Hoekzema, A. J. A. Vicinal fluorine-fluorine coupling constants: Fourier analysis. *J. Chem. Phys.* **2004**, *121*, 6268-6276.

(34)   Alkorta, I.; Elguero, J. E. Fluorine-Fluorine Interactions: NMR and AIM Analysis. *Struct. Chem.* **2004**, *15*, 117-120.

(35)   Tuttle, T.; Grafenstein, J.; Cremer, D. Analysis of NMR through-space coupling mechanism between ^{19}F atoms. *Chem. Phys. Lett.* **2004**, *394*, 5-13.

(36)   Bartolome, C.; Espinet, P.; Martin-Alvarez, J. M.; Villafane, F. Bis(fluoromesityl) Palladium Complexes, Archetypes of Steric Crowding and Axial Protection by *ortho* Effect - Evidence for Dissociative Substitution Processes - Observation of [19]F-[19]F Through-Space Coupling. *Eur. J. Inorg. Chem.* **2004**, 2326-2337.

(37)   Schwarz, R.; Seelig, J.; Kunnecke, B. Structural properties of perfluorinated linear alkanes: a ^{19}F and ^{13}C NMR study of perfluorononane. *Magn. Reson. Chem.* **2004**, *42*, 512-517.

(38)   Hierso, J.-C. Indirect Nonbonded Nuclear Spin−Spin Coupling: A Guide for the Recognition and Understanding of "Through-Space" NMR J Constants in Small Organic, Organometallic, and Coordination Compounds. *Chem. Rev.* **2014**, *114*, 4838-4867.

(39)   Kimber, B. J.; Feeney, J.; Roberts, G. C. K.; Birdsall, B.; Griffiths, D. V.; Burgen, A. S. V. Proximity of 2 Tryptophan Residues in Dihydrofolate-Reductase Determined by F-19 NMR. *Nature* **1978**, *271*, 184-185.

(40)   Arnold, W. D.; Mao, J.; Sun, H.; Oldfield, E. Computation of Through-Space [19]F–[19]F Scalar Couplings via Density Functional Theory. *J. Am. Chem. Soc.* **2000**, *122*, 12164-12168.

(41)   Bukovsky, E. V.; Larson, B. W.; Clikeman, T. T.; Chen, Y. S.; Popov, A. A.; Boltalina, O. V.; Strauss, S. H. Structures and structure-related electronic properties of new $C_{60}(CF_3)_{10}$ isomers. *J. Fluorine Chem.* **2016**, *185*, 103–117.

(42) Shustova, N. B.; Kuvychko, I. V.; Boltalina, O. V.; Strauss, S. H. 1,7,16,30,36,47-Hexakis(perfluoroisopropyl)-1,7,16,30,36,47-hexahydro(C$_{60}$-I$_h$)[5,6]fullerene. *Acta Crystallogr., Sect. E: Cryst. Commun.* **2007**, *E63*, o4575.

(43) Boltalina, O. V.; Popov, A. A.; Kuvychko, I. V.; Shustova, N. B.; Strauss, S. H. Perfluoroalkylfullerenes. *Chem. Rev.* **2015**, *115*, 1051-1105.

(44) Myhre, P. C.; Edwards, J. W.; Kruger, W. D. Long-Range Spin-Spin Coupling in Alkylfluorobenzenes. The Stereochemical Requirements for Coupling of Fluorine and Hydrogen Separated by Five Bonds. *J. Am. Chem. Soc.* **1966**, *88*, 2459-2466.

(45) Abushanab, E. Long-range Hydrogen-Fluorine Spin-Spin Coupling. Further Support for the "Through-Space" (Direct) Mechanism. *J. Am. Chem. Soc.* **1971**, *93*, 6532-6536.

(46) Schaefer, T.; Chum, K.; Marat, K.; Wasylishen, R. E. The sign of the 'through-space' spin-spin coupling between methyl protons and the fluorine nucleus in 2,6-dimethylbenzoyl fluoride. *Can. J. Chem.* **1976**, *54*, 800-804.

(47) Lyga, J. W.; Henrie, R. N.; Meier, G. A.; Creekmore, W.; Patera, R. M. 'Through-Space Hydrogen–Fluorine, Carbon–Fluorine and Fluorine–Fluorine Spin–Spin Coupling in 2-Phenyl-3alkyl-4,5,6,7-tetrahydroindazoles. *Magn. Reson. Chem.* **1993**, *31*, 323-328.

(48) Favaro, D. C.; Contreras, R. H.; Tormena, C. F. Unusual Through-Space, TS, Pathway for the Transmission of J_{FHf} Coupling: 2-Fluorobenzaldehyde Study Case. *J. Phys. Chem,. A* **2013**, *117*, 7939-7945.

(49) Chaudhari, S. R.; Mogurampelly, S.; Suryaprakash, N. Engagement of CF$_3$ Group in N−H⋯F−C Hydrogen Bond in the Solution State: NMR Spectroscopy and MD Simulation Studies. *J. Phys. Chem. B* **2013**, *117*, 1123-1129.

(50) Mishra, S. K.; Suryaprakash, N. Organic fluorine involved intramolecular hydrogen bonds in the derivatives of imides: NMR evidence corroborated by DFT based heoretical calculations. *RSC Adv.* **2015**, *5*, 86013-86022.

(51) Dalvit, C.; Piotto, M.; Vulpetti, A. Fluorine NMR spectroscopy and computational calculations for assessing intramolecular hydrogen bond involving fluorine and for characterizing the dynamic of a fluorinated molecule. *J. Fluorine Chem.* **2017**, *202*, 34-40.

(52) Cosimi, E.; Trapp, N.; Ebert, M.-O.; Wennemers, H. Combined experimental and theoretical study of long-range H–F interactions in α-fluoro amides. *Chem. Comm.* **2019**, *55*, 2253-2256.

(53) Patel, A. K.; Mishra, S. K.; Krishnamurthy, K.; Suryaprakash, N. Retention of strong intramolecular hydrogen bonds in high polarity solvents in binaphthalene–benzamide derivatives: extensive NMR studies. *RSC Adv.* **2019**, *9*, 32759-32770.

(54) San, L. K.; Spisak, S. N.; Dubceac, C.; Deng, S. H. M.; Kuvychko, I. V.; Petrukhina, M. A.; Wang, X.-B.; Popov, A. A.; Strauss, S. H.; Boltalina, O. V. Experimental and DFT Studies of the Electron-Withdrawing Ability of Perfluoroalkyl (R_F) Groups: Electron Affinities of PAH(R_F)$_n$ Increase Significantly with Increasing R_F Chain Length. *Chem. Eur. J.* **2018**, *24*, 1441-1447.

(55) Castro, K. P.; Bukovsky, E. V.; Kuvychko, I. V.; DeWeerd, N. J.; Chen, Y.-S.; Deng, S. H. M.; Wang, X.-B.; Popov, A. A.; Strauss, S. H.; Boltalina, O. V. PAH/PAH(CF$_3$)$_n$ Donor/Acceptor Charge-Transfer Complexes in Solution and in Solid-State Co-Crystals. *Chem. Eur. J.* **2019**, *25*, 13547-13565.

(56) Bordwell, F. G. Equilibrium Acidities in Dimethyl Sulfoxide Solution. *Acc. Chem. Res.* **1988**, *21*, 456-463.

APPENDIX A

SUPPLEMENTAL INFORMATION FOR CHAPTER 2

Table S2-1. Crystal data and final refinement parameters for the single-crystal X-ray CORO and H$_2$CORO structures

compound	CORO-4-1	H$_2$CORO-7-1	H$_2$CORO-7-2	H$_2$CORO-8-1	H$_2$CORO-8-2
formula	C$_{28}$H$_8$F$_{12}$	C$_{31}$H$_7$F$_{21}$	C$_{31}$H$_7$F$_{21}$	C$_{32}$H$_6$F$_{24}$	C$_{32}$H$_6$F$_{24}$
formula wt, g mol^{-1}	572.34	778.37	778.37	846.37	846.37
X-ray wavelength, Å	0.41328	0.41328	0.41328	0.41328	0.41328
crystal system	orthorhombic	monoclinic	monoclinic	triclinic	orthorhombic
space group, Z	Ibam	P2$_1$/c	P2$_1$	P-1	Pna2$_1$
a, Å	12.484(4)	11.9692(4)	13.4625(6)	8.1278(4)	14.697(3)
b, Å	23.207(8)	27.7144(9)	7.9058(3)	13.1666(6)	23.300(4)
c, Å	7.222(3)	8.0855(3)	14.4223(6)	13.8141(7)	8.1423(17)
α, deg	90	90	90	73.1890(10)	90
β, deg	90	93.6170(10)	117.7620(10)	89.6170(10)	90
γ, deg	90	90	90	79.1220(10)	90
V, Å^3	2092.3(13)	2676.77(16)	1358.30(10)	1387.91(12)	2788.3(9)
ρ_{calc} g cm^{-3}	1.817	1.931	1.903	2.025	2.016
T, K	100	100	100	100	100
$R(F)$ ($I > 2\sigma(I)$)[a]	0.089	0.0509	0.0507	0.0456	0.0688
$wR(F^2)$ [all data][a]	0.2819	0.1533	0.1373	0.1327	0.2147
GOOF	−0.575, 0.999	−0.464, 0.509	−0.350, 0.362	−0.38, 0.44	−0.476, 0.715

[a] $R(F) = \Sigma\|F_o| - |F_c\|/\Sigma|F_o|$; $wR(F^2) = (\Sigma[w(F_o^2 - F_c^2)^2]/\Sigma[w(F_o^2)^2])^{1/2}$.

Table S2-2. The retention times for the major $H_2CORO(CF_3)_n$ fractions collected by HPLC.

Designation	Retention Time (min)	Molecule Name
F0	3.4 – 3.7	N/A
F1	7.6 – 8.4	N/A
F2	10.4 – 11.3	H_2CORO-8-1
F3	13.6 – 14.9	H_2CORO-8-2/H_2CORO-8-3
F4	21.0 – 22.2	H_2CORO-7-1
F5	45.2 – 47.7	H_2CORO-7-2

Separation performed in 100% toluene on the Cosmosil Buckyprep column at a flow rate of 5 mL min^{-1}. Pure fractions with compounds which were characterized and identified are named.

Table S2-3. Results of mass spectrometric analysis of the isolated fraction from MTR-HP.

Fraction	m/z present by MS†	Number of CF$_3$ groups	Number of C(sp^3) bonded H
F0	984.00	10	4
F1	777.08‡	7	2
F2	846.08	8	2
F3	846.08	8	2
F4	778.08	7	2
F5	778.08	7	2

† Most abundant ion is given

‡ Shows a mass that is one proton less than the theoretical mass for an $H_2CORO(CF_3)_7$.

Table S2-4. Chemical shifts for the fluorine signals on the major products from MTR-HP.

H$_2$CORO-8-1	H$_2$CORO-8-2	H$_2$CORO-7-1	H$_2$CORO-7-2
F_a −71.4 (ap) J_{FF} = 8	$F_{a,b}$ −71.0, −71.1 (ap) J_{FF} = 8, 8	$F_{a,b}$ −71.1 (ap) J_{FF} = 8 6F	$F_{a,b}$ −71.1 (ap) J_{FF} = 8 6F
F_b −71.1 (ah) J_{FF} = 7	$F_{c,h}$ −60.65, −60.78 (q) J_{FF} = 8, 8	$F_{c,g}$ −60.5, −60.6 (q) J_{FF} = 8, 8	$F_{c,g}$ −60.5 (q) J_{FF} = 8 6F
F_c −60.5 (q) J_{FF} = 8	F_d −63.42 (s)	$F_{d,f}$ −60.4, −60.4 (s)	$F_{d,f}$ −63.4, −63.5 (s)
$F_{d,f}$ −63.3, −63.4 (s)	F_e −61.46 (s)	F_e −61.2 (s)	F_e −61.2 (s)
F_e −61.3 (s)	$F_{f,g}$ −54.39, −54.67 (abq) J_{FF} = 15, 15		
F_g −52.8 (abq) J_{FF} = 16			
F_h −53.16 (um)			

Multiplets are listed as singlet (s), quartet (q), ab quartet (abq), apparent pentet (p), apparent heptet (ah), and unresolved broad envelope multiplet (um). All shifts are reported in ppm. All J_{FF} values are ±1 Hz due to second order effects. All integration values are 3F unless otherwise stated.

Table S2-5. ^1H NMR chemical shifts of the 4 isolated and characterized major products from MTR-HP.

H$_2$CORO-8-1	H$_2$CORO-8-2	H$_2$CORO-7-1	H$_2$CORO-7-2
$H_{a,b}$ 5.1, 5.3 (q) J_{HF} = 9 Hz	$H_{a,b}$ 5.1 (q) J_{HF} = 7 Hz 2H	$H_{a,b}$ 5.1 (ap)† J_{HF} = 6 Hz 2H	$H_{a,b}$ 5.1 (uq)‡ J_{HF} = 8 Hz 2H
$H_{c,d,f}$ 9.1, 9.2, 9.2 (s)	$H_{c,d,f}$ 9.1 (s), 9.1, 9.2 (broad s)	$H_{c,d}$ 8.8, 8.9(s)	H_d 8.9 (s)
H_e 9.3 (s)	H_e 9.3 (s)	$H_{f,g}$ 9.1, 9.1 (s)	$H_{c,g}$ 9.1 (s)
		H_e 9.3 (s)	$H_{e,f}$ 9.1, 9.1 (broad s)

† The C(sp^3) bonded protons ideally are quartets however, the 5.1 ppm signal appears to be a pentet due to the overlap of the two quartets.

‡ The C(sp^3) bonded protons on H$_2$CORO-7-2 shows a poorly resolved quartet. The poor resolution is due to the small sample size.

Multiplets are listed as singlet (s), quartet (q), unresolved quartet (uq), and apparent pentet (ap). All shifts are reported in ppm. All J_{FH} values are ±1 Hz due to second order effects. All integration values are 1H unless otherwise stated.

Table S2-6. Retention times for isolated $CORO(CF_3)_n$ derivatives

Designation	Retention Time
CORO-1-1	6.0 – 8.0 min
CORO-4-1	12.7 – 14.5 min
CORO-4-2	20.7 – 22.9 min
CORO-5-1	31.3 – 33.7 min
CORO-5-2	33.9 – 37.2 min
CORO-5-3	42.9 – 50.0 min

Table S2-7. CORO(CF$_3$)$_n$ derivatives listed by their substitution pattern and their corresponding energy levels and heats of formation.

CORO(CF$_3$)$_2$	ΔE, kJ/mol	HOMO, eV	LUMO, eV	Gap, eV
1,7	0.00	-5.735	-3.035	2.700
1,8	0.33	-5.736	-2.994	2.742
1,5	0.46	-5.755	-3.003	2.751
1,6	0.52	-5.741	-3.060	2.681
1,10	0.85	-5.766	-3.008	2.759
1,4	0.90	-5.762	-3.016	2.746
1,3	2.18	-5.746	-3.011	2.735
1,12	64.15	-5.720	-3.083	2.637
1,2	64.48	-5.681	-3.112	2.569

CORO(CF$_3$)$_3$	ΔE, kJ/mol	HOMO, eV	LUMO, eV	Gap, eV
1,5,9	0.00	-6.028	-3.228	2.800
1,4,8	0.32	-5.996	-3.239	2.757
1,4,7	0.37	-6.000	-3.293	2.707
1,5,10	0.43	-6.014	-3.303	2.711
1,3,7	1.22	-5.986	-3.285	2.701
1,3,9	1.23	-5.985	-3.286	2.699
1,3,8	1.61	-5.978	-3.300	2.678
1,3,10	1.95	-5.992	-3.235	2.757
1,3,6	2.16	-5.998	-3.316	2.683
1,3,5	3.32	-6.010	-3.234	2.776

CORO(CF$_3$)$_4$	ΔE, kJ/mol	HOMO, eV	LUMO, eV	Gap, eV
1,4,7,10*	0.00	-6.253	-3.552	2.700
1,3,7,10	1.16	-6.237	-3.514	2.723
1,3,6,9	1.30	-6.242	-3.560	2.682
1,3,6,10	1.63	-6.245	-3.535	2.711
1,3,7,9	1.65	-6.223	-3.538	2.686
1,3,5,9	2.07	-6.237	-3.507	2.730
1,3,8,10	2.74	-6.219	-3.510	2.710
1,3,5,10	2.81	-6.234	-3.510	2.724
1,3,5,8	2.86	-6.228	-3.530	2.697
1,3,6,8	2.92	-6.216	-3.571	2.645

| 1,3,5,7 | 3.67 | -6.228 | -3.495 | 2.733 |

*"dead-end" - i.e. further addition to this structure is not possible hence it may be accumulated (it is symmetric CORO-4 isomer)

CORO(CF$_3$)$_5$	ΔE, kJ/mol	HOMO, eV	LUMO, eV	Gap, eV
1,3,5,7,10	0.00	-6.474	-3.753	2.721
1,3,5,8,10	0.39	-6.459	-3.764	2.695
1,3,5,7,9*	0.42	-6.465	-3.732	2.732

*On the route to the sole CORO-6 structure without close CF$_3$-CF$_3$ contact

Two isomers with close positions of CF$_3$ groups (1,2 and 1,12) have similarly high relative energies of 64 kJ/mol. For comparisons, the isomer of CORA-2 with similar relative location of CF$_3$ groups have the energies of 43.9 (peri) and 55.4 (ortho). Thus, inter-CF$_3$ repulsion in planar CORO-2 seems to be stronger than in the bowl-shaped CORA-2. For a series of CORA(CF$_3$)x derivatives, our analysis have shown that relative energies can be predicted using energy increments for different structural fragments. If similar rule holds for CORO, we do not need to compute relative energies of isomers with para or ortho fragments. We therefore focused on finding all isomers avoiding close CF$_3$ contacts. It can be seen that the relative energies of isomers vary in a very small range, and one can hardly find any reasons for the preferable formation of this or that isomer. My suggestion was that maybe it can be explained by statistics – i.e., imagine that we start with CORO-1 and count how many CF$_3$ addition sequences lead to a certain structure. But this does not work. For CORO-5 isomers, I counted totally 356 addition sequences leading to three isomers, of them 120 lead to 1,3,5,7,9-isomer (which means there should be roughly a third of it in the mixture). Another suggestion is that the "dead-end" isomers should be accumulated. For instance, among 11 isomers of CORO-4, there is only one structure, 1,4,7,10, which cannot react further without addition of CF3 groups to adjacent positions. Therefore, 1,4,7,10-isomer is a "dead-end" and should be accumulated in the product mixture (whereas other CORO-4 isomer react further to form CORO-5 etc). Among three isomers of CORO-5, only 1,3,5,7,9-isomer can react further without addition of CF$_3$ groups to adjacent position, whereas 1,3,5,7,10 and 1,3,5,8,10 cannot. Therefore, one can expect a smaller amount of 1,3,5,7,9 in the products, but then CORO-6 should be formed (unless it also reacts further).

Table S2-8. Isolated yields of the various product types from GTGS-3.

	CORO + CORO-1	CORO-2 + CORO-3	CORO-3 + CORO-4	CORO-5-1	CORO-5-2	CORO-5-3
Isolated yield based on recovered material	14.40%	7.00%	13.60%	8.60%	19.80%	2.30%
Isolated yield based on starting material	6.40%	2.20%	3.80%	1.98%	4.60%	0.54%

Due to the loss of material from charring, the yields based on recovered material as well as the true isolated yields based on the starting material are reported. The specific reaction conditions are discussed in the experimental section. The missing percentage of material is due to compounds which elute before coronene and by mass spectrometry appear to be dihydrocoronene compounds similar to the ones isolated from MTR-HP.

CORO-1-1	1-(trifluoromethyl)coronene
CORO-4-1	**1,4,7,10-tetrakis(trifluoromethyl)coronene**
CORO-4-2	1,3,8,10-tetrakis(trifluoromethyl)coronene
CORO-5-1	1,3,5,7,10-pentakis(trifluoromethyl)coronene
CORO-5-2	1,3,5,8,10-pentakis(trifluoromethyl)coronene
CORO-5-3	1,3,5,7,9-pentakis(trifluoromethyl)coronene
H_2CORO-7-1	**1,2,3,5,7,9,12-heptakis(trifluoromethyl)-1,2-dihydrocoronene**
H_2CORO-7-2	**1,2,3,5,7,10,12-heptakis(trifluoromethyl)-1,2-dihydrocoronene**
H_2CORO-8-1	**1,2,3,4,6,8,10,12-octakis(trifluoromethyl)-1,2-dihydrocoronene**
H_2CORO-8-2	**1,2,3,5,6,8,10,12-octakis(trifluoromethyl)-1,2-dihydrocoronene**
H_2CORO-8-3	1,2,3,5,7,8,10,12-octakis(trifluoromethyl)-1,2-dihydrocoronene
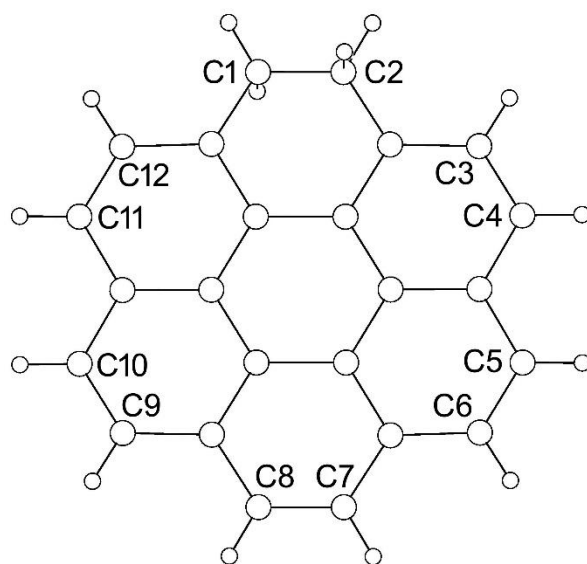
Figure S2-1. The IUPAC numbering for H_2CORO, which is the same for CORO. Also shown are the abbreviations for the 12 compounds characterized in this work. The structures in bold were characterized by single-crystal X-ray diffraction.
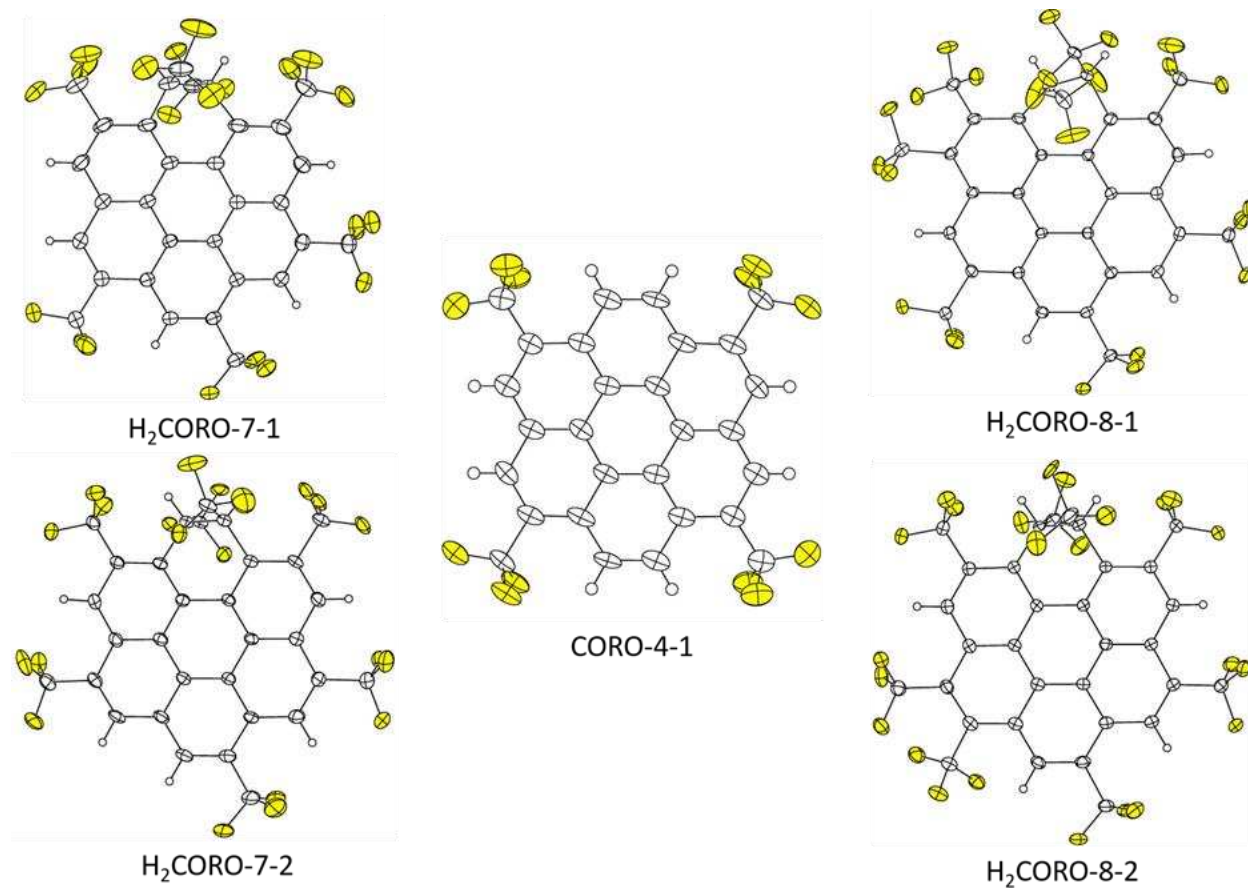
Figure S2-2. The five structures reported in this work (H atoms shown as spheres of arbitrary size; this is the same as Figure 10 in the main paper). Except for H_2CORO-8-2 (30% probability ellipsoids), the drawings are shown with 50% probability ellipsoids.

Details of X-ray structure refinement and disorder modeling

CORO-4-1. The structure of CORO-4-1 exhibited a rotational disorder about the center of the central hexagon. The minor portion (8%) is rotated ca. 15° with respect to the major portion (92%). This disorder was modeled using a combination of SADI and EADP commands. The 92:8 rotational disorder model resulted in a 22% improvement in $wR2$ and a 12% improvement in $R1$. This structure was also evaluated as monoclinic $C2/m$, with two unique molecules, each molecule related by a 90° rotation. However, the similarity in the two molecules resulted in ADDSYM errors associated with missed higher symmetry and never yielded a unit cell without all cell angles being 90°, a clear sign that the correct crystal system is orthorhombic, with two superimposed molecules. This was further evaluated by solving the structure as triclinic and using the Platon ADDSYM commands to find higher symmetry, and this resulted in the final solution reported here. In addition, there are indications that the crystals are twinned. However, there were not enough reflections from the twin cell to allow for a twin refinement. The result is that R-int is relatively high, 20.4%.

H₂CORO-7-1. The structure of H₂CORO-7-1 exhibited positional disorder of the H atoms and CF₃ groups on C1 and C2, resulting in the superposition of two enantiomers of unequal population. The disorder was refined with a free variable so that each molecule is the superposition of opposite enantiomers in a 61:39 ratio.

H₂CORO-7-2. The structure of H₂CORO-7-2 also exhibited positional disorder of the H atoms and CF₃ groups on C1 and C2. The positional disorder extends to C3 and C18 and their CF₃ substituents, showing that the flex of the two enantiomers can extend beyond C1 and C2. The occupancy for these disordered atoms was constrained to be 50:50.

H₂CORO-8-1. The structure of H₂CORO-8-1 also exhibited positional disorder of the H atoms and CF₃ groups on C1 and C2, with the major enantiomer component constrained to 70% (based on the average free-variable occupancy of the C atoms of a given enantiomer. In addition, the CF₃ group on C12 was rotationally disordered and was modeled as two CF₃ components with the major component being 70.9%.

H₂CORO-8-2. The structure of H₂CORO-8-2 also exhibited positional disorder of the H atoms and CF₃ groups on C1 and C2, with the major enantiomer component constrained to 61%. In addition, it appears that a small percentage of another isomer, designated as H₂CORO-8-3, is present in the crystal. This isomer differs from H₂CORO-8-2 in the position of one CF₃ group:

H$_2$CORO-8-2 is 1,2-H$_2$-1,2,3,5,6,8,10,12-CORO(CF$_3$)$_8$ and H$_2$CORO-8-3 is 1,2-H$_2$-1,2,3,5,7,8,10,12-CORO(CF$_3$)$_8$, which has C_2 molecular symmetry. This assignment is based on the mass spectrum and ^{19}F NMR spectrum of the sample of H$_2$CORO-8-2, which show a symmetric impurity with the same mass as H$_2$CORO-8-2. However, it was not possible to isolate H$_2$CORO-8-3 separately. In addition, several of the CF$_3$ groups exhibit rotational disorder. The presence of the small percentage of H$_2$CORO-8-3 and the CF$_3$ disorder in the structure of H$_2$CORO-8-2 lead to several unusual bond distances and angles. Therefore, bond distances and angles in this structure will not be discussed.
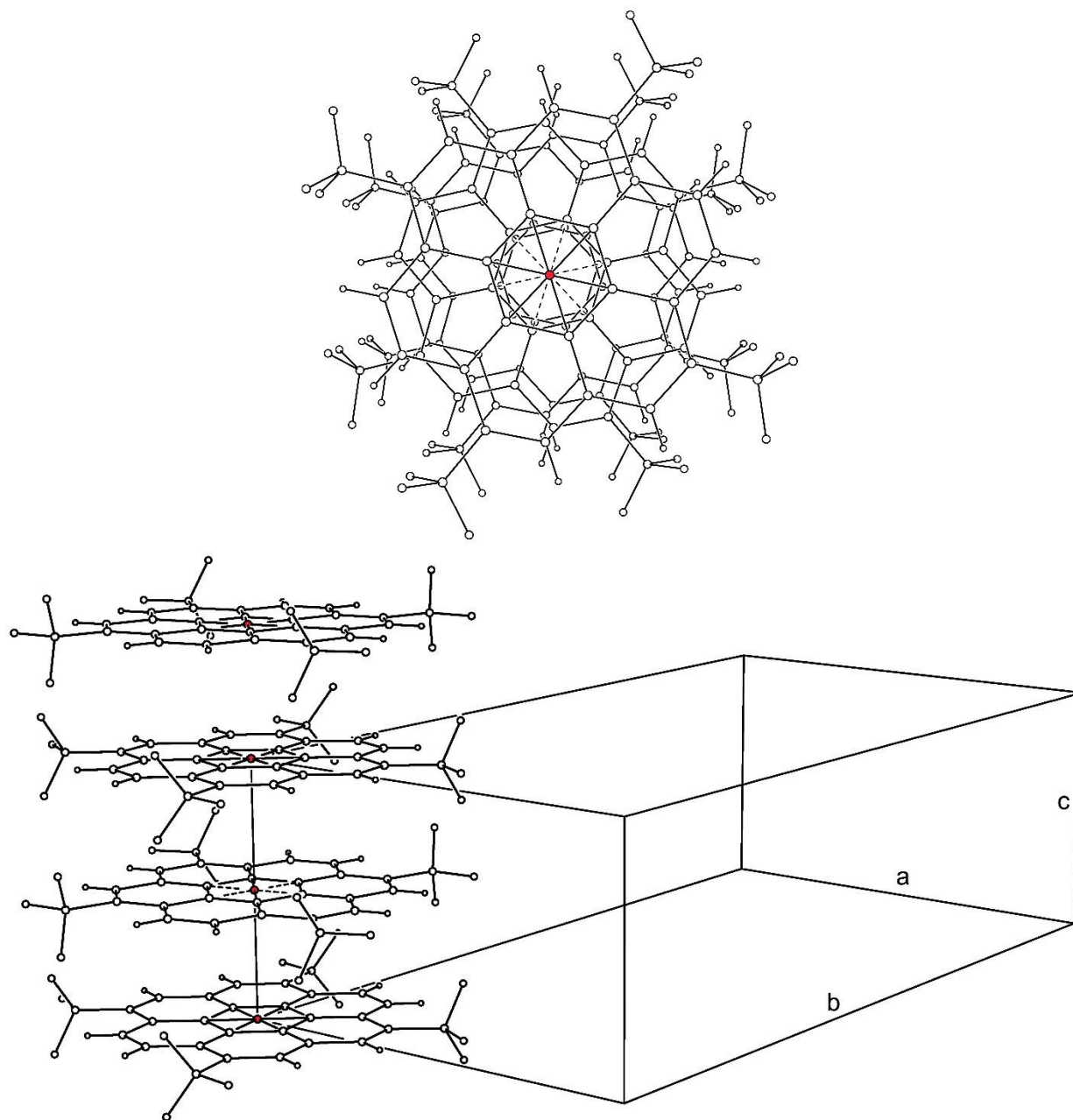
Figure S2-3. Drawings of the stacks of molecules in the structure of CORO-4-1 (only the 92% components are shown). The C and H atoms in each molecule are rigorously co-planar, and those planes are rigorously perpendicular to the crystallographic *c* axis. The red dots are the centroids of the central hexagons. These centroids are aligned along the crystallographic *c* axis, resulting in a 3.611 Å (*c*/2) separation of the π systems in adjacent molecules. Molecule in the stack are rotated 25° relative to one another so that every second molecule is perfectly aligned.
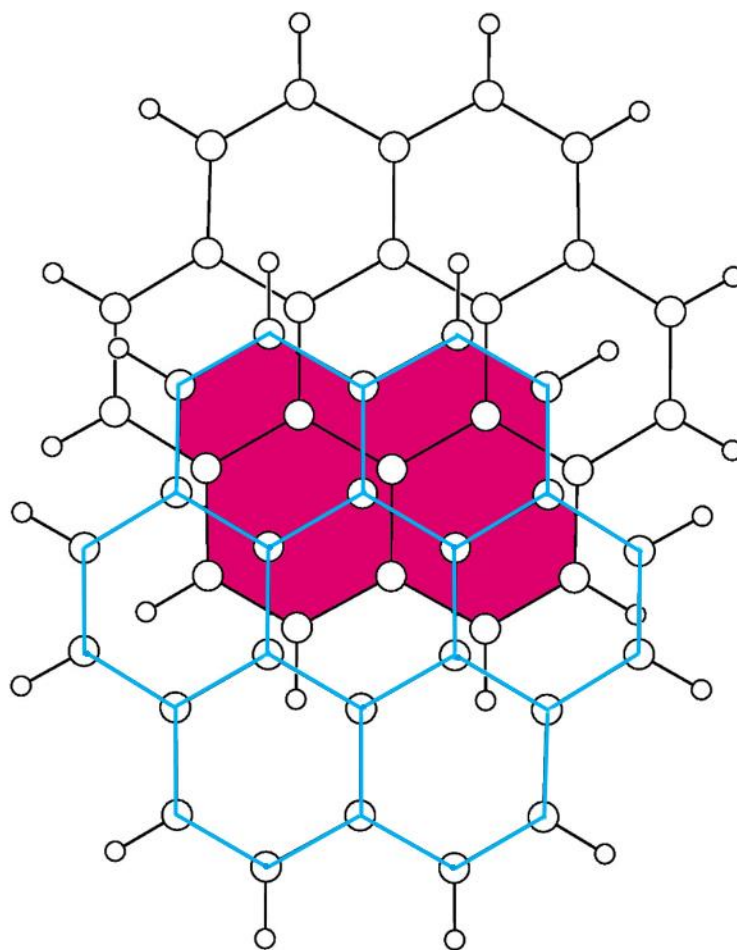
Figure S2-4. Adjacent molecules in the structure of unsubstituted coronene from the Kataeva 2016 paper.[1] Degree of π–π overlap is 28%.
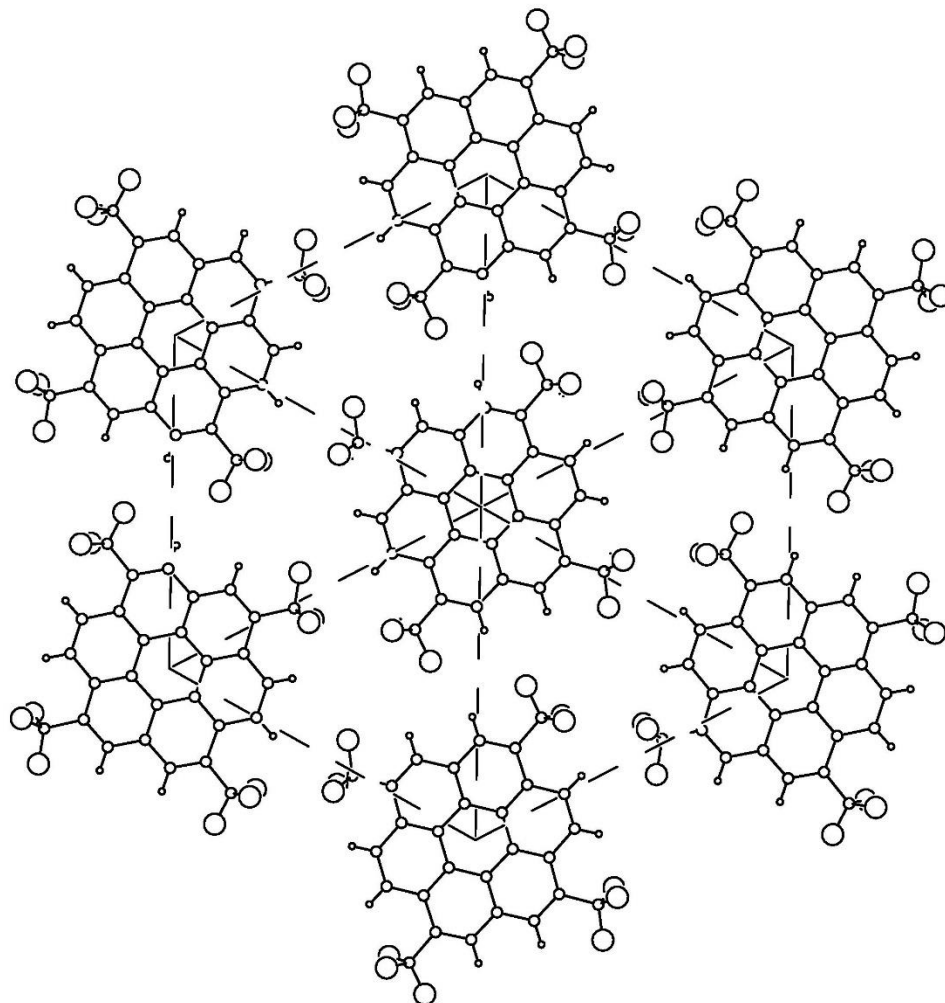
Figure S2-5. One layer of molecules in the structure of CORO-4-1, with F atoms highlighted as large spheres. The molecules lie in the crystallographic ab plane, which is parallel to the plane of the page in this drawing. The closest intermolecular F···F and F···H distances are 3.11 and 2.61 Å, respectively.
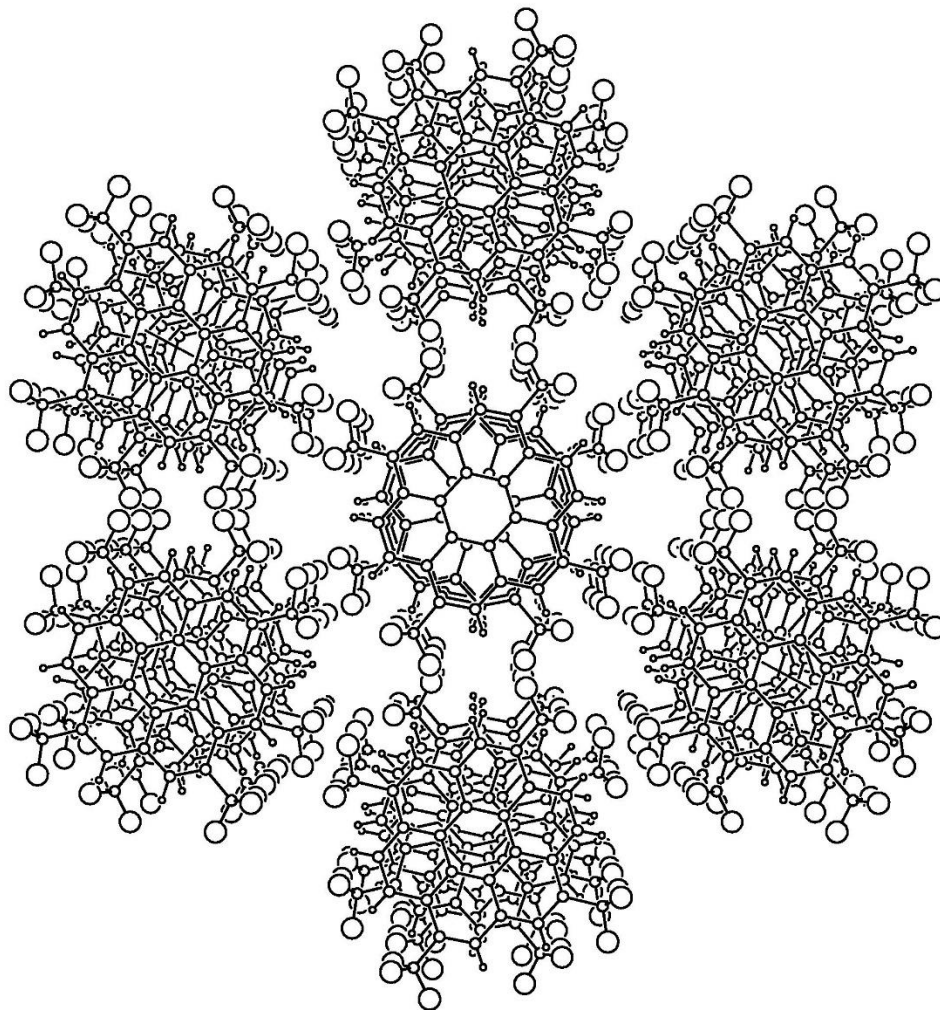
Figure S2-6. Hexagonal array of stacks of molecules in the structure of CORO-4-1. The view is looking down the crystallographic *c* axis. The empty spaces between major component molecules can be seen. These spaces may be the reason for the facile rotational disorder of the minor component molecules.
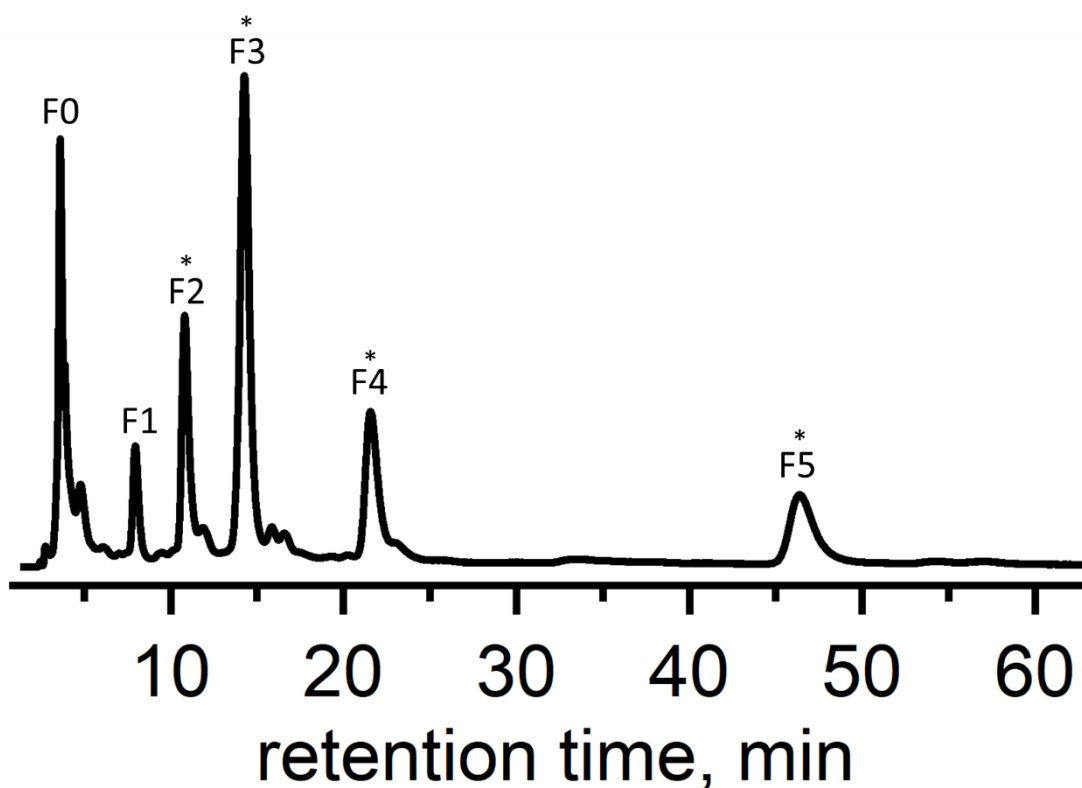
Figure S2-7. HPLC chromatogram of MTR-HP. All compounds shown above have more than 6 CF$_3$ groups according to mass spectrometry. The best eluent found for these compounds was heptane, showing these compounds have weak interactions with the pyrene based stationary phase, resulting in excellent separation while the single run allows for efficient separation/purification protocol. All of the fractions with asterisks represent compounds where crystal structures were obtained, see Figure S2-2.
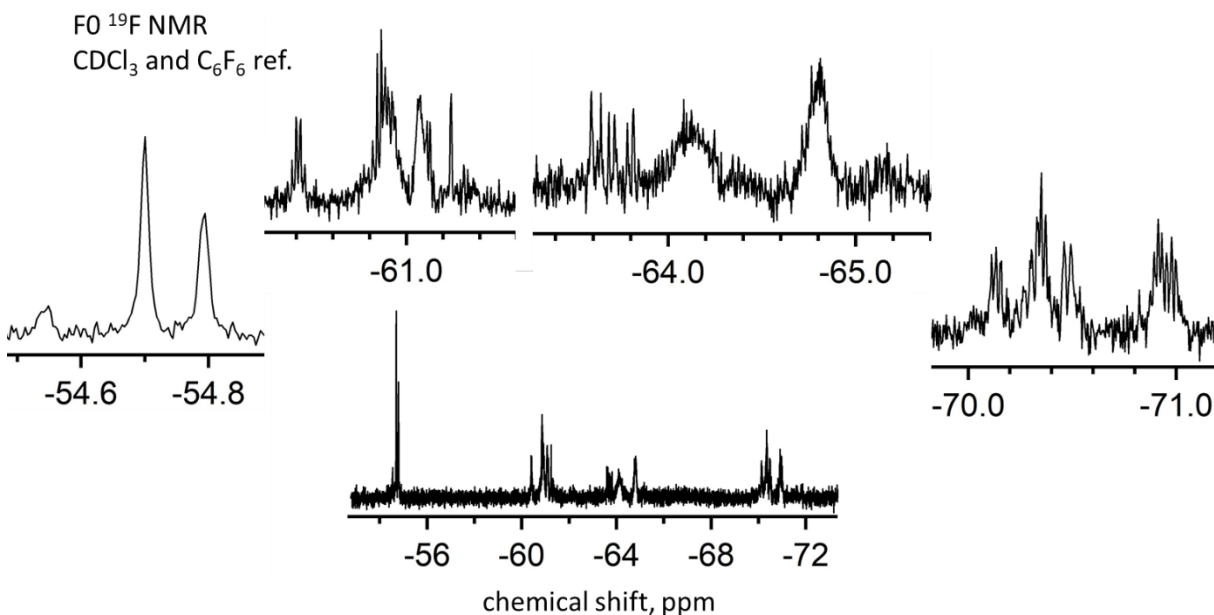
Figure S2-8. The ^{19}F NMR spectrum of F0, see Table S2-3. The mass spectrum results suggest that the majority of the material has ten CF$_3$ groups with four sp^3 protons. The multiplets at -70 to -71 ppm are indicative of the sp^3 functionality. There are few singlet signals in the -60 to -65 ppm range showing there are few CF$_3$ groups that are not adjacent to at least one other CF$_3$ group. The ^{1}H NMR of this fraction was collected but due to the large number of compounds there are no discreet signals which can be observed.
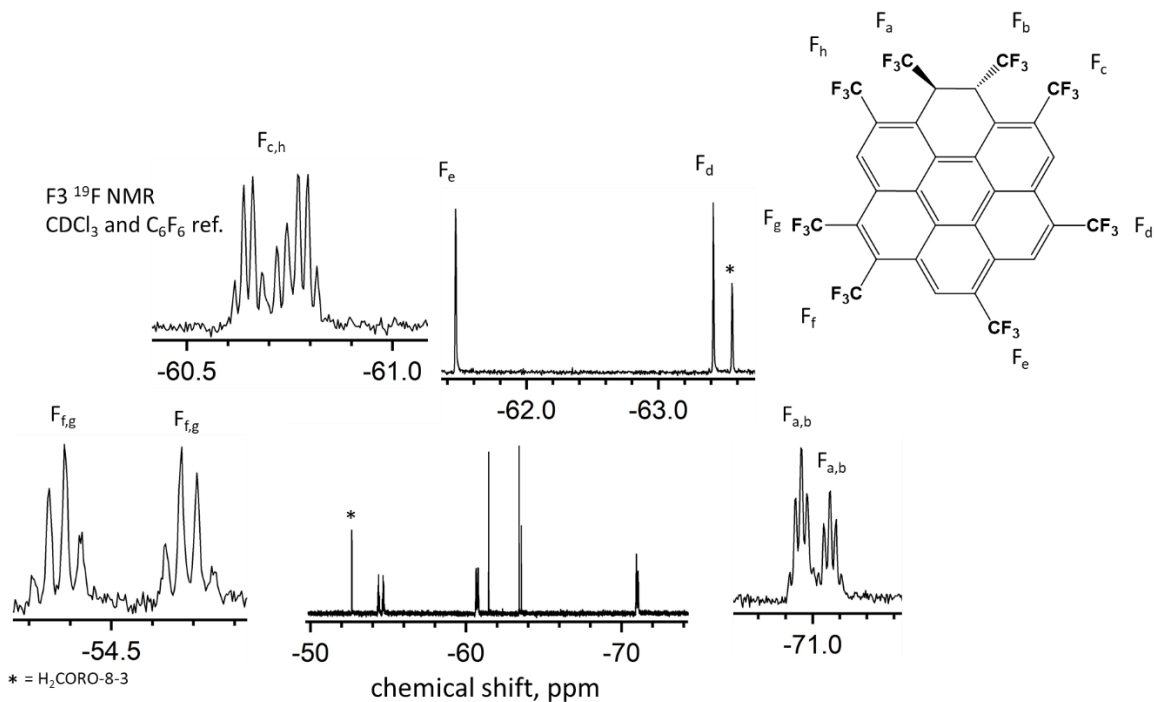
Figure S2-9. ^{19}F NMR of H$_2$CORO-8-2 with peaks assigned to specific CF$_3$ groups on the molecule. The spectrum contains signals from an impurity which integrates to 25% of the total sample assuming the visible singlets represent one CF$_3$ group each. There is also evidence for signals underneath the multiplets at −60 and −71 ppm resulting in elevated integration values. These signals appear to be due to a second isomer, H$_2$CORO-8-3 aka 1,2,3,5,7,8,10,12-octakis(trifluoromethyl)-1,2-dihydrocoronene. The crystal structure of H$_2$CORO-8-2 supports this assignment, see Figure 2-7. Measurement recorded in CDCl$_3$ with C$_6$F$_6$ as a reference.
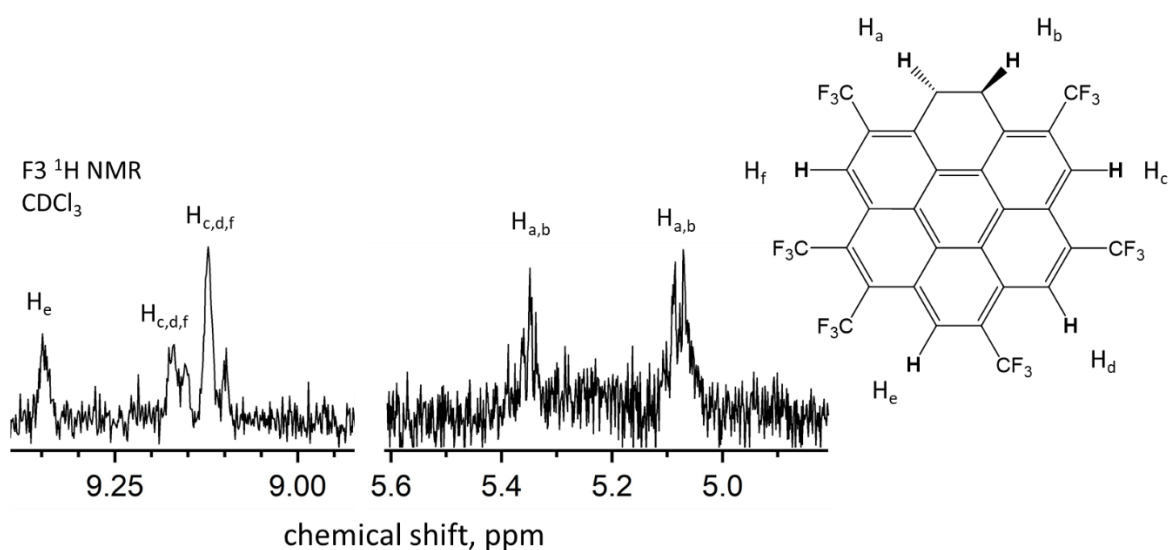
Figure S2-10. ^{1}H NMR of H$_2$CORO-8-2. The spectrum is very noisy due to the small amount of material. The spectrum was recorded in CDCl$_3$ with chloroform as a reference (7.26 ppm).

There are no unique signals for the H$_2$CORO-8-3 protons. This appears to be due to the poor signal to noise ratio for the ^{1}H NMR spectrum which is due to the small amount of material available for the measurement.
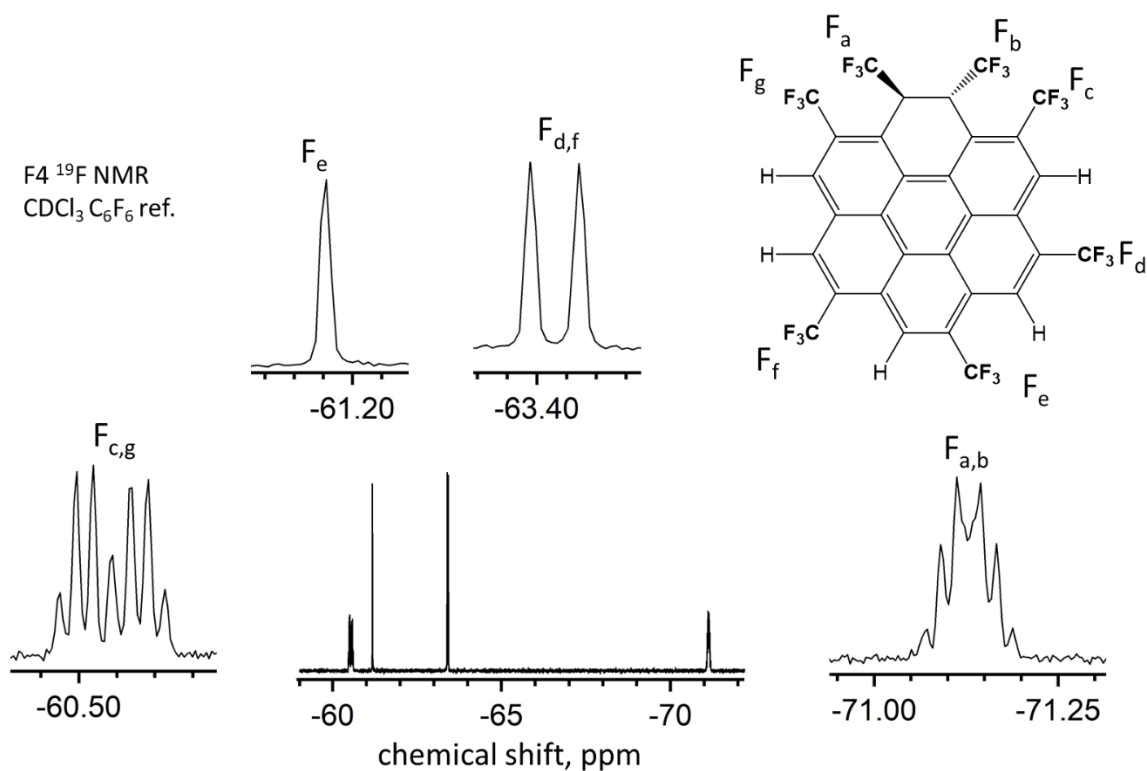
Figure S2-11. The ^{19}F NMR of H_2CORO-7-1. ^{19}F NMR (CDCl$_3$, internal ref. C$_6$F$_6$, 375 MHz). The multiplet at -71 ppm is a pair of near isochronous quartets arising from the two adjacent C(sp^3) bonded CF$_3$ groups, it is listed as an apparent septet in Table S2-4. On this molecule as well as H$_2$CORO-7-2 the CF$_3$ groups are in nearly identical chemical environments causing the chemical shift difference to be very small for those two CF$_3$ groups, labeled F$_a$ and F$_b$, resulting in the unique multiplet. Measurement recorded in CDCl$_3$ with C$_6$F$_6$ as a reference.
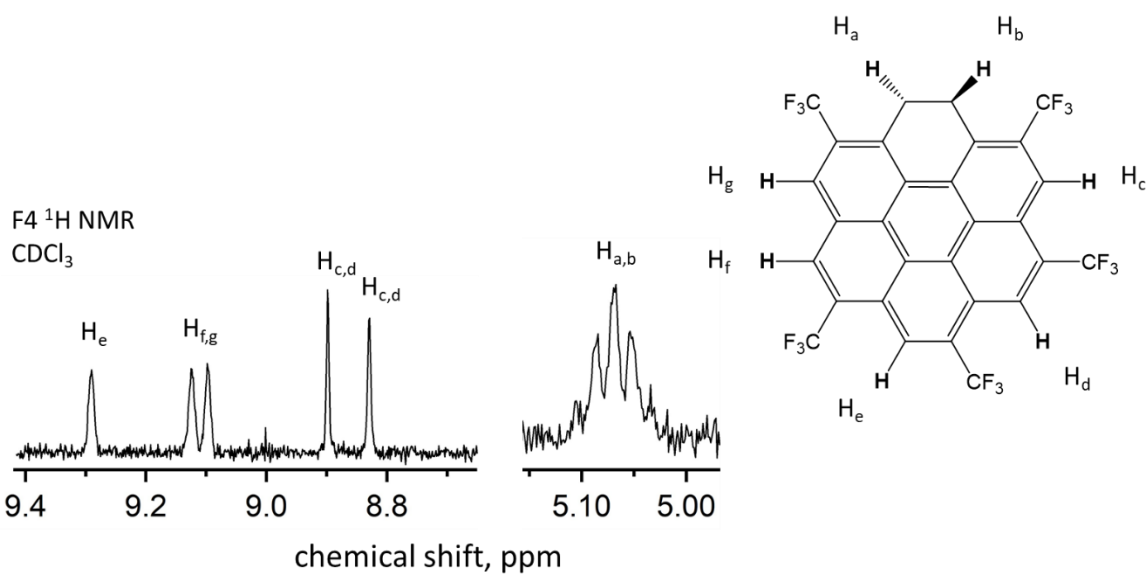
Figure S2-12. ^{1}H NMR of H_2CORO-7-1. The chemical environment for the two sp^3 protons is nearly identical resulting in coincidental isochrony giving rise to an apparent pentet. The spectrum was recorded in $CDCl_3$ with chloroform as a reference (7.26 ppm).
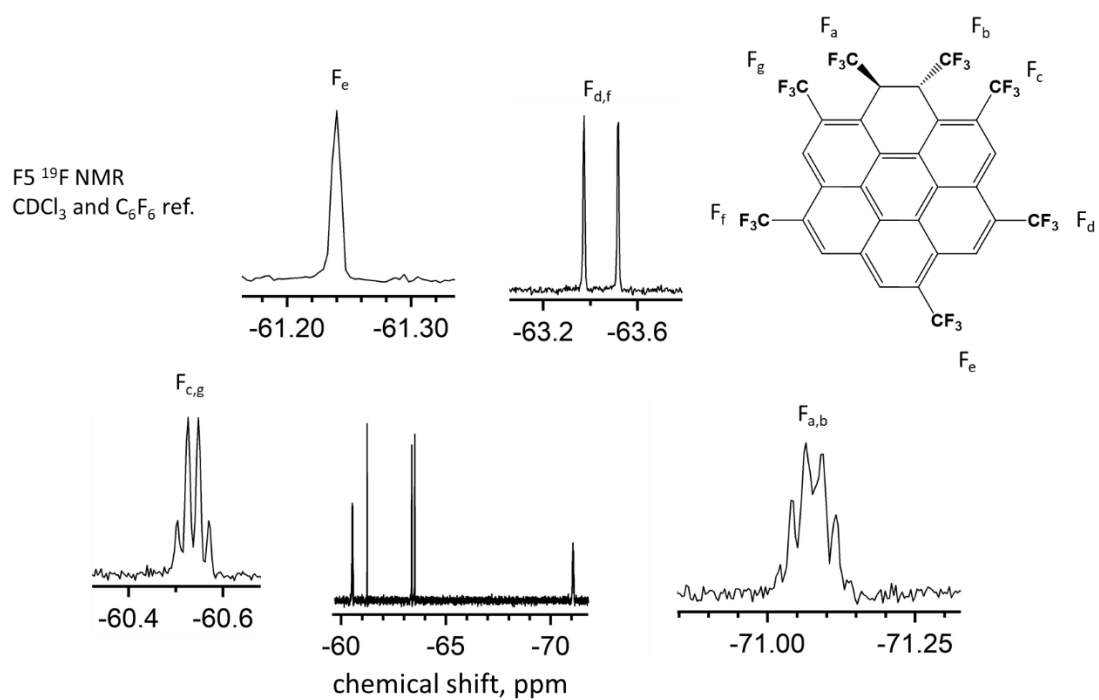
Figure S2-13. ^{19}F NMR of H2CORO-7-2 with all assignable peaks labeled. Measurement recorded in CDCl$_3$ with C$_6$F$_6$ as a reference.
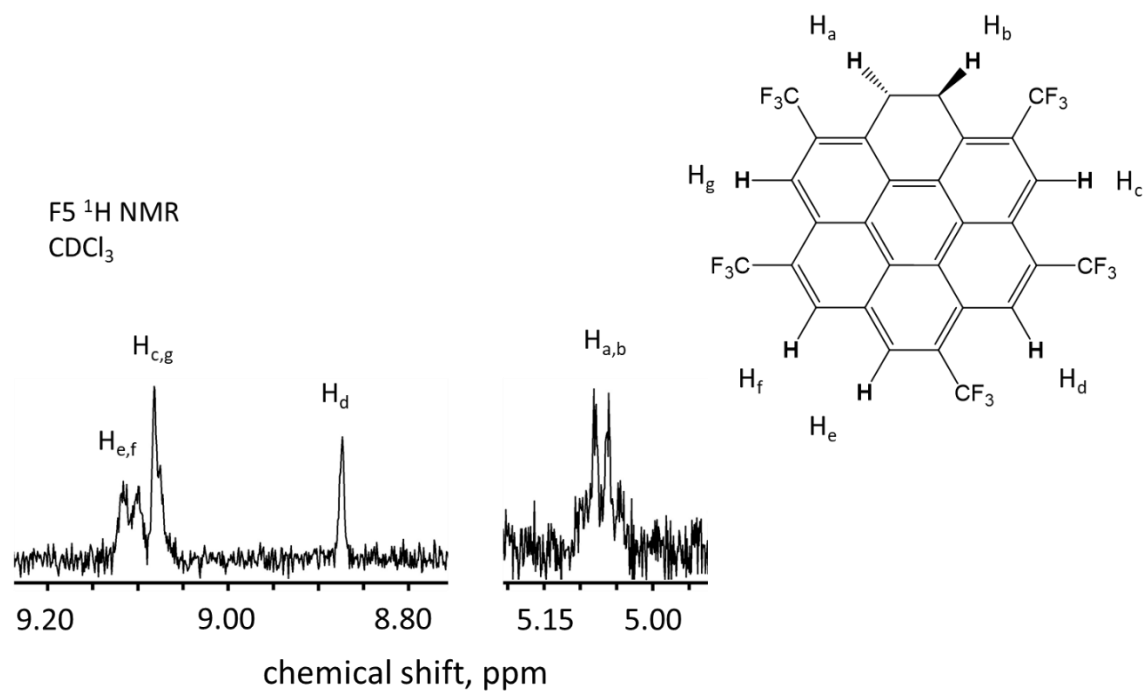
Figure S2-14. ^{1}H NMR of H$_2$CORO-7-2. The spectrum was recorded in CDCl$_3$ with chloroform as a reference (7.26 ppm).
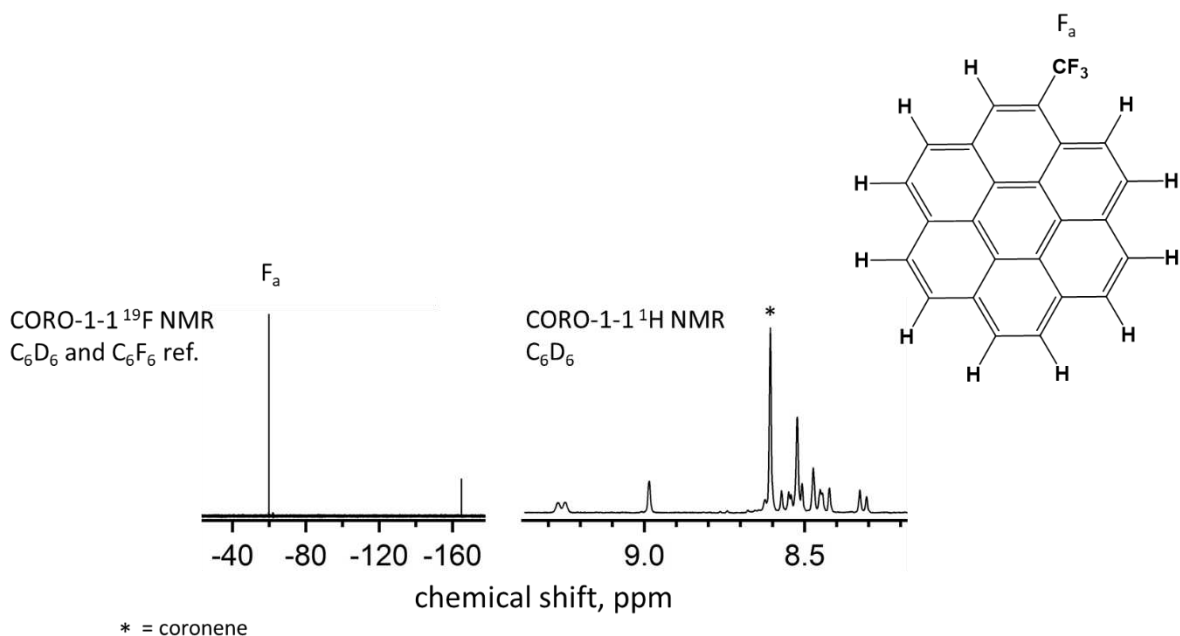
Figure S2-15. ^{19}F and ^{1}H NMR spectra for CORO-1-1. ^{19}F NMR (C_6D_6, internal ref. C_6F_6, 375 MHz): δ −59.89 (s, 3F). ^{1}H NMR (C_6D_6, 400 MHz) δ 8.3 (d, 1H, $J = 9$ Hz); δ 8.4 (d, 1H, $J = 9$ Hz); δ 8.5 (d, 2H, $J = 9$ Hz); δ 8.5 (overlapped d, 1H); δ 8.5 (s, 2H); δ 8.5 (overlapped d, 1H); δ 8.6 (d, 1H, $J = 9$ Hz); δ 9.0 (s, 1H); δ 9.3 (d, 1H, $J = 9$ Hz,). The multiplets of the overlapped signals were determined using the integration values of each signal. Unfortunately, the J coupling values could not be determined reliably for the overlapped doublets. Spectrum recorded in C_6D_6 with C_6F_6 used as an internal standard for the ^{19}F NMR. Peak identified with an asterisk is due to the 12 symmetric protons from residual coronene which coelutes with CORO-1-1. The proton NMR agrees well with the previously reported 1-chlorocoronene and the recently reported 1-trifluoromethylcoronene recorded in CD_2Cl_2.[2-3]
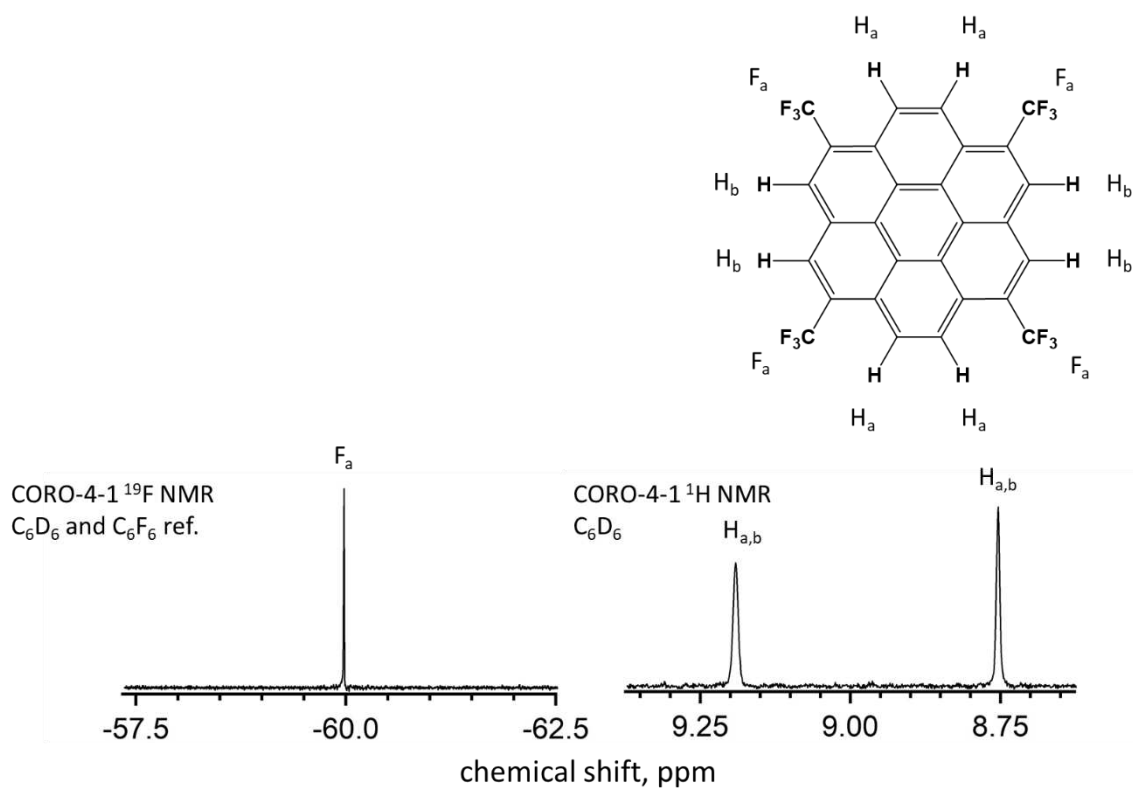
Figure S2-16. ^{19}F and ^{1}H NMR spectra for CORO-4-1. ^{19}F NMR (C_6D_6, internal ref. C_6F_6, 375 MHz): δ −60.0 (s, 12F). ^{1}H NMR (C_6D_6, 400 MHz) δ 8.8 (s, 4H); δ 9.2 (s, 4H).
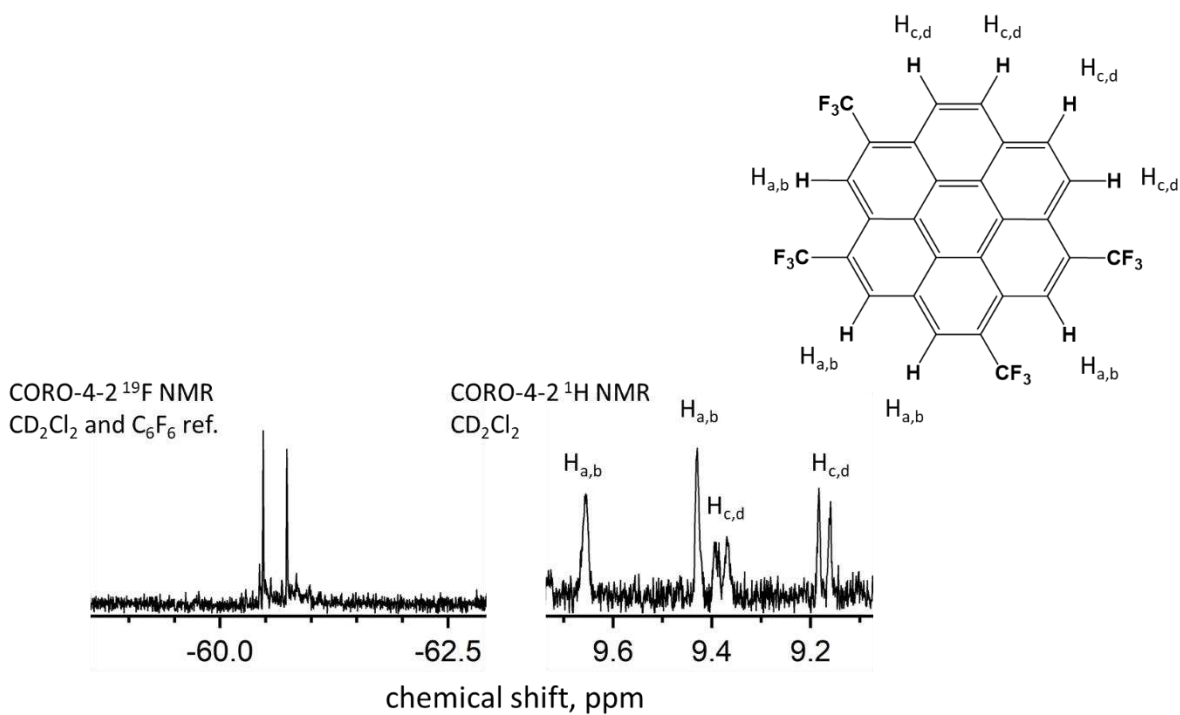
Figure S2-17. ^{19}F and ^{1}H NMR spectra for CORO-4-2. ^{19}F NMR (CD$_2$Cl$_2$, internal ref. C$_6$F$_6$, 375 MHz): δ −60.5 (s, 6F); δ −60.7 (s, 6F). ^{1}H NMR (CD$_2$Cl$_2$, 400 MHz) δ 9.2 (d, 2H, J = 9 Hz); δ 9.4 (d, 2H, J = 10); δ 9.4 (s, 2H); δ 9.7 (s, 2H).
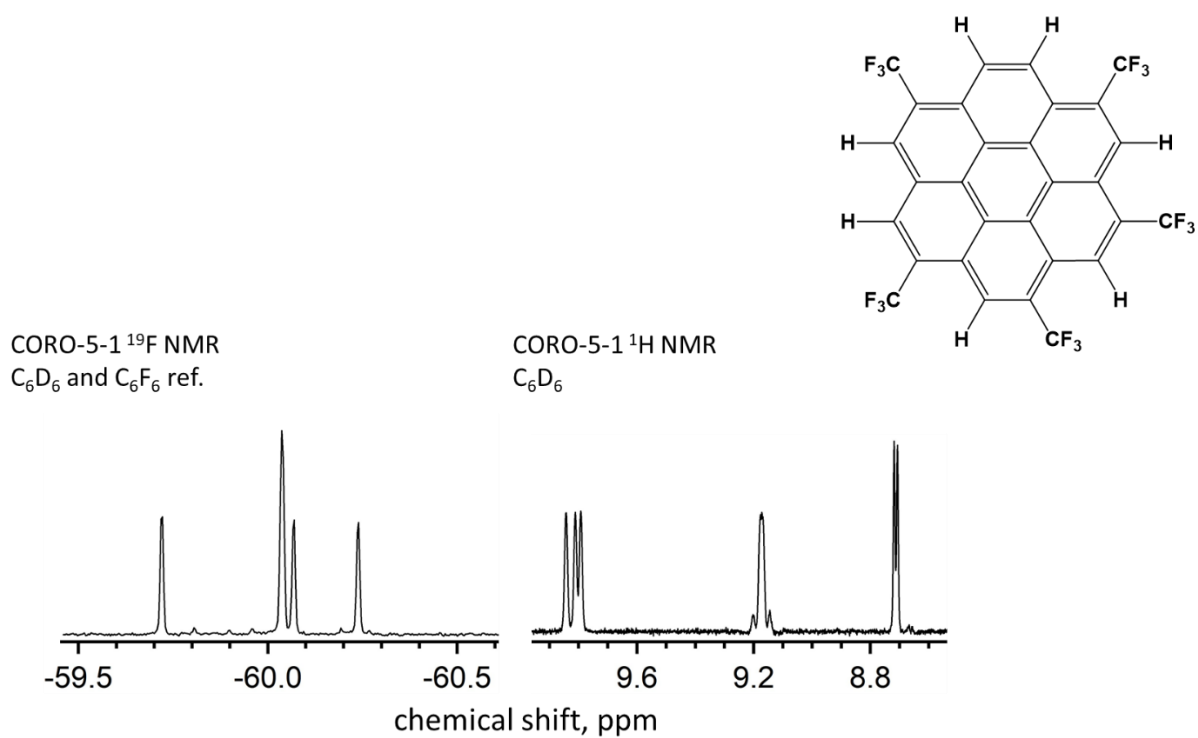
Figure S2-18. ^{19}F and ^1H NMR spectra for CORO-5-1. ^{19}F NMR (C_6D_6, internal ref. C_6F_6, 375 MHz): δ −59.7 (s, 3F); δ −60.0 (s, 2F) δ −60.1 (s, 3F); δ −60.2 (s, 3F). ^1H NMR (C_6D_6, 400 MHz) δ 8.7 (d, 2H, J = 5 Hz,); δ 9.2 (m, 2H, J = 11); δ 9.8 (d, 2H, J = 7 Hz); δ 9.8 (s, 1H)
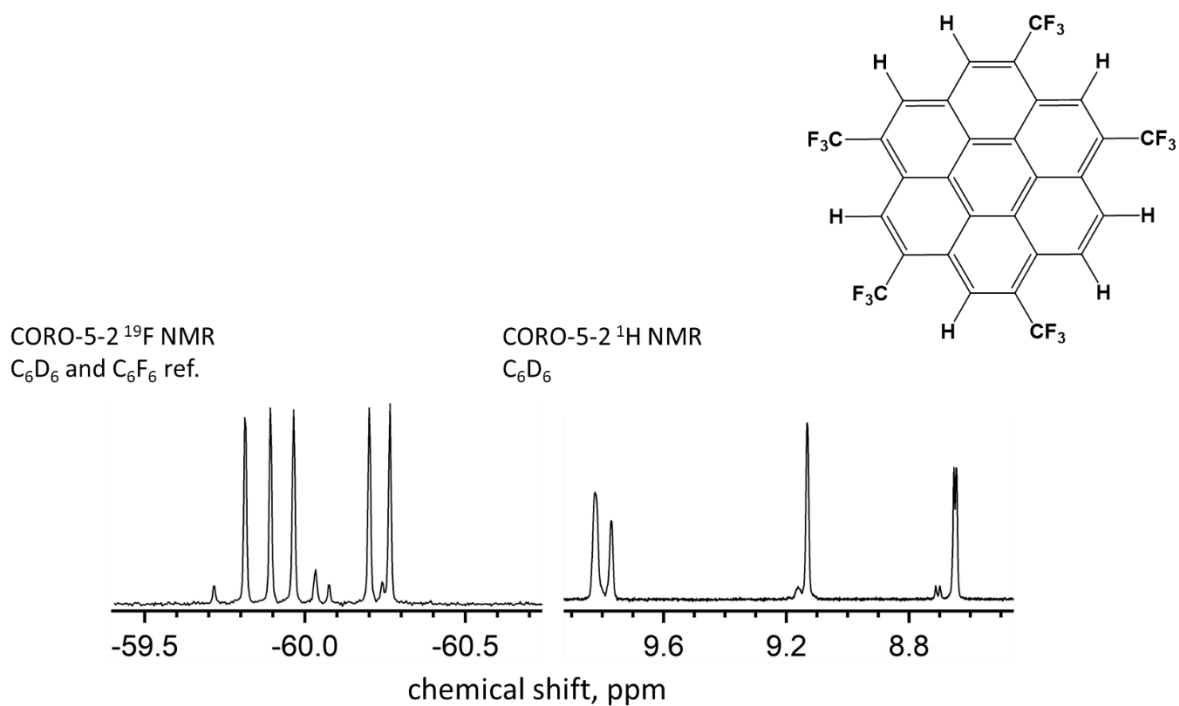
Figure S2-19. ^{19}F and ^{1}H NMR spectra for CORO-5-2. ^{19}F NMR (C$_6$D$_6$, internal ref. C$_6$F$_6$, 375 MHz): δ −59.8 (s, 3F); δ −59.9 (s, 3F) δ −60.0 (s, 3F); δ −60.2 (s, 3F); δ −60.3 (s, 3F). ^{1}H NMR (C$_6$D$_6$, 400 MHz) δ 8.7 (d, 2H, J = 3 Hz); δ 9.1 (s, 2H); δ = 9.8 (s broad, 1H); δ = 9.8 (s broad, 2H).
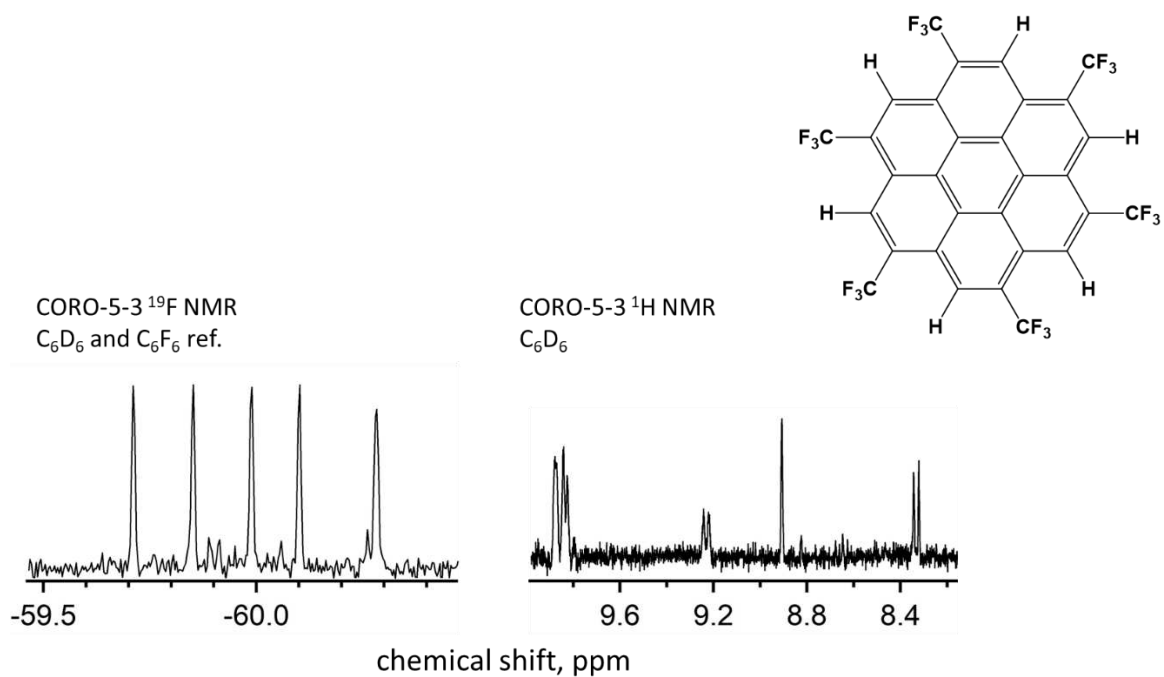
Figure S2-20. ^{19}F and ^1H NMR spectra for CORO-5-3. ^{19}F NMR (C_6D_6, internal ref. C_6F_6, 375 MHz): δ −59.7 (s, 3F); δ −59.9 (s, 3F) δ −60.0 (s, 3F); δ −60.1 (s, 3F); δ −60.3 (s, 3F). ^1H NMR (C_6D_6, 400 MHz) δ 8.3 (d, 1H, J = 9 Hz); δ 8.9 (s, 1H); δ 9.2 (d, 1H); δ 9.8 (s broad, 1H); δ 9.8 (d, 2H, J = 6 Hz); δ 9.9 (s broad, 2H).
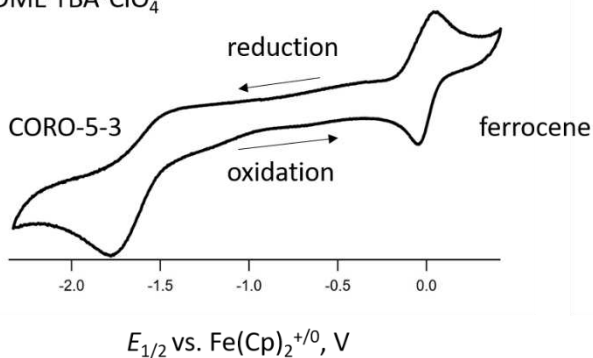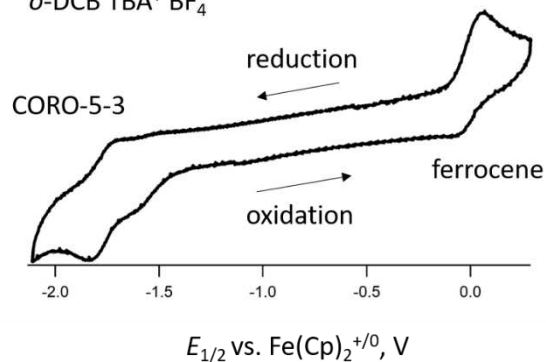
Figure S2-21. Cyclic voltammograms of CORO-5-3 in dimethoxyethane (**Left**) and *ortho*-dichlorobenzene (**Right**). The solvent effect on the $E_{1/2}$ results in approx.. 150 mV decrease for the aromatic solvent. $E_{1/2}$ for CORO-5-3 is −1.62 V in DME and −1.77 V in *o*-DCB. Both voltammograms were recorded at 500 mV s^{-1}.

CORO-1-1

CF₃
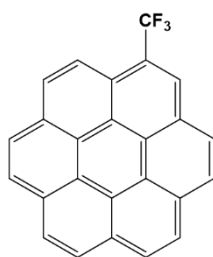
1-(trifluoromethyl)coronene
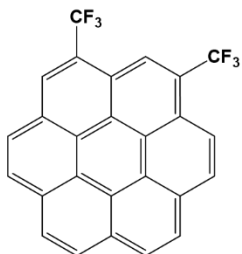
1,3-bis(trifluoromethyl)coronene
2.18 kJ/mol
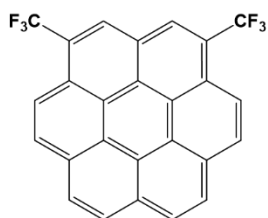
1,4-bis(trifluoromethyl)coronene
0.9 kJ/mol
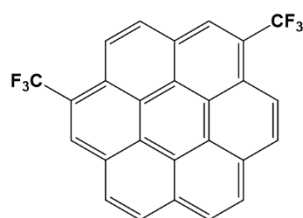
1,5-bis(trifluoromethyl)coronene
0.46 kJ/mol
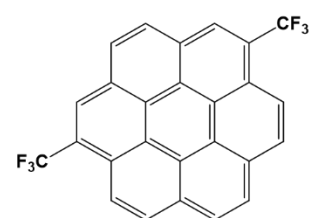
1,6-bis(trifluoromethyl)coronene
0.52 kJ/mol
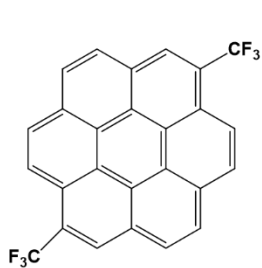
1,7-bis(trifluoromethyl)coronene
0.0 kJ/mol
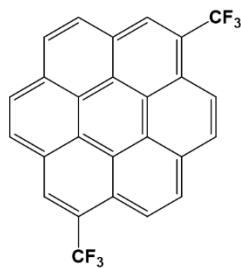
1,8-bis(trifluoromethyl)coronene
0.33 kJ/mol
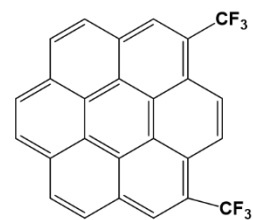
1,10-bis(trifluoromethyl)coronene
0.85 kJ/mol

380
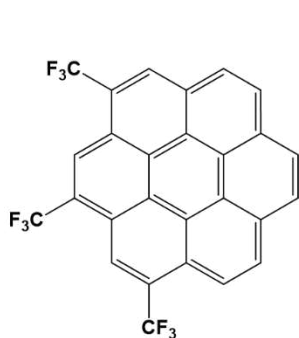
1,3,5-tris(trifluoromethyl)coronene

3.32 kJ/mol
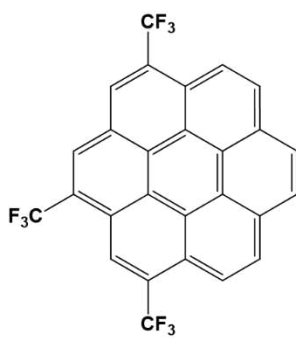
1,3,6-tris(trifluoromethyl)coronene

2.16 kJ/mol
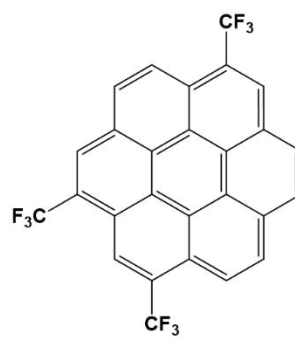
1,3,7-tris(trifluoromethyl)coronene

1.22 kJ/mol
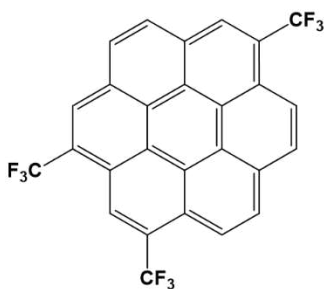
1,3,8-tris(trifluoromethyl)coronene

1.61 kJ/mol
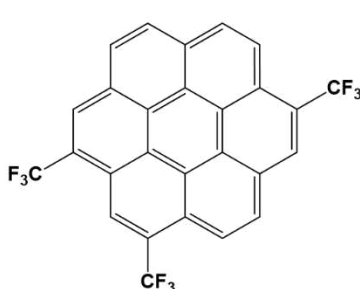
1,3,9-tris(trifluoromethyl)coronene

1.29 kJ/mol
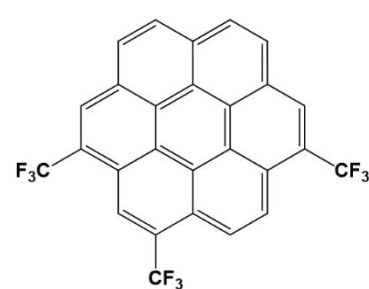
1,3,10-tris(trifluoromethyl)coronene

1.95 kJ/mol
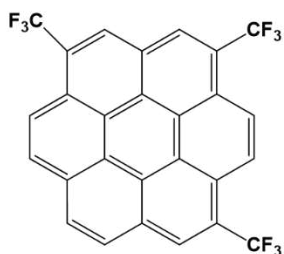
1,4,7-tris(trifluoromethyl)coronene

0.37 kJ/mol
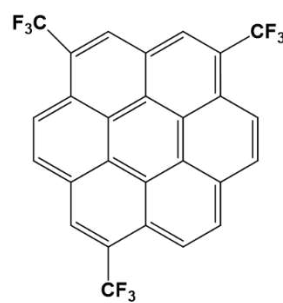
1,4,8-tris(trifluoromethyl)coronene

0.32 kJ/mol
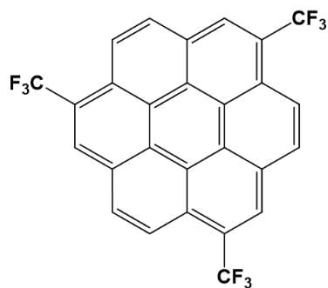
1,5,9-tris(trifluoromethyl)coronene

0.00 kJ/mol
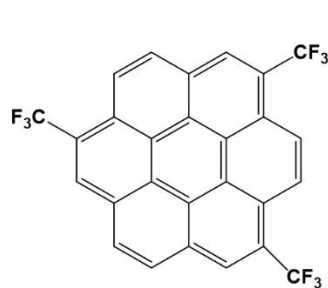
1,5,10-tris(trifluoromethyl)coronene

0.43 kJ/mol

381

CORO-4-1

1,4,7,10-tetrakis(trifluoromethyl)coronene

0.00 kJ/mol

1,3,6,9-tetrakis(trifluoromethyl)coronene

1.30 kJ/mol

1,3,7,10-tetrakis(trifluoromethyl)coronene

1.16 kJ/mol

1,3,5,10-tetrakis(trifluoromethyl)coronene

2.81 kJ/mol

CORO-4-2

1,3,6,8-tetrakis(trifluoromethyl)coronene

2.92 kJ/mol

1,3,5,7-tetrakis(trifluoromethyl)coronene

3.67 kJ/mol

1,3,5,8-tetrakis(trifluoromethyl)coronene

2.86 kJ/mol

1,3,8,10-tetrakis(trifluoromethyl)coronene

2.74 kJ/mol

1,3,6,10-tetrakis(trifluoromethyl)coronene

1.63 kJ/mol

1,3,7,9-tetrakis(trifluoromethyl)coronene

1.65 kJ/mol

1,3,5,9-tetrakis(trifluoromethyl)coronene

2.07 kJ/mol

382

CORO-5-1

1,3,5,7,10-pentakis(trifluoromethyl)coronene

0.00 kJ/mol

CORO-5-2

1,3,5,8,10-pentakis(trifluoromethyl)coronene

0.39 kJ/mol

CORO-5-3

1,3,5,7,9-pentakis(trifluoromethyl)coronene

0.42 kJ/mol

1,3,5,7,9,11-hexakis(trifluoromethyl)coronene

Figure S2-22. Structures and names of all possible isomers with the stipulation that no CF$_3$ groups are adjacent to each other. There are in total 1 single substitution product, 7 two substitution products, 10 three substitution products, 11 four substitution products, 3 five substitution products, and only 1 six substitution product. The relative energies of each isomer are shown below the structure name. Compounds which were isolated and characterized are labeled with the reference used in this publication.
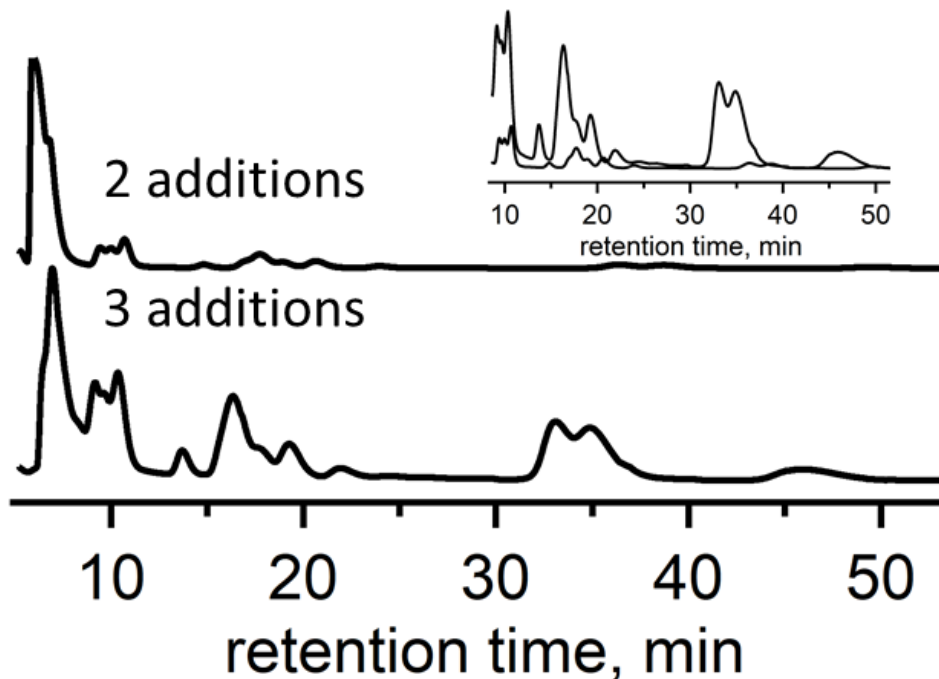
Figure S2-23. Stacked plot showing the HPLC trace for GTGS-2 and GTGS-3. The top chromatogram shows the result of using two additions of CF_3I gas at 700 Torr, GTGS-2, and the bottom chromatogram shows the result from 3 additions of CF_3I at the same temperatures, pressures, and reaction times, GTGS-3.

It is evident that higher substituted coronenes have been produced in larger relative amounts. The inset shows even more clearly the large difference in product distribution where the CORO-1-1 peak, not shown, is normalized to 1 in both chromatograms. The result shows the relative distribution increasing for the higher substituted products, especially the CORO-5s, over subsequent additions. The retention time shift is due to varying concentrations of different coronene derivatives having a strong interaction with the elute resulting in a measurable change in retention. This concentration dependent retention time effect was tested and the resulting HPLC traces are shown in Figure S2-24.
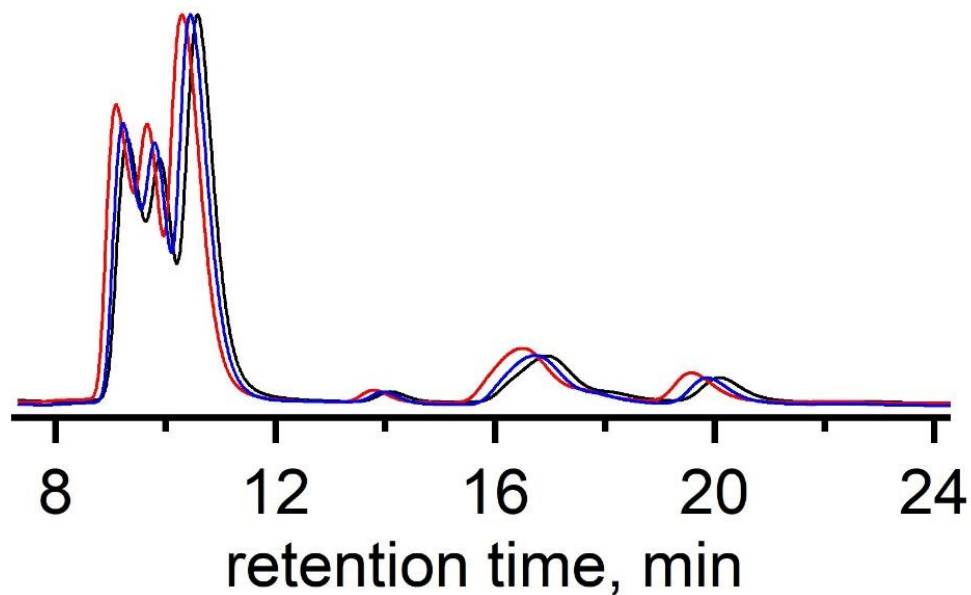
Figure S2-24. The effect of concentration on retention time of aromatic coronene derivatives. The blue trace and red trace are double and triple the concentration of the black trace, respectively. Increasing concentration results in earlier elution times due to increasing the favorability of the elute to interact with itself in solution.
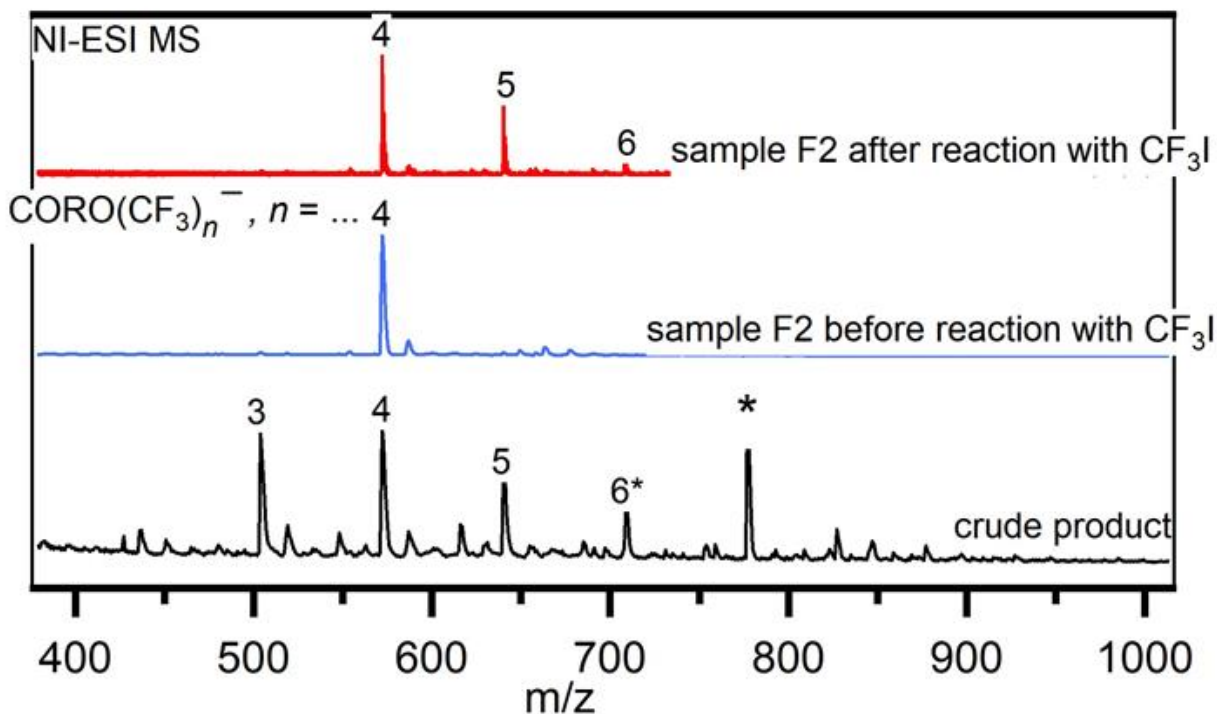
Figure S2-25. Stacked mass spectra showing the crude reaction mixture from GTGS-4 on the bottom, the middle spectrum shows the mass of a fraction isolated from the crude product material containing four CF_3 isomers, the top spectrum shows the result of reacting the material measured in the middle spectrum with CF_3I. The peak labeled 6* is a six isomer with one proton extra or possible evidence of a derivative with two sp^3 carbons with one proton lost as a result of the ionization event. The second starred peak shows the m/z value, 777, corresponding to a dihydrocoronene derivative with seven CF_3 groups and one extra proton suggesting two sp^3 carbons with a loss of one of the protons during ionization. This signal is identical to the F1 fraction from MTR-HP, see Table S2-3.
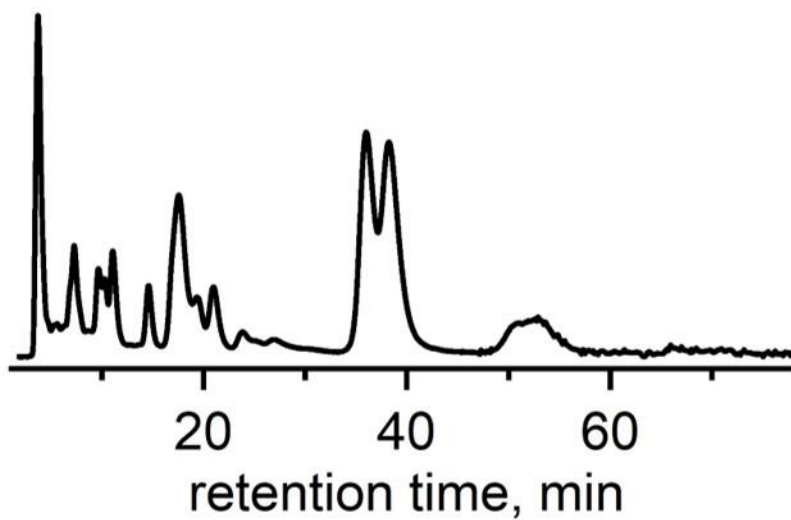
Figure S2-26. HPLC chromatogram of ROCK-1. The karpatite reaction favors $CORO(CF_3)_5$ isomers predominantly, 47% collectively by HPLC peak area.
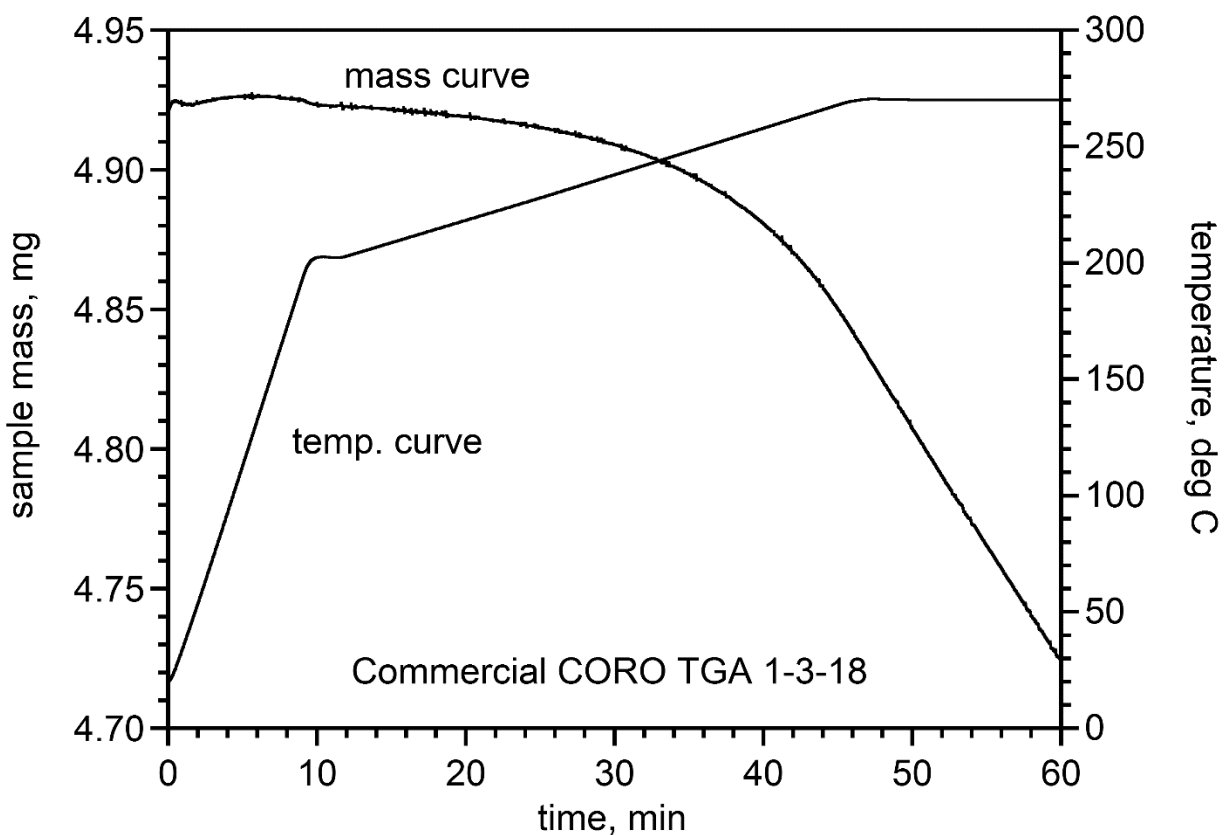
Figure S2-27. TGA thermogram of commercial coronene sample showing the rate of sublimation of the coronene starting material. Sublimation is noticeable at 200 °C and then the rate steadily increases above 200 °C.
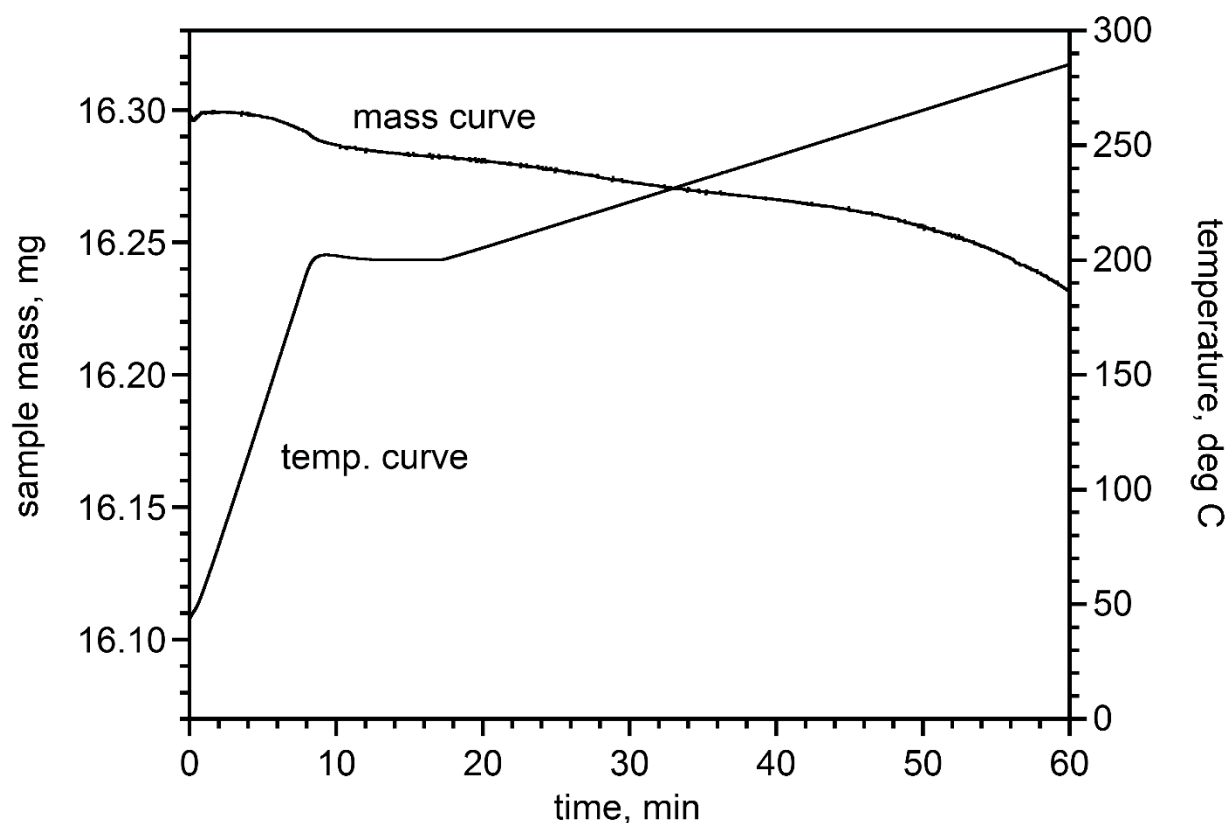
Figure S2-28. TGA thermogram of the karpatite mineral sample showing the rate of sublimation of the coronene inside the karpatite sample. Sublimation is noticeable at 200 °C and continues to fall over the duration of the experiment.

A possible explanation for the elevated concentration of the CORO-5 isomers is that the sublimation rate of coronene out of the karpatite mineral matrix is slower than the commercial coronene sublimation rate. Crystals of coronene were excavated from the mineral sample and tested in the TGA experiment as well. Producing an identical thermogram as is shown in Figure S2-29.
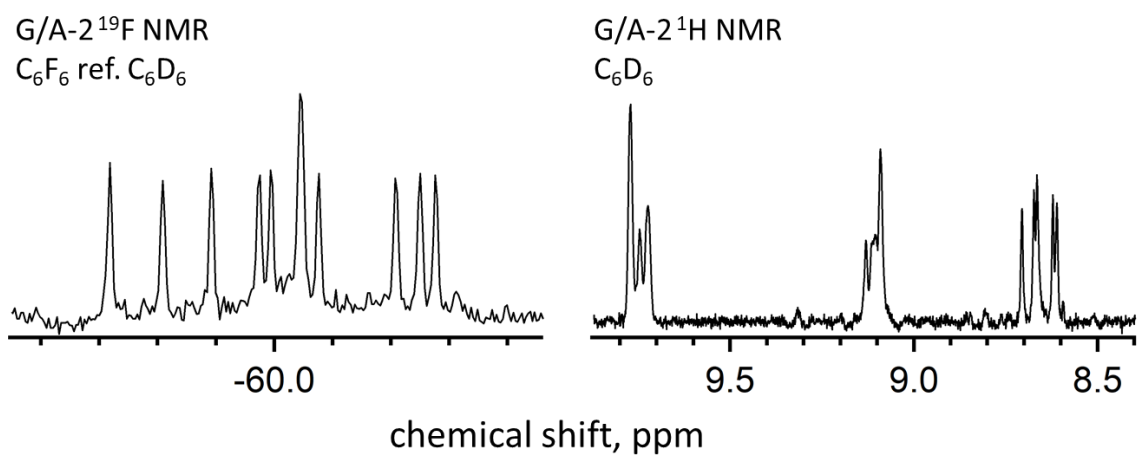
Figure S2-29. ^{19}F and ^{1}H NMR of G/A-2. The chemical shifts line up with CORO-5-1 and CORO-5-2 which agrees well with the HPLC chromatogram.

390
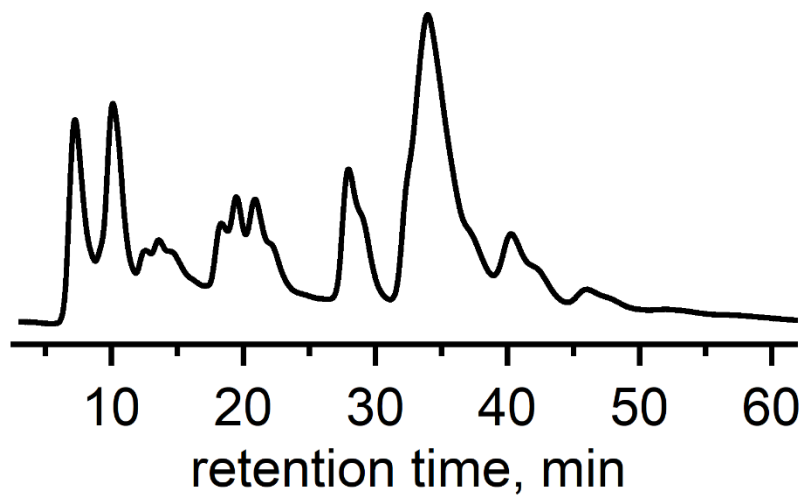
Figure S2-30. HPLC chromatogram for G/A-1.
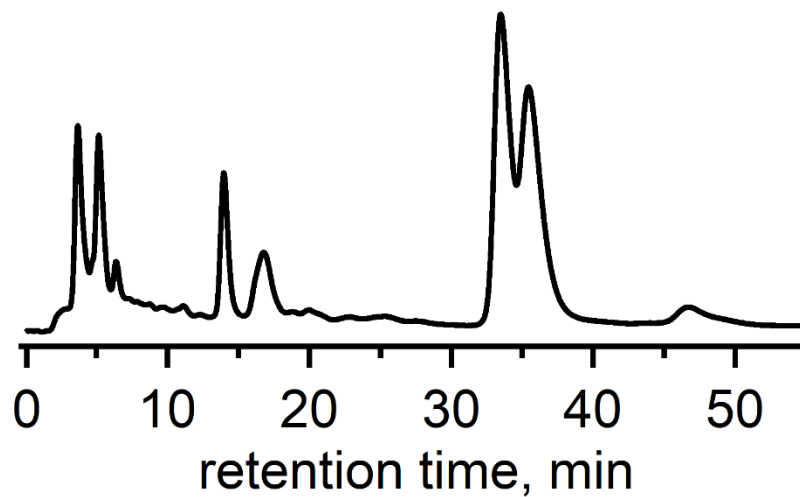
Figure S2-31. HPLC chromatogram for G/A-2.
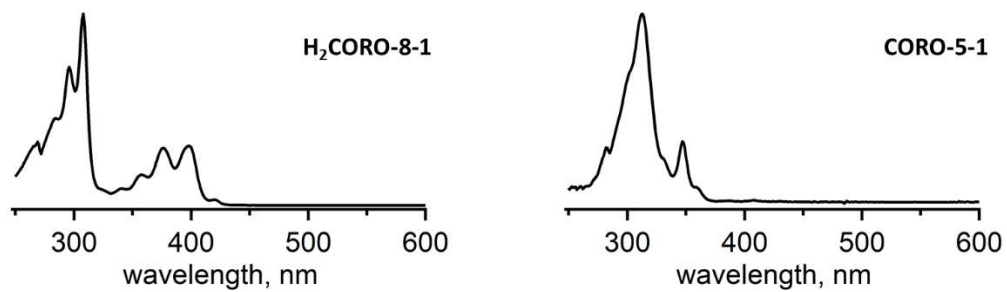
Figure S2-32. UV-vis spectra for (**Left**) H$_2$CORO-8-1 and (**Right**) CORO-5-1. Spectrum for H$_2$CORO-8-1 was collected in heptane. Spectrum for CORO-5-1 was collected in toluene.

Electronic Spectra of H$_2$CORO-8-1

$S_0 \rightarrow S_1$ $S_1 \rightarrow S_0$

wavelength, nm

$$\Phi_x = \Phi_{std}\left(\frac{1-10^{-A_{std}}}{1-10^{-A_x}}\right)\left(\frac{\int F_x}{\int F_{std}}\right)\left(\frac{n_x^2}{n_{std}^2}\right)$$

Absorption Spectra

wavelength, nm

Emission Spectra Overlay

standard

wavelength, nm
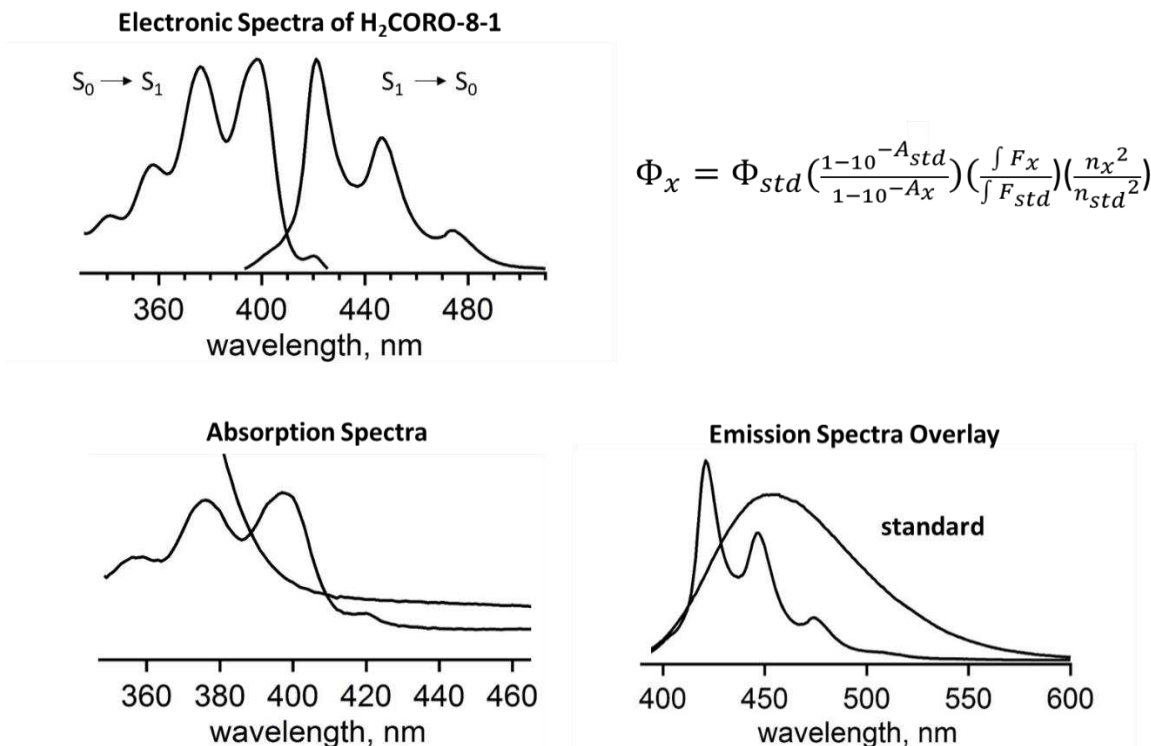
Figure S2-33. Electronic spectra associated with the calculation of the quantum yield of H$_2$CORO-8-1. Quantum yield was recorded as 0.35. The spectra were recorded in cyclohexane with the concentration of the H$_2$CORO-8-1 being 3.6×10^{-6} M. The standard, quinine hemisulfate monohydrate, was dissolved in 0.105 M HClO$_4$ aqueous solution. The quantum yield was calculated using the equation shown (**Top Right**) where x represents the sample, std represents the standard, Φ is the quantum yield, $\int$F is the integrated fluorescence intensity, A is the absorbance at the excitation wavelength, and η is the refractive index of the solvent.

REFERENCES S2.

1.   Kataeva, O.; Khrizanforov, M.; Budnikova, Y.; Islamov, D.; Burganov, T.; Vandyukov, A.; Lyssenko, K.; Mahns, B.; Nohr, M.; Hampel, S.; Knupfer, M., Crystal Growth, Dynamic and Charge Transfer Properties of New Coronene Charge Transfer Complexes. *Cryst. Growth Des.* **2016,** *16*, 331-338.

2.   Shen, H.-C.; Tang, J.-M.; Chang, H.-K.; Yang, C.-W.; Liu, R.-S., Short and Efficient Synthesis of Coronene Derivatives via Ruthenium-Catalyzed Benzannulation Protocol. *J. Org. Chem.* **2005,** *70*, 10113-10116.

3.   Pal, A. K.; Li, C.; Hanan, G. S.; Zysman-Colman, E., Blue-Emissive Cobalt(III) Complexes and Their Use in the Photocatalytic Trifluoromethylation of Polycyclic Aromatic Hydrocarbons. *Angew. Chem Int. Ed.* **2018,** *57* (27), 8027-8031.

APPENDIX B

SUPPLEMENTAL INFORMATION FOR CHAPTER 3

Table S3-1. Table of NMR chemical shifts reported in ppm. Solvent $CS_2/CDCl_3$ 9/1 for all FHF compounds and neat $CDCl_3$ for Bn_F compounds.

	C$_{70}$FHF-1	C$_{70}$FHF-2	C$_{70}$FHF-3		C$_{70}$Bn$_F$-1
F$_a$	−75.5 (d)	−74.2	−74.4(abq)	F$_a$	−99.1(t)
J (AB)	4 Hz	4 Hz	343, 256 Hz		31 Hz
F$_e$	−140.0	−139.4	−142.6	F$_{bb}$	−138.7
F$_b$	−142.2	−142.7	−142.8	F$_d$	−151.3(tt)
F$_c$	−148.9	−148.3	−148.7	F$_{cc}$	−163.4
F$_d$	−153.1	−153.4	−153.4		
				H$_a$	5.1

All chemical shifts other than where stated in the table are complex multiplets due to second order effects.

Table S3-2. Peak maxima for the UV-vis spectrum of both the mixture of $C_{70}FHF$-1 and 2 and $C_{70}FHF$-3

$C_{70}FHF$-3 (nm)	$C_{70}FHF$-1 and 2 mixture (nm)
288	290
-	310
321	338
364	399
400	-
440	465
-	537
592	661

Table S3-3. Table of relative energies of C$_{70}$FHF theoretical isomers calculated by two different levels of theory. The first three isomers are C$_{70}$FHF-1, 2, and 3.

	PBE-D3BJ/def2-TZVP, opt		
	dE, kJ/mol	HOMO, eV	LUMO, eV	d-LUMO (vs C70), eV
C70FHF_a1	0.0	-5.735	-4.106	0.004
C70FHF_a2	0.7	-5.730	-4.117	-0.008
C70FHF_b	15.2	-5.665	-4.158	-0.048
C70FHF_d	38.0	-5.548	-4.387	-0.277
C70FHF_e	65.3	-5.613	-4.714	-0.604
C70FHF_f1	66.2	-5.427	-4.563	-0.453
C70FHF_f2	66.7	-5.430	-4.559	-0.449
C70FHF_c2	67.6	-5.642	-4.298	-0.188
C70FHF_c1	68.0	-5.643	-4.303	-0.194
C70FHF_g1	76.5	-5.355	-4.657	-0.547
C70FHF_g2	78.1	-5.351	-4.649	-0.539
C70FHF_h	147.0	-5.535	-4.392	-0.283
C70		-5.824	-4.110	0.000
C60		-5.823	-4.173	-0.063
C60FHF		-5.723	-4.228	-0.119
PCBM		-5.493	-4.009	0.100

Table S3-4. Table of relative energies of C_{70}FHF theoretical isomers calculated by two different levels of theory. The first three isomers are C_{70}FHF-1, 2, and 3.

	B3LYP-D3BJ/def2-TZVP, single-point			
	dE, kJ/mol	HOMO, eV	LUMO, eV	d-LUMO (vs C70), eV
C70FHF_a1	0.0	-6.100	-3.610	-0.022
C70FHF_a2	0.6	-6.097	-3.610	-0.022
C70FHF_b	13.5	-6.091	-3.651	-0.063
C70FHF_d	37.7	-5.962	-3.898	-0.310
C70FHF_e	73.8	-6.047	-4.262	-0.674
C70FHF_f1	76.7	-5.828	-4.101	-0.513
C70FHF_f2	77.3	-5.831	-4.096	-0.508
C70FHF_c2	74.2	-6.053	-3.819	-0.231
C70FHF_c1	74.6	-6.049	-3.825	-0.237
C70FHF_g1	95.7	-5.656	-4.297	-0.709
C70FHF_g2	97.4	-5.649	-4.287	-0.699
C70FHF_h	169.9	-5.946	-3.918	-0.330
C70		-6.225	-3.588	0.000
C60		-6.284	-3.607	-0.019
C60FHF		-6.191	-3.691	-0.103
PCBM		-5.942	-3.456	0.132

Reactions of fullerene and SF$_5$CF$_2$CF$_2$I

C$_{60}$ powder (18.7 mg, 0.026 mmol) was mixed with *ortho*-dichlorobenzene (*o*-DCB, 3 mL) in a 10-mL Schlenk flask equipped with a PTFE-protected high vacuum valve and a magnetic stirring bar. The flask was placed in ultrasonic water bath for 1 h, and then the mixture was stirred overnight to form a homogeneous solution. To the liquid obtained, 4 equiv of SF$_5$CF$_2$CF$_2$I (16.6 μL, 0.104 mmol) was added via a micro syringe, then 1.85 g copper powder was carefully transferred into the flask, and the mixture was diluted with another 3 mL of *o*-DCB. The Schlenk flask was connected to a vacuum line to remove air, and then the reaction vessel was placed in oil bath that had been preheated to the desired temperature. The color of solution changed from violet to deep brown during the period of heating. After 72 h, the reaction flask was cooled with cold water and then stored in a refrigerator overnight. The reaction mixture was then filtered, and the resulting solid residue was washed with *o*-DCB. A deeply brown-colored crude compound was collected after removing the solvent via high vacuum at 55 °C.

In the reaction carried out at 145 °C, the amount of the unreacted reagent of SF$_5$CF$_2$CF$_2$I was estimated as 16%, according to the ^{19}F NMR spectrum (with C$_6$H$_5$CF$_3$ as internal standard) of the crude product. ^{19}F NMR (crude product, 300 K, toluene-D$_8$, 282.40 MHz): δ 66 (bs, 1F,), 45 (dm, 4F), –88 (bm, 2F), –107 to –111 (m, 2F).

before heating　　　　**after heating**

Figure S3-1. Reaction mixture before and after heating the mixture of fullerene extract, $SF_5CF_2CF_2I$, and Cu powder in o-DCB.
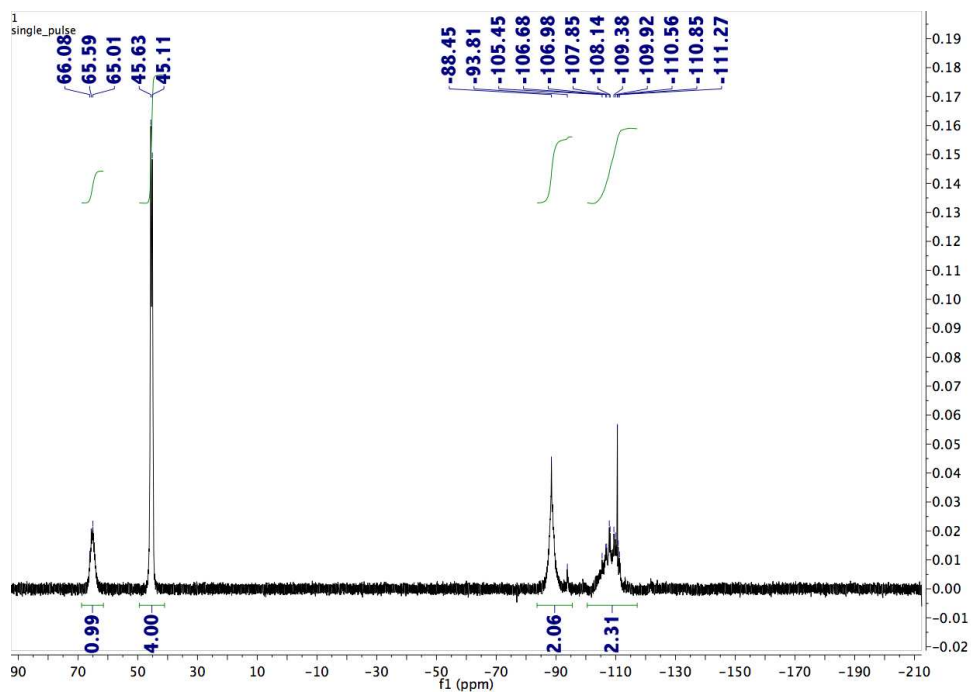
Figure S3-2. ^{19}F NMR spectrum of the crude product of the reaction of SF$_5$CF$_2$CF$_2$I and fullerene extract at 145 °C.
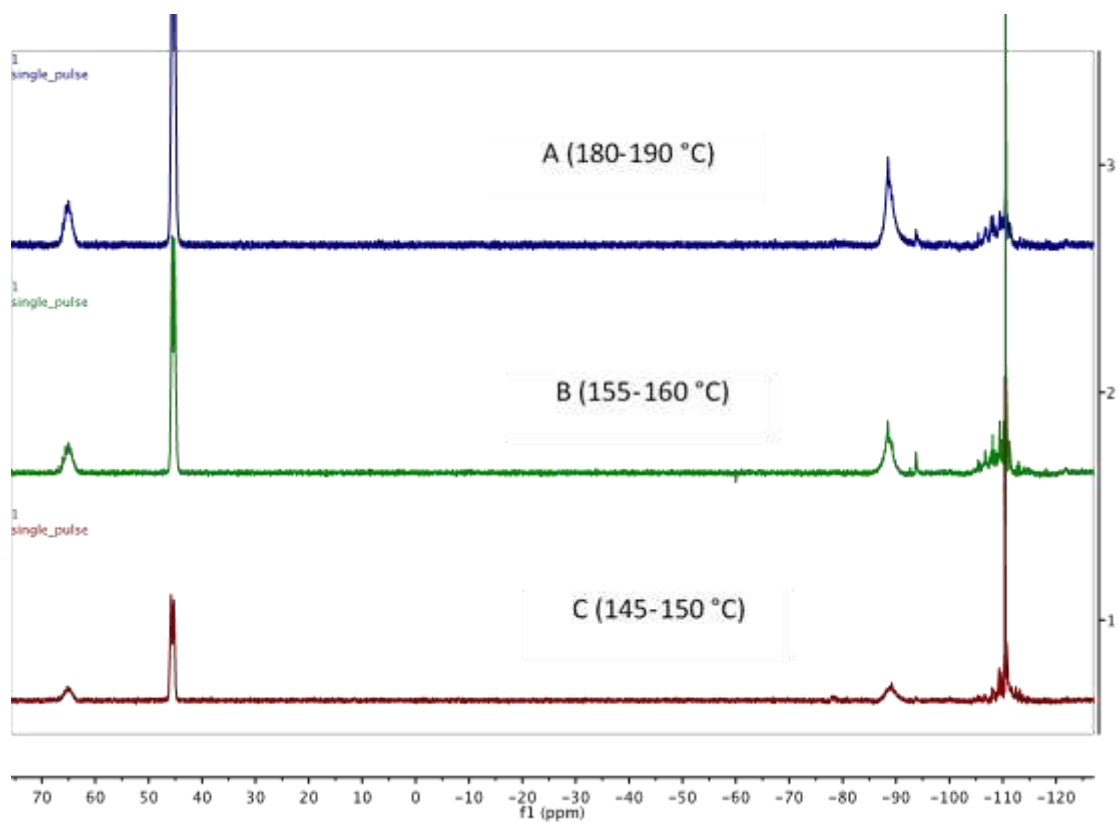
Figure S3-3. Effect of reaction temperature on the product distribution in the reaction of $SF_5CF_2CF_2I$ with C_{60}/C_{70}. Note increase in the relative intensities of the signals due to fullerene derivatives $C_{60}(CF_2)_n$ (resonances at –90 and –110 ppm), indicative of the lower stability of $C_{60}(SF_5CF_2CF_2)_n$ compounds at higher temperature.
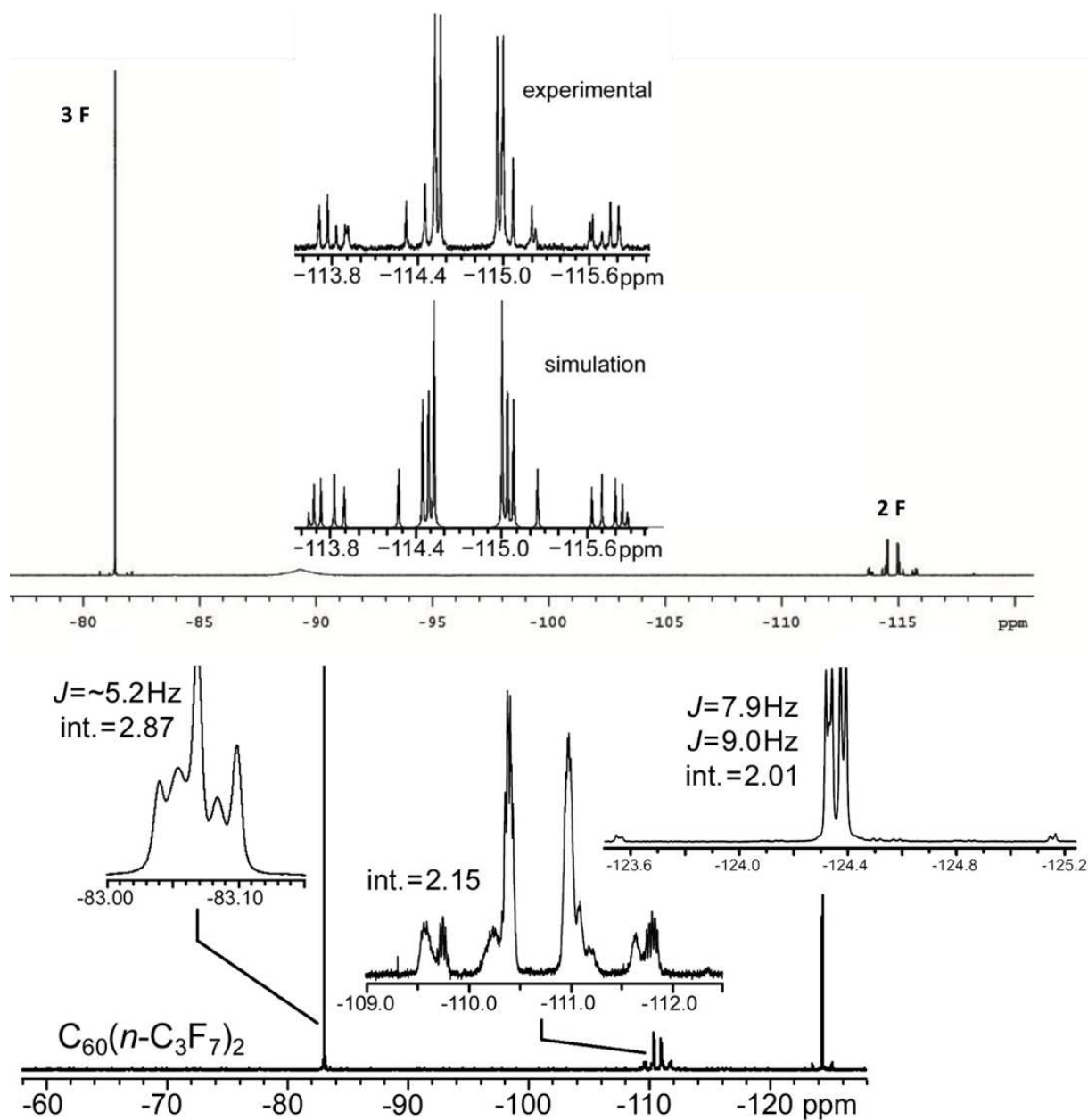
Figure S3-4. (**Top**): Full-range ^{19}F NMR spectrum of *para*-$C_{60}(C_2F_5)_2$. Inset: expansion of the CF_2 region of the ^{19}F NMR spectrum of *para*-$C_{60}(C_2F_5)_2$ (**Top**) and a spin simulation of the AA'BB' pattern of the spin ½ nuclei (**Bottom**). The spin simulation was performed using SpinNMR software (original DOS version). (**Bottom**) ^{19}F NMR spectrum of 1,7-$C_{60}(n$-$C_3F_7)_2$. Data are taken from the Supporting Information of the 2012 paper by Dr. Kuvychko et. al.[1]
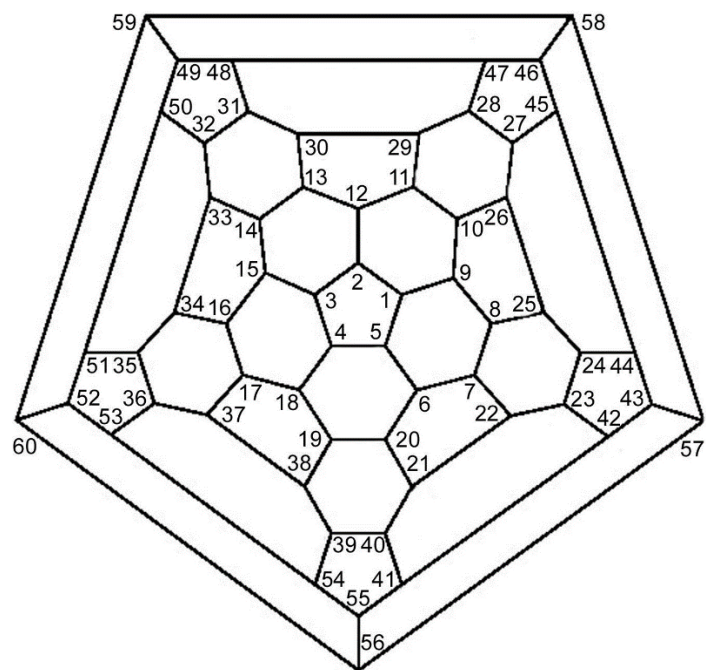
Figure S3-5. Schlegel diagram of C_{60} with IUPAC numbering.

Reaction of C$_{60}$/C$_{70}$ fullerene substrate with SF$_5$CF$_2$I

A quantity of fullerene substrate powder (0.02 g) was mixed with 1.9 g of Cu and then *o*-DCB (5 mL) in a 10-mL Schlenk flask equipped with a PTFE-protected high-vacuum valve and a magnetic stirring bar. The mixture was stirred for 3 hours at room temperature, and SF$_5$CF$_2$I (0.2 g) was added. The reaction flask was connected to a vacuum line, frozen with liquid nitrogen and evacuated. Then, the flask was placed in oil bath and the reaction mixture was stirred at 150–155 ℃ for 76 hours. After that the reaction mixture was kept at room temperature for three days, it was then filtered. The resulting solid residue was washed with *o*-DCB and acetone. The solvent was distilled off on a vacuum line, initially at room temperature and then with heating of the sample in oil bath at 95–100 ℃.

The ^{19}F NMR spectrum of the reaction mixture prior to solvent removal contained two dominant peaks around –62 ppm that could tentatively be assigned to trifluoromethyl derivatives of aromatic solvent. The ^{19}F NMR spectrum after solvent removal (Figure S3-4) contained the same peaks due to residual solvent, but only in small amounts. Two groups of broad peaks characteristic of the two types of fluorine atoms of the SF$_5$ group, in the 1:4 ratio, were present at 68 and 44 ppm, respectively. The resonances in the –60 to –70 ppm region are characteristic of fluorine atoms of CF$_3$ groups in trifluoromethylfullerenes. A group of poorly resolved peaks in the –105 to –110 ppm region are likely due to the fluorine atoms of the CF$_2$ group in the SF$_5$CF$_2$ moiety.
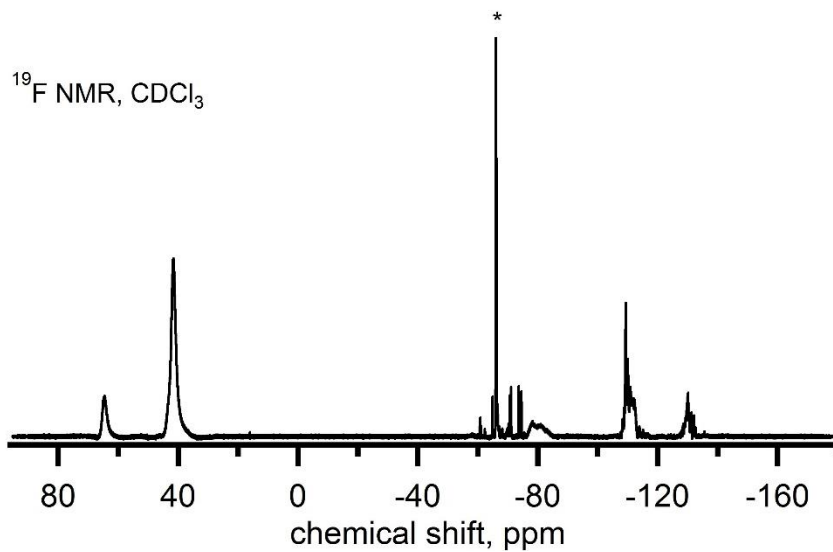
Figure S3-6. ^{19}F NMR spectrum of the crude product of the reaction of SF_5CF_2I and fullerene extract at 150–155 °C. The * denotes the reference, PTFMB ($\delta = -67.9$).
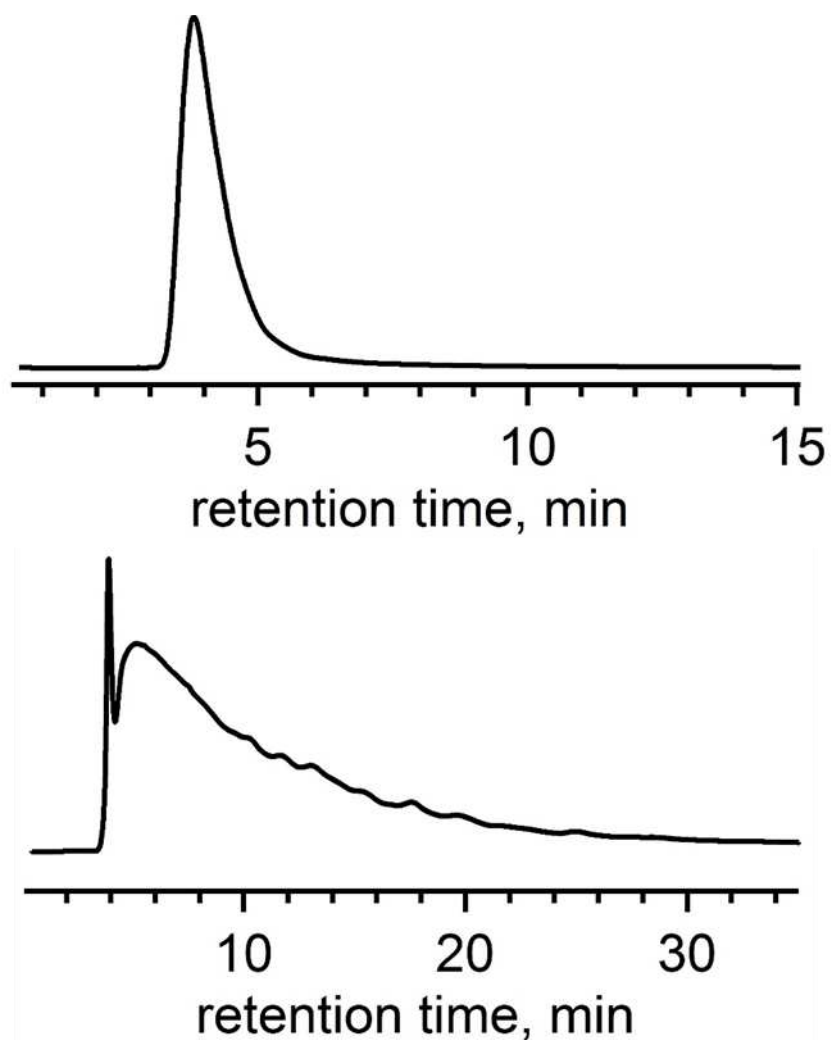
Figure S3-7. HPLC chromatogram of the crude product of the reaction of SF_5CF_2I and fullerene extract at 150–155 °C. Top: recorded in 100% toluene eluent; bottom: recorded in 20/80 v/v toluene/heptane. Note absence of resolved peaks in both traces, which is indicative of presence of many compounds with similar properties.
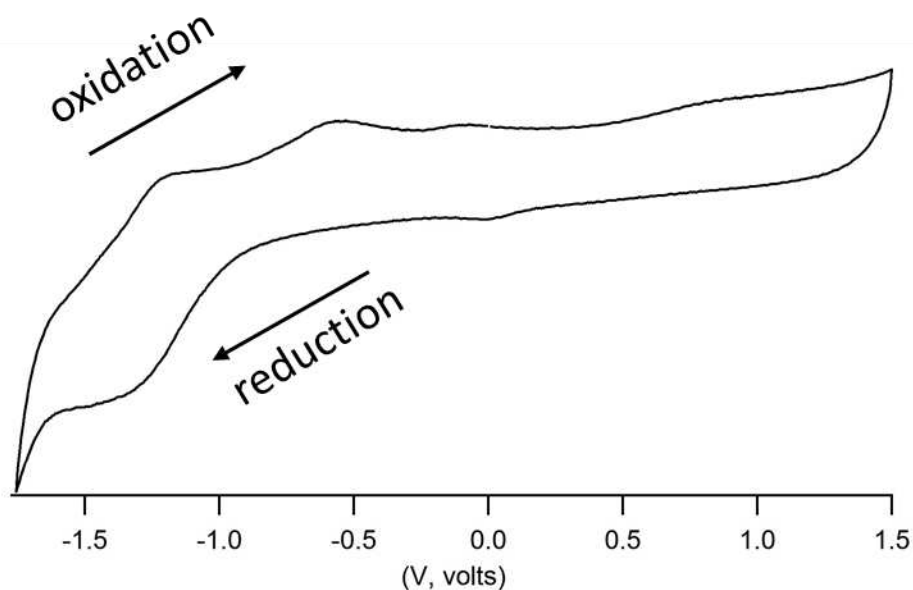
Figure S3-8. The cyclic voltammogram of 1,7-$C_{60}(SF_5CF_2CF_2)_2$ showing irreversible electrochemical behavior. Cyclic voltammograms were recorded in an inert atmosphere using PAR 263 potentiostat/galvanostat. 2 mM *o*-DCB solutions of the 1,7-$C_{60}(SF_5CF_2CF_2)_2$ fullerene with 0.1 M N(*n*-butyl)$_4$Cl as the electrolyte were prepared. The electrochemical cell used was equipped with 0.125 mm diameter platinum working and counter electrodes and a 0.5 mm diameter silver reference electrode. The scan rate was 100 mV s^{-1}. Experiments were performed at 500 mV s^{-1} as well but did not show improved electrochemical behavior. Attempts to use ferrocene as an internal standard resulted in degradation of the ferrocene redox event and a loss of reversible behavior. The above voltammogram shows the initial reduction of the fullerene but due to the broadness of the reduction event it was concluded that this reduction was not chemically stable and resulted in a multitude of reduction products. This is further supported by the non-reversible nature of the following oxidation events.
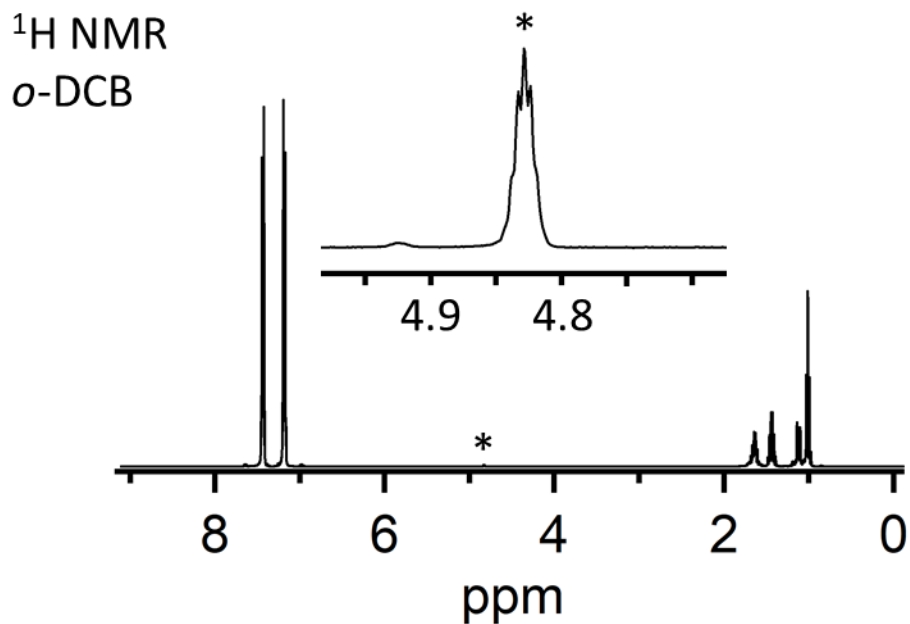
Figure S3-9. ^{1}H NMR of SnH in *o*-DCB with a minimal amount of anhydrous CDCl$_3$ for locking. The residual hydride is only 10% based on the butyl peak area ratio. The hydride signal is denoted with an asterisk.
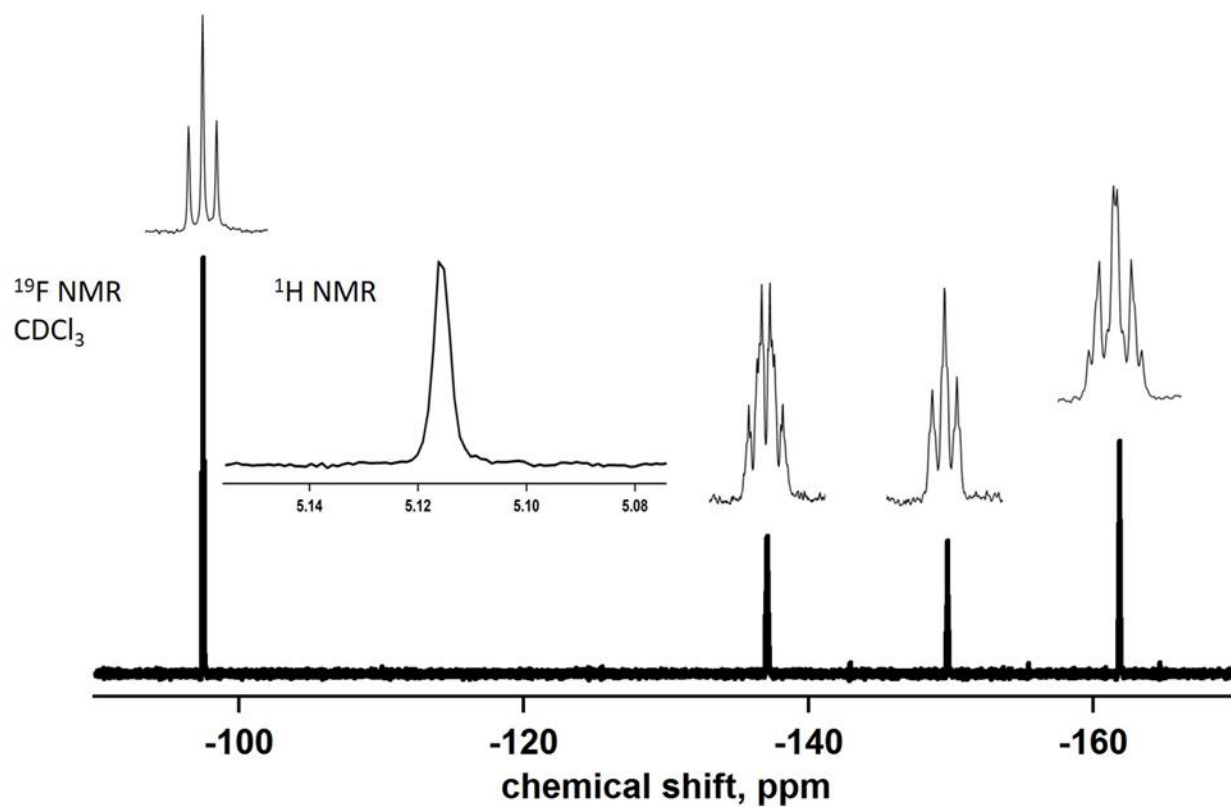
Figure S3-10. NMR spectroscopy of $C_{70}(Bn_F)H$-1. The ^1H NMR signal of the hydrofullerene is shown in the middle inset, δ 5.1. Reference (residual CHCl₃ int. std. (δ = 7.25)). ^{19}F NMR ref (1,4-trifluoromethylbenzene int. std. (δ = −67.9))
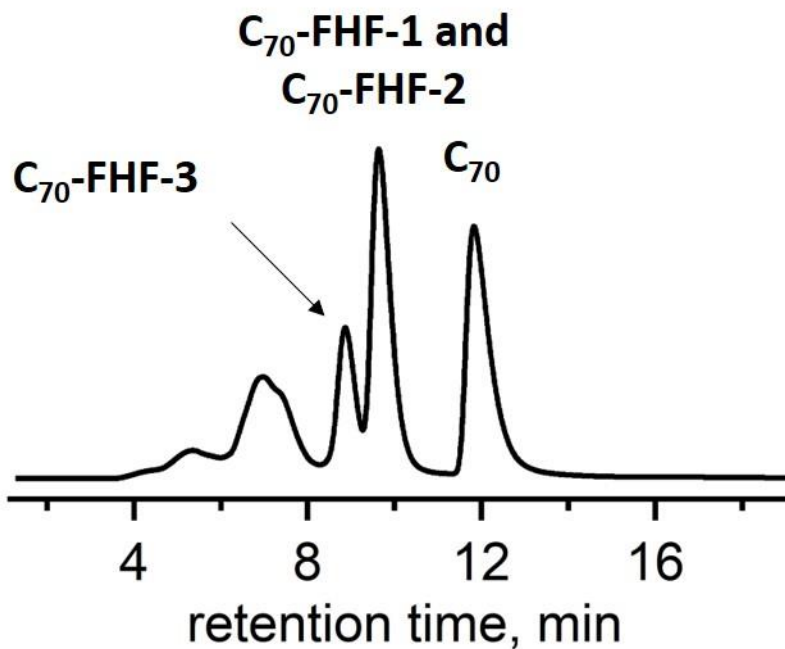
Figure S3-11. HPLC chromatogram of the crude reaction mixture from method 2. Chromatograms were collected at 300 nm using toluene as the eluent with a flow rate of 5 mL min^{-1}. Elution times at 8.4–9.2 and 9.2–10.4 minutes for C_{70}FHF-3 and the mixture of C_{70}FHF-1 and 2 isomers respectively. The unreacted C_{70} was collected for future use. Ratio of C_{70}FHF-3 to the mixture of C_{70}FHF-1 and 2 isomers was approximately 1:2.
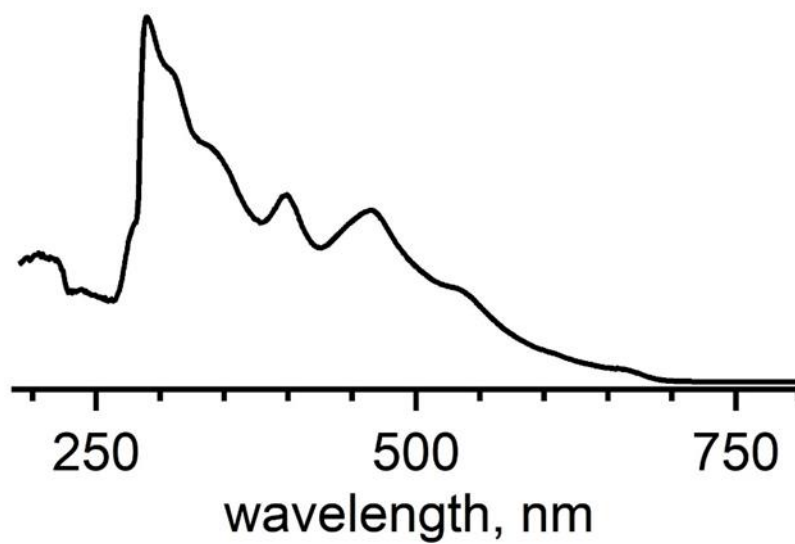
Figure S3-12. UV-vis spectrum of the C$_{70}$FHF-1 and C$_{70}$FHF-2 recorded in toluene.
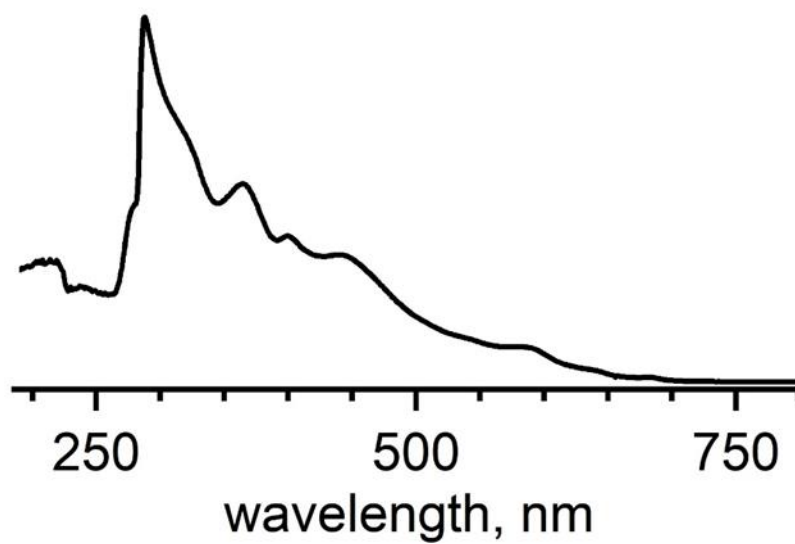
Figure S3-13. UV-vis spectrum of the $C_{70}FHF$-3 recorded in toluene.
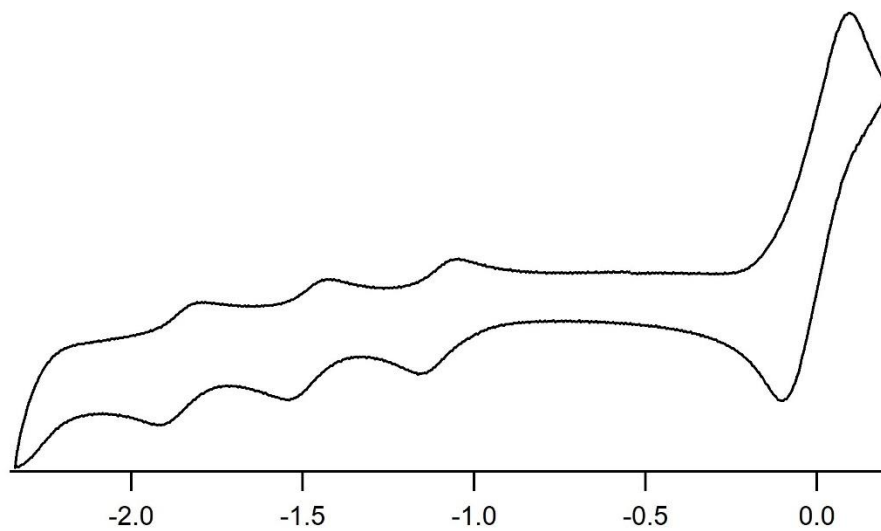
Figure S3-14. The cyclic voltammogram of $C_{70}FHF$-1 and 2 mixture versus ferrocene recorded in 0.1 M TBABF$_4$ o-DCB solution with a cycle rate of 250 mV s^{-1}. $E_{1/2}$ (1st red.) vs Ferrocene -1.11 V
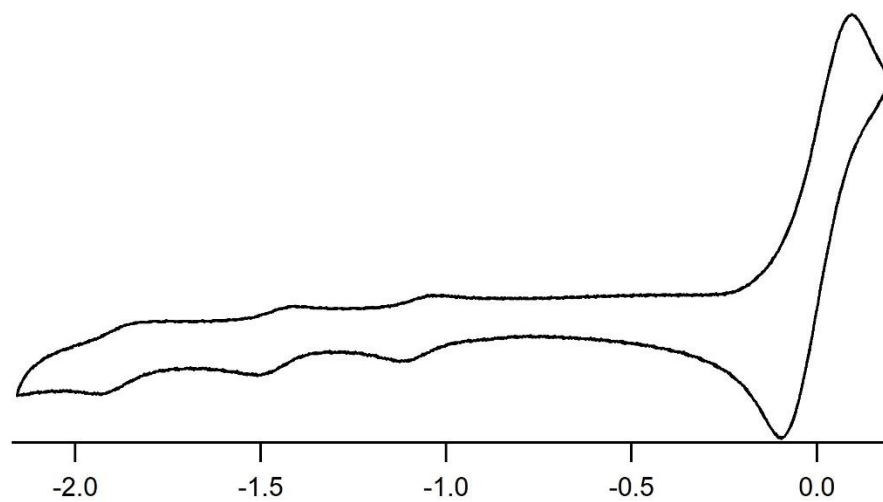
Figure S3-15. The cyclic voltammogram of $C_{70}FHF$-3 versus ferrocene recorded in 0.1 M TBABF$_4$ o-DCB solution with a cycle rate of 250 mV s^{-1}. $E_{1/2}$ (1st red.) vs Ferrocene -1.09 V
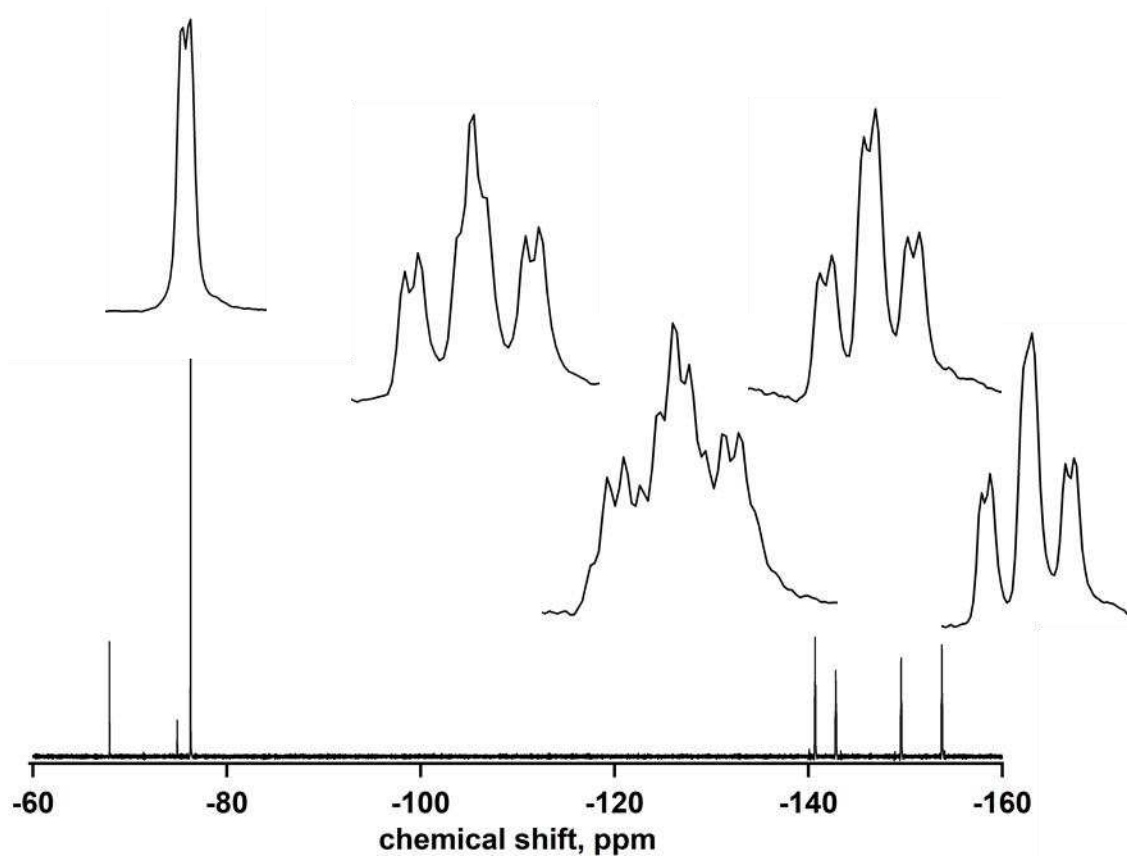
Figure S3-16. ^{19}F NMR of isolated $C_{70}FHF$-1. Synthesized directly by method 1 using proton sponge as an organic base. (1,4-trifluoromethylbenzene int. std. (δ −67.9)) Solvent 60/40 $CS_2/CDCl_3$.
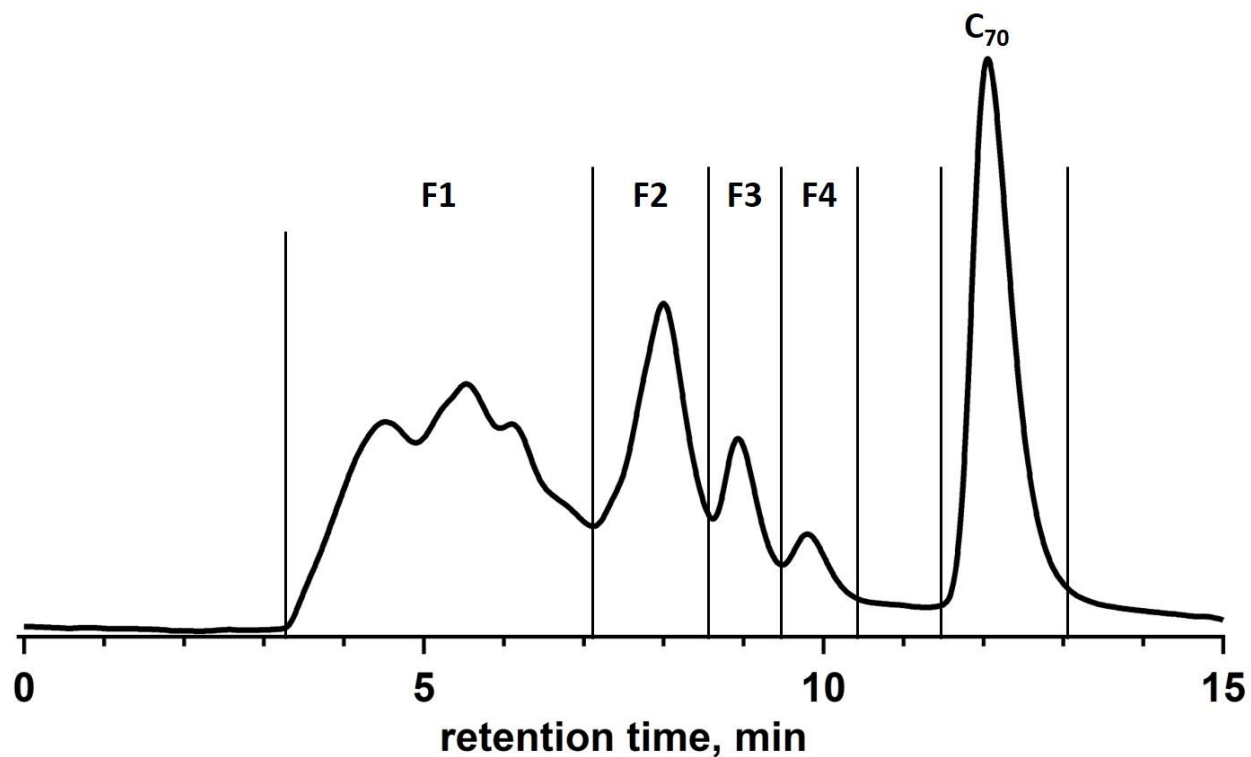
Figure S3-17. HPLC chromatogram from step one of method 1. F1 fraction contains multiple perfluorobenzyl-C_{70} products and possibly other hydrofullerenes. F2 fraction contains a mixture of the $C_{70}FHF$-3 and at least three hydrofullerenes. F3 is a mostly pure fraction containing $C_{70}(Bn_F)H$-1 and a small amount of C_{70}-FHF-3. F4 contains a small amount of $C_{70}FHF$-1 and $C_{70}FHF$-2. Final peak was identified as C_{70}. Separated in 100% toluene at 5 mL min^{-1}, 370 nm.
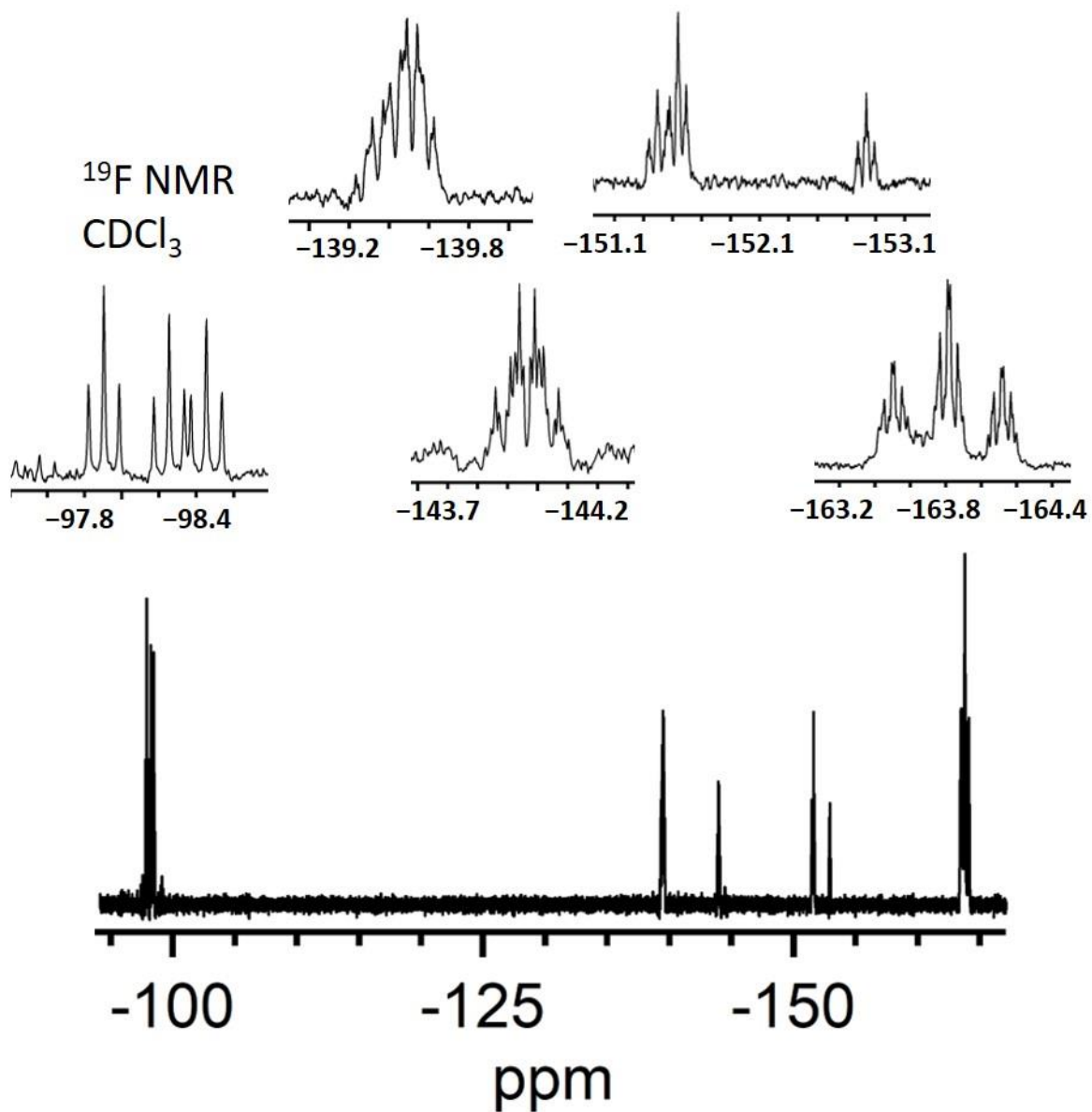
Figure S3-18. ^{19}F NMR for the F2 fraction from method 1. At least three hydrofullerenes are present in the fraction. (1,4-trifluoromethylbenzene int. std. (δ −67.9)) Solvent CDCl$_3$.

420
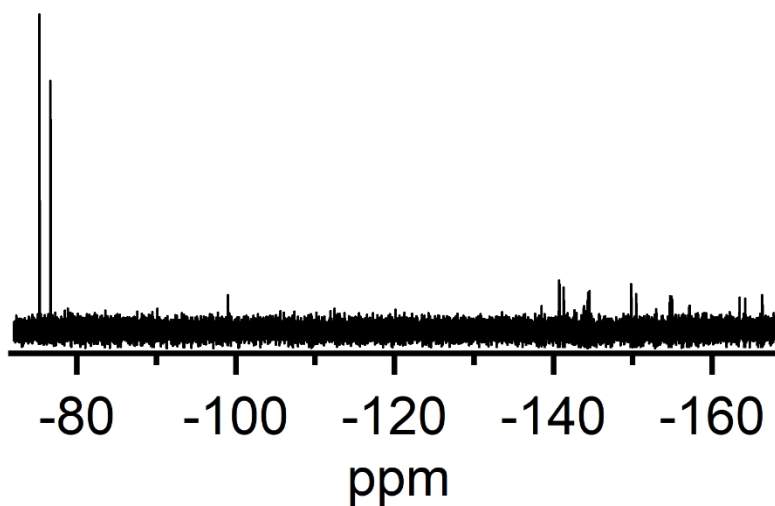
Figure S3-19. ^{19}F NMR of the F4 fraction from method 1. The two compounds present are C$_{70}$FHF-1 and 2 based on the chemical shifts. The ratio between the two compounds is approximately 1:1 based on the ratio of the integrals of the CF$_2$ fluorines. (1,4-trifluoromethylbenzene int. std. (δ −67.9)) Solvent CDCl$_3$.
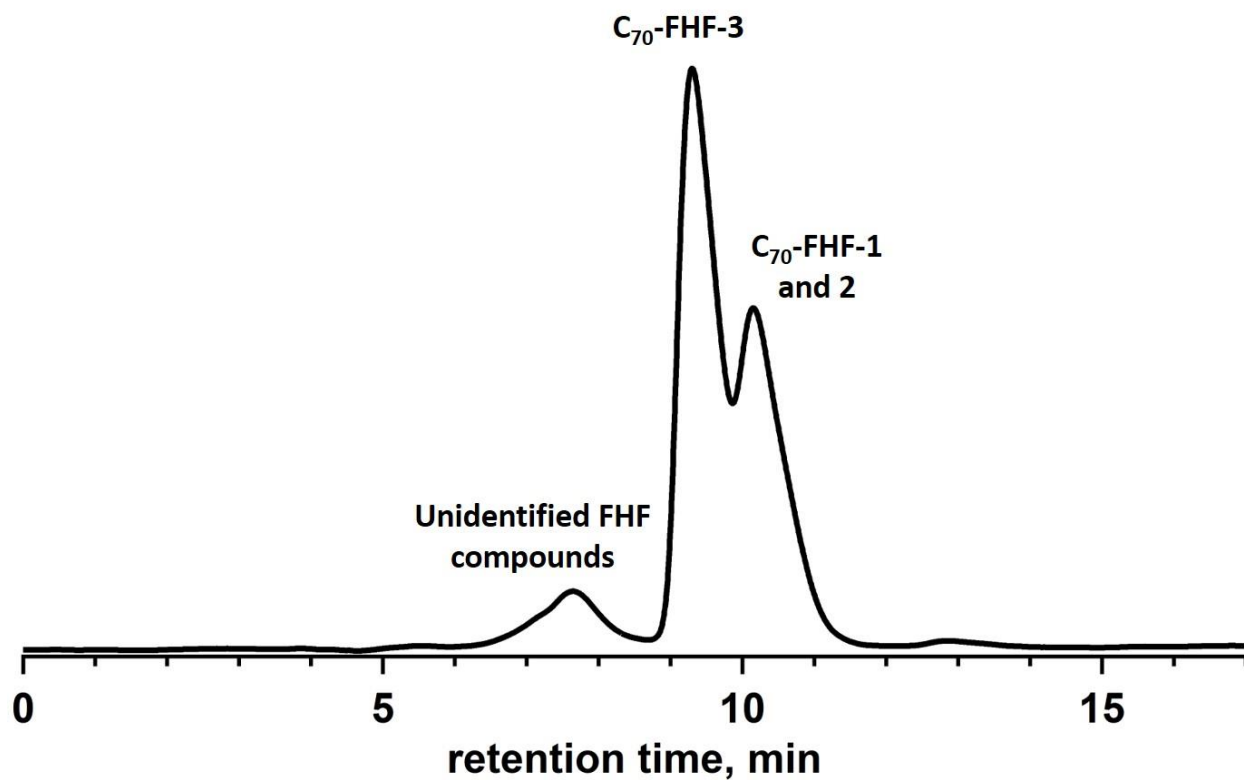
Figure S3-20. HPLC chromatogram of the crude material from the reaction of F2 from method 1 with proton sponge. Toluene used as the eluent on buckyprep semiprep stationary phase. Flow rate 5 mL min^{-1}, 300 nm. F2F1 fraction t_R = 5–9 min, F2F2 fraction t_R = 9–9.8 min, and F2F3fraction t_R = 10–11.5 min.
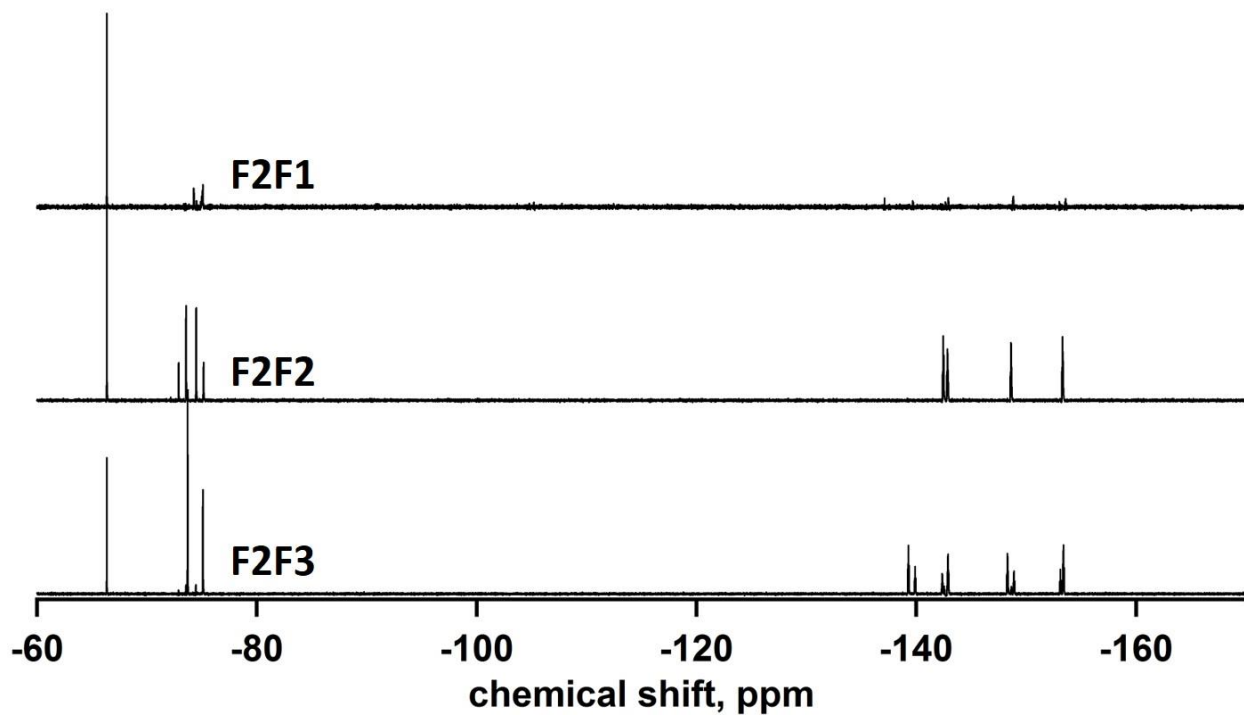
Figure S3-21. ^{19}F NMR spectra of the three fractions collected from the reaction of F2 from method 1 with proton sponge. The separation of these compounds is shown in S-13. F2F1 shows a mixture of unidentified FHF compounds. F2F2 is predominantly C_{70}FHF-3. F2F3 is a mixture of C_{70}FHF-1 and 2. (1,4-trifluoromethylbenzene int. std. (δ −67.9)) Solvent 60/40 CS_2/CDCl$_3$.
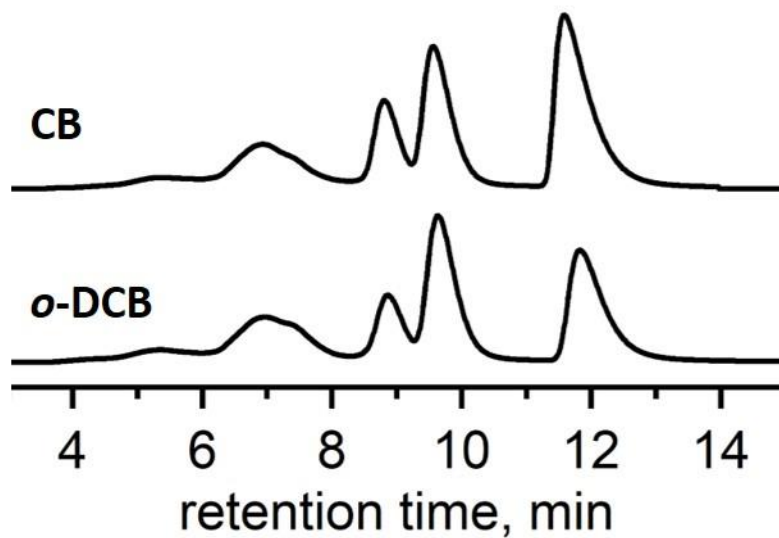
Figure S3-22. Comparison of the effect of changing solvent on product distribution using method 2. (**Top**) HPLC chromatogram of a crude product mixture from a method 2 reaction using chlorobenzene as the solvent. (**Bottom**) HPLC chromatogram of a crude product mixture from a method 2 reaction using *o*-DCB as the solvent. Both reactions were performed at 145 °C to control for temperature.
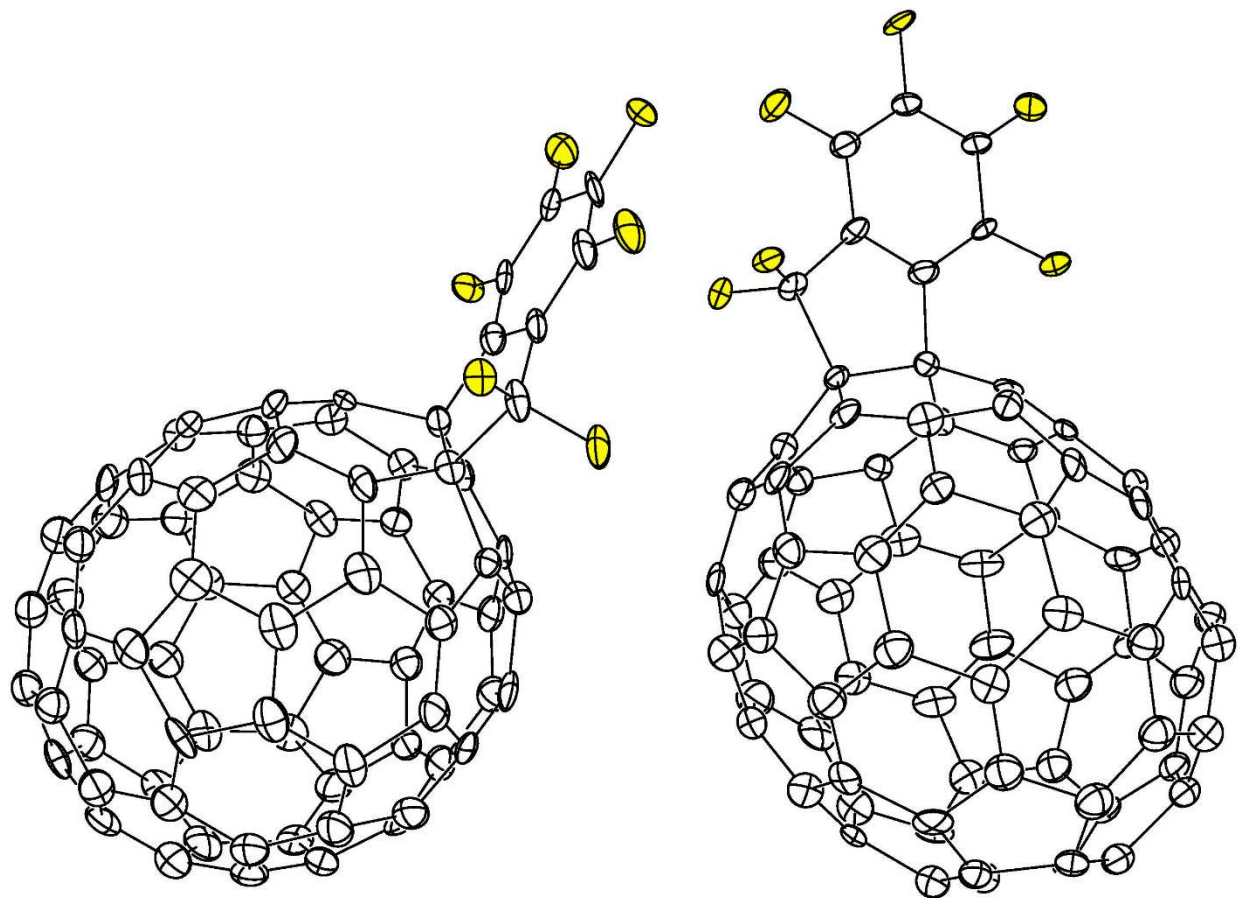
Figure S3-23. Drawings of the two independent molecules in the structure of 25,8-$C_{70}(CF_2(2'\text{-}C_6F_4))\cdot0.5$ CS_2 (50% probability ellipsoids).
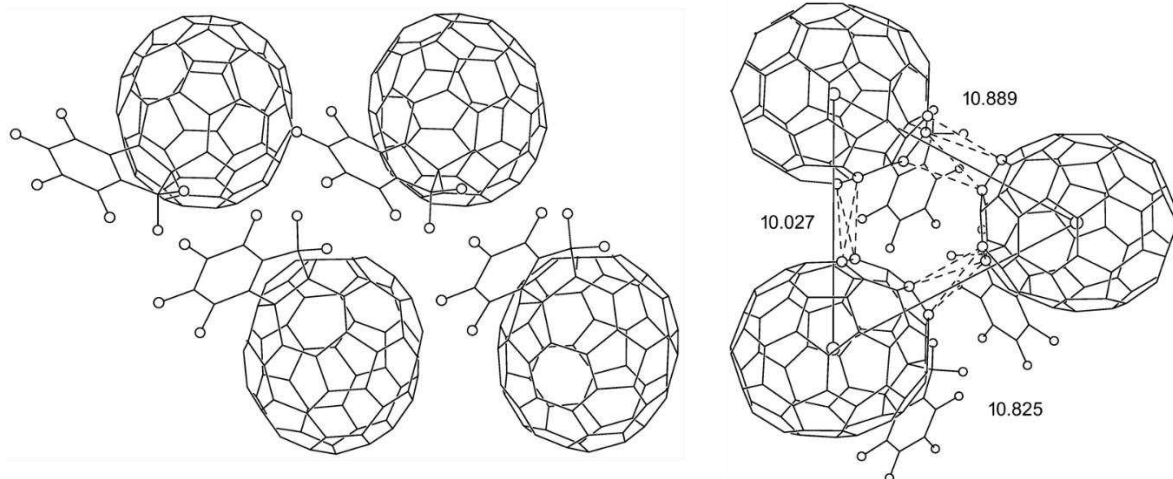
Figure S3-24. Two views of the packing of $C_{70}FHF$-1 molecules within the planar hexagonal arrays (see Figure 3-17 and 3-18 in the main text).
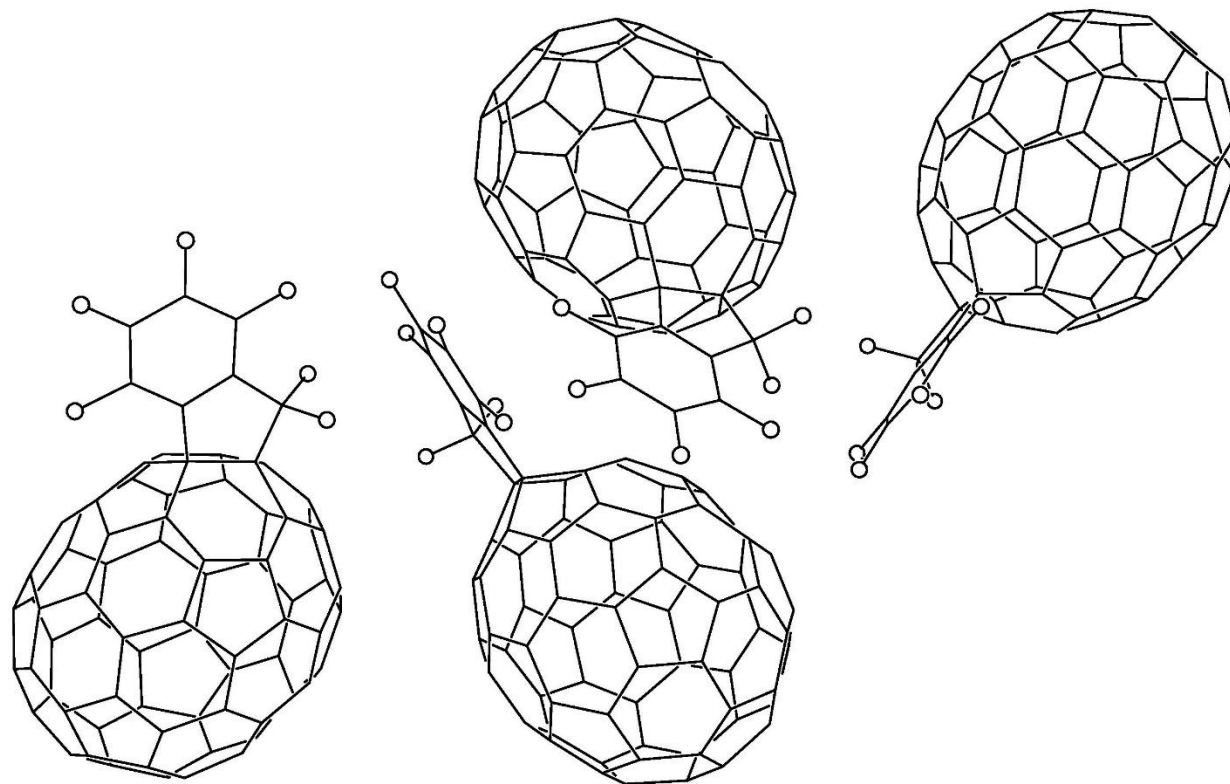
Figure S3-25. The packing of C$_{70}$FHF-1 molecules on either side of the layer of fluorous faux hawk substituents.
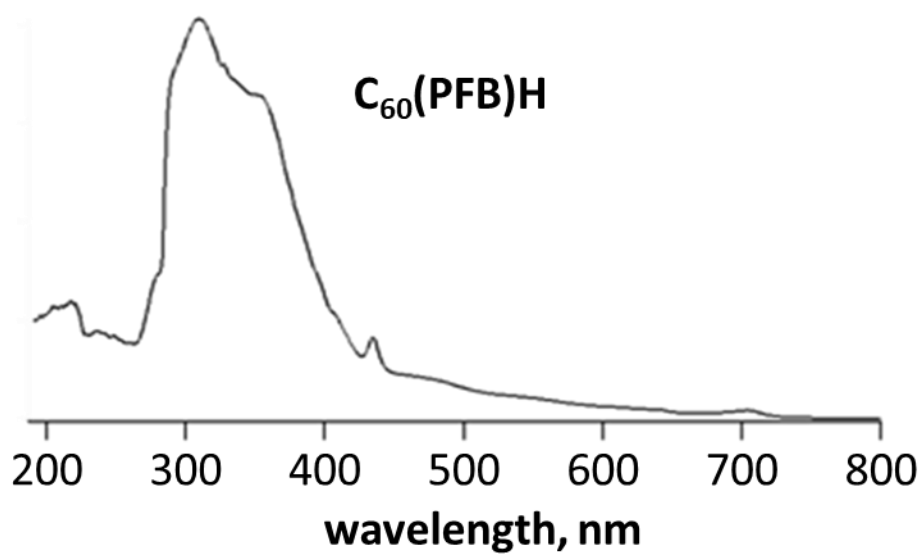
Figure S3-26. UV-vis spectrum of $C_{60}(PFB)H$ recorded in toluene.
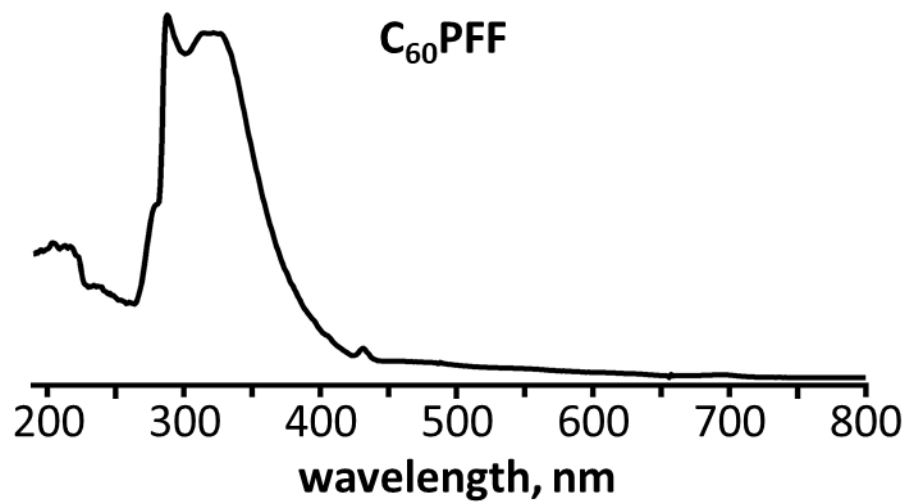
Figure S3-27. UV-vis spectrum of C_{60}PFF recorded in toluene.
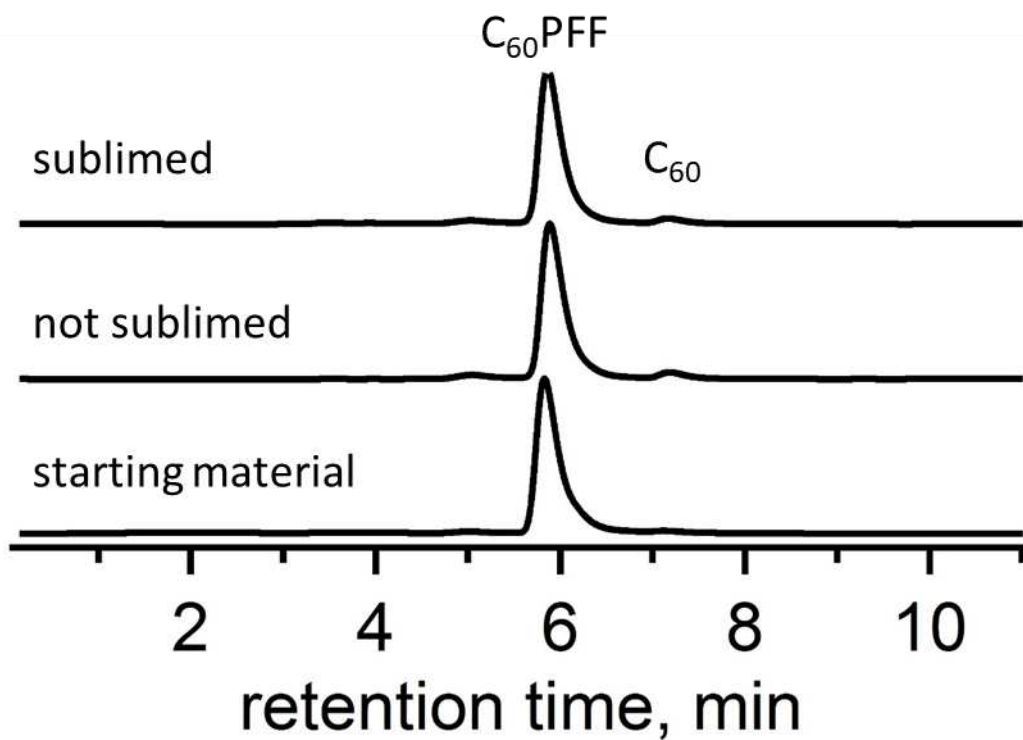
Figure S3-28. HPLC chromatograms showing $C_{60}PFF$ is stable to sublimation. Stationary phase is Cosmosil Bucky-M semi-preparative column, eluent is 100% toluene, and excitation wavelength is 300 nm. Sublimation occurred rapidly at 350 °C. Minimal residue from C_{60} is present in all three traces apparently as contamination from the initial separation.

REFERENCES S3.

1.   Kuvychko, I. V.; Whitaker, J. B.; Larson, B. W.; Folsom, T. C.; Shustova, N. B.; Avdoshenko, S. M.; Chen, Y. S.; Wen, H.; Wang, X. B.; Dunsch, L.; Popov, A. A.; Boltalina, O. V.; Strauss, S. H., Substituent effects in a series of 1,7-C-60(R-F)(2) compounds (R-F = CF3, C2F5, n-C3F7, i-C3F7, n-C4F9, s-C4F9, n-C8F17): electron affinities, reduction potentials and E(LUMO) values are not always correlated. *Chem. Sci.* **2012,** 3, (5), 1399-1407.

APPENDIX C

SUPPLEMENTAL INFORMATION FOR CHAPTER 4

Table S4-1. Comparison of electron mobilities of C_{60} and C_{70} OFET devices.

	$\mu_e\ (\text{cm}^2\,\text{V}^{-1}\text{s}^{-1})\ C_{60}$	$\mu_e\ (\text{cm}^2\,\text{V}^{-1}\text{s}^{-1})\ C_{70}$
pristine[a1]	0.08	2×10^{-3}
PCBM[b2]	0.21	0.1
PCBM[b3]	0.104	0.066
ICMA[c3]	0.04	0.01
BBF[d3]	0.012	0.008

[a] underivatized fullerene
[b] phenyl[fullerene]butyric acid methyl ester
[c] indene[fullerene]mono adduct
[d] 1,7-bis-4-methoxybenzyl fullerene

Figure S4-1. (**Left**) Air-tight vessel for thermal cycling of OPV active layers. The glass tube shows the arrangement of the slides inside the chamber. (**Right**) Low temperature chamber, −78 °C. High temperature chamber, 100 °C, was a lab grade oven.
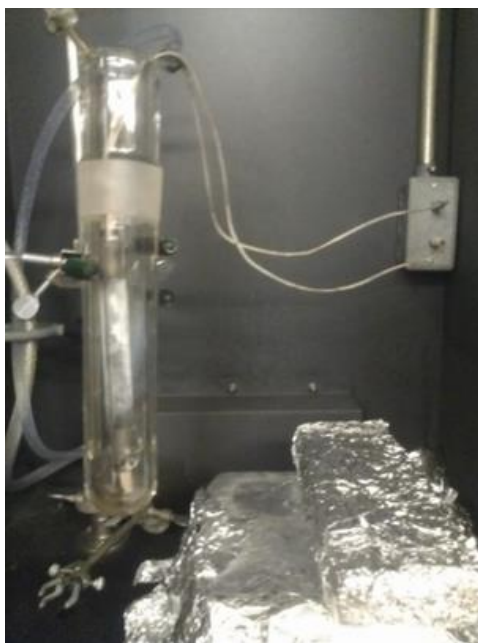
Figure S4-2. 450 W high-pressure mercury-arc lamp for UV radiation exposure tests. The films were placed along the aluminum wrapped lead brick to minimize the variation in exposure based on position for the films.
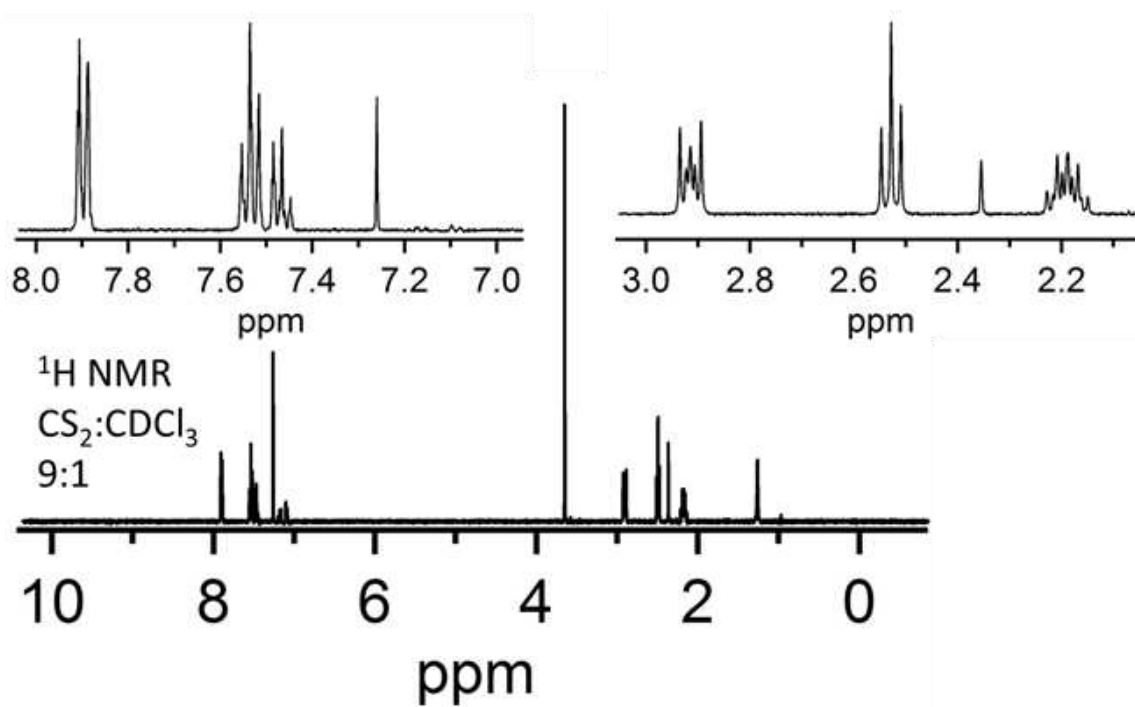
**Figure S4-3.** Proton NMR of PCBM used to make films in a mixture of 9/1 v/v CS$_2$/CDCl$_3$.
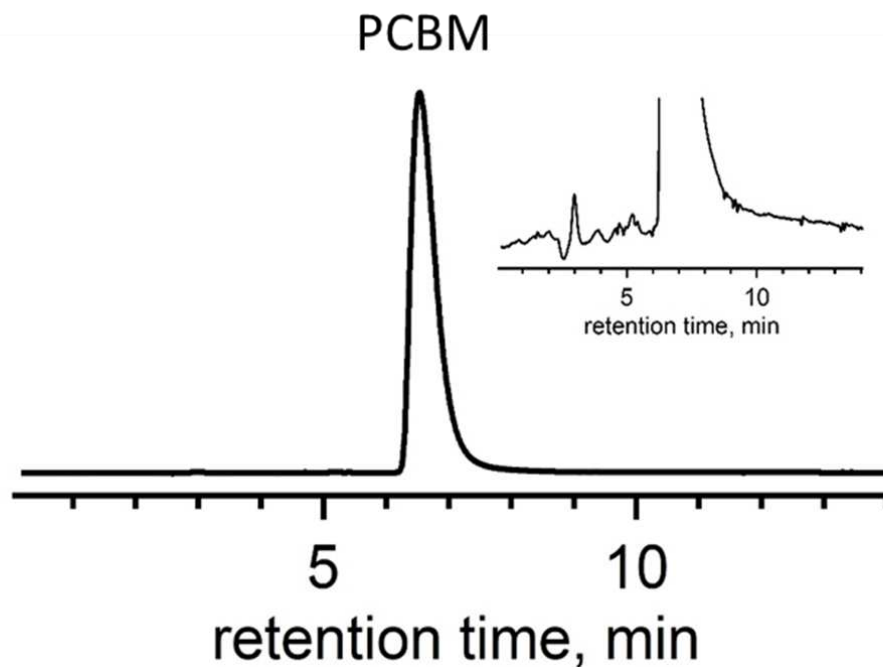
Figure S4-4. HPLC chromatogram of PCBM sample in 100% toluene on the Cosmosil Buckyprep semiprep column at a flow rate of 5 mL min^{-1}. The inset shows a 100× magnification of the chromatogram showing no observable impurities. The peak at 3 minutes is due to residual solvent in the sample.
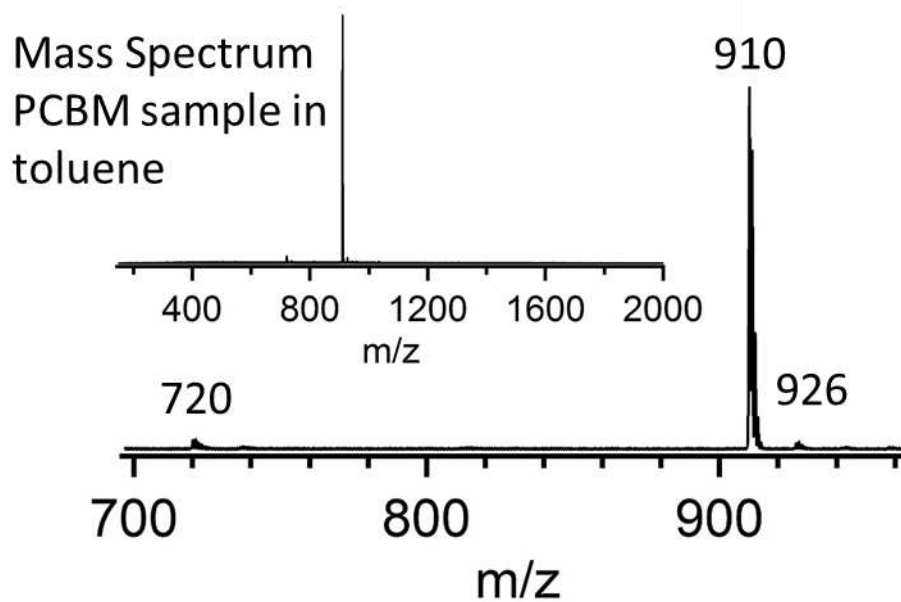
Figure S4-5. Mass spectrum of the PCBM sample in toluene, electrospray ionization source in negative ion mode. In addition to the *m/z* 910 signal for the molecular ion of PCBM, there are detectable signals at m/z 926 and 720 due to oxide of PCBM and parent fullerene, C_{60}, respectively.
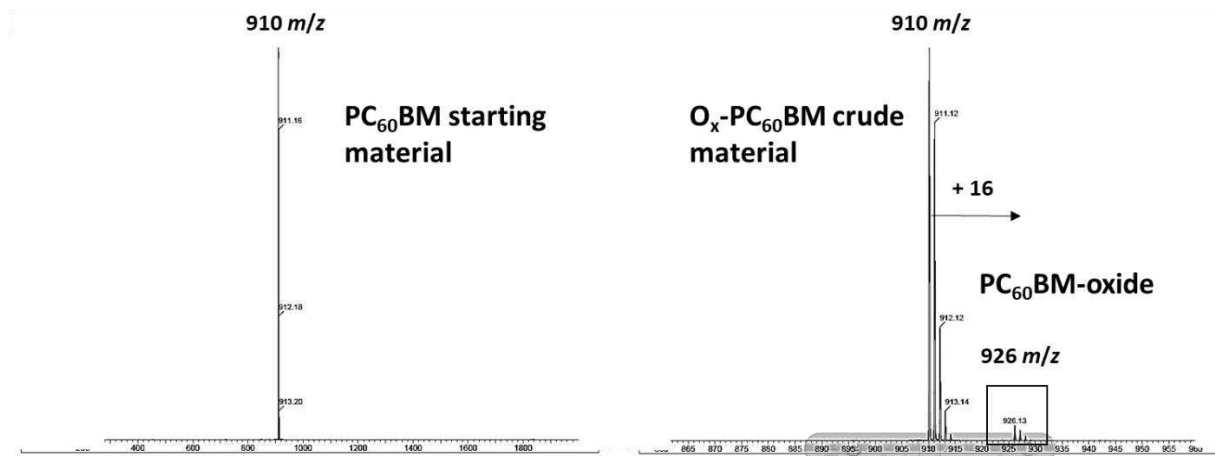
Figure S4-6. Positive-ion field desorption mass spectra related to O_x-PCBM characterization. The mass spectrum (**Left**) shows the PCBM starting material used in the O_x-PCBM synthesis. (**Right**) shows the mass spectrum of the resulting crude mixture, O_x-PCBM.
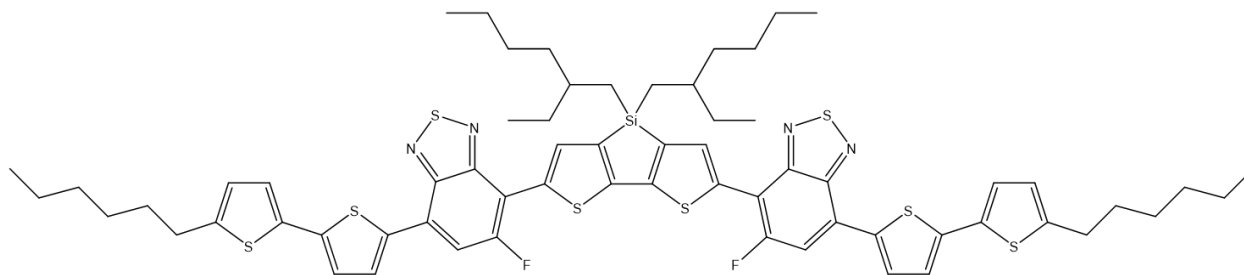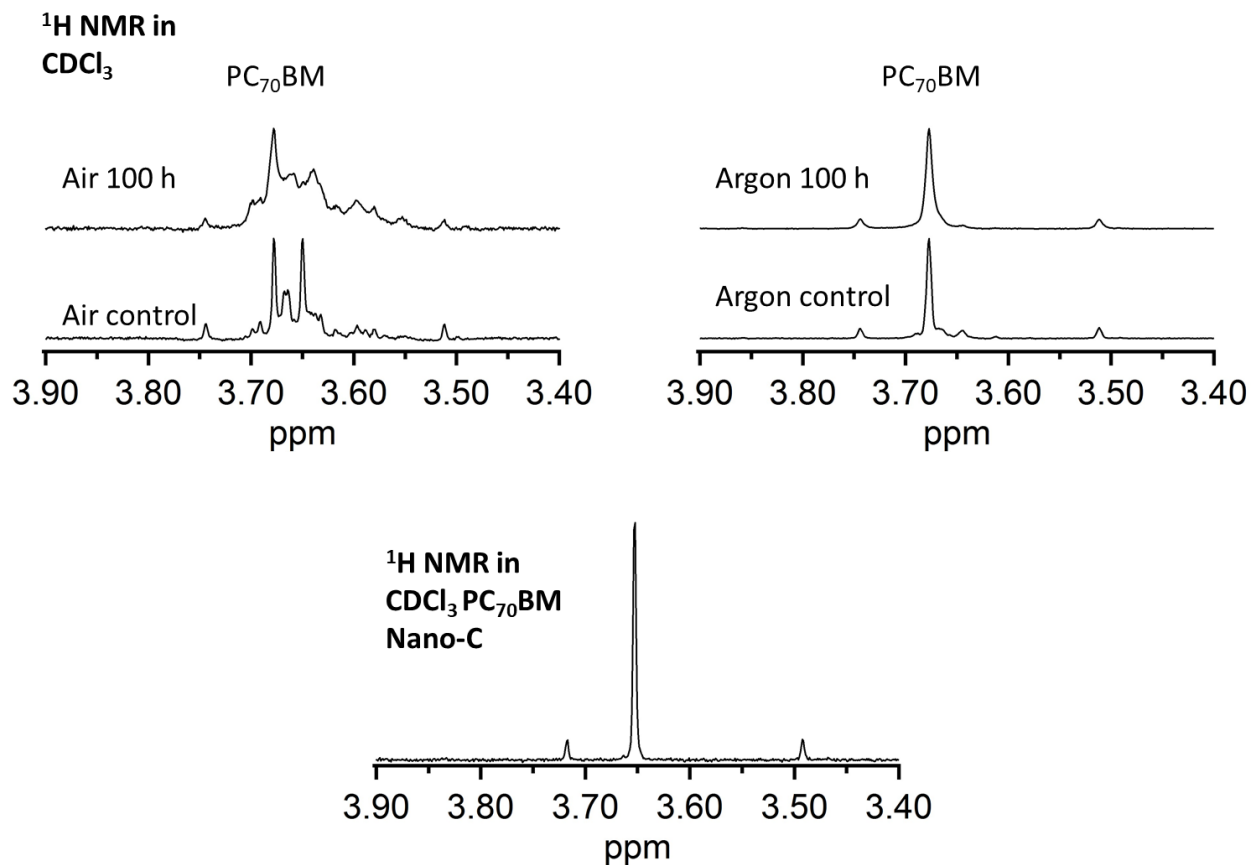
7,7'-(4,4-bis(2-ethylhexyl)-4H-silolo[3,2-b:4,5-b']dithiophene-2,6-diyl)bis(6-fluoro-4-(5'-hexyl-[2,2'-bithiophen]-5-yl)benzo[c][1,2,5]thiadiazole)

Figure S4-7. Molecular structure and IUPAC name for the small molecule donor referred to as monofluoro.
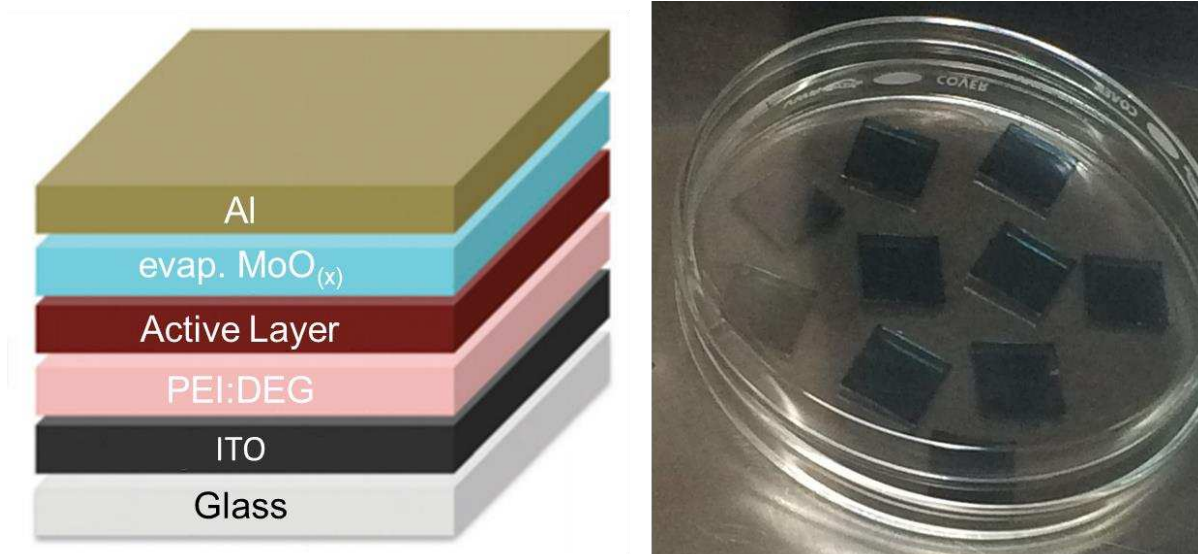
Figure S4-8. (**Left**) Device architecture for SMD/PCBM devices. (**Right**) Mock-up of active layers.

Figure S4-9. Degradation results from PC$_{70}$BM studies. The air exposed films (**Left**) are clearly more severely degraded than the argon films (**Right**). The reference spectrum for PC$_{70}$BM is shown (**Bottom**). The two small singlets at δ 3.7 and 3.5 are due to the two other PC$_{70}$BM isomers which are present as virtually inseparable biproducts in most syntheses of PC$_{70}$BM.
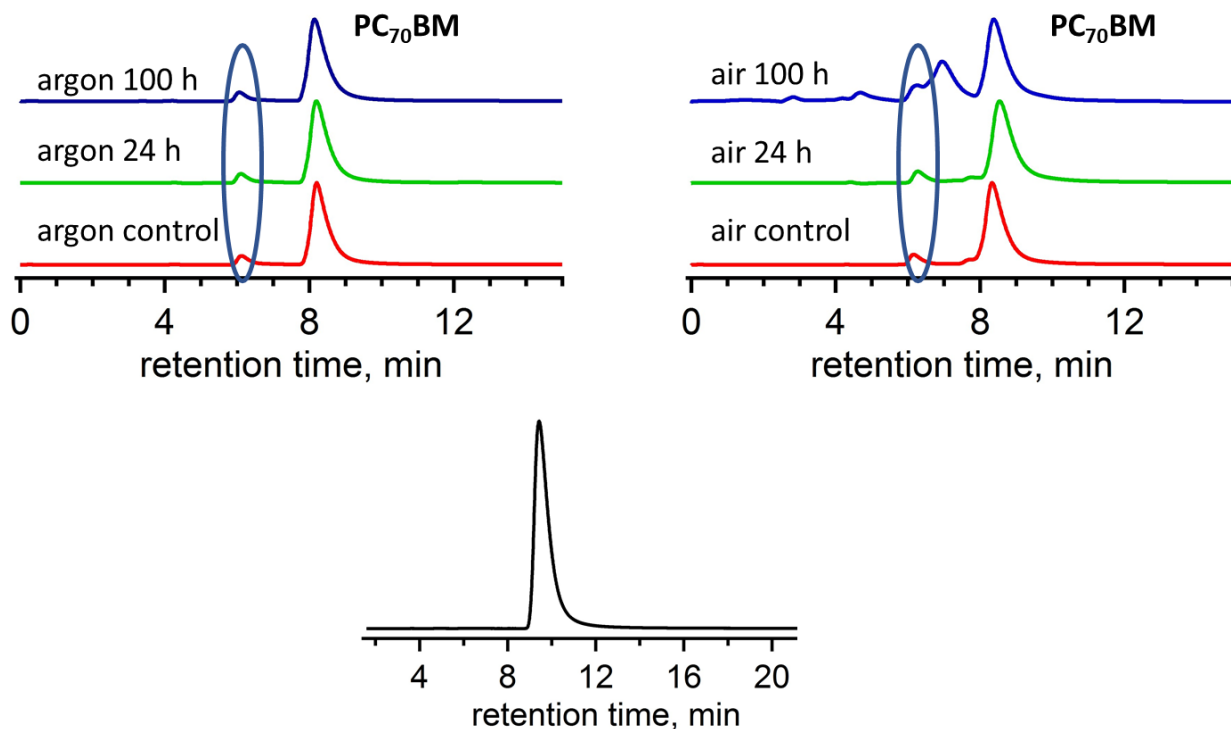
Figure S4-10. HPLC chromatograms showing the results of the degradation studies on PC$_{70}$BM. All separations were performed on a Buckyprep semipreparative column in 100% toluene with a 5 mL min^{-1} flow rate. In both aged samples there is evidence of a new compound which is not present in the reference sample (**Bottom**). Attempts to characterize this fraction were unsuccessful which may mean it is a residual solvent impurity which evaporated over time. Once again, the air aged films (**Left**) are more degraded than the argon aged films (**Right**).
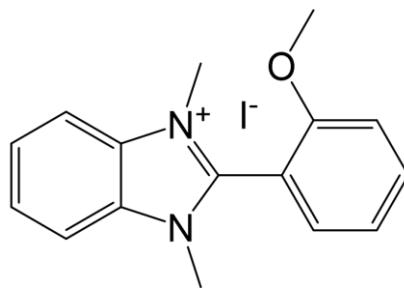
2-(2-Methoxyphenyl)-1,3-dimethyl-1H-benzoimidazol-3-ium iodide

Figure S4-11. Structure and IUPAC name for *o*-MeO-DMBI-I, *n*-type dopant used in contact materials either as a bulk layer or co-deposited with C_{60}.

REFERENCES S4.

1.   Zhang, Y.; Murtaza, I.; Meng, H., Development of fullerenes and their derivatives as semiconductors in field-effect transistors: exploring the molecular design. *J. Mater. Chem. C* **2018,** 6, (14), 3514-3537.

2.   Wöbkenberg, P. H.; Bradley, D. D. C.; Kronholm, D.; Hummelen, J. C.; de Leeuw, D. M.; Cölle, M.; Anthopoulos, T. D., High mobility n-channel organic field-effect transistors based on soluble C60 and C70 fullerene derivatives. *Synthetic Metals* **2008,** 158, (11), 468-472.

3.   Li, C.-Z.; Chueh, C.-C.; Yip, H.-L.; Zou, J.; Chen, W.-C.; Jen, A. K. Y., Evaluation of structure–property relationships of solution-processible fullerene acceptors and their n-channel field-effect transistor performance. *Journal of Materials Chemistry* **2012,** 22, (30), 14976-14981.